University of California
Lawrence Livermore
National Laboratory

UCRL-LR-124998

Volume II: Near-Field and Altered-Zone Environment Report

Chapters 2–11 and Appendix

Dale G. Wilder

August 23, 1996

Volume II:
Near-Field and Altered-Zone Environment Report

Dale G. Wilder
Scientific Editor

August 1996

DISCLAIMER

Prepared by Yucca Mountain Site Characterization Project (YMP) participants as part of the Civilian Radioactive Waste Management Program. The YMP is managed by the Yucca Mountain Site Characterization Project Office of the U.S. Department of Energy, Las Vegas, Nevada.

Contents

Acronyms and Abbreviations

ACD	advanced conceptual design
APD	areal power density
ASTM	American Society for Testing and Materials
bfs	blast furnace slag
BHW	borehole wall
CEC	cation exchange capacity
CHnv	Calico Hills, nonwelded, vitric
CHnz	Calico Hills, nonwelded, zeolitized
DFM	discrete fracture model
DHLW	defense high-level waste
DOE	U.S. Department of Energy
DST	drift scale test
EBS	engineered barrier system
EBSFT	engineered barrier system field tests
ECM	equivalent continuum model
ERT	electrical resistivity tomography
ESF	Exploratory Studies Facility
ESFTT	ESF thermal tests
FMM	fracture-matrix model
GTUF	G-Tunnel Underground Facility
GWTT	groundwater travel time
HLW	high-level waste
LA	license application
LAD	license application design
LBT	large block tests
LLNL	Lawrence Livermore National Laboratory
LSLDT	large-scale long-duration tests
MPBX	multiple borehole extensometer
NF	near field
NFE	near-field environment
NFER	*Near-Field Environment Report*
NTS	Nevada Test Site
NWTRB	Nuclear Waste Technical Review Board
PEBSFT	prototype engineered barrier system field test
PPw	Prow Pass, welded
PTn	Paintbrush, nonwelded
QA	quality assurance
REKA	rapid estimation of K (thermal conductivity) and alpha (diffusivity)
RIB	*Reference Information Base* (DOE, 1990)
RMR	rock-mass rating
RTD	resistance temperature device
SCP	*Site Characterization Plan* (DOE, 1988)
SCPCDR	Site Characterization Plan Conceptual Design Report
SCSSS	Standard Canadian Shield Saline Solution
SEAMIST	Science Engineering Associate Mambrane Insitu Sampling Technology
SEM	scanning electron microscopy
SF	spent fuel
SHT	single-heater tests
SIMS	secondary ion mass spectrometry
SP	spontaneous electrical potentials
TCw	Tiva Canyon, welded
TMHC	thermal-mechanical-hydrological-chemical

Acronyms and Abbreviations (continued)

Tpt	Topopah Spring Member of the Paintbrush tuff
TSw1	Topopah Spring, welded, lithophysae-rich
TSw2	Topopah Spring, welded, lithophysae-poor
TSw3	Topopah Spring, welded, vitric
UNE	underground nuclear explosion
WP	waste package
WPP	*Waste Package Plan* (Harrison-Giesler et al., 1991)
XRD	x-ray diffraction
YM	Yucca Mountain
YMP	Yucca Mountain Site Characterization Project
YMPO	Yucca Mountain Site Characterization Project Office

Contents

Chapter 2.0 Laboratory-Determined Hydrologic Properties and Processes

W. Lin and J. Roberts

Understanding the movement of moisture—including liquid water, steam, and vapor—in the near-field environment (NFE) of the potential nuclear-waste repository at Yucca Mountain, Nevada, is one of the goals of the waste-package environment hydrologic investigations. This chapter discusses how thermal loading resulting from waste package emplacement will affect the preconstruction hydrologic properties and processes of the NFE.

One of the main concerns about the NFE of a nuclear-waste repository is the quantity and quality of water that may be present and that may contact the waste and waste packages (near field) and be in the rock mass surrounding the repository. Water can cause property changes in the altered zone. Processes that may affect the quantity and quality of water are coupled thermal-mechanical-hydrological-chemical (TMHC) processes. The TMHC processes may involve the *in-situ* pore water in the Topopah Spring tuff, water present in fractures, and/or condensate that results from water mobilized by heat, as well as any water introduced (either naturally or artificially) after the emplacement of the wastes. Field and laboratory tests are conducted to enhance our understanding of the coupled TMHC processes and to measure physical properties. The field tests are reported in Chapter 9.0. The laboratory tests of hydrologic properties and processes will be used as input data to model calculations of the coupled TMHC processes, to improve the understanding of the model calculations, to gain insight into physical processes and thus learn under what conditions specific coupled processes become dominant or important, and to help in analyzing the results of the field tests. The laboratory-determined hydrologic properties reported in this document include moisture-retention curves at elevated temperatures, water permeability at elevated temperatures and pressures, electrical resistivity as a function of water saturation at elevated temperatures, and relative humidity as a function of water saturation at elevated

temperatures. The laboratory studies of the thermal-hydrological-chemical processes include fracture flow vs. matrix imbibition at elevated temperatures, fracture healing, and condensation along a fracture. All of the laboratory test results are not qualified, as defined in the quality assurance procedures.

2.1 Laboratory-Determined Hydrologic Properties

The work described here can generally be classified into two different areas with regard to the NFE: (1) preconstruction conditions and processes and (2) the perturbed environment. Preconstruction conditions and processes are those processes that occur prior to any disturbance; that is, they occur naturally.

The perturbed environment is the region that has changed because of some human activity. During the post-emplacement period, the near field may experience at least one dehydration-rehydration cycle. After waste emplacement, the rock in the near field is expected to dehydrate as a result of heating. The rate of dehydration and the movement of moisture in the rock will depend on, among other factors, the initial moisture content in the rock, the geometry and configuration of fractures, and the force of gravity. Later, as the rock temperature decreases below the boiling point of water, rehydration of the near field is expected to occur. The dehydration and rehydration processes and the effect of temperature on the hydrologic properties of tuff are discussed below.

The laboratory work described in the NFER Rev. 0 was divided into these two sections. Because of the increased number of experiments, many of them performed over a range of conditions including ambient condition, it was decided in this report to describe each experiment and the results separately. In addition, in reporting laboratory test results, it is easier to appreciate the effect of temperature on the properties if the results at room temperature and elevated temperatures are presented together. Generally, work performed at near-ambient temperatures (20–25°C) applies to preconstruction conditions, while work at higher temperatures is relevant to the perturbed environment. Obvious exceptions to this are the

measured physical properties at ambient conditions after a cycle of heating, pressure, or fluid flow.

2.1.1 Moisture Retention at Elevated Temperatures

The suction potential of rock determines the imbibition of water in the matrix. That, in turn, affects the relative importance of matrix flow and fracture flow because greater suction potential enhances matrix flow. Moisture content as a function of matric potential (moisture retention curves) of Topopah Spring tuff samples at elevated temperatures was determined using a constant-relative-humidity chamber. The method of measurement was described in Daily and Lin (1991), Roberts and Lin (1995a), and Roberts and Lin (1996a). Some of the test results have been published in Daily and Lin (1991), Roberts and Lin (1995a), and Roberts and Lin (1996a). Daily and Lin (1991) reported results of measurements at 20 and 70°C on Topopah Spring tuff samples from the USW H-1 borehole at a depth range from 333 to 350 m and from outcrops at Fran Ridge, Nevada Test Site. The Topopah Spring tuff samples used in the tests by Roberts and Lin included cores from borehole USW G-4 at a depth of about 360 m (1147 ft) and cores from the Large Block Test. Figures 2-1 to 2-4 show the results of Daily and Lin (1991). As noted on the figures, suction potential is a strong function of saturation below 20–30% saturation but is less dependent on saturation above 30% (varying between 200–400 atm). At near-ambient temperatures the suction potential decreases much more rapidly with increasing saturation during wetting than it does during drying (samples from USW H-1). This difference in behavior between wetting and drying is also seen at elevated temperatures, although the difference is not as pronounced as for ambient temperatures. Figure 2-5 summarizes the results of Roberts and Lin (1995a and 1996a) and shows the moisture retention curves of USW G-4 samples at temperatures of 24.8, 78.4, and 93.6°C for both drying and wetting phases. In this study there was not a consistent difference between wetting and drying curve shape, although there is a difference in the curves for 93.6°C.

Peters et al. (1984) and Klavetter and Peters (1987) used psychrometers to measure the suction potential of both welded and non-welded tuff from Yucca Mountain at

20°C during the dehydration phase. Our data at 20°C are within the spread of corresponding results of Klavetter and Peters, as noted on Fig. 2-3 of NFER Rev. 0.

Results from another experiment using five samples of Grouse Canyon tuff from the G-Tunnel showed that in a 100% relative humidity environment, the suction of water into rock samples is quite different from that in an environment of liquid water, although both have zero water potential (NFER Rev. 0). The samples were placed in a constant-humidity chamber at 100% humidity for more than 917 hours, after which they were removed and submersed in liquid water. Under 100% humidity the suction of moisture was limited to no more than 20% of the sample porosity. Yet, when the samples were removed from the 100% humidity environment and submersed in liquid water, the degree of saturation increased overnight to ~70% of their porosity, and then continued to increase. This implies that in the NFE the moisture-content change in the matrix during the flow of steam or vapor through fractures will be quite different from that of the change during the flow of liquid water, also indicating that after the liquid water has been driven off as a result of thermal loading from waste emplacement, the rock's saturation level will not be elevated to above ~20% until liquid water is able to return to the NFE. During the G-Tunnel field experiments, rehydration took place much more slowly than did dehydration, supporting the observation that saturation levels do not increase without liquid water (Ramirez et al., 1991).

Generally speaking, water saturation at a constant matric potential decreases with increasing temperature. Hysteresis between the drying and wetting phases exists at most of the temperatures. The hysteresis at 78.4°C is much smaller than at other temperatures. For most of the samples the hysteresis is that more moisture is retained in the samples during drying than during wetting. However at 93.6°C the hysteresis was reversed. The explanation for this discrepancy requires further investigation. No process has been identified that can explain smaller hysteresis at 78.4°C than at other temperatures, or explain the hysteresis reversal at 93.6°C. However, in this test the samples were heated from 24.8°C to 93.6°C then cooled to 78.4°C. This heating history may have some effect on the moisture-retention curves.

2.1.2 Water Permeability at Elevated Pressures and Temperatures

Water permeability in Topopah Spring tuff samples as functions of pressure and temperature has been measured to provide input data for model calculations. The techniques used to measure the permeability were described by Lin and Daily (1984). As expected, water permeability in intact Topopah Spring tuff samples was different than in fractured samples; however, it was determined that permeabilities of fractured samples responded to elevated temperature in a fundamentally different way than for unfractured samples (see Section 2.2.3) (Lin and Daily, 1984; Daily et al., 1987; Lin and Daily, 1988; Lin, 1991; Roberts and Lin, 1995b; Lin et al., 1995). The water permeability of intact Topopah Spring tuff samples is reported in this section. The water permeability of fractured tuff samples is reported in Section 2.2.3, "Fracture Healing."

An intact Topopah Spring tuff sample machined from an outcrop at Fran Ridge, Nevada Test Site, was used by Lin and Daily (1984) to measure water permeability at various times during a series of three dehydration and rehydration cycles. The sample was under a constant confining pressure of about 5 MPa, and temperatures up to 140°C. The water permeability of the intact tuff sample was independent of temperature, time, and dehydration and rehydration cycles. At 21°C, before starting the dehydration-rehydration processes, the permeability was 0.34×10^{-18} m^2 (0.34 μD); after the first drying phase, at 98°C, the permeability was 0.32×10^{-18} m^2 (0.32 μD); then at 140°C, also after the first drying phase, the permeability was 0.31×10^{-18} m^2 (0.31 μD); after three drying phases at 98°C the permeability was 0.35×10^{-18} m^2 (0.35 μD). The steam permeability after two drying phases, at 140°C, was 1.99×10^{-18} m^2 (1.99 μD). The greater steam permeability may be a result of the effect of gas flow on permeability, as normally seen in gas permeability measurements due to the Klinkenberg effect. Recently, water permeability of an intact core from the Large Block Test was measured by Lin and Roberts. The results are shown in Table 2-1. The water permeability of the intact tuff sample is again independent of temperature and ranges from 0.09 to 0.67×10^{-18} m^2 (0.09 to 0.67 μD). For

comparison, Ramirez et al. (1991) reported water permeability, at 20°C, of intact Grouse Canyon tuff from G-Tunnel, Nevada Test Site, to be about 10^{-18} m^2 (1 μD). Moore et al. (1986) reported that the water permeability of Topopah Spring tuff samples at 20°C ranged from 0.85 to 64 × 10^{-18} m^2 (0.85 to 64 μD). It is not clear if the samples used by Moore et al. were intact or fractured.

2.1.3 Electrical Resistivity as a Function of Water Saturation at Elevated Temperatures

Spatial distribution and temporal variation of moisture content in the rock mass in the repository horizon are among the most important parameters needed to understand the coupled TMHC processes. There are no direct methods for measuring moisture content other than drying and weighing, therefore geophysical methods are required to determine the moisture content in a rock mass. Electrical resistivity tomography (ERT) is one of the few geophysical methods that can effectively determine the distribution of moisture content in a two-dimensional plane and/or a three-dimensional region. ERT determines the distribution of electrical resistivity in an imaging region. Laboratory-determined relationships between electrical resistivity and moisture content over a range of temperatures are required to interpret the ERT results in terms of moisture content. Measuring the electrical resistivity as a function of moisture content at various frequencies can also provide information about the microscopic wetting and drying processes in rocks (Roberts and Lin, 1996b).

Laboratory-determined electrical resistivities of Topopah Spring tuff as a function of water saturation at elevated temperatures have been reported by Roberts and Lin (1994a, 1994b, and 1996b). Topopah Spring tuff samples used in this study were from holes U3hg-1 at 399-m depth, USW GU-3 at 330-m depth, and USW G-4 at 374-m depth. The connected porosity of the samples were 25–28% for U3hg-1, 9–14% for USW G-4, and 9–10% for USW GU-3. The electrical properties measurement techniques were described in Roberts and Lin (1994a and 1994b). Briefly, the two-electrode method was used on thin disc-shaped samples that had sputtered gold electrodes backed by gold foil. Samples were placed in holders to

inhibit the uptake or loss of moisture to the surrounding atmosphere. Water was added to the samples in small increments, and saturations were determined gravimetrically. Electrical resistivity measurements were conducted after each addition of water until a constant value was reached, at which point it was assumed the water was evenly distributed throughout the sample. This redistribution of fluid generally took between 4 and 6 hours but was dependent on saturation and the amount of sample area to which fluid was added. The time-dependent monitoring of samples was discontinued after the length of time for re-equilibration to occur was established, and measurements were made approximately daily (or 4 to 6 times as long as needed for re-equilibration to occur). We used four samples of each rock, each having a different thickness. This was done for several reasons: to check the effect of electrode contact impedance on the measurement (minimal at 1 kHz), to measure heterogeneity (most of the scatter in Figs. 2-6 through 2-9 results from the multiplicity of samples for each rock), and to provide more data points.

Figures 2-6 to 2-8 show the electrical resistivity of these rock samples at room temperature as a function of water saturation. The resistivity measured during the drying process is slightly greater than that measured during the wetting process. For all of these rocks the resistivity is most sensitive to the water saturation when the water saturation is below 20%. The slope of the resistivity vs. saturation trend is related to the connected porosity: the U3hg-1 samples had the steepest slope; the USW G-4 samples had the most gentle slope. Roberts and Lin (1994b) also reported that the electrical resistivity in USW G-4 has only slight anisotropy: that is the rock is slightly less resistive for electrical current that flows along the bedding planes, but the difference in the resistivity is small and most likely will not affect the use of electrical resistivity measurements for determining water saturation in laboratory and field tests.

Figure 2-9 shows the electrical resistivity of samples from USW G-4 as a function of water saturation at various temperatures from 23 to 95°C during wetting. As expected, the resistivity decreases with increasing temperature. The temperature effect is very small when the water saturation is less than 10%. The maximum decrease in resistivity as a result of temperature occurs in the 20–40% saturation

range, when the decrease in resistivity due to increased saturation is also very high. Above 40% saturation the difference due to temperature is greater than the difference due to saturation.

Figure 2-10 shows the resistivity of USW G-4 samples as a function of temperature for 40 and 75% saturation. The individual data points were selected from the total data set for points that ended up having similar saturations. This means that the curve for 40% saturation, for instance, might have data points for different G-4 samples; thus there is some inherent scatter in the data. Despite this, there is a clear trend in the data. Note that the resistivity axis is linear in this case. Resistivity decreases by about a factor of 3 to 4 from 20 to 100°C. The data are described by simple power-law fits of the form $\rho = a(T^{-b})$ where ρ is the resistivity in ohm-m, T is temperature in °C, and a and b are fitting parameters. The fits shown have values of 23920 and 19896 for a and values of 0.9184 and 0.9811 for b for 40 and 75% saturation respectively. These values are relevant only to the specific data set for which they were derived, and we caution that more data points are needed to confirm any systematic relationship.

Based on these results, we conclude that using electrical resistivity to determine the distribution and variation of moisture content in Topopah Spring tuff is most effective when the saturation is less than 40%. For greater levels of saturation, the method is still useful but potentially with less accuracy, depending on how well temperature changes can be determined. It will be necessary to have a separate determination of temperature to get the most accurate saturation estimates. For water saturation greater than 50%, relative permittivity (dielectric constant) may be more sensitive to water saturation than resistivity (Roberts and Lin, 1994b).

2.1.4 Relative Humidity as a Function of Water Saturation at Elevated Temperatures

Relative humidity in the waste package environment is a key factor affecting the integrity of the waste canister. The purposes of determining the relative humidity as a function of water saturation in Topopah Spring tuff are to provide experimental data for comparison with the calculated relative humidity in the near-field

environment, to assess the ambient (pre-heat) relative humidity in the repository, and to understand the diffusion process of vapor through the matrix of the tuff.

The technique of measuring the relative humidity as a function of water saturation was described in Lin et al. (1996). One cylindrical Topopah Spring tuff sample was machined from a small block of the tuff collected at the Large Block Test site. A Humicap humidity sensor was sealed in a hole about 1.0 cm in diameter, in the central portion of the sample. Distilled water was added to the outer surface of the sample, and the relative humidity was monitored continuously until a steady state was reached. The experiment is still under way, and at this reporting time the experiment has only been completed at room temperature. Although it is planned to conduct the experiment at elevated temperatures, we do not believe that increasing temperature in the sample will change the conclusions reported here.

Figure 2-11 shows the current status of the test results. Prior to adding water to the sample, as is indicated by the first spike in the figure, the relative humidity in the entire system was monitored for about one week. Because the experiment started with a dry sample, the relative humidity inside the sample was approximately zero during the pre-test monitoring period, while the room humidity was about 30 to 40%. Water was added to the sample in increments. Each spike in the figure was due to exposing the Humicap to the room air during the water-adding processes. The three spikes in the last segment of the relative-humidity curve were due to some electronic noise of unknown source occasionally received by the data acquisition system. The noise does not seem to affect the quality of the data. The water saturation at each increment of relative humidity shown in the figure was determined based on the amount of water in the sample (by weighing the sample) when the relative humidity had reached a steady state. Currently the relative humidity in the sample is approaching 95% with a saturation level of about 15.9%.

These experimental results indicate that in a closed system very high relative humidity can be reached with very small moisture content. The ambient moisture content in the Exploratory Studies Facility (ESF) is estimated to be about 85%. With this ambient moisture content we expect that the relative humidity in the waste

package environment, without drying out the rock and without considering thermal gradients, to be near 100%. Corrosion rates in AISI carbon steel were observed to increase notably at relative humidities above 75–80% (Estill and Gdowski, 1996). The moisture content in the rock will have to be below about 10% saturation to maintain an environment that dry. At greater temperatures we expect the relative humidity at a given saturation level to be less than shown here, but we don't expect the temperature effect to be great enough to alter the conclusion for the rock itself. However, thermal gradients can modify the relative humidity in drifts or near waste packages by a significant amount. Another observation in this test is the slowness of the vapor diffusion in an intact rock. If this process also occurs in the Topopah Spring tuff rock mass, the increase of moisture content in the matrix due to vapor flow in the fractures will be very slow. Earlier tests indicate that moisture content increases via vapor diffusion are limited to about 20% saturation. This is consistent with data presented in Section 2.1.1 that show a large decrease in suction potential at saturations near 20%. For greater saturations, the suction potential decreases very little with increasing saturation, an indication that matrix saturation above 20% by way of vapor transport alone is unlikely.

2.2 Laboratory Study of Thermal-Hydrological-Chemical Processes

2.2.1 Condensation Along a Fracture

Thermal-hydrological model calculations predict that radioactive decay heat from the waste packages will dry out the surrounding rock mass by evaporating the pore water and will move the vapor away from the waste packages. Based on hydrological tests, both in the laboratory and in the field, and on model calculations, it is believed that fractures are fast paths for the movement of vapor and steam. How the vapor flows within fractures and how the water, which is condensed from the vapor/steam, moves within the fractures affects the moisture distribution in the near field environment. To help understand the thermal-hydrological model predictions and future field thermal tests, we are conducting a laboratory test on a core to study the condensation of vapor in a single fracture.

The core is about 5 cm in diameter and 35.56 cm in length. It was machined from a Topopah Spring tuff block that was collected from the Large Block Test site. The core was split in two by a longitudinal saw cut. Eleven pairs of gold shims, 25 μm in thickness, were placed evenly along both edges of the saw cut to serve as electrodes and to control the aperture. The 11 electrode pairs were used to measure electrical resistance in the saw cut, and the measured electrical resistance was used to detect moisture movement within the saw cut. A high-input impedance bridge was used to measure the resistance (1 kHz measurement frequency) of each electrode pair at regular time intervals. The largest resistance measurable was 100 MΩ. Ten thermocouples were mounted in holes in the sample 90° from the plane of the saw cut. One thermocouple was placed in each of the top and bottom brass end-caps; one thermocouple was placed in the rock about 2 mm from the top and bottom ends; six thermocouples were placed within the core, evenly spaced along its axis. The measuring tips of the thermocouples were located very close to the saw cut (within ~3 mm). Water was added to the core to obtain a water saturation level of about 95%. The cylindrical surface of the core was coated with high-temperature RTV silicon cement to prevent moisture loss. The sample assembly was placed vertically on a hot plate. A vapor release tube was installed in the top end-cap and connected to a water collecting bottle. Fiberglass insulation was used to cover the entire cylindrical surface of the core. The core was heated to a constant temperature of about 160°C at the bottom; the temperature at the top of the core reached and stayed at about 33°C. Copper coils for a heat exchanger to control the top temperature were installed on the top of the core, but it was not necessary to use the heat exchanger in this test. Ambient temperature and electrical resistance data were collected for a few hours before the heating started. The sample was heated for about 245 hours, then the heater was turned off. The experiment is now at about 700-hour elapsed time. Data acquisition continued throughout the heating and cool-down phases. Some observations of the test are summarized in the following paragraph. The test is still in progress, therefore the observations and conclusions presented below are preliminary and are subject to reinterpretation upon conclusion of the test.

Figure 2-12 shows the temperature distribution in the sample assembly for the first 300 hours of the test. For the rest of the test beyond 300-hour elapsed time, the temperatures in the sample are all at room temperature. Thermocouple #1 (Tc1) and thermocouple #10 (Tc10) were in the bottom brass end-cap and top brass end-cap respectively. Tc2 and Tc9 were located about 2 mm from the bottom and top of the core respectively. Tc3 to Tc8 were evenly distributed along the core axis from bottom to top respectively. During most of the test the temperatures in the sample were constant. The step-down in temperature at the 200-hour mark was probably caused by an unplanned decrease in the power output from the hot plate. Just before the heater was turned off, at about 245 hours, we opened the insulation material to inspect the integrity of the RTV moisture coating. No obvious breakage in the RTV was observed. Based on the temperature distribution in the core, cooling of the core seems to be slightly faster than the heating. This may be related to the different thermal capacities of the saturated versus partially saturated rock. The reason for the step-up in temperature at the 100-hour mark (Tc2 to Tc10) is unknown. It was probably a real temperature increase, because there was a simultaneous resistance decrease at electrode pairs 6 to 8. Figure 2-13 shows the electrical resistance measured from electrode pairs 1 to 8 for the entire 700-hour duration of the test. The resistance of electrode pairs 9 to 11 were off-scale during the entire period of this test, and therefore are not shown in Fig. 2-2 through 2-13. The high resistance in the upper portion of the core was probably due to water loss in the upper portion of the core. The water loss was likely due to gravity drainage to the lower portion of the core or through a leak near the vapor collection system at the top of the sample. The resistance of all electrode pairs went off-scale at about the 220-hour mark, indicating substantial dry-out before the heater was turned off. This figure shows sequential drying of the saw cut from the bottom upward. Figures 2-14 and 2-15 show more detailed variance of the resistance at electrode pairs 1-4 and 5-8 respectively. The resistance decreased at the beginning of the experiment because of the heating of the pore water. As heating continued, resistance increased when the saw cut was drying out because of evaporation. The changing slope of the resistance-time trend in electrode pairs 3 to 8 may be caused by the slowing down of the dry-out process in

these portions of the saw cut. The slowing down of the dry-out process may be caused by many factors, such as slower dry-front propagation rate into the matrix, and moisture supply from above, in the form of condensate refluxing. In addition, the resistivity as a function of saturation and temperature for tuff is not a simple relationship, as demonstrated in Section 2.1.3. More detailed observation will be conducted in the future to determine the real cause of this phenomenon.

No vapor was observed to exit the top of the core, and no water was collected in the bottle. The temperature in the core has been decreased to room temperature for at least 350 hours, but no change in the electrical resistance, which would indicate re-wetting, has been observed. Future tests to verify the current observations will be conducted. Those include model calculation of the experimental setup, measurement of electrical resistance perpendicular to the saw cut, thickening the RTV layer to minimize vapor loss, and an improved vapor collection system at the top.

2.2.2 Fracture Flow vs. Matrix Imbibition at Elevated Temperatures

As mentioned in Section 2.1.4, the diffusion of vapor into the matrix because of the vapor flow in fractures may not be very effective in transporting moisture. The understanding of how water imbibes into the matrix during fracture flow will become more important for enhancing our knowledge about the coupled TMHC processes. The purpose of this test is to visualize the fracture flow and matrix imbibition process when the sample is at elevated temperatures. By this visualization we hope to determine the parameters, such as fracture aperture, infiltration rate (i.e., the fracture flow rate), initial moisture content of the matrix, and thermal gradient, that may affect the coupling between water flow in fractures and the imbibition into the matrix. The experimental techniques and procedures, and some of experimental results were reported by Roberts and Lin (1996c). Basically, a linear x-ray source of 160 kVp was used to conduct vertical scans of blocks of Topopah Spring tuff containing vertical fractures. Water, doped with KI to enhance the x-ray attenuation contrast, was introduced into the top of the fracture. X-ray radiographs were taken periodically to image the movement of water in the fracture

and the matrix. Images were normalized using aluminum standards. After the normalization, difference images were created by subtracting a beginning image from the subsequent images. In this manner only the relative changes in the x-ray images are studied. All the x-ray images presented in this report use the following convention: darker shades indicate higher x-ray attenuation (or changes in attenuation) and imply higher water content, and lighter shades indicate relatively low x-ray attenuation (or changes in attenuation) and imply lower water content. Quantitative saturation fields can be calculated but are not presented here (see Tidwell and Glass, 1994, or Roberts and Lin, 1996c).

So far four experiments have been conducted: (1) fracture flow and matrix imbibition in an artificially induced tensile fracture without shims; (2) fracture flow and matrix imbibition in the same fracture as in experiment (1) with four shims of 25-μm thickness; (3) after completion of test (2), dehydration of the sample under a thermal gradient of about 95°C at the bottom and 33°C at the top; and (4) fracture flow and matrix imbibition against a thermal gradient, tested in another Topopah Spring tuff block that contained nine 25-μm gold shims. The results of the first three experiments were reported in Roberts and Lin (1996c) and are summarized later in this report. The sample dimensions for experiments (1), (2), and (3) were 14 × 10 × 2.5 cm (length, height, width). Experiment (4) is described in the following paragraph, and its results are summarized later, along with the results of the first three experiments.

In the fourth experiment, a dry block of Topopah Spring tuff machined from a small block of the rock collected at the Large Block Test site was used. The dimensions of the block were 29.21 cm tall by 15.1 cm wide by 2.65 cm thick. The sample preparation and test procedures were similar to the preceding experiments, with the exceptions noted here. Nine 25-μm gold shims were placed inside the tensile fracture at regular intervals. Five thermocouples were placed inside the rock at 0.2, 7.5, 14.8, 22.1, and 29.1 cm, from the bottom of the sample to the top, respectively. The temperatures in the dry rock prior to flow were 115, 48.4, 33.8, 29.4, and 28.1°C, from bottom to top. The temperature between the heater and the bottom

of the sample was 126°C. Even though insulation was used wherever possible, a relatively large temperature gradient existed at the bottom of the sample. Initial images were taken, and then water was permitted to pond on the sample. Only the fractured region on top (~1 cm wide) was exposed directly to the ponded water, the other areas having been coated with RTV.

The results of the four fracture flow and matrix imbibition experiments are summarized here. Figure 2-16 shows the x-ray difference image of fracture flow and matrix imbibition in a tensile fracture without shims, at room temperature. The fracture is located near the left edge of the image. Water was ponded at the top of the image. The darker region represents the region where water has wetted the sample, 47.3 hours after the ponding started. The roughly V-shaped wetted region, with the tip of the "V" at the front of the fracture flow, is very similar to that of fracture flow in a block of plaster of Paris with 25-μm shims that had been used as a test of analytical approaches of fracture/matrix interactions (Fig. 2-17). The matrix permeability of the tuff is about 3 orders of magnitude less than that of the plaster of Paris. The result of this experiment indicates that fracture flow and matrix imbibition in an unshimmed tensile fracture in tuff is qualitatively similar to that in a material with a higher permeability matrix that contains a fracture with greater aperture. Figure 2-18 shows a sequence of x-ray difference images of fracture flow and matrix imbibition in the same fracture shown in Fig. 2-16, except that four gold shims of 25-μm thickness were placed in the fracture. The test was also conducted at room temperature. There is no V-shaped wetted region, as seen in Figs. 2-16 and 2-17. Water flowed through the fracture within a couple of minutes (Fig. 2-18a), then matrix imbibition began. The imbibition into the matrix was faster on the right side of the sample as compared to the left side. This is more evident at longer times (Fig. 2-18c). Examination of the fractured sample after the experiment revealed pumice fragments near the areas where lateral imbibition was the fastest. Small microfractures around the edges of these fragments are believed responsible for the enhanced lateral imbibition.

The larger fracture aperture changed significantly both the volume of flow through the fracture and the rate and amount of imbibition into the matrix. These effects are being studied further because they have bearing on models of repository performance.

Figure 2-19 shows the movement of the wetting front versus the square root of time for three locations: within the fracture (~1/3 the distance from the top of the sample on both sides of the fracture) and the top of the sample (~3.5 cm from the left edge of the sample). The wetting front was arbitrarily defined as 75–80% saturated. The large variability in matrix imbibition is evident in this figure. The imbibition from ponded water on top of the sample was slowed considerably by a relatively impermeable crystal-lined cavity (low attenuation region—may be porous area) ~1 cm beneath the surface. After an initial time lag, all three locations are linear with respect to time$^{1/2}$. The slope of this line is related to permeability.

Figure 2-20 shows the x-ray image of the drying process of the sample as in experiment (2) after the infiltration had totally wetted the sample. Again, as in the previous experiment, the fracture had four shims of 25-μm thickness within it. The drying was created by using a heater at the bottom of the sample to maintain the temperature there at about 95°C, while the temperature at the top of the block was about 30°C. The image shows that the fracture was dried out within hours after the heater was turned on. A darker horizontal region near the lower part of the image seems to indicate greater x-ray attenuation. The greater attenuation may be because of increase in water saturation or deposition of KI. Because the higher attenuation band changed shape and moved up and down slightly during the sequence, it is believed that it represents increased saturation in this instance.

As mentioned previously, the fourth experiment was designed to visualize the fracture flow and matrix imbibition in a heated block of fractured Topopah Spring tuff. Based on examination of difference images, several important features were noted. Figure 2-21(a, b, c) shows images taken at 1.7, 73.5, and 360 hours respectively and illustrates most of the following points. Initially, water flowed relatively quickly into the rock with minimal lateral imbibition into the matrix from the fracture,

similar to that in Experiment (2). By 1.6 hours, water had flowed ~16 cm down the fracture with the width of the highly saturated zone ~0.8 to 1.5 cm (Fig. 2-21a). At this point, downward flow slowed considerably and lateral imbibition continued. The most likely reason for the stop in downward flow is the existence of a low density (i.e., more porous) pumice fragment at ~16 cm from the top. After ~23 hours the water began to move past this region as a V-shaped wetting front. The highly saturated zone was ~2.2 to 3.5 cm wide. Water continued to travel down the fracture until ~27 hours, when a narrow region of high x-ray attenuation began to develop in the fracture between ~22.6 and 26.3 cm (from top). At longer periods of time, a circular region of high x-ray attenuation developed near the bottom of the sample, centered on the fracture (Fig. 2-21b). Because this is the hottest region of the rock, where temperature was above the boiling point of water, a likely reason is the concentration of KI (used as a dopant to increase x-ray attenuation) in these regions. Water never penetrated the entire sample; that is, water never was observed to exit the bottom of the sample past the "boiling zone." Although dependent upon many factors (i.e., hydraulic head, porosity, permeability, pore size distribution), this could be a very important observation because it indicates that condensate will not penetrate the boiling zone for fractures less than some critical aperture. Additional studies are needed to verify and determine the aperture dependence. Continued lateral imbibition was observed up until the experiment was stopped at ~360 hours elapsed time; however, it appeared that the rate of advancement of the wetting front slowed as time progressed (Fig. 2-21c).

The results of this experiment suggest that rock heterogeneity plays a significant role in the speed at which water flows down gradient in a fracture. Although not conclusive, the existence of a boiling region stopped downward flow, while lateral imbibition continued. Post-experimental examination of the fracture surface near the boiling zone revealed small crystals. It is thought that these are KI crystals indicative of boiling and would explain the higher x-ray attenuation discussed above. Thus the resultant increased x-ray attenuation in the boiling region was probably a result of crystal formation rather than of increased saturation.

2.2.3 Fracture Healing

As mentioned in Section 2.1.2, the laboratory-determined water permeability of fractured Topopah Spring tuff samples at elevated temperatures behaves differently than that of intact samples. The water permeability in the fractured tuff samples decreases with increasing temperature. A series of laboratory experiments were conducted to understand the mechanism(s) that may cause the fracture healing. Those experiments have been reported by Lin and Daily (1984), Daily et al. (1987), Lin and Daily (1988), Lin (1991), Roberts and Lin (1995b), and Lin et al. (1995). The experimental techniques were described in Lin and Daily (1984). All of these experiments were designed to measure water permeability in fractured Topopah Spring tuff samples as functions of temperature, under various sample and experimental conditions that included reopened natural fractures, introduced tensile fracture, saw cut without shims, naturally fractured sample in a thermal gradient, and naturally fractured sample with variable pressure differences (confining pressure minus pore pressure). To understand the fracture healing process, we also conducted tests to investigate the effects of temperature and pressure on dry gas permeability, the effect of heating a saturated sample with water not flowing on the water permeability at room temperature, and the effect of flowing steam on gas permeability. In some of these experiments, the water that flowed through the samples was analyzed for concentration of certain elements, such as Si, Ca, K, etc. Also for some experiments the scanning electron microscope (SEM) was used to image the fracture surfaces before and after the experiments. The results of earlier experiments and a discussion of the mechanisms of fracture healing were reported in NFER Rev. 0. The results of these experiments are summarized in the following paragraphs.

The results of all of these experiments showed that flowing high-temperature (greater than 90°C) water through fractured tuff samples under compression caused water permeability to decrease significantly. This was true for both uniformly heated samples and samples under a thermal gradient. Flowing steam through a naturally fractured sample for about one week also decreased the dry N_2 permeability

measured at room temperature before and after the steam-flowing by about one order of magnitude. Flowing dry N_2 gas in fractured tuff samples under the same temperature and pressure conditions did not affect the gas permeability. Heating a saturated fractured tuff sample when water was not allowed to flow during heating did not affect the water permeability at room temperature. Based on these observations and the results of chemical analyses of the water, and SEM studies of the fracture surfaces, we concluded that dissolution and deposition of minerals, such as silica by the water in the fracture surfaces, may smooth out asperities and cause the fracture aperture to decrease under confining pressure. These processes are relatively insensitive to the type of fracture surface, such as natural fracture, rough tensile fracture, and smooth saw cut (NFER Rev. 0).

Recent study of fracture healing at various differential pressures reveals more detailed information about the healing mechanism. Figure 2-22 shows the water permeability of a naturally fractured tuff sample with respect to time. The figure also shows water permeability and confining pressure with respect to time during the experiment. The pore pressure in the sample was kept constant at 0.5 MPa, therefore the variation of confining pressure equals the variation of differential pressure. The experiment consisted of several parts. First the confining pressure was cycled from 1 to 5 to 1 MPa at ambient temperature. Next were several cycles in temperature, from approximately 25 to 150 to 25°C at constant confining pressures (1, 2, 3, and 5 MPa).

The first decrease in permeability, as shown in Fig. 2-22 at about 400 hours elapsed time, was caused by increasing confining pressure at room temperature. When the confining pressure was released, the permeability recovered to its original value. This shows that a confining pressure of 5 MPa at room temperature is not enough to cause any nonelastic deformation on the fracture surfaces. Upon heating, the permeability began to decrease as soon as temperature started to increase, even at the lowest differential pressure, 0.5 MPa. For the entire experiment the permeability decreased from about 18×10^{-15} m^2 (18 mD) to about 2×10^{-15} m^2 (2 mD). Most of that decrease in permeability was accomplished during the first heating cycle.

Figure 2-23 shows the Si concentration in the water that flowed through the sample during the test, and temperature as a function of the elapsed time. The two x's at the zero elapsed time are the Si concentration in the virgin J-13 water, before it flowed through the sample. With regard to Si concentration and permeability decreases, the experiment can be divided into two parts as indicated by the line at ~2000 hr on both Figure 2-22 and 2-23. The largest decrease in permeability occurred during the first thermal cycle prior to 2000 hr (from 18×10^{-15} m^2 to about 6×10^{-15} m^2 [18 to 6 mD]). Also note that during the first thermal cycle the Si concentration in the water was below that in the virgin J-13 water until the temperature reached 150°C, and the fluid exiting the sample was undersaturated with respect to Si during this period. This indicates that during the first heating phase Si may have been deposited on the fracture surfaces. After 2000 hr, during subsequent heating cycles, the permeability change is much less than the first thermal cycle (about 6×10^{-15} m^2 to 2×10^{-15} m^2 [6 to 2 mD]) and the water is saturated with respect to Si (α-cristobalite; W. Glassley, personal communication, 1995). As observed in Figure 2-23, the Si concentration is strongly correlated with temperature during this period. During this period permeability does show a relationship with confining pressure, because permeability decreases with increasing confining pressure. As shown in Fig. 2-22, slight increases in permeability were observed at the end of thermal cycles because of cooling (e.g., 2900 hr). Under the condition of Si saturation, both dissolution and deposition of Si can occur. However, the dissolution and deposition were probably not very active because the corresponding decreases in permeability were not significant. In addition, during the later part of the test the fracture surfaces may be smoother than before; therefore the effect of dissolution and deposition on permeability may be reduced.

The coupled processes that are evident in this experiment demonstrate a complex relationship, and the subsequent effect they have on the permeability is often difficult to fully understand. This experiment provides us with some indication of which specific process is active during the different portions of the test. During the first temperature cycle, thermal-chemical processes seem to dominate

hydrologic changes. Later, when the Si concentration reached saturation, thermal-mechanical processes appear to most affect the permeability. This test confirms the previous conclusion that rock-water interaction is probably the cause of the fracture healing. In addition, it shows that permeability in fractured tuff samples can decrease even at very low pressure. It also indicates that the rock-water interaction was most active during the initial heating of the sample. In terms of modeling and understanding repository design and performance, this is an extremely important result and is worthy of more study. If the laboratory-observed phenomena also occur *in situ*, these coupled processes can have a potentially large effect on the movement of condensate, the importance of preferential pathways, and the effective local permeability, as well as on other issues related to repository design.

2.3 References

Daily, W., W. Lin, and T. Buscheck, 1987, "Hydrology of Topopah Spring Tuff—Laboratory Measurements," *J. Geophys. Res.* 92, No. B8, pp. 7854–7864. NNA.19900123.0064

Daily, W., and W. Lin, 1991, "Laboratory Determined Suction Potential of Topopah Spring Tuff at High Temperatures," *Proceedings of the Second Annual International Conference on High Level Radioactive Waste Management*, Las Vegas, NV, April 28–May 3, 1991, American Nuclear Society, Inc., La Grange Park, IL, pp. 583–588. NNA.19910304.0097

Estill, J.C., and G.E. Gdowski, 1996, "Water vapor effects of the corrosion of carbon steel," *Proceedings of the Seventh Annual International Conference on High Level Radioactive Waste Management*, Las Vegas, NV, April 29–May 3, 1996, American Nuclear Society, Inc., La Grange Park, IL, pp. 457–458.

Klavetter, E.A., and R.R. Peters, 1987, *An Evaluation of the Use of Mercury Porosimetry in Calculating Hydrologic Properties of Tuff from Yucca Mountain, Nevada*, SAND86-0286, Sandia National Laboratory, Albuquerque, NM. NNA19890327.0056

Lin, W., 1991, "Variation of Permeability with Temperature in Fractured Topopah Spring Tuff Samples," *Proceedings of the Second Annual International Conference on High Level Radioactive Waste Management*, Las Vegas, NV, April 28–May 3, 1991, American Nuclear Society, Inc., La Grange Park, IL, pp. 988–993. NNA.19910523.0105

Lin, W., and W. Daily, 1984, *Transport Properties of Topopah Spring Tuff*, Lawrence Livermore National Laboratory UCRL-53602, Livermore, CA. NNA.19891026.0025

Lin, W., and W. Daily, 1988, "Hydrological Properties of Topopah Spring Tuff under a Thermal Gradient, Laboratory Results," *International Journal of Rock Mechanics*, 27, #5, pp. 373–385. NNA.19880503.0014

Lin, W., J.J. Roberts, W. Glassley, and D. Ruddle, 1995, *The Effect of Rock-water Interaction on Permeability*, Lawrence Livermore National Laboratory UCRL-JC-119574, Livermore, CA. MOL.19960416.0275

Lin, W., J.J. Roberts, and D. Ruddle, 1996, "Relative humidity in the near-field environment," *Proceedings of the Seventh Annual International Conference on High Level Radioactive Waste Management*, Las Vegas, NV, April 29–May 3, 1996, American Nuclear Society, Inc., La Grange Park, IL, pp. 128–129. MOL.19960422.0127

Moore, D.E., C.A. Morrow, and J.D. Byerlee, 1986, "High-temperature permeability and groundwater chemistry of some Nevada Test Site Tuffs," *J. Geophys. Res.*, 91, No. B2, pp. 2163–2171.

Peters, R.R., E.A. Klavetter, I.J. Hall, S.C. Blair, P.R. Heller, and W.G. Gee, 1984, *Fracture and Matrix Hydrologic Characteristics of Tuffaceous Materials from Yucca Mountain, Nye County, Nevada*, SAND84-1471, Sandia National Laboratory, Albuquerque, NM. NNA.19900810.0674

Ramirez, A., T. Buscheck, R. Carlson, W. Daily, K. Lee, W. Lin, N. Mao, T. Ueng, H. Wang, and D. Watwood, 1991, *Prototype Engineered Barrier System Field Test (PEBSFT) Final Report*, A. Ramirez, Scientific Editor, Lawrence Livermore National Laboratory UCRL-ID-106159, Livermore, CA. NNA.19910711.0047

Roberts, J.J., and W. Lin, 1994a, *Hydrological Property Measurements of Topopah Spring Tuff*, Lawrence Livermore National Laboratory UCRL-ID-119033, Livermore, CA. MOL.19950501.0032

Roberts, J.J., and W. Lin, 1994b, "Electrical properties of Topopah Spring tuff as a function of saturation," *Proceedings of the Fifth Annual International Conference on High Level Radioactive Waste Management*, Las Vegas, NV, May 22–26, 1994, American Nuclear Society, Inc., La Grange Park, IL, pp. 2112–2120. NNA.19940524.0018

Roberts, J.J., and W. Lin, 1995a, *Hydrological Property Measurements of Topopah Spring Tuff*, Lawrence Livermore National Laboratory UCRL-ID-119033, Livermore, CA. MOL.19950501.0032

Roberts, J.J., and W. Lin, 1995b, "Permeability of Fractured Tuff as Functions of Temperature and Confining Pressure," *Proceedings of the Sixth Annual International Conference on High Level Radioactive Waste Management*, Las Vegas, NV, April 30–May 5, 1995, American Nuclear Society, Inc., La Grange Park, IL, pp.44–45. MOL.19960109.0097

Roberts, J.J., and W. Lin, 1996a, *Report on Laboratory Tests of Drying and Re-Wetting of Intact Rocks*, Lawrence Livermore National Laboratory UCRL-ID-121513, Livermore, CA. MOL.19960409.0179

Roberts, J.J., and W. Lin, 1996b, *Electrical Properties of Partially Saturated Topopah Spring Tuff: Water Distribution as a Function of Saturation*, Lawrence Livermore National Laboratory UCRL-JC-123763, Livermore, CA. (submitted to Water Resources Research)

Roberts, J.J., and W. Lin, 1996c, "X-ray radiography of fracture flow and matrix imbibition," *Proceedings of the Seventh Annual International Conference on High Level Radioactive Waste Management*, Las Vegas, NV, April 29–May 3, 1996, American Nuclear Society, Inc., La Grange Park, IL, pp. 128–129. MOL.19960409.0159

Tidwell, V.C., and R.J. Glass, 1994, "X-ray and visible light transmission for laboratory measurement of two-dimensional saturation fields in thin-slab systems," *Water Resources Research*, 30, 2873–2882.

Data Tracking Information in this Chapter:

2.1.1 Moisture Retention at Elevated Temperatures
(Data Tracking Numbers: LL950404604242.012 and LL950812704242.017)

2.1.3 Electrical Resistivity as a Function of Water Saturation at Elevated Temperatures
(Data Tracking Numbers: LL950404604242.012 and LL960201404244.011)

2.1.4 Relative Humidity as a Function of Water Saturation at Elevated Temperatures
(Data Tracking Numbers: LL960100604244.007 and LL960201304244.010)

2.2.2 Fracture Flow vs. Matrix Imbibition at Elevated Temperatures
(Data Tracking Number: LL960100704244.008)

2.2.3 Fracture Healing
(Data Tracking Numbers: LL950404604242.012, LL950916504242.018, LL950406104242.016, and LL940800704242.002)

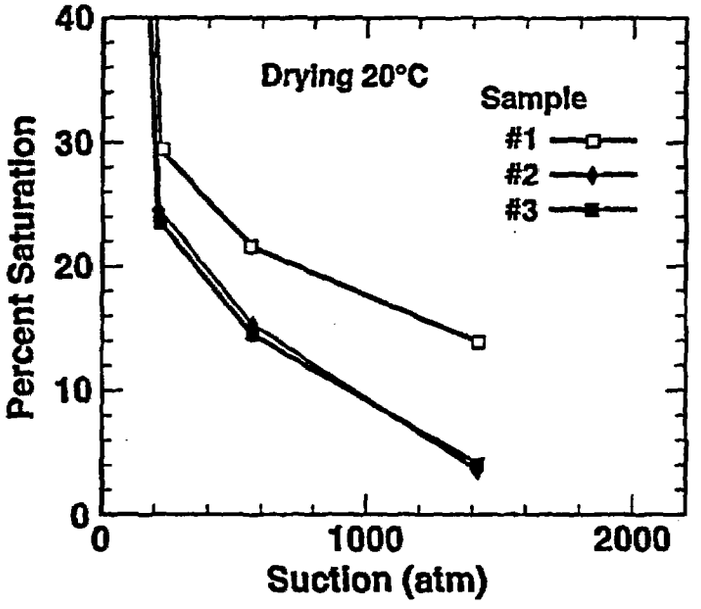

Figure 2-1. Percent saturation as a function of suction potential measured at 20°C for three samples of Topopah Spring tuff. Samples were initially saturated so that these data are the capillary suction for drying. All samples were taken from USW H-1 core.

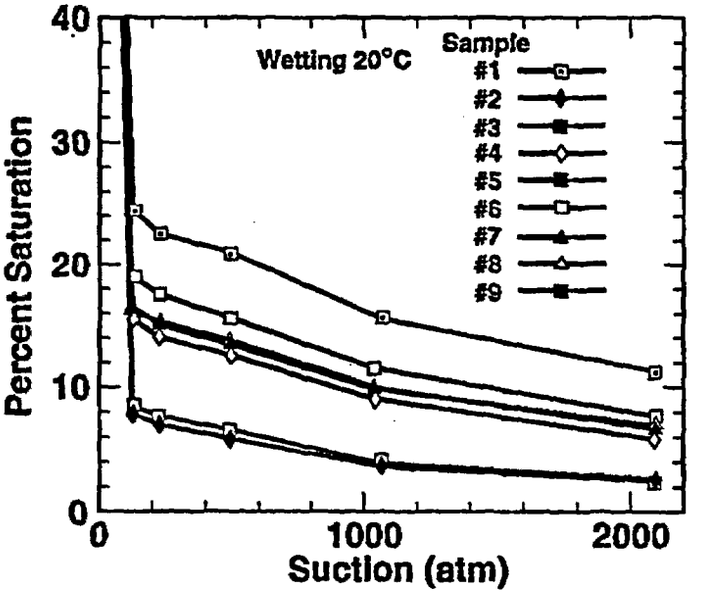

Figure 2-2. Percent saturation as a function of suction potential measured at 20°C for nine samples of Topopah Spring tuff. Samples were initially dry so that these data are the capillary suction for wetting. Samples 1–3 were taken from USW H-1 core; samples 4–9 were taken from Fran Ridge outcrop.

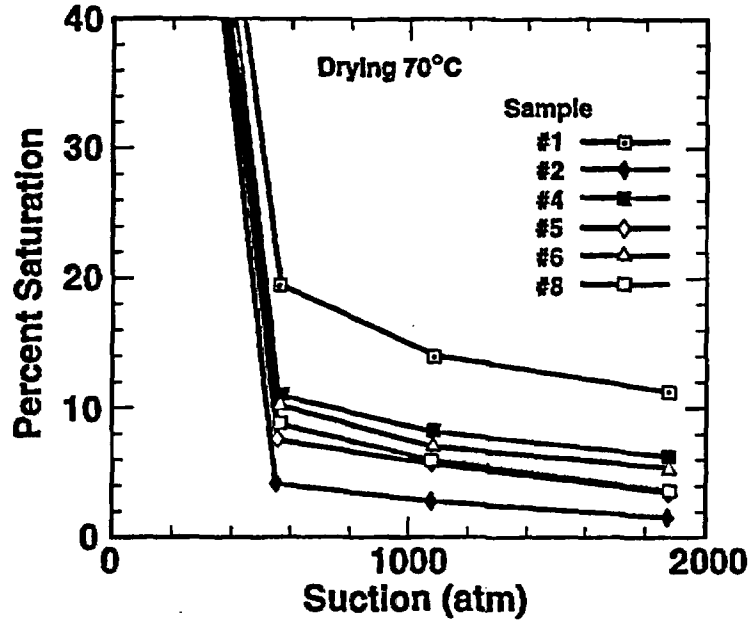

Figure 2-3. Percent saturation as a function of suction potential measured at 70°C for six samples of Topopah Spring tuff. Samples were initially saturated so that these data are the capillary suction for drying. Samples 1 and 2 were taken from USW H-1 core, and the others were taken from Fran Ridge outcrop.

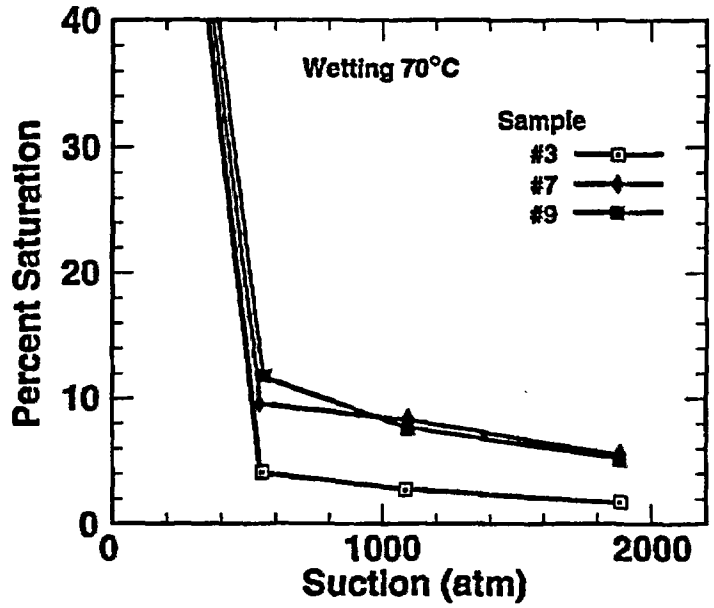

Figure 2-4. Percentage saturation as a function of suction potential measured at 70°C for three samples of Topopah Spring tuff. Samples were initially dry so that these data are the capillary suction for wetting. Sample 3 was taken from USW H-1 core; samples 7 and 9 were taken from Fran Ridge outcrop.

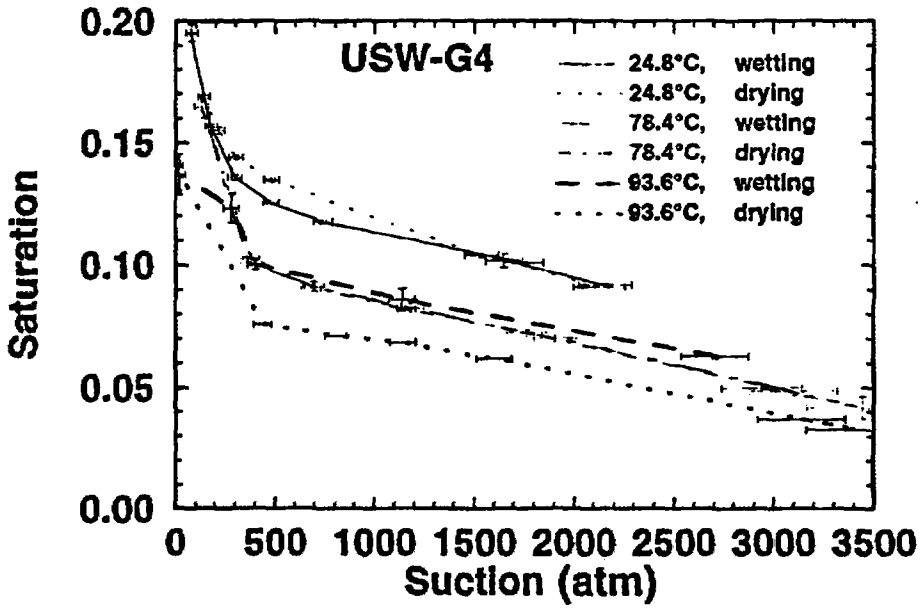

Figure 2-5. Saturation as a function of suction (atmospheres) for USW G-4. Wetting and drying curves are shown for three temperatures. The lines are not fitted curves but indicate the connection between points that are averaged for several samples. Error bars for suction assume 2% error in the relative humidity measurement. Note the reversal in hysteresis from low to high temperature.

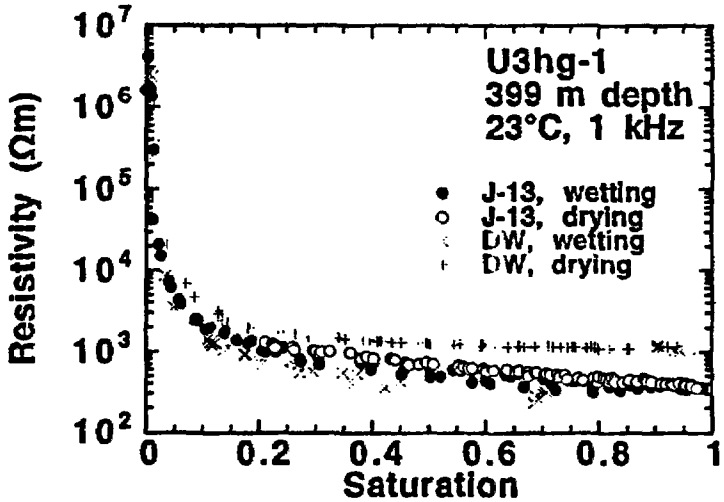

Figure 2-6. Electrical resistivity of U3hg-1 samples as a function of water saturation at room temperature, using J-13 water and distilled water (DW) as saturating fluid.

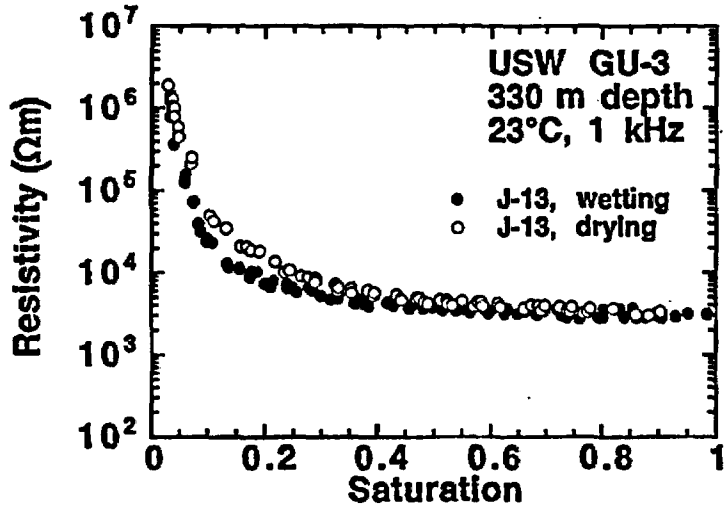

Figure 2-7. Electrical resistivity of USW GU-3 samples as a function of water saturation at room temperature, using J-13 water as saturating fluid.

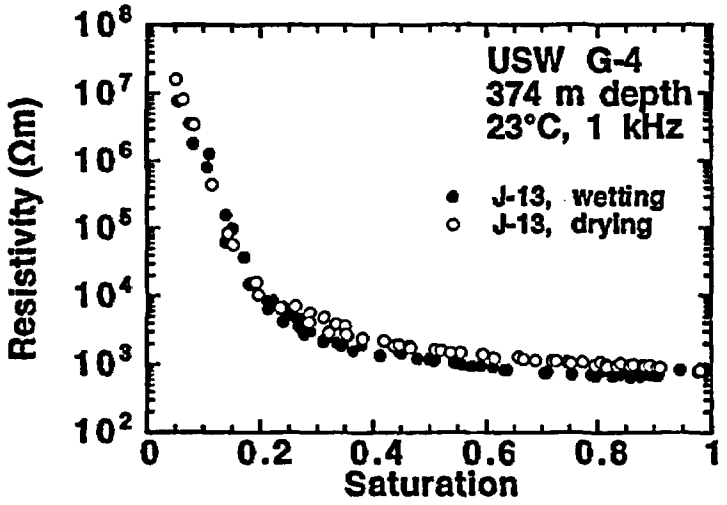

Figure 2-8. Electrical resistivity of USW G-4 samples as a function of water saturation at room temperature, using J-13 water as saturating fluid.

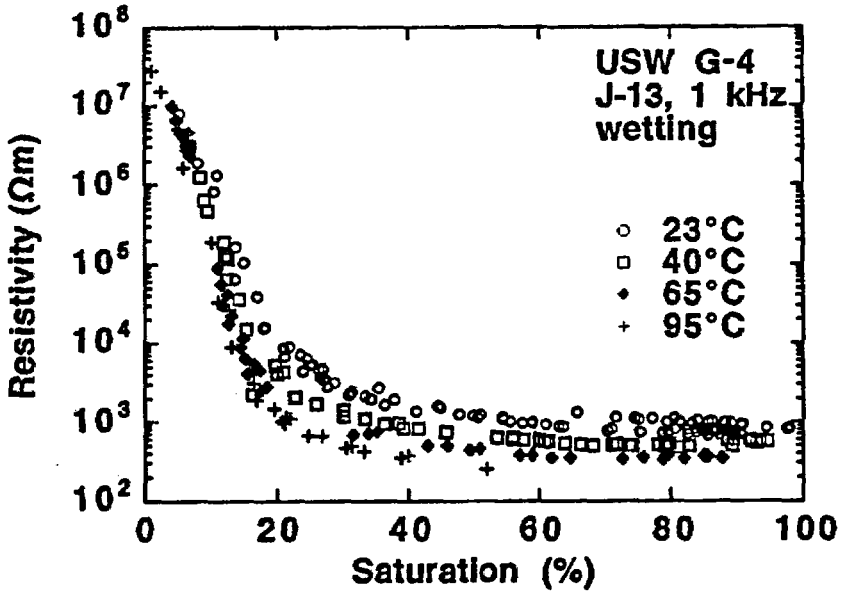

Figure 2-9. Electrical resistivity of USW G-4 samples as a function of water saturation at elevated temperatures, using J-13 water as saturating fluid.

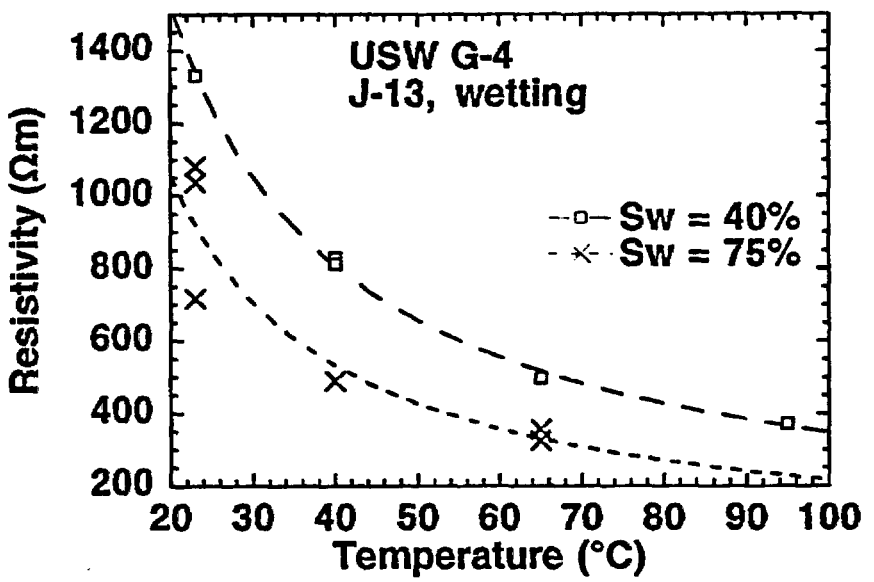

Figure 2-10. Resistivity (Ωm) of Topopah Spring tuff as a function of temperature for two saturations, 40 and 75%. Data are for the saturation cycle of samples from USW G-4 using J-13 water. Curves are power law fits. Between 20 and 100°C there is approximately a factor of 3 to 4 reduction in resistivity. Over the same temperature span the resistivity of J-13 water decreases by about a factor of 2.

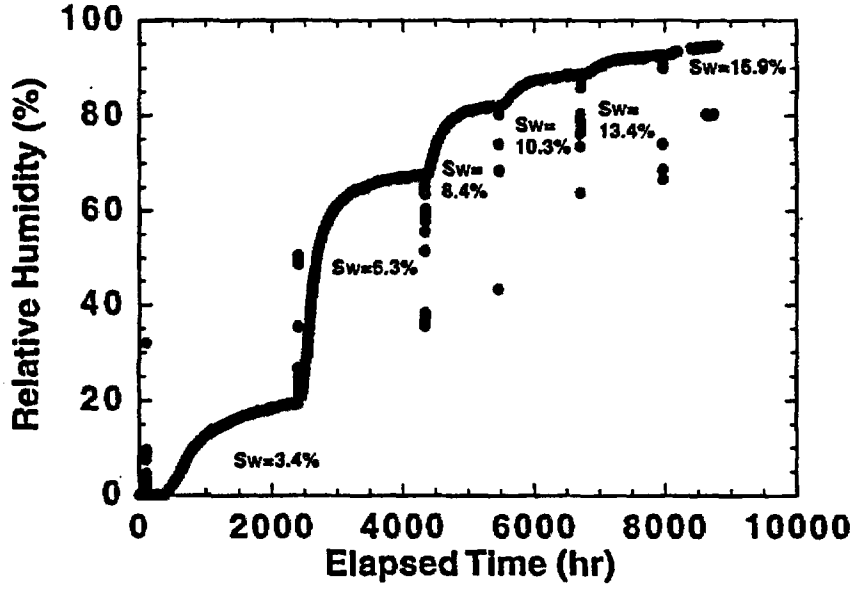

Figure 2-11. Relative humidity in an intact Topopah Spring tuff sample and water saturation as a function of elapsed time.

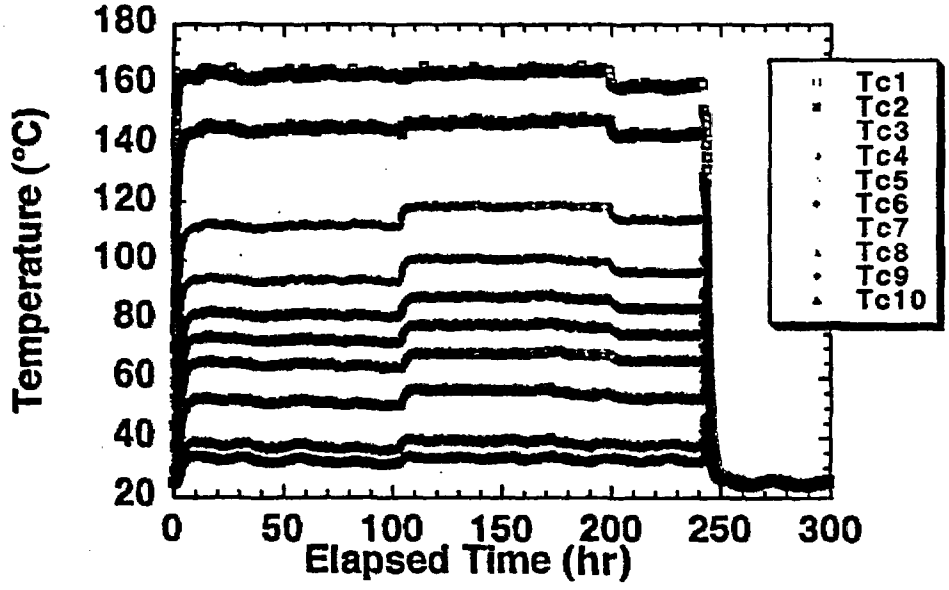

Figure 2-12. Temperatures in the 35.56-cm core during the vapor condensation along a fracture experiment as a function of time. Thermocouples Tc1 to Tc10 are from the bottom to the top of the sample, respectively.

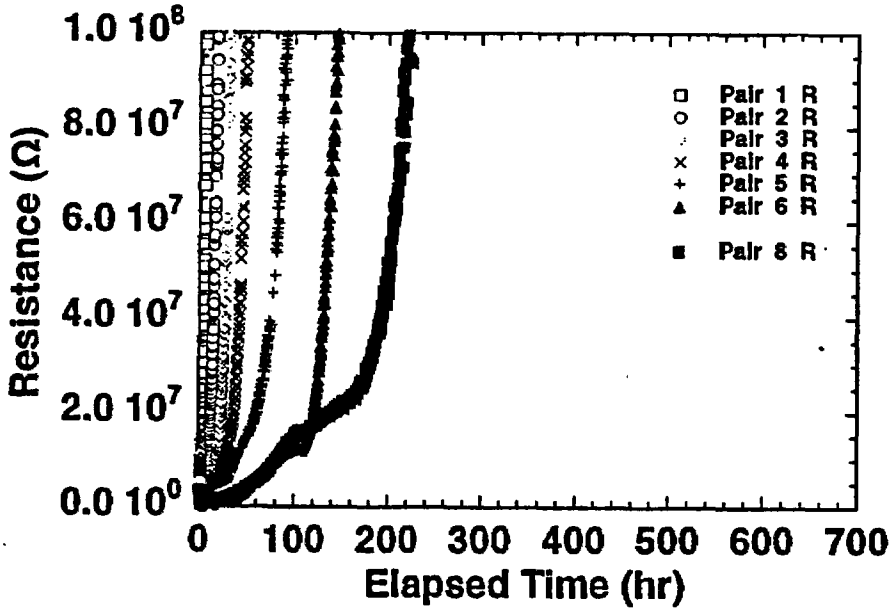

Figure 2-13. Electrical resistance in the 35.56-cm core during the vapor condensation along a fracture experiment as a function of time. Electrode pairs 1 to 8 are from the bottom to the top of the sample, respectively.

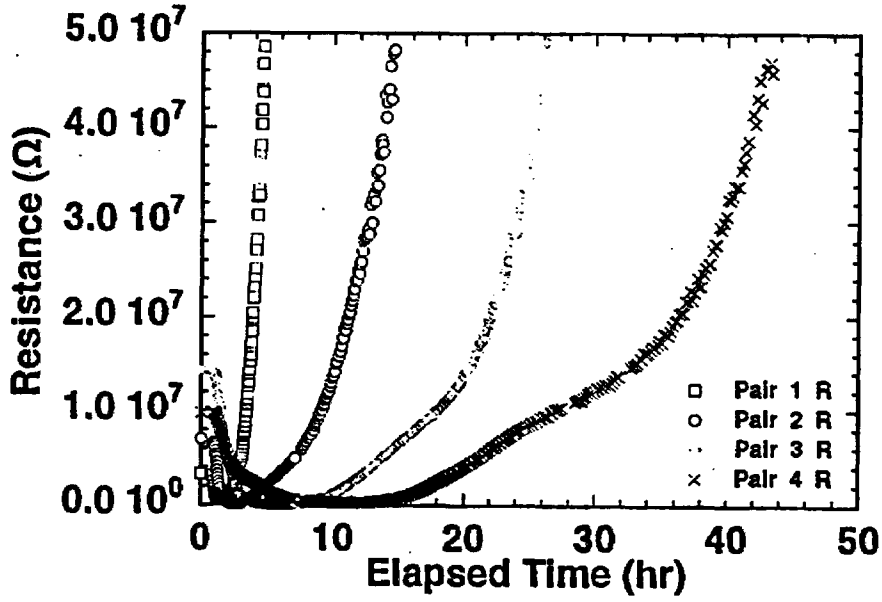

Figure 2-14. Electrical resistance at electrode pairs 1 to 4 in the 35.56-cm core during the vapor condensation along a fracture experiment as a function of time.

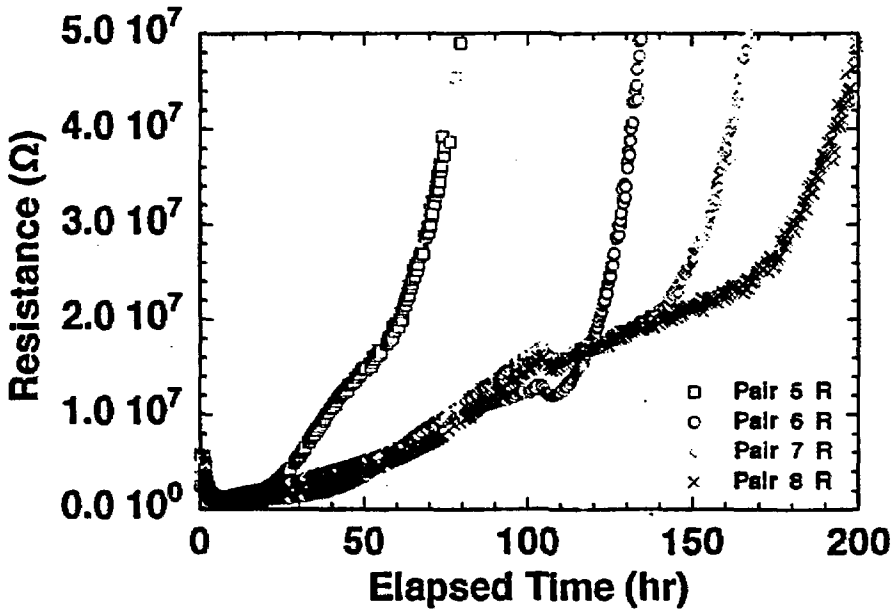

Figure 2-15. Electrical resistance at electrode pairs 5 to 8 in the 35.56-cm core during the vapor condensation along a fracture experiment as a function of time.

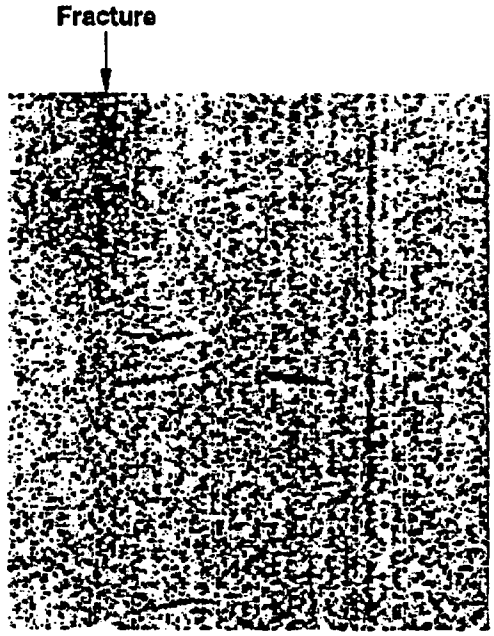

Figure 2-16. X-ray difference image sequence of radiographs of tuff containing a tensile fracture. No shim was put in the fracture. The experiment was performed at room temperature. Water containing KI to enhance attenuation of x rays was ponded on top of the sample. A roughly V-shape wetting front was observed at 47.5 hours.

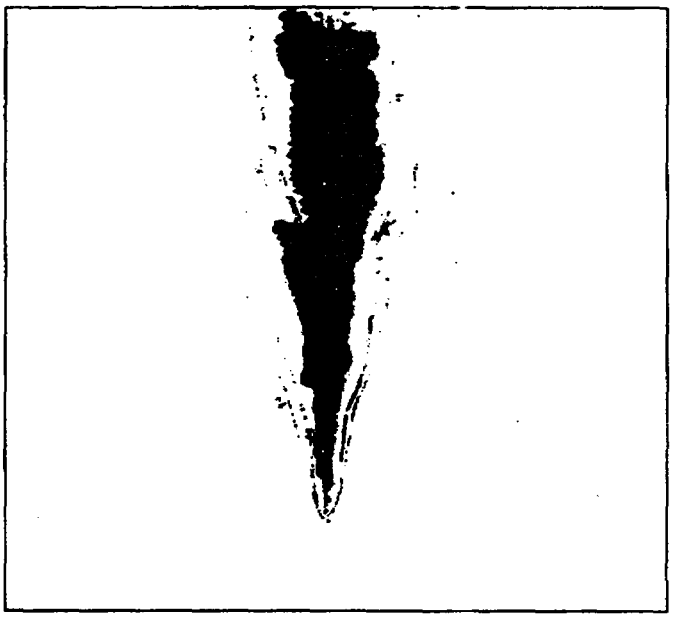

Figure 2-17. Fracture flow and matrix imbibition in plaster of Paris. Liquid containing dye was ponded on top of the sample and flowed into the fracture. The fracture was held open by 25-μm gold shims. The lines indicate the progress of the wetting front as a function of time (hours).

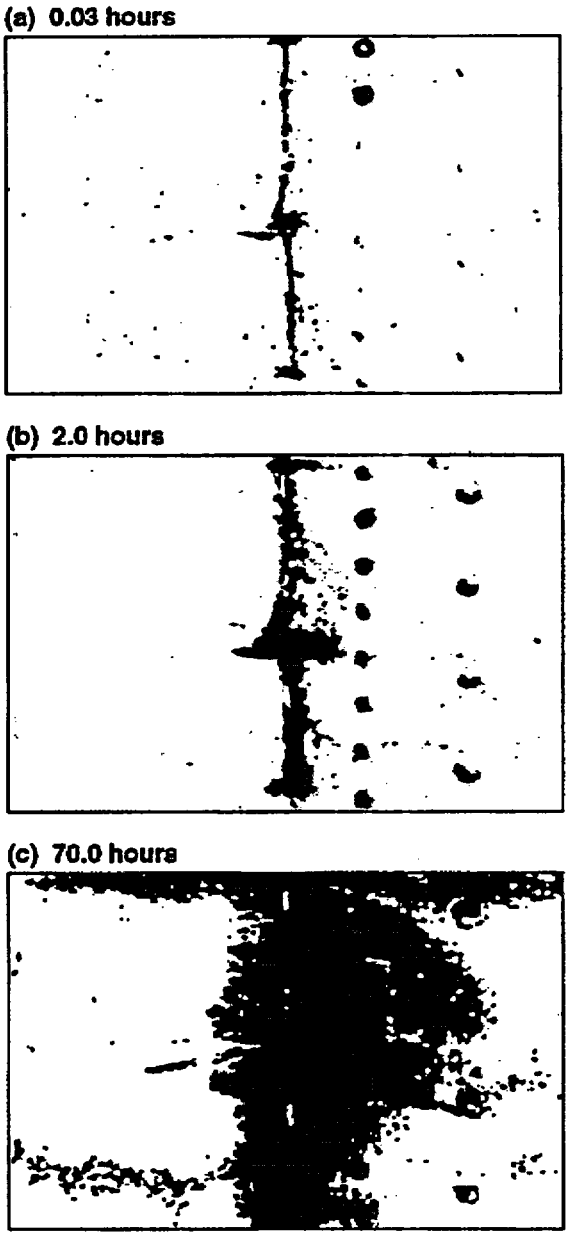

Figure 2-18. X-ray difference image sequence of radiographs of tuff containing a tensile fracture. Four 2-μm gold shims held the fracture open. The experiment was performed at room temperature. Water containing KI to enhance attenuation of x rays was ponded on top of the sample. The elapsed time of each image is (a) 0.03, (b) 2.0, and (c) 70.0 hours. Darker shades represent a large change in attenuation (the addition of water from the first radiograph). The spots on the right side of the images are holes that were plugged with RTV after the start of the experiment. (a) After 0.03 hours, water had already flowed the length of the fracture. (b) At later times, 2.0 hours, water began to imbibe laterally into the matrix. (c) After 70 hours the non-uniformity of matrix imbibition is evident (see text).

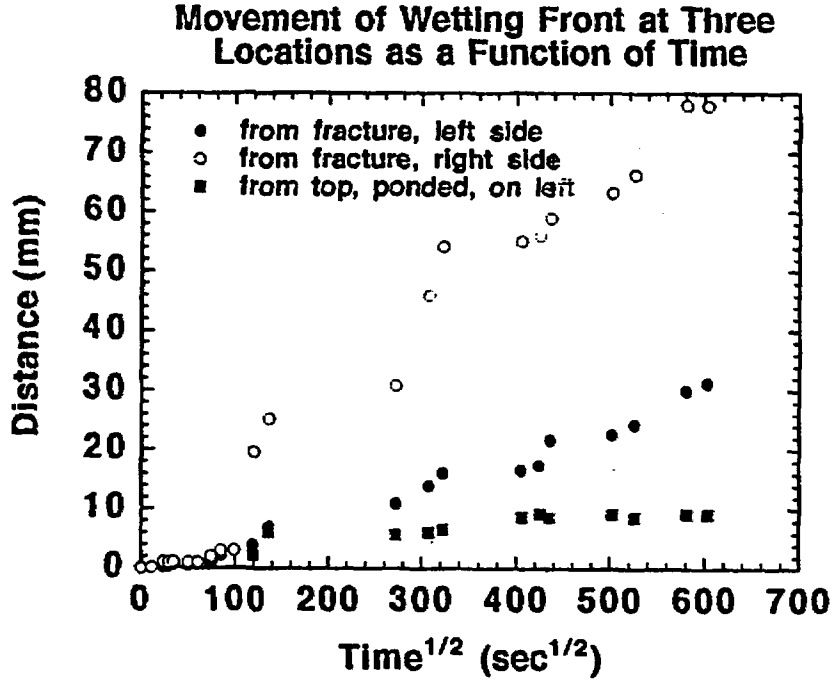

Figure 2-19. Tracking of the wetting front in the experiment shown in Fig. 2-18 plotted as distance (mm) vs the square root of time for three separate locations. The different slope of each line indicates difference imbibition rates for each location, demonstrating the heterogeneity of the rock.

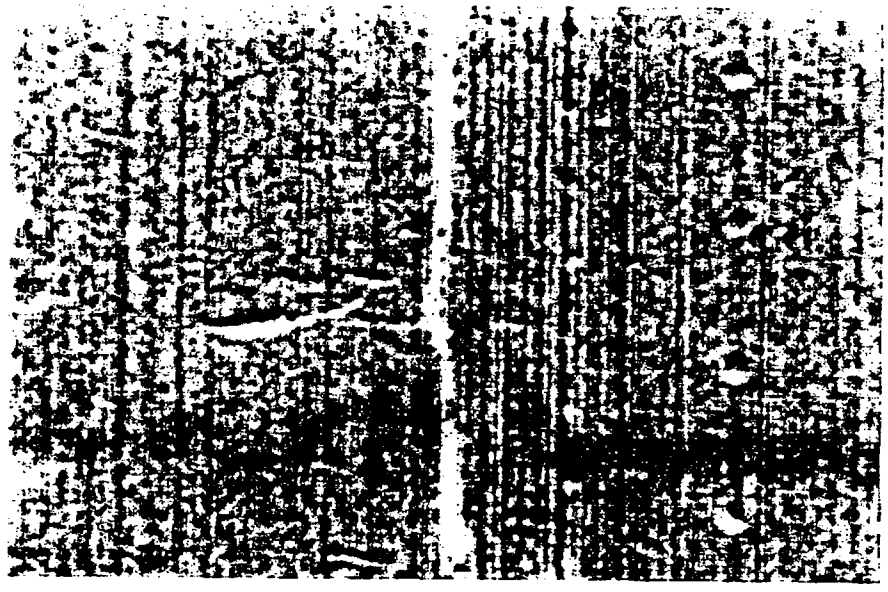

Figure 2-20. X-ray radiography image of the dry-out of the same fracture as in Fig. 2-18 after it was wetted.

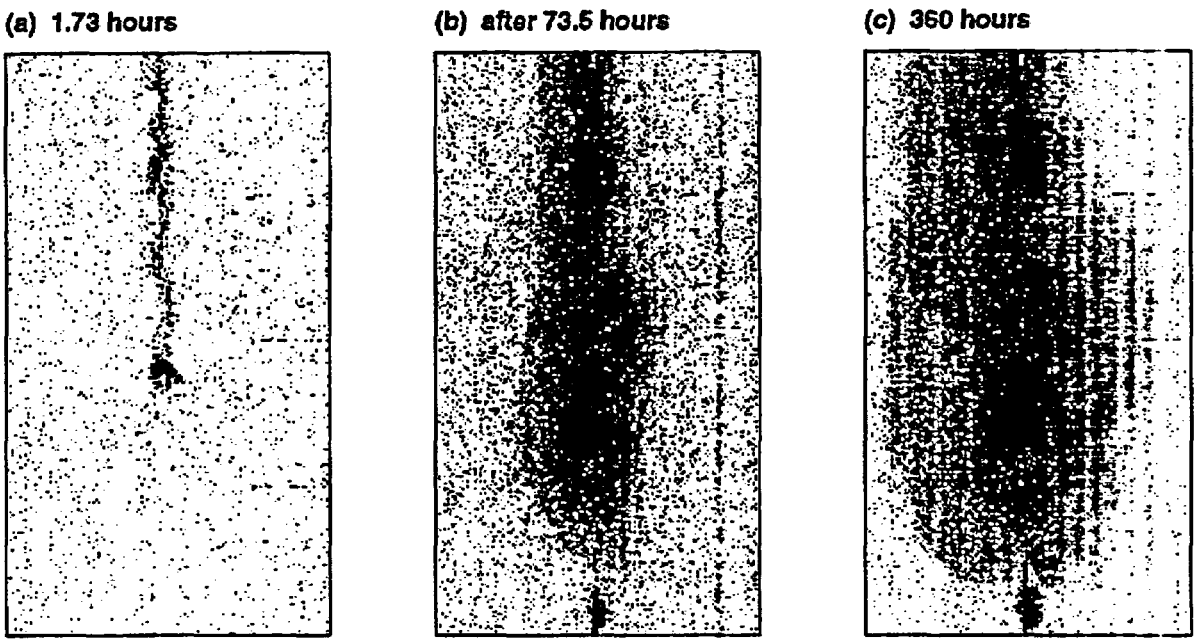

Figure 2-21. X-ray difference image sequence of radiographs of tuff containing a natural fracture. Nine 25-μm gold shims held the fracture open. The sample was initially heated (faint traces of the thermocouples can be seen) to above boiling at the bottom of the sample. The top of the sample was approximately 28°C. Water was ponded on top of the sample near the fracture only (as opposed to the entire sample top). Water quickly flowed into the fracture (similar to the unheated experiment in Fig. 2-18) after which the progress of the fracture flow slowed, shown in (a) 1.73 hours. The point at which flow slowed was found to be a relatively porous low x-ray attenuation region intersected by the fracture. At greater times, flow eventually proceeded past this region (after ~23 hours). There was also considerable lateral imbibition by this time. (b) Shows progress of fluid after 73.5 hours. The darkest region indicates the porous region now highly saturated. At the bottom of the sample centered on the fracture is a second dark region. This is interpreted as a region of high attenuation because of KI precipitation during boiling. (c) At 360 hours, water continued to imbibe laterally but never penetrated past the bottom of the sample.

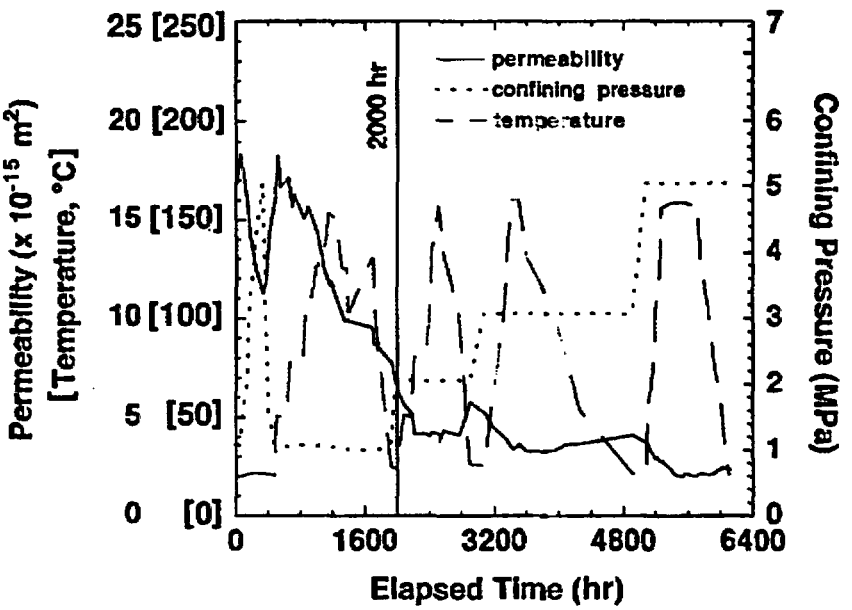

Figure 2-22. Permeability, confining pressure, and temperature of tuff containing a single fracture as a function of elapsed time. The vertical line at 2000 hr is explained in the text.

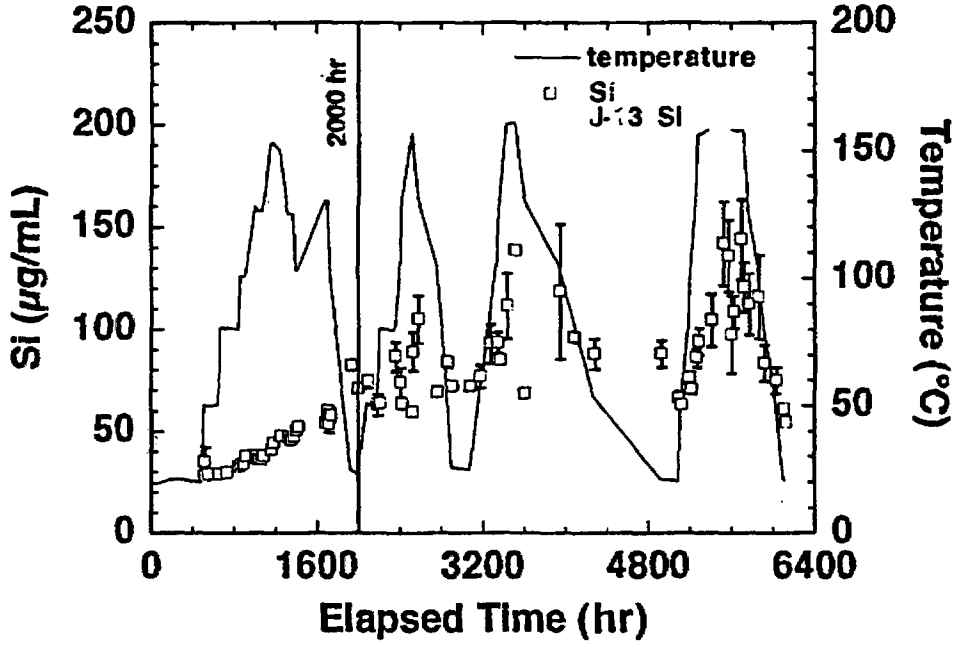

Figure 2-23. Si concentration at selected times during the experiment. Temperature of the experiment is also shown. During the initial pressure and heating cycles before 2000 hr, the Si concentration is relatively low. This is the period of the largest decrease in permeability. After 2000 hr, Si concentration is correlated with temperature (and is saturated with respect to α-cristobalite). Only a small decrease in permeability occurred during the period after 2000 hr.

Table 2-1. Permeability Measurements on Intact Core Sample SPC00504573.4

Temperature, °C	Confining Pressure, MPa	Differential Pressure, MPa	Permeability, µD
23	5.06	1.92	0.12
25	5.07	2.47	0.14
26	5.06	2.59	0.67
26	5.06	2.61	0.20
53	5.06	2.42	0.11
53	5.06	1.91	0.15
83	5.06	2.02	0.17
91	5.06	2.17	0.14
92	5.06	1.60	0.14
130	5.05	1.46	0.13
130	5.05	2.04	0.11
154	5.06	1.61	0.09

Contents

Chapter 3.0 Geochemistry

3.1 Summary of Recent Studies Concerning Geochemical and Mineralogical Evolution of the Near-Field Environment

This section provides a brief summary of the more detailed results presented in Sections 3.4 and Chapters 10.3 and 10.4 of this report. As appropriate, reference is made to the relevant subsections where the detailed information can be located. The results described here use, as a basis, the research summarized in the Preliminary Near-field Environment Report, Volumes I and II. The primary change between the PNFER and this report reflects a change in modeling approach, rather than a change in models or data. The results described in Sections 3.4.2, 3.4.3, and Chapters 10.3 and 10.4, document that limitations in thermodynamic and kinetic data, which are used to describe future mineralogical and chemical changes, constrain our ability to simulate future mineralogical and chemical conditions. Therefore an approach is proposed in which general mineral assemblages ('facies') will be used to describe future mineralogical and chemical conditions, rather than detailed descriptions of mineral assemblages that include specific mineral types and compositions. See Section 3.4.2 for a thorough discussion of this issue.

3.1.1 Near-Field Environment

The results of three studies are reported here that consider the geochemical and mineralogical evolution of the NFE. Since the temperature in this region will be significantly above ambient for many years, evaporation of pore water will occur. One study (Section 3.4.1, Equilibrium Bounds on Water Chemistry and Mineralogical Changes Produced by Near-Field Relative Humidity Changes) examines these effects through numerical simulation of water chemistry changes resulting from evaporation. This study found that the main controls on water composition, and the secondary minerals precipitated as water evaporates, are the composition of the gas phase in equilibrium with the water, and the degree of

evaporation. The numerical simulations show that the coexisting gas phase composition primarily influences pH and redox state of the pore water. If the water remains in equilibrium with air, for example, pH increases significantly, reaching values in excess of 9.5, while the Eh decreases to values on the order of +500 mv. On the other hand, if the water is isolated from the atmosphere and the coexisting gas phase evolves in equilibrium with the water, pH decreases to values less than 6.75 and the Eh becomes more oxidizing, reaching values in excess of +650 mv.

The numerical simulations show that carbonates, phosphate, Al-silicates, and Si polymorphs are saturated in the water at very low degrees of evaporation (<10%). However, the only phases that may develop in significant abundance ($>10^{-3}$ moles per kilogram of water) are carbonate and Si-polymorphs, even at relatively high degrees of evaporation (70% to 90%). At higher degrees of evaporation, chloride salts may precipitate, in volumes that are ca. 10^{-6} of the original fluid volume. However, it is also to be expected that, as evaporation approaches 100%, very small volume films of high salinity brines will form in restrictions (pore throats, restricted channels, etc.), and persist to high temperatures due to the effect of salinity on water vapor pressure. These results suggest that the initial volumes of water entering the dry-out region, after the initial thermal pulse, should be expected to have ionic strengths and salinities that are elevated above ambient, due to dissolution of the previously precipitated mineral phases.

A second study (Section 3.4.2, Testing EQ3/6 and GEMBOCHS Using Fluid-Mineral Equilibria in the Wairakei Geothermal System) was undertaken to determine the extent to which numerical simulations could provide detailed descriptions of which minerals may develop as the repository heats up and cools down. This study used detailed chemical and mineralogical data obtained from the Wairakei Geothermal system in New Zealand, where rocks that are virtually identical to those that make up Yucca Mountain are undergoing alteration as they interact with water at elevated temperatures.

These observational data were compared to the results of numerical simulations, which used thermodynamic data from different sources. Employing a technique which considers the computed temperature-dependent affinity of several different

mineral species, it is possible to identify suites of minerals that are predicted to stably coexist.

Comparison of these predicted mineral suites to the observed mineral assemblages in the Wairakei rocks, allows one to determine the adequacy of different thermodynamic data sets. In all cases, it was possible to select a thermodynamic data set that best reproduced the observed mineral assemblages. Nevertheless, regardless of the data set employed, some minerals are predicted to occur which are not observed in the natural assemblages. This result leads to the conclusion that a facies concept should be used when describing the mineralogical evolution of the repository block. In such a concept, it is recognized that a specific suite of mineral types are expected to occur, but precise prediction of the mineral structures and compositions is not attempted, since small, local variations in intensive and extensive parameters, and uncertainties in thermodynamic and kinetic data, will lead to variations among the mineral assemblages that may actually form.

A third study (Section 3.4.3 Mineralogy-Petrology Observations Regarding the Near-Field Environment; also see "Summary and Synthesis Report on Mineralogy and Petrology Studies for the Yucca Mountain Site Characterization Project," 3-volume report, in preparation) summarizes host rock mineralogy, and some data on mineral stability relevant for near-field processes. The bulk-rock mineralogy within the near-field environment varies with depth and laterally across Yucca Mountain. Comparatively soluble silica phases, including cristobalite, tridymite, opal-CT, and volcanic glass are ubiquitous within the NFE. Limited data illustrate that major amounts of clinoptilolite and mordenite are common directly underlying the host rock in the eastern portion of Yucca Mountain, in and below the lower vitrophyre of the Topopah Spring Tuff. Natural alteration in the lower vitrophyre exemplifies hydrothermal modification of rock porosity by the dissolution of volcanic glass and precipitation of smectite, zeolite, and silica. This is consistent with several previous detailed studies which documented that significant changes in bulk rock solid volume will occur during rock-water interaction and temperature change, and that these changes may significantly modify rock and

fracture porosity and permeability (Meike and Glassley, 1990; Glassley, 1993; Glassley et al., 1994; Lin et al., 1995). Simplified mass balance calculations are presented in Section 3.4.3 that substantiate those previous conclusions. The rates at which mineral reactions will occur in the presence of water are dependent upon dissolution and precipitation kinetics of mineral phases. This was pointed out in the PNFER, where studies completed to 1990 were sumarized in Section 3.3.2, "Kinetics". Since then, several additional studies have been completed (kaolinite, Carroll and Walther, 1990, Nagy, et al., 1991, Nagy and Lasaga, 1993; gibbsite, Nagy and Lasaga, 1992; heulandite, Ragnarsdottir, 1993; cristobalite, Carroll et al., 1995, Renders et al., 1995) that established the kinetics of dissolution for a variety of phases important for modeling repository-relevant rock-water interaction as a function of time. As an addition to this database, recent results of dissolution kinetics experiments on clinoptilolite and analcime are discussed in Section 3.4.3, as well as recent data on the thermodynamic properties of analcime and clinoptilolite. Based on existing data, the dissolution of clinoptilolite appears to be slower than analcime, by a factor near 100. The energetics of solid-solutions and cation exchange models were discussed in the PNFER, Section 3.3.3. In this report, additional models for exchange are discussed in Section 3.4.3.

3.2 Ambient Conditions

The rock unit that is being characterized for waste emplacement is within the Topopah Spring member of the Paintbrush Tuff and has been designated as unit TSw2 on the thermal and mechanical stratigraphic map of the region (Ortiz et al., 1985). TSw2 is a devitrified, welded, rhyolitic tuff and consists of intact blocks separated by fractures. Price et al. (1987) report that the majority of the rock contains fine-grained matrix regions and gray-colored, vapor-phase-altered regions. In addition to these main components, the rock contains small lithophysae (open and closed) and fractures, some of which are filled with quartz, calcite, or other minerals. The porosities of the matrix and vapor-phase-altered regions are between 8 and 49% (Price et al., 1985; 1987). The matrix in the potential repository horizon has an

estimated mean water saturation of 65% (Montazer and Wilson, 1984). Existing data also indicate that the fracture density may be approximately 40 per m^3, and predominantly oriented in the vertical direction (Scott and Castellanos, 1984).

Field, petrographic, electron microprobe, scanning electron microscopy, and X-ray diffraction analyses (Carlos, 1985, 1987, 1989; Schuraytz et al., 1986; Broxton et al., 1987, 1989; Bish and Chipera, 1989; Chipera and Bish, 1989; Carlos et al., 1990, 1993; 1995; Levy et al., 1996) have shown that the tuff consists of both primary and secondary minerals. The primary minerals (sanidine, plagioclase, quartz, biotite, Fe-Ti oxides, allanite, and zircon) were formed at temperatures in excess of 600°C in a magma chamber prior to eruption of the tuff. Secondary minerals such as cristobalite, opal, tridymite, quartz, alkali feldspar, carboantes, and smectite collectively make up a substantial portion of the rock and were formed at temperatures less than 500°C, either during cooling, or later as alteration products. See Section 3.4.3 for a more detailed discussion.

3.3 Processes That Will Modify Ambient Conditions Within the Near-Field Environment

Emplacement of waste packages in this environment will modify the thermal and radiation fields experienced by the host rock, and may lead to complex chemical reactions between the near-field fluids and minerals. The nature of these reactions will depend on a variety of parameters, including the temperature of the environment, the composition of the fluid phase, the rate at which the thermal field changes, the kinetics of reactions, fluid movement rates and pathways, and the amount and nature of radiolysis products. The values of these parameters will change through time as the thermal and radiation fields decay.

Numerous simulations of the hydrological evolution of the WP environment (Nitao and Buscheck, 1989; Buscheck et al., 1991, 1993, 1994; Buscheck and Nitao, 1992, 1993; Nitao et al., 1992) have suggested that four different hydrothermal regimes will form in the vicinity of WPs:

A. A regime in which temperatures are elevated, but are below the boiling point;
B. A regime in which boiling occurs;
C. A regime in which temperatures are above boiling and relative humidities may be low (<95%)
D. A regime in which rock properties are permanently modified, such that rock characteristics during cool down do not recover to pre-emplacement state or values.

These regimes form because pore water will be heated as energy is transferred from the WPs to the surrounding rock. This heating will lead to (1) evaporation of pore water as temperature rises, (2) condensation of water vapor in cooler regions, and (3) boiling and dessication in those regions that reach or exceed the nominal boiling temperature. The local heat budget will thus reflect the local balance between convective and conductive processes. The kinds of processes and effects that may develop are described below.

Regime A: Temperature < $T_{boiling}$. This regime encompasses those areas in which the temperature is between ambient and boiling. It is therefore significant for all regions that undergo heating. As heating occurs, *in situ* pore water is heated and evaporates. Water vapor moving in fractures to lower temperature regions will condense on fracture surfaces. The condensed water either will be imbibed into the matrix by capillary suction or will flow along fracture surfaces, depending on the degree of matrix saturation and the permeability of the fracture surfaces.

Within a few tens of meters of the walls of drifts within which waste has been emplaced, Regime A will persist for a very brief period of time (less than 10 years) because of the rapid rate of heat deposition. In contrast, rock that is hundreds of meters from emplacement drifts will heat up slowly, resulting in the persistence of Regime A for hundreds to thousands of years.

Regime B: $T = T_{boiling}$. Between Regime A and the WPs, temperatures will eventually reach the boiling point for virtually all scenarios with APDs greater than 20 kW/acre. When this condition is met, pore water will vaporize and the resulting steam will migrate to cooler regions where it will condense. Imbibition of the

condensed steam into the matrix of fracture-bound blocks will eventually result in fully saturated rock adjacent to fractures transporting steam. Thus, this rock volume is one in which temperature is essentially constant at the nominal boiling point (~96°C), and much of the rock may be at 100% saturation. Above the repository, this may lead to a region of water refluxing in which water will cycle from the boiling zone to the condensation front (as vapor), and back again (as liquid). Below the repository, refluxing will not occur, but the saturation zone will be widened as condensed hot water flows downward along fractures.

The water that condenses is distilled, and thus must be treated as a liquid that is far from equilibrium with either the host rock or fracture lining minerals. Extensive dissolution of rock matrix and fracture lining minerals must be anticipated for this region.

This regime grows in volume as long as the thermal envelope around the repository is expanding. The regime thickness varies, being virtually zero at the edge of emplacement drift walls when the boiling point is first reached shortly after waste emplacement, to thicknesses that may be in excess of 100 meters several hundred to thousands of years after the repository is closed. This regime will be one of the most chemically active since a high temperature is achieved at full saturation for long time periods (10's to 100's of years).

Regime C: $T > T_{boiling}$. Regime C is bounded by the boiling point isotherm outward, and the repository inward, and represents the region within which temperatures are above the boiling point and relative humidity is variable (<90%). Local persistence of liquid water to very high temperatures, perhaps as high as 150 to 210°C, may result from (1) vapor pressure lowering due to increased salinity of trapped water in restricted pores, (2) boiling point elevation associated with high vapor pressures in block interiors, where vapor migration to fractures may be restricted, or (3) water adsorbed onto mineral surfaces. In general, however, it is expected that this regime will be one dominated by relative drying of the rock, with a persistent but very small volume of water remaining.

Regime D: $T < T_{local\ max}$. This regime develops after the local thermal maximum has been achieved. It encompasses rock that has been physically modified during the

heat-up period, either as a result of mineral dissolution or precipitation or both, or because of mechanical effects. These effects will be evident as changes in bulk and fracture porosity and permeability, and mineralogy. In those regions where saturation had increased above pre-emplacement ambient values, slow removal of water will lead to decreasing saturation. Those regions that had experienced decreased saturation relative to pre-emplacement ambient saturations will begin to rehydrate slowly as the local thermal maximum passes. Current modeling suggests that the rates of resaturation are so slow that it will be 100's of 1000's of years before pre-emplacement ambient saturations are approached. This regime could be realized in all of the other regimes, as cooldown proceeds.

Preliminary modeling has suggested that regimes A and B may quickly pass through the NFE, if thermal loadings are > 100 kw/acre (Nitao, 1988). Nevertheless, complex coupling of fluid velocities and mineralogical reactions in fractures and matrix blocks suggests that mineralogical equilibrium may be approached for some portions of the NFE, even under these conditions (Glassley, 1993). This work has shown that, as evaluated using classic Damkohler numbers or characteristic times of silicate reactions, reaction rates are fast enough to establish chemical steady state relative to transport rates in all regions except the immediate vicinity of emplacement drifts, or in regions of rapid refluxing and rapid fracture flow. At lower thermal loadings, or for certain scenarios in which there is wide spacing between emplacement drifts, regimes A and B may persist within portions of the NFE for hundreds of years. For this reason, the effects of all regimes must be considered as potentially significant for the NFE.

The composition of water that may contact waste containers will depend on the mineralogy of the near-field which, in turn, will be influenced by recrystallization processes that will occur during the period of time prior to incursion of liquid water (see Bish et al., this volume), and on the presence of materials placed within emplacement drifts during construction (see the Introduced and Man-Made Materials Chapter in this report). Within this section (Section 3) only those effects that result from interaction with the *in situ* rock will be discussed.

The primary chemical and mineralogical effects will be the result of interaction of the distilled, condensed water with rock matrix and fracture lining minerals. The main mechanisms responsible for the chemical evolution of the water will be dissolution and precipitation of along flow pathways. Water composition will also be influenced by evaporation, boiling, mixing of waters from different sources or regions, and infiltration. The effects of some of these processes on near-field water composition are discussed in Sections 3.4 and Chapter 10.3.

Such effects of rock-water interaction will change the local hydrological properties of the rock by dissolving pre-existing materials, and thus increasing local porosity and permeability, or precipitating minerals, thus decreasing porosity and permeability. Efforts to characterize these effects along flow pathways are in progress.

3.3.1 References for Sections 3.1, 3.2 and 3.3

Bish, D.L. and S.J. Chipera (1989), *Revised Mineralogical Summary of Yucca Mountain, Nevada,* Los Alamos National Laboratory, NM, LA-11497-MS, 57p.

Broxton, D.E., Bish, D.L., and Warren, R.G., 1987, Distribution and chemistry of diagenetic minerals at Yucca Mountain, Nye County, Nevada. Clays and Clay Minerals, v. 35, p. 89–110.

Broxton, D.E., Warren, R.G., and F.M. Byers, 1989, Chemical and mineralogic trends within the Timber Mountain-Oasis Valley caldera complex, Nevada: evidence for multiple cycles of chemical evolution in a long-lived silicic magma system. J. Geophys. Res., v. 94, p.5961–5985.

Bruton, C.J., Glassley, W.E., and Meike, A., 1995, *Geothermal Areas As Analogues To Chemical Processes In The Near-Field And Altered Zone of Potential Yucca Mountain, Nevada Repository,* Lawrence Livermore National Laboratory, Livermore, Calif., UCRL-ID-119842.

Buscheck, T. A., and J. J. Nitao (1992), *The Impact of Thermal Loading on Repository Performance at Yucca Mountain,* Lawrence Livermore National Laboratory, Livermore, Calif., UCRL-JC-109232.

Buscheck, T. A., and J. J. Nitao (1993), *The Impact of Repository Heat on Thermo-hydrological Performance at Yucca Mountain,* Lawrence Livermore National Laboratory, Livermore, Calif., UCRL-JC-114791.

Buscheck, T. A., D.G. Wilder, and J. J. Nitao, 1993, *Large-scale in situ heater tests for hydrothermal characterization at Yucca mountain,* Lawrence Livermore National Laboratory, Livermore, Calif., UCRL-JC-112445.

Buscheck, T. A., J. J. Nitao and S.F. Saterlie (1994), *Evaluation of Thermo-Hydrological Performance in Support of the Thermal Loading Systems Study,* In Proceedings of the 5th International High Level Nuclear Waste Management Conference, Las Vegas, NV, American Nuclear Society, La Grange, IL, p. 592-610.

Buscheck, T. A., J. J. Nitao, and D.A Chesnut, 1991, *The impact of episodic nonequilibrium fracture-matrix flow on repository performance at the potential Yucca mountain site,* Lawrence Livermore National Laboratory, Livermore, Calif., UCRL-JC-107920.

Carlos, B.A., 1985, Minerals in fractures of the unsaturated zone from drill core USW G-4, Yucca Mountain, Nye County, Nevada. Los Alamos National Laboraotry, LA-10415-MS.

Carlos, B.A., 1987, Minerals in fractures of the saturated zone from drill core USW G-4, Yucca Mountain, Nye County, Nevada. Los Alamos National Laboraotry, LA-10927-MS.

Carlos, B.A., 1989, Fracture-coating minerals in the Topopah Spring Member and Upper Tuff of Calico Hills from drill hole J-13. Los Alamos National Laboraotry, LA-11504-MS.

Carlos, B.A., Bish, D.L., and Chipera, S.J, 1990, Manganese oxide minerals in fractures of the Crater Flat Tuff in drill core USW G-4, Yucca Mountain, Nevada, Los Alamos National Laboratory, LA-11787-MS.

Carlos, B.A., Chipera, S.J., Bish, D.L., and Craven, S.J., 1993, Fracture-lining manganese oxide minerals in silicic tuff, Yucca Mountain, Nevada, U.S.A. Chemical Geology, v. 107, p. 47–69.

Carlos, B.A., Chipera, S.J., Bish, D.L., and Raymond, R., 1995, Distribution and chemistry of fracture-lining zeolites at Yucca Mountain, Nevada, in Natural Zeolites '93 (D.W. Ming and F.A. Mumpton, eds), Int. Comm. Natural Zeolites, Brockport, N.Y., p. 547–563.

Carroll S. A., Mroczek, E., Bourcier, B., Alai, M. and Ebert, M. (1995) Comparison of field and laboratory precipitation of amorphous from geothermal waters at 100°C. Lawrence Livermore National Laboratory Yucca Mountain Site Characterization Project Milestone MOL207.

Carroll, S.A. and Walther, J. V., 1990. Kaolinite dissolution at 25oC, 60oC, and 80oC. Amer. j. Sci., v. 290, p. 797-810.

Chipera, S. J., and D. L. Bish (1989), *Quantitative X-ray Diffraction Analyses of Samples Used for Sorption Studies by the Isotope and Nuclear Chemistry Division, Los Alamos National Laboratory,* Los Alamos National Laboratory, Los Alamos, NM, LA-11669-MS, 19 pp.

Glassley, W.E. (1993), Coupled Hydro-Geochemical Processes and Their Significance for Yucca Mountain Site Characterization, in *Proceedings of FOCUS '93,* Las Vegas, NV, American Nuclear Society, La Grange, IL, p. 221–224

Glassley, W.E., Bruton, C.J., Bourcier, W.L., 1994, Testing long-term predictions from hydrogeochemical models. Materials Res. Soc. Symposium Proc. Vol 333, p.805-810.

Levy, S.S., Norman, D.I., and Chipera, S., 1996, Alteration history studies in the exploratory studies facility, Yucca Mountain, Nevada, USA *Mat. Res. Soc. Symp.,* v. 412, p. 783–790.

Lin, W., Roberts, J.J., Glassley, W.E., and Ruddle, D., 1995. The effect of rock-water interaction on permeability. Proceedings of the Eigth International Congress on Rock Mechanics, Tokyo, Japan, and Lawrence Livermore National Laboratory UCRL-JC-119574.

Meike, A. and Glassley, W.E., 1990, In situ observation of the alpha/beta cristobalite transition using high voltage electron microscopy. Materials Res. Soc. Symposium Proc. Vol 178, p. 631-639.

Montazer, P., and W. E. Wilson, 1984, *Conceptual Hydrologic Model of Flow in the Unsaturated Zone, Yucca Mountain, Nevada,* U.S. Geol. Survey, Denver, CO, Water Resources Inv. Rep. 84-4345.Scott and Castellanos, 1984

Nagy, K.L., and Lasaga, A.C., 1992, Dissolution and precipitation kinetics of gibbsite at 80oC and pH 3: The dependence on solution saturation state. Geochim. Cosmochim. Acta, v. 56, p.3093-3111.

Nagy, K.L., and Lasaga, A.C., 1993, Simultaneous precipitation kinetics of kaolinite and gibbsite at 80oC and pH 3. Geochim. Cosmochim. Acta, v. 57, p.4329-4336.

Nagy, K.L., Blum, A.E., and Lasaga, A.C., 1991, Dissolution and precipitation kinetics of kaolinite at 80oC and pH 3: The dependence on solution saturation state. Amer. J. Sci., v. 291, 649-686.

Nitao, J.J. (1988), *Numerical Modeling of the Thermal and Hydrological Environment Around a Nuclear Waste Package Using the Equivalent Continuum Approximation: Horizontal Emplacement,* Lawrence Livermore National Laboratory, Livermore, CA, UCID-21444.

Nitao, J.J. and T.A. Buscheck, 1989, *On the movement of a liquid front in an unsaturated, fractured porous medium, Part I.* , Lawrence Livermore National Laboratory, Livermore, Calif., UCID-21714.

Nitao, J.J., T.A. Buscheck and D.A. Chesnut, 1992, *The implications of episodic nonequilibrium fracture-matrix flow on site stability and total system performance* , Lawrence Livermore National Laboratory, Livermore, Calif., UCRL-JC-109216.

Ortiz, T. S., R. L. Williams, F. B. Nimick, B. C. Whittet, and D. L. South (1985), *A Three-Dimensional Model of Reference Thermal/Mechanical and Hydrologic Stratigraphy at Yucca Mountain, Southern Nevada,* Sandia National Laboratories, Albuquerque, NM, SAND84-1076.

Price, R. H., F. B. Nimick, J. R. Connolly, K. Keil, B. M. Schwartz, and S. J. Spence (1985), *Preliminary Characterization of the Petrologic Bulk and Mechanical Properties of a Lithophysal Zone within the Topopah Spring Member of the Paintbrush Tuff,* Sandia National Laboratories, Albuquerque, NM, SAND84-0860.

Price, R. H., J. R. Connolly, and K. Keil (1987), *Petrologic and Mechanical Properties of Outcrop Samples of the Welded, Devitrified Topopah Spring Member of the Paintbrush Tuff,* Sandia National Laboratories, Albuquerque, NM, SAND86-1131.

Ragnarsdottir, K.V., 1993, Dissolution kinetics of heulandite at pH 2-12 and 25 degrees C. Geochim. Cosmochim. Acta, v. 57, p. 2439-2449.

Renders, P. J. N., Gammons, C. H., and Barnes, H. L. (1995) Precipitation and dissolution rate constants for cristobalite from 150 to 300°C. *Geochimica et Cosmochimica Acta,* 59, 77-85.

Schuraytz, B. C., T. A. Vogel, and L. W. Younker (1986), *Geochemical Gradients on the Topopah Spring Member of the Paintbrush Tuff: Evidence for Eruption Across a Magmatic Interface,* Lawrence Livermore National Laboratory, Livermore, CA, UCRL-53698.

3.4 Results of Recent Geochemical Research Relating To Near-Field Geochemistry And Mineralogy

3.4.1 Equilibrium Bounds on Water Chemistry and Mineralogical Changes Produced by Near-Field Relative Humidity Changes, by William E. Glassley, Lawrence Livermore National Laboratory

3.4.1.1 Introduction. Radioactive decay heat will lead to interaction of rock and water at high temperatures in the vicinity of emplacement drifts (Buscheck and Nitao, 1992; Nitao et al., 1992; Buscheck, et al., 1993). In order to determine how possible thermal histories will affect water chemistry and near-field mineralogy, the evolution of water compositions over a range of scenarios must be determined. This section describes how water chemistry may change due to evaporation. It does not consider the role of rock-water interaction, or the role of boiling, in the development of water compositions. Those aspects will be treated in a later report.

Evaporation of water is an important consideration for establishing the nature of secondary precipitates that may be deposited along fracture surfaces, in rock pores during various phases of the thermal evolution of the repository, or on waste containers from dripping water. The specific precipitates that may develop will reflect the initial water composition. In using J-13 well water (see below) this study considers those scenarios in which water evaporation begins with a dilute water that is close to equilibrium with high silica rhyolite similar to that which makes up the repository horizon at Yucca Mountain.

The chemical consequences of evaporation are distinct from those of boiling, due to the contrast in behavior of dissolved gases during evaporation and boiling. During open-system boiling, dissolved, volatile weak electrolytes (e.g., CO_2, H_2S) will exsolve from the liquid phase to varying degrees, depending upon the water composition. Their behavior can be described by means of Henry's law relationships which can take into account the relative "volatilities" of the dissolved species (Drummond and Ohmoto, 1985). Rayleigh distillation models can then be used to describe the overall evolution of the water chemistry during boiling (e.g., Arthur and Murphy, 1989; Criscenti and Arthur, 1991). Evaporation, on the other hand, can

be approximated as a simple removal of water from a system, with the dissolved gas behavior expressed by temperature-dependent changes in the equilibrium partial pressure of the gas coexisting with the water.

3.4.1.2 Previous Work. Numerous studies have summarized the chemical characteristics of natural ground waters and pore waters in the vicinity of the repository block (Ogard and Kerrisk, 1984; Benson and McKinley, 1985; Yang et al., 1988; Bruton, et al., 1993). Those waters provide an indication of the degree of local compositional variability that may be expected. As a step in determining how these water compositions may be influenced by evaporation, a water composition typical of well J-13 was used in the simulations described here. This water was selected because it is a typical example of the type of water that occurs in the region, that is, it is a relatively dilute chloride- and sulfide- and sulfate-poor, bicarbonate groundwater (Glassley, 1986; Harrar, et al, 1990; Bruton, Glassley and Viani, 1993). Other water compositions will be considered as funding permits.

3.4.1.3 Approach. Evaporation of J-13 water was simulated using the EQ3/6 code package (Wolery, 1992 a,b; Wolery and Daveler, 1992) by removing water at a specified rate during reaction progress in an EQ6 simulation (Wolery and Daveler, 1992). Water was evaporated at constant temperatures of 31°C and 90°C. It was also evaporated at increasing temperatures using arbitrary relationships between amount of water evaporated, and temperature change, from 31°C to 95°C (see Fig. 3.4-1 for the different temperature-evaporation trends used). Differences in the relationship between temperature and the moles of water evaporated had no discernible effect on the results. The variable temperature calculations allowed consideration of the effects of disequilibrium between heating and evaporation rate.

These simulations were conducted with and without controls on the composition of the coexisting gas phase. The simulations done without gas-phase controls simulate scenarios in which there is no influence of atmospheric gases on the composition of the evolving gases or water. Simulations conducted in which O_2 and CO_2 gas fugacities were assumed to remain constant at their atmospheric values (.2 and .0004 bars, respectively) address scenarios in which equilibration of atmospheric gases with pore waters is rapid, relative to the rate at which

evaporation occurs. Although disequilibrium may occur between water and gas, these simulations bound the extreme case where equiulibrium is achieved, and water pH may be most severely affected by carbonate.

Simulations were conducted with and without precipitation of quartz, tridymite and talc. Suppression of these phases simulates scenarios in which metastable precipitation of other phases is allowed to occur. This is consistent with experimental studies in which the aqueous SiO_2 concentration is controlled by the least stable silica polymorph present in the coexisting rock, and the fact that, at low temperatures similar to those considered here, the minerals that form most readily are those which most significantly lower the system's free energy and not necessarily the phases that are thermodynamically stable (see summary in Bruton et al., 1993). Although a number of other phases could also be justifiabley suppressed, these particular ones were selected because they are among those phases which commonly occur as precipitates in simulations, but which are not observed in experimental studies. Simulations in which these minerals were not suppressed consider scenarios in which the most thermodynamically stable phases precipitate. These contrasting approaches allow consideration of the relative importance of metastable precipitation of phases on the aqueous chemistry.

As a note of caution, it must be pointed out that the phases which occur as the "most thermodynamically stable" are identified as such on the basis of the thermodynamic properties compiled in the EQ3/6 database. Uncertainties in the values of thermodynamic properties, which are inherent in a compilation of this sort (see Johnson, et al., 1992 for discussion of this issue), make problematic the identification of the actual phases that would precipitate during evaporation. The phases that appear in the simulations, therefore, must be viewed as an approximation to the mineral assemblages that would develop in the course of evaporation. In addition, metastable crystallization of phases, due to nucleation or other kinetic effects in real systems, may also influence the actual sequence of minerals that would form during evaporation. Hence, the general sequence of precipitation that is obtained during the simulations may not be the same as that observed in the laboratory or in nature. However, efforts to evaluate the accuracy of

simulations have been undertaken, using data from the New Zealand geothermal system (see Section 3.4.2).

Interaction with rock was not considered. These simulations, therefore, apply to the extreme case where evaporation occurs at very high rates, relative to the rates of dissolution or precipitation of rock components. Although later studies were planned that would consider the consequences of reacting rock with evaporating waters, such studies have been indefinitely postponed due to budgetary and schedule constraints. Laboratory studies and simulations of rock interacting with J-13 well water have been carried out over a range of conditions, and are reported elsewhere (Knauss and Peiffer, 1986; Knauss et al., 1986; Knauss, 1987; Delaney 1985; Bruton et al, 1993).

The simulations reported here were conducted using the extended Debye-Hückle activity coefficient model (Helgeson, 1969; Helgeson et al., 1970). This model is applicable only to systems in which the ionic strength is less than ca. 0.5 molal, which is approximately equivalent to evaporation of 55 moles of water from 1 kg of J-13 well water (1 kg of water equals ca. 55.51 moles of water). Although the simulations were carried to higher degrees of evaporation, only the results that were obtained well within the region over which the extended Debye-Hückle approach is valid (i.e., for <53 moles of evaporated water, which is approximately 95% evaporation) are reported here. Simulations at higher ionic strengths, using more appropriate models of ion interactions, will be conducted when applicable data are available.

3.4.1.4 Results and Discussion. The results of the simulations are shown in Figs. 3.4-2 through 3.4-14.

The effect of controlling gas composition can be dramatic, for some aqueous species and solids. In those cases where the effect is evident, *circles* are used in the figures to indicate values computed with no gas phase controls. *Squares* are used to indicate cases where gas phase controls were implemented. Solid symbols indicate simulations in which quartz, tridymite and talc precipitation was not suppressed, and *open* symbols are used for cases where they were suppressed.

Although calculations were conducted for both constant temperature and varying temperature conditions, the results were similar. Hence, the following discussion and data presentations only deal with the case in which temperature changed during evaporation.

Evaporation that occurs in the absence of any controls on the composition of the coexisting gases results in water compositions in which the pH remains near neutral, and the Eh slightly oxidizing (Figs. 3.4-2 and 3.4-3). In addition, Na (Fig. 3.4-4), S (Fig. 3.4-5), Cl (Fig. 3.4-6), and F (Fig. 3.4-7) concentrations increase linearly as the activity of H_2O decreases. For Na, S, and Cl, no solids precipitate that incorporate these elements, hence their concentrations increase by the same factor (i.e., 23 times). F, on the other hand, is incorporated into fluor-apatite and fluorite during evaporation. However, fluor-apatite precipitates during the very early stages of evaporation and remains constant in abundance, and fluorite only occurs in small concentrations toward the end of the evaporation, hence the relative behavior of F in solution mimics that of Na, S, and Cl, but at a lower degree of enrichment (ca. 15 times).

The concentrations of Ca (Fig. 3.4-8), P (Fig. 3.4-9), and Si (Fig. 3.4-10), on the other hand, are effected by precipitation of carbonates, phosphates, and silicates as evaporation proceeds. Changes in Ca concentration mainly correlate with precipitation of calcite, which is the most abundant precipitate formed, after the silica polymorphs (Fig. 3.4-11). Dolomite precipitation also influences Ca concentration, but to a small degree (Fig. 3.4-12). P variation reflects the effects of precipitation of fluor-apatite. Si variation is controlled by the solubility limits of quartz and chalcedony, with which the waters are saturated; the particular polymorph that occurs in the simulations reflects whether quartz precipitation was inhibited.

For conditions in which the coexisting gas phase is fixed at atmospheric O_2 and CO_2 fugacities, the fluid composition evolution is significantly different in pH, Eh, Ca, and Si. Because of the effect CO_2 fugacity has on the stability of carbonate and bicarbonate ions, the pH is more alkaline, reaching values >9.0. In addition, the Eh is more oxidizing at low temperature, but becomes more reducing at high

temperatures, than for the simulations in which the gas composition is uncontrolled. This behavior reflects both the effect of CO_2 abundance on the carbonate-bicarbonate system, and the retrograde solubility of calcite at elevated temperatures. Together, these processes influence the relative solubilities of components that make up the main redox couples in the system (ferric-ferrous and sulfide-sulfate). These effects lead to much greater Ca and Si concentrations in solution. Cl, F, S, and P concentrations are virtually the same as in the case where gas composition is not controlled.

It is clear in these simulations that the specific silica polymorph that is allowed to precipitate has only a second order effect on the solution composition. This is mainly expressed in the Si and Ca concentrations. The latter is sensitive to the impact of Si concentration on the occurrence of Ca-bearing aluminosilicates (e.g, saponite clays and the zeolite stilbite; Figs. 3.4-13 and 3.4-14).

In all of these simulations, regardless of the specific conditions imposed on the system, fluor-apatite, nontronite, and pyrolusite occur as small abundance precipitates at constant concentration regardless of the degree of evaporation. Their occurrence reflects the low solubilities of these solids.

3.4.1.5 Conclusions. Simulated evaporation of J-13 well water suggests that the most significant variable that controls the evolution of the water chemistry and the solids that precipitate, is the composition of the coexisting gas phase, and whether that gas phase is in equilibrium with the water. The most significant effects can be seen in the divergence of pH and Eh (Figs. 3.4-2 and 3.4-3) as evaporation proceeds with and without equilibrium with a gas phase. These effects influence total concentration of elements that occur in silicates and carbonates that have solubilities sensitive to moderate changes in solution pH. Conservative elements (Cl, F, S) change concentration linearly as evaporation proceeds, since they do not play a role in any of the precipitates that form.

Further work should focus on how these changes will be modified by rock-water interaction during evaporation, and on bounding the range of water variability using the spectrum of water chemistries exhibited by the analyzed groundwaters.

3.4.1.6 References

Arthur, R.C., and W.M. Murphy, 1989, An Analysis of Gas-Water-Rock Interactions During Boiling in Partially Saturated Tuff, Sci. Geol. Bulletin, vol. 42, #4, p. 313–327.

Benson, L.V., and P.W. McKinley, 1985. Chemical Composition of Groundwater in the Yucca Mountain Area, Nevada, 1971-1984, U.S. Geological Survey, Denver, CO, OFR-85-484. (NNA.900207.0281)

Bruton, Carol, William E. Glassley, and Brian E. Viani, 1993. *Preliminary Near-Field Environment Report Volume II: Scientific Overview of Near-Field Environment and Phenomena, Chapter 3, Geochemistry,* Lawrence Livermore National Laboratory UCRL-LR-107476 Vol. 2, p. 37–60.

Buscheck, T.A., and John. J. Nitao, 1992, *The Impact of Thermal Loading on Repository Performance at Yucca Mountain,* in Proceedings of the Third International Conference on High Level Radioactive Waste Management, Las Vegas, Nevada, p. 1003–1017.

Buscheck, T.A., John. J. Nitao, and Dwayne A. Chesnut, 1993, *Preliminary Near-Field Environment Report Volume II: Scientific Overview of Near-Field Environment and Phenomena, Chapter 1 Hydrothermal Modeling,* Lawrence Livermore National Laboratory UCRL-LR-107476.Vol. 2, p. 5–27.

Criscenti, L.J., and R.C. Arthur, 1991, The Calculated Effects of Isothermal Boiling on Tuff-Water Interactions, Radiochimica Acta, v. 52/53, p. 513–517.

Glassley, W.E., 1986. Reference Waste Package Environment Report. Lawrence Livermore National Laboratory, Livermore, CA UCRL-53726 (NNA.920506.0035)

Harrar, J.E., J.F. Carley, W.F. Isherwood, E.Raber, 1990. Report of the Committee to Review the Use of J-13 Well Water in Nevada Nuclear Waste Storage Investigations. Lawrence Livermore National Laboratory, Livermore, CA UCID-21867 (NNA.910131.0274)

Helgeson, H.C., 1969. Thermodynamics of Hydrothermal Systems at Elevated Temperatures and Pressures. American Journal of Science, vol. 267, pp. 729–804.

Helgeson, H.C., T.H. Brown, A. Nigrini, and T.A. Jones, 1970. Calculation of Mass Transfer in Geochemical Processes Involving Aqueous Solutions. Geochimica Cosmochimica Acta, vol. 34, pp. 569–592.

Johnson, J. W., Eric H. Oelkers, and Harold C. Helgeson, 1992. SUPCRT92: A Software Package For Calculating The Standard Molal Thermodynamic Properties of Minerals, Gases, Aqueous Species, and Reactions From 1 to 5000 Bars and 0 to 1000°C. Computers and Geosciences, vol. 18. p. 899–947.

Knauss, K.G., 1987. Zeolitization of Glassy Topopah Spring Tuff Under Hydrothermal Conditions, Mat. Res. Soc. Symp. Proc., vol. 84, p. 737–745. (NNA.920302.0050)

Knauss, K.G., J.M. Delany, W.J. Beiriger, and D.W. Peiffer, 1986, Hydrothermal Interaction of Tonopah Spring Tuff with J-13 Water As a Function of Temperature, Mat. Res. Soc. Symp. Proc., vol. 44, pp. 539–546 (NNA.870407.0364)

Knauss, K.G., and D.W. Peiffer, 1986, Reaction of Vitric Topopah Spring Tuff and J-13 Groundwater Under Hydrothermal Conditions Using Dickson-Type, Gold-Bag

Rocking Autoclaves, Lawrence Livermore National Laboratory, Livermore, CA UCRL-53795 (NNA.891102.0117)

Nitao, J.J., T.A. Buscheck, and D.A. Chesnut, 1992, The Implications of Episodic Nonequilibrium Fracture-Matrix Flow on Site Suitability and Total System Peformance, in Proceedings of the Third International Conference on High Level Radioactive Waste Management, Las Vegas, Nevada, p. 279–296.

Ogard, A.E., and J.F. Kerrisk, 1984. Groundwater Chemistry Along Flow Paths Between a Proposed Repository Site and the Accessible Environment. Los Alamos National Laboratory, Los Alamos, NM, LA-10188. (NNA.890907.0118)

Wolery, T.J., 1992a, EQ3/6, A Software Package for Geochemical Modeling of Aqueous Systems: Package Overview and Installation Guide. Lawrence Livermore National Laboratory, Livermore, CA UCRL-MA-110662 PT. I

Wolery, T.J., 1992b, EQ3NR, A Geochemical Program For Aqueous Speciation-Solubility Calculations: Theoretical Manual, User's Guide, and Related Documentation. Lawrence Livermore National Laboratory, Livermore, CA UCRL-MA-110662 PT. III

Wolery, T.J., and S. A. Daveler, 1992, EQ6, A Computer Program for Reaction Path Modeling of Aqueous Geochemical Systems: Theoretical Manual, User's Guide, and Related Documentation (Version 7.0). Lawrence Livermore National Laboratory, Livermore, CA UCRL-MA-110662 PT. IV

Yang, I.C., A.K. Turner, T.M. Sayre, and P. Montazar, 1988. *Triaxial-Compression Extraction of Pore Water from Unsaturated Tuff, Yucca Mountain, Nevada,* U.S. Geological Survey, Water Resources Investigations Report 88-4189 (NNA.890309.0161)

3.4.2 Testing EQ3/6 and GEMBOCHS Using Fluid-Mineral Equilibria in the Wairakei Geothermal System, by Carol Bruton, Lawrence Livermore National Laboratory

3.4.2.1 Introduction. It is necessary to establish well defined bounds on the range of chemical conditions that may develop within a nuclear waste repository in order to evaluate the extent to which corrosion of waste containers, dissolution of waste forms, and transport of radionuclides may occur. This information forms part of the basis for total system and sub-system performance assessment evaluations, and site suitability determination.

To achieve this goal, simulations of geochemical processes over long time periods (i.e., thousands of years) are required, since experimental studies can be conducted only for a few years, at most. However, the accuracy and precision of numerical simulations is often limited by the supporting thermodynamic and kinetic data that are used in the simulations. One method for ascertaining the accuracy and precision of simulation capabilities is to compare the results of simulations with observed geochemical and mineralogical characteristics of natural systems in which the same processes occur that are anticipated in the potential repository.

The ability of the EQ3 and EQ6 geochemical modeling codes and the GEMBOCHS thermodynamic data bases (Wolery, 1992; Wolery and Daveler, 1992) to simulate geochemical changes in the post-emplacement environment at the potential repository at Yucca Mountain was tested using observed mineral-fluid relations in the Taupo Volcanic Zone of New Zealand. This site was selected for use in the comparisons because of its close geological similarity to the potential repository site, and because processes of interest and an extensive data base are accessible for study (Bruton et al., 1995). Comparisons between observed equilibria and simulations of field relations in the Wairakei geothermal system were used to test the codes and data bases in high temperature (>200°C) systems. Tests at lower temperatures have been planned, but have yet to receive funding.

The conditions selected for initial evaluation are those that most closely approximate processes in the near-vicinity of emplacement drifts. Numerical models of the post-emplacement temperature field (Buscheck and Nitao, 1993) show the potential for peak temperatures about 200°C near the waste, and attendant changes in relative humidity, "drying-out," boiling, condensation, one- and two-phase fluid flow, mineral precipitation and dissolution, ion exchange, and surface complexation. The work described here documents tests conducted to evaluate the ability of the EQ3/6 geochemical modeling codes and their associated GEMBOCHS thermodynamic data bases to model mineral-fluid relations in order to:

1. Test the conditions and manner in which EQ3/6 can be used to forecast changes in rock and fluid chemistry during the flow of heated fluids through silicic rocks;
2. Test the thermodynamic data in GEMBOCHS and to select appropriate thermodynamic data when multiple sources exist.

To accomplish this work, it is necessary to select representative water and gas compositions from Wairakei wells (called boreholes), reconstruct downhole fluid compositions, calculate the minerals predicted to be in equilibrium with each fluid, and compare simulation results with observed vein and vug mineralogy.

All calculations described were carried out using version 7.2a R134 of EQ3 and version 7.2a R130 of EQ6. The SUPCRT and COM subsets of the R24 version of GEMBOCHS were used as indicated.

3.4.2.2 Fluid chemistry: choice of representative waters and gases. Reyes, Giggenbach and Christenson (1993) reviewed available well discharge data for the Wairakei area. Details of the process of reconstructing downhole fluid chemistry from surface gas and water analyses are described in Bruton (1995). Tables 3.4-1 and 3.4-2 summarize the as-analyzed and reconstructed fluid analyses used in this study.

Redox state was set by the $SO_4^{=}/H_2S$ buffer, assuming an initial concentration of aqueous H_2S of 0.3 mg/kg in WK-28 based on concentration data from nearby wells. This assumption represents an initial test of modeling strategies regarding control of redox in the subsurface. This initial study did not focus on phases containing Mg, Fe,

and/or S as primary components. The latter two elements are strongly dependent on redox state, which can vary significantly in hydrothermal systems owing to boiling. Chlorite is the major mineral phase containing Mg in these systems, but no chlorite solid solutions are provided for in the SUPCRT data base. The COM data file provides for an ideal solid solution model for chlorite as well as saponites, which are Mg-rich smectites.

3.4.2.3 Alteration mineralogy. Alteration mineralogy seems to be strongly controlled by temperature. A representative set of minerals, called a mineral facies, is composed of secondary minerals which commonly occur in a given temperature range. The minerals in the facies occur in various combinations, called mineral assemblages. Different mineral assemblages in a given facies can coexist on spatial scales as small as a single hand specimen or petrographic thin section (Bruton, et al., 1994).

Mineral assemblages identified at downhole temperatures of 240-260°C in the main feed zones at Wairakei (wells WK-28, 72 and 81) (Reyes, Giggenbach and Christenson, 1993; Steiner, 1977) include: wairakite; adularia (a variety of K-feldspar); epidote solid solution; wairakite ± quartz; quartz + adularia; wairakite+epidote±calcite; albite+quartz+epidote+chlorite+calcite; prehnite; wairakite+prehnite.

The above mineral assemblages represent the secondary minerals that coexist with the fluids described in the previous section.

3.4.2.4 Calculational approach. Three reconstructed downhole fluids were used to compute predicted secondary mineralogy at depth, which was then compared to observed mineral assemblages.

The approach taken was as follows.

- Select representative sets of coexisting water and gas analyses from Wairakei wells and reconstruct downhole fluid chemistry by adding steam and gases lost during production back into the liquid phase.
- Identify mineral assemblages along fractures and flow zones closely associated with source of produced fluids.

- Calculate affinity (A) of potential secondary minerals where $A=RT\ln(Q/K)$[1] using version R24 of the SUPCRT and COM subsets of the GEMBOCHS thermodynamic data base.
- Compare calculated and observed mineral assemblages.

Phase relations were examined with the use of affinity-temperature diagrams. Affinity is a measure of a mineral's saturation state. If:

A=0, the mineral is at equilibrium with the solution

A<0, the mineral is undersaturated with respect to the solution

A>0, the mineral is supersaturated with respect to the solution.

Potential mineral assemblages are inferred when multiple affinity-temperature curves have a common intersection at A=0. Identification of potential mineral assemblages in this manner is especially useful when thermodynamic data may be suspect or kinetics controls the formation of precipitates. Downhole temperature can be estimated by noting the temperature at which the affinity curves converge on zero (equilibrium).

Calculations assume that pressures correspond to the liquid/vapor saturation curve for H_2O. Solid solutions for epidote and muscovite were considered. Clinozoisite as used in this paper refers to the clinozoisite end member of an ideal epidote solid solution (Bird and Helgeson, 1980) with an activity of 0.4, as calculated from microprobe analyses of epidote at Wairakei. Muscovite refers to the muscovite end member of an ideal illite solid solution with an activity of 0.5, estimated by analogy to illite from the Kawerau geothermal field in New Zealand.

3.4.2.5 Results: Water-rock equilibrium calculations. Comparisons between predicted and observed mineral stabilities that will be described in the following sections allowed us to determine:

1. Quartz solubility data that best describes controls of aqueous silica concentrations at temperatures greater than about 200°C.
2. Importance of gas phase chemistry to mineral equilibria, and mineral indicators of variations in pH.

---

1. Q = ion activity product; K = equilibrium constant; R = gas constant; T = temperature in K.

3. Thermodynamic data for aqueous Al species that best describe mineral stabilities at temperatures greater than about 200°C.
4. Corrections to thermodynamic data for wairakite, a high temperature zeolite.
5. Need for better usage and interpretation of calorimetric thermodynamic data for zeolites.
6. Appropriateness of utilizing the mineral facies concept to infer mineral stability rather than exact prediction of the precise secondary minerals to precipitate at temperature.

In all affinity-temperature diagrams shown below, some discretion was used to select the minerals to be plotted. Phases were chosen based on their occurrence in observed mineral assemblages, and their extent of supersaturation or closeness to equilibrium. Minerals that were generally depicted on the diagrams include: quartz, K-feldspar, albite, muscovite, calcite, prehnite, wairakite and clinozoisite. These minerals most often appear in stable mineral assemblages identified by Reyes in the temperature range 240-260°C (Reyes, et al., 1993).

3.4.2.5.1 Choice of quartz solubility data: Well WK-81. Figure 3.4-15 shows differences in the concentrations of SiO_2 (aq) predicted according to quartz solubility data from Walther and Helgeson (1977) and Fournier (1983). Fournier's data predict significantly higher SiO_2 (aq) concentrations in solution than the quartz solubility data of Walther and Helgeson (1977) at temperatures exceeding about 150°C.

Figures 3.4-16 and 3.4-17 contrast computations of mineral equilibria in Wairakei well WK-81 using Fournier (1983) and Walther and Helgeson (1977) data, respectively. The adiabatic quartz geothermometer based on data from Walther and Helgeson predicted a downhole temperature of 263°C, whereas that of Fournier predicted 240°C. As can be seen from Figs. 3.4-16 and 3.4-17, the affinity curves seem to converge more closely on the downhole temperature predicted using the Fournier (1983) quartz solubility data. It is apparent that calculated mineral equilibria more closely correspond to observed mineralogy when Fournier's (1983) quartz geothermometer is used.

Ragnarsdottir and Walther (1983) measured the pressure dependence of quartz solubility at 250°C, and concluded that the pressure dependence accounts for the

discrepancy between results of Fournier and Walther and Helgeson. Calculations with GEMBOCHS are currently restricted to the liquid/vapor saturation curve for H_2O. However, according to the results of Ragnarsdottir and Walther (1983), the hydrostatic fluid pressures maintained at Wairakei are not large enough to impact quartz solubility significantly.

For calculations of quartz solubility above about 200°C at the present time, the quartz solubility data of Fournier (1983) should be used in place of that of Walther and Helgeson (1977), which is contained in all current versions of GEMBOCHS.

3.4.2.5.2 Impact of changes in gas chemistry: WK-72. Vapor compositions vary with time owing to production and the partitioning of components between vapor and liquid phases. Figure 3.4-18 shows the variation of CO_2 with time in wells WK-28, 72 and 81. Changes of this magnitude will greatly impact calculated fluid-mineral equilibria owing to its impact on pH. The variation of component ratios, discharge enthalpy and other well parameters with time can be used to try to derive reasonable estimates of the quantity of volatile species in the original, undisturbed fluids. However, uncertainties persist.

Use of different gas compositions for a given fluid analysis can produce significant changes in predicted mineralogy owing to the impact of CO_2 on pH. The greater the CO_2 content of the produced vapors, the lower the predicted pH of the reconstructed downhole fluid. For example, the calculated downhole pH is reduced from 6.2 to 5.9 when the 3/78 gas analysis for WK-72 with 258 mmol CO_2/mol TD is used rather than the 5/61 analysis with 102 mmol CO_2/mol TD, where TD is defined as the total discharge, that is, the combined chemistry of the steam and liquid phases.

Figures 3.4-19 and 3.4-20 illustrate the mineralogical consequences of using the high (3/78) and low (5/61) CO_2 gas estimates, respectively. The stabilities of K-feldspar and albite are largely unaffected by changes in pH, whereas the stabilities of prehnite, muscovite and calcite are sensitive to pH, as reflected by the shift of their affinity-temperature curves. The dissolution/precipitation of muscovite, prehnite and calcite may thus serve as sensitive indicators of changes in downhole fluid

chemistry. In contrast, the stabilities of K-feldspar and albite are largely unaffected by uncertainties in gas chemistry and pH, and are therefore good tests of equilibrium and the adequacy of thermodynamic data for aqueous Al species.

Figures 3.4-19 and 3.4-20 also suggest that the earlier, lower CO_2 gas analysis better represents downhole conditions, as shown by the fact that the curves tend to converge more closely on the downhole temperature than in the high CO_2 gas case.

This finding may have implications for Yucca Mountain with regard to the timing and mass of ^{14}C release. If released as CO_2 and in sufficient quantities while water is present, the waters can be made more chemically aggressive if initially neutral, or neutralized if initially alkaline from contact with cementitious materials in the engineered barrier system. The consequences of interactions with cementitious materials before contact with tuff must also be taken into account.

Of perhaps more importance is the variation in gas phase chemistry, particularly CO_2 content, in the vapor phase in the two-phase (gas and water) zones predicted to occur by Buscheck and Nitao (1993). The CO_2 content will control the pH of the fluid with which it is in contact, and thus the extent and type of fluid-rock interaction. The fluid-rock interaction, in turn, may have a large impact on tuff permeability and fluid flow pathways. Bruton and Viani (1992) suggested that water may behave as if it were 100% saturated at liquid saturations greater than about 20% at temperatures up to 100°C. However, the coexisting gas phase will have a large impact on the water's chemical reactivity. Any forecasts of fluid-rock interaction in two-phase zones will require the gas phase chemistry to be considered, as addressed in the boiling scenarios evaluated by Criscenti and Arthur (1991) and Arthur and Murphy (1989).

3.4.2.5.3 Thermodynamic data for aqueous Al species: WK-28. Downhole mineral equilibria in well WK-28 were calculated using two different data bases that are in current use. One is based on SUPCRT92, and the other is an updated version of the same data base but with thermodynamic data for aqueous Al species from Pokrovskii and Helgeson (1995) (SUPCRT R24). The latter data will be used in GEMBOCHS.

Figure 3.4-21 shows the simulation results using data from Pokrovskii and Helgeson, whereas Fig. 3.4-22 was constructed using the SUPCRT92 data base. The convergence of affinity curves at zero affinity (equilibrium) at the downhole temperature in Fig. 3.4-21 for phases that are observed as secondary phases suggests that Pokrovskii and Helgeson's data for aqueous Al species work quite well. In contrast, the data in SUPCRT92[2] do not reproduce downhole mineralogy well. In these calculations, measured Al concentrations were used; that is, they were not automatically set using mineral equilibria as is often done, especially at lower temperature (e.g Bowers and Burns, 1990; Chipera, Bish and Carlos, 1995).

Given the above results, thermodynamic data for aqueous Al species should be sourced from Pokrovskii and Helgeson (1995). Further simulations should be undertaken in the range 100-200°C to evaluate the Al data bases at lower temperature. However, less discrepancy may be observed at lower temperatures because the main cause of discrepancy is the log K for reaction between Al^{3+} and AlO_2^-. The two log Ks agree well at low temperature, but deviate increasingly with increasing temperature until a difference of about 0.4 log units exists at 250°C, producing the observed differences in the affinity vs. temperature figures.

The log K for reaction between Al^{3+} and AlO_2^- from Bourcier and Knauss (1993) used in GEMBOCHS COM versions prior to R24 also reproduces observed mineralogy well. Users of GEMBOCHS data bases should identify the $Al(OH)_4^-/Al^{3+}$ log K specified in the data base they are using, and ascertain that it is appropriate for their needs. Of course, reactions which are written balanced on Al, such as those incorporated in many activity diagrams (e.g Bowers and Burns, 1990; Chipera, Bish and Carlos, 1995), will not be affected.

3.4.2.5.4 Thermodynamic data for wairakite. Figures 3.4-17 through 3.4-22 illustrate that wairakite is predicted to be about 1 to 1.5 kcal/mol undersaturated in all wells at about 250°C. In contrast, wairakite commonly occurs at Wairakei as a

2. Versions of SUPCRT have been published and distributed without data for AlO_2^-, the most important Al aqueous species under many conditions. The calculations in this paper provided for this species.

secondary phase at this temperature. Therefore, the calculations suggest that the free energy of formation from the elements of wairakite in SUPCRT92 (Helgeson et al., 1978), and in all current verions of GEMBOCHS, should be decreased by approximately 1-1.5 kcal/mol at about 250°C to increase its stability.

Thermodynamic data for wairakite may not seem to be relevant to the Yucca Mountain Project. However, if temperatures exceed 200°C with water present, wairakite would tend to be the stable zeolite relative to clinoptilolite, heulandite, and mordenite. Given the uncertainty in thermodynamic data for lower temperature zeolites such as clinoptilolite, heulandite, and mordenite (discussed below), it is useful to have some measure of data reliability for at least one zeolite with which to reference the other zeolites.

3.4.2.5.5 Thermodynamic data for zeolites. The simulations represented in Figs. 3.4-17 through 3.4-22 were run with the SUPCRT data base instead of the COM data file in part because the COM file contains thermodynamic data for zeolites such as analcime, clinoptilolite, mordenite, heulandite, stilbite, mesolite, scolecite and natrolite from Johnson and co-workers (1982, 1983, 1985, 1991, 1992) and Howell et al. (1990). These data were obtained through careful calorimetric studies. When kinetic constraints are not considered and purely thermodynamic equilibrium calculations are made, one of the above zeolites is present in the computed equilibrium assemblage at temperatures as high as 250°C, even though they are generally not expected to be stable at such high temperature in natural systems.

Figure 3.4-23 shows a calculation of zeolite stability in well WK-28 under conditions identical to that in Fig. 3.4-21, but using GEMBOCHS version COM R24 which contains Johnson's calorimetric data for zeolites. Figure 3.4-21 can be combined with Fig. 3.4-23 to show the affinities of zeolites relative to other minerals. Note the supersaturation with respect to scolecite, mesolite, stilbite and the Ca end-member of a clinoptilolite solid solution (discussed by Viani and Bruton, 1992) at the downhole temperature of 246°C.

Owing to this discovery, the first tests of the codes were made using data bases that do not contain Johnson's data for zeolites. At this time, simulations using the COM data base containing Johnson's zeolites must be made by suppressing the

zeolites to artificially reflect their disappearance from natural assemblages at temperatures greater than about 200°C.

The thermodynamic data at elevated temperature for the above zeolites from Johnson and co-workers are uncertain for a number of reasons.

First, the third law entropies (S^o) for clinoptilolite, mordenite, stilbite, mesolite, scolecite, and natrolite in the COM data file are actually values for $S^o(T)-S^o(0)$, because the configurational entropies at 0 K ($S^o(0)$) were not available. Johnson and co-workers attempted to estimate configurational entropies when possible, and warned that the configurational entropy must be taken into account when computing mineral equilibria. We have not devoted effort to estimating configurational entropies because their contribution would increase zeolite stability, whereas the problem is that they seem to be too stable already.

Secondly, it is possible that H_2O vapor adsorption occurred during the cooling of Johnson's drop calorimetry experiments. The exothermic reaction would produce excess heat capacity at elevated temperature (see Carey, 1993 for full discussion). Carey (1993) suggested that the heat capacity of H_2O in clinoptilolite is temperature-insensitive, rather than increasing monotonically with temperature, as shown by Johnson et al. (1991).

Thirdly, the hydration state of zeolites may decrease with increasing temperature, which would affect their stability. Water in zeolites is generally considered to have a lower free energy than bulk water, such that water desorption is endothermic. Johnson measured the thermodynamic properties of his zeolites at 50% relative humidity in recognition of their potential for changing hydration state. This potential for changing hydration state is not currently provided for in the EQ3/6 codes and data bases, however.

If the configurational entropy were appropriately accounted for, and the heat capacities corrected for readsorption phenomena, the stability of zeolites would increase because their free energies of formation would be more negative. However, zeolite stability would have to decrease if errors in thermodynamic data were the cause for the predicted stability of zeolites at temperatures greater than about 200°C.

Clearly, alternate approachs similar to that illustrated by the affinity-temperature diagrams should be adopted to determine the potential for mineral stability. The calculations described in Figs. 3.4-3 through 8 suggest that fluid-mineral equilibria determined in this manner agree well with observed mineralogy.

3.4.2.5.7 Vein/vug vs. matrix mineralogy and mineral assemblages. Alteration mineralogy at Wairakei is controlled strongly by temperature in veins and vugs, and by both temperature and mineralogy in the matrix. Replacement minerals in the matrix are controlled in identity, morphology and location by the primary mineralogy. That is, replacement mineralogy is controlled by the dissolving phase; the components of the dissolving mineral tend to re-precipitate as secondary minerals next to the dissolving grain. This link is much weaker or non-existent, in vein- and vug-fills.

The stabilities of fracture-, vein- and vug-filling minerals are controlled by solution composition and temperature with apparently limited control by the matrix. Alteration minerals in veins and vugs are the same as those found as replacement minerals in the matrix, but they occur in assemblages composed of fewer phases. It is striking that vein and vug fills, which obviously have precipitated from solution, are characterized by one to three secondary minerals, fewer than the number of different replacement minerals in the matrix as a whole. The above findings suggest that the fractures, veins and vugs represent fluid-dominated systems, whereas the matrix represents a rock-dominated system.

Petrographic observations suggest that the minerals replacing plagioclase in the matrix are those that commonly comprise fracture/vein/vug mineralogy; both seem to be Ca-dominated systems. At this time, our working hypothesis is that vein mineralogy is controlled mainly by fluid chemistry in the flowing system with negligible interaction with the host rock. The number of fracture-filling minerals may be controlled by the phase rule for mobile components.

In the post-emplacement environment at Yucca Mountain, replacement mineralogy in the matrix would be expected to be controlled by temperature and primary mineralogy, provided sufficient water is present to effect such changes, whereas the stability of minerals along flow paths such as fractures would be

controlled by the evolution of water composition as well as temperature. Factors that could effect impact water composition include boiling/condensation, interactions with cementitious and other manufactured materials including metal waste package components, and so on.

The degree of mass transfer between matrix and fractures in the New Zealand systems should be evaluated. If there is little chemical exchange between the matrix and fractures, mineral dissolution/precipitation during fluid flow in coupled hydrogeochemical models can be simulated much more simply because diffusion to and from the matrix does not have to be considered.

3.4.2.6 Conclusions. Vein and matrix minerals are predicted to be in equilibrium with subsurface fluids at downhole temperatures greater than 240°C. The proximity of a variety of minerals to equilibrium suggests that small differences in fluid chemistry, temperature or pressure can significantly impact mineral assemblages. This might account for the wide variety of mineral assemblages observed at Wairakei.

The SUPCRT92 data base, combined with the data of Pokrovskii and Helgeson (1995) for aqueous Al species describes, equilibrium relations between measured Al concentrations and observed mineral equilibria better than data in the current SUPCRT92 data base. Observed changes in the stability of calcite, prehnite and illite (muscovite) can be indicative of changes in the gas content of the downhole fluid. Feldspar stabilities are largely independent of pH provided that pH values do not deviate greatly from neutrality.

Quartz solubility data from Fournier (1983) describe observed mineral assemblages better than data from Walther and Helgeson (1977). The free energy of wairakite from Helgeson et al. (1978) should be decreased by approximately 1–1.5 kcal/mole at about 250°C. Additional work is required to determine why calorimetric data for clinoptilolite, stilbite and other zeolites from Johnson and co-workers appear to overestimate the stability of these minerals at elevated temperature.

Fluid-mineral interactions at temperatures >200°C are generally believed to be controlled by equilibrium, and so were chosen as the starting point for the EQ3/6

code and data base tests. This assumption is supported by the excellent convergence observed for computed and observed assemblages. Further studies should focus on fluid-mineral reactions in the temperature range of about 100–200°C at the Wairakei and Kawerau geothermal fields. Zeolites such as mordenite, dachiardite and clinoptilolite have been identified in this temperature interval. Extension of the tests to lower temperature allows us to address the controls of kinetics vs. equilibrium on mineral stability, and to determine the stability of zeolites similar to those found at Yucca Mountain.

3.4.2.7 References

Arthur, R.C. and Murphy, W.M., 1989, An analysis of gas-water-rock interactions during boiling in partially saturated tuff: Soc. Geol., Bull., v. 42, p. 313–327.

Bird, D.K. and Helgeson, H.C., 1980, Chemical interaction of aqueous solutions with epidote-feldspar mineral assemblages in geologic systems. 1. Thermodynamic analysis of phase relations in the system CaO-FeO-Fe_2O_3-Al_2O_3-SiO_2-H_2O-CO_2: Am. Jour. Sci., v. 280, p. 907–941.

Bourcier, W.L. and Knauss, K.G., 1993, Aluminum hydrolysis constants to 250°C from boehmite solubility measurements: Geochim. et Cosmochim. Acta, v. 57, p. 747–762.

Bowers, T.S. and Burns, R.G., 1990, Activity diagrams for clinoptilolite: Susceptibility of this zeolite to further diagenetic reactions: Am. Min., v. 75, p. 601–619.

Bruton, C.J., 1995, Testing EQ3/6 and GEMBOCHS using fluid-mineral equilibria in the Wairakei geothermal system: Yucca Mountain Project letter report, Milestone MOL206, Chemical and Mineralogical Properties of the Waste Package Environment:, Natural System Simulations, WBS Element 1.2.3.12.1), August 28, 1995.

Bruton, C.J., Glassley, W.E. and Bourcier, W.L., 1994, Field-based tests of geochemical modeling codes using New Zealand hydrothermal systems: Lawrence Livermore National Laboratory UCRL-ID-118009.

Bruton, C.J., Glassley, W.E. and Meike, A., 1995, Geothermal areas as analogues to chemical processes in the near-field and altered zone of the potential Yucca Mountain, Nevada, repository: Lawrence Livermore National Laboratory UCRL-ID-119842.

Bruton, C.J. and Viani, B.E., 1992, Geochemical modeling of water-rock interactions in the unsaturated zone: In Water-Rock Interaction 7, Y.K. Kharaka and A.S. Maest, eds., A.A. Balkema, Netherlands, p. 705–708.

Buscheck, T.A. and Nitao, J.J., 1993, Repository-heat-driven hydrothermal flow at Yucca Mountain, Part 1: Modeling and analysis: Nuclear Tech., v. 104, p. 418–448.

Carey, J.W., 1993, The heat capacity of hydrous cordierite above 295 K: Phys. Chem. Min., v. 19, p. 578–583.

Chipera, S.J., Bish, D.L. and Carlos, B.A., 1995, Equilibrium modeling of the formation of zeolites in fractures at Yucca Mountain, Nevada: In D.W. Ming and

F.A. Mumpton, eds., Natural Zeolites '93: Occurrence, Properties, Use: Intl. Comm. on Natl. Zeolites, Brockport, N.Y., p. 565–577.
Criscenti, L.J. and Arthur, R.C., 1991, The calculated effects of isothermal boiling on tuff-water interactions: Radiochim. Acta, v. 52/53, p. 513–517.
Fournier, R.O., 1983, A method of calculating quartz solubilities in aqueous sodium chloride solutions: Geochim. et Cosmochim. Acta, v. 47, p. 579–586.
Howell, D.A., Johnson, G.K., Tasker, I.R. and O'Hare, P.A.G., 1990, Thermodynamic studies of the zeolite stilbite: Zeolites, v. 10, July/August, p. 525–531.
Johnson, G.K., Flotow, H.E. and O'Hare, P.A.G., 1982, Thermodynamic studies of zeolites: analcime and dehydrated analcime: Am. Min., v. 67, p. 736–748.
Johnson, G.K., Flotow, H.E. and O'Hare, P.A.G., 1983, Thermodynamic studies of zeolites: natrolite, mesolite and scolecite: Am. Min., v. 87, p. 1134–1145.
Johnson, G.K., Flotow, H.E. and O'Hare, P.A.G., 1985, Thermodynamic studies of zeolites: heulandite: Am. Min., v. 70, p. 1065–1071.
Johnson, G.K., Tasker, I.R., Flotow, H.E., O'Hare, P.A.G. and Wise, W.S., 1992, Thermodynamic studies of mordenite, dehydrated mordenite, and gibbsite: Am. Min., v. 77, p. 85–93.
Johnson, G.K., Tasker, I.R., Jurgens, R. and O'Hare, P.A.G., 1991, Thermodynamic studies of zeolites: clinoptilolite: J. Chem. Thermo., v. 23, p. 475–484.
Pokrovskii, V.A. and Helgeson, H.C., 1995, Thermodynamic properties of aqueous species and the solubilities of minerals at high pressures and temperatures - The system Al_2O_3-H_2O-NaCl: Am. Jour. Sci., v. 295, p. 1255–1342.
Ragnarsdottir, K.V. and Walther, J.V., 1983, Pressure sensitive "silica geothermometer" determined from quartz solubility experiments at 250°C: Geochim. et Cosmochim. Acta, v. 47, p. 941–946.
Reyes, A.G., Giggenbach, W.F. and Christenson, B.W., 1993, First Report for the LLNL-Inst. Geol. Nuclear Sciences EQ3-EQ6 Code Validation Contract: Inst. Geol. Nuclear Sciences Client Report 722305.15A.
Steiner, A., 1977, The Wairakei geothermal area, North Island, New Zealand: New Zealand Geological Survey Bull. 90.
Viani, B.E. and Bruton, C.J., 1992, Modeling fluid-rock interaction at Yucca Mountain, Nevada: A progress report: Lawrence Livermore National Laboratory UCRL-ID-109921.
Walther, J.V. and Helgeson, H.C., 1977, Calculation of the thermodynamic properties of aqueous silica and the solubility of quartz and its polymorphs at high pressures and temperatures: Am. Jour. Sci., v. 277, p. 1315–1351.
Wolery, T.J., 1992, EQ3NR, A computer program for geochemical aqueous speciation-solubility calculations: Theoretical manual, user's guide, and related documentation (Version 7.0): Lawrence Livermore National Laboratory Report UCRL-MA-110662 PT III.
Wolery, T.J. and Daveler, S.A., 1992, EQ6, A computer program for reaction path modeling of aqueous geochemical systems: theoretical manual, user's guide, and related documentation (Version 7.0): Lawrence Livermore National Laboratory Report UCRL-MA-110662 PT IV.

3.4.3 Mineralogy-Petrology Observations Regarding the Near-Field Environment, by David L. Bish, J. William Carey, Schon S. Levy and Steve J. Chipera, Los Alamos National Laboratory

3.4.3.1 Introduction. In order to model accurately the short- and long-term effects of repository-induced heating on the properties of rocks in the near-field environment (NFE) at Yucca Mountain, an understanding of the host rock mineralogy, past mass transfer in the host rocks, and the anticipated changes in mineral and glass stability due to emplacement of high-level radioactive waste are required. Bish and Chipera (1989) compiled a summary of mineral distributions with depth in drill holes at Yucca Mountain using available non-Q core. A more recent report (Chipera et al., 1995b) has provided similar mineralogical information using Q core. Levy (1991) and Levy and O'Neil (1989) described the application of petrologic and isotopic methods to the understanding of past mass transfer in the host rocks. A large amount of research has been conducted on the effects of repository-induced heating on the long-term stability of minerals and glasses in the near-field environment. This includes studies of the dehydration behavior of clays and zeolites in tuffs (Bish, 1984, 1988a, 1988b, Kranz et al., 1989; Carey and Bish, 1994, 1996; Chipera et al., 1994) and on the hydrothermal stability of tuffs (Blacic et al., 1986; Duffy, 1983a, 1983b, 1993). The data reported here from drill holes USW NRG-6 and UE-25 UZ#16 are the only Q data available; all other mineralogical data are non-Q as they were obtained from non-Q core and cuttings.

3.4.3.2 Host Rock Mineralogy. The discussion of host-rock mineralogy will be confined primarily to portions of Yucca Mountain most likely to experience repository-induced conditions departing significantly from ambient conditions. This region consists primarily of the Topopah Spring Tuff and the underlying Calico Hills Formation within the repository exploration block (Fig. 3.4-24).

3.4.3.2.1 Mineralogical Data. The thin but hydrologically important upper vitrophyre of the Topopah Spring Tuff lies beneath the nonwelded Paintbrush bedded tuffs. This vitrophyre has a significant hydrologic effect despite its meager thickness (3–7 m) because it is the greatest single barrier to downward recharge into the unsaturated zone (Flint et al., 1993).

One of the important features examined in this vitrophyre across Yucca Mountain has been the extent of alteration, indicating whether this glassy barrier has been compromised by 12 Myr of potential recharge into the unsaturated zone. The upper vitrophyre is composed primarily of unaltered volcanic glass. There is some noteworthy alteration of up to 11% smectite in the glassy portions. More detailed sampling in drill hole UE-25 UZ#16 showed that the upper vitrophyre has been altered significantly by past fluid flow, with up to 18% smectite and 18% clinoptilolite-group zeolite.

The clinoptilolite-group zeolites in this zone have 020:200 intensity ratios indicative of heulandite. To confirm the identification of heulandite, aliquots of samples from drill hole UE-25 UZ#16 were heated overnight at 400°C and 550°C. The samples were analyzed by X-ray diffraction after each heating to determine if the structure had collapsed as expected for heulandite (Mumpton, 1960; Alietti, 1972). Although heating produced significant collapse, the structure was not completely destroyed below 350°C as expected for a "type 1" heulandite (Mumpton, 1960). Likewise, the zeolite cannot be a pure clinoptilolite which should remain stable to temperatures in excess of 700°C.

The amount of collapse observed suggests that the zeolite in these samples is either a mixture of heulandite with minor clinoptilolite, or it is structurally and compositionally an intermediate "type 2" heulandite (Alietti, 1972). The presence of zeolites and smectite in this zone suggests "ponded" alteration above the relatively impermeable upper vitrophyre, it is, however, impossible, given existing data, to determine whether the extent of alteration in the upper Topopah vitrophyre is variable across Yucca Mountain. If such variability could be documented, it might then be possible to map those portions of the mountain where recharge has been, and is likely to be, concentrated.

The restriction of zeolites to the thin interval above the upper vitrophyre of the Topopah Spring Tuff, and the identification of a heulandite component in these zeolites associated with abundant cristobalite, may indicate a very early episode of zeolitization during initial heat loss from the underlying vitrophyre. This interpretation is in accord with studies of the lower vitrophyre of the Topopah

Spring Tuff, where the formation of heulandite at the margin of the vitrophyre is related to the moderate-temperature events that occurred with late-stage cooling of the tuff (Levy and O'Neil, 1989).

One of the inferences that can be drawn from this interpretation is that the zeolitization observed sporadically above the upper vitrophyre of the Topopah Spring Tuff does not represent any significant accumulation of water over the last 12 million years. This inference should be considered critically in further studies of mineralogy from this interval, for although the occurrences of heulandite-above-glass are similar in both the lower and upper Topopah Spring vitrophyres, the alteration setting is quite different. Heulandite formation in the lower vitrophyre is associated with passage from the overlying devitrification front into the vitrophyre, whereas the heulandite that formed above the upper vitrophyre marks a boundary between two vitric zones (welded and nonwelded) with markedly different porosity and transmissivity. It is also possible that the formation of this upper zeolitic zone was favored by the presence of minor amounts of perched water captured due to the low permeability of the underlying upper vitrophyre. Whatever the timing and mode of heulandite formation above the upper vitrophyre, the upper vitrophyre itself is remarkably unaltered, indicating little water/rock interaction in this relatively impermeable interval since tuff emplacement.

Mineralogic evidence of ongoing infiltration may best be found in the potentially ongoing alteration of glass to smectite and in the minor but significant accumulation of calcite in the lower part of the Paintbrush Tuff nonwelded interval in drill hole UE-25 UZ#16. It is important to note that the quantities of smectite and calcite that occur in this interval vary markedly across Yucca Mountain. Up to 40% calcite and 40% smectite occur to the north in USW G-2, and 40% smectite but only a trace of calcite occur in UE-25a#1. A possible implication of this variability is that those portions of the mountain where recharge has been greatest might be delineated by examining the extent of underlying alteration in the nonwelded tuffs between the Tiva Canyon and Topopah Spring Tuffs. This implication deserves serious consideration.

The main central portion of the Topopah Spring Tuff, which consists of densely welded, devitrified rhyolitic tuff (e.g., Broxton et al., 1989), is critical to site characterization because it is the host rock for the potential high-level nuclear waste repository.

The potential repository horizon includes the interval below the zone of abundant (>15%) lithophysal cavities in the upper Topopah Spring Tuff and above the unit's basal vitrophyre. The Topopah Spring Tuff is chemically homogeneous, but the mineralogy is variable, primarily in the relative abundances of silica polymorphs (quartz, cristobalite, and tridymite).

Hematite and smectite are common minor phases, and Mn-oxides are common fracture coatings in the upper portion of the unit. However, within the exploration block, there is little variation in the mineralogy of the repository horizon, and over 98% of the mineral content of the rocks can be ascribed to tridymite, cristobalite, quartz, and alkali feldspar. The abundance of feldspar varies between about 55 and 65%, with the remainder of the rock consisting of variable proportions of crystalline silica polymorphs. Thus, the *total* of the crystalline silica polymorphs is quite consistent throughout much of the Topopah Spring Tuff.

In most cores, tridymite occurs throughout this interval of the Topopah Spring Tuff but is most abundant in the upper portion. Quartz is often absent in the upper portion of this interval but occurs in the lower portions in tuffs with reduced tridymite abundance. Based on higher sampling densities in UE-25 UZ#16 and USW NRG-6, there appears to be a pronounced break in the distribution of silica polymorphs at between 15 and 20% of the way downward through the Topopah Spring Tuff. This is where the transition from quartz-latite to rhyolitic composition occurs. At this point, a maximum in tridymite abundance is reached and quartz becomes more important.

Cristobalite varies markedly in relation to quartz below this transition depth. X-ray diffraction data suggest that there may be a general reduction in cristobalite and rise in quartz with depth, beginning near the middle nonlithophysal zone.

These silica polymorphs are important, because the least stable of them (cristobalite and tridymite) can elevate the aqueous silica activity in local

unsaturated-zone waters. These less stable silica minerals provide a ready source of silica for dissolution, transport, and deposition under the thermal perturbations of a repository. Cristobalite is particularly abundant in the potential repository horizon (Bish et al., 1984), and as such may be an important health hazard consideration. In addition to effects on aqueous silica activity, cristobalite is important in the near-field environment because it undergoes a displacive phase transformation, with an associated 5% volume increase, at about 220°C (Peacor, 1973).

Recent studies of drill hole UE-25 UZ#16 (Chipera et al., 1995b) emphasized our limited understanding of the rocks within the exploration block. In this drill hole, stellerite, a Ca-rich ($Ca_4Al_8Si_{28}O_{72}•28H_2O$) orthorhombic mineral similar to stilbite, was discovered in significant amounts in the central 50% of the Topopah Spring Tuff. This zeolite occurs in bulk-rock samples between 191.5 and 332.4 meters in depth, in concentrations up to 14 wt% (avg. ~3 wt%) and is obviously not restricted to fractures. The occurrence of this hydrous mineral within the potential repository horizon was completely unexpected as it had previously been found only in fractures from drill holes USW G-1, G-2, and UE-25a#1. Its significance in the remainder of the exploration block is unknown. Future analyses of cores from drill holes SD-7, SD-9, and SD-12 may clarify the stellerite distribution with the exploration block. Naturally this hydrous mineral will be particularly sensitive to changes in temperature and water-vapor pressure, and it loses most of its water below 200°C (Gottardi and Galli, 1985).

The effects of thermal alteration by hot emplaced waste may be most pronounced in the basal vitrophyre of the Topopah Spring Tuff, closely underlying the potential repository horizon. This vitrophyre is variably altered across Yucca Mountain, with devitrification-associated heulandite formation penetrating its highly irregular upper surface (Levy and O'Neil, 1989).

As noted by Bish et al. (1984), the so-called Zeolite Interval I occurs at the top of the basal vitrophyre. This is a 2–5-m thick interval, commonly containing up to 30% of a clinoptilolite-heulandite mineral and 45% smectite. Alteration to zeolites and smectite is often gradational in the upper and lower margins of the basal vitrophyre,

and smaller amounts of other zeolites (e.g., erionite) also invade the lower and upper margins, usually in fractures. The minerals in Zeolite Interval I are potentially quite important in the near-field environment because (1) they represent the first occurrence of significant amounts of sorptive minerals beneath the repository horizon; and (2) they represent the first occurrence of minerals that are particularly sensitive to changes in temperature and/or water-vapor pressure.

The basal vitrophyre itself is a 10- to 30-m thick zone consisting predominantly of densely welded glass (40-90%), with smaller amounts of feldspar, quartz, and opal-CT. Perlitic fractures in the vitrophyre are commonly lined with smectite or zeolites. The perlitic glass in this interval contains from 2.8 to 4.6% water, approximately three-fourths of which is lost at temperatures below 300°C in dry heating experiments (Vaniman et al., 1993).

In the eastern portion of Yucca Mountain, the nonwelded base of the Topopah Spring Tuff and all of the underlying Calico Hills Formation are extensively zeolitized to clinoptilolite and mordenite. These zeolitic rocks contain up to 83% clinoptilolite and up to 43% mordenite. The primary silica phase associated with this zeolitization is authigenic opal-CT, with minor amounts of quartz and alkali feldspar in the highly zeolitized horizons. Percentages of smectite up to 50% occur in the Topopah Spring Tuff bedded tuffs immediately underlying the lower vitrophyre, but the thoroughly zeolitized rocks at greater depth typically contain very little smectite. In the western portion of Yucca Mountain, the few core samples available suggest that this entire interval is vitric and largely unaltered. This vitric interval consists of moderately welded to non-welded glassy tuffs, with 30 to 80% glassy shards and minor amounts of alkali feldspar, cristobalite, and quartz. Alteration to smectite is minor in this interval.

The available data suggest that an alteration front may have been associated with past rises in the static water level (SWL), giving rise to zeolitized Calico Hills Formation rocks to the east. However, the nature of this zeolitic/vitric transition and the implications for past fluctuations in the SWL will remain speculative until further core samples from the potential repository block (e.g., SD-7, -9, and -12) are

analyzed. The nature of the lateral and vertical transitions between zeolitic and vitric portions of the Calico Hills Formation is of fundamental importance to understanding (1) the maximum amount of zeolitic tuff between the host rock and the static water level; (2) the transport pathways from the potential repository toward the saturated zone and (3) the potential for thermal alteration or dehydration of existing zeolites and possible formation of new zeolites from heated glass (Vaniman and Bish, 1995).

The Calico Hills Formation at the potential repository site is underlain by the mostly devitrified, poorly welded Prow Pass Tuff of the Crater Flat Group. The devitrified portions of the Prow Pass Tuff are composed of feldspar and a silica mineral. Available data show that cores taken from locations in which the Prow Pass is high above the SWL and underlies vitric portions of the Calico Hills Formation contain the same variable silica-polymorph associations (tridymite, cristobalite, and quartz) found in the devitrified Topopah Spring Tuff (e.g., USW H-3 and H-5). In cores where the Prow Pass is closer to or within the saturated zone and is overlain by zeolitized portions of the Calico Hills Formation, only quartz is preserved. If borne out in further drill cores, this alteration-associated variability in the Prow Pass may prove to be an important component in predicting the future silica activity, and hence the extent of silica mobilization, to be expected in thermally-perturbed portions of the Prow Pass Tuff.

3.4.3.2.2 Distribution of Silica Phases. As noted above, the nature of the silica phases is particularly important in the NFE. Alteration reactions in the tuffs involving zeolites and smectite are quite sensitive to the aqueous silica activity (e.g., Chipera et al., 1995a). In addition, cristobalite and the hydrous silica phases are susceptible to thermally induced modifications.

The variability of silica polymorph distributions throughout the unsaturated zone reveals a stratigraphy of minerals capable of generating widely varying silica activity in water/rock interactions. Earlier studies (Bish et al., 1984) of core samples showed a crude stratigraphy of silica polymorphs in the Topopah Spring Tuff, with tridymite concentrated in the upper portions of the devitrified tuff. It was principally concentrated in the quartz-latite portion that was erupted from a

significantly hotter part of the magma chamber than the rhyolite; see Lipman, 1971. Quartz was restricted to the lower, rhyolitic portions where tridymite is only a minor phase. Cristobalite is ubiquitous throughout the Topopah Spring Tuff.

More recent studies show that although this stratigraphic model continues to be upheld, the lower portion of the Topopah Spring devitrified zone generally contains all three of these crystalline silica polymorphs. Small amounts of tridymite (~0–6%) and larger amounts of cristobalite (typically 10–20%) occur throughout the rhyolitic portion of the Topopah Spring Tuff. Thus, in most drill holes examined within the repository block, even at the potential repository horizon, cristobalite and usually tridymite are present to provide relatively soluble silica for dissolution, transport, and deposition under repository thermal conditions.

Recently completed analysis of samples from the Exploratory Studies Facility (ESF) suggest that the ratio of total crystalline silica polymorphs to alkali feldspar is reasonably constant at 0.75±0.03 within the host rock. Within the host rock in the ESF, cristobalite is the dominant silica polymorph at 23±5%, with quartz at 12±5% and tridymite at 4±1%.

The distribution of the least-stable silica form in Yucca Mountain cores (apart from volcanic glass), opal-CT, was outlined by Bish and Chipera (1989). The occurrence of this phase is strongly correlated with stratified occurrences of zeolites (clinoptilolite/mordenite), where it averages 18% of zeolitic rocks, and with the lower vitrophyre of the Topopah Spring Tuff, where it averages 10% of these glassy rocks. Opal-CT in earlier-analyzed drill cores was lumped together with cristobalite, hence one can obtain the mistaken impression from the earlier data that this correlation does not hold. The occurrence of opal-CT in the lower vitrophyre is not universal (e.g., absent in core UE-25a#1; Bish and Chipera, 1989). Moreover, opal-CT has not been found in the upper vitrophyre, although small amounts of cristobalite occur there (1–2% in UE-25 UZ#16 and in trace amounts in other cores near the exploration block). The presence or absence of opal-CT in glassy tuffs is important to note, suggesting different environments of alteration. As with the potentially different origins of heulandite in upper and lower vitrophyres, the silicification of

the lower vitrophyre and not of the upper vitrophyre point to different alteration regimes. It is possible that alteration was predominantly associated with the advancement of a devitrification front into the lower vitrophyre, whereas alteration may be largely associated with "ponding" above the upper margin of the upper vitrophyre.

3.4.3.3 Past Mass Transfer in Host Rock Tuffs

3.4.3.3.1 Syngenetic Alteration of the Topopah Spring Tuff. The Topopah Spring Tuff was emplaced at temperatures up to 700 to 800°C and probably required about 10^2 to 10^3 years to cool (Riehle, 1973). Early in the cooling period, the interior welded by viscous flow and compaction of the glass particles. The process of welding continued to temperatures as low as 475°C in the basal vitrophyre (Rosenbaum, 1986). After substantial welding had occurred, the tuff in the hottest parts of the interior devitrified, that is, it crystallized to an assemblage of feldspars and silica minerals. Escaping gases created gas cavities (lithophysae or lithophysal cavities) with vapor-phase mineral deposits. The faster cooling upper and lower margins of the deposits did not weld and experienced little or no devitrification. Some of the moderately to densely welded portions toward the outer margins did not devitrify and have survived in a glassy state (upper and lower vitrophyres). Localized alteration, caused by a combination of trapped water and infiltrating meteoric water that interacted with the rock, occurred during the very late stages of cooling, at near-ambient temperatures. The tuffs were also subject to fracturing, faulting, and brecciation during cooling.

The alteration history of the Topopah Spring Tuff have been reconstructed from field studies and examination of outcrop samples, drill core and cutting samples, and rock samples from the ESF. Thin sections of samples were examined by optical microscopy. Scanning-electron microscopy, using an ISI model DS-130 scanning electron microscope (SEM) operated at 19 kV with a Kevex model 7000 energy-dispersive X-ray analytical system, provided details of textural relations. Minerals were identified from energy-dispersive X-ray spectra and crystal morphology. X-ray powder diffraction data and quantitative mineral analyses were obtained as

described above. All of the data in this section are non-Q because they are derived from non-Q drill core. The data-tracking numbers are LA000000000024.001 and LA000000000101.001. The record packages containing traceability information are EES-1-9-92-5 and LA-EES-1-TIP-94-008.

3.4.3.3.2 Alteration in the lower Topopah Spring Devitrified-Vitric Transition Zone. The lower Topopah Spring Tuff devitrified-vitric transition zone marks the downward change from the pervasively devitrified, densely welded tuff (Tptpln) to underlying vitrophyre (Tptpv3: densely welded, glassy tuff). The transition zone is an interval of slightly to almost completely devitrified vitrophyre in which devitrification is sporadic and localized around fractures (Levy, 1984a). In the uppermost parts of the transition zone, where devitrification is almost complete, the tuff is distinguishable from ordinary devitrified tuff by the presence of incompletely devitrified pumice clasts that have been replaced primarily by clinoptilolite-heulandite. Further down, the most common alteration features are fractures with devitrified borders up to 0.3 m thick. Some of the devitrified borders are downward extensions from the overlying completely or predominantly devitrified tuff.

The transition zone is an interval of variable vertical dimension, extending from about 3 m to 30 m downward into the vitrophyre, with discontinuous distributions of secondary minerals both vertically and horizontally. This altered zone does not possess the attribute of thickness in the sense that intervals of zeolitized nonwelded tuffs elsewhere in the pyroclastic section have reliably measurable thicknesses and km-scale lateral continuity.

The devitrified fracture borders have a common textural and mineralogic zonation developed more or less symmetrically about the fracture traces. The inner margins of devitrified borders are mineralogically and texturally similar to the overlying devitrified rock, but with increasing amounts of yellow cryptocrystalline devitrification toward the outer margins. The outermost margins of devitrified borders contain clinoptilolite-heulandite, smectite, and minor silica. Dissolution cavities may be present in the adjacent vitrophyre. Quartz, chalcedony (microscopically fibrous quartz), opal, and clinoptilolite-heulandite are locally

abundant as fracture and void fillings, along with small quantities of iron and manganese minerals. Minute to major quantities of erionite may also be present.

Field and microscopic textural relations show a ubiquitous association between the hydrous minerals and devitrification features within the transition zone. The relations indicate that hydrous mineral crystallization was connected to devitrification during cooling of the pyroclastic unit. The observed textural relations, together with evidence for abundant fluid flow along fractures downward into the vitrophyre, indicate that devitrification, glass dissolution, and hydrous mineral deposition were caused by downward movement of heated water from the central hottest part of the cooling tuff. Temperatures calculated from oxygen isotope geothermometry of quartz associated with zeolite in fracture fillings and secondary pore fillings are in the range of 40° to 100°C (Levy and O'Neil, 1989).

There is textural evidence that alteration in the transition zone resulted in the genesis, transport, and deposition of colloidal material (Levy, 1992). Pores and fractures contain layered or nonlayered accumulations of colloidal particles. These accumulations, or gels, later crystallized to clinoptilolite-heulandite, silica, and zeolite-silica mixtures. Silica products include opal, chalcedony, and cristobalite, locally in combination with each other. Additional minor gel products include hematite and manganese minerals. Relict colloidal accumulations also fill primary and secondary pores in moderately welded tuffs below the vitrophyre.

3.4.3.3.3 Mass Transfer During Natural Alteration. Glasses representative of the starting materials, smectite, and zeolites in the altered rocks were analyzed by electron probe microanalysis using a Cameca model Camebax electron microprobe operated at 15kV accelerating potential and 5 to 15 nA beam currents. Normalized analyses of starting materials and secondary mineral products, plus the calculated elemental mass per unit volume for selected elements, are presented in Table 3.4-3. Glass analyses used as input for mass balance calculations were recalculated to a uniform 3 wt % water content. The 3% value falls within the range of 2.8% to 4.6% water measured in Topopah Spring Tuff lower vitrophyre samples (Vaniman et al., 1993). The materials used in those studies were not collected as natural-state samples

to preserve *in situ* moisture contents. In addition, the samples are perlitic and may not represent the water content of glasses at the onset of alteration.

Normalization of the water content in glasses, as well as in clay and zeolites, eliminates compositional variability due solely to differences in water content at the time of analysis. The use of this convention means that chemical changes during glass hydration (i.e., the earliest stage of alteration) are not represented in the calculations and are not accounted for in mass-transport determinations. Clinoptilolite-heulandite analyses were recalculated to a water content of 17 wt % corresponding to measured values at ~100% relative humidity and 23°C; smectite analyses were recalculated to a water content of 30 wt % (Chipera, personal communication, 1994).

Mass-balance and transport calculations used published density data for minerals. The composition of cristobalite was assumed to be 100% SiO_2 with a density of 2.30 (Deer et al., 1963), yielding a calculated value of 0.03828 mole Si/cm^3. A grain density value for Topopah Spring Tuff lower vitrophyre from a depth of 369.9 m in drill hole GU-3 (Anderson, 1984) was used for the calculations.

3.4.3.3.4 Alteration of Topopah Spring Basal Vitrophyre Glass. The effects of vitrophyre glass alteration on rock porosity depend in part on the amounts of secondary minerals formed during the alteration process, whether natural or repository-related. There is substantial lateral variation in the abundances and proportions of alkali feldspar, smectite, clinoptilolite-heulandite, and silica that comprise the characteristic secondary-mineral assemblage (Table 3.4-4). Instead of attempting to determine abundance values of general validity, the alternative approach taken here is to calculate bounding values for the amounts of secondary minerals that could form from the constituents of dissolved glass.

Alkali feldspar is typically the most abundant component of the natural alteration in the upper part of the devitrified-vitric transition zone, closest to the completely devitrified rock (candidate host rock). However, alteration assemblages from lower in the transition zone, with little or no feldspar, are simpler to model and may be more representative of alteration products to be expected in a waste repository-induced hydrothermal regime (Knauss and Peifer, 1986).

Dissolution of vitrophyre glass and precipitation of secondary minerals is represented qualitatively by the reaction

glass → smectite + heulandite + cristobalite (1)

Smectite and zeolite, alone or in combination, were typically the first-formed alteration products of glass dissolution. SEM photographs suggest that these minerals were commonly deposited at or near the dissolution sites. Silica was more likely to be transported and deposited elsewhere as fracture or pore fillings of cristobalite, chalcedony, quartz, or opal. Aluminum was the limiting constituent that determined the maximum amount of smectite or zeolite that was produced, so long as no additional Al was introduced in solution or colloidal suspension. Figure 3.4-25 is a graphic representation of reaction (1), balanced for all possible combinations of smectite and clinoptilolite-heulandite. Input values for the figure are from Table 3.4-3. The graph balances the reaction with respect to Al and Si, but not Na, Ca, K, or other elements. Also, the very small primary porosity was not factored into the calculations.

The most important result illustrated in Fig. 3.4-25 is that any combination of secondary minerals produces an increase in volume of 13 to 24 % over the volume of the reacted glass. The higher volume increase is for a smectite-rich assemblage in which the smectite accounts for less than the original glass volume and cristobalite is almost half of the original volume. In a zeolite-dominated assemblage, the volume of zeolite produced is approximately equal to the volume of glass consumed, with cristobalite comprising the additional 13%.

For vitrophyre with a bulk porosity around 1.4% (Anderson, 1984), alteration products in principle could seal all of the porosity in a volume of rock at least ten times larger than the volume of altered vitrophyre. This has not been observed in the naturally altered rock. Bulk porosity in the vitrophyre probably corresponds to the pervasive perlitic fracture system (Blacic et al., 1982), but larger-aperture through-going fractures also exist. The wider fractures, along with devitrification cavities, provided pathways for fluid flow and space for secondary-mineral

deposition during the period of alteration. The alteration must have caused an overall reduction in porosity, but this does not appear to have resulted in pervasive sealing or plugging of flow paths below the repository horizon.

3.4.3.4 Effects of Repository-Induced Thermal Load on Minerals And Glasses in the Near-Field Environment

3.4.3.4.1 Rationale and approach. The purpose of this section is to summarize thermodynamic and kinetic data on minerals and glass relevant to the near-field environment. These data are necessary to model mineral development in the near-field environment as a function of their thermodynamic properties and of the mineral reaction kinetics. The implications of the thermodynamic and kinetic data on the factors controlling stability of minerals and glasses at Yucca Mountain and anticipated changes in these factors are discussed in some detail. The observed range of mineral assemblages at Yucca Mountain as a function of depth and paleotemperatures suggests that the following materials are the likely reactants and products of any mineralogical reactions in response to heat derived from the high-level nuclear waste: (1) Reactions of unstable silica polymorphs tridymite, cristobalite, and opal-CT to quartz; (2) Reaction of alkali feldspar under hydrothermal conditions to gibbsite, kaolinite, illite, smectite, analcime, and/or clinoptilolite; (3) Hydrothermal alteration of vitric units to assemblages of smectite, clinoptilolite/heulandite, and mordenite; (4) Dehydration/hydration reactions of clinoptilolite, mordenite, and smectite in response to changing temperature and fluid saturation; (5) Decomposition of clinoptilolite and smectite in response to elevated temperatures or changed fluid compositions.

The minerals discussed in detail here are clinoptilolite (hydration/dehydration reactions, solubility, kinetics of dissolution/precipitation), analcime (solubility and kinetics of dissolution/precipitation), smectite (hydration/dehydration reactions), and cristobalite (solubility and kinetics of dissolution/precipitation). Additional data gathered from the recent literature are presented on the thermodynamic and kinetic properties of these and other minerals.

3.4.3.4.1.1 Silica polymorph control of mineral stability. Mineral assemblages observed in a wide variety of low-temperature volcanic environments indicate that

the silica polymorph plays a determinative role in mineral stability. For example, it has been observed that the presence of clinoptilolite is correlated with the occurrence of cristobalite or opal-CT, and analcime with that of quartz (Duffy, 1993). These relations indicate that metastable silica polymorphs allow other metastable mineral assemblages to persist and suggest that the evolution of mineral assemblages may be at least partly controlled by the kinetics of silica reactions.

The primary silica phases at Yucca Mountain are quartz, cristobalite, tridymite, and opal-CT. The ground water sampled at Yucca Mountain and vicinity is generally supersaturated with respect to quartz and cristobalite, with an aqueous silica activity between amorphous silica and opal-CT solubility. The equilibrium silica polymorph is quartz. Because the solutions are saturated or even supersaturated with respect to cristobalite, there is no thermodynamic driving force for the dissolution of cristobalite, even though it is metastable with respect to quartz. In such aqueous systems, the primary thermodynamic driving force is for the precipitation of quartz. Therefore, the rate-limiting step for the conversion of cristobalite to quartz appears to be the precipitation of quartz. As quartz precipitates, the aqueous silica content decreases, and then some cristobalite can dissolve. This is consistent with the model presented by Duffy (1993). Similarly, analcime may be stable with respect to clinoptilolite at quartz saturation but metastable at cristobalite saturation. As a consequence, there is no thermodynamic driving force for the dissolution of clinoptilolite and precipitation of analcime until the silica solubility drops below that of cristobalite.

Duffy (1993) considered the reactions of clinoptilolite to analcime, clinoptilolite to smectite, analcime to albite, and feldspar to illite, to all be effected by the silica polymorph in equilibrium with the fluid.

3.4.3.4.2 Stability of Selected Minerals and Glass

3.4.3.4.2.1 Clinoptilolite (and heulandite). Compositions of clinoptilolite and heulandite at Yucca Mountain are highly variable, with Si/Al ratios between 3 and 5 and the dominant exchangeable cation varying between Na^+, K^+, and Ca^{2+} (Broxton et al., 1987). Consequently, it is evident that thermodynamic and kinetic models capable of addressing the effect of compositional variations in clinoptilolite

minerals are essential for accurate prediction of the dissolution or precipitation of clinoptilolite and heulandite. Because clinoptilolite is the most abundant zeolite at Yucca Mountain, considerable attention has been focused on the thermodynamic properties of this mineral. The work that will be reviewed here includes the following:

1. The effect of exchangeable cation in clinoptilolite on molar volumes (Bish, 1984);
2. Thermal analysis investigations of the dehydration behavior of clinoptilolite and heulandite (Bish, 1988a);
3. The effect of dehydration on molar volume (Bish, 1995);
4. Estimation of the thermodynamic properties of clinoptilolite and heulandite as a function of chemical composition (Chipera et al., 1995a);
5. Determination of the equilibrium water content of clinoptilolite as a function of exchangeable cation (Carey and Bish, 1996a);
6. Determination of the energetics of hydration and dehydration processes in clinoptilolite as a function of exchangeable cation (Carey and Bish, 1996b); and
7. The solubility and kinetics of dissolution and precipitation of Na-clinoptilolite (MacInnis et al., 1995; Barnes and Wilkin, 1995).

3.4.3.4.2.2 Thermodynamic Stability. The thermodynamic properties of clinoptilolite and heulandite have been investigated by modeling, calorimetry, and solution chemistry. The various results are difficult to compare because of differences in Si/Al ratio and exchangeable cation (Table 3.4-5). Note that Barnes and Wilkin (1995) conducted solubility measurements on an almost completely exchanged Na-clinoptilolite that should be a very useful end-member in thermodynamic calculations. The complete results of Barnes and Wilkin's solubility data from 25 to 265°C are summarized in Table 3.4-6. The Gibbs free energy of formation of Na-clinoptilolite calculated from the measured solubility products is almost linear in temperature (Fig. 3.4-26). A linear regression of these values provided the enthalpy of formation and the third-law entropy for Na-clinoptilolite (Table 3.4-5).

3.4.3.4.2.3 Effect of cation-exchange. The thermodynamic data for Na-clinoptilolite (Barnes and Wilkin, 1995) provide a basis for the calculation of the end-member thermodynamic properties of K- and Ca- and Sr-clinoptilolite by incorporating the results of Pabalan (1994) and Pabalan and Bertetti (1994). The latter studies are binary cation-exchange experiments for Na-K, Na-Ca, and Na-Sr compositional pairs. Calculation of the integral Gibbs free energy of exchange combined with the Gibbs free energy of formation of the aqueous cations and Na-clinoptilolite gives end-member thermodynamic properties that differ by 180 to 97 kJ/mol from Na-clinoptilolite (72 oxygen basis; Table 3.4-7). These differences are small compared with the differences reported in Table 3.4-3. Consequently, the variability of results in Table 3.4-3 reflects either the large energetic affect of Si/Al substitutions or some other source of difference or error (e.g., Al/Si order/disorder).

As is common with many other natural zeolites, the energetic preference for cations is in the order K>Sr>Ca>Na (cf., Sherry 1969). Pabalan (1995) demonstrated that clinoptilolite is enriched in K relative to Na in aqueous solutions. The situation for the exchange of Ca and Sr for Na is more complex: dilute, Na-rich solutions favor preferential sorption of Ca and Sr; whereas concentrated, Na-poor solutions show enrichment of Na in clinoptilolite. These relations indicate that the presence of K-rich, Ca-poor, dilute solutions will result in clinoptilolite with compositions significantly removed from the Na end-member. In such solutions, clinoptilolite will be stabilized relative to Na-rich minerals that do not readily cation exchange, such as analcime and albite.

3.4.3.4.2.4 Effects of hydration/dehydration of clinoptilolite. Hydration and dehydration of clinoptilolite may have significant consequences in the near-field environment. Dehydration will destabilize clinoptilolite relative to less hydrous assemblages (albite and analcime); release significant amounts of H_2O; have a significant effect on the thermal budget; and result in porosity changes due to changes in molar volume. The experimental data necessary to assess all of these factors have been obtained by Bish (1995) and Carey and Bish (1996a and b).

3.4.3.4.2.5 Equilibrium. The equilibrium H_2O contents of clinoptilolite as a function of temperature (25–250°C), water-vapor pressure (0–35 mbar), and

exchangeable cation (Na^+, K^+, and Ca^{2+}) were determined by Carey and Bish (1996a). These experiments were conducted by determining the equilibrium mass of clinoptilolite at a measured temperature and water-vapor pressure using a thermogravimetric balance.

These experiments show that clinoptilolite hydrates and dehydrates reversibly up to temperatures ≤215°C (Fig. 3.4-27). Above 215°C, Na-clinoptilolite suffers a slight loss in water adsorption capacity. K- and Ca-exchanged clinoptilolite maintain reversibility to temperatures >250°C. Equilibration time for hydration and dehydration of powders is on the order of an hour, so that the kinetics of hydration/dehydration do not appear to be relevant to processes at Yucca Mountain. The H_2O content of clinoptilolite is a smooth function of temperature and pressure (Fig. 3.4-28), and there are no discontinuities in the dehydration behavior at the boiling point of water. Clinoptilolite retains substantial H_2O to temperatures > 150°C, even in a nominally dry atmosphere.

The measured thermogravimetric equilibrium data were fit to a thermodynamic function describing the reaction:

anhydrous clinoptilolite (aCpt) + H_2O ↔hydrous clinoptilolite (hCpt) (2)

The equilibrium constant, K_{ideal}, containing ideal mixing terms for this reaction is:

$$\ln K_{ideal} = \left(\frac{\theta}{(1-\theta) f_{H_2O}} \right) \quad (3)$$

where θ is the ratio of the amount of H_2O in clinoptilolite relative to the maximum amount clinoptilolite contains.

The thermodynamic function was determined by analysis of the equilibrium constant as a function of temperature and composition (Fig. 3.4-29). The variations

in K were described with an equation giving the Gibbs free energy of hydration, the enthalpy of hydration, and two mixing parameters (W_1 and W_2):

$$-R\ln K = {}^{\Delta\mu^o_{Hy}}/_{T_o} + \Delta\bar{H}^o_{Hy}\left({}^1/_T - {}^1/_{T_o}\right) - 3R\left(\ln\left({}^T/_{T_o}\right) + \left({}^{T_o}/_T - 1\right)\right) + {}^{W_1}/_T\theta + {}^{W_2}/_T\theta^2 \qquad (4)$$

Fits of the data yielded thermodynamic parameters describing hydration in Na-, K-, and Ca-exchanged clinoptilolite (Table 3.4-8; Figs. 3.4-28 and 3.4-29). The results indicate that the energetics of hydration increase from K<Na<Ca clinoptilolite (Table 3.4-9).

The results for clinoptilolite are energetically similar to those of mordenite and intermediate between strongly (analcime) and weakly (cordierite) interacting systems. The similarity of the integral values of hydration for mordenite and clinoptilolite suggest that in the absence of additional thermodynamic data the hydration energetics of mordenite may be approximated by those of clinoptilolite. Note that the energetics of hydration are significantly greater than condensation of water vapor.

As discussed by Pabalan (1994), cation-exchange in clinoptilolite is accompanied by hydration and dehydration reactions. Consequently, the Gibbs free energy of exchange measured by Pabalan contains a contribution due to hydration reactions in addition to cation-exchange. The results described here may be used to "correct" the Gibbs free energy of exchange data to give energetics solely due to cations.

The equation of state for clinoptilolite (Equation 4) allows calculation of the equilibrium water content of clinoptilolite under conditions of interest in the NFE. Under conditions of rising temperature, clinoptilolite dehydrates even in the presence of an aqueous phase (Fig. 3.4-30). However, if dryout of the rock units occurs, as may happen if temperatures rise above 100°C, the degree of dehydration of clinoptilolite increases markedly. The equilibrium water content as a function of maximum sustainable water-vapor pressure, is shown in Fig. 3.4-30 for maximum pressures ranging between 1 and 20 bars.

3.4.3.4.2.6 Energetics. The energetics of hydration and dehydration of clinoptilolite have been measured calorimetrically by Carey and Bish (1996b). In these experiments, Na-, K-, and Ca-exchanged clinoptilolite samples were partially dehydrated, sealed in an evacuated ampoule, and placed in water where the heat of immersion was measured. The enthalpy of hydration (which is equivalent to the heat of immersion in the experiments) increases with decreasing water content in clinoptilolite (Fig. 3.4-31). This demonstrates that the energetic cost of dehydration increases as dehydration proceeds. The partial molar enthalpy of hydration was fit to an equation of the form (Table 3.4-10; Fig. 3.4-32):

$$\Delta\bar{H}_{Hy} = \Delta\bar{H}^{o}_{Hy} + W_1\theta + W_2\theta^2 \qquad (5)$$

A combination of the equilibrium and calorimetry studies can be used to assess the potential effects of hydration and dehydration processes on heat flow and pore saturation at Yucca Mountain. A simple numerical model was used that considers the thermal and hydrologic evolution of a thermally insulated block of clinoptilolite that receives a constant source of thermal energy. In the model, a 1 m^3 box has 10% porosity, is initially at 25°C, 100% relative humidity, and receives a thermal flux of 14 watts while maintaining a uniform temperature (the value of the thermal flux is representative of those considered for Yucca Mountain). The thermal flux is consumed by the heat capacity of clinoptilolite and by dehydration processes. It is assumed that the box is porous to water vapor and a maximum pressure of 1 bar is attained. The temperature achieved by the box is dramatically lower when clinoptilolite is allowed to dehydrate (Fig. 3.4-33). The model without dehydration reached 395°C after 844 days, whereas that allowing dehydration reached only 250°C over the same period. The kink in the temperature evolution at 100°C is the point at which the pores attained the maximum water-vapor pressure of 1 bar. During the dehydration process, the clinoptilolite released 1.63 pore volumes of liquid water. In other words, the model constraints require that an amount of water equal to 16% of the rock volume must drain away (10% porosity).

These calculations demonstrate that dehydration and hydration of clinoptilolite can affect the temperature and saturation field in the NFE. Whether clinoptilolite has a significant effect depends on the interplay of factors such as: the rate of heating versus the rate of thermal dissipation; and the ratio of water released by clinoptilolite to the amount infiltrating the rock unit in a given period of time. These can only be quantitatively addressed using coupled numerical models of clinoptilolite hydration/dehydration and thermo-hydrologic processes.

3.4.3.4.2.7 Changes in Molar Volume of Clinoptilolite. The molar volume of clinoptilolite is a sensitive function of temperature, exchangeable cation, and hydration state (Bish, 1984; Bish, 1995). Changes in molar volume of clinoptilolite may be important in the Calico Hills Formation, where clinoptilolite constitutes from 50 to 70% of the rock. Bish (1984) observed that decreases in molar volume on heating to 300°C ranged from 1.6 to 3.6 to 8.6% for K-, Ca-, and Na-exchanged samples, respectively. Apparently the bulk of the volume decrease was a direct result of dehydration. For a rock with 50% clinoptilolite, an 8% decrease in volume could result in the development of 4% additional rock porosity.

3.4.3.4.2.8 Analcime

3.4.3.4.2.8.1 Thermodynamic Stability. Natural analcime is Na-rich with a Si/Al ratio that varies from nearly stoichiometric (Si/Al = 2) in hydrothermal environments to siliceous compositions (Si/Al = 2.55) typical of sedimentary or diagenetic environments (e.g., Gottardi and Galli, 1985). The analcime at Yucca Mountain is a siliceous, sodic variety with Si/Al ~ 2.75 (Broxton et al., 1987). Most studies of the thermodynamic properties of analcime have been conducted on nearly stoichiometric material derived from hydrothermal environments. Thus the important effect of variations in Si/Al ratio on the stability of analcime were largely unknown until recently.

As a part of the mineralogical investigations at Los Alamos National Laboratory, a study of the solubility of two analcime samples with Si/Al ratios of 2.0 and 2.55 were conducted in collaboration with Pennsylvania State University and Yale University (Barnes and Wilkin, 1995). These data complement the calorimetric studies reported by Robie et al. (1979) and Johnson et al. (1982) and the solubility

study of Murphy et al. (1996) on stoichiometric analcime. The study by Barnes and Wilkin allows the direct calculation of the energetic effect of the substitution Na + Al = Si and, as discussed below, provides a basis for determining the effect of similar substitutions in other zeolites, such as clinoptilolite.

The reported uncertainty in the measured Gibbs free energy of formation of analcime varies between 3 and 5 kJ/mol (Table 3.4-11; Fig. 3.4-34). Note, however, that Johnson et al. (1992) revised their measured value for analcime by almost 9ÊkJ/mol due to a change in the reference value of silica and gibbsite used in the solution calorimetry. This revised value may be more accurate than the earlier result, but earlier work and many internally consistent thermodynamic data bases are implicitly built on the previous reference states. As a consequence, it is probably advisable to retain the old value until a consensus on the most useful reference value for silica can be achieved. The results of Barnes and Wilkin (1995) for both samples (Si/Al = 2 and 2.55) were obtained by extrapolation from experiments at 50 to 300°C. The *measured* solubility at 25°C for the Mt. St. Hilaire (Si/Al = 2) sample is also provided in Table 3.4-11, but Barnes and Wilkin showed that their results at 25°C are not consistent with results extrapolated from higher temperatures.

Thermodynamic values for analcime have also been derived from phase equilibria constraints by Helgeson et al. (1978) and estimated by using polyhedral summation methods by Chermak and Rimstidt (1989) and Chipera et al. (1995a; Table 3.4-12 and Fig. 3.4-34). The summation methods allow calculation of the Gibbs free energy of formation for arbitrary compositions, but such summations must be checked against actual measurements.

The data presented by Barnes and Wilkin allow calculation of an empirical relationship giving the relationship of the Gibbs free energy of formation of analcime as a function of Si/Al ratio:

$$\Delta G_f^{analcime} = -3090 + 98.8\left(Si/_{Al} - 2\right) \qquad (6)$$

Their results agree well with the intermediate value measured by Johnson et al. (1982; Fig. 3.4-34), and they noted that their results are consistent with the ideal solution model of Wise (1984) for Si/Al mixing in analcime.

The value derived by Helgeson et al. (1978) is also in good agreement with the measurements. The estimation methods of Chermak and Rimstidt (1989) are slightly high and those of Chipera et al. (1995a) are somewhat better. Interestingly, these estimation methods also provide reasonable-estimates of the trends in the value of the Gibbs free energy of hydration as a function of Si/Al ratio. The equation derived from Chermak and Rimstidt is (in kJ/mol):

$$\Delta G_f^{analcime} = -3099 + 298(Si - 2) \tag{7}$$

and that of Chipera et al. is

$$\Delta G_f^{analcime} = -3094 + 281(Si - 2) \tag{8}$$

These conclusions regarding the compositional effects of analcime thermodynamics are consistent with the calorimetric study of Petrovic and Navrotsky (1995) on the energetics of the Na + Al = Si substitution in faujasite. They found that the increase in the enthalpy of formation per mole of Si was 267±kJ/mol, very similar to the values of 281 and 298 for the Gibbs free energy of formation obtained by estimation (Equations 7 and 8).

For a variety of common reactions involving analcime, the relations in Equations 6, 7, and 8 indicate that siliceous analcime is destabilized relative to stoichiometric analcime with respect to sodium end-member phases such as albite or clinoptilolite (Fig. 3.4-35). The degree of destabilization for a reaction balanced on aluminum of analcime relative to another sodic framework-aluminosilicate (such as albite or clinoptilolite) can be calculated with the aid of one of these equations. For example, for the reaction

$$(18\text{-}3x/(1\text{-}x))\ SiO_{2\,aq} + 6/(1\text{-}x)\ Na_{1-x}Al_{1-x}Si_{2+x}O_6 \cdot H_2O + 19\ H_2O =$$
$$Na_6Al_6Si_{30}O_{72} \cdot 20H_2O \qquad (9)$$

the degree of destabilization corresponds to

$$\frac{1}{RT2.303}\left(\Delta G_f^{o,\,anal}\left(\frac{-x}{1-x}\right) - 98.8\left(\frac{3x}{(1-x)^2}\right) + \Delta G_{f,\,SiO_2}^{o,\,aqueous}\left(\frac{3x}{1-x}\right)\right) = \left(\frac{3x}{1-x}\right) log\left(a_{SiO_2}^{aqueous}\right) \qquad (10)$$

where Equation 7 has been used to calculate the effect.

The effects of a 5 kJ/mol uncertainty in the Gibbs free energy of formation on phase relations involving analcime are considerable (Fig. 3.4-36). The uncertainty introduced by analcime for a given reaction in terms of the equilibrium constant can be calculated as

$$log\,K = \pm n\frac{5000\ J/mol}{2.303RT} = \pm n(0.876)@25\ ^oC \qquad (11)$$

where n is the stoichiometric coefficient of analcime in the reaction. For example, the breakdown of clinoptilolite to analcime calculated by Chipera et al. (1995a):

$$(K_{0.3}Na_{0.1}Ca_{1.5})Al_{3.4}Si_{14.6}O_{36} \cdot 10.8H_2O\ (clinoptilolite) + 3.3Na^+ + 3.95\ H_2O \Leftrightarrow$$
$$4.25Na_{0.8}Al_{0.8}Si_{2.2}O_6 \cdot H_2O\ (analcime) + 0.3\ K^+ + 1.5\ Ca^{2+} + 5.25Si(OH)_4 \qquad (12)$$

is shifted by ±2.5 log units on activity-activity diagrams commonly used to analyze phase relations at Yucca Mountain (Fig. 3.4-36).

Thermodynamic data for analcime at elevated temperature was obtained by Barnes and Wilkin (1995) using solubility data at temperatures between 25 and 300°C. The Gibbs free energy of formation of analcime was calculated from these data (Table 3.4-13). Linear regression of the Gibbs free energy of formation as a function of temperature provided the enthalpy of formation and standard state

entropy (the heat capacity of the dissolution reaction was assumed to be zero; Table 3.4-14). Additional high-temperature data include heat capacity measurements of analcime between 25 and 350°C (Johnson et al., 1992). However, Carey (1993) argued that the heat capacity of hydrous analcime above 25°C is more accurately given by the sum of the heat capacities of anhydrous analcime (Johnson et al., 1992), H_2O vapor (Robie et al., 1979), and a constant factor accounting for H_2O sorption which is equal to the gas constant.

3.4.3.4.2.8.2 Estimated Thermodynamic Properties of Zeolites and Clays. Thermodynamic data are limited for several important zeolites and clays and still less available for treating compositional variation of these phases (see also Section 3.4.2). One method of addressing this deficiency is to make semi-quantitative calculations using estimated thermodynamic properties. Chipera et al. (1995a) provide the most comprehensive example of this method, obtaining estimated Gibbs free energies and enthalpies of formation, third-law entropies, and heat capacity values for zeolites and clays with compositions representative of those at Yucca Mountain (Table 3.4-15). These data provide a very useful framework for understanding potential reactions among zeolites and clays as a function of temperature, pressure, and solution chemistry (Chipera et al., 1995a).

3.4.3.4.2.9 Smectite. Hydration and dehydration reactions in smectite have a H_2O significant effect on smectite stability and molar volume (due to swelling/collapse of the aluminosilicate layers). These reactions may also affect pore-water saturation, fracture filling, and the osmotic swelling capacity (Bish, 1988b). The hydration and dehydration behavior of smectite is difficult to model thermodynamically because of the pronounced hysteresis in molar volume and water content (Fig. 3.4-37). Although the hydration/dehydration behavior of smectite is an important component in modeling the effects of repository-induced heating on the repository water budget, the highly reversible nature of these reactions suggests that the long-term effects on rock properties may be minor. One of the most important phenomena observed during heating of smectites is the dramatic decrease in osmotic swelling ability after only short-term heating under steam conditions (e.g., Couture, 1985). Such behavior can have very important implications for the long-

term behavior of smectites in the NFE and for their importance in affecting transport. For example, it is likely that NFE conditions will be conducive to the total loss of osmotic swelling capacity of smectites that occur both in fractures in the host rock and in the altered zone immediately underlying the host rock. Such a reaction would thus dramatically increase the hydraulic conductivity of smectite-lined fractures.

Data obtained from drill cores taken from the north and east of the exploration block show that the well-known reaction of smectite to interstratified illite/smectite occurs with increasing depth (Bish, 1989). Both experimental data and field observations demonstrate that this transformation develops progressively from 100 to 250°C. The swelling capacity of smectite is steadily reduced during this diagenetic reaction from 25 to 100°C (cf. Bish, 1989, for a more complete discussion).

3.4.3.4.2.10 Vitrophyre (volcanic glass). The effects of elevated temperatures on Yucca Mountain volcanic glasses have been studied experimentally (see Chapter 10 for a discussion of glass alteration in the presence of water, and Knauss and Peiffer, 1986, Knauss, 1987). Dehydration and hydration of a sample of the basal vitrophyre of the Topopah Spring Tuff were studied by thermogravimetry and by long-term dry heating experiments (Vaniman et al., 1993). The glass initially contained 2.8 to 4.6 wt% H_2O. Approximately three-fourths of the water was lost during long-term heating at 200°C, but ~1 wt% H_2O was not lost at temperatures less than 400°C, even after long-term heating. Rehydration of the samples at room temperature and 79% relative humidity was continuous but did not reach completion after 10,000 hours. No devitrification reactions were observed during the dry heating experiments, even at 400°C for 10,000 hours, but up to 60% of the fluorine in the glass was evolved.

3.4.3.4.2.11 Kinetics of Dissolution and Precipitation. The long-term fate of minerals in the NFE cannot be determined without measurements of the kinetics of reactions as a function of degree of saturation and temperature. These measurements are usually made by dissolution or precipitation of a given mass of material of known surface area (typically a BET surface area) in a known volume of fluid. The studies are conducted either in a batch mode with continuously changing

solution compositions (e.g., Murphy et al., 1996) or preferably in flow-through devices at constant solution composition (e.g., Nagy et al., 1991). The results reported below have been interpreted using transition state theory (e.g., Nagy et al., 1991) in which the rate of dissolution or precipitation is expressed as

$$R(\text{moles/m}^2\text{-s}) = -k_{diss}\left(1 - IAP/K_{eq}\right) \quad (13)$$

where the ratio of the ion-activity-product (IAP) to the equilibrium constant (K_{aq}) expresses the degree of saturation and k_{diss} is the rate constant for the dissolution reaction. The parameter k_{diss} is not an intrinsic rate parameter but may depend on pH and other surface-adsorbed species (Nagy et al., 1991). Equation 13 indicates that the rate of dissolution reaches a constant value ($-k_{diss}$) for significant degrees of undersaturation but that the rate of precipitation increases without bound for increasing supersaturation. Table 3.4-16 summarizes relevant data pertinent to phases important at Yucca Mountain, in addition to more recent data obtained for clinoptilolite and analcime by Murphy et al. (1996) and MacInnis et al. (1995).

3.4.3.4.2.12 Kinetic data for clinoptilolite and analcime. The dissolution rate obtained for clinoptilolite by MacInnis et al. (1995) using a flow-through apparatus appears to be anomalous with respect to other minerals and is not in agreement with the batch study of Murphy et al. (1996). Unfortunately, the study of MacInnis et al. is the only source of data for dissolution rates of clinoptilolite at elevated temperatures (50, 80, and 125°C). Their results were expressed as

$$R = -k_o \exp\left(-E_a/RT\right) a_{H^+}^{-0.54}\left(IAP/K_{eq}\right) \quad (14)$$

where $k_o = 2 \pm 27 \times 10^5$ mol/m^2-s; $E_a = 35.1 \pm 9.2$ kcal/mol; and the experiments were conducted at pH 7.5 to 9.0. The difference between Equations 13 and 14 is a consequence of the fact that MacInnis et al. did not observe a constant dissolution rate at significant undersaturation, but they showed data indicating a linear

relationship between rate and undersaturation. Consequently, the dissolution process they observed may be distinct from that modeled by transition state theory (Equation 13). MacInnis et al. also observed some evidence of inhibition by aqueous Al, but were unable to quantify this effect.

There is no single study providing rate data for analcime at more than one temperature. Lasaga et al. (1994a) determined the dissolution of analcime at 80°C with flow-through methods. Their rate equation is similar to that determined by MacInnis et al. (1995) in which the rate depends linearly on the degree of saturation:

$$R = -10^{-12.4} a_{Al(OH)_4^-}^{-0.27} \left(\left| \Delta G \text{ kcal mol}^{-1} \right| \right)^{1.05} \quad (15)$$

where the measurements were made at pH 8.6-8.9 and the degree of saturation is represented by the Gibbs free energy of the dissolution reaction. Typical values at 80°C for the net dissolution rate constant, $\log(k_{diss})$, are approximately -11. Again, these rate constants do not agree well with the batch study values of Murphy et al. (1996) where rates were -11 at 25°C.

In summary, the available kinetic data for both analcime and clinoptilolite are not well constrained and reflect the incomplete status of kinetic data measurement for these minerals. Based on existing data, the dissolution of clinoptilolite does appear to be slower than analcime, by a factor near 100.

3.4.3.5 Acknowledgements

We are grateful to D. Vaniman for a thorough review of this manuscript.

3.4.3.6 References

Alietti, A. (1972) Polymorphism and crystal-chemistry of heulandites and clinoptilolites. *American Mineralogist*, 57, 1448–1462.

Anderson, L. (1984) Rock property measurements on large-volume core samples from Yucca Mountain USW GU-3/G-3 and USW G-4 boreholes, Nevada Test Site, Nevada. *U. S. Geological Survey Open-File Report*, USGS-OFR-84-552, 39 p.

Barnes, H. L., and Wilkin, R. T. (1995) Kinetic measurements on the silicates of the Yucca Mountain potential repository (Yucca Mountain final report for FY95, Los Alamos National Laboratory).

Barrer, R. M., and Cram, P. J. (1971) Heats of immersion of outgassed and ion-exchanged zeolites. In *Molecular Sieve Zeolites-II*, E. M. Flanigen, and L. B. Sand , eds., 105-131. American Chemical Society, Washington, D.C.

Berman, R. G., and Brown, T. H. (1985) Heat capacity of minerals in the system Na_2O-K_2O-CaO-MgO-FeO-Fe_2O_3-Al_2O_3-SiO_2-TiO_2-H_2O-CO_2: Representation, estimation, and high temperature extrapolation. *Contributions to Mineralogy and Petrology*, 89, 168–183.

Bish, D. L. (1984) Effects of exchangeable cation composition on the thermal expansion/contraction of clinoptilolite. *Clays & Clay Minerals*, 32, 444–452.

Bish, D. L. (1988a) Effects of composition on the dehydration behavior of clinoptilolite and heulandite. In *Occurrence, Properties and Utilization of Natural Zeolites*, D. Kallo and H. S. Sherry, eds. Akademiai Kiado, Budapest.

Bish, D. L. (1988b) Smectite dehydration and stability: Applications to radioactive waste isolation at Yucca Mountain. *Los Alamos National Laboratory Report*, LA-11023-MS, 31 pp.

Bish, D. L. (1989) Evaluation of past and future alterations in tuff at Yucca Mountain, Nevada, based on the clay mineralogy of drill cores USW G-1, G-2, and G-3. *Los Alamos National Laboratory Report*, LA-10667-MS, 40 pp.

Bish, D. L. (1995) Thermal behavior of natural zeolites. In *Natural Zeolites '93: Occurrence, Properties, Use*, D. W. Ming and F. A. Mumpton, eds., 259–269.

Bish, D. L., and Chipera, S. J. (1986) Mineralogy of drill holes J-13, UE-25A#1, and USW G-1 at Yucca Mountain, Nevada. *Los Alamos National Laboratory Report*, LA-10764-MS. HQS.880517.1957

Bish, D. L., and Chipera, S. J. (1988) Problems and solutions in quantitative analysis of complex mixtures by X-ray powder diffraction. *Advances in X-Ray Analysis*, 31, 295-308. NNA.890405.0178

Bish, D. L., and Chipera, S. J. (1989) Revised mineralogic summary of Yucca Mountain, Nevada. *Los Alamos National Laboratory Report*, LA-11497-MS, 68 pp. NNA.891019.0029.

Bish, D. L., and Chipera, S. J. (1991) Detection of trace amounts of erionite using X-ray powder diffraction: Erionite in tuffs of Yucca Mountain, Nevada, and central Turkey. *Clays & Clay Minerals*, 39, 437–445.

Bish, D. L., and Chipera, S. J. (1995) Accuracy in quantitative X-ray powder diffraction analyses. *Advances in X-ray Analysis*, 38 47–57.

Bish, D. L., and Reynolds, R. C., Jr. (1989) Sample preparation for X-ray diffraction. In *Modern Powder Diffraction*, D. L. Bish and J. E. Post, eds., Mineralogical Society of America, Washington, D.C., Vol. 20, 73–99.

Bish, D. L., Ogard, A. E., Vaniman, D. T., and Benson, L. (1984) Mineralogy-petrology and groundwater geochemistry of Yucca Mountain tuffs. *Materials Research Society Symposium Proceedings*, 26, 283–291.

Blacic, J., Carter, J., Halleck, P., Johnson, P., Shankland, T., Anderson, R., Spicochi, K., and Heller, A. (1982) Effects of long-term exposure of tuffs to high-level nuclear waste-repository conditions: Preliminary report. *Los Alamos National Laboratory Report*, LA-9174-PR.

Blacic, J. D., Vaniman, D. T., Bish, D. L., Duffy, C. J., and Gooley, R. C. (1986) Effects of long-term exposure of tuffs to high-level nuclear waste repository conditions: Final Report. *Los Alamos National Laboratory Report*, LA-9330-MS, 33 pp.

Broxton, D. E., Warren, R. G., Hagan, R. C., and Luedemann, G. (1986) Chemistry of diagenetically altered tuffs at a potential nuclear waste repository, Yucca Mountain, Nye County, Nevada: *Los Alamos National Laboratory Report*, LA-10802-MS, 160 pp.

Broxton, D. E., Bish, D. L., and Warren, R. G. (1987) Distribution and chemistry of diagenetic minerals at Yucca Mountain, Nye County, Nevada. *Clays and Clay Minerals*, 35, 89–110.

Broxton, D. E., Warren, R. G., Byers, F. M., Jr., and Scott, R. B. (1989) Chemical and mineralogic trends within the Timber Mountain-Oasis Valley caldera complex: Evidence for multiple cycles of chemical evolution in a long-lived silicic magma system. *Journal of Geophysical Research*, 94, 5961–5985.

Buscheck, T. A., and Nitao, J. J. (1992) The impact of thermal loading on repository performance at Yucca Mountain. *High-Level Radioactive Waste Management, Proceedings of the 3rd Annual International Conference*, April 27–May 1, 1992, Las Vegas, Nevada.

Byers, F. M., Jr. (1985) Petrochemical variation of Topopah Spring tuff matrix with depth (stratigraphic level), drill hole USW G-4, Yucca Mountain, Nevada. *Los Alamos National Laboratory Report*, LA-10561-MS.

Byers, F. M., Jr., and Moore, L. (1987) Petrographic variation of the topopah spring tuff matrix within and between cored drill holes, Yucca Mountain, Nevada. *Los Alamos National Laboratory Report*, LA-10901-MS.

Carey, J. W. (1993) The heat capacity of hydrous cordierite above 295 K. *Physics and Chemistry of Minerals*, 19, 578–583.

Carey, J. W. (1995) A thermodynamic formulation of hydrous cordierite. *Contributions to Mineralogy and Petrology*, 119, 155–165.

Carey, J. W., and Bish, D. L. (1994) Hydration energetics of zeolites. *Proceedings of the 31st Annual Meeting of the Clay Minerals Society*, Saskatoon, Saskatchewan, p. 52.

Carey, J. W., and Bish, D. L. (1996a) Equilibrium in the clinoptilolite-H_2O system. *American Mineralogist* (in press).

Carey, J. W., and Bish, D. L. (1996b) Calorimetric measurement of the enthalpy of hydration of clinoptilolite (submitted to Clays and Clay Minerals).

Carlos, B. A. (1987) Minerals in fractures of the saturated zone from drill core USW G-4, Yucca Mountain, Nye County, Nevada. *Los Alamos National Laboratory Report*, LA-10927-MS, 32 pp.

Carlos, B. A., Chipera, S. J., Bish, D. L., and Raymond, R. (1995a) Distribution and chemistry of fracture-lining zeolites at Yucca Mountain, Nevada. In *Natural Zeolites '93: Occurrence, Properties, Use*, D. W. Ming and F. A. Mumpton, eds., 547_563.

Carlos, B. A., Chipera, S. J., and Bish, D. L. (1995b) Distribution and chemistry of fracture-lining zeolites at Yucca Mountain, Nevada. *Los Alamos National Laboratory Report*, LA-12977-MS, 92 pp.

Carlos, B. A., Chipera, S. J., and Snow, M. G. (1995c) Multiple episodes of zeolite deposition in fractured silicic tuff. In *Proceedings of the 8th International Symposium on Water-Rock Interaction—WRI-8*, Y. K. Kharaka and O. V. Chudaev, eds; Balkema, Rotterdam, 67–71.

Chermak, J. A., and Rimstidt, J. D. (1989) Estimating the thermodynamic properties (Gf and Hf) of silicate minerals at 298 K from the sum of polyhedral contributions. *American Mineralogist*, 74, 1023–1031.

Chipera, S. J., and Bish, D. L. (1988) Mineralogy of drill hole UE-25P#1 at Yucca Mountain, Nevada. *Los Alamos National Laboratory Report*, LA-11292-MS.

Chipera, S. J., and Bish, D. L. (1995) Multi-reflection RIR and intensity normalizations for quantitative analyses: Applications to feldspars and zeolites. *Powder Diffraction*, 10, 47–55.

Chipera, S. J., Carey, J. W. and Bish, D. L. (1994) The nature of interlayer water in smectite. *Proceedings of the 31st Annual Meeting of the Clay Minerals Society*, Saskatoon, Saskatchewan, p. 53.

Chipera, S. J., Bish, D. L., and Carlos, B. A. (1995a) Equilibrium modeling of the formation of zeolites in fractures at Yucca Mountain, Nevada. In *Natural Zeolites '93: Occurrence, Properties, Use*, D. W. Ming and F. A. Mumpton, eds., 565–577.

Chipera, S. J., Vaniman, D. T., Carlos, B. A., and Bish, D. L. (1995b) Mineralogic variation in drill core UE-25 UZ#16, Yucca Mountain, Nevada. *Los Alamos National Laboratory Report*, LA-12810-MS, 39 pp.

Chung, F. H. (1974) Quantitative interpretation of X-ray diffraction patterns of mixtures. I. Matrix-flushing method for quantitative multicomponent analysis. *Journal of Applied Crystallography*, 7, 519–525. NNA.890405.0179

Couture, R. A. (1985) Steam rapidly reduces the swelling capacity of bentonite. *Nature*, 318, 50_52.

Czarnecki, J. B. (1985) Simulated effects of increased recharge on the ground-water flow system of Yucca Mountain and vicinity, Nevada-California. *U. S. Geol. Survey Water Resources Invest. Report*, 84-4344.

Deer, W., Howie, R., and Zussman, J. (1963) *Rock-Forming Minerals*. Vols. 3 and 4. Longmans, London.

Domenico, P. A., and Schwartz, F. W. (1990) *Physical and Chemical Hydrogeology*. John Wiley & Sons, New York.

Duffy, C. J. (1983a) Hydrothermal stability studies. In *Research and Development Related to the Nevada Nuclear Waste Storage Investigations July 1-September 30, 1982*, W. R. Daniels, B. R. Erdal, and D. T. Vaniman, compilers, *Los Alamos National Laboratory Progress Report*, LA-9577-PR.

Duffy, C. J. (1983b) Permeability, porosity, and hydrothermal reactions. In *Research and Development Related to the Nevada Nuclear Waste Storage Investigations January 1–March 30, 1983*, K. Wolfsberg, D. T. Vaniman, and A. E. Ogard, compilers, *Los Alamos National Laboratory Progress Report*, LA-9793-PR.

Duffy, C. J. (1993). Preliminary conceptual model for mineral evolution in Yucca Mountain. *Los Alamos National Laboratory Report*, LA-12708-MS.

Ervin, E. M., Luckey, R. R., and Burkhardt, D. J. (1993) Summary of revised potentiometric-surface map for Yucca Mountain and vicinity, Nevada. In *High*

Level Radioactive Waste Management, American Nuclear Society and American Society of Civil Engineers, Proceedings of the 4th Annual International Conference, Las Vegas, Nevada, 1554–1558.

Fabryka-Martin, J., Dixon, P., Levy, S., Liu, B., Turin, J., and Wolfsberg, A. (1996) Systematic sampling for chlorine-36 in the Exploratory Studies Facility. Las Alamos National Laboratory YMSCP letter report.

Flint, A. L., Flint, L. E., and Hevesi, J. A. (1993) The influence of long term climate change on net infiltration at Yucca Mountain, Nevada. In *High Level Radioactive Waste Management*, American Nuclear Society and American Society of Civil Engineers, Proceedings of the 4th Annual International Conference, Las Vegas, Nevada, 152–159.

Glassley, W. E. (1995) Characterization of chemical and mineralogical changes in the post-emplacement environment. YMSCP Study Plan for SCP Section 8.3.4.2.4.1, R1, p. 69.

Gottardi, G., and Galli, E. (1985) *Natural Zeolites*. Springer-Verlag, Berlin, 409 pp.

Helgeson, H. C., Delany, J. M., Nesbitt, H. W., and Bird, D. K. (1978) Summary and critique of the thermodynamic properties of rock-forming minerals. *American Journal of Science*, 278-A, 229 p.

Hemingway, B. S., and Robie, R. A. (1984) Thermodynamic properties of zeolites: low-temperature heat capacities and thermodynamic functions for phillipsite and clinoptilolite. Estimates of the thermochemical properties of zeolitic water at low temperature. *American Mineralogist*, 69, 692_700.

Holland, T. J. B. (1989) Dependence of entropy on volume for silicate and oxide minerals: A review and a predictive model. *American Mineralogist*, 74, 5_13.

JCPDS (1986) *Mineral Powder Diffraction File Data Book*. International Centre for Diffraction Data, Swarthmore, Pennsylvania.

Johnson, G. K., Flotow, H. E., O'Hare, P. A. G., and Wise, W. S. (1982) Thermodynamic studies of zeolites: Analcime and dehydrated analcime. *American Mineralogist*, 67, 736–748.

Johnson, G. K., Flotow, H. E., O'Hare, P. A. G., and Wise, W. S. (1985) Thermodynamic studies of zeolites: Heulandite. *American Mineralogist*, 70, 1065–1071.

Johnson, G. K., Tasker, I. R., Jurgens, R., and O'Hare, P. A. G. (1991) Thermodynamic studies of zeolites: Clinoptilolite. *Journal of Chemical Thermodynamics*, 23, 475–484.

Johnson, G. K., Tasker, I. R., Flotow, H. E., O'Hare, P. A. G., and Wise, W. S. (1992) Thermodynamic studies of mordenite, dehydrated mordenite, and gibbsite. *American Mineralogist*, 77, 85–93.

Klug, H. P., and Alexander, L. E. (1974) *X-ray Diffraction Procedures for Polycrystalline and Amorphous Materials*, John Wiley & Sons, Inc., New York.

Knauss, K. (1987) Zeolitization of glassy Topopah Spring tuff under hydrothermal conditions. Mat. Res. Soc. Symposium, v. 84, p. 737–745.

Knauss, K., and Peifer, D. (1986) Reaction of vitric Topopah Spring Tuff and J-13 ground water under hydrothermal conditions using Dickson-type, gold-bag rocking autoclaves. *Lawrence Livermore National Laboratory Report*, UCRL-53795.

Kranz, R. L., Bish, D. L., and Blacic, J. D. (1989) Hydration and dehydration of zeolitic tuff from Yucca Mountain, Nevada.. *Geophysical Research Letters*, **16**, 1113–1116.

Lasaga, A. C. (1984) Chemical kinetics of water-rock interactions. *Journal of Geophysical Research*, **89**, 4009–4025.

Lasaga, A. C., Ganor, J., and MacInnis, I. N. (1994a). Progress report on the kinetic measurements of the reactions of the silicates at the Yucca Mountain potential repository site (August, 1994) Los Alamos National Laboratory.

Lasaga, A. C., Soler, J. M., Ganor, J., Burch, T. E., and Nagy, K. L. (1994b) Chemical weathering rate laws and global geochemical cycles. *Geochimica et Cosmochimica Acta*, **58**, 2361_2386.

Levy, S. S. (1984a) Studies of altered vitrophyre for the prediction of nuclear waste repository induced thermal alteration at Yucca Mountain, Nevada. In: *Scientific Basis for Nuclear Waste Management VII*, G. L. McVay, ed., Elsevier, New York, 959–966.

Levy, S. S. (1984b) Petrology of samples from drill holes USW H-3, H-4, and H-5, Yucca Mountain, Nevada. *Los Alamos National Laboratory Report*, **LA-9706-MS**, 77 pp.

Levy, S. S. (1991) Mineralogic alteration history and paleohydrology at Yucca Mountain, Nevada. In *High Level Radioactive Waste Management*, American Nuclear Society and American Society of Civil Engineers, Proceedings of the 4th Annual International Conference, Las Vegas, Nevada, 477–485.

Levy, S. S. (1992) Natural gels in the Yucca Mountain area, Nevada, USA. *Applied Clay Science*, **7**, 79_85.

Levy, S. S., and O'Neil, J. R. (1989) Moderate-temperature zeolitic alteration in a cooling pyroclastic deposit. *Chemical Geology*, **76**, 321–326.

Lipman, P. W. (1971) Iron-titanium oxide phenocrysts in compositionally zoned ash-flow sheets from southern Nevada. *Journal of Geology*, **79**, 438–456.

MacInnis, I. N., Wilkin, R. T., Mercy, M. A., Barnes, H. L., and Lasaga, A. C. (1995) A rate law for clinoptilolite dissolution/precipitation at 50–125°C in basic solutions. YMSCP Milestone No. LA3445. Los Alamos National Laboratory, LA-EES-1-TIP-95-017.

Marshall, B. D., Peterman, Z. E., and Stuckless, J. S. (1993) Strontium isotopic evidence for a higher water table at Yucca Mountain. In *High Level Radioactive Waste Management*, American Nuclear Society and American Society of Civil Engineers, Proceedings of the 4th Annual International Conference, Las Vegas, Nevada, 1948_1952.

Mumpton, F. A. (1960) Clinoptilolite redefined. *American Mineralogist*, **45**, 351–369.

Murphy, W. M., Pabalan, R. T., Prikryl, J. D., and Goulet, C. J. (1996) Reaction kinetics and thermodynamics of aqueous dissolution and growth of analcime and Na-clinoptilolite at 25°C. *American Journal of Science*, **296**, 128–186.

Nagy, K. L., Blum, A. E., and Lasaga, A. C. (1991) Dissolution and precipitation kinetics of kaolinite at 80 C and pH 3: The dependence on solution saturation state. *American Journal of Science*, **291**, 649–686.

Pabalan, R. T. (1994) Thermodynamics of ion exchange between clinoptilolite and aqueous solutions of Na^+/K^+ and Na^+/Ca^{2+}. *Geochimica et Cosmochimica Acta*, **58**, 4573–4590.

Pabalan, R. T., and Bertetti, F. P. (1994) Thermodynamics of ion exchange between Na^+/Sr^{2+} solutions and the zeolite mineral clinoptilolite. In *Scientific Basis for Nuclear Waste Management XVII*, Barkatt, A., and Van Konynenburg, R. A., eds., Materials Research Society Symposium Proceedings 333, 731–738.

Paces, J. (1996) "Submission of Milestone: 3GQH455, Due February 29, 1996," Memorandum to R. W. Craig, Chief, Yucca Mountain Project Branch, WRD, Las Vegas, NV, February 23, 1996.

Peacor, D. R. (1973) High-temperature single-crystal study of the cristobalite inversion. *Zeitschrift für Kristallographie*, 138, 274–298.

Petrovic, I., and Navrotsky, A. (1995) Thermochemistry of Na-faujasites with varying Si/Al ratios (submitted to Microporous Materials).

Renders, P. J. N., Gammons, C. H., and Barnes, H. L. (1995) Precipitation and dissolution rate constants for cristobalite from 150 to 300°C. *Geochimica et Cosmochimica Acta*, 59, 77–85.

Riehle, J. R. (1973) Calculated compaction profiles of rhyolitic ash-flow tuffs. *Geological Society of America Bulletin*, 84, 2193–2216.

Rimstidt, J. D., and Barnes, H. L. (1980) The kinetics of silica-water reactions. *Geochimica et Cosmochimica Acta*, 44, 1683–1699.

Robie, R. A., Hemingway, B. S., and Fisher, J. R. (1979) Thermodynamic Properties of Minerals and Related Substances at 298.15 K and 1 Bar (10^5 Pascals) Pressure and at Higher Temperature. *U. S. Geological Survey Bulletin*, 1452.

Rosenbaum, J. G. (1986) Paleomagnetic directional dispersion produced by plastic deformation in a thick miocene welded tuff, southern Nevada: Implications for welding temperatures. *Journal of Geophysical Research*, 91, 12,817–12,834.

Sheppard, R. A., Gude, A. J., 3rd., and Fitzpatrick, J. J. (1988) Distribution, characterization, and genesis of mordenite in Miocene silicic tuffs at Yucca Mountain, Nye County, Nevada. *U. S. Geological Survey Bulletin*, 1777, 22 pp.

Sherry, H. S. (1969) The ion-exchange properties of zeolites. In *Ion Exchange*, J. A. Marinsky , ed., Marcel Dekker, Inc., New York, 89–133.

Smith, D. K., Nichols, M. C., and Zolensky, M. E. (1983) POWD10, A FORTRAN IV Program for Calculating X-Ray Powder Diffraction PatternsÑVersion 10. Pennsylvania State University, College of Earth and Mineral Sciences report. NNA.890602.0030

Smyth, J. R., and Bish, D. L. (1988) *Crystal Structures and Cation Sites of the Rock-Forming Minerals*. Allen & Unwin, London, 332 pp.

Vaniman, D. T., and Bish, D. L. (1995) The importance of zeolites in the potential high-level radioactive waste repository at Yucca Mountain, Nevada. In *Natural Zeolites '93: Occurrence, Properties, Use*, D. W. Ming and F. A. Mumpton, eds., 533–546.

Vaniman, D., Bish, D., and Chipera, S. (1993) Dehydration and rehydration of a tuff vitrophyre. *Journal of Geophysical Research*, 98, 22309–22320.

Wise, W. S. (1984) Thermodynamic studies of zeolites. Analcime solid solutions. In *Proceedings of the Sixth International Zeolite Conference*, D. Olson , and A. Bisio, eds., Butterworths, Surrey, UK, 616–622.

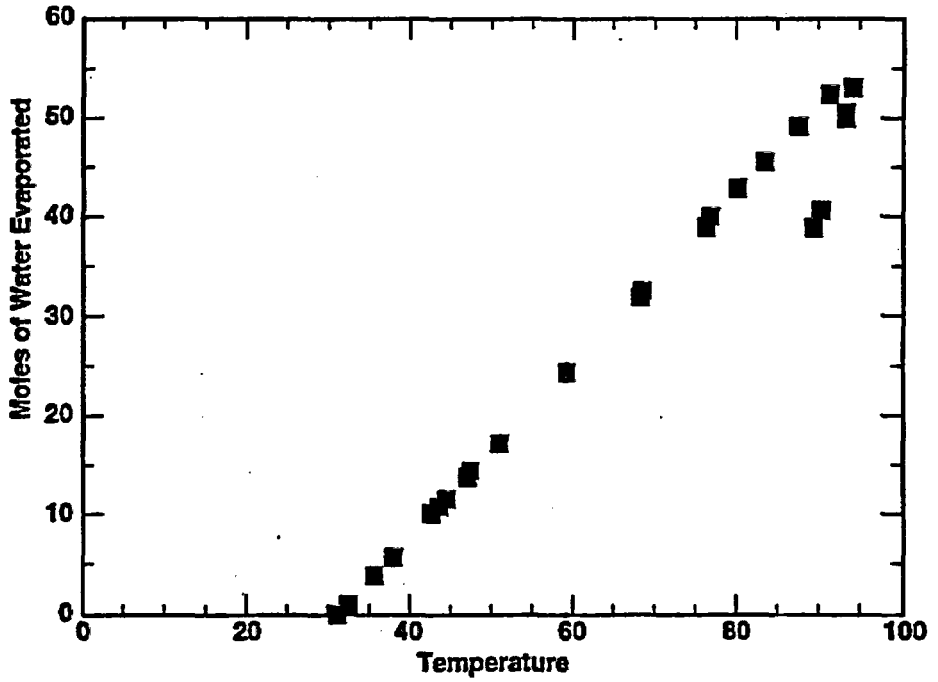

Figure 3.4-1. The trend of number of moles of water evaporated, as a function of temperature. Two different trends at the high temperature end of the sequence were used in the calculations to determine to what extent such differences would influence the chemical and mineralogical evolution of the system. In all cases, the results derived from the two trends differed by less than 1% (relative).

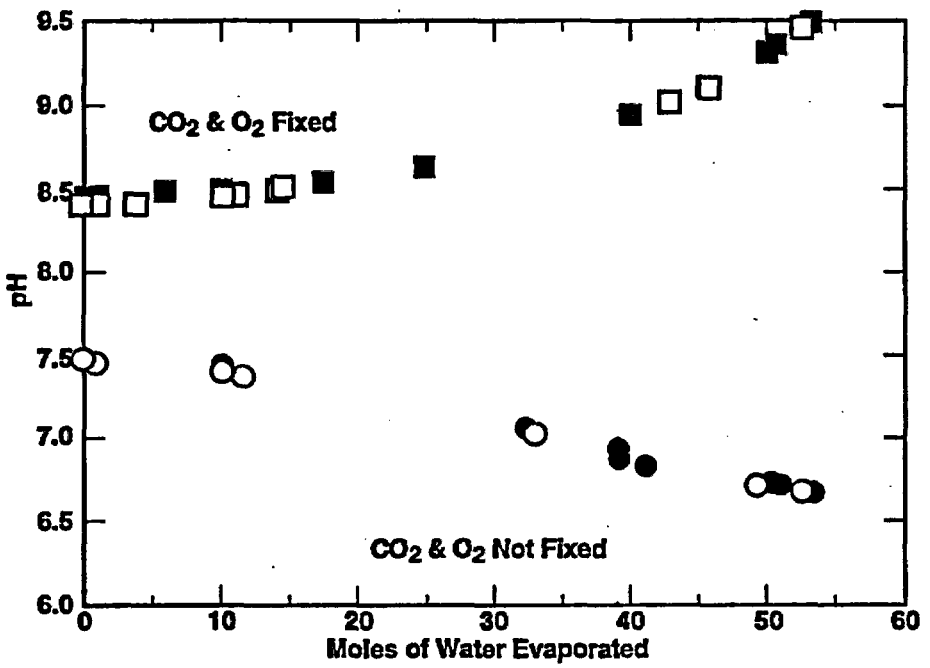

Figure 3.4-2. pH as a function of moles of water evaporated. In this, and in all subsequent figures, square symbols represent results obtained from simulations in which CO_2 and O_2 fugacities were fixed at atmospheric values throughout the runs, circles represent results obtained from simulations in which CO_2 and O_2 fugacities were not fixed, filled symbols indicate runs in which precipitation of solids was not restricted, and open symbols indicate runs in which quartz, tridymite, and talc were suppressed.

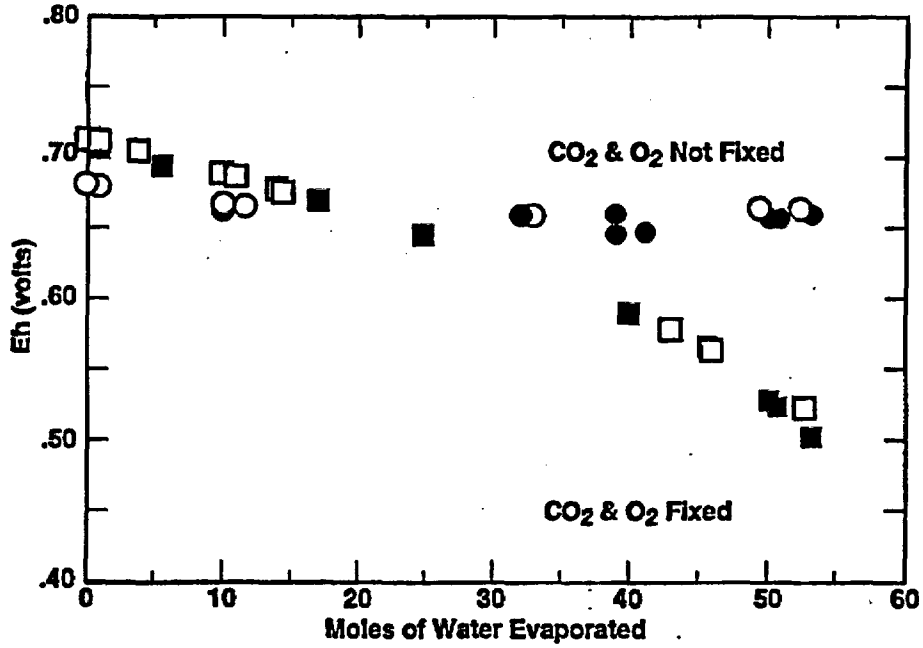

Figure 3.4-3. Eh, in volts, as a function of moles of water evaporated. Symbols as described in caption to Figure 3.4-2.

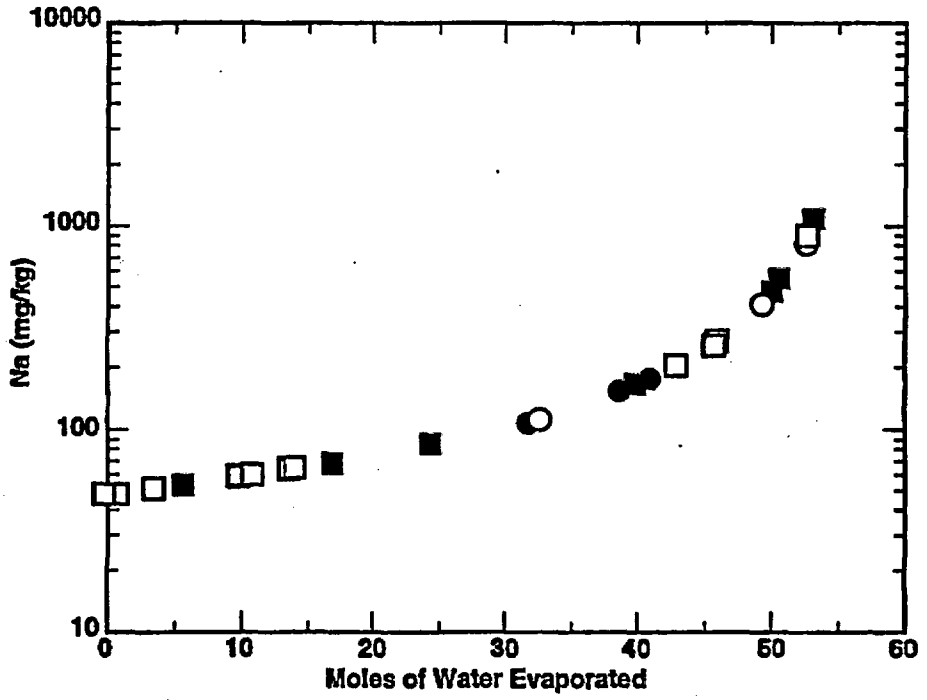

Figure 3.4-4. Total Na in solution, in mg/kg, as a function of moles of water evaporated. Symbols as described in caption to Fig. 3.4-2.

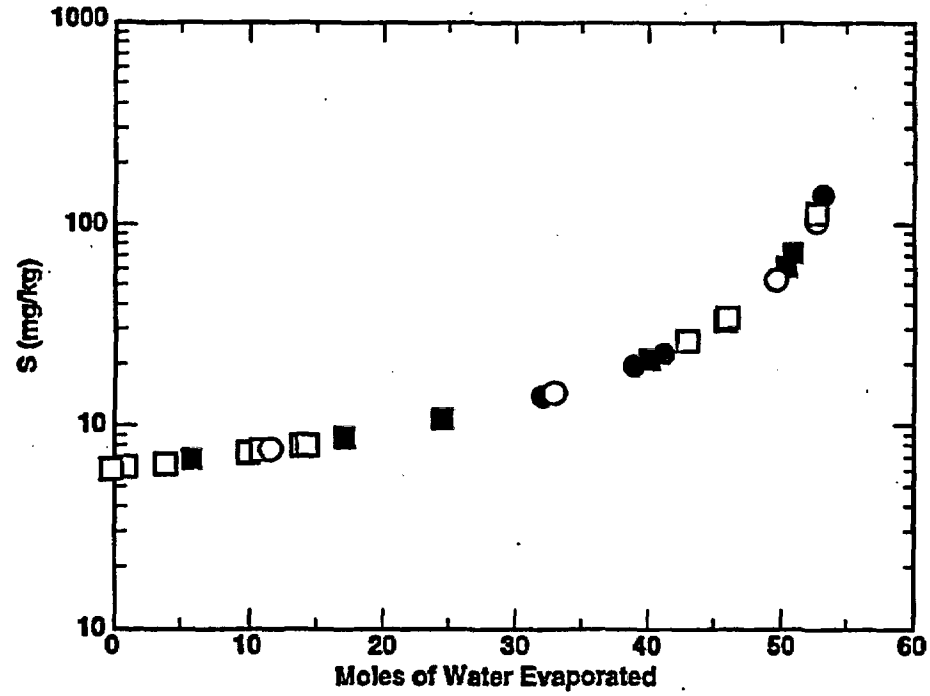

Figure 3.4-5. Total S in solution, in mg/kg, as a function of moles of water evaporated. Symbols as described in caption to Fig. 3.4-2.

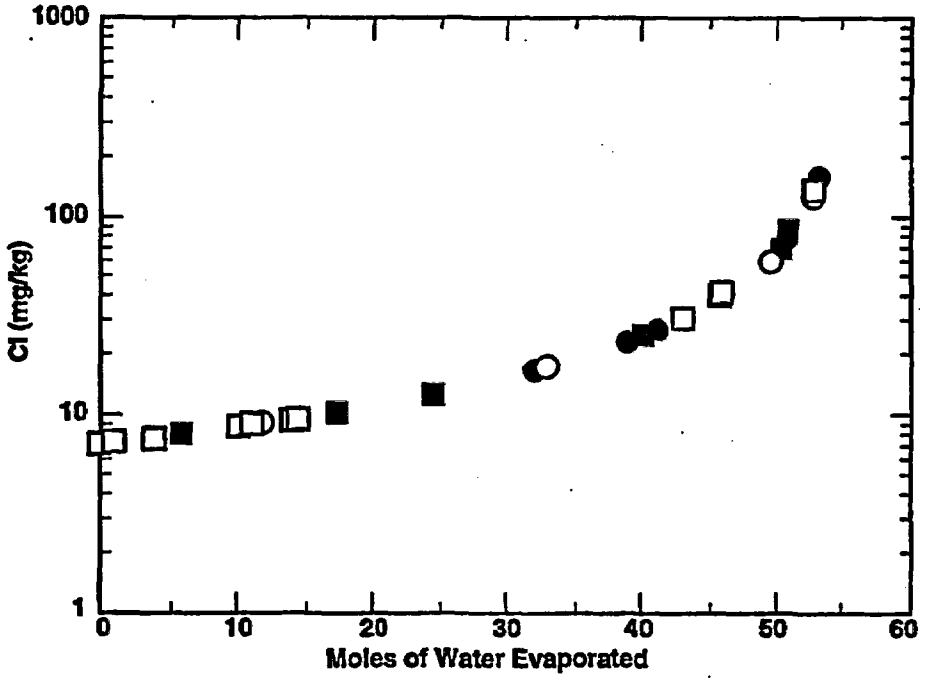

Figure 3.4-6. Total Cl in solution, in mg/kg, as a function of moles of water evaporated. Symbols as described in caption to Fig. 3.4-2.

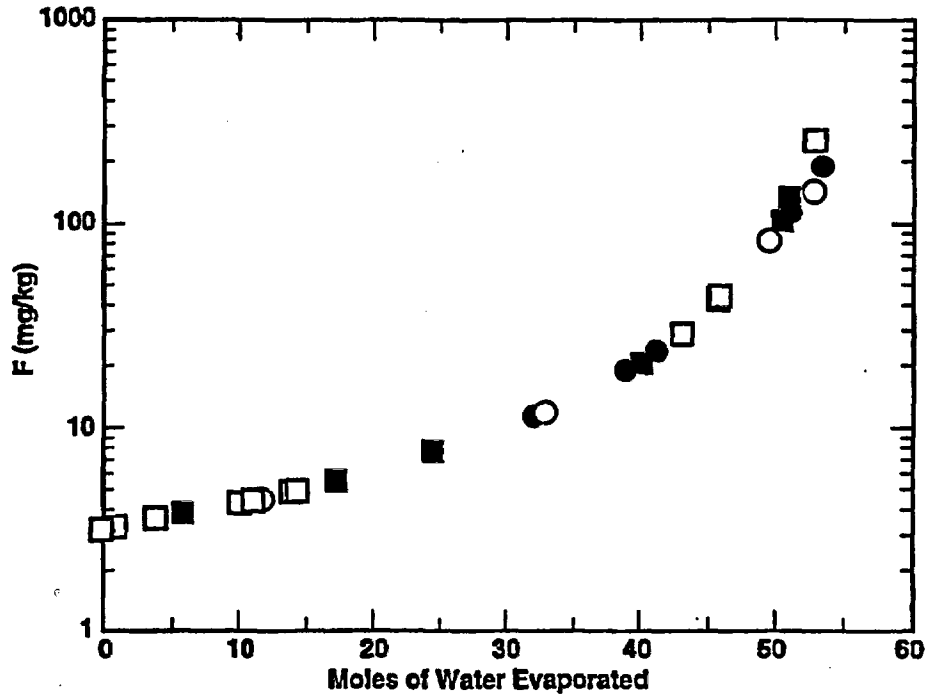

Figure 3.4-7. Total F in solution, in mg/kg, as a function of moles of water evaporated. Symbols as described in caption to Fig. 3.4-2.

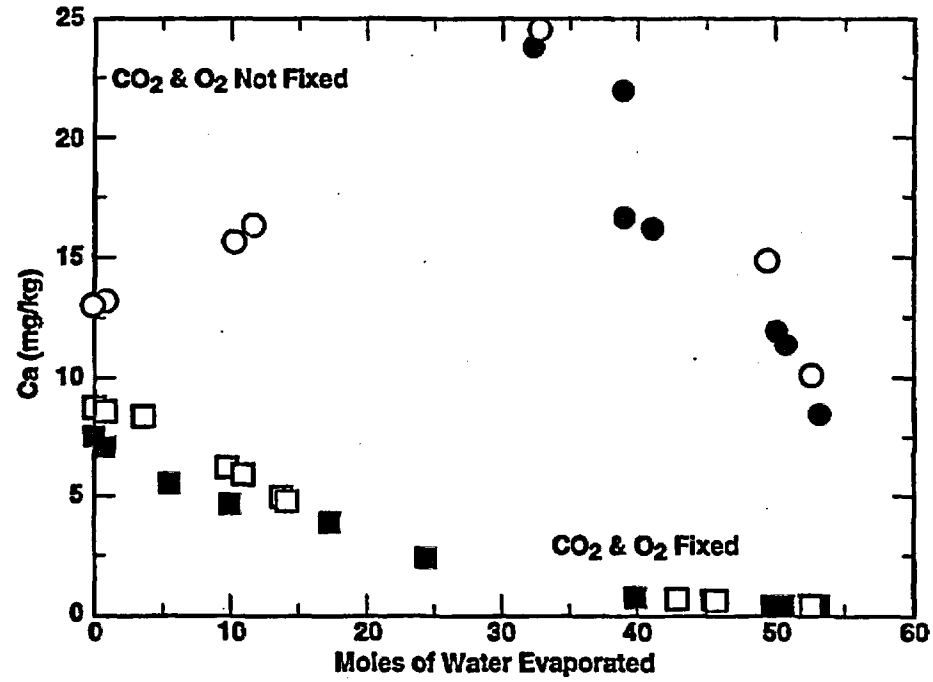

Figure 3.4-8. Total Ca in solution, in mg/kg, as a function of moles of water evaporated. Symbols as described in caption to Fig. 3.4-2. Note that the peak concentration for the uncontrolled CO_2 and O_2 case corresponds to calcite saturation (compare with Fig. 3.4-11).

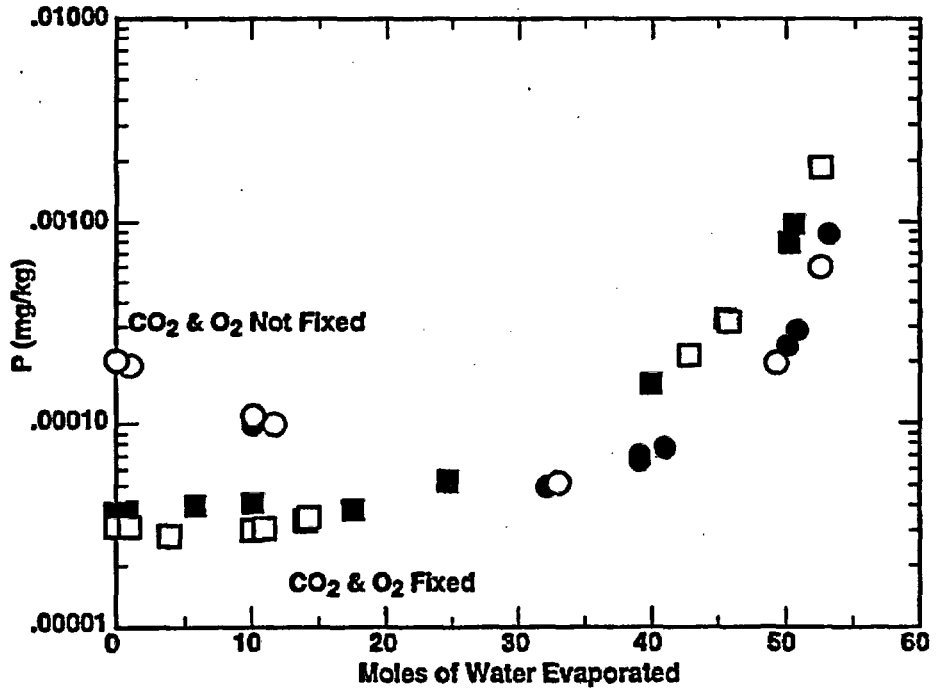

Figure 3.4-9. Total P in solution, in mg/kg, as a function of moles of water evaporated. Symbols as described in caption to Fig. 3.4-2.

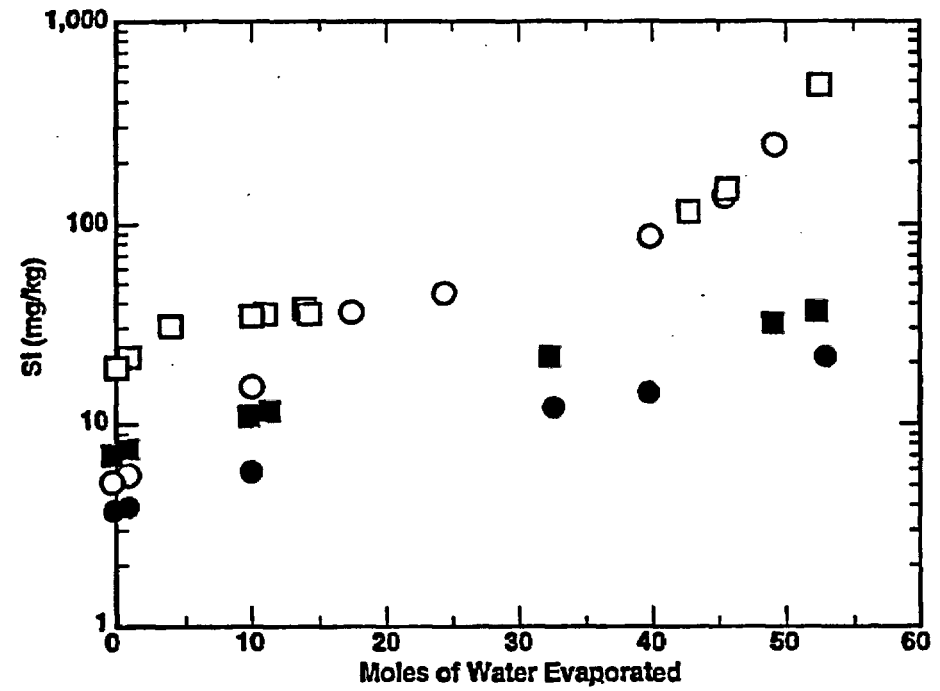

Figure 3.4-10. Total Si in solution, in mg/kg, as a function of moles of water evaporated. Symbols as described in caption to Fig.3.4-2.

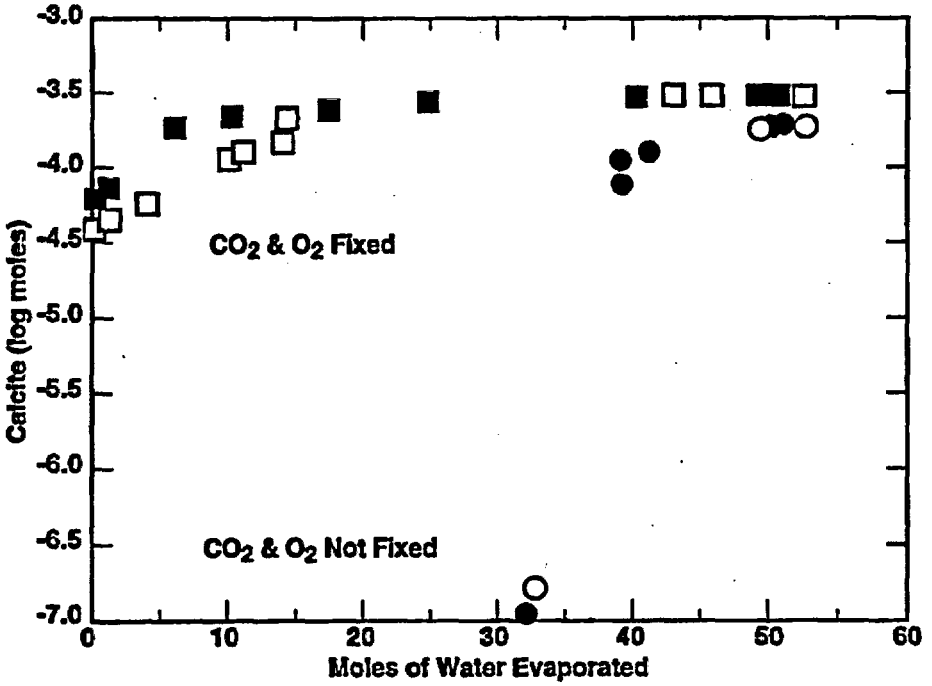

Figure 3.4-11. Log of the number of moles of calcite precipitated, as a function of moles of water evaported. Symbols as described in caption to Fig. 3.4-2.

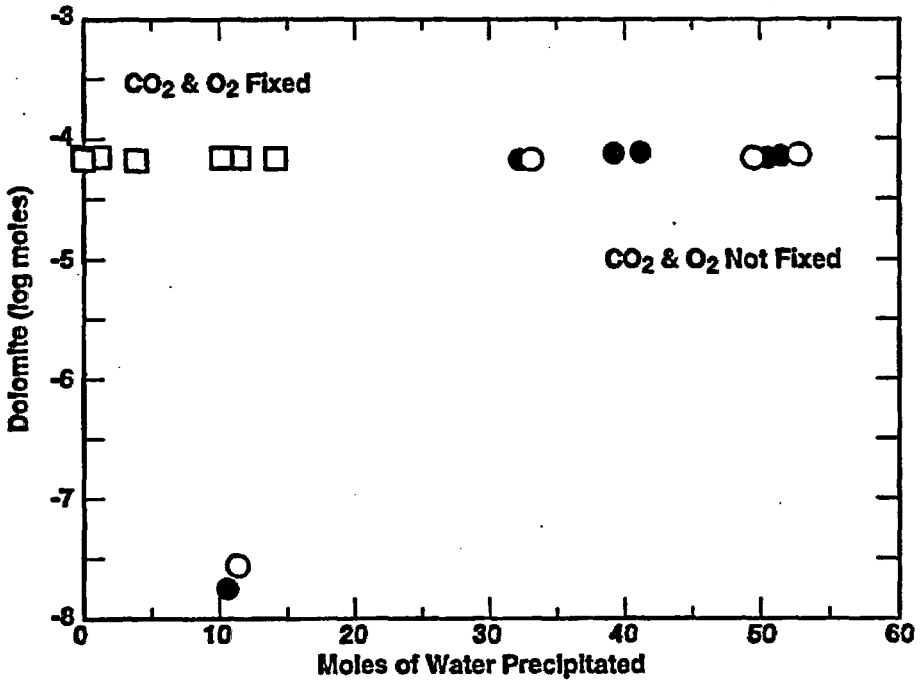

Figure 3.4-12. Log of the number of moles of dolomite precipitated, as a function of moles of water evaported. Symbols as described in caption to Fig.3.4-2.

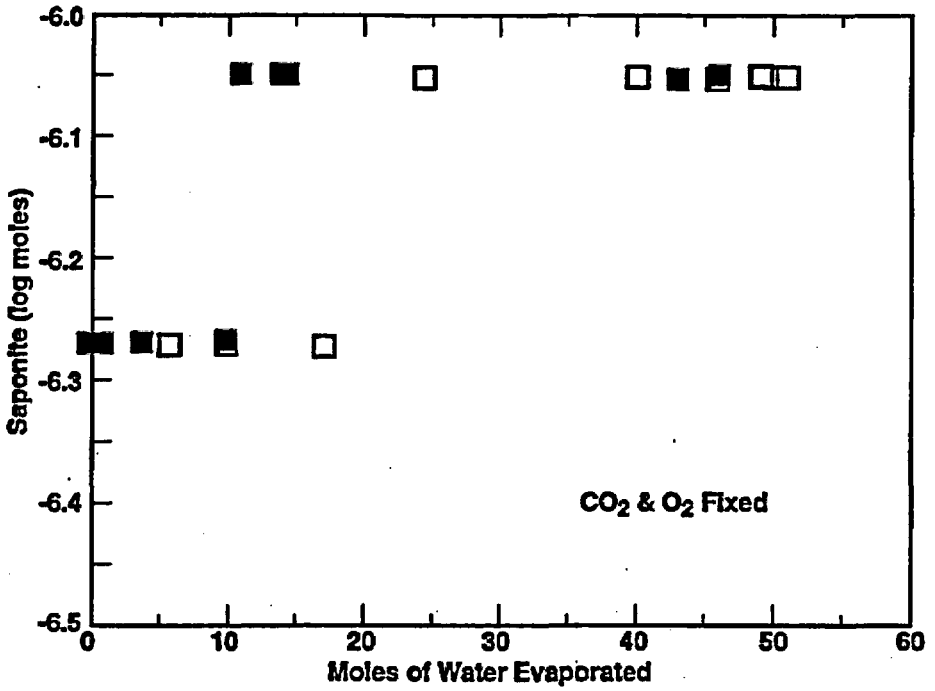

Figure 3.4-13. Log of the number of moles of saponite precipitated, as a function of moles of water evaported. Symbols as described in caption to Fig. 3.4-2.

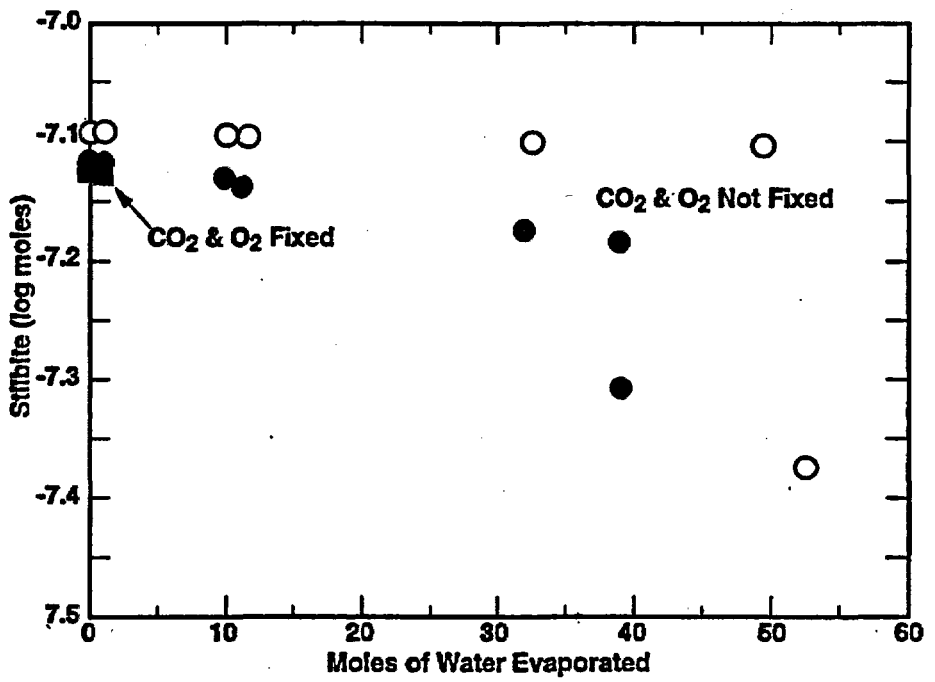

Figure 3.4-14. Log of the number of moles of stilbite precipitated, as a function of moles of water evaported. Symbols as described in caption to Fig. 3.4-2.

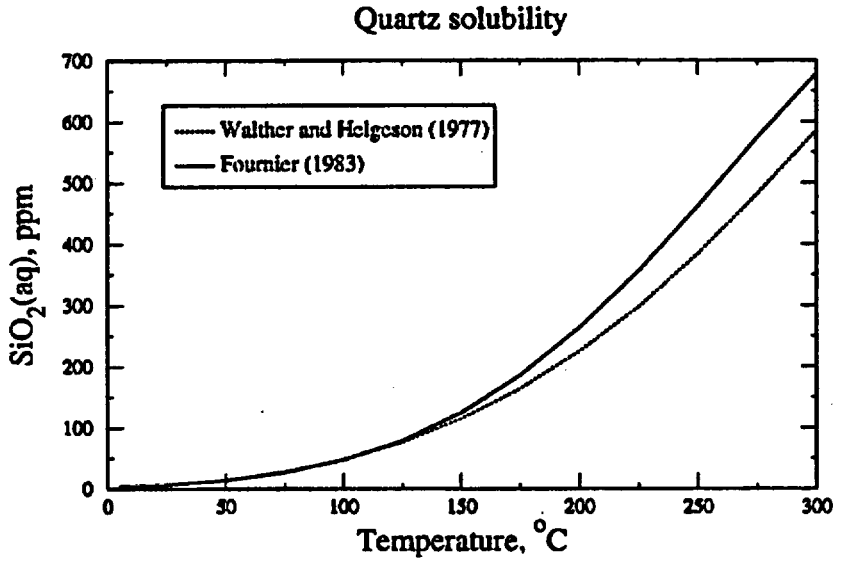

Figure 3.4-15. SiO_2(aq) concentrations in equilibrium with quartz using thermodynamic data from Walther and Helgeson (1977) and Fournier (1983).

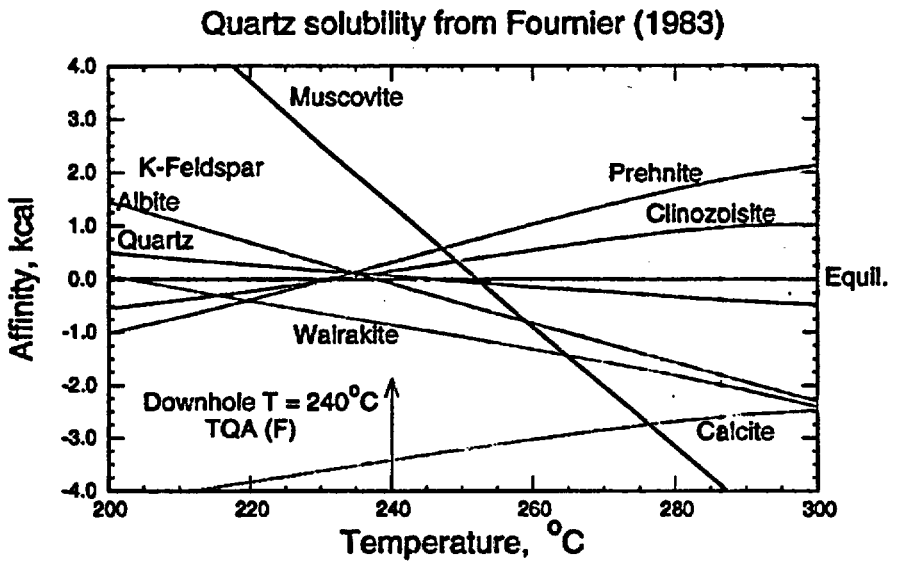

Figure 3.4-16. Affinity vs. temperature diagram for well WK-81 using quartz solubility from Fournier (1983).

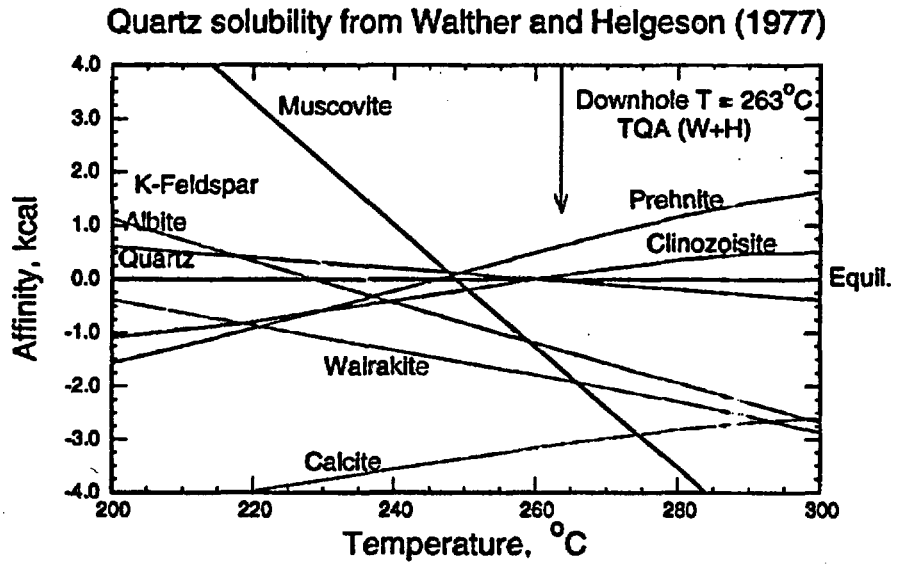

Figure 3.4-17. Affinity vs. temperature diagram for well WK-81 using quartz solubility from Walther and Helgeson (1977).

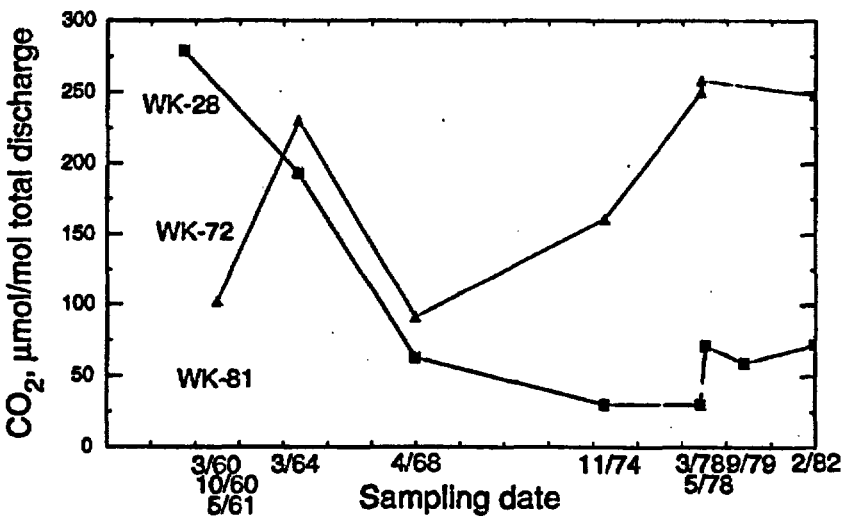

Figure 3.4-18. CO_2 concentrations (in µmol/mol water) measured in Wairakei wells WK-28, 72 and 81 as a function of time.

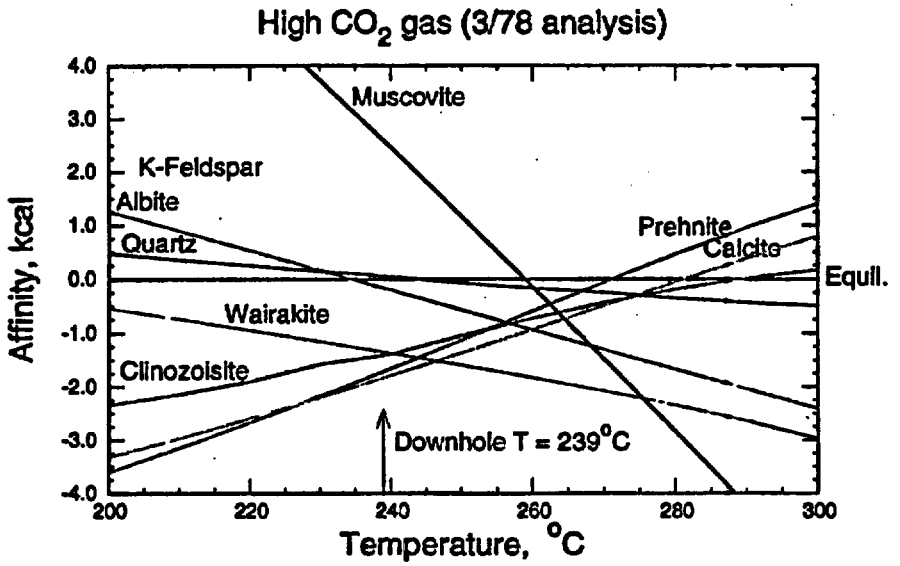

Figure 3.4-19. Affinity vs. temperature diagram for well WK-72 using 3/78 gas analysis with 258 mmol CO_2/mol TD (see text). Quartz data from Fournier (1983).

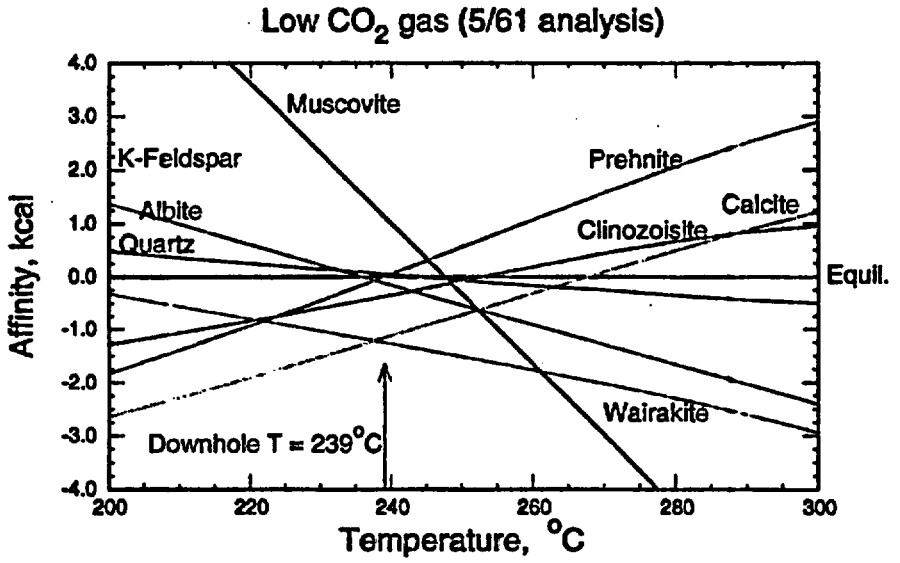

Figure 3.4-20. Affinity vs. temperature diagram for well WK-72 using 5/61 gas analysis with 102 mmol CO_2/mol TD (see text). Quartz data from Fournier (1983).

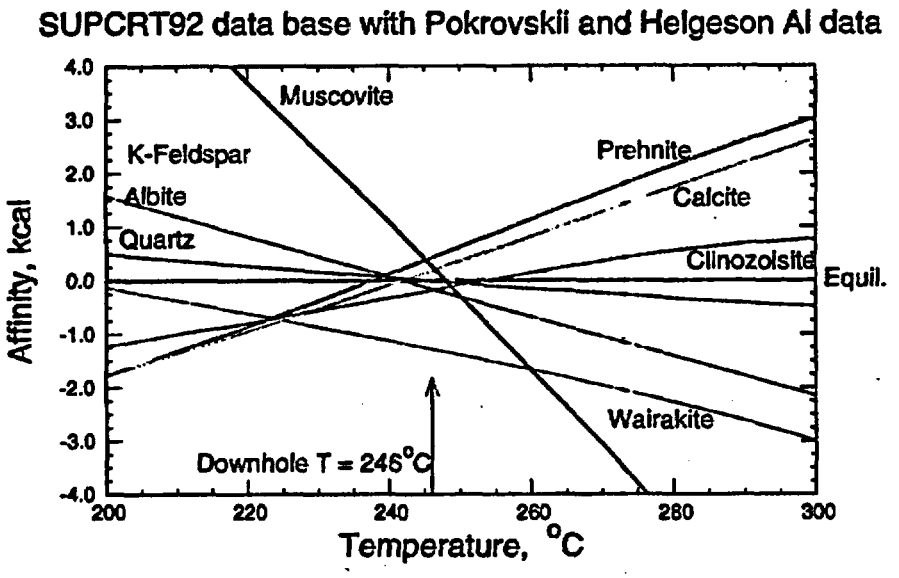

Figure 3.4-21. Affinity vs. temperature diagram for well WK-28 using thermodynamic data for Al aqueous species from Pokrovskii and Helgeson (1995). Quartz data from Fournier (1983).

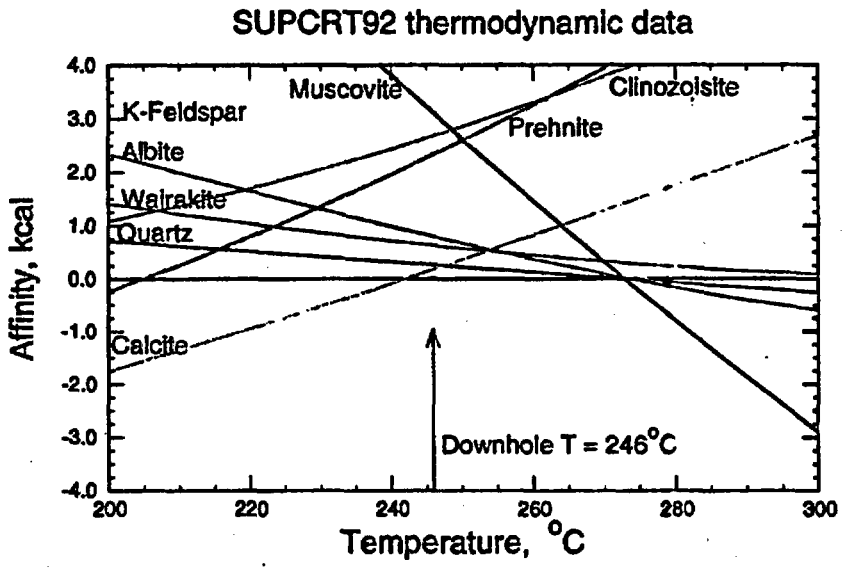

Figure 3.4-22. Affinity vs. temperature diagram for well WK-28 using thermodynamic data for Al aqueous species from the SUPCRT92 version of the GEMBOCHS data base. Quartz data from Fournier (1983).

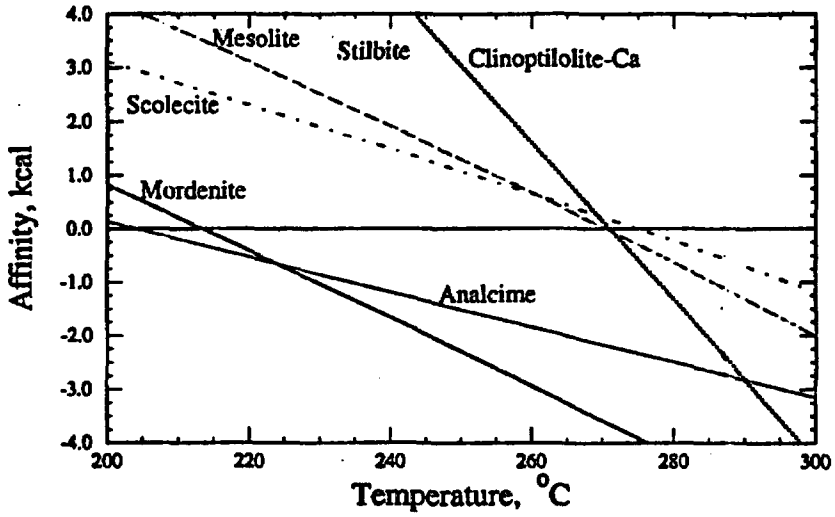

Figure 3.4-23. Zeolite affinities vs. temperature diagram for well WK-28 using thermodynamic data for Al aqueous species from Pokrovskii and Helgeson (1995). See Figure 7 for stabilities of additional minerals. Clinoptilolite-Ca refers to the Ca end-member of a clinoptilolite solid solution. Quartz data from Fournier (1983).

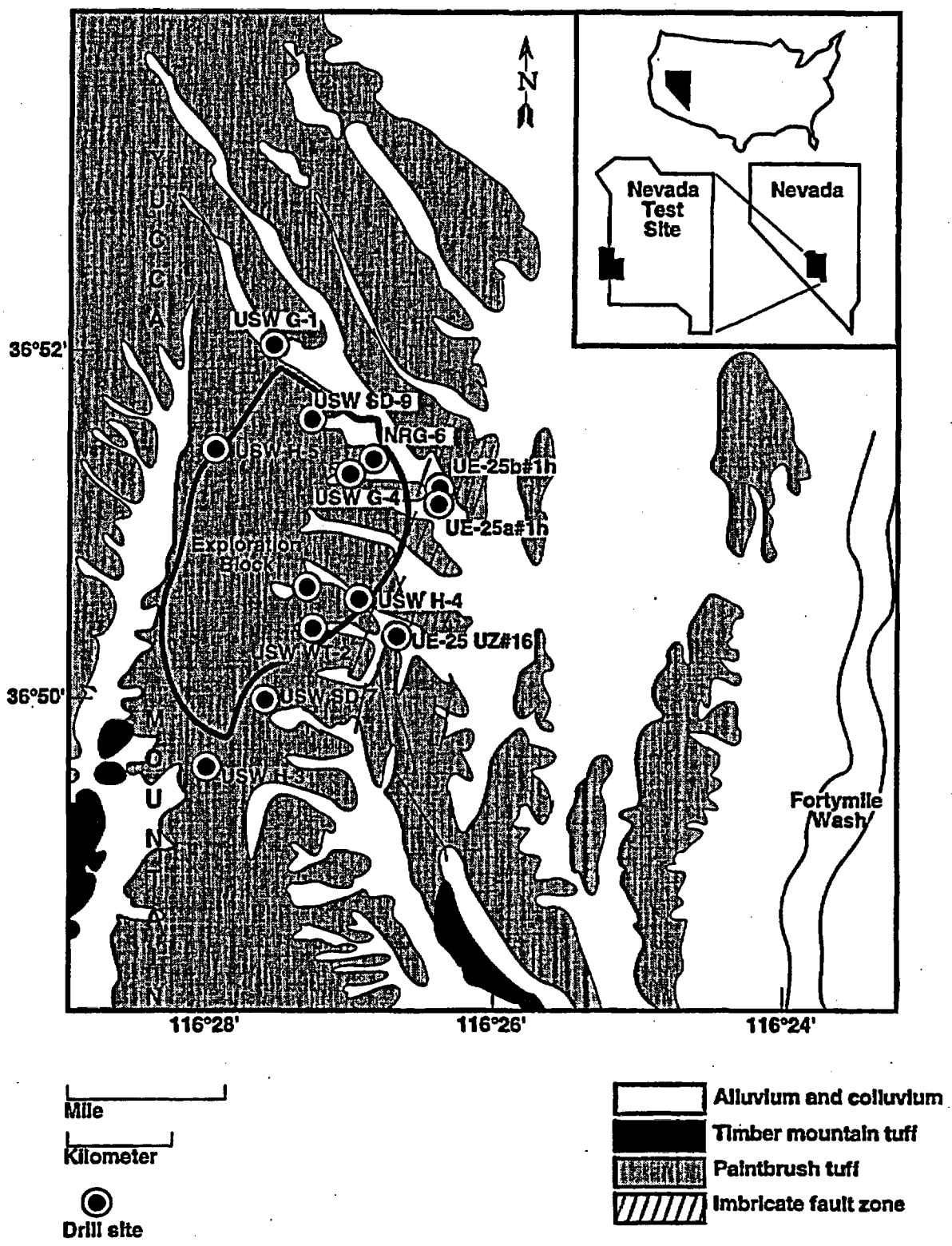

Figure 3.4-24. Map of Yucca Mountain, Nevada, showing locations of drill holes within or near the exploration block where mineralogical data have been collected mentioned in the appendices.

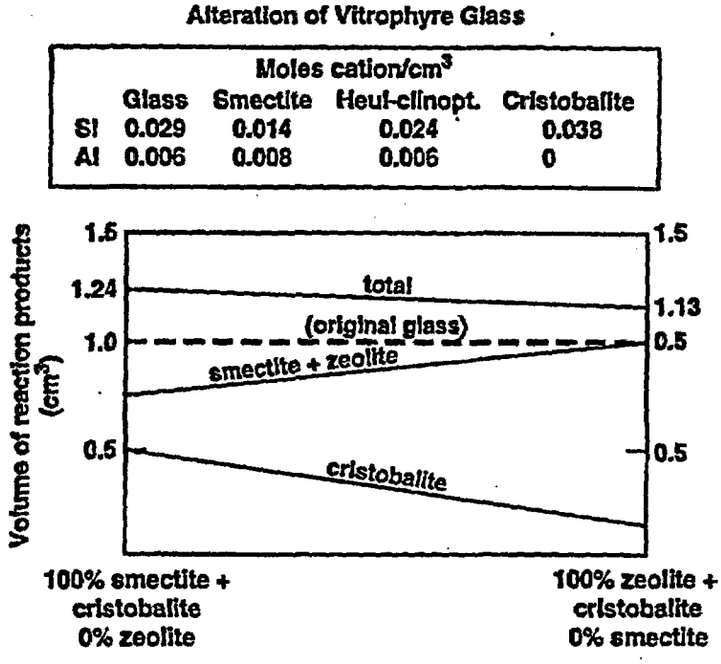

Figure 3.4-25. Graphic representation of reaction (1), balanced for all possible combinations of smectite and clinoptilolite-heulandite.

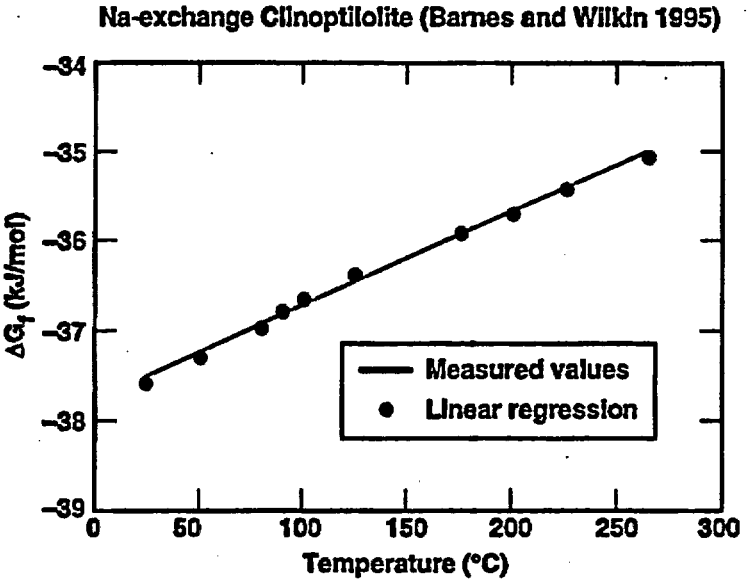

Figure 3.4-26. The Gibbs free energy of formation of Na-exchanged clinoptilolite derived from solubility measurements (Barnes and Wilkin, 1995). The solid line is a linear regression of the data from 50 to 265°C.

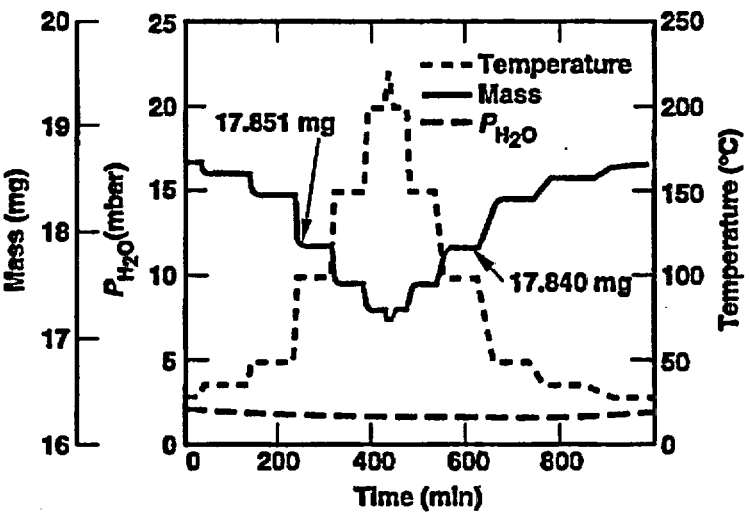

Figure 3.4-27. Results of a single thermogravimetric experiment on Ca-clinoptilolite conducted over a series of isothermal stages from 25 to 220 °C at an approximately constant water-vapor pressure of 2 mbar (Carey and Bish 1996a). Two mass measurements at 100°C are indicated to illustrate reversible hydration and dehydration.

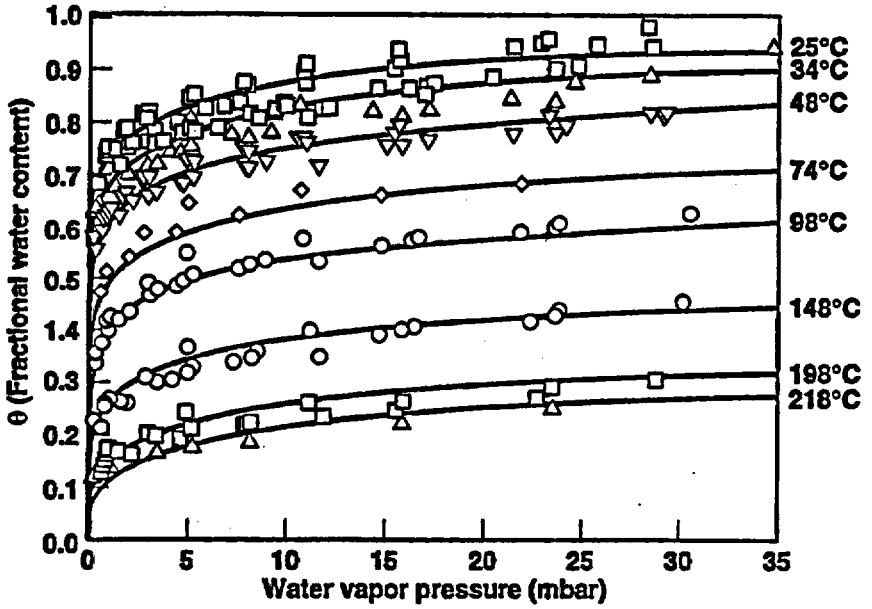

Figure 3.4-28. Equilibrium H_2O content of Na-clinoptilolite determined by thermogravimetry between 25 and 218 °C (Carey and Bish 1996a). The fractional water content, θ, is the observed H_2O content divided by the maximum H_2O content. The calculated lines were derived by a single linear regression of all the data.

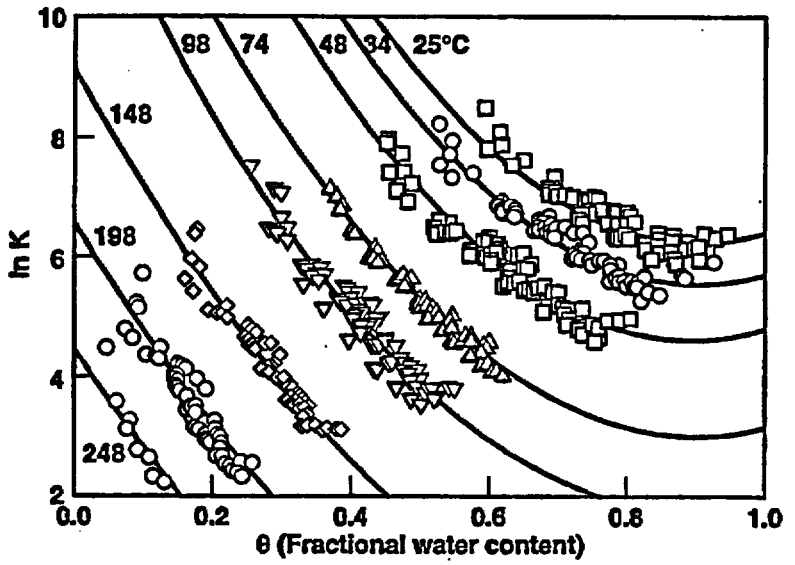

Figure 3.4-29. Comparison of the experimental data for K-clinoptilolite (symbols) with the calculated fit (solid lines) for water content versus equilibrium constant at several temperatures (Carey and Bish 1996a). The numbers labeling the curves are the temperature (°C) of the experiment. lnK is defined as $\ln(\theta/(1-\theta)/P)$, and θ is the ratio of the observed water content to the maximum water content at 25°C.

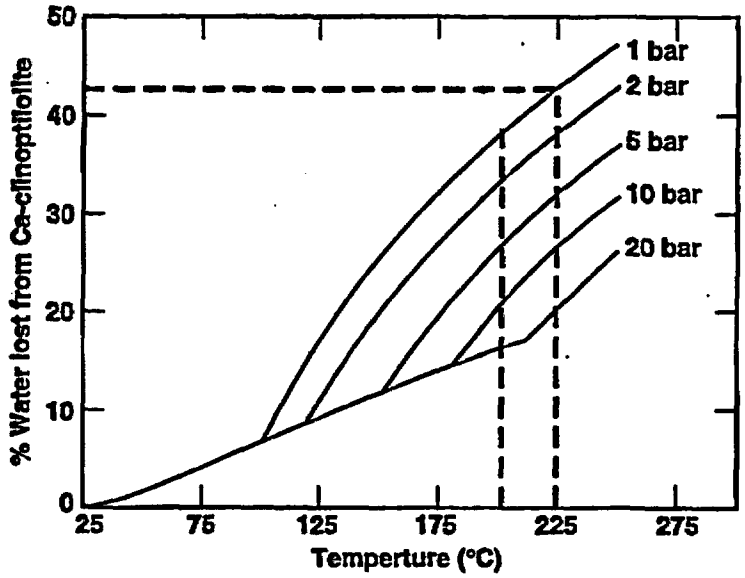

Figure 3.4-30. Calculated dehydration evolution of Ca-clinoptilolite under conditions of rising temperature and differing maximum pressures. Dehydration occurs along the boiling curve until the maximum pressure is reached (Carey and Bish 1996a).

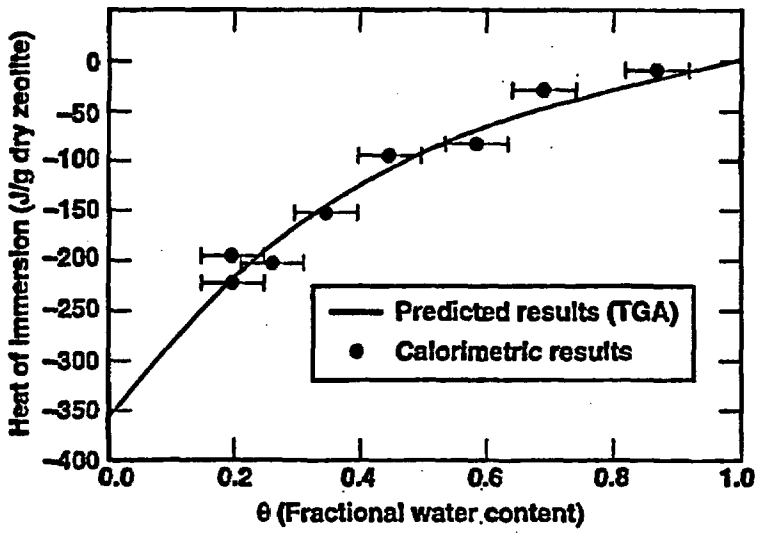

Figure 3.4-31. Calorimetric measurements of the integral heat of immersion of Ca-clinoptilolite (Carey and Bish 1996b) and calculated heats of immersion (TGA) from the study of Carey and Bish (1996a).

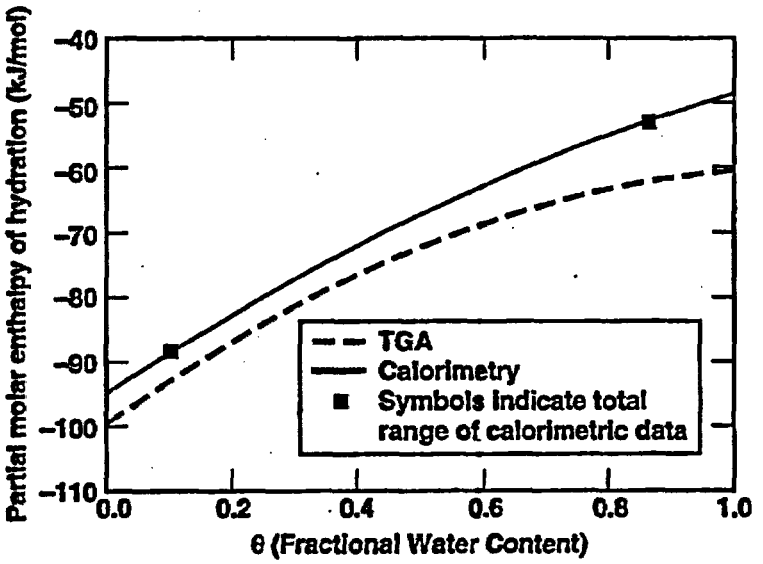

Figure 3.4-32. Partial molar enthalpy of hydration of Na-clinoptilolite derived from linear regression of the immersion calorimetry data (Carey and Bish 1996b) compared to the thermogravimetric results (TGA) of Carey and Bish (1996a).

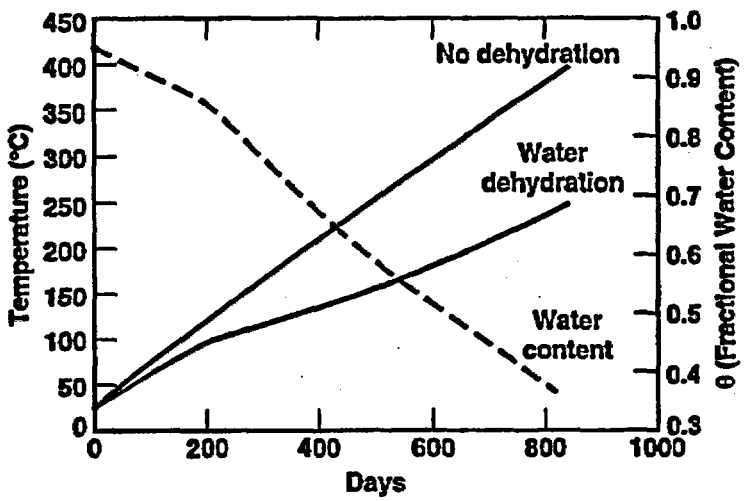

Figure 3.4-33. Calculated thermal and hydrologic evolution of a 1 m^3 block of K-clinoptilolite with 10% porosity, insulated boundaries, maximum water-vapor pressure of 1 bar, and receiving 14 watts of thermal energy. The two solid lines show the temperature of a block with K-clinoptilolite that dehydrates and one which does not dehydrate. The dotted line shows the water content of the clinoptilolite in the dehydrating block (Carey and Bish 1996a).

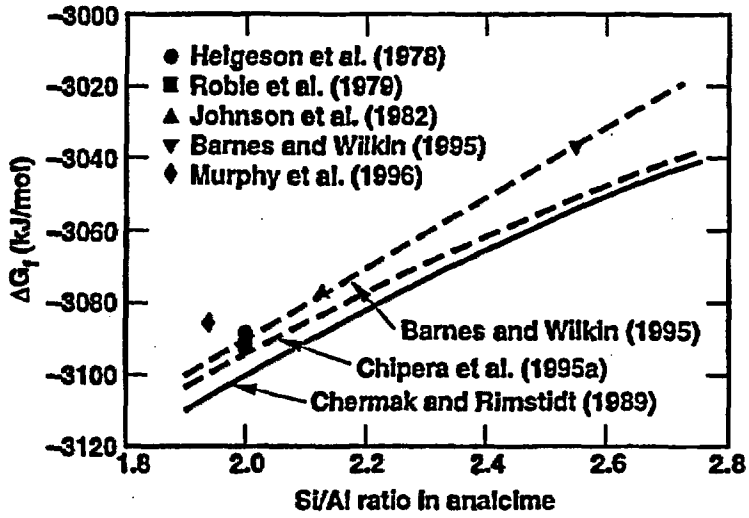

Figure 3.4-34. The Gibbs free energy of formation of analcime of differing Si/Al ratio determined by calorimetry, solubility measurements, phase equilibria analysis, and by estimation methods.

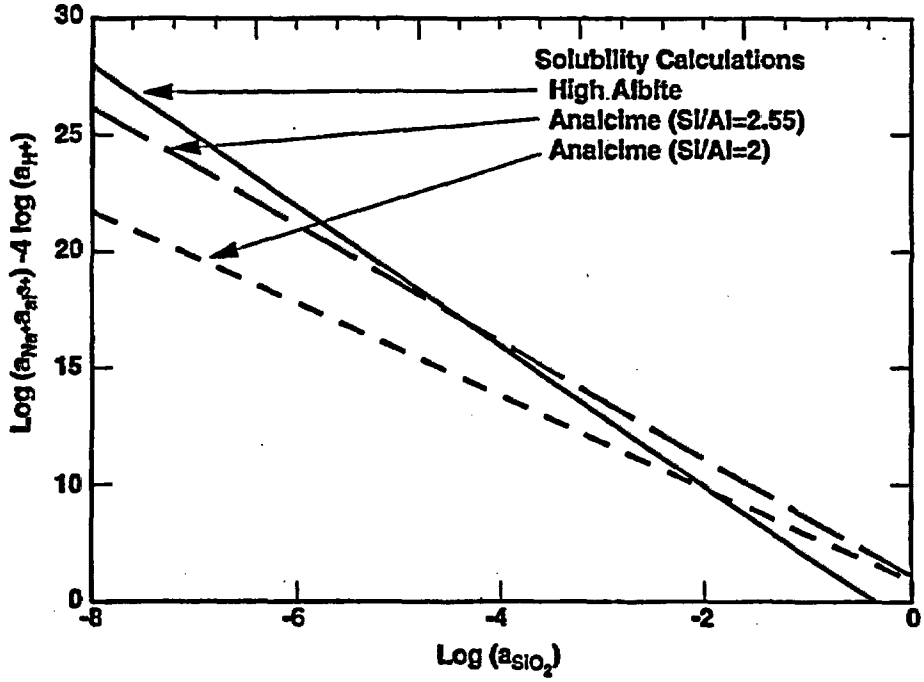

Figure 3.4-35. Solubility of stoichiometric and siliceous analcime (Barnes and Wilkin 1995) compared to the solubility of high albite (EQ3 Com data base).

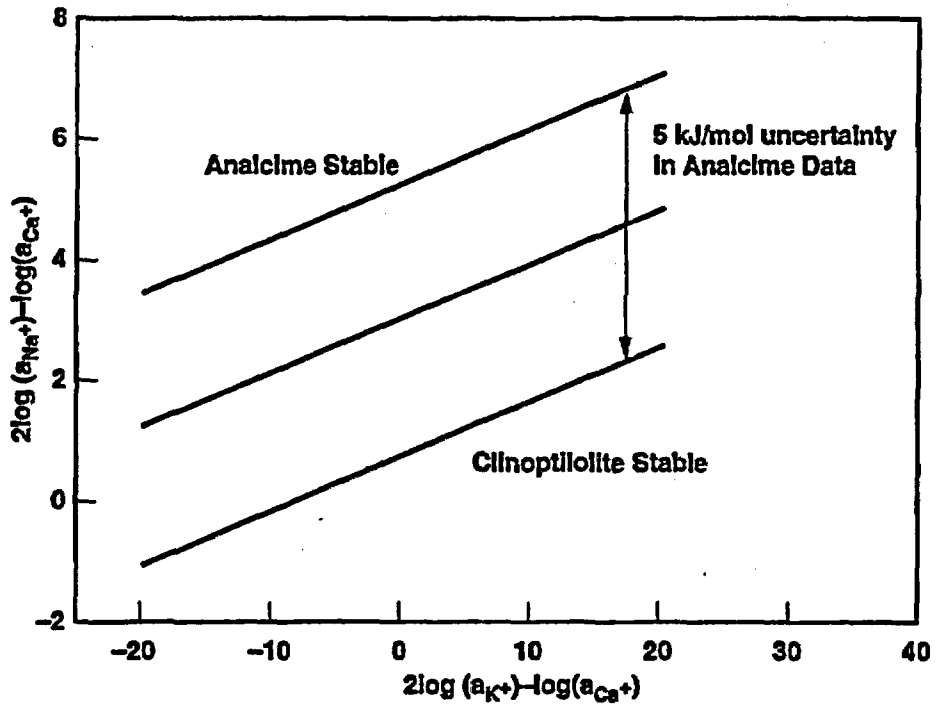

Figure 3.4-36. Reaction of clinoptilolite and analcime, balanced on aluminum, and plotted at cristobalite saturation. The reaction corresponds to Equation 12 of the text and uses the thermodynamic properties of analcime and clinoptilolite shown in Table 3.4-15.

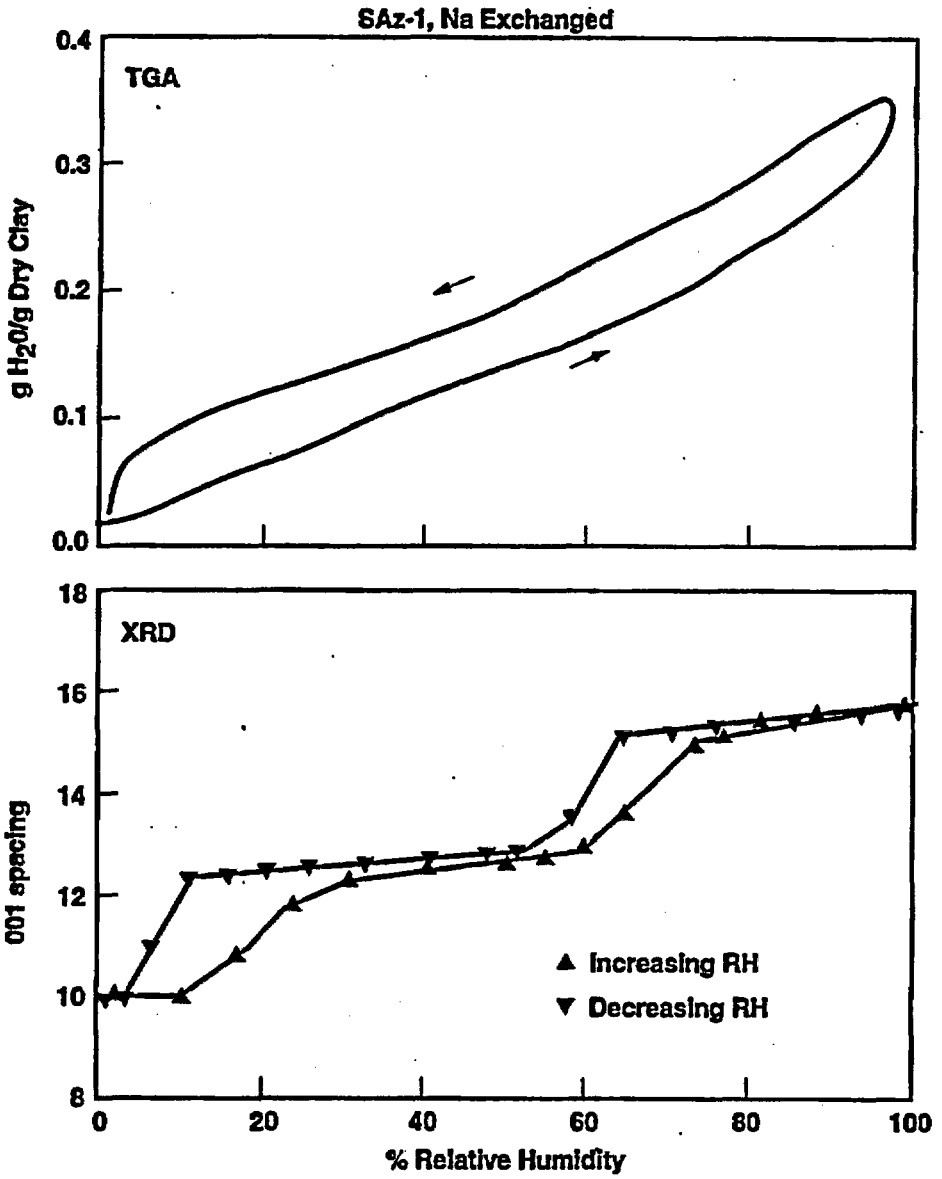

Figure 3.4-37. Hysteresis in Na-exchanged smectite as a function of relative humidity at 25°C. The H_2O contents were determined by thermogravimetry and the 001 d-spacings were determined by X-ray diffraction.

Table 3.4-1. Major constituents of discharge from Wairakei wells WK-28 (sampled on 3/60), WK-72 (sampled on 4/61) and WK81 (sampled on 10/74) (in mg/kg) (from Reyes, Giggenbach and Christenson, 1993).

Component	WK-28 analyzed	WK-28 corrected*	WK-72 analyzed	WK-72 corrected*	WK-81 analyzed	WK-81 corrected*
Na	1260	898	1295	942	1256	917
K	200	142	215	157	182	133
Ca	16	11.4	18	13	22	16
Mg	0.035	0.025	0.014	0.01	0.0035	0.0026
Fe *	NA	0.6e-6	NA	0.38e-3	NA	0.19e-2
Al **	NA	0.27	NA	0.26	0.37	0.27
Rb	NA	NA	NA	NA	2.52	1.8
Li	14	10	12.9	9.4	11.8	8.6
Cs	NA	NA	NA	NA	2.4	1.8
B	28.2	20	NA	NA	25.3	19
Cl	2213	1530	2241	1636	2083	1587
HCO_3	48	979	NA	345	NA	41
SO_4	34	24	34***	20	34	25
H_2S****	NA	15	NA	9	NA	4
SiO_2	660	470	600	438	612	447
pH	8.2(20°C)	6.3 (246°C)	8.3 (20°C)	6.2 (239°C)	7.4 (20°C)	6.1 (240°C)
TQA*****		246°C		239°C		240°C

* Corrected for steam and gas loss; calculated assuming equilibrium with pyrite at TQA; Cl adjusted to obtain electrical neutrality

** From analysis of other samples from same wells3

*** From average of other samples from WK-72

**** Analyzed value for all samples assumed to equal 0.3 mg/kg, typical of WK-28 waters.

***** Downhole temperature calculated from the adiabatic quartz geothermometer (TQA) using quartz solubility data from Fournier (1983)4

3 The previous study by Bruton, Glassley and Bourcier (1994) assumed that Al concentration was controlled by equilibrium with K-feldspar.

4 Implications of using data from Fournier (1983) vs. Walther and Helgeson (1977) for quartz solubility are discussed in the text.

Table 3.4-2. Major chemical components of vapors discharged from Wairakei wells WK-28, 72 and 81 sampled on 3/60, 5/61 and 11/74, respectively (in μmol/mol water)

Component	WK-28	WK-72	WK-81
CO_2	279	102	12
H_2S	8	4.5	1.9

Table 3.4-3. Chemical Compositions of Glass and Secondary Minerals

	GU-3 1195C glass	H-5 1666 smectite	GU-3 1195 heulandite
Weight Percent			
SiO_2	74.1	43.2	64.8
TiO_2	0.09	0.13	0.00
Al_2O_3	12.4	21.4	12.0
FeO	0.82	1.57	n.d.*
MnO	0.00	0.05	0.09
MgO	0.02	0.89	0.88
CaO	0.19	2.48	3.84
BaO	0.06	0.00	0.00
Na_2O	3.55	0.14	0.59
K_2O	5.77	0.15	0.78
H_2O	3.0	30.0	17.0
Total	100.0	100.0	100.0
Density, g/cm^3			
	2.36†	2.00‡	2.20‡
Mole/cm^3			
Si	0.02904	0.01437	0.02372
Al	0.00560	0.00840	0.00550
Ca	0.00008	0.00088	0.00160
Na	0.00270	0.00009	0.00045
K	0.00288	0.00006	0.00039

*n.d. = not detected
†Anderson (1984)
‡Deer et al.(1963)

Table 3.4-4. X-ray diffraction mineralogy of altered Topopah Spring vitrophyre (weight percent)

Sample	Depth (m)	Smectite	Heulandite	Quartz	Cristobalite	Alkali feldspar	Opal-CT	Other
GU-3*								
1195.7	364.5	n.d.§	~1	8±2	22±3	70±5	n.d.	trace†
G-4*								
1299	395.9	2±1	5±2	8±2	23±4	62±10	n.d.	trace†
1314	400.5	45±10	28±5	2±1	14±4	11±5	n.d.	
H-5								
1666	507.8	37±16	20±5	3±1	n.d.	24±7	15±7	~0.6‡

*From Bish and Chipera (1989).
§n.d. = not detected.
†mica.
‡erionite. Special techniques to detect erionite were used for this sample only (Bish and Chipera , 1991).

Table 3.4-5. Summary of standard state thermodynamic data for clinoptilolite and heulandite.

Reference	Johnson et al. (1991)	Johnson et al. (1991)*	Hemingway and Robie (1984)	Murphy et al. (1996)	Barnes and Wilkin (1995)	Johnson et al. (1985)	Johnson et al. (1985)*
Sample	Malheur, OR clinoptilolite	Malheur, OR clinoptilolite	Mojave county, AZ clinoptilolite	Death Valley Junction, CA clinoptilolite	Castle Creek, ID clinoptilolite	Gunnadah, Australia, heulandite	ref. state modified heulandite
Study type	Calorimetric	Calorimetric	Calorimetric	Solubility	Solubility	Calorimetric	Calorimetric
Na (72 O)	1.908		0.56	5.412	6.36	1.532	
K	1.086		0.98	0.369	0.18	0.528	
Ca	1.522		1.50	0.009	0	2.34	
Mg	0.248		1.23	0.105	0	0	
Mn	0.004			0	0	0	
Ba	0.124			0	0	0.26	
Sr	0.072			0	0	0.7	
Fe	0.034		0.3	0.132	0	0	
Al	6.900		6.7	5.841	6.6	8.66	
Si	29.066		29	30	29.4	27.34	
O	72		72	72	72	72	
H_2O	21.844		22	22.29	21	24	
Si/Al	4.21		4.33	5.14	4.45	3.16	
ΔG_f kJ/mol	-38156.8	-38042.4		-38124	-37506	-39228	-39114
ΔH_f kJ/mol	-41290	-41176			-40646	-42490	-42376
S° J/mol-K	2966.10	2966.10	2872.3		2830.32	3068.72	3068.72
high T data**	yes		no	no	yes		yes

*These values have been corrected back to a reference state based on quartz (cf. Johnson et al., 1992 and discussion in the section on analcime).
**Indicates whether data at temperatures above 25°C were collected.

Table 3.4-6. Gibbs free energy of formation of Na-clinoptilolite determined by solubility measurements (Barnes and Wilkin, 1995).

Temperature (°C)	ΔG_f° kJ/mol
25	-37577.4
50	-37282.8
80	-36958.2
90	-36785.4
100	-36633.0
125	-36375.6
175	-35910.0
200	-35679.0
225	-35404.8
265	-35031.0

Table 3.4-7. Calculated Gibbs free energies of formation of end-member clinoptilolite.

	ΔG binary exchange for Na J/mol	ΔG_f kJ/mol
Na-clinoptilolite	0	-37506
K-clinoptilolite	-7980	-37688
Ca-clinoptilolite	-925	-37604
Sr-clinoptilolite	-1371	-37624

Table 3.4-8. Standard-state values for the thermodynamics of hydration in cation-exchanged clinoptilolite with errors derived from regression analysis. The values (except entropy) are used in Equation 4.

Parameter*	Ca-Exchanged		Na-Exchanged		K-Exchanged	
	Value	std error	Value	std error	Value	std error
$\Delta\mu^{o}_{Hy}$ (J/mol)	-79685	2414	-55080	3273	-48949.2	1171
$\Delta\bar{H}^{o}_{Hy}$ (J/mol)	-120477	2232	-99593	2910	-91183	1031
$\Delta\bar{S}^{o}_{Hy}$ (J/mol/K)	-136.82	3.08	-149.30	5.03	-141.65	1.86
W_1 (J/mol)	137070	3332	72214	34123	74649	1277
W_2 (J/mol)	-74935	2129	-32111	2248	-41726	920

*Excess significant figures are retained for calculations.

Table 3.4-9. Molar values of the thermodynamics of hydration for cation-exchanged clinoptilolite determined in this study compared with values measured in clinoptilolite, other zeolites, and H_2O.

Material	$\Delta\tilde{G}_{Hy}$ (kJ/mol-H_2O)	$\Delta\tilde{H}_{Hy}$ (kJ/mol-H_2O)	$\Delta\tilde{S}_{Hy}$ (J/mol-H_2O/K)
Ca-Cpt[1]	-36.13 ± 3.02	-76.92 ± 2.88	-136.8 ± 3.1
Na-Cpt[1]	-29.68 ± 3.77	-74.19 ± 3.46	-149.3 ± 5.0
K-Cpt[1]	-25.53 ± 1.37	-67.78 ± 1.25	-141.7 ± 1.9
Sodic-Cpt[2]	n.d.	-65.5	n.d.
Na-Cpt[3]	n.d.	-66.1	n.d.
H_2O[4]	-8.57	-44.02	-118.9
Cordierite[5]	-9.5	-41.8	-108.2
Analcime[6]	-44.9	-84.9	-133.8
Mordenite[7]	-33.5	-73.8	-134.8

[1]This study. Uncertainties are derived from the standard errors of the egression coefficients.
[2]Johnson et al. (1991) adiabatic and solution calorimetry.
[3]Barrer and Cram (1971) immersion calorimetry.
[4]Robie et al. (1979) condensation of water vapor.
[5]Carey (1995) phase equilibria.
[6]Johnson et al. (1982) adiabatic and solution calorimetry.
[7]Johnson et al. (1992) adiabatic and solution calorimetry.

Table 3.4-10. Parameters for the calculation of the partial and integral molar enthalpy of hydration from calorimetric data (cal). Also included are the less accurate values derived from the thermogravimetric experiments (TGA).

Clinoptilolite	$\Delta\bar{H}^{o}_{H_2O}$ J/mol	W_1 J/mol	W_2 J/mol	$\Delta\bar{H}_{H_2O}$ kJ/mol
Ca (Cal)	-95274	34169	14400	-73.4
Na (Cal)	-94760	66112	-19468	-68.2
K (Cal)	-99161	100460	-52575	-66.5
Ca (TGA)	-120477	1370706	-74935	-76.9
Na (TGA)	-99593	72214	-32111	-74.2
K (TGA)	-91183	74649	-41726	-67.8

Table 3.4-11. Standard-state Gibbs free energy of formation of analcime from the elements determined from calorimetric and solubility measurements.

Sample	Si/Al Ratio	ΔG_f kJ/mol	Uncertainty kJ/mol	Reference
Mt. St. Hilaire	1.94	-3085.4	5	Murphy et al. (1996)
Table Mountain	2	-3091.73	3.682	Robie et al. (1979)
Mt. St. Hilaire	2	-3090*	5	Barnes and Wilkin (1995)
Mt. St. Hilaire	2	-3105.3**	5	Barnes and Wilkin (1995)
Skookumchuck	2.125	-3077.2	3.3	Johnson et al. (1982)
Skookumchuck	2.125	-3086.1†	3.3	Johnson et al. (1982)
Wikieup	2.55	-3036	5	Barnes and Wilkin (1995)

*Value obtained by linear regression from 50 to 300°C
**Actual value measured at 25°C (Barnes and Wilkin, 1995).
†Revised value (Johnson et al., 1992).

Table 3.4-12. Standard-state thermodynamic properties of analcime derived from phase equilibria constraints or by polyhedral estimation techniques.

Sample	Si/Al Ratio	ΔG_f kJ/mol	Reference
Phase equilibria studies	2	-3088.22	Helgeson et al. (1978)
Arbitrary composition	2	-3093.77	Chipera et al. (1995a)
Arbitrary composition	2.75	-3037.5	Chipera et al. (1995a)
Arbitrary composition	2	-3099.72	Chermak and Rimstidt (1989)
Arbitrary composition	2.75	-3040.1	Chermak and Rimstidt (1989)

Table 3.4-13. Gibbs free energy of formation (kJ/mol) of analcime determined from solubility data by Barnes and Wilkin (1995). Predicted values from linear regression

Temperature (°C)	Mt. St. Hilaire*	Predicted	Wikieup**	Predicted
25	-3105.3	-3089.95		-3035.82
50	-3080.5	-3071.31		-3017.49
80	-3048.1	-3048.95		-2995.5
90	-3036.2	-3041.49	-2989	-2988.17
125	-3010.4	-3015.4	-2961.7	-2962.5
175	-2977.5	-2978.13	-2925.2	-2925.84
225	-2939.8	-2940.86	-2889.8	-2889.19
275	-2905	-2903.59		-2852.53
300	-2887.2	-2884.96		-2834.2

*$Na_{0.99}AlSi_2O_6 \cdot H_2O$ (minor K ignored).
**$Na_{0.86}Al_{0.84}Si_{2.14}O_6 \cdot H_2O$ (minor K, Ca, Mg ignored).

Table 3.4-14. Enthalpy of formation and standard-state entropy of analcime derived by linear regression of the solubility data of Barnes and Wilkin (1995). Johnson et al.'s (1982) data on Mt. St. Hilaire analcime are shown for comparison.

	Mt. St. Hilaire	Wikieup	Johnson et al. (1982)
ΔH_f kJ/mol	-3312.19	-3254.42	-3296.9
S° J/mol-K	220.05	223.71	226.75

Table 3.4-15. Thermodynamic data estimated using representative chemical formulae for Yucca Mountain zeolites.

Mineral and Representative Formula	ΔG_f° (kJ/mol)	ΔH_f° (kJ/mol)	S° (J/mol•K)	Volume (cm^3/mol)	k_0 x100	k_1 $x10^{-2}$	k_2 $x10^{-5}$	k_3 $x10^{-7}$
Analcime (Broxton et al., 1986)								
$Na_{0.9}Al_{0.9}Si_{2.2}O_6 \cdot 1.0H_2O$	-3040.1	-3256.2	220.2	97.3	380.95	-22.05	-94.81	139.49
Chabazite (Gottardi and Galli, 1985)								
$K_{0.6}Na_{0.2}Ca_{1.5}Al_{3.8}Si_{8.2}O_{24} \cdot 10.0H_2O$	-13850.3	-15047.4	1194.3	499.4	2022.86	-138.50	-301.581	419.459
Clinoptilolite (Broxton et al., 1986)								
$K_{0.6}Na_{0.2}Ca_{3.0}Al_{6.8}Si_{29.2}O_{72} \cdot 1.6H_2O$	-38078.2	-41247.2	2897.0	1264.0	5206.30	-348.32	-902.94	1271.38
Erionite Approximated from USW UZ-14 1364 data								
$K_{2.5}Na_{0.1}Ca_{3.1}Al_{8.8}Si_{27.2}O_{72} \cdot 28.0H_2O$	-43261.3	-43751.1	3317.0	1344.0	5848.04	-401.03	-896.74	1260.92
Erionite USW H-5 1666 (Levy, 1984b)								
$K_{2.6}Na_{0.4}Ca_{3.2}Al_{8.8}Si_{27.2}O_{72} \cdot 28.0H_2O$	-40252.4	-43743.4	3310.4	1344.0	5842.07	-399.82	-904.39	1272.49
Heulandite USW UZ-14 1364								
$K_{2.9}Na_{0.1}Ca_{3.6}Al_{9.3}Si_{26.7}O_{72} \cdot 26.0H_2O$	-39936.6	-43324.2	3150.9	1266.4	5671.68	-385.22	-895.82	1253.00
Heulandite USW H-5 1666 (Levy, 1984b)								
$K_{0.4}Na_{0.5}Ca_{3.3}Al_{7.5}Si_{28.5}O_{72} \cdot 26.0H_2O$	-39348.6	-42746.9	3091.5	1266.4	5606.63	-381.26	-909.32	1280.34
Heulandite USW G-2 1488 "prismatic" (Carlos et al., 1995b)								
$K_{0.4}Na_{0.3}Ca_{2.3}Sr_{0.2}Mg_{1.0}Al_{7.7}Si_{28.3}O_{72} \cdot 26.0H_2O$	-39373.0	-42776.5	3081.6	1266.4	5604.98	-380.84	-917.90	1289.88

Table 3.4-15: continued.

Heulandite USW G-2 1505 "prismatic" (Carlos et al., 1995b)								
$K_{0.5}Na_{0.3}Ca_{2.5}Sr_{0.2}Mg_{0.0}Al_{7.8}Si_{28.2}O_{72}$•26.0 H_2O	-39413.9	-42815.8	3087.3	1266.4	5609.67	-381.20	-914.91	1285.32
Heulandite UE-25a#1 1243 "tabular core" (Carlos et al., 1995c)								
$K_{0.2}Na_{0.5}Ca_{2.8}Sr_{0.7}Mg_{0.1}Al_{7.9}Si_{28.1}O_{72}$•26.0 H_2O	-39364.4	-42771.6	3069.6	1266.4	5609.98	-381.02	-909.99	1277.85
Heulandite UE-25a#1 1243 "tabular rim & prismatic" (Carlos et al., 1995c)								
$K_{0.1}Na_{0.2}Ca_{2.3}Sr_{0.2}Mg_{1.2}Al_{7.7}Si_{28.3}O_{72}$•26.0 H_2O	-39469.8	-42869.2	3091.0	1266.4	5596.09	-380.29	-918.16	1287.96
Laumontite (Gottardi and Galli, 1985)								
$K_{0.3}Na_{0.2}Ca_{1.8}Al_4Si_8O_{24}$ • 8.0H_2O	-13431.2	-14525.9	1011.2	406.4	1842.70	-122.73	-301.22	414.72
Mordenite (Carlos, 1987; Broxton et al., 1987; Sheppard et al., 1988)								
$K_{0.3}Na_{0.7}Ca_{0.5}Al_2Si_{10}O_{24}$ • 7.3H_2O	-12621.0	-13677.6	986.1	424.5	1752.07	-116.17	-317.63	456.08
Phillipsite USW GU-3 1200.1 (Carlos et al., 1995b)								
$K_{0.7}Na_{0.7}Ca_{2.1}Al_{5.6}Si_{12.4}O_{32}$ • 12.6H_2O	-17817.7	-19375.1	1491.9	609.2	2608.70	-177.81	-415.85	591.77
Stellerite USW G-2 1488.5 and 1505 (Carlos et al., 1995b)								
$Ca_{8.9}Na_{0.1}Al_{7.9}Si_{28.1}O_{72}$ • 28.0H_2O	-39960.1	-43468.5	3224.3	1331.0	5774.01	-396.39	-898.38	1257.38

[1] Gibbs free energies and enthalpies of formation were estimated using Chermak and Rimstidt (1989).
[2] Entropies of formation were estimated using Holland (1989).
[3] Volumes from Smyth and Bish (1988).
[4] Heat capacity terms (k) estimated using Berman and Brown (1985) for equation $C_p = k_0 + k_1T^{-0.5} + k_2T^{-2} + k_3T^{-3}$ in units of J/mol·K.

Table 3.4-16. Summary of 25°C dissolution rate constants for minerals.

Mineral	Log k_{diss}*	Log K normalized to 2 structural oxygen	Molar Volume (cc/mole)
analcime**	-11	-11.48	97.1
gibbsite	-11.45	-11.63	31.956
sanidine	-12	-12.60	109.008
albite	-12.26	-12.86	100.07
prehnite	-12.41	-13.19	140.33
microcline	-12.50	-13.10	108.741
epidote	-12.61	-13.42	139.2
Na-clinoptilolite**	-13.15	-14.23	420.87
amorphous silica†	-12.2	-12.20	29
β-cristobalite†	-12.34	-12.34	27.38
muscovite	-13.07	-13.85	140.71
kaolinite	-13.28	-13.93	99.52
α-cristobalite†	-12.77	-12.77	25.74
quartz	-13.39	-13.39	22.688
Na-clinoptilolite‡	-15.623	-17.18	1262.6

*k_{diss} in moles/m^2-s
All values from Lasaga et al. (1994b) except as noted.
**Murphy et al. (1996)
†Rimstidt and Barnes (1980)
‡MacInnis et al. (1995)

Contents

Chapter 4.0 Geomechanics

Stephen C. Blair
Patricia A. Berge

4.1 Introduction

Information on the geomechanical characteristics of the near-field environment (NFE) is needed for design of the waste package (WP) and engineered barrier system (EBS) and for the assessment of their performance over the lifetime of the repository. Specifically, information is needed on (1) the amount and type of rock-induced loading that might be expected on the waste package, (2) the geomechanical properties of rock in the NFE and how they will change over time, and (3) any coupling of changing geomechanical properties to other near-field properties (e.g., geochemical or hydrologic). Two types of rock-induced loading need to be considered: impact loads and static loads. Impact loads may be caused by the sudden movement of blocks of rock along pre-existing fractures, or by sudden spalling of excavation walls. The WP must be able to withstand the maximum expected impact load without damage. Static loads may result from spalling or sloughing of rock chips from the drift walls, or from slow movement of rock blocks. Static loads provide contact between the rock and the Waste Package, transport pathways into the wall rock, and sites for surface corrosion of the WP. The WP and EBS must be designed to accommodate the expected static loads and still meet the performance objectives over the lifetime of the repository.

Changes in the mechanical properties of the near-field rock over time are also very important. Several processes including creep, microfracturing, radiation damage, and others could contribute to changes in hydrologic and geochemical processes that affect transport. Information on the geomechanical properties of near-field rock away from excavations is also needed to assess the transport properties of the NFE over time.

4.2 Ambient Conditions

4.2.1 Physical, Thermal, and Mechanical Properties of Rock Mass and Intact Rock

The most effective way to determine the ambient physical, thermal and mechanical properties of the rock mass forming the NFE is to tunnel into the rock mass, observe composition and fracture distributions, take samples of the rock for laboratory testing, and perform in situ tests of the thermal-hydrologic-mechanical-chemical (THMC) performance. At the time of writing of this report a tunnel boring machine (TBM) is creating a tunnel through the potential repository horizon, a thermal testing alcove is under construction, and rock samples obtained from the tunnel are being tested in various laboratory facilities. In addition, a series of boreholes has been drilled into the potential repository horizon, and these holes have been logged and samples from them have been tested and characterized in several ways. The ESF operations and studies of associated boreholes have produced a significant amount of new data describing the properties of the ESF. However, because the studies at the ESF are ongoing at this time of writing, the ESF data presented here are subject to frequent revision, and the reader is cautioned to check for updates to the data base.

An extensive series of laboratory tests on core samples obtained from boreholes that intersect the potential repository horizon has been done over a period of several years. The results of these tests have been compiled in the *Yucca Mountain Project Reference Information Base* (*RIB*) (DOE, 1994). It is important to note that the values presented in the *RIB* are subject to frequent revision and that references for some of the values in the *RIB* are not readily available. Consequently, an evaluation of the significance of differences between values reported in the *RIB* and published values cannot be made at this time.

4.2.1.1 Physical Properties. Physical properties including porosity, grain density, bulk density at in situ saturation, and dry bulk density have been determined from core samples and values for these parameters are given in Table 4-1. These values were obtained from a statistical analysis of available data and can be found in chapter 1, sections 1.1321 and 1.1325 of the *RIB*; additional data can be found in Price et al. (1985), Martin et al. (1994), and Roberts and Lin (1995).

4.2.1.2 Thermal Properties. Thermal properties of the repository horizon are presented in Tables 4-1, 4-2, and 4-3. The values for matrix and in situ thermal conductivity in Table 4-1 are from Nimick (1990) and reflect the values from the

RIB. The coefficient of thermal expansion for welded tuff is determined by the tuff's mineralogy (as reflected in matrix conductivity), matrix porosity, matrix saturation, and fracture porosity.

Measurements of linear thermal expansion have been made on samples from the Topopah Spring welded unit, lithophysae-poor layer (TSw2) and Table 4-2 presents the coefficients of linear thermal expansion. These coefficients are the tabulated results of a statistical analysis of thermal expansion data and can also be found in Chapter 1, section 1.1326 of the *RIB*. The values represent coefficients of linear thermal expansion during heating, and the coefficients shown for the intact rock should be used for calculations that do not involve very near-field regions. Coefficients of linear thermal expansion during heating for very near-field regions are also shown and apply only to welded, devitrified tuffs that are near or at a free surface and are in an essentially unconfined initial-stress state. Table 4-2 gives the mean coefficient of linear thermal expansion ($\bar{\alpha}$); the standard deviation of the sample group (s); and the number of samples analyzed (n). Note that these coefficients should not be used for calculations of displacements or stresses during cooling; thermal expansion behavior is hysteretic and depends on the maximum temperature reached by the material. Coefficients of linear thermal expansion ($\bar{\alpha}$) are assumed to be identical for both intact rock and the rock mass. This assumption will be evaluated during the underground heater tests that are currently planned to be conducted in the ESF.

Unconfined thermal expansion measurements on silicate rocks generally show an increase in the expansion coefficient as temperature increases. This is thought to result from a mismatch between the expansion coefficient of constituent grains, which results in local distortions and the formation of new microcracks in an uncracked material or in the shear-related opening of pre-existing microcracks (Cooper and Simmons, 1977). The presence of a mineral, such as cristobalite, that undergoes a phase transformation at a temperature of about 230° C (±20° C) (Meike and Glassley, 1990) with an accompanying 5% increase in volume (Cohen and Klement, 1975), will also cause thermal expansion to vary with temperature. The SiO_2 polymorphs cristobalite and tridymite make up as much as 30% by volume of Topopah Spring tuff groundmass in some parts of the formation (Connolly, 1991, 1994). However, the volume of rock expected to be heated above 200° C is a small percentage of the total rock mass.

Martin et al. (1996) conducted thermal expansion measurements as a function of confining pressure and at temperatures to 250°C on core samples of Topopah Spring

tuff. These authors found that the coefficient of thermal expansion for welded tuff increased with temperature. At temperatures below 100°C the value of this parameter was in the range 7.7 to 10.8 x 10^{-6} °C^{-1}, and as temperature was increased to near 250°C, values of the coefficient of thermal expansion increased to between 14.2 and 20.6 x 10^{-6} °C^{-1}. These authors found that confining pressure had a small effect of the coefficient of thermal expansion.

Thermal capacitance has also been estimated for the Topopah Spring welded unit, lithophysae-poor layer (TSw2) for various temperatures, and the values listed in Table 4-3 are reported in section 1.1326 of the *RIB*. This value incorporates an estimate of rock-heat capacity based on bulk chemical analyses of the rock, the effects of the transformation of the minerals tridymite and cristobalite, the boiling of pore water, and the decrease in saturation of pore water as temperature is increased from 95 to 115 °C. Figure 4-1 is taken from the *RIB* and shows thermal capacitance in more detail. This figure plots values computed from a series of equations presented in section 1.1326 of the *RIB* for thermal capacitance of unit TSw2.

4.2.1.3 Mechanical Properties. To properly characterize the mechanical behavior of the NFE it is necessary to know the mechanical properties of the rock mass forming the NFE. The mechanical properties of a rock mass are difficult to measure directly and depend on the properties of both the intact rock and the fractures making up the rock mass.

The mechanical properties for intact rock of the potential repository horizon have been extensively studied via tests on core samples (Martin et al., 1995a, 1994, Price et al., 1987; Price, 1983; Price and Jones, 1982; Price, 1986; and Nimick et al., 1987). Mechanical properties for TSw2 have been analyzed statistically; the results of the statistical analysis are included in section 1.322 of the *RIB* and are summarized here in Table 4-4. Recent measurements of mechanical properties such as ultimate strength and elastic moduli for tuff by Teufel and McNamee (1991) and Martin et al. (1993, 1994, 1995a) are in general agreement with the values given in Table 4-4. Lin et al. (1993b) used information about intact rock mass properties and fracture/joint characteristics to develop models of rock mass properties and rock mass qualities.

The mechanical data indicate that the intact rock is quite strong with a uniaxial strength of 155 MPa (±59 MPa) and a high deformation modulus. Uncracked samples have stress-strain curves that show nearly linearly elastic behavior until failure. Samples with cracks exhibit nonlinear stress-strain behavior as expected when stress is above 50% of the failure stress. Typical stress-strain curves for 50.8-mm-diam saturated samples are shown in Fig. 4-2.

Martin et al. (1993, 1994, 1995a) measured unconfined compressive strength, static Young's modulus and Poisson's ratio, and elastic wave velocities for Topopah Spring tuff samples from Busted Butte and from the USW NRG-6 and USW NRG-7/7A boreholes at Yucca Mountain. These holes intersected the path of the north ramp of the Exploratory Studies Facility (ESF) and are part of a series of holes identified as the North Ramp Geotechnical (NRG) holes. All measurements were made at ambient temperature conditions. They also made confined compressive strength and indirect tensile strength measurements for the samples from the boreholes. The unconfined compressive strength and static Young's modulus and Poisson's ratio values that they found showed more scatter than the results reported in the *RIB*, and some of the values were much lower than corresponding *RIB* results. The Topopah Spring tuff samples are apparently quite heterogeneous, representing a wide range of porosities, and some samples can be much weaker than those described in the *RIB*. For example, some of the borehole samples failed at pressures well below 100 MPa (Martin et al., 1994, 1995a) rather than having strengths between approximately 100 and 200 MPa as described in the *RIB*. Poisson's ratio values for the borehole samples of TSw2 ranged from about 0.14 to 0.40 (Martin et al., 1994, 1995a), and the TSw2 samples from Busted Butte had static Poisson's ratio values of about 0.09 (Martin et al., 1993).

Elastic wave velocity measurements on laboratory samples are useful as they provide data for comparison with velocities measured in the field, and a means of estimating the dynamic moduli, including Poisson's ratio for the rock. They also provide a convenient method for characterizing anisotropy in the rock behavior. Compressional and shear wave velocity measurements were made at frequencies of about 300 to 800 kHz for the Busted Butte samples and about 300 kHz to 1 MHz for the borehole samples, for both the dry and the saturated cases by Martin et al., 1993, 1994, 1995a. This corresponds to wavelengths of a few mm to a few cm in the tuff. Measurements were made along the core axis for the Busted Butte samples, and both parallel to and perpendicular to the core axis for the borehole samples. But since the shear wave velocities were not measured for waves propagating perpendicular to the core axis and having polarization perpendicular to the core axis (i.e., the expected fast shear wave direction for the case of transverse isotropy), these data cannot be used to quantify any velocity anisotropy. Further discussion of anisotropy in Topopah Spring tuff can be found in Martin et al. (1992).

The compressional wave velocities for the Busted Butte samples were about 4.5 to 4.7 km/s for both the dry and the saturated cases (Martin et al., 1993). The

borehole samples had similar velocities except that a few samples had velocities as low as 4.0 to 4.3 km/s (Martin et al., 1994, 1995a). These velocities found for cores measuring a few cm are higher than the velocities found for the G-tunnel heated block experiment at the 1-m scale (Zimmerman et al., 1986), but are in excellent agreement with compressional wave velocities measured at ambient temperature and pressure conditions for a block of Topopah Spring tuff at the 0.5 m scale (Blair and Berge, 1996).

The shear wave velocities for the Busted Butte samples were about 2.5 to 2.8 km/s for the saturated case, and 2.7 to 2.8 km/s for the dry case (Martin et al., 1993). The borehole samples of tuff had only two shear wave velocity measurements for the saturated case, 2.7 and 2.9 km/s (Martin et al., 1994, 1995a). For the dry case, the borehole samples had shear wave velocities of 2.4 to 3.0 km/s (Martin et al., 1994, 1995a).

Martin et al. (1993) used the velocity measurements to estimate dynamic Young's modulus and Poisson's ratio for the Busted Butte samples. They found values of about 41 to 44 GPa for dynamic Young's modulus in the dry case, and about 39 to 45 GPa for the saturated case. The Poisson's ratio estimates were about 0.20 to 0.22 in the dry case and about 0.23 to 0.28 for the saturated case. The dynamic Young's modulus values were slightly higher than the measured static values for the Busted Butte samples (about 34 GPa). A separate study of the effect of frequency on Young's modulus and elastic wave attenuation (Price et al., 1994) found that Young's modulus for Topopah Spring tuff varied slightly with frequency, having values near 38 GPa for frequencies of about 10^{-2} Hz and higher values near 40 GPa for frequencies up to about 10^{6} Hz. For these measurements, saturation had a greater effect on Young's modulus than the frequency had.

The values that Martin et al. (1993) observed for Poisson's ratio are quite low, 0.09±0.067, when compared to values presented in the *RIB*, about 0.22 to 0.30. Martin et al. (1993) were unable to explain these anomalously low values for Poisson's ratio. One likely explanation is that their samples may have contained significant amounts of α-cristobalite. This mineral has a negative Poisson's ratio for single crystals and polycrystalline aggregates (Yehaneh-Hari et al., 1992; Keskar and Chelikowsky, 1993), which means that rocks containing significant amounts of α-cristobalite may have anomalously low values for Poisson's ratio.

Price (1986) studied the effect of sample size on mechanical properties of Topopah Spring tuff (Tpt) and found that both the ultimate strength and axial strain at failure are inversely related to sample diameter, while Young's modulus and

Poisson's ratio are independent of sample diameter. Price (1986) used power-law models to describe the behavior of ultimate strength and axial strain at failure as a function of sample size and proposed the following two equations:

$$s_u = (1944)\,(D)^{-0.846} + 69.5 \qquad (4\text{-}3)$$

and

$$e_u = 11.6\,D^{-0.268}, \qquad (4\text{-}4)$$

where

s_u = ultimate strength (uniaxial) (MPa),
e_u = axial strain at failure (millistrain),
D = sample diameter (mm).

Price illustrates the effect of sample size on ultimate strength using saturated samples in Fig. 4-3.

To date, most compressive-strength experiments have used samples that were saturated with water and then tested under drained conditions. The results represent a minimum value because rocks are generally weaker when saturated with water. Olsson and Jones (1980) show that for Grouse Canyon tuff, which is similar to rock in the potential NFE, saturated samples are about 24% weaker than dry samples in unconfined compression.

The physical properties of the rock mass must also be determined for evaluation of the NFE. Rock-mass compressive strength is defined as the strength of a representative volume of intact- and jointed-rock matrix material. Estimates of rock-mass strength are based on (1) the known behavior of intact rock, (2) the known joint characteristics, and (3) the presence of applied or confining stresses. A rock-mass strength criterion of

$$(\sigma_1)_{ultimate} = 16.0 + 10.2\,(\sigma_3)^{0.602}, \qquad (4\text{-}5)$$

where $0 < \sigma_3 < 25$ MPa, is presented in item 1.2.6 of the *RIB*. Equation (4-5) is based on an assumed rock-mass rating (RMR) of 61 and an unconfined compressive strength of 16.0 MPa. The equation reflects the current understanding of the nonlinear empirical relationship between rock-mass strength and confining stress and is subject to revision as more field and laboratory data for rock characteristics become available.

4.2.2 Temperature and Stress

In situ stress values for the potential repository horizon have been determined from measurements in drill holes USW G-1, USW G-2, and USW G-3 (Stock et al., 1984, 1985). Table 4-5 shows the average mean value and range for vertical stress, which is the maximum principal stress and is due to the overburden rock at the site, in addition to the ratios of minimum and maximum horizontal stresses to vertical stress, and the bearings of minimum and maximum horizontal stresses.

A calculated stress profile for the in situ stress near the Exploratory Studies Facility (ESF) is reported in chapter 1, section 1.27 of the *RIB*. The results of the analysis are shown in Fig. 4-4. The stress values are estimated using two-dimensional finite-element analysis in which the gravitational stress is the only loading mechanism modeled (Bauer et al., 1985). The calculated values are similar to those reported in both Bauer et al. (1985) and Bauer and Holland (1987), and to the values of Yucca Mountain in situ stress measurements (Stock et al., 1985). The calculations assumed plane-strain conditions and a linearly elastic material response. The maximum horizontal stress was assumed to be equal to twice the minimum horizontal stress. The values of in situ bulk density and elastic properties for the rock mass used in the finite-element analysis were slightly different than those reported in Table 4-5 and can be found in section 1.27 of the *RIB*.

4.2.2.1 Cracks and Fractures. Current knowledge of cracks and fractures in the potential repository horizon is based on observations in exploratory vertical drill holes and from recent observations made in the Exploratory Studies Facility. However, at the time of this writing, fracture mapping from the ESF are not available, but preliminary analysis indicates that the main observations determined from the drill hole data are representative of the data derived from the ESF. The drill hole indicates that jointing in the Topopah Spring welded unit, lithophysae-poor layer is mostly vertical. Scott and Catellanos (1984) reported a fracture density of about $40/m^3$ in the potential repository horizon, and evaluation of these data (Wilder, 1990) indicate that the fracture spacing in the rock mass may be less than ~30 cm (1 ft). Fracture data are also given in chapter 1, section 1.142 of the *RIB*. Data on the distribution and characteristics of fractures in the Topopah Spring welded unit, lithophysae-poor layer (TSw2) along the 2800 m route of the north ramp of the Exploratory Studies Facility have been collected from several boreholes by Brechtel et al. (1995). Brechtel et al. (1995) averaged values over 3 m, (10 ft) lengths along the boreholes and found that the most frequent joint spacing was from 60 - 200mm, with the joint condition characterized as slightly rough, separation < 1mm, and

slightly weathered walls. These data confirm the conclusions of earlier work by Scott and Catellanos (1984) which indicated that potential repository horizon contained a significant number of fractures.

Lin et al. (1993a) reviewed the fracture data from drill holes USW G-1, USW G-4, USW GU-3 and UE-25a#1 and present a description of the fracture spatial location and abundance and physical characteristics and estimated Rock Quality Designation (RQD) for the Topopah Spring member and other geologic formations intersected by the drill holes. Table 4-6 summarizes their findings for the potential repository horizon. These values are similar to those presented by MacDougall (1987). However, because these data are generated from only four exploratory vertical drill holes, additional data and analyses are needed to fully assess the potential for block movement for either borehole or drift emplacement. Moreover, additional data are currently being collected from the ESF, but these data are not available at the time of this writing.

The constitutive properties of fractures and joints present in the potential repository horizon are also important for assessment of the thermal-mechanical and thermal-hydrologic behavior of the rock. Olsson and Brown (1994) measured constitutive properties of seven fractures from drill holes NRG-4 and NRG-6 using a rotary shear apparatus. They found that the peak friction ranged from 0.89 to 1.11, and residual friction ranged form 0.76 to 1.00. They also report that dilation angle ranged from 5.29° to 11.28°, and that the roughness characteristics for the fracture surfaces are in qualitative agreement with the mathematical model of Brown (1994). Olsson also examined the effect of sliding velocity on the mechanical response of an artificial joint in Topopah Spring tuff to determine the velocity-dependence of shear strength. Olsson found that different initial conditions affected the character of the stress-slip curve. In particular, slide-hold-slide tests exhibited time-dependent strengthening, while hold-slide tests produced slip weakening. No joint creep was observed in these tests.

Blair and Berge (1996) monitored the deformation under compression of a fracture zone in a 0.5m scale block of Topopah Spring welded unit, lithophysae-poor layer (TSw2). The test is shown schematically in Fig. 4-5, and a stress-strain curve is shown in Fig. 4-6. This figure shows that deformation is nonlinear with increasing stress, and modulus increases as vertical stress increases above 4 MPa. The modulus value computed for vertical stress below 4 MPa is ~ 4 GPa, and that value increases to ~ 6 GPa as applied stress is raised above 4 MPa. These values are considerably lower than modulus values measured on core samples, and reflect that the block

contains vugs and fractures. The increase in deformation modulus with increasing vertical stress can be attributed to closure of fractures and vugs that occur in the subhorizontal zone. Moreover, the curve exhibits the banana shape that is associated with the hysteretic behavior of fractures. The hysteresis shown during the initial stage of unloading is attributed to the cohesion of fractures. The plot shows that the cohesion for this zone is ~ 1 MPa, which is an order of magnitude weaker than values often used in numerical models of rock behavior that incorporate discrete joints and fractures. As the load continues to decrease, the slope of the unloading curve decreases gradually. This is relevant to hydrologic calculations of flow during the cool down period when stresses are expected to decrease, as the opening of fractures will increase the permeability of the near field region.

Knowing the properties of the intact rock and the fractures provides basic elements for understanding rock mass behavior, and empirical methods have been developed that use information on the properties of intact rock and fractures, as well as the number and orientation for fractures to estimate properties of the rock mass. The two most widely used methods are the Rock Mass Rating (RMR) method (Bieniawski, 1979), and the "Q" method (Barton et al., 1994). Brechtel et al. , 1995) used data from the NRG holes in conjunction with other data from standard laboratory tests on cores from the drill holes to estimate the condition of the rock mass using these two methods. Results indicate fair to good rock conditions in the Topopah Spring welded unit, lithophysae-poor layer. Brechtel et al. (1995) also analyzed the rock quality data using the methodology of Hardy and Bauer (1991) to estimate values of the mechanical properties of the rock mass. These estimates are derived from the RMR and Q values and were computed for input for numerical modeling of thermomechanical and seismic loading of the ESF. Results of their analysis for the TSw2 layer are summarized in Table 4-7. This table shows that estimated rock mass strengths are substantially lower than strength values determined from laboratory measurements on intact rock samples form the NRG drill holes. In particular, the estimated compressive strength for unit TSw2 is 18.8 MPa, which is approximately 10% of the mean value of compressive strength measured from intact core samples. It is interesting that the estimated Young's modulus is similar to that measured on intact core. However, these are only estimated values and more tests and analyses in both the laboratory on blocks containing multiple fractures, and in the field need to be conducted to better define the anticipated rock mass compressive strength.

Comparison of the estimated mechanical properties for the rock mass and the values measured on intact core, indicates that the properties of the rock mass are scale dependent. This is primarily due to the presence of cracks and fractures, and unfortunately, the scaling relations for the behavior and properties of fractured tuff are not well developed. Recently, Lin et al. (1995) proposed an intermediate scale test to aid in the development of scaling relations. This test is known as the Large Block Test and is described in detail in Chapter 9 of this report. Also, Blair and Berge (1996) have measured deformation on a 0.5m scale block of Topopah Spring welded unit, lithophysae-poor layer (TSw2) that contained several cracks and fractures. These authors observed Young's modulus to be about 6 GPa, with most of the deformation occurring across fractures. This indicates that the estimated value of Young's modulus given in Table 4-4 may be too high.

4.3 Processes That Perturb the Waste Package Environment

Development of a subsurface nuclear waste repository will significantly affect the geomechanical conditions of the near-field rock. Excavation of the repository drifts will increase the level of stress in the rock within a few meters of the excavations. Emplacement of the waste containers will cause an immediate and rapid increase in temperature in the walls of the excavations. The maximum temperature reached will depend on the nature of the waste emplaced and the repository design, but temperatures as high as 230 °C are predicted (O'Neal et al., 1984). The thermal loading will affect the stress, strength, and other properties of the rock near the excavations. The overall stress in the WP environment will increase as the rock heats and tries to expand. As heating proceeds, however, some zones of the repository may actually experience tension due to excavation and heating geometries. During cooling, the overall stress will decrease and zones put in tension will return to a compressive state. The heating and cooling of the near-field rock will also cause moisture distribution in the near field to be time-dependent and will impose a drying and rewetting cycle on the rock. Since the rock strength at elevated temperature is also a function of the water content, this must be considered in analysis of near field behavior. Finally, the emplacement of waste may impose a radiation field on rock in the first few centimeters of an excavation wall.

When imposed over long time periods, these changes in the environmental conditions may cause physical and mechanical changes in the rock that need to be considered in the design and assessment of the waste package. While the effect of

these parameters on the mechanical behavior of the NFE has not been studied for the period after closure, it has been studied for the period before closure; the results of some of these studies are summarized below.

4.3.1 Excavation of the Repository

The excavation of repository drifts can alter the mechanical properties of the rock near the openings. Blasting creates fractures while damage due to mechanical excavation depends on the particular technique used. Pusch (1989) evaluated the influence of several excavation techniques on the structure and physical properties of rock around large boreholes and found that "the procedure employed in the excavation of canister disposition holes affects the structure and physical properties of the 'near-field rock.'" Pusch considered percussion, full-face and core drilling, and smooth blasting and found that "except for smooth blasting, the generated damage appears to be less important than the increase in 'axial' hydraulic conductivity that is caused by stress-release effects, but both combine to yield significant local flow passages. This is particularly obvious where the rock structure yields steep wedges." Pusch concludes that core drilling has the least effect, while percussion drilling causes fine-fissuring and discing within one centimeter of the borehole wall. Full-face drilling causes more extensive fissuring and the generation of new fractures in addition to the growth of pre-existing ones within several decimeters from the borehole wall. Pusch's results also indicate that smooth blasting produces a particular form of regular fractures that appear to control the hydraulic conductivity of the near-field rock. Pusch did not consider excavation of the drifts by tunnel-boring machines. It is expected that this method would minimize rock damage around the drifts. While not directly applicable to the drift excavation, Pusch's results are indicative of the types of effects that could be expected in drift excavation.

Excavation of emplacement drifts will also alter the stress field in the rock near because the repository horizon is under lithostatic and regional tectonic stress. When sections of the rock are removed, the stress previously supported by the excavated rock is redistributed in the remaining rock. Generally, stress levels and stress gradients near the excavated openings increase and can result in time-dependent deformation of the excavations.

4.3.2 Thermal Effects of Waste Emplacement

The thermal cycle, during which the rock will rapidly heat and then slowly cool, will affect the geomechanical behavior of the NFE. Figure 4-7 shows temperature

profiles predicted at 150, 500, 1,000, 5,000, and 10,000 yr after waste emplacement at a density of 83.4 mtu. This figure shows that temperatures in the near-field will remain in excess of 100°C for over 1,000 yr. Additional estimates of temperatures in the near field are shown in Fig. 1.10.5.2.1. The thermal loading of the NFE will alter the stress in the rock near the emplacement excavation as a function of time. During the period of temperature increase, the stress in the rock will increase as the rock tries to expand. However, because of the geometry of the excavated drifts, the stress field in the NFE will be complex and, as stated previously, some zones may even be put in tension for an extended period of time. As the temperature decreases, the overall stress levels will decrease and the entire stress field will again be compressive.

In addition, the effect of temperature on the strength of near-field rock is not well defined at this time. Rock strength, however, generally decreases with increasing temperature. Price et al. (1987) report that for samples from the potential repository horizon, Young's modulus decreases an average of 16% as temperature is raised from 22 to 150°C. The mean ultimate strength also decreases 16% as temperature is raised from 22 to 150°C at both 0 and 5 MPa confining pressures.

Several numerical modeling studies have been conducted to assess the stability of underground excavations at Yucca Mountain for the preclosure period and a synopsis of these studies is presented by Ehgartner and Kalinski (1988). All of the studies cited by Ehgartner and Kalinski show that drifts and shafts should be stable through repository decommissioning. However, none of the studies examined the stability of openings at times beyond decommissioning.

Several studies have also evaluated the stability of boreholes if borehole emplacement is selected including Arulmoli and St. John (1987) and Christianson and Brady (1989). Moreover, Christianson and Brady (1989) in investigating the stress field around boreholes for both vertical and horizontal emplacement geometries found for specific geometries that there were locations where compressive stresses were adequate to form zones of rock failure that occurs either prior to heating or develops as heating progresses. Christianson and Brady (1989) also estimated that for horizontal emplacement, zones of joint slip will develop prior to heating. Except for joints dipping at 45°, heating has the effect of reducing the tendency for joint slip, implying that there should be no progressive deformation of the borehole as heating proceeds. The opposite conclusion applies to joints dipping at 45° with a local principal stress ratio of unity. In that case, progressive deterioration of the borehole may accompany heating.

To predict the postclosure geomechanical environment, time-dependent rock properties may be important because stresses in the near field are predicted to remain at levels of 20–40 MPa for well over 100 years. Estimates of the geomechanical behavior of rock around the emplacement drift that incorporate time-dependent rock properties are still to be made. In addition, it is important to note that spalling and/or slip along fractures is expected to occur within the first 50 yr. after waste emplacement at a time when (1) the monitoring of drifts will be practical, and (2) drift support could be relied on.

4.3.3 Time-Dependent Effects

4.3.3.1 Microcracking and Subcritical Crack Growth. Microcracking and subcritical crack growth in the near-field rock over long periods of time is of concern because the formation, growth, and coalescence of microcracks in the rock at or near excavations could lead to excavation damage and the formation of rock chips or blocks. These chips or blocks might passively load the container and form transport pathways. The formation of microcracks may also change the physical and geochemical properties of rock in the NFE. Very little work has been done in this area. Kemeny and Cook (1990), however, used a probabilistic approach, which included time-dependent crack growth, to examine borehole emplacement. They estimated that over the lifetime of the repository, slabbing is likely to occur in a significant portion of the emplacement boreholes.

One mechanism that may cause microcracking of the matrix is the phase transformation of the mineral cristobalite. Cristobalite may occur in significant amounts in the repository horizon (Connolly, 1994), and it has been shown to invert from a tetragonal to cubical structure at approximately 230° C (±20° C) (Meike and Glassley, 1990) with an accompanying 5% increase in volume (Cohen and Klement, 1975). This phase transformation could increase stresses on a local scale and cause cracking of the rock matrix.

At the elevated temperature and stress conditions expected in the near field, significant crack growth may occur even at low-crack-growth rates. Moreover, rates of subcritical crack growth may be such that, when considered over the lifetime of the repository, changes in crack length and density cannot be dismissed when estimating rock behavior. Increases in stress, temperature, and moisture have been shown to cause substantial increases in subcritical crack-growth rate for such rock types as granite and gabbro (Atkinson and Meredith, 1987). Although tests of this type are still to be made on tuff, a similar effect is expected.

Martin et al. (1995b) performed laboratory experiments to investigate creep in Topopah Spring tuff samples at ambient and elevated temperatures. They found that the observed creep deformation was consistent with a mechanism of time-dependent crack growth, particularly at stresses above 90% of the uniaxial compressive strength of the tuff. The stress necessary to produce failure appeared to decrease with increasing temperature, but the data were not sufficient to quantify that effect. Temperature did cause a reduction in strength, but further tests would be required to constrain the strength and creep deformation of tuff as a function of temperature, saturation, and applied load.

Blair and Berge (1996) found that imposing low levels of compressive stress for periods of a few days on 0.5m blocks of Topopah Spring tuff caused time-dependent inelastic crack closure to occur for cracks oriented parallel to the applied stress.

4.3.3.2 Joint Properties. MacDougall et. al (1987) have reported the following joint mechanical properties: joint cohesion = 0.1 MPa and joint-friction angle = 28.4°. Olsson (1987, 1988) investigated joint properties in rock samples from the potential repository horizon and found that the strength of a joint may increase with the time of stationary contact and that joint properties are dependent on stress history. However, he indicated that the latter area needs to be investigated further. To date, data on the effect of environmental variables (e.g., temperature, moisture content, and stress history) on joint properties are not available.

Lin et al. (1993a) present a description of the abundance, orientation, and physical characteristics of fractures and rock quality designation for the stratigraphic units of the potential repository at the Yucca Mountain site. Wibowo et al. (1993) and Olsson (1994) conducted laboratory experiments on fractures and joints in tuff to examine slip behavior and fracture surface damage during shear.

Blair and Berge (1996) found that imposing low levels of compressive stress for periods of a few days on 0.5m scale blocks of Topopah Spring tuff caused time-dependent, non-repeatable behavior to occur for cracks oriented both parallel and perpendicular to the applied stress. Under the long-term loading cracks/vugs oriented perpendicular to the applied stress showed significant closure beyond that observed in the 1-day tests performed by these authors and discussed earlier. In addition, the long-term loading caused pre-existing hairline cracks oriented in the direction parallel to the applied stress to open, which significantly reduced compressional wave velocities in this direction. Increasing temperature caused closure of some of the vertical cracks, which increased horizontal velocities.

Increasing the temperature also caused a softening of the mechanical response in the direction of loading.

Blair and Berge (1996) postulate that some properties of the rock mass may become increasingly anisotropic with time. For instance, if cracks, vugs and fractures oriented parallel to the maximum principal stress undergo time-dependent closing, permeability in this direction will be reduced and deformation modulus will increase. Moreover, opening of pre-existing hairline cracks that occur near the drift wall and are oriented parallel to it, will increase the permeability in this direction and will change the geochemical environment by exposing different mineral assemblages.

4.3.4 Radiation Effects of Waste Emplacement

The effect of radiation on the geomechanical properties of rock from the potential repository horizon is uncertain. Radiation is expected to have a negligible effect on the overall geomechanical behavior of the rock mass. This supposition is based on the work of Durham et al. (1986) who conducted a series of unconfined compression tests on cylinders of quartz monzonite, half of which were irradiated with gamma radiation and half of which were not. A similar series of tests were conducted by Durham et al. on samples of Westerly granite. These experiments showed no statistically significant change in unconfined compressive strength for either rock type. Null results were also found for the effect of gamma irradiation on Young's modulus and Poisson's ratio. Durham et al. concluded that gamma irradiation has no effect on the strengths of either rock type.

However, more recently Blair et al. (1996) have presented results of a suite of uniaxial compressive tests conducted to provide laboratory data to determine how radiation affects the compressive strength of Topopah Spring tuff. This study was patterned after that of Durham et al. (1986), mentioned above. Results indicate that for homogeneous, uncracked samples of Topopah Spring welded unit, lithophysae-poor layer, TSw2, exposure to gamma radiation had no discernible effect on the unconfined compressive (peak) strength or the Young's modulus. However, results for samples that contained partially healed, preexisting vertical or subvertical cracks, indicate that radiation may cause some degradation of the strength and Young's modulus.

A possible explanation of the observed behavior for the cores containing partially healed cracks is that exposure to radiation weakened the cementing material in the cracks and fractures that were present in these samples, leading to the lower values

of peak strength and Young's modulus. The cementing material is thought to be largely composed of carbonates and the authors discuss two possible mechanisms that could weaken the cementing material when it is exposed to radiation (Blair et al., 1996).

These results are preliminary, and additional studies are warranted to evaluate whether radiation does weaken cementing materials in welded tuff. However, if this is a real phenomenon, it has implications for the behavior of rock in the near-field region of a nuclear waste repository. The radiation field is expected to affect only rock exposed on the surface of excavated drifts and to penetrate only a few centimeters into the rock. However, the rock in this region will also experience the highest temperatures and stresses in a repository as well as high humidity. Weakening of fracture-filling materials may cause unanticipated spalling, which may change the amount and nature of rock fragments that come in contact with the waste containers. However, there are several processes that would be likely to occur that would minimize the impact of the radiation. First, radiation penetration is limited to a few centimeters of rock, and if spalling were to occur, the rubble would bulk up and form a radiation shield.

4.3.5 Seismic Loading

Earthquakes and explosions generally affect underground excavations through either fault slip or shaking. Damage due to fault slip will occur when an emplacement drift passes through a fault zone. Under such circumstances, damage is generally restricted to the fault zone, and may range from minor cracking of a tunnel liner to collapse of a portion of the excavation, depending on the fault displacement and the engineering properties of the NFE. If an emplacement drift is found to cross an active or potentially active fault zone, the appropriate sections of the drift will be abandoned because fault slip cannot be prevented.

Excavation damage as a result of shaking or vibratory motion has been widely investigated. For unlined underground excavations in rock, such damage occurs as rock fall, spalling, local opening of rock joints, and block motion. Subramanian et al. (1990) have provided recommendations for seismic parameters for the design of the shafts associated with the ESF. Their recommendations are summarized in section 1.22 of the *RIB*. They concluded that the shafts need only be designed to adequately ensure worker safety and reasonably uninterrupted functions. The working group concluded that deterministic methods were appropriate for establishing conservative levels of ground motion for consideration in the ESF design, and

probabilistic methods were appropriate for confirming that the resulting motions are unlikely to be exceeded during the operating lifetime of the ESF. The recommendations, which were based on available site-specific seismic and geologic data, include design parameters for natural earthquakes that may occur at or near the potential repository site and for underground nuclear explosions (UNE) that may occur at the Nevada Test Site (NTS) and are given in Table 4-8.

Recommended surface-control motion values that are used for the natural earthquake design are 0.30 g horizontal acceleration and 30.0 cm/s peak horizontal velocity (Subramanian et al., 1990; Table 2-1). Subramanian et al. recommend the use of control motions 1.67 times these design-basis values for performance evaluations of the ESF.

Attempts to catalogue records of the performance of underground excavations subjected to seismic loading and develop simple empirical design criteria have indicated a damage threshold of approximately 20 cm/s (8 in./s). No damage should be experienced if the peak particle velocity is beneath that threshold. It is important to note, however, that ground motion resulting from earthquakes can last for several seconds, subjecting the excavation to repeated stress cycles; the number of stress cycles is critical to determining how much permanent deformation will occur within a rock mass around a tunnel when subjected to earthquake loading.

Phillips and Luke (1991) conducted at Tunnel Dynamics Experiment (TDE) to document tunnel damage corresponding to measured and observed ground motions and compared the TDE ground motions with the design basis motions for Yucca Mountain. Their analysis indicated that the design basis motions are relatively small and can be accommodated in the design of the repository drifts.

Implications of seismic loading for the near field environment are that over extended times, the drifts may experience shaking. At the elevated temperature and stress conditions around openings, they may be less stable than during the preclosure and spalling may occur. Backfill of the drifts will prevent contact between this rock and the surface of the cansiter. Kana et al. (1989) recently reviewed the literature on seismic loading for an underground repository and found that because studies completed to date have ignored both time-dependent fracture properties and the duration of shaking, they are of limited use in predicting the rock response to seismic loading by earthquakes. They conclude that further investigation is needed to resolve this issue.

4.4 Geomechanics Modeling

4.4.1 Discussion of Model Approaches

Available Approaches

As mentioned in the above discussion, the rock mass forming the NFE is expected to be a fractured, welded tuff. Several numerical codes have been developed for simulation of rock mass behavior which provide for discrete cracks and fractures. These codes employ finite element (FEM), distinct element, and boundary element numerical techniques, and can incorporate a wide variety of constitutive models. Some have been generalized to three dimensions. To predict rock damage over long periods, and at changing temperature and moisture conditions, existing codes must accommodate the appropriate constitutive equations for elasto-plastic moduli of the rock mass, nonlinear properties of the joints, and fracture propagation. Included properties of the rock are compressive and tensile strength, coefficient of friction, fracture stiffness, and fracture toughness, among others. The codes use these parameters along with boundary stresses and thermally induced stresses to obtain a stress distribution throughout the region of interest in the NFE.

The most common modeling approach utilizes either the finite element or finite difference technique. In this approach, the rock mass is assumed to be a continuum, and the network of cracks and fractures contained in the rock behave in a manner similar to an individual crack. Equations describing the response of an ensemble of cracks is assumed to be identical in form to that describing the response of a single isolated crack. These models handle the creation of new cracks and fracture in various ways. One method is to derive a damage vector D which describes the number of cracks and fractures accumulated during the entire history of deformation (Costin, 1987).

One numerical code which uses a time-dependent finite difference algorithm is called FLAC, which is an acronym for Fast Lagrangian Analysis of Continua. This code is capable of treating both mechanical and thermally induced stresses and deformations. In this code, materials are represented by arbitrarily shaped, quadrilateral zones, and several built-in constitutive models are available for describing material behavior. FLAC is often used in 2-D, assuming plane strain geometry, and linear mechanical and thermal properties where mechanical properties (e.g., elastic moduli) and thermal properties (e.g., thermal expansion

coefficient) are independent of stress and temperature. Constitutive relations are often either isotropic elastic or else make use of the ubiquitous joint model capability of the FLAC code. The thermal response is usually isotropic heat conduction. FLAC has recently become available in 3-D, and this new version is currently being configured to allow simulation of the 3-D stress and displacement field in the NFE over time (see discussion below).

Another widely available code is ABAQUS. This is a 3-D finite element code with capability for time-dependent analysis of thermal and mechanical behavior. The numerical model is weakly coupled in the sense that the temperature field produces thermal stresses, but that these stresses do not in turn influence temperatures. The temperature field is calculated as a function of time from a thermal diffusion model. The mechanical model uses the temperature field at various times to apply thermal loading.

The distinct element approach represents a fundamentally different approach to analysis of the mechanical behavior of a fractured rock mass. In the distinct element method, the rock mass is composed of an assembly of deformable blocks that are interfaced by discontinuities. In some of the distinct element models the blocks are discretized by means of triangular zones where the strains are assumed to be constant. In a distinct element code, fractures in the rock mass are entered individually. One of the most commonly used distinct element codes is called UDEC, and Millard et al. (1995) discuss the use of UDEC in a thermal-hydro-mechanical simulation.

Another very different type of modeling available for study of the NFE is statistical modeling. This type of modeling can be used to study fracture processes as well a deformation and stress in rock especially at elevated temperatures and at long times (Blair, 1994). It can be used to construct ideal systems in which all physical properties are known; this allows the effect of rock heterogeneity on the overall rock behavior to be examined in a quantitative way. In a statistical model, the body of interest is simulated using a lattice or a network of sites, bonds, or both. The behavior of each site or bond is governed by simple, one-dimensional (1-D) rules. For instance, a material may be represented by a network of springs, and each spring is assigned a modulus and a breaking strength. Stress, displacement, and/or temperature contidions are then applied, and the network is solved to determine the stress in each spring. If for a particular spring the stress exceeds the strength assigned to the spring, it is "broken" and removed from the network. Lattices of sites can be used in the same manner, or a network of sites and bonds can be

constructed where both sites and bonds have properties. This approach provides a way to study complex systems using simple elements. Using simple brittle-bond elements this type of model can produce globally ductile behavior for a network where material shows strain-softening.

One of the major advantages of a statistical model for studying fracture in rock is that local heterogeneity can be incorporated very easily. Statistical models include a variety of lattice, network, molecular-dynamics, cellular-automata, field-theory, and other pseudo-continuum models. Herrmann and Roux (1990) have compiled a comprehensive volume describing statistical models and how they can be used to study fracture in rock.

Validity Studies

An international co-operative research project was established for theoretical and experimental studies of coupled thermal, hydrological, and mechanical processes in hard rocks. This project is called DECOVALEX and is described by Jing, Tsang, and Stephansson (1995). In this work, different mathematical models and computer codes have been used to study problems of interest to geologic disposal of nuclear waste. In particular, 11 codes were evaluated including both 2-D and 3-D finite element codes in which the rock was modeled as a porous/fracture media and a 2-D discrete element code in which the rock was modeled as discrete deformable block assemblages. Much of the work done for DECOVALEX is documented in a special issue of the *International Journal of Rock Mechanics* (Stephansson, 1995).

As part of the DECOVALEX program, two inter-code bench mark comparisons were carried out. The bench mark test BMT1 considered a large-scale (km) mass of rock and is described by Millard et al. (1995). The bench mark problem BMT2 involved a system of nine blocks of intact hard rock separated by two pairs of soft fractures and is described by Chan et al. (1995). For each of these exercises, both finite element and distinct element methods were used. Chan et al. (1995) found that for BMT2, heat convection significantly affects the distribution of temperature, thermal stresses, and displacements, and that the predominant coupled effect is fracture closure caused by thermal expansion of the rock blocks. Thus, coupled models of the near field need to incorporate this effect. Results for DECOVALEX also indicate that for studies BMT1 and BMT2, the different modeling techniques produced very similar results. This indicates that use of the continuum codes is merited for study of the near field. This is important because continuum codes are generally easier to use than the distinct element codes.

Other work conducted in conjunction with the DECOVALEX program includes development of an analytical solutions for coupled thermo-hydro-mechanical behavior by Rehbinder (1995), and study of thermal-mechanical-hydrological behavior of sparsely fractured rock by Nguyen and Selvadurai (1995). In addition, Jiao and Hudson (1995) have presented a fully coupled model for rock engineering systems.

Model Development

One of the necessary tasks for simulation of the geomechanical behavior in the near field is coupling of the thermal-mechanical models to the sophisticated hydro-thermal models used by the hydrologic community (discussed in Chapter 1). Recently, we have initiated coupled 3-D modeling of thermal-mechanical-hydrologic behavior of the near field. The methodology being used to model the coupled behavior is as follows. Thermal-hydrologic models are used to compute the temperature distribution, this information is then passed to the thermal-mechanical model for computation of stress and deformation fields. The thermal-mechanical model is set-up with the same grid as the thermal-hydrologic model (see Chapter 1, Fig. 1.10.5.2.1). The particular models being used are NUFT for the thermal-hydrologic behavior, and FLAC-3D for the thermal-hydrologic behavior. Progress to date includes completion of the translating program which passes the NUFT grid into FLAC-3D, and initial testing of the mechanical behavior using this grid.

As mentioned above, statistical methods also offer promise for the study of rock behavior over long periods in the NFE and Blair (1994) has developed a statistical model for fracture of rock in compression that allows rock heterogeneity to be introduced at a variety of scales. This model utilizes a *field theory* approach to the analysis of fracture, and incorporates the concept of superposition and the techniques of boundary element analysis and percolation theory to form a simple yet powerful method for the study of progressive fracture of rock. A conduction temperature model has been implemented into this *field-theory* code and using this or other statistical models, temperature-dependent behavior could be linked to the chemical state of any given site. This could be used to evaluate the behavior of Topopah Spring Tuff at conditions equivalent to those expected in the NFE. This formation is known to contain significant amounts of the mineral cristobalite and at temperatures between 175° and 225°C this mineral undergoes a phase transformation and expands in volume by 5% or more. In addition, bound water may be given off and flash to steam when this phase transformation occurs. This

provides a considerable amount of energy at the site of the mineral. The model could be used to simulate the mechanical effects of this phase transformation by assigning a portion of the sites to be cristobalite sites and imparting some special properties to these sites. When temperature reaches the transformation temperature, these sites break and impart strain energy to the system. Chemistry-dependent properties could also be included by assigning to each site an appropriate chemical parameter(s) that represent the chemical state and a timer. For time-dependent strength, or strength that is dependent on time and chemical environment, the time and chemical environment can be tracked and at time *t* the strength of the site is decreased.

4.4.2 Applications to the Near Field Environment at Yucca Mountain

Blair, Berge, and Wang (1995) analyzed the thermal mechanical behavior of a 3m x 3m x 5m block of fractured rock as part of the analysis done in anticipation of the Large Block Test (LBT) planned for Fran Ridge near Yucca Mountain (Lin et al. 1995). The purpose of this work was to provide analysis and interpretation of coupled thermal-mechanical-hydrological behavior of the block as it is heated. Particular objectives of the modeling were to aid in the experimental design of the test, to evaluate different thermal and constitutive models, and to evaluate different numerical methods. In this study, thermal-mechanical simulations of the heat-up phase of the LBT were conducted using two different numerical codes that are commercially available, a 2-D finite difference model (FLAC, Itasca, 1993) and a 3-D finite element model (ABAQUS).

The purpose of this initial numerical modeling was to calculate temperatures, stresses, and displacements in two and three dimensions for a simplified representation of the large block. In reality, numerous joints and fractures complicate the behavior of the large block significantly. Nonetheless, these simulations provide a general understanding of the thermal-mechanical behavior to be expected in the LBT.

In these simulations, the gridding used in the FLAC models was similar to that used by Lee (1995) for hydrothermal modeling. The second method considered is the 3-D finite element method, and the code ABAQUS was used to evaluate this method. In the 3-D simulations only one-quarter of the block was modeled; therefore, the two symmetry planes were given boundary conditions of zero displacement normal to the plane. ABAQUS requires many of the same material properties as FLAC, and for the simulations conducted in this study, the mechanical

and thermal properties input to ABAQUS were identical to those used in the FLAC elastic model. In the ABAQUS modeling, an elastic model was used to simulate the large block, and no viscoelastic properties or fracture zones were used.

Blair, Berge, and Wang (1996) show that the predicted temperature fields agree well with those predicted by Lee (1995) using a code that incorporates a more sophisticated thermal-hydrological model. Two simulations were conducted in which discrete fractures present in the large block were simulated, and lower levels of stress were predicted in these simulations, indicating that the presence of compliant fractures may reduce the stress levels.

The 2-D, plane strain, FLAC model was constructed in a plane orthogonal to the heater holes proposed for the LBT. The thermal predictions made with this code show a 2-D temperature field near the heaters at early times. At later times, the code predicts a temperature field that is nearly 1-D because all the walls are insulated. Temperature fields in the 3-D simulation were very similar to those predicted by the 2-D FLAC model. For example, the temperature at the top of the block is approximately 65°C after 60 days in the 3-D model and approximately 70°C after 55 days in the 2-D model.

The differences are greater between the 2-D and 3-D mechanical models. The plane strain approximation used in the 2-D model assumes that the length of the heater direction is long compared with the height and width of the block. Further, the plane strain model does not incorporate the stress-free boundary faces parallel to the model plane. The plane strain model generates a large, compressive normal stress in the heater direction to suppress the thermal expansion in that direction.

Blair, Berge, and Wang (1995) conclude that the thermal-mechanical FLAC and ABAQUS modeling produced temperature fields similar to that of Lee (1995) who used a code which contains a more sophisticated thermal-hydrologic model. This suggests that the FLAC and ABAQUS codes could be used with a thermal-hydrological model to better investigate coupled processes. The 2-D modeling was faster and was useful for exploring effects of different constitutive models, but was unable to simulate the outside face of the large block where stresses are highest. This is because the plane strain assumption is equivalent to assuming that the 2-D model lies at the center of the block. Note that most of the instrumentation in the LBT will be located on the outside surface of the block. The 3-D modeling required an order of magnitude more in computer time, but was able to estimate maximum stresses and displacements everywhere in the block's volume.

4.5 References

Arulmoli, K., and C. M. St. John (1987), *Analysis of Horizontal Waste Emplacement Boreholes of a Nuclear Waste Repository in Tuff*, Sandia National Laboratories, Albuquerque, NM, SAND86-7133.

Atkinson, B. K., and P. G. Meredith (1987), "The Theory of Subcritical Crack Growth with Applications to Minerals and Rocks," Fracture Mechanics of Rocks, B. K. Atkinson, Ed. (Academic Press, London).

Barton, N. R., R. Lien and J. Lunde, 1994, "Engineering Classification of Rock Masses for the Desing of Tunnel Support," *Rock Mechanics*, 6, 189-236, (NNA.870406.0237)

Bauer, S. J., and J. F. Holland (1987), "Analysis of In Situ Stress at Yucca Mountain," Proc. of the 28th U.S. Symp. on Rock Mechanics, I. Farmer, Ed. (A. A. Balkema, Rotterdam, The Netherlands), pp. 707–713.

Bauer, S. J., J. F. Holland, and D. K. Parrish (1985), "Implications About In Situ Stress at Yucca Mountain," Proc. of the 26th U.S. Symp. on Rock Mechanics, E. Ashworth, Ed. (A. A. Balkema, Rotterdam, The Netherlands), pp. 1113–1120.

Bieniawski, Z.T., 1979. Engineering Rock Mass Classification, Wiley-Interscience Publication, John Wiley & Sons, New York. (NNA.901005.0044)

Blair, S. C. (1994), "Analysis of compressive fracture in rock using statistical techniques," Ph.D. Thesis, Dept. of Materials Science and Mineral Engineering, U. C. Berkeley, Berkeley, CA.

Blair, S. C. and P. A. Berge, "Uniaxial compression behavior of small blocks of welded tuff," in *Proceedings of the 1996 Int'l High Level Radioactive Waste Management Conference*, April 29 - May 3, 1996, Las Vegas, NV, published by American Nuclear Soc and American Society of Civil Engineers, pp. 409-411.

Blair, S. C, P. A. Berge, and H. F. Wang (1995), "Geomechanical Analysis of the Large Block Test," UCRL-ID-122898, Lawrence Livermore National Laboratory, Livermore, CA.

Blair, S. C., J. M. Kelly, O. Pine, R. Pletcher, and P. A. Berge, "Effect of radiation on the mechanical properties of Topopah Spring tuff," UCRL-ID-122899, Lawrence Livermore National Laboratory, Feb. 1996.

Brechtel, C.E., M. Lin, E. Martin, and D.S. Kessel, 1995. Geotechnical Characterization of the North Ramp of the Exploratory Studies Facility, SAND95-0488/1 and -0488/2, Yucca Mountain Site Characterization Project, Sandia National Laboratories, Albuquerque, NM. (MOL.19950502.0004)

Brechtel, C.E., S. C. Carlisle, and J. Pott, 1993. "Rock Mass Quality Estimation, North Ramp Starter Tunnel, Upper Bench," SLTR93-7001, DTN:SNF28021693001.001, Sandia National Laboratories, Albuquerque, NM.

Brown, S.R. 1994. Simple Mathematical Model of a Rough Fracture, SAND92-2216J, Sandia National Laboratories, Albuquerque, NM. MOL 19941006.0040.

Chan, T, K., Khair, L. Jing, M. Ahola, J. Noorishad, and E. Vuillod (1995), "International comparison of coupled thermo-hydro-mechanical models of a multiple-fracture bench mark problem: DECOVALEX Phase I, bench mark test

2," in Thermo-Hydro-Mechanical Coupling in Rock Mechanics, *Int. J. Rock Mech. Min. Sci. & Geomech. Abstr.*, 32(5).

Christianson, M. C., and B. Brady (1989), *Analysis of Alternative Waste Isolation Concepts*, U.S. Nuclear Regulatory Commission, Washington, DC, NRC-FIN D1016, NUREG/CR-5389.

Cohen, L. H., and W. Klement, Jr. (1975), "Differential Thermal Analysis Investigation of the High-Low Cristobalite Inversion under Hydrostatic Pressure to 7 kbar," *Jour. Am. Cerm. Soc.* 58(5-6), 206–208.

Connolly, J. R. (1991), Mineralogy, Petrology and Whole-Rock Chemistry of Selected Mechanical Test Samples of Yucca Mountain Tuffs, Sandia National Laboratories, Albuquerque, NM, SAND90-7058. (101 pp., accession number NNA.911202.0029)

Connolly, J. R. (1994), Mineralogical, Petrologic, and Whole-Rock Chemical Analysis of Fran Ridge Tuff Used in the SNL Backfill Thermal Properties Experiment, FR-88-62-SNL Petrology Report, written communication from Univ. of New Mexico to Sandia National Laboratories.

Cooper, H. W., and G. Simmons (1977), "The Effects of Cracks on Thermal Expansion of Rocks," *Earth and Planetary Science Letters* 36, 404.

Costin, L. S. (1987), "Time-dependent deformation and failure in Fracture Mechanics of Rock," B. K. Atkinson editor, pp. 167–215, Academic Press, London. ISBN: 0-12-066265-5.

DOE (U.S. Department of Energy) (1994), *Yucca Mountain Project Reference Information Base, Version 4*, Yucca Mountain Site Characterization Project Office, Las Vegas, NV, YMP/CC-0002. (NNA 890330.0077)

Durham, W. B., J. M. Beiriger, M. Axelrod, and S. Trettenaro (1986), "The Effect of Gamma Radiation on the Strength and Elasticity of Climax Stock and Westerly Granites," *Nuclear and Chemical Waste Management* 6, 159–168.

Ehgartner, B. L., and R. C. Kalinski (1988), *A Synopsis of Analyses (1981–1987) Performed to Assess the Stability of Underground Excavations at Yucca Mountain*, Sandia National Laboratories, Albuquerque, NM, SAND88-2294.

Gertsch, R. and L. Ozdemir (1992), Performance Prediction of Mechanical Excavators from Linear Cutter Tests on Yucca Mountain Welded Tuffs, Sandia National Laboratories, Albuquerque, NM, SAND91-7038. (accession number NNA.920819.0247)

Hardy, M.P., and S.J. Bauer, 1991. Drift Design Methodology and Preliminary Application for the Yucca Mountain Site Characterization Project, SAND89-0837, Sandia National Laboratories, Albuquerque, New Mexico. (NNA.910808.0105)

Herrmann, H. J., and S. Roux (1990), *Statistical Models for the Fracture of Disordered Media* (North-Holland Elsevier Science Publishers B. V.).

Itasca Consulting Group, Inc. (1993), *FLAC User's Manual*, vol. I-III, Minneapolis, MN.

Jiao, Y., and J. A. Hudson (1995), "The full-coupled model for rock engineering systems", *Int. J. Rock Mech. Min. Sci. & Geomech. Abstr.* 32(5).

Jing, L., C.-F. Tsang, and O. Stephansson (1995), "DECOVALEX-an international co-operative research project on mathematical models of coupled THM processes

for safety analysis of radioactive waste repositories," *Int. J. Rock Mech. Min. Sci. & Geomech. Abstr.* 32,5.

Kana, D. D., B. H. G. Brady, B. W. Vanzant, and P. K. Nair (1989), *Critical Assessment of Seismic and Geomechanics Literature Related to a High-Level Nuclear Waste Underground Repository*, Nuclear Regulatory Commission, Center for Nuclear Waste Regulatory Analyses, San Antonio, Texas.

Kemeny, J., and N. Cook (1990), "Rock Mechanics and Crustal Stress," Demonstration of a Risk-Based Approach to High-Level Waste Repository Evaluation, R. K. McGuire, Ed., Electric Power Research Institute, Palo Alto, CA, EPRI-NP-7057.

Keskar, N. R., and J. R. Chelikowsky (1993), Anomalous Elastic Behavior in Crystalline Silica, *Phys. Rev. D*, 48, 16,227-16,233.

Lee, K. H. (1995), "Progress report on pre-test calculations for the Large Block Test," UCRL-ID-118669, Lawrence Livermore National Laboratory, Livermore, CA.

Lin, M., M. P. Hardy, and S. J. Bauer (1993a), Fracture Analysis and Rock Quality Designation Estimation for the Yucca Mountain Site Characterization Project, Sandia National Laboratories, Albuquerque, NM, SAND92-0449. (accession number NNA.921204.0012)

Lin, M., M. P. Hardy, J. F. T. Agapito & Associates, and S. J. Bauer (1993b), Rock Mass Mechanical Property Estimations for the Yucca Mountain Site Characterization Project, Sandia National Laboratories, Albuquerque, NM, SAND92-0450. (accession number NNA.921204.0013)

Lin, W. L., D. G. Wilder, J. A. Blink, S. C. Blair, et al. (1994), "The testing of thermal-mechanical-hydrological-chemical processes using a large block," in *Proceedings of the 5th Intl. High-Level Rad. Waste Mgmt. Conf.*, Las Vegas, ASCE (May, 1994).

Lin, W. D.G. Wilder, J. A. Blink, S. C. Blair, T. A. Buscheck, W. E. Glassley, K. Lee, M. W. Owens, & J. J. Roberts, (1995) "A heated large block test for high level nuclear waste management," in *Proceedings of the Second International Conference on the Mechanics of Jointed and Faulted Rock*, Vienna, Austria, April, 1995.

MacDougall, H. R., L. W. Scully, and J. R. Tillerson, (Compilers) (1987), *Site Characterization Plan Conceptual Design Report*, Sandia National Laboratories, Albuquerque, NM, SAND84-2641.

Martin, R. J., III, R. H. Price, P. J. Boyd, and J. S. Noel (1993), Unconfined Compression Experiments on Topopah Spring Member Tuff at 22° C and a Strain Rate of 10^{-9} s^{-1}: Data Report, Sandia National Laboratories, Albuquerque, NM, SAND91-0894. (accession number NNA.930728.0088)

Martin, R. J., III, R. H. Price, P. J. Boyd, and R. W. Haupt (1992), Anisotropy of the Topopah Spring Member Tuff, Sandia National Laboratories, Albuquerque, NM, SAND91-0894. (28 pp., accession number NNA.920522.0041)

Martin, R. J., J.S. Noel, P.J. Boyd, and R.H. Price, 1996, "Thermal expansion as a function of confining pressure for welded tuff from Yucca Mountain," in *Proceedings of the 2nd North American Rock Mechanics Symposium*, Montreal, Canada, June 19-21, 1996, Aubertin, Hassani, and Mitri eds. Balkema. Rotterdam.

Martin, R. J., R. H. Price, P. J. Boyd, and J. S. Noel (1994), Bulk and Mechanical Properties of the Paintbrush Tuff Recovered from Borehole USW NRG-6: Data

Report, Sandia National Laboratories, Albuquerque, NM, SAND93-4020. (92 pp., accession number MOL.19940811.0001)

Martin, R. J., R. H. Price, P. J. Boyd, and J. S. Noel (1995a), Bulk and Mechanical Properties of the Paintbrush Tuff Recovered from Borehole USW NRG-7/7A: Data Report, Sandia National Laboratories, Albuquerque, NM, SAND94-1996. (93 pp., accession number MOL.19950316.0087)

Martin, R. J., III, R. H. Price, P. J. Boyd, and J. S. Noel (1995b), Creep in Topopah Spring Member Welded Tuff, Sandia National Laboratories, Albuquerque, NM, SAND94-2585. (53 pp., accession number MOL.19950502.0006)

Meike, A., and Glassley, W. E. (1990), In-Situ Observation of the Alpha/Beta Cristobalite Transition Using High Voltage Electron Microscopy, MRS Symp. Proc., 176, 631-639.

Millard, A., N. Durin, A. Stietel, A. Thoraval, E. Vuillod, H. Baroudi, F. Plas, A. Bougnoux, G. Vouille, A. Kobayashi, K. Hara, T. Fujita and Y. Ohnishi (1995), "Discrete and continuum approaches to simulate the thermo-hydro-mechanical couplings in a large, fractured rock mass," *Int. J. Rock Mech. Min. Sci. & Geomech. Abstr.* 32(5).

Nguyen, T. S., and A. P. S. Selvadurai (1995), "Coupled thermal-mechanical-hydrological behaviour of sparsely fractured rock: implications for nuclear fuel wasted disposal," *Int. J. Rock Mech. Min. Sci. & Geomech. Abstr.* 32(5).

Nimick, F. B. (1990), *The Thermal Conductivity of Seven Thermal Mechanical Units at Yucca Mountain, Nevada*, Sandia National Laboratories, Albuquerque, NM, SAND88-1387.

Nimick, F. B., R. G. Van Buskirk, and A. F. McFarland (1987), *Uniaxial and Triaxial Compression Test Series on Topopah Spring Member from USW G-2, Yucca Mountain, Nevada*, Sandia National Laboratories, Albuquerque, NM, SAND85-0703.

Olsson, W. A. (1987), *Rock Joint Compliance Studies*, Sandia National Laboratories, Albuquerque, NM, SAND86-0177.

Olsson, W. A. (1988), *Compliance and Strength of Artificial Joints in Topopah Spring Tuff*, Sandia National Laboratories, Albuquerque, NM, SAND88-0660.

Olsson, W. A. (1994), The Effect of Sliding Velocity on the Mechanical Response of an Artificial Joint in Topopah Spring Member Tuff, Sandia National Laboratories, Albuquerque, NM, SAND92-2333. (18 pp., accession number NNA.940209.0001)

Olsson, W. A., and S. R. Brown (1994), Mechanical Properties of Seven Fractures from Drillholes NRG-4 and NRG-6 at Yucca Mountain, Nevada, Sandia National Laboratories, Albuquerque, NM, SAND94-1995. (29 pp., accession number MOL.19941007.0081)

Olsson, W. A., and A. K. Jones (1980), *Rock Mechanics Properties of Volcanic Tuffs from the Nevada Test Site*, Sandia National Laboratories, Albuquerque, NM, SAND80-1453.

O'Neal, W. C., D. W. Gregg, J. N. Hockman, E. W. Russell, and W. Stein (1984), *Preclosure Analysis of Conceptual Waste Package Designs for a Nuclear Waste Repository in Tuff*, Lawrence Livermore National Laboratory, Livermore, CA, UCRL-53595.

Phillips, J. S., and B. A. Luke (1991), Tunnel Damage Resulting from Seismic Loading, Sandia National Laboratories, Albuquerque, NM, SAND90-1721C. (27 pp., accession number NNA.910424.0001)

Price, R. H. (1983), *Analysis of Rock Mechanics Properties of Volcanic Tuff Units from Yucca Mountain, Nevada Test Site*, Sandia National Laboratories, Albuquerque, NM, SAND82-1315.

Price, R. H. (1986), *Effects of Sample Size on the Mechanical Behavior of Topopah Spring Tuff*, Sandia National Laboratories, Albuquerque, NM, SAND85-0709.

Price, R. H., and A. K. Jones (1982), *Uniaxial and Triaxial Compression Tests Series on Calico Hills Tuff*, Sandia National Laboratories, Albuquerque, NM, SAND82-1314.

Price, R. H., F. B. Nimick, J. R. Connolly, K. Keil, B. M. Schwartz, and S. J. Spense (1985), *Preliminary Characterization of the Petrologic, Bulk, and Mechanical Properties of a Lithophysal Zone Within the Topopah Spring Member of the Paintbrush Tuff*, Sandia National Laboratories, Albuquerque, NM, SAND84-0860.

Price, R. H., J. R. Connolly, and K. Keil (1987), *Petrologic and Mechanical Properties of Outcrop Samples of the Welded, Devitrified Topopah Spring Member of the Paintbrush Tuff*, Sandia National Laboratories, Albuquerque, NM, SAND86-1131.

Price, R. H., R. J. Martin, III, and R. W. Haupt (1994), *The Effect of Frequency on Young's Modulus and Seismic Wave Attenuation*, Sandia National Laboratories, Albuquerque, NM, SAND92-0847. (50 pp.)

Pusch, R. (1989), *Influence of Various Excavation Techniques on the Structure and Physical Properties of Near-Field Rock around Large Boreholes*, Swedish Nuclear Fuel and Waste Management Co. (SKB), Stockholm, Sweden, Technical Report 89-32.

Rehbinder (1995), "Analytical solutions of stationary coupled thermo-hydro-geomechanical problems," *Int. J. Rock Mech. Min. Sci. & Geomech. Abstr.* 32(5).

Roberts, J. R. and W. Lin, 1995, "Permeability of Fractured Tuff as Functions of Temperature oand Confining Pressure, in *Proceedings of the 19965Int'l High Level Radioactive Waste Management Conference*,, Las Vegas, NV, published by American Nuclear Soc and American Society of Civil Engineers

Scott, R. B., and M. Catellanos (1984), *Stratigraphic and Structural Relations of Volcanic Rocks in Drill Holes USW GU-3 and USW G-3, Yucca Mountain, Nye County, Nevada*, U.S. Geological Survey, Denver, CO, OFR-84-491.

Stephansson, O. (1995), "Introduction to Special Issue on Thermo-Hydro-Mechanical Coupling in Rock Mechanics," *Int. J. Rock Mech. Min. Sci. & Geomech. Abstr.* 32(5).

Stock, J. M., J. H. Healy, and S. H. Hickman (1984), *Report on Televiewer Log and Stress Measurements in Core Hole USW G-2, Nevada Test Site*, U.S. Geological Survey, Denver, CO, OFR-84-172.

Stock, J. M., J. H. Healy, S. H. Hickman, and M. D. Zoback (1985), "Hydraulic Fracturing Stress Measurements at Yucca Mountain, Nevada, and Relationship to Regional Stress Field," *J. Geophys. Res.* 90(B10), 8691–8706.

Subramanian, C. V., J. L. King, D. M. Perkias, R. W. Modd, A. M. Richardson, J. C. Calovini, E. VanEeckhout, and D. D. Emerson (1990), *Exploratory Shaft Seismic*

Design Basis Working Group Report, Sandia National Laboratories, Albuquerque, NM, SAND88-1203.

Teufel, L. A., and M. J. McNamee (1991), Tensile Strength Testing of Topopah Spring Tuff, Sandia National Laboratories, Albuquerque, NM, SAND91-0044. (13 pp., accession number NNA.910322.0056)

Wibowo, J., B. Amadei, S. Sture, R. H. Price, and A. B. Robertson (1993), Effect of Boundary Conditions on the Strength and Deformability of Replicas of Natural Fractures in Welded Tuff: Data Report, Sandia National Laboratories, Albuquerque, NM, SAND92-1853. (accession number NNA.930907.0001)

Wilder, D. G. (1990), "Engineered Barrier Systems and Canister Orientation Studies for the Yucca Mountain Project, Nevada," Proc. of International Symp. on Unique Underground Structures (Colorado School of Mines Press, Colorado).

Yehaneh-Hari, A., D. J. Weidner, and J. B. Parise (1992), Elasticity of α-Cristobalite: A Silicon Dioxide with a Negative Poisson's Ratio, Science, 257, 650-652.

Zimmerman, R. M., R. L. Schuch, D. S. Mason, M. L. Wilson, M. E. Hall, M. P. Board, R. P. Bellman, and M. L. Blanford (1986), Final Report: G-Tunnel Heated Block Experiment, Sandia National Laboratories, Albuquerque, NM, SAND84-2620.

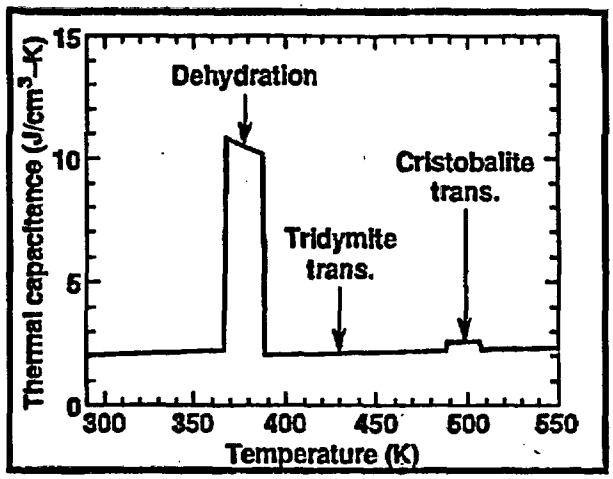

Figure 4-1. Rock-mass thermal capacitance of unit TSw2 showing the effects of dehydration and cristobalite transformation. The temperature of tridymite transformation is shown for reference. Adapted from the Yucca Mountain Project Reference Information Base (DOE, 1994).

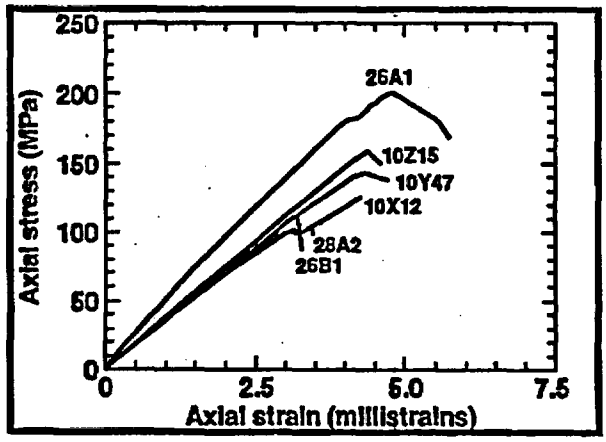

Figure 4-2. Plots of axial stress vs axial strain for uniaxial measurements on 50.8-mm saturated Tpt samples at 22°C. Measurements were taken at a strain rate of $10^{-5}s^{-1}$. Adapted from Price (1986).

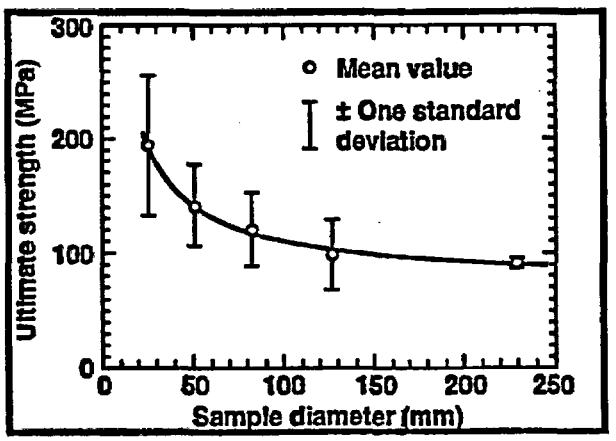

Figure 4-3. Plot of ultimate strength vs sample diameter for uniaxial measurements on saturated Tpt samples at 22°C. Measurements were taken at a strain rate of $10^{-5}s^{-1}$. Adapted from Price (1986).

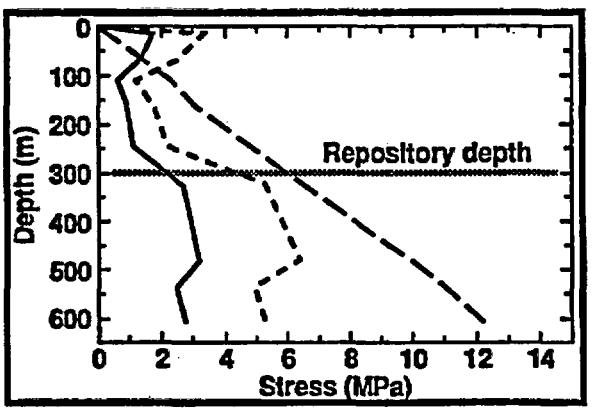

Figure 4-4. Stress profile along an exploratory shaft near the Exploratory Studies Facility. The solid line is the minimum horizontal stress, the long dashed line is the maximum horizontal stress, and the short dashed line is the vertical stress. Adapted from the *Yucca Mountain Project Reference Information Base* (DOE, 1994).

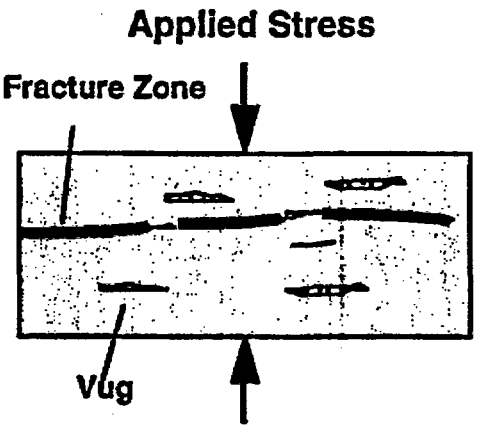

Figure 4-5. Schematic of compression test on 0.5m scale block of Topopah Spring tuff.

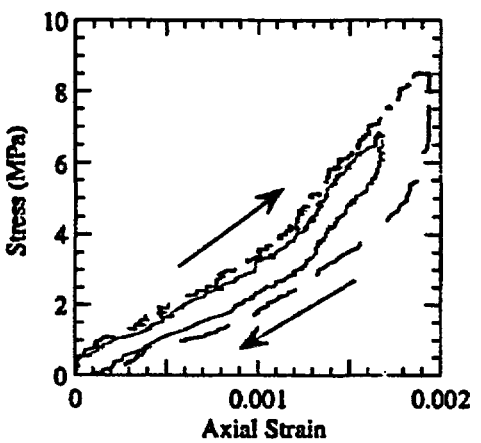

Figure 4-6. Stress-strain behavior for repeated loading of a single fracture in a 0.5m block of Topopah Spring tuff. Adapted from Blair and Berge, 1996.

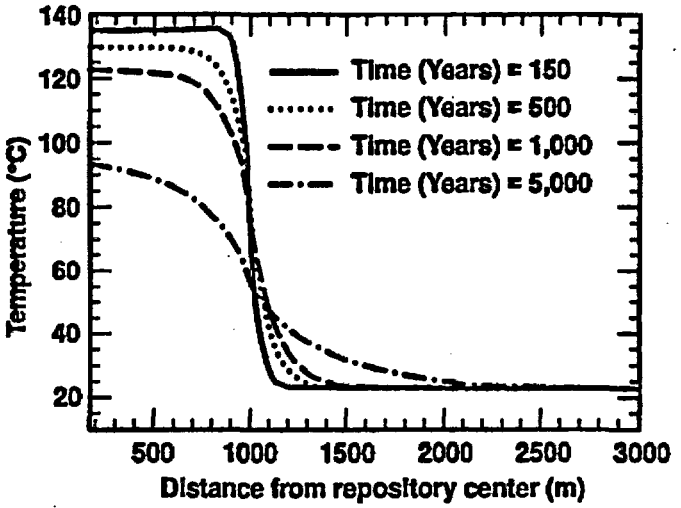

Figure 4-7. Temperature profile predicted in the rock forming the repository at 150, 500, 1000, and 5000 yrs after emplacement of waste at a thermal density of 83.4 MTU per acre.

Table 4-1. Physical and thermal properties of rock in the Topopah Spring welded unit, lithophysae-poor layer (TSw2).

Parameter	Value
Physical Properties	
Porosity (%)	12 ± 4a
Grain density (g/cm^3)	2.55 ± 0.03a
Bulk density at in situ saturation (g/cm^3)	2.30 ± 0.09a
Dry bulk density (g/cm^3)	2.22 ± 0.10a
Thermal Properties	
Dry matrix thermal conductivity (W/mK)	2.51 ± 0.17[b]
Saturated matrix thermal conductivity (W/mK)	—
Dry in situ thermal conductivity (W/mK)	2.1 ± 0.2[b]
Saturated in situ thermal conductivity (W/mK)	2.1 ± 0.2[b,c]

a DOE (1994)
b Nimick (1990)
c 0.65 ± 0.19 in situ saturation with lithophysal cavities and fractures assumed dry.

Table 4-2. Coefficients of linear thermal expansion (10^{-6}/°C) for Topopah Spring welded unit, lithophysae-poor layer (TSw2) during heating.

	Temperature Range (°C)											
	25–50°		50–100°		100–150°		150–200°		200–250°		250–300°		
Type	$\bar{\alpha}$	s	$\bar{\alpha}$	s	$\bar{\alpha}$	s	$\bar{\alpha}$	s	$\bar{\alpha}$	s	$\bar{\alpha}$	s	n	s
Intact rock	9.1	1.3	8.2	0.8	6.8	0.5	9.7 —	1	—	—	—	—	9	
Very near field	5.4	2.2	8.0	1.5	9.8	1.7	17.0 11.6	12	25.0 15.7	11	35.6 10.8	7	12	

$\bar{\alpha}$ = mean coefficient of linear thermal expansion
s = standard deviation of the sample group
n = number of samples analyzed

Table 4-3. Values of rock-mass thermal capacitance for Topopah Spring welded unit, lithophysae-poor layer (TSw2) at selected temperatures (DOE, 1994).

Temperature (°C)	Thermal capacitance (J/cm3K)
25	2.0324
50	2.1280
94	2.2638
95	10.7683
105	10.4690
114	10.1984
115	2.0065
155	2.1114
195	2.1912
235	2.2692
275	2.3410

Table 4-4. Mechanical properties of intact rock for unit TSw2 (DOE, 1994).

Mechanical property	Value
Unconfined compressive strength (MPa)	155 ± 59
Young's modulus (GPa)	32.7 ± 4.6
Poisson's ratio	
USW G-1, USW GU-3	0.22 ± 0.03
USW G-4	0.30 ± 0.05
Cohesion (MPa)	
USW G-2	18.3 ± 5.2
UE-25a#1, USW G-4, USW GU-3	37.8 ± 12.4
Angle of internal friction	
USW G-2	19.7° ± 5.2°
UE-25a#1, USW G-4, USW GU-3	36.5° ± 9.0°

Table 4-5. Values and ranges of principal stresses in the potential repository horizon at Yucca Mountain (Stock et al., 1984, 1985).

Parameter	Average value[a]	Range
Maximum principal stress (vertical)	7.0 MPa (1015 psi)	5.0 to 10.0
Ratio of minimum horizontal stress to vertical stress	0.5	0.3 to 0. 8
Ratio of maximum horizontal stress to vertical stress	0.6	0.3 to 1.0
Bearing of minimum horizontal stress	N57°W	N50°W to N65°W
Bearing of maximum horizontal stress	N32°E	N25°E to N40°E

[a] Average value for a depth of about 0.3 km (1000 ft).

Table 4-6. Corrected linear fracture frequency (m^{-1}) the Topopah Spring welded unit, lithophysae-poor layer (TSw2) at Yucca Mountain (Lin, 1993a).

	0 –10°	10– 20°	20– 30°	30– 40°	40– 50°	50– 60°	60– 70°	70– 80°	80– 90°
Upper range	0. 50	0.6 0	0.4 6	0.3 5	0.3 5	0.4 4	0.8 9	5.9 2	24.0 7
Mean	0. 25	0.2 9	0.2 5	0.2 2	0.2 3	0.2 4	0.5 6	2.5 1	11.2 8
Lower bound	0. 05	0.0 5	0.0 7	0.0 5	0.0 5	0.0 6	0.1 9	0.8 1	2.99

Table 4-7. Comparison of Rock Mass Strength Estimates to Intact Strength Data for Topopah Spring welded unit, lithophysae-poor layer (TSw2), adapted from Brechtel (1995).

Estimated Rock Mass Strength (MPa)	Intact Strength (MPa)	Intact Standard Deviation (MPa)	Ratio of Rock Mass to Intact Strength (%)	Rock Mass Elastic Modulus (GPa)	Rock Mass Poisson's Ratio
18.8	178.5	78.3	10.6	23.51	0.21

All values were computed using Hardy and Bauer (1991) classification 5 which is designed to include 90% of the rock in a particular unit.

Table 4-8. Recommended motions for the design-basis UNE (Subramanian et al., 1990).

Component	Median predicted value	Design-basis UNE values [95% nonexceedance level (1.65 σ)]
Vertical acceleration (g)	0.05	0.2
Radial acceleration (g)	0.03	0.1
Transverse acceleration (g)	0.03	0.1
Vertical velocity (cm/s)	4	9
Radial velocity (cm/s)	4	12
Transverse velocity (cm/s)	3	12
Vertical displacement (cm)	1	2
Radial displacement (cm)	1	3
Transverse displacement (cm)	1	4

Contents

Chapter 5.0 Radiation Effects

Richard A. Van Konynenburg

When the previous report version was being written, we considered waste packages with relatively thin-walled containers. The gamma-ray dose rates outside such packages would be high enough that observable radiation–chemical effects would be produced in the near field, so a detailed discussion of such effects was presented. Since that time, a new waste package design philosophy has emerged. For this design, our objective is to make the waste package walls sufficiently thick, providing enough radiation shielding to reduce the dose rates to levels that will eliminate concerns about radiation–chemical effects on package corrosion (100 R/hr or less and uneventful). No experiments have been funded to determine the dose rate at which effects on corrosion are no longer observed, but based on the literature, it is probably an order of magnitude higher than 100 R/hr, although experiments would be required to confirm this. At such levels, it is likely that effects on important near-field geochemical parameters such as pH and Eh will also be minimal. Certainly, radiation effects will not extend beyond a few centimeters of rock or backfill. Therefore, no further discussion of radiolytic effects will be presented here. Refer to the PNFER (Wilder, 1993) for a discussion of the environmental effects that could occur if the radiation dose were many times higher than the current design allows.

5.1 Reference

Wilder, D. G. (1993), *Preliminary Near-Field Environment Report Volume II: Scientific Overview of Near-Field Environment and Phenomena,* Lawrence Livermore National Laboratory, Livermore, CA, UCRL-LR-107476.

Contents

Chapter 6.0 Introduced (Man-Made) Materials

Annemarie Meike

6.1 Materials Identification and Evaluation

The present appraisal of the potential effects of introduced materials on the chemistry and mineralogy of the post-emplacement environment is presented in three sections. The first section of this chapter seeks to identify potential inherent chemical reactions and uncertainties that are inherent in the pre-closure repository design.

The chemical significance of the materials and the chemical processes that involve them are influenced by temperature, degree of water saturation, fluid composition, and the ratio of material surface area to fluid volume. We expect heat to be generated by the waste packages and some water to enter the near-field environment, which will affect the character of the chemical and hydrological processes and the timing of their occurrence. These processes, which are part of the post-closure perturbation of the repository, are addressed in the second section.

The third section is a discussion of the status of modeling intended to predict the processes, their outcomes, and the timing of events discussed in section 6.5. Ultimately these models will be used in conjunction with geological and hydrological models to describe likely chemical and hydrological interactions among water, the host rock, the waste packages, introduced materials, and organisms. However, even in the absence of such sophisticated modeling capability, an iterative exchange between the identification and evaluation of materials, computer modeling, and performance assessment can positively influence design decisions.

6.1.1 Original Post-Construction Conditions

The original as-built design has inherent chemical reactions which become important parameters for predicting the chemical environment of a waste package (WP). A broad spectrum of materials and organisms may be introduced into a radioactive-waste repository as a result of its construction and operation. More than 260 items used in a mine construction setting (the Exploratory Shaft Facility) were inventoried by West (1988), together with the known chemical effects of those materials at 25°C. A further discussion of materials that could be located in the near-field

environment and some potential chemical consequences has been presented in Rev. 0 of the Near Field Environment Report. However, it is not sufficient to simply identify materials and their chemical effects in isolation. The chemical impact of a material depends upon its context: its concentration, distribution, reaction rates and products, and other materials with which it is in contact or in close proximity. In addition, the heterogeneous distribution of materials will create pH and chemical concentration gradients that may in themselves drive chemical reactions. The examination and comparison of these materials assemblages as chemical systems that influence water chemistry and hydrology will most effectively support design decisions. In order to develop a useful system of comparison and decision making, we identify materials assemblages, or collections of materials that represent the various options that are available to perform a specific function (e.g., transportation, mucking, excavation, and stabilization). The materials assemblages are based on observations drawn from the construction of the Exploratory Studies Facility (ESF).

In this chapter we will need to depart from the terminology of the Waste Isolation Evaluations (WIE) in which it is recognized that the terms "permanent," "non-permanent," and "temporary" are used for materials disbursement in a specific manner. For materials disbursement purposes "temporary" and "non-permanent" refer to items that are removed prior to operation of a potential repository. "Permanent" refers to materials that are used at the site during the operations period, but which may be removed at closure of the potential repository. The WIE therefore uses the words "committed" and "non-committed," in which "non-committed" refers to substances are only those which are not being purposely introduced into the environment and for which reasonable assurance exists that the bulk of the substance would be removed at closure and "committed" refers to substances that are expected to be retained in the environment after closure. Because all of these terms have been applied in such a way as to imply intent, none of them are applicable to the present study. The purpose of the present study is to identify materials that may be introduced into a repository setting, and to determine the longevity of the potential chemical impact, part of which depends on the residence time of the substance. Other factors include concentration, degradation rate and environmental factors. We will use different terminology to underscore our purpose, which is to discover the residence time from actual usage data rather than to record the original intent. For our purpose we will use the terms "short-residence" and "extended-residence."

At present, although the Advanced Conceptual Design (ACD) for the potential Yucca Mountain Repository has been released, many aspects of drift engineering that

are required to carry out that design are not complete. Some materials such as metals, bonding agents, and concrete may serve as active parts of the designed engineered barrier. Other materials that are introduced to serve other purposes, including surveillance (thermocouples, gauges), construction and operation (drilling rigs, roadbeds, exhaust fumes, chemical toilets, concrete, grout, rebar), and lubrication (petroleum-based products, rope dressing) may not be removed because they have either become inaccessible or have not been identified as items to be removed. In normal mining operations extended residence materials also include waste material and spills. The introduced materials will exist in gas, liquid, and solid phases, as inorganic and organic compounds, and in various reactive states. Some materials, such as concrete, may be present in large quantities. As of this writing, precast concrete is being considered as a major part of the non-removable mechanical support system as well as invert material.

Although this lack of information directly affects our present ability to predict the chemistry of the near-field environment, we have the potential to provide input to those engineering decisions that may increase the confidence of future predictions by examining and assessing materials that have a high probability of being used in a repository setting.

6.1.1.1 Evaluation of Materials from ESF Construction

We have monitored excavation practices at the Exploratory Studies Facility (ESF) assuming that the construction methods used at the ESF represent a baseline for standard construction activities in a repository setting. Based on an examination of ESF construction techniques, we have concluded that detailed relational information is key to obtaining good estimates of construction material usage and, thus, our ability to model drift-scale chemical, hydrological and mechanical processes. Our purpose has been to obtain relational information and methods for estimating materials usage during the construction of a proposed repository at Yucca Mountain. Work in this area was initiated in December 1994 and halted in September 1995. We have attempted to determine the extent to which actual materials usage during construction and operation of an actual repository may be known or predicted, in order to more tightly constrain bounding conditions for the chemical impact of introduced materials in the near-field environment.

Materials used. Our expectation and that of many contacts from whom we requested information was that much of the materials usage information should be archived and readily available from the Tracers, Fluids and Materials (TFM) database.

However, these data were not readily available (Meike and Spragge, 1995) as of September 1995. Inadequacies exist in the areas of obtaining, archiving and retrieving data. We understand that, partly because of our needs in this area, some of these inadequacies are presently being addressed.

More specific compositional information will be needed to support the needs of drift-scale modeling. However, in the absence of that information, we have begun to identify and quantify materials usage, and to recognize patterns of usage and deviations from those patterns, in order to build estimation methods and bounding parameters for the usage of various materials. In this report we identify and demonstrate important factors that affect the patterns of usage and, if monitored, will ultimately lead to more accurate predictive capabilities include geology, construction function, regulations, and procedural developments. For example, the pattern of variation between estimated and as-built materials is a function of structural and stratigraphic geological factors. The following observations have been made about materials usage and the relationship of these materials to materials called out in a design plan. In our description of materials usage we will make these important distinctions explicit.

Clearly, extended residence materials will have chemical effects, some of which may significantly impact the post-closure chemistry. What may not be so obvious is that extended residence materials include not only those materials that are explicitly named in a repository design, but also the unspecified and necessary associated materials. For example, a repository design concept that calls for precast invert sections does not necessarily explicitly include the polymer gasket that appears between many of the invert sections in the ESF. Similarly, excelsior, pine 4x4's (cribbing) and other cellulose materials have been placed in open fractures and behind steel sets for stabilization purposes and will probably remain in place permanently. Our documentation of the use of these materials and their functional relationships is well underway, although actual quantities are still to be retrieved from the TFM database when that becomes a possibility. Another category of extended residence, non-explicit materials is spills. Although major efforts have been taken to minimize the accidental introduction of material by reducing the occurrence of spills, cleaning them up when they occur, and reporting them, it is important to quantify that minimum. This includes a thorough documentation of reporting limits (e.g., how much diesel fuel can be spilled before a report must be filed?) and relational information (e.g., hydraulic oil is usually spilled near the TBM), as well as reported amounts.

Even "non-permanent" materials can affect the post-closure chemical environment. Short residence materials may leave a residue of significant chemical or hydrological importance, even after they have been removed. For example, a conveyor belt is used for mucking operations in the ESF. It appears to be depositing a fine layer of black organic matter on the left drift wall. More obvious are the talus piles of conveyer belt shreds and rock powder that pile up at the junction between conveyor segments. With respect to such short-residence materials, we document residual effects as a function of quantity, usage, and duration of emplacement.

We have aimed to recognize useful classification schemes and significant categories of materials for the purpose of supporting design decisions. A useful and elucidative category for discussion is the materials assemblage that represent functional units. Some of these functional units (e.g., for mechanical stabilization: steel sets or fibercrete) are substitutional.

There is also a certain amount of flexibility that is an inherent and necessary part of any construction design. For example, it is not possible to predict precisely how many rockbolts will be required to stabilize a particular section of drift. This depends on information that is acquired as the drift is excavated and must be determined to some extent by the contractor.

6.1.1.2 Uncertainty and Variability in Materials Used

The ability to translate from repository design concepts to the realities of the as-built drift, which may be the greatest source of uncertainty in estimating materials usage, has developed substantially from observations of ESF construction. We have aimed to recognize useful methods of quantification, whether they are threshold values, mean values and deviations, or degrees of uncertainty.

For data that can be quantified, we wish to obtain materials usage data at a resolution significant to the Yucca Mountain Project, which can be determined through sensitivity tests using chemical modeling codes. This degree of resolution is expected to vary depending on the material.

For data that cannot be estimated, such as unpredictable events or the results of irregular activities, we wish to determine first the significance of the information using sensitivity analyses and secondly whether bounding or statistical analyses can be used to bracket or otherwise characterize the data. This type of determination is critical to performance assessment evaluations.

Clearly, adequate data is not yet available to be used as described above. However, these goals are reflected in the manner in which the data is presented below.

6.1.1.3 Materials explicitly named in construction drawings

Metals

Steel Sets. Steel set and lagging installation documentation is in hand for the ESF North ramp from the start of TBM operation at tunnel segment 00+58 through section 06+00, with tunnel sections divided into and reported by the following 200 m tunnel increments:

00+58 to 02+00

02+00 to 04+00

04+00 to 06+00

Within these 200-m sections of tunnel the as-built quantities of the following construction items are documented:

Steel Set, five-piece ring (reference drawing BABEAB000-01717-2100-41101-03):

1. Top component, MK#1A
2. Bottom components, MK#1B (two parts per set)
3. Side components, MK#1C (two parts per set)
4. Steel set, shims and Dutchmen (two parts per set)
5. Steel set shims (reference drawing BABEAB000-01717-210041102-03)
6. Steel lagging, C8 x 11.5# channel for steel sets ~4 ft in length
7. Tie rods for steel sets (reference drawing BABEAB000-01717-2100-41102-03)

All components are of steel (see Table 6-1). Specific tunnel locations (other than the 200 m range cited) are not supplied. The lengths of tie rods used are not specified despite the notation of two different lengths on the drawing (see Table 6-2). According to a cover letter sent by the Kiewit/PB project manager, W. Wightman, these were the first of many actual-use TFM reports planned for input to the TFM database by early September. It was the only report available as of November 1995.

Rockbolts. An investigation of rockbolt usage in the ESF has shown that far more rockbolts are used in some sections of drift than are specified in the drawings. This is understandable and necessary because ground support depends on the type of rock encountered and must be left to the discretion of the construction company. However, a few useful observations that can be made. First, the number of rockbolts used is dependent on rock type, and secondly the rockbolt distributions referenced on engineering drawings can be considered minimum (non-conservative) values.

Rails. It is evident that rails are used presently for hauling personnel and materials in the ESF. Ultimately, rails may be used for the emplacement of waste packages. It is possible that these rails will not be removed.

Concrete

Fibercrete™. Fibercrete™ is composed of ordinary Portland cement (OPC) grout, sand, and short, flat Flex-Ten steel fibers combined in a slurry that has a viscosity low enough to be extruded at high velocity through hoses. It is used primarily for drift consolidation, often in combination with wire mesh and after rockbolts have been emplaced. Table 6-3(a–c) shows the composition of the cementitious material in the Fibercrete™. The source of the sand is specified in the MSDS. Although this provides tracking information, the mineralogy can vary considerably. The MSDS composition lists quartz, calcite, clinozoisite, and feldspars (albite and anorthite), as identified by x-ray diffraction (XRD). Gypsum, phlogopite, and bassanite may also be present.

Rockbolt Grout. The grout composition for the Williams™ rockbolts is stipulated by a Transmittal of Shop Drawings, Equipment Data, Materials Samples, or Manufacturer's Certificates of Compliance (SDT) (Form #AP-5.26) dated 16 January 1995. It stipulates that the grout is type E-1 (K) and specifies the brand Wil-X-Cement™ thixotropic grout. A water/cement ratio (w/c) of 0.4 by weight is stipulated, not to exceed 0.5. It should be noted, however, for the purpose of establishing water introduced into the repository environment, that the mixing of concrete is not exact. According to the SDT, the actual amount of water is left to the operator's discretion, as it needs to be. The operator must assure that w/c does not exceed 0.5, even though 5/6 of the total amount of water to be used is added to the tank before the grout is added.

Invert. The composition of grout and aggregate for the precast invert have not yet been obtained. However, it is clear that each invert segment is reinforced with a rebar cage. Figure 6-1 illustrates the shape of an individual segment.

6.1.1.4 Materials Implicit in Construction and Operation

Fluid Reports and Consumables. Reports of water usage and equipment fluid consumption have been requested. The inventory of all water documented as used in the ESF will be complete upon the receipt of this information. As of November 1995 informal records of materials which are logged into the Exploratory Studies Facility and assumed consumed within a certain segment of tunnel had not been provided. These "records" have been described as having been made without standard documentation. Examples of these materials are paints and sealers (D. Wayman, personal comm.). However, to this date no records separate from the provided as-builts have been obtained.

A separate, but similar issue has to do with materials that may be used in much larger quantities. These materials included cribbing (metal and wood) and excelsior,

which, according to LANL's weekly ESF reports, were used when poor ground conditions rendered the tunnel boring machine (TBM) gripping mechanisms inadequate. LANL's weekly reports cite use of wood cribbing, fibercrete, shotcrete, sand, and a cement-water slurry. For the same time period that these LANL's weekly reports cover, use of these materials is not documented in the Kiewit/PB TFM reports. A list of materials that were used in construction of the tunnel, but were missing from any of the materials records were requested (from D. Wayman). The response indicated a belief that no materials were missing from the records (Meike and Spragge, 1995). We suspect that some of the missing materials may be listed as "consumed." This category of materials is misleading if it includes both items that are consumed and removed (e.g., compressed air, packaging materials), as well as items that remain as a permanent part of the ESF structure (e.g., cribbing, excelsior, sand, and fibercrete).

The TFM data record sheets of the as-built starter tunnel were obtained from REECO. Quantities are given of each material used, and annotations as to whether the materials were considered permanently or temporarily emplaced are included. We noted that materials were listed (and archived into the TFM database) by brand name, which will render retrieval of this information very time-consuming, if not impossible. We suggest that a classification system such as the one already used for construction specifications (and thus easily accessible to the construction engineer who must fill out the TFM data record) would also be useful for retrieval of the information from the TFM database and should be part of the Determination of Importance Evaluation (DIE) record requirement. LANL continues to provide, on a weekly basis, information detailing the position of the tunnel face, the advancement of the tunnel boring machine, and the total quantity of water introduced to the tunnel from holding tanks.

Water. Water brought into the ESF from the holding tanks is measured. It is used for dust control, cleanup, and excavation. The weekly ESF TCO report provides information on the amount of actual water use per week and the cumulative amount of water used. However, the term "water use" is actually employed to specify the quantity of water transported into the tunnel. These reports do not specify how much water was removed from the ESF, e.g., by evaporation or sorbed to rock and removed during the mucking operation. Thus, the water value represents a maximum value of water introduced from the holding tanks. Although this is not an issue at ambient temperature, water introduced and stored in solid form (e.g., cement) will be available to the drift environment upon heating and dehydration. Thus, although it is an important component, an estimate of water usage based on the holding tank usage does

not necessarily represent a complete or "conservative" estimate of the introduced water budget in a post-construction repository setting.

We present the available water usage data in order to illustrate a number of the data evaluation methods that will be used. In the future it should be possible to further constrain estimates of the amount of water that remains on the site in both fluid forms by obtaining better information on water retrieval.

The water usage limit specified in the DIE of no more than 7.4 cubic meters of water per linear meter of tunnel excavated has not been exceeded (Fig. 6-2). An average of the total amount of water used to date is 2.47 kL/m. Figure 6-3 illustrates a more detailed week-by-week analysis of water usage. Figure 6-3(a) shows that to a first approximation, water usage mirrors excavation progress. From Fig. 6-3(b) it is clear that normal weekly amounts of water usage of between 2 and 4 kL/m, which is by and large a function of excavation progress, are punctuated by events of large or excess water usage. Therefore, rather than averaging total water usage, we aim to establish an average water usage per meter (of roughly between 2 and 5 kL/m) that can be modified by a statistical distribution of excess water events. The character of the statistical distribution will be determined by further monitoring of water usage in the ESF. The next step is to relate these events to known functions in order to predict water usage more accurately.

Spills. Kiewit/PB has maintained records of spills/releases in the method of the Kiewit/PB Spill Response Plan in accordance with the requirements of YAP-2.8Q. They include:

- Date and time of the spill/release
- Type of material
- Source of spill/release
- Tunnel location
- Quantity
- Estimate of unrecovered quantity
- Time at completion of clean-up
- Whether follow-up cleaning was required

Records of spills for the period 10-December-94 through 09-August-95 were submitted to the TDB for input to the TFM database. Copies of the records signed by the walker/shift superintendent, environmental supervisor, and M&O A/E site representative have been obtained for the period from 10-December-94 through April-14-95. During this period, eleven underground spills/releases were reported (Table 6-4). All were fluid spills, described as hydraulic oil or hydraulic fluid with the

exception of one described as TBM lube oil (See Meike and Spragge, 1995). No specifics as to type or manufacturer were provided by these reports. However, efforts to retrieve these specifics from Kiewit/PB (through D. Wayman) have yielded some material safety data sheets (MSDS) and chemical compositions of the fluids.

Another thirteen spills/releases were recorded from 6-May-95 through 9-August 95 (Table 6-5). However, the only information available to date regarding these spills is the spill number (SRP #) of each and the dates the spills occurred. All other information has been reported to the TFM administrator for entry in the TFM database. Because the spill number (SRP #) of 6-May-95 is consecutive with the SRP of the last April spill reported, it is assumed that no spills were recorded between these two reports.

Cellulose. The use of excelsior for ground stabilization behind steel sets has been observed in the ESF and noted in LANL's TCO report. The use of wood 4x4's (pine or fir) has been similarly noted. These materials, although extended residence by the nature of the way that they are used, have either not been recorded or are recorded with consumables and thus are indistinguishable from items that may be removed (see the discussion above). This category of materials also includes trash that may be incorporated into invert fill material.

Polymers. Polymers are composed of long, chain-like molecules which are formed by the bonding together of relatively small molecular subunits (monomers). Although proteins (i.e., wool and silk), carbohydrates (i.e., starch and cellulose), and condensation polymers (i.e., shellac and "glue"), polynucleotides (DNA), and cellulose are also polymers, the focus here is on the synthetic polymers which have been created over the past 60 years whose many useful properties have lead to incorporation into everyday construction operation. The matter of identification is an issue because there are many "hidden" sources of polymers. For example, almost all paper products contain polymers such as phenol formaldehyde and polyvinyl alcohol. Furthermore, most adhesives are polymers, and polymers are often added to drilling water to increase laminar flow. Given the combination of reporting issues discussed above, and the inexplicit nature in which polymers can be used, our initial aim with respect to polymers has been to review the types of polymers that may be used in a construction setting independent of the ESF context. Below we first present some of the characteristics that are used to evaluate polymers, and then we review the relevant polymer classes. Some comments are made on the relevance of the polymers to the ESF and to a potential radioactive-waste repository. The review is useful in discovering polymers and their usages in the ESF as well as pointing out important distinctions that can be made. Some thermal and degradation mechanisms are mentioned. In section

6.2.1.4 the discussion of relevant degradation mechanisms is continued, as well as the potential significance of these characteristics to the design of a radioactive-waste repository. Concepts fundamental to polymer characterization that are significant to predicting their long-term degradation are outlined in Appendix A.

Relevant Polymers. *Epoxy resin* systems are made up of resin and hardener. There are literally hundreds of epoxies with different chemical structures dependent upon the resin and hardener used. Epoxy is classified as a thermosetting resin and cures from internally generated heat. When the resin and hardener are mixed together, a chemical reaction occurs which causes hardening. Because epoxy easily reacts, chain extension and crosslinking can occur without the elimination of a small molecule such as water. Thus epoxy does not shrink as much as many other thermosets. Curing, which can be carried out either through the epoxy or hydroxyl groups, gives epoxy its crosslinked character. Either catalytic systems or polyfunctional crosslinking agents may be used to link the epoxy resin molecules together. Amines, acids, anhydrides, and mercaptans all may be used as curing agents.

The range of epoxy resin applications becomes apparent when one examines its properties. The high reactivity of the three membered epoxy ring leads to many unique and desirable properties. First, epoxy resins have high chemical and corrosion resistance. This leads to many protective coating applications. Epoxies are heat resistant, with a T_m of approximately 260°C (Brandup and Immergut, 1975). Low shrinkage, high flexibility, high strength and high impact resistance lend epoxy to many mechanical uses. Epoxy also has good electrical properties, is waterproof, and is lightweight. The most well known property of epoxy, however, is its great adhesion. Epoxies are used to bond metals to glass and plastics and even concrete to concrete. In fact, epoxy is often significantly stronger than the material it is bonding. Steel rebar is coated with epoxy to prevent corrosion. However, the long-term effectiveness is questionable, especially if the coating is not uniform. Corrosion can occur at the interface between the epoxy coat and cold-rolled and galvanized steel (Dickie et al.,1990). Another potential use of epoxy at Yucca Mountain will be as rockbolt grout.

Neoprene rubber is a chloroprene polymer and was the first commercially successful synthetic elastomer. It is a thermoset which is crosslinked using the vulcanization process. Vulcanization involves crosslinking of the highly reactive allylic chlorine. The accelerator is usually zinc oxide or magnesium oxide (however, other metal oxides may be used) to create a sulfide crosslink. There are two types of neoprene: dry neoprene and neoprene lattices, each of which may be further classified as general-purpose or specialty types. Latex rubbers are examples of lattice neoprenes. General purpose

neoprenes include those that are used for molding and other product applications. Specialty types, used for adhesives and sealants, tend to crystallize much faster.

Neoprene rubber tubing, probably dry neoprene, has been used in the ESF. It is likely that it contains antioxidants, fillers and plasticizer additives, because these are often present in neoprene rubber. Antioxidants are necessary since neoprene is quite susceptible to oxidation. Processing aids are added which lubricate and tackify. Examples of these are stearic acid, microcrystalline waxes, and low molecular-weight polyethylenes. Carbon black and mineral fillers are used to give more hardness and to increase abrasion and tear resistance. Hydrated calcium silicate and precipitated silicon dioxide fillers of fine particle size are added to neoprene vulcanizates for tensile strength and hot-tear and abrasion resistance (Mark et al., 1985). Inexpensive petroleum derivatives are used as plasticizers, to lower the T_g.

Polyamide is a condensation polymer made from dibasic acid and diamine derived from oil and natural gas. These polymers contain amide groups as part of their monomer unit. Nylon is the most prevalent polyamide used today, with nylon 6,6 being the most preferred due to its properties and manufacturing cost. Nylons are used primarily for fibers and engineering resins. Aromatic polyamides (Kevlar, nomax) exhibit especially good strength and temperature properties. *Nylon* was the first synthetic fiber forming polymer developed. It is strong, tough, lightweight, abrasion and puncture resistant, and resistant to chemicals. Nylon has a very low glass transition temperature of 50°C and degrades thermally to hydrocarbons and carboxyls at 265°C. Nylon is also quite hydrophilic relative to other synthetic fibers and water acts as a plasticizer for nylon. A completely dry nylon fiber will be quite brittle whereas a fiber which is in a humid environment will be more flexible. Nylon ropes have been used at the ESF. Thus, at least some of the possible nylon usage in the potential repository will be in fiber form. *Kevlar* falls into the category of liquid crystalline polymers and is considered a thermoplastic polymer. Kevlar is close to completely crystalline and, thus, is quite strong. The production of Kevlar requires very strong solvents to achieve the maximum liquid crystalline phase. The linear aromatic structure of kevlar yields more strength and high-temperature stability. Kevlar ropes are used in the ESF. Although kevlar has very good thermal stability relative to other polymers, it will degrade in a high-temperature environment. Long-term chemical effects are unknown.

Polybutadiene rubber is the main component of Liquid Nails caulk which is used at the ESF. Polybutadiene is a synthetic rubber which is thermoset via vulcanization. It has a long-chain molecular structure, which gives it toughness and chemical resistance. The structure of polybutadiene has long been of interest due to its symmetry and simplicity.

Its monomer, butadiene, is a highly reactive colorless gas which reacts with the characteristic of having conjugated double bonds. Butadiene reacts through a self condensation reaction to form the polymer. Dependent on length and conformation, the polymer has a melting temperature ranging from 2 to 156°C and a T_g below 0°C.

Polycarbonate (PC) is a thermoplastic of very high molecular weight. It is strong, rigid, transparent, non-toxic, and weather and impact resistant, though it tends to suffer from stress cracking. It has a high glass transition temperature of 135°C and melting temperatures up to 200°C. Since polycarbonate is used for many electrical applications, flame retardants are often added. There are two types of polycarbonate: aliphatic and aromatic. Of the two, aromatic is by far the most prevalent and also the most useful. Aromatic polycarbonates are prepared from a condensation reaction between bisphenols and carbonic acid derivatives. Plexiglas™ covers (e.g., for the ESF percolation test) are made of polycarbonate. It is likely that Plexiglas™ used during the construction of a repository can be removed and, in that case, polycarbonate will be of little or no concern.

Polyester is classified by carboxylate groups in the backbone of the polymer. They are produced by a condensation reaction of ethylene glycol and propylene glycol which are derived from petrochemicals. There are many different polyesters produced for many different chemicals and glycol derivatives, but terephthalate polyester (PET) products appear to be the dominant type used at the ESF. Polyester rope and rein-anchored bolt systems are used. The rope is a thermoplastic polyester which will soften at high temperatures before degrading. PET is produced from a reaction between a terphthalic acid and ethylene glycol. Impurities are then removed in water at elevated temperatures and pressure. Purity is especially important in PET manufacture since the final quality is affected by very small amounts of impurity. Because the intermolecular interactions in polyesters are relatively weak, small changes in structure lead to large differences in properties. PETs have melting temperatures as high as 270°C. The degree of branching of PET determines the crystallinity (less branching, more crystallinity) and thus the toughness and stability. Polyesters are also hydrophobic and oleophillic. Polyesters are useful as both thermosets and thermoplastics. If the resins are saturated, there are no free radicals in the molecular chain for crosslinking to take place, and therefore the material remains thermoplastic. Likewise, if the resins are unsaturated, there are free radicals and crosslinking can take place.

Polyethylene (PE) is a thermoplastic which is polymerized from the monomer ethylene, obtained from the cracking of petroleum or from natural gas. It was polymerized at high temperatures until the birth of the Ziegler-Natta catalyst, which

eliminated the need for high pressures. There are two primary types of polyethylene. High-density polyethylene (HDPE) is processed by low-pressure polymerization. It is tougher than low-density polyethylene (LDPE) and has better chemical and impact resistance. Low-density polyethylene is odorless and non-toxic. Polyethylene is tough, flexible and a good insulator. However, it is easily scratched, stress cracking is common and it has a low T_g (80 to 130°C). Its properties are affected by side branching. During thermal degradation, polyethylene breaks down to hydrocarbons. One use of polyethylene at Yucca Mountain is in the form of sand bags and tubing. Polyethylene is one of the most prevalent polymers and it is likely that it will also be present in other forms.

Polyisocyanate (PI) is manufactured by a condensation reaction of isocyanate monomers. Isocyanates are primarily used to manufacture polyurethanes. Isocyanates are made in the form of diisocyanates from amines. It is a highly reactive monomer and degrades from about 175°C. In addition, it is highly reactive with water. The polymerization of pure diisocyanate leads to polymers (called nylon-1 polymers) that have T_g ranging from 40 to 180°C. These temperatures are dependent upon the length of side chains; the longer the side chains, the less thermally stable. Polyisocyanate has been used above ground at the ESF in the form of foam sealant and synthetic enamel. In addition, it is possible that these products are actually polyurethanes which have been labeled polyisocyanates due to the prevalence of polyurethanes as foams and coatings.

Like polyethylene, *polypropylene (PP)* is an olefin made from carbon and hydrogen and is derived from petroleum. It is formed using the Ziegler-Natta catalyst (consisting of titanium and aluminum). It is a thermoplastic which degrades readily requiring the use of stabilizers. Polypropylene has high impact resistance and flex strength, is scratch resistant and hydrophobic. There is a strong correlation between average molecular weight and the properties of polypropylene. It is possible to have atactic, syndiotactic and isotactic forms, three different conformations, of polypropylene. The isotactic and syndiotactic forms are more readily packed and thus more crystalline than the atactic form. Higher crystallinity leads to a higher melting temperature and greater toughness. Polypropylene has been used in the form of rope and tubing at the ESF. In addition, since it is one of the most prevalent polymers, it may be present in the form of packaging.

Polystyrene (PS) is a thermoplastic. The styrene monomer is made from benzene and ethylene, both of which are petroleum feedstocks. Polystyrene is used for its high-frequency electrical insulation and its optical clarity. It is very brittle; this can be improved with orientation and the addition of plasticizers. It also has a low glass

transition temperature of 80 to 90°C. However, polystyrene has a relatively high melting point of 274°C (syndiotactic PS) (Ravinetti and Zini, 1992). Polystyrene "Styrofoam" insulation has been used at the ESF. In addition, polystyrene auto body filler and fiberglass resin will be used above ground. Because foam has more surface area, it is likely that the Styrofoam will degrade more quickly than a solid chunk of polystyrene.

Polytetrafluoroethylene (Teflon, or PTFE) was first discovered in 1938 by accident while scientists were attempting to produce a new type of Freon. Since then, it has been used for a wide variety of applications, most of which take advantage of its high-temperature stability (the highest of any non-aramid thermoplastic) and its low friction. The frictionless property is due to the strong bond between the fluorine and the carbon backbone, so strong that it repels other substances. Teflon's electrical properties are unchanged by temperature and frequency, lending teflon to radio and power cable applications.

Teflon is polymerized with a peroxide catalyst in the presence of water from a monomer which is a poisonous gas. The result is a polymer which is very inert, chemically resistant (there are no solvents for teflon) and self lubricating. Teflon coating called by the trademarked name Gortex serves as a waterproof coating on the roof of the Denver airport. Teflon will be used for tubes for the heater tests in the ESF. It has also been used as wire pulling lubricant and as lubricating spray. Although not used in large quantities at present, Teflon's applications continue to grow. Its high melting point (330°C) may lend it to more applications in a high-level radioactive-waste repository. If so, a major effort should be conducted to understand its biodegradation.

Polyurethane (PUR) is synthesized in a condensation reaction between isocyanate and a hydroxyl compound. Isocyanate is an ester of isocyanic acid, HNCO. A wide range of physical properties can be obtained due to flexibility in selection of the reacting hydroxyl compound. Although originally produced in the form of fibers competitive with nylon, the main products of polyurethane are a variety of crosslinked polymers foams, coatings, and elastomers. Other applications of polyurethanes are adhesives, sealants, binders, and mine reinforcements. The flammability of polyurethane is reduced with the addition of flame retardants.

No other foam-producing system compares with that of polyurethane. It is easy to produce at a reasonable cost. Flexible and rigid foams can both be produced using polyurethane because catalysts precisely control the balance between polymerization and expansion. Flexible foams are produced by simultaneous polymerization and expanding with carbon dioxide gas. Flexible foams are used mostly as protective and

cushioning materials. The production of rigid foams is similar to that of flexible foams except that expansion is achieved using a low boiling solvent. Rigid foams are used as thermal insulating materials. Although polyurethane has a tendency to burn, this is lessened by the addition of flame retardants and the bulky foam structure lends itself to good insulation properties.

Polyurethane coatings are quite hard yet are flexible. They are also resistant to abrasion, chemicals and solvents. Finally, polyurethane coatings have high light stability and weatherability.

Polyurethane elastomers may be considered block copolymers consisting of alternating polyurethane and polyol segments. Primary or secondary amines, polyester and polyether are all polyol segments which may be used. Some of the main components of polyurethane elastomers are polyester and polyether diols, diisocyantes and chain extenders. Although different polyurethane elastomers possess different properties, they usually have wonderful tear, abrasion, impact and wear resistance as well as resistance to hydrocarbon and aromatic oils.

Cast elastomers are produced from liquid starting materials which differentiates them from other natural and synthetic rubbers. Examples of cast elastomer products are skateboard wheels and O-rings. Thermoplastic elastomers are processed as thermoplastics and hence can be used for various purposes. Examples of thermoplastic elastomer products are adhesives, hose lines and films for laminating. Millable polyurethane gums are used in synthetic rubber application such as machine parts.

Reaction injection molding is a process in which a mixture of two or more reactive low-viscosity materials is injected into a mold where it polymerizes. This process yields crosslinked, network structures. The product is a solid skin over a low-density microcellular core (foam structure) in a single operation. These structural foams use the smooth hard skins as a source of impact strength, heat-distortion, temperature and combustion resistance. An example of a use for reaction injection molding is in the production of automotive body panels. In this case, the car body would be durable yet lightweight. At Yucca Mountain, polyurethane is used for insulation purposes, probably as a foam.

Polyvinyl Chloride (PVC) is one of the oldest and most widely used synthetic polymers. In the past, the vinyl monomer was formed by a reaction between hydrochloric acid (HCl) and acetylene, which is derived from calcium carbide. More recently, however, PVC has been formed from ethylene, which is cheaper than acetylene (Nass and Heiberger, 1986). PVC is a thermoplastic which is used in rigid, non-plasticized form, and flexible, plasticized form. Although the chemical structure of

PVC appears to be quite stable, there are many deviations from the ideal structure. Structural irregularities result from polymerization defects such as branching and double bonds and from oxygenated groups such as carbonyls and peroxide groups. Thus, the commercial success of PVC is dependent on stabilizers. PVC has a glass transition temperature of about 80°C and easily degrades to HCl without stabilizers. In addition, it has very poor chemical resistance. Thus, almost all PVC products contain a significant amount of additives, which can vary their properties greatly. Polyvinyl chloride is widely used in the ESF as cable sheath, cement for pipes, cement primer, conduit, containers, hose piping, portable toilets, sheeting and tubing. Because of its potential acidic degradation products, PVC should be either not used or should be removed from areas of drift excavation in which local acidity is a significant issue.

Silicone is derived from silica or quartz and can have diverse properties dependent upon the length of chain and organic groups, but all silicones are based on a backbone of alternating oxygen (O) and silicon (Si) atoms. Silicones have outstanding resistance to aging and weathering, good thermal stability (up to about 315° C), water repellency, and toughness. In addition, they are inert and frictionless. The first step of production of silicones involves the conversion of silica to silicone in an electric arc furnace. The silicon is then converted to methylchlorosilanes by a direct process reaction with methyl chloride in the presence of copper as a catalyst (Lynch, 1978).

This product then reacts with water to form siloxane monomers, dimers and trimers, which continue to react until termination is reached. The result is a siloxane polymer. Silicone rubber is the crosslinked form of this polymer. At Yucca Mountain, silicone rubber is used as caulk, desiccant and lubricating spray. The thermal degradation products of silicone are low-molecular-weight cyclic oligomers, which are quite inert (Brandup and Immergut, 1975). Thus, the primary concern will be failure of the products used in the repository.

6.1.2 Evaluation of Materials by Function

It is evident that the blueprints show a minimum of materials that are actually used in construction. The following evaluation is intended to categorize standard suites of materials by construction function and, if more than one construction option exists for a particular function, to discriminate suites of materials by construction option. The presentation below represents the state of the work, which was in progress until November 1995. We do not present information on the following functions: utility piping and ventilation, power distribution, or communication and instrumentation.

6.1.2.1 Transportation

Invert. The exact number of invert segments placed in the tunnel has been provided. The tunnel has been divided into the same sections as for the steel sets. All inverts are precast prior to emplacement and are of concrete composition. Rail placement and invert segment plan and sections and detail are shown in reference drawing BABFCCOOO-01717-2100-40178-02, and BABFCCOOO-01717-2100-40179-02. The use of hardware, including lifting anchors, rebar, and strap anchors, is evident from the drawings. A polyethylene foam fill material is explicitly mentioned for placement between invert sections and between invert and the drift wall. Fill material cannot be tracked in this way unless it is on structural drawing 41099. It is not included in the inventory of inverts and is unaccounted for. Further chemical and physical analysis should be conducted on this fill/invert area, given that in an emplacement drift, with the appropriate design, the invert may constitute an engineered barrier.

Crushed rock, an option that has been discussed for emplacement drifts, has not been tried in the ESF.

Rail system. Documentation of the materials used in the rail system had not been initiated when this work was halted. However, it is clear that the system involves the rail, anchors, ceramic inserts and rubber insulation. These aspects should be clarified in the future because they impact the ability to predict microbiology and chemistry in regions close to the waste package.

Diesel Exhaust and Fuel. One of the early concerns of the Yucca Mountain Project, in the area of materials usage, was diesel fuel and its hydrous pyrolysis products. Diesel-powered vehicles are standard and economical for hauling activities, and if they were used, spilled diesel fuel and exhaust products might become part of the post-closure repository environment.

Electric Rail. Use of electrically powered vehicles is an option that has been considered for the ESF and may be considered again for use in a potential repository at Yucca Mountain. The residual material that may be left behind by such a system could be examined by investigating the Bay Area Rapid Transit (BART) or other electric rail systems. Even a cursory examination of BART and other tunnels indicates that a carbon deposit is a likely result from the use of such a system. This and other aspects of environmental modification will need to be examined if electric rail is to be an option in a repository setting.

6.1.2.2 Stabilization

To a great extent the amount of stabilization that is required within a section of tunnel is unknown until that section is reached. However, accurate mapping of the construction materials and correlation with the ESF geologic assessment should allow us to predict materials usage in the repository more accurately than simply from blueprints.

Cribbing. In the ESF, in sections of drift where large fractures have been exposed, both wood and metal cribbing has been used for stabilization.

Steel sets. Steel sets have been used in areas of extreme rock instability, where rockbolts are insufficient. At times stabilization is required behind the steel sets. In the ESF this stabilization material has consisted of sand or excelsior (wood fiber).

Rockbolts. As mentioned above, rockbolts of a number of different lengths and designs are used in the ESF. The emplacement of some rockbolts require grout, while others require a rather large quantity of water (nine gallons per bolt). The number of rockbolts used in a given section of drift varies and is dependent on the stability of the rock and the other components of the stabilization system (Table 6-2). Rockbolts can be associated with wire mesh and with wire mesh and Fibercrete (refer to portal area of the ESF).

Pre-cast Concrete. Although it has not been used in the ESF, pre-cast concrete is presently being considered as a mechanical stabilization method in the context of a potential repository design. Presumably these pre-cast concrete sections will require a polymer material between the sections similar to the invert sections.

Fibercrete. Fibercrete has been used for stabilization in the portal area of the ESF (see the rockbolt discussion above).

6.1.2.3 Mucking, Dust Control and Ventilation

Conveyor system. Although it is believed that a conveyor system used for mucking during repository construction would be removed, it is clear from observation of the ESF conveyor system that the *operation* of the conveyor modifies the environment chemically and physically. The moving conveyor belt generates a lot of rock powder which settles on the walls and floor of the tunnel. This could affect drift-scale hydrological properties. In addition, due to the length of the mucking operation the conveyor is composed of segments. Each segment consists of a belt, which dumps its load on the next belt and so on until the excavated rock is removed from the drift. At the junction between segments, talus piles of rubble and shredded conveyor belt (see

polymer section) are evident. A very fine black deposit is also visible on the left drift wall (rib) throughout the tunnel.

Dust control. Given that the basis for the nuclear waste strategy is the minimization of water in contact with the waste packages, our goal is to minimize, to the extent possible, the amount of introduced water. Data is not available for water usage by function, so water usage is discussed below in terms of total amounts. In addition to the chemical issues, the physical modification of the environment should be acknowledged. Dust control (even pure water) will cause the heterogeneous dispersion of a coagulated rock powder, the long-term impact (hydrological and chemical) of which we have yet to understand. However, in view of the fact that for health reasons a dust suppressant must be used, and that pure water may not be the best option (due to the larger amounts needed in the absence of a surfactant), the present discussion is limited to the dust control products that were under consideration in 1995 and 1996 (see Table 6-6). The salient issues are outlined in memo LLYMP9603087.

The additives were evaluated based on the MSDS information provided for the products. Although the chemical information provided in most cases was not adequate, eight were found to contain hydrocarbons/polymers. From the perspective of test interference in the ESF, we were concerned about the introduction of compounds that might alter the baseline of chemical analyses, which had the potential of severely interfering with and rendering useless the planned Swipe Tests, which were intended to obtain sensitive isotope data of hydrocarbon compounds and air samples in the ESF. The dust control chemicals are especially invasive to those experiments due to the dispersed nature of their usage. If dust suppression is to be conducted in the ESF using these additives, an additional program will be required in order to discriminate between airborne diesel exhaust and vapors, and these dust suppression agents. These distinctions are critical to our ability to supply baseline information toward the understanding of potential ESF test interferences. No chemical information was provided for the last additive considered, Bio Cat 300-1, and therefore no determination can be made at this point. Based on these considerations we advised against the use of the additives that contained hydrocarbons and against Bio Cat 300-1 due to the lack of information. Given that Dustcon™ degrades rapidly, we would want to understand the chemical nature of the biodegradation products in order to make a complete assessment of test interference in the ESF.

Over the long term we are concerned about the formation of colloids and the alteration of the chemical composition of water. However, we can make some preliminary assessments. It is our understanding that tracers are introduced into the

water that is used for dust control. If this is accurate, then although the dust control compound may affect chemical analysis, at least the investigator will be alerted to that fact. In a gross sense the big distinction over the long term between Dustcon™ and the other products appears be pH, because the documentation provided cites the prevention of limestone and salt that otherwise build up at a number points in the dust control system. With the exception of pH, the chemical effects can be considered grossly of the same type at the concentrations under consideration.

Dustcon™ appears to need much less water (especially less than non-modified water) to reduce dust to the required level than the other products under consideration, even though the amount of additive used per volume of water appears to be less than the other products. This has two advantages: first, the dust control agent is minimized, thus limiting the impact on data collected from experiments conducted in the ESF, and secondly, the amount of water introduced into the ESF for the purpose of dust control is minimized. Similar arguments could be applied to the construction of a radioactive-waste repository.

6.1.2.4 Excavation

The tunnel boring machine (TBM) is electrically powered. However, its hydraulic system requires the use of petroleum products. These have been introduced into the tunnel through spillage during maintenance and equipment failure. As mentioned above, a policy is in place regarding the reporting and clean-up of spills. According to the policy, not every spill needs to be reported, but only that above a certain value. Because not every spill is recorded, the spills on record must be regarded as a minimum number. Therefore, in estimates of material usage, the uncertainty factor may be included to account for the spills that are thought to be below the reporting limit and therefore not recorded. Water usage accompanies the excavation operation through the actual excavation, dust control and clean-up of the "dance floor."

6.1.3 Tracers, Fluids and Materials Database: Retrieval of Information

Much of the initial information depends upon the retrieval of large amounts of data supposedly archived in the Tracers Fluids and Materials (TFM) database. Yucca Mountain Project YMP procedural documents identify explicit methods and channels through which this data should be retrievable. Our attempt to retrieve data that has been archived in the TFM database suggests that the large effort expended on developing procedures to collect and archive data is not reflected in the data that can be

obtained. At the time of the assessment, which ended in November 1995, searches have retrieved far more procedural documents than data. Since the assessment was conducted, the operation of the database and collection has been turned over to another group. In order to enhance the utility and retrievability of information we suggest that ANSI or other standard construction material reference numbers be used in addition to brand name. Our experiences suggest that since November 1995 some of these suggestions are being incorporated into the database. We look forward to an improved state of access to archived data and better communication between the construction team, DIE, TFM database and those that require the data, given that, as time progresses, both the quantity of data and the demand for it will increase. This data, once available, will be incorporated and interpreted in subsequent revisions of the NFER.

Routes of information retrieval (other than archival work) that have been explored include the first-hand study of the ESF and interviews with on-site construction staff. These options appear at first glance to be more time intensive than the retrieval of archived data. However, they promise to provide a more comprehensive understanding of materials usage that will ultimately be useful in extrapolating information from the ESF setting to the prediction of materials usage in a potential radioactive-waste repository.

6.1.3.1 GENISES

As should become apparent from the above review, tracers, fluids, and materials data in the form of TFM usage requests and estimates and reports of actual use of TFMs (also known as "as-builts") are a critical aspect of developing the capability to relate a repository design to a materials usage prediction. However, at present, such data remains virtually inaccessible from the YMP TFM database. The current state of the database is such that it is much less easily accessed than both status reports provided by and personal communication with the database administrator would lead one to believe. Currently, there are three databases of TFMs, as cited in the Tracers, Fluids, and Materials (TFM) Database Status Report for the Period April 1995–June 1995. The first consists of the original TFM data compiled by LANL and entered into a system provided by Computer Applications Group, Inc. The transfer of this data into the GENISES database is on hold according to the status report dated June 30, 1995. The second database was compiled and input by EG&G/EM. Because the data was submitted without standards on a variety of forms, the database will need to be retrofitted to the revised TFM system to facilitate retrieval of data. The third database conforms to the specifications of YAP-2.8Q. This database, according to the

aforementioned TFM status report, contains only data reported after May 8, 1995, the effective date of YAP-2.8Q. However, to quote the status report, "no new data have been provided under this procedure." To summarize, it seems that the only readily accessible TFM database contains no data.

The only other self-evident option for obtaining specifics of TFM usage and requests was to request it from the originator. That method resulted in limited amounts of information pertaining to the following construction categories being supplied by D. Wayman of Klewit/PB:

1. North ramp spill reports
2. North ramp steel sets
3. North ramp rail/segments

This information is reflected in the discussion of materials and materials usage in the previous sections.

6.1.4 Assessment of Materials Considered for Repository Construction

Progress in this area consists primarily of the initiation of modeling capabilities to assess the drift-scale heterogeneity of materials and their distribution, the quantities and location of materials and the chemical composition of some of the more critical materials. To this point, materials have been considered critical if they have the potential of being located in the emplacement drift and in fairly large quantities. This work is of fundamental importance to ability to respond to the needs of Performance Assessment, Repository Design and Waste Package Design Areas of the Yucca Mountain Project.

6.1.4.1 Heterogeneity

It is clear that the emplacement drifts will be both hydrologically and chemically heterogeneous. Given that the driving force behind many important chemical processes are chemical, thermal or other gradients, and that microbial activity is frequently most active in crevices, and that permeability variations in space will affect hydrological properties, attention to heterogeneity is very important. The drift modeling work described later in this report includes an assessment of the chosen software to identify interfaces and to manipulate the level of detail required by this inherent heterogeneity of the as-built system.

6.1.4.2 Materials

The potential significance of a material to the repository environment will be determined by its modification potential (chemical or hydrological), its quantity and its location. Given that some materials may be exposed to temperatures above the standard conditions to which we are accustomed and to a time frame outside of our experience (or even, for that matter, longer than the period of time that the material has been known, e.g., plastics), it is clear that once materials are identified, it may be necessary to conduct experiments or analyze historical analogs in order to understand their potential significance in this environment. The beginning of the materials identification and quantification work has been outlined above. This information is evaluated through the experimental and modeling activities discussed below. The drift-scale model has been chosen to be able to interface with existing hydrological, chemical and coupled codes to create three dimensional renderings of drift-scale processes through time.

6.1.4.3 Materials juxtapositions

Attention to the juxtaposition of materials is critical, not only to identify potential locations of microbial activity and possible microenvironments, but because it is highly likely that the effects of materials in contact at elevated temperatures may also be outside our standard experience. Identifying these juxtapositions is also a goal of the drift-scale modeling activities.

6.2 Post-Closure Chemical Processes That May Modify Predicted Geochemistry

Modifications of the natural environment due to construction of an underground repository would, in themselves, alter the natural chemistry, some aspects of which may be critical to the robustness of the waste package or to the chemistry of the fluid leaving the repository. However, once the materials are emplaced, in the absence of changing extrinsic properties, the chemical evolution of the repository would be fixed to a specific path and hypothetically predictable. The first section of this chapter on introduced materials described the chemical evolution that is brought about by the intrinsic nature of a repository design, and the initial steps that we have taken toward quantifying aspects of repository construction. The present section discusses the aging of repository materials in response to extrinsic conditions such as temperature, relative humidity and aqueous chemistry that will vary during the lifetime of the repository. The ultimate goal of this work is use a combination of post-closure chemical processes

and processes that are determined by repository design and construction to identify the resultant chemistries that are outside the envelope of possible natural chemistries.

The product phases of materials disintegration, biodegradation and corrosion may include oxides of metals, sulfides, chlorides, carbonates, and silicates, as well as organic compounds, alkali metals, and halogen elements. These materials have the potential to alter the pH, ionic strength, and composition of water that may be present at some time in the lifetime of the repository. In addition to aging, gamma radiation effects must be considered in the WP environment as discussed in Van Konynenburg (1986b). The chemical effects of gamma radiation on man-made materials remain largely uninvestigated even though it is known that aggressive substances such as nitric acid can be a product of such processes.

The quality of water, whether present in an aqueous or vapor phase, will directly affect the dissolution of spent fuel, waste glass, and ultimately, the concentration of dissolved or suspended radionuclides in water that exits breached containers. Therefore, the introduction of some man-made materials into the WP environment may influence WP performance. The chemical data for these materials will be gathered from a wide variety of sources that represent their usage in both modern and ancient societies. This data is essential because many chemical consequences specific to the repository setting are to a large extent unknown. The information that is known, summarized below, comes from literature searches that have been initiated for some of the major categories of materials. Therefore the preponderance of data on cement-based materials represents the preliminary nature of this task rather than the relative significance of any of the materials.

In the sections that follow we distinguish between those chemical processes that are biotic, or mediated by living organisms from those that are abiotic, or not dependent on living organisms. As will be discussed in the next section, most of our predictive chemical modeling capabilities are abiotic. Thus to use that modeling capability without explicit recognition of biotic chemical processes implicitly assumes that they are insignificant compared to abiotic processes. Clearly this is untrue for some materials such as some organic compounds over long periods of time in natural environments. Given the potential confusion in terminology, we define at the outset "organic chemistry" as those processes that involve organic compounds as distinct from "biotic chemistry" which involves a living intermediary such as a colony of microbes. As will be discussed in Section 6.2.2, microbially mediated (biotic) processes do not necessarily depend on the presence of organic compounds and can significantly affect inorganic chemistry.

6.2.1 Abiotic Chemistry

In this section the chemistry of inorganic materials and organic materials that are relevant to a high level radioactive waste repository is examined. The choice of subjects examined and the length of the studies was strongly determined by the needs of the project on a yearly and some times shorter term basis.

6.2.1.1 Organic Materials. This examination of potential chemical effects of organic materials concerns two very different goals. The first goal is to assess the potential contamination of studies conducted in the ESF by introduced materials. This work supports the determination of importance evaluation of materials used in the ESF. The second goal is to examine organic materials in the context of a radioactive waste repository and whether they may react with the surrounding rocks causing changes in repository porosity, or react with the waste package or waste form and enhance the mobility of radionuclide species. It does not, however, address microbially mediated degradation.

Diesel Exhaust. A study of long term diesel exhaust effects was conducted using N-Tunnel (Nevada Test Site) as a historical analog (Meike et al., 1995). The study represents a broad approach to material degradation that aimed first to assess the rate determining processes before embarking on the detailed experiments. Biotic and abiotic processes were considered and organic and inorganic materials were analyzed. This study is described in Meike (1995).

Diesel Fuel. Two studies have been conducted on different aspects of diesel fuel contamination. The first was conducted primarily to assess the potential impact of diesel operation on geochemical studies conducted in the ESF. The other study was oriented toward understanding the significant long term degradation processes.

^{14}C in Diesel Fuel from the ESF. Chemical isotope studies of selected introduced materials were conducted in the ESF in support of geochemical tests to determine what the potential effect of contamination would be to those geochemical studies. One effect is the potential contamination of ^{14}C from a number of sources. The objectives of the first stage of the study were threefold. Our first objective was to verify that the sample collection protocol did not contribute "modern" ^{14}C to the fuel sample. The second was to demonstrate reproducibility between samples collected at the same location. The third objective was to verify that the fuel collected from the locomotive motor was isotopically equivalent to fuel collected directly from the fuel tank. This first stage was intended to demonstrate unequivocally that (1) our sample collection protocol was appropriate for these measurements and (2) future samples could be collected exclusively from the storage tank, thus simplifying future collection. These were

necessary precursors to give credence to the second stage of the study which was the actual analysis of the diesel fuel.

Eight samples of ~50 mL each were collected at the ESF at YMP. Five of the eight samples were taken from the storage tank and 3 were collected from the locomotive motor. The ^{14}C in each sample was measured using accelerator based mass spectrometry (AMS). Prior to measurement an aliquot from each sample was combusted to graphite at the LLNL environmental-level graphitization laboratory. The technique used to graphitize samples at LLNL is in widespread use at other AMS laboratories around the world and cross-calibrations with other laboratories are performed routinely. In addition to the samples procedural blanks are also graphitized to verify background activity.

From the AMS measurement an isotopic ratio ($^{14}C/^{13}C$) is derived. The AMS measurement of ^{14}C and ^{13}C is converted to an isotopic ratio by referencing to standards measured during the measurement cycle of the unknowns. The accuracy of the standards is <1%. Within counting statistics all of the samples measured were identical and their ^{14}C activity was not distinguishable from background, i.e., they were ^{14}C dead. The limits on their ages are shown in Table 6-7. All of the samples measured have ^{14}C ages of >48 Kyr. This is essentially the background of the graphitizer-spectrometer system. These samples are unequivocally ^{14}C dead. Furthermore, they are all identical, thus verifying the efficacy or the sample collection protocol. Since the samples collected from the locomotive motor were indistinguishable from those collected directly from the storage tank any future measurements could be performed exclusively on samples collected from the storage tank.

A preliminary interpretation of these results is that any possible contamination of geologic samples taken from ESF by diesel fuels would result in apparent ^{14}C ages older than their real ages. The extent to which mixing of C indigenous to geologic samples taken from ESF with fuel-derived C can be assessed however this task is beyond the scope of this preliminary report. It is significant that apparent young ^{14}C ages from materials taken from could not have been produced by contamination with fuel or exhaust from diesel fuel.

Hydrous Pyrolysis of Diesel Fuel. This study examined the hydrothermal production of carboxylic acid and other aqueous organic species due to thermal degradation of diesel fuel at elevated temperatures. Carboxylic acids are particularly significant because they are known to form complexes with common rock forming cations, and thus can enhance mineral dissolution rates and mineral solubility (e.g., Bell et al., 1992; Gestsdottir and Manning, 1992; Hajash et al., 1992; Fein, 1991; Bennett et al.,

1988). Carboxylic acids are also known to accelerate the corrosion of steel and other alloys (Jones, 1992; Fontana and Green, 1978; Larrabee and Mathay, 1963). Furthermore, carboxylic acids are kinetically metastable for geologically long periods of time at 100-200°C (Palmer and Drummond, 1986). Other hydrocarbons that may be derived from diesel fuel and its degradation products are potential sources of colloidal material for radionuclide transport. These experiments were carried out at 200 and 315°C, temperatures somewhat higher than those expected within a repository emplacement drift of the present reference design, in order to directly determine the rate and products of diesel fuel degradation within a 2 to 3 month laboratory experiment. They thus provide an upper limit for the rate of abiotic degradation within the chemical system studied.

Experimental. Given the complex nature of the potential interactions between diesel fuel, other relevant man-made materials, groundwater, and Yucca Mountain geology, a series of scoping experiments with increasing degree of chemical complexity were undertaken. The experiments (see Table 6-8) also represent an evolution in the development of experimental and analytical protocols. The studies of diesel fuel hydrous pyrolysis were conducted (1) at 200°C (Jackson and Carroll, 1994), (2) at 315°C to accelerate the reactions, (3) in the presence of cementitious material and analog J-13 well water to examine reactions at elevated pH, (4) in the presence of Topopah Spring tuff and analog J-13 well water to examine possible catalytic effects, and (5) in the presence of cementitious material, Topopah Spring tuff, and analog J-13 well water. In addition, a scoping study of hydrothermal cement reactions 200°C was conducted for comparison with the more complicated chemical systems (3 and 5 above).

A wide range of analytical techniques were used because no single instrument is capable of adequately analyzing all of the wide range of substances of interest. Gas Chromatography (GC) with flame ionization (FID) and thermal conductivity (TCD) detectors or Gas Chromatography Mass Spectrometry (GCMS) were used to analyze organic phases (aromatics and alkanes in aqueous and organic solution. Gas Mass Spectrometry (GMS) was used to analyze gas phase extracted from the liquid samples. Liquid Chromatography (HPLC) was used to analyze for dissolved carboxylic acids. Inorganic aqueous species were analyzed with one of two instruments. Cations were detected using Inductively-Coupled Plasma, Atomic Emission Spectrometer (ICP-AES). Anions were detected using Ion Chromotography (IC). Inorganic carbon was detected using a CO_2 Gas Analyzer. The solids were characterized mineralogically using X-Ray Diffractometry (XRD) and morphologically and chemically using Scanning Electron Microscopy (SEM) with energy dispersive spectrometer (EDS) and a beryllium window.

The diesel fuel used in these experiments was obtained from the LLNL motor pool. It is composed primarily of alkanes ranging from C_6 to C_{26} (Table 6-9). The total sulfur concentration is 0.55 wt%, as measured by combustion using a LECO SC132 analyzer. Fibercrete™ wafers, weighing approximately 3 g each were prepared from a sample obtained from the ESF, and is described in Section 6.1.1.3. Topopah Spring Tuff (Tpt) cores taken 1232.2-1232.3 feet below the surface from drill hole USWG-1 were sliced into wafers weighing approximately 3 grams (Knauss et al., 1985a). It consists of a devitrified matrix containing plagioclase phenocrysts, alkali feldspar, cristobalite, quartz, biotite, magnetite, ilmenite, and accessory zircon and apatite, and has an average pore diameter of 0.025 μm and a porosity of 6.54% (see also Warren et al., 1984; Bish et al., 1981). All waters used in the experiments were either distilled MilliQ (17.5 MΩ) filtered water or 3 mM $NaHCO_3$ solution in MilliQ water. The latter composition reflects the most salient chemical feature of J-13 well water (~3 mM $NaHCO_3$) for the purpose of the experiment and will be referred to as J-13 analog water (JAW). J-13 water is considered representative of the natural ground water from Yucca Mountain (Knauss and Peifer, 1986).

The high temperature pyrolysis experiments were run in Dickson-type, gold bag autoclaves (Seyfried et al., 1987). The apparatus has been used extensively for hydrothermal experimentation, and its use in the experimental study of the hydrous pyrolysis of hydrocarbons is well established (Jackson et al., 1992). Within the Yucca Mountain Project the apparatus is standard equipment and is described elsewhere in geochemical studies (Knauss and Beiriger, 1984; Knauss et al., 1985a; Knauss et al., 1985b, Knauss and Peifer, 1986 and Knauss et al., 1987).

During fluid sample extraction autoclave rocking was stopped, but the experimental pressure was maintained by externally pumping deionized water into the pressure vessel. The sampling port was positioned so as to sample the desired immiscible liquid phase: the down position sampled the more dense aqueous phase, and the up position sampled the less dense organic phase. All samples were extracted from the sample port with gas-tight syringes. Approximately 1 mL of liquid was extracted to clear the sampling line, which was not maintained at temperature and pressure, and thus could be contaminated with precipitated phases. Another 1 mL of liquid was taken to measure pH at room temperature, which is not necessarily equal to the pH at temperature. However, given the experimental difficulties of measuring the pH at experimental temperature and the straightforward nature of the calculation, it is standard practice to calculate the value at temperature based on thermodynamic principles. In any case, the trend of pH changes is the same.

An additional two samples were filtered (0.4 μm filter) for ICP-AES analysis of cations: a 3 mL undiluted sample acidified with concentrated nitric acid for trace element analysis, and a 1 mL sample diluted by a factor of 10 with 3 mM $NaHCO_3$ and acidified with concentrated nitric acid for major element analysis. Approximately 0.5 to 1.0 mL of the aqueous phase was sampled for organic analyses. A 1 mL aqueous sample was taken to measure organic anions using HPLC. Prior to filtering samples for HPLC analyses, the gas phase, which exsolves from the sample at room temperature, was removed by passing 20 mL of He gas at atmospheric pressure in a gas-tight syringe through the liquid sample syringe, then the liquid sample was gently shaken for about 1 minute to allow the gas exchange to occur, and the gas was re-injected into the 25 mL He syringe. The total gas volume was measured after adjusting to atmospheric pressure and injected into an evacuated sampling steel cylinder for GMS analysis. This extraction procedure was repeated with the same liquid sample. The gas extractions were analyzed for inorganic and organic gases. Approximately 1 mL of the aqueous phase was sampled for inorganic carbon analysis with the CO_2 gas analyzer.

Simulations using the Geochemist's Workbench (GW) equilibrium geochemical code (Bethke, 1994), and COM.R16 thermodynamic data base (Johnson and Lundeen, 1995) were used to interpret the experimental solution concentrations and solid end products. These calculations were evaluated at 200°C. Sulfur was assumed to be in the form $(SO_4)^{-2}$ and the solutions were charge balanced with Na^+. The lack of detectable $H_2(g)$ in the diesel fuel hydrous pyrolysis experiments suggested that oxidizing conditions existed in the experiments, which were simulated by setting Eh = 0.4 V.

Results. Diesel fuel hydrous pyrolysis is limited at 200 and 315°C over a two to three month reaction period. Low carbon number alkanes and aromatics were dissolved in the aqueous phase (Table 6-10). Carboxylic acids, such as acetic acid and perhaps formic acid, may have been present in the aqueous samples, but their concentrations were below the HPLC working detection limit (4 ppm). The room temperature pH of the sample taken at the end of experiment DF1, equaled 4.5. In experiment DF2, the room temperature pH decreased from 6 to 4.9 during the first 30 days of reaction followed by a slower decrease to pH 4.7 at the end of the experiment. The exception to this trend was taken at approximately 65 days (Fig. 6-4). No $H_2(g)$ or $O_2(g)$ were detected by GMS and $CO_2(g)$ concentrations were on the order of 10^{-5} M. There was no measurable change in the proportions of the alkanes, as illustrated by the normalized concentrations of n-C_{10}, n-C_{12} and n-C_{14} with respect to hexadecane, n-C_{16} for experiment DF1 (Fig. 6-5) or in the final diesel fuel analysis for experiment DF2.

The results of Fibercrete™-water interactions (DF3 and DF4) appear to be independent of the presence of diesel fuel (Fig. 6-6 through 6-8). Solution pH (200°C) decreases from approximately 8.8 to 8.4 in both experiments. Similarly, total sulfur concentrations increase to approximately 15 mM and initial inorganic carbon concentrations decrease from 3 mM to concentrations near the detection limit (~1mM) after the first few days of reaction. The aqueous Si concentrations increase rapidly during the first few days of reaction, followed by a slower increase to approximately 5 mM, whereas the aqueous Al concentrations decrease steadily from 2 to 1 mM. The aqueous Ca concentrations increase as a function of time, however the concentrations measured in the presence of diesel fuel are a factor of two lower than the concentrations measured in the absence of diesel fuel. Aqueous Fe and Mg concentrations hover around 1 mM, near the detection limit of the ICP-AES analytical technique.

In both experiments DF3 and DF4, the reacted Fibercrete™ consists of quartz, calcite, clinozoisite, feldspars (albite and anorthite), and 11Å-tobermorite as identified by XRD (Fig. 6-9). Of these, only 11Å-tobermorite is not found in the unreacted Fibercrete™. Other crystalline Ca-Si-hydrate phases (but not all) that are associated with reactions above 100°C (see Meike et al., 1994); afwillite, xonotlite and foshagite, were not identified in the unreacted Fibercrete™. The absence of xonotlite, afwillite, foshagite, bassanite, phlogopite, and mesolite were not unambiguously determined by XRD, because their major peaks overlap with quartz, calcite, clinozoisite, and 11Å-tobermorite. Two XRD peaks remain unidentified. SEM photomicrographs of unreacted and reacted Fibercrete™ (Fig. 6-10) show dissolution etch pits as well as prismatic growth features in the larger aggregate minerals, quartz and feldspar of the reacted crystal. The Ca-rich precipitate covering the majority of the wafer surface does not form on the aggregate or penetrate the wafer at depth. No Si was detected in association with the Ca, thus it is possible that the Ca-rich precipitate is calcite or an amorphous calcium hydroxide (portlandite) because CO_3 and OH are not detected by these analytical methods. No portlandite was identified by the bulk XRD analysis. Steel fibers were not detected in the reacted Fibercrete™ with backscattering electron imaging (BEI) using SEM. However, because iron was not detected in the solution or the Ca-rich precipitate, it is likely that the corrosion of the steel fibers was minimal and that they were masked by the Ca-rich precipitate.

Modeling simulations regarding Ca-bearing phases must be considered with caution because the COM.R16 database does not contain thermodynamic data for many of the amorphous and crystalline Ca-Si-H_2O phases that are pertinent to this chemical system at this temperature (see e.g., Meike et al., 1994) and that data that is available is not

internally consistent. These simulations suggest that the aqueous phase was supersaturated with respect to mesolite (Na-Ca-Al zeolite), close to saturation with respect to wollastonite, albite, K-feldspar, quartz and calcite, and undersaturated with respect to bassenite (least soluble of the calcium sulfates), anorthite, and gyrolite and 11Å-tobermorite (crystalline Ca-Si-H_2O phases that are found in the COM.R16 database).

GCMS analyses of the organic phases indicated no significant difference between the starting and post-experimental sample (Table 6-11). These results suggest that neither alkaline pH nor the phases present in Fibercrete™ catalyzed the hydrous pyrolysis of diesel fuel at 200°C. However, organic compounds such as the BTEX (benzene, toluene, ethylbenzene, and xylene) compounds are water soluble at this temperature and did partition into the aqueous phase. The aqueous solubility of organic phases has significant implications for their transport which is significant to both colloidal interaction and microbial activity. However, the aqueous organic species did not appear to evolve over the course of the experiment. Within the scatter of the data: average benzene, toluene, ethylbenzene, and p-xylene are 0.04 (±0.01), 0.06 (±0.02), 0.02 (±0.01), and 0.07 (±0.02) mM respectively. The concentrations of aqueous alkanes were approximately an order of magnitude less than the aqueous aromatic hydrocarbons. Little significant change was detected with respect to gases although O_2 gas decreased from 21 to 20 mole percent. No H_2 gas was detected in the GMS analyses.

The results of DF 5, the diesel fuel-Tpt-JAW experiment at 200°C (Figs. 6-11 through 6-13), was similar to previous hydrothermal Topopah Spring Tuff experiments carried out in the absence of diesel fuel (Knauss and Beiriger, 1984; Knauss et al., 1985b; Knauss and Peifer, 1986; Knauss et al., 1987). At 200°C, the system quickly reached a metastable equilibrium. The pH (200°C) decreased slowly from 7.7 to 7.5 over the duration of the experiment. The aqueous sulfur concentration remained constant for the duration of the experiment (near 1 mM). The unusually high value of 5 mM at the end of the experiment requires verification. The inorganic carbon concentration remained constant for the duration of the experiment near its initial concentration of 3 mM. The aqueous Si concentration increased rapidly during the first few days of reaction to approximately 8 mM. The aqueous Al and K concentrations decreased rapidly and reach a constant concentration after 30 days of reaction. The aqueous Ca concentration was constant and close to the detection limit of the analytical technique for the duration of the experiment. No Fe or Mg were detected in the aqueous phase.

XRD analyses revealed no mineralogical differences between the reacted and unreacted tuff. Quartz, cristobalite plagioclase, alkali feldspar, ilmenite, and biotite

were unambiguously identified. SEM photomicrographs of unreacted and reacted Topopah Spring tuff (Fig. 6-14) reveal a Si-rich precipitate on tuff surface. Cristobalite would be consistent with geochemical modeling. The aqueous solutions are calculated to be supersaturated with respect to mesolite (Na-Ca-Al-zeolite) and albite, close to saturation with respect quartz, cristobalite, muscovite, and calcite, and undersaturated with respect to anorthite, wollastonite, and bassenite.

Similar to the Fibercrete™ results (DF3 and DF4), the Topopah Spring tuff did not catalyze the pyrolysis of diesel fuel. No chemical difference was found between the constituents of the final the organic phase and the beginning diesel fuel. The dissolved organics were dominated by aromatic hydrocarbons (Table 6-12). Within the scatter of the data, the BTEX concentrations were seen to increase to a constant value after 30 days of reaction. Average values of benzene, toluene, ethylbenzene, m/p-xylene and o-xylene concentration were 0.030 (±0.003), 0.072 (±0.006), 0.013 (±0.005), 0.04 (±0.01) and 0.013 (±0.004) mM respectively. The concentrations of aqueous alkanes are approximately an order of magnitude less than the aqueous aromatic hydrocarbons. The O_2 gas concentration decreased from 21 to 20 mole percent. No H_2 gas was detected by GMS analyses.

The results of DF6, the diesel fuel-Fibercrete™-Tpt-JAW experiment (Figs. 6-15 through 6-17), indicated little to chemically distinguish it from the Fibercrete experiments (DF3 and DF4). The solution pH (200°C) decreased from 8.5 to 8.2 indicating that the cementitous material dominated the system and that the tuff has little buffering capacity. The total sulfur concentration increased linearly from 1 to 14 mM over the course of the experiment. The inorganic carbon concentration decreased from 3 mM to a final value of 1.5 mM. During the first few days of reaction, the aqueous Si concentration increased rapidly to approximately 10.5 mM, followed by a slower decrease to 9.5 mM at the end of the experiment. The aqueous K concentration decreases from 0.9 mM to a steady-state concentration of 0.25 mM during the first 40 days of reaction. The aqueous Al concentration decreases from a maximum of 0.075 mM to a minimum of 0.025 mM after 15 days of reaction, followed by a slow increase to 0.04 mM by the end of the experiment. The aqueous Ca concentration increases linearly throughout the experiment, with the exception of the questionably high final data point. The aqueous Mg concentrations are at the detection limit of the ICP-AES spectrometer. No aqueous Fe was detected in the aqueous phase.

SEM analysis indicate that the majority of the reacted Fibercrete™ surface is covered with a well crystallized layered Ca-silicate (Fig. 6-18) distinct from the precipitate formed in experiments DF3 and DF4 (Fig. 6-10). This phase does not penetrate the

wafer. An amorphous/poorly crystalline phase can be seen in the spaces between overlapping sheets of the precipitate. It is approximately 5 to 10 μm thick, leaving open pores by not precipitating on the aggregate, as is observed in experiment DF3 and DF4, or around pores of the starting cement material. Although not rigorously determined, the ratio of Ca to Si is similar to that found in tobermorite, which was identified independently by XRD. This phase also contains minor amounts of Al, which is frequently a substitutional element (for Si) in tobermorite. No steel fibers in the reacted Fibercrete™ are observed with backscattered electron imaging (BEI) and no measurable amounts of iron were found in the solution and surface precipitate, indicating little reaction of the steel fibers, indicating that the fibers were covered by the Ca-silicate sheet precipitate. Three different precipitates were observed on the Topopah Spring tuff: (1) small 10-20 micron wide books of the layered Ca-silicate identical to the precipitate found on the Fibercrete™, (2) calcite rhombs, and (3) Si-rich matrix covering the surface, which may have been amorphous silica or cristobalite.

The aqueous organics were dominated by aromatic hydrocarbons (Table 6-11). Average benzene, toluene, ethylbenzene, m/p-xylene and o-xylene are 0.033 (±0.004), 0.081 (±0.011), 0.013 (±0.006), 0.05 (±0.02) and 0.015 (±0.007) mM respectively similar to the previous experiments. The concentrations of aqueous alkanes are approximately an order of magnitude less than the aqueous aromatic hydrocarbons. No H_2 gas is detected with GMS analyses. Analysis of the organic phase at the end of the experiment yields no discernible change from the starting diesel fuel.

At 200°C, this system quickly reaches a steady state, which, according to geochemical calculations is a metastable equilibrium. The aqueous solutions were calculated to be supersaturated with respect to mesolite (Na-Ca-Al-zeolite) and albite, close to saturation with respect quartz, cristobalite, wollastonite, K-feldspar, muscovite and calcite, and undersaturated with respect to anorthite, 11Å-tobermorite, gyrolite, and bassenite.

Discussion. The experiments indicate that the abiotic degradation of diesel fuel is slow with respect to repository lifetime and, unaided by biotic degradation, would remain almost indefinitely. Our experimental results show that hydrothermal degradation of diesel fuel is minimal at mildly acid and alkaline pH over two to three month reaction periods at 200°C and 70 bars. At 200 and 315°C, low carbon number aromatics and alkanes dissolve into the aqueous phase, but the production of carboxylic acids is limited. It is possible that the soluble aromatics and alkanes are intermediate degradation products between diesel fuel and carboxylic acids. The dominant water-soluble organics are aromatic compounds, not aliphatic carboxylic acids. At 315°C, the

diesel fuel is significantly more reactive, although the net production of carboxylic acids is minimal. However, soluble alkanes, aromatics, and carboxylic acids may be intermediates between the unstable diesel fuel and the equilibrium thermal degradation products. A probable reaction path for diesel fuel hydrous pyrolysis may be:

Diesel Fuel ⇒ soluble aromatics and alkanes ⇒ carboxylic acids ⇒ carbonic acid (1)

Although production rates of carboxylic acids at 200 and 315°C are too low to be quantified directly, the final pH values for experiments DF1 and DF2 support the presence of acetic acid, which has a pK_a of 4.8 at 25°C. In contrast to the reaction path proposed above, (Kharaka et al., 1993) and (Lundegard et al., 1992) interpret measured concentrations of carboxylic acids from oil hydrous pyrolysis experiments as simple partitioning between the aqueous and organic phases. However, if that were the case, then the organic acid concentrations and the pH should have been constant over time. In experiments DF1 and DF2, the solution pH continues to decrease slowly as a function of time.

A conservative rate of diesel fuel hydrous pyrolysis can be made from the pH data (measured at 25°C) as a function of time from experiment DF2 (315°C). To make these calculations, it is assumed that the decrease in pH reflects a net increase in total dissolved inorganic carbon (carbonic acid) or total dissolved acetate. In the inorganic carbon system, a total inorganic carbon concentration can be calculated from pH and the carbonic acid dissociation mass balance, charge balance, and total carbon equations. The dissociation reaction (K_a) and mass balance expression for carbonic acid are:

$$CO_2(aq) + H_2O \Leftrightarrow H^+ + HCO_3^- \qquad K_a = ([H^+][HCO_3^-]/[CO_2(aq)]) \qquad (2)$$

where the $pK_a(25^\circ C) = 6.35$ (and $pK_a = \log K_a$). Total inorganic carbon mass balance (C_T) and charge balance equations at the experimental pH are:

$$C_T = [CO_2(aq)] + [HCO_3^-] \qquad (3)$$

and

$$[H^+] = [HCO_3^-], \qquad (4)$$

respectively.

Similar calculations can be made assuming the decreasing pH reflects an increase in the total acetate concentrations as a function of time. The acetate system is chosen to represent carboxylic acids, because the final pH of both experiments DF1 and DF2 is near the acetic acid pK_a. The dissociation reaction for acetic acid and corresponding mass balance expression are:

$$HAc \Leftrightarrow Ac^- + H^+ \quad K_a = ([H^+][Ac^-]/[HAc]) \tag{5}$$

where $pK_a(25^\circ C) = 4.87$. In this model system, the total carbon mass balance and charge balance equations for the experimental pH may be written as:

$$C_T = [HAc] + [Ac^-] \tag{6}$$

and

$$[H^+] = [Ac^-], \tag{7}$$

respectively. The results of both of these simple systems are shown in Fig. 6-19. The calculated inorganic carbon concentrations increase linearly as a function of time, approaching the measured values near the detection limit after 100 days. The calculated total acetate concentrations increase linearly as a function of time, and remain well below the detection limit of the LC analytical technique, 0.4 mM. The calculated increases of inorganic carbon or total acetate can be used as conservative rates of diesel fuel hydrous pyrolysis: 8.3×10^{-6} M C/day from the inorganic carbon model or 7.8×10^{-7} M C/day from the acetate model. In all likelihood, the decrease in pH as a function of time represents contributions from both increasing concentrations of carbonic and carboxylic acids. These low concentrations cannot be accurately measured and thus long term effects remain unknown, however they can be bounded by using the detection limit as a guide.

Thermal degradation of diesel fuel is not enhanced in the presence of cementitious material or at alkaline pH. Similarly, diesel fuel hydrous pyrolysis is not catalyzed by Fibercrete™ or by Topopah Spring Tuff and does not accelerate dissolution of silicate minerals found in these solids at 200°C. These results agree with previous studies that show that water inhibits the catalytic effects of clay minerals in contact with alkanes, alkenes, alcohols, and ethers (Weres et al., 1988; Tannenbaum and Kaplan, 1985). In a preliminary study, Bell et al. (1992) show that acetate decarboxylation reactions are enhanced in the presence of magnetite, hematite, Ca- and Fe- montmorillonite, and non-

stoichiometric pyrite, indicating the Fe^{3+} - Fe^{2+} redox couple as an important catalyst. However, in this study, the presence of metal iron in the steel fibers did not catalyze the hydrous pyrolysis of the complex organic mixture.

Secondary results support the understanding that the presence of cementitious materials will react, affecting the chemistry of the water with which it is in contact, the repository rock its own porosity, as well as its own permeability and mineral assemblage.

6.2.1.2 Cementitious Materials. The number, identity, and significance of potential coupled interactions between man-made materials are as yet not determinable. However, interactions between concrete and some other materials are known to be significant for the chemical environment. The oxidation of rebar creates a chemical environment that increases the degradation rate of concrete. Examples of this effect can be seen in many major bridges and thoroughfares, but knowledge of these processes remains qualitative. Tests in which concretes were leached at 100 to 200°C with either distilled water or Standard Canadian Shield Saline Solution (SCSSS) in contact with a sodium-bentonite, a waste glass, or a silica fume additive have indicated that the identity and concentration of species in solution is time-dependent (Komarneni and Roy, 1983; Burnett et al., 1985; Heimann and Hooton, 1986; Onofrei, 1987; Heimann, 1988a,b).The fate of C-S-H and the cement minerals, and their interaction with the aggregate, are a function of time, temperature, solid and aqueous solution compositions, and the availability of water. Of particular chemical concern is whether the concrete is exposed to air, CO_2 or water, the aluminate and ferrite content of the cement, and the activities of carbonate and sulfate in the water. The preferred rheology of the cement at the time of emplacement dictates the quantity of water added to the dry cement mix and usually exceeds that required for complete hydration. Therefore, extra water is expected in any situation in which wet grout is emplaced. Physical properties, such as interconnected porosity, can regulate the rate of, and the long term susceptibility to chemical attack. Porosity is affected by initial water:cement (w/c) ratios and thus potentially by the method of emplacement. Leaching will preferentially dissolve some minerals such as portlandite from the set material and thus can increase permeability, which will influence the rate of degradation. Sufficiently high activities of sulfate or CO_2 can react with concrete. At elevated temperatures, residual portlandite reacts with carbonates to form calcite (Milestone et al., 1987).

Disintegration and dissolution of cementitious materials may change the pH of water to values as high as 11.5 at 100°C. Tobermorite (14 Å) forms in water at temperatures below 80°C (Fujii and Kondo, 1983). This phase begins to lose interlayer

water at 70°C in dry CO_2-free air to give 11Å tobermorite (Taylor, 1987). Sulfate-resistant cements (Soo and Milian, 1989) are formulated to have a relatively low aluminum content so as to minimize the possibility of forming ettringite after the cement has set. Minimization of the volume of portlandite in the set cement controls the reaction of $Ca(OH)_2$ with sulfate to form gypsum. The large volume increases associated with both ettringite and gypsum formation cause cracking and increase the surface area exposed to degradation.

Insight into the long-term performance of cements has been gained from examinations of (1) groundwaters that issue from rocks containing cement-type minerals, and (2) ancient concretes. Water with a pH as high as 12.5 has been collected from rocks containing portlandite, ettringite, tobermorite, and higher temperature minerals (Khoury et al., 1985; Neal and Stanger, 1984). A preliminary calculation of phases in equilibrium with the water (Barnes et al., 1982) is consistent with these natural data. Ancient Roman concretes often incorporated pyroclastics, including acidic tuffaceous material that may be applicable to modern portland cements in the sense that similar aggregate is being considered for use in the repository. Examination of these ancient materials demonstrates that low-permeability cements, and particularly pozzolanic cements, have the greatest durability (Roy and Langton, 1983, 1989). Optical and compositional comparisons between modern portland cement and a relatively young portland cement that had been submerged in water for 63 years (Rhoderick, 1981) have revealed no significant differences. Whether the resolution of data acquisition in this study is appropriate to predict change over 10,000 years has not yet been established.

The presence of cementitious material may greatly alter the geochemistry of the repository by providing a large reservoir of unstable Ca-silicate phases which will dissolve and reprecipitate at the rock-water interface. Chemical interactions between water and non-thermally treated grout at 20-60°C may well be dominated by the dissolution kinetics of the unstable amorphous and crystalline phases and precipitation kinetics of the metastable or stable phases (e.g., Atkins et al., 1991). This type of low temperature interaction has received much attention internationally and can be found in the radioactive waste disposal literature.

A unique aspect of the Yucca Mountain strategy relative to other high level radioactive waste strategies around the world is that water will probably contact the cementitious material only after it has been exposed to elevated temperatures (>100°C) for an extended period of time (>150 years). It is likely that the cementitous materials will have dehydrated and transformed to a more crystalline mineral assemblage. Many

phases in the crystalline Ca-Si-H_2O system can develop in cement exposed over long periods of time to temperatures above 25°C. The phases themselves are found both naturally and in synthetic systems. As a consequence of their appearance in cements exposed to elevated temperatures, chemical reactions involving these phases can affect not only water chemistry, but also the relative humidity of a radioactive waste repository that contains significant amounts of cement. In order to predict and simulate these chemical reactions, we are developing an internally consistent database of crystalline Ca-Si-hydrate structures. The experimental aspects of the synthesis and characterization of pure phases for the purpose of measuring thermodynamic parameters is discussed elsewhere (e.g., Barnes et al., 1996; Martin, 1995; Bruton et al., 1994; Meike et al., 1994). A complete synopsis of the work in the cement area is not ready at present due to the premature halt of a five year study in this area.

Other reactions known to occur in cementitious materials over time would contribute to alterations in the mineral assemblage and contribute to their degradation and reduction of mechanical strength. These are chloride attack, the alkalai silica reaction (ASR) and delayed ettringite formation. Chloride attack works by the ingress of chloride bearing water through permeable grout or cracks to contact and corrode the metal reinforcement (rebar). Expansion of the rebar due to corrosion causes the cementitious materials to crack and spall. One of the notable sources of chloride attack for the present application is the use of aggregate from desert climates that may contain evaporated salts (Taylor, 1990). Alkali silica reaction occurs when silica bearing aggregate reacts with alkali impurities in the cement paste. As with chloride attack, expansion occurs due to formation of the product phases, causing cracking (Taylor, 1990). Delayed ettrigite formation is also a cracking process due to the late formation of sulfate bearing phases (Taylor, 1990). There is still much debate about the causes of DEF. However, some significant DEF has been related to the heat-curing of sulfate-bearing cements. A phenomenon similar to DEF occurs through the formation of thaumasite, a sulfate-carbonate mineral (Crammond, 1995).

Roy and Langton (1983, 1989) have studied ancient concretes, to ascertain mineral stabilities and instabilities that may be applicable to modern Portland cements. The ancient concretes, which were made from lime formulations, are not completely analogous to the modern concretes which are composed of "alite" and "belite" and require higher temperatures for manufacture. Although made with unknown processes as well as varying starting materials, and mixed using unknown water/cement ratios, ancient Roman concretes often incorporated pyroclastics, including tuffaceous material. A main conclusion that Roy and Langton draw from examination of ancient materials is

that low permeability cements, and particularly pozzolanic cements, have the greatest durability. A study of mortars from the Byzantine basilica of Hagia Sophia, Istanbul suggests that a calcium silicate hydrate phase is present. The degree of crystallinity is not well constrained, however, and the mortar appears to be dominated by a calcium carbonate phase. A cursory examination of a Portland cement that had been submerged in water for 63 years (Rhoderick, 1981a, b, c) suggested no "significant effect" on either composition or microstructure. Notably lacking for the purpose of the Yucca Mountain Project are studies of cementitious materials that have been exposed to elevated temperatures for extended periods of time. It is clear that at elevated temperatures will cause changes in both composition and microstructure, which would ultimately affect the chemistry of the water in contact with the material, as well as its structural integrity.

A different approach to evaluating the long-term performance of cements is to examine the occurrence of hyper alkaline groundwaters issuing from rocks that contain cement-type minerals. One such occurrence had been noted (Khoury, 1985; Neal, 1984): in Jordan, a pH 12.5 water issuing from rocks containing portlandite, ettringite, tobermorite, and higher temperature minerals. Combustion of bituminous marl generated a pre-cursor assemblage of minerals similar to modern cement. Upon contact with water, recognizable calcium silicate hydrate minerals were formed. A somewhat incomplete calculation of phases in equilibrium with the water was reported by Barnes et al. (1982). Since important constituents of the water analysis were not reported, an exact replication of the calculation using EQ3 could not be made. By using additional data from the later literature cited above, the phases showing supersaturation and the degree of saturation via an EQ3 calculation were parallel those reported in Barnes et al. (1982).

Tobomorite synthesis and stability with respect to CO_2. Observations of the extreme sensitivity of tobermorite, a cement phase expected under repository conditions, during its synthesis (Martin et al., 1994) indicate that the formation of tobermorite is sensitive to the partial pressures of CO_2, and at partial pressures of CO_2 greater than ambient compositional and microstructural changes are also to be expected. Ultra-pure samples tobermorite and other crystalline Ca-Si-hydrates have been synthesized and characterized in order to obtain thermodynamic data. The purpose of this thermodynamic is to fill a need for fundamental parameters that are not available in the literature. These parameters are required in order to model the interaction between water and cementitious materials (see the Fibercrete-water experiment discussed above, and Meike et al., 1994).

The starting materials for synthesis were CaO and an aqueous suspension of fumed SiO_2 ("Cab-o-sperse") in a molar ratio of 5:6. The CaO was prepared from $CaCO_3$ heated to 1050°C for >4 hours. The highly reactive SiO_2 had a surface area of 100 m^2/g. In one case hydrochloric acid (HCl) was added before mixing with CaO to neutralize the SiO_2 suspension which had a pH of 9.8. The constituents were mixed in an argon filled glove box to inhibit CO_2 uptake. CO_2 free water was added in excess to obtain a homogeneous sol/gel. The gels were autoclaved at 90 and 120°C in pressure vessels. Individual vessels were sampled multiple times over the total length of the run in the argon glove box. Post run treatment of the aliquots included washing the product with milli-Q water and ethanol before drying in desiccators. To hinder calcite formation and remove excess CaO in the product some of the reacted samples were titrated with HCl to a pH of 7-8.

Powder x-ray diffraction (XRD) was used to identify the mineralogical phases. Two types of run products were obtained, a mixture of 1.1 and 1.4 nm tobermorite at 90°C, and a 1.1 nm tobermorite at 120°C. For the mixed phase runs the intensity of the 1.4 nm peak decreased and the 1.1 nm peak increased over time as the tobermorite became less hydrated (Fig. 6-20). Mixed phase samples heated and dried at 100°C produced a 1.1 nm tobermorite. X-ray diffraction of the higher temperature run indicated a single phase, 1.1 nm tobermorite (Fig. 6-20). In general, tobermorite became more crystalline over time and at higher temperature. Scanning electron microscopy (SEM) was used to determine particle morphology. Photomicrographs of the reacted material showed an aggregation of platy particles similar to those shown by Suzuki and Sinn[3]. No distinct morphological differences were noted between the 1.1 nm tobermorite and the mixed 1.1 and 1.4 nm tobermorite.

Measures were taken to preclude calcite formation but calcite was detected in the product and was probably due to unreacted CaO reacting with atmospheric CO_2 (pH measurements of the run products were high, 11.3). The formation of calcite was not instantaneous. X-ray diffraction patterns indicated an increase in calcite concentration in the longer runs and was most pronounced in the longest run of 161 days. Although aliquots were taken in the argon glove box, they were cooled outside of the box in the laboratory. Carbon dioxide may have diffused through the Teflon lined vessels into the run product.

Carbon dioxide concentrations were measured with a CO_2 analyzer and indicated equivalent $CaCO_3$ concentrations of up to 6%. Calcite concentrations were the highest in samples exposed to atmospheric CO_2 for longer periods of time. Samples titrated with HCl immediately after synthesis did not contain calcite, and XRD analysis of shelved

samples containing calcite indicated that the calcite was removed from the sample with acid titration without affecting the tobermorite. The volume of HCl added to reduce the pH to approximately 8 was equivalent to an excess CaO concentration of approximately 8%, which correlates to a $CaCO_3$ concentration of approximately 14% if completely reacted.

The extreme sensitivity of tobermorite and other crystalline Ca-Si-hydrates that may exist in ordinary portland cement to the partial pressure of CO_2 suggests that, in a repository environment, much of the cementitious material could evolve into $CaCO_3$ phases such as calcite and vaterite. The consequences to the pH are significant. Whereas a young cement- water system could register pH values of 11 or 12, a calcite water dominated system would have a significantly lower pH.

Significance to YMP. It is clear from the extant literature and studies that have been conducted to date, that at temperatures near 25°C water in contact with modern ordinary portland cement can obtain extremely high pHs. However, the effects of other factors, such as microbes, heating and pCO_2 above ambient have not been well established and therefore cannot be well constrained. Therefore for the purpose of chemical performance assessment the addition of cementitious materials widens boundary conditions and increases uncertainty. With regard to the potential survival of concrete, we recognize an important distinction between "performance lifetime," which is linked to the mechanical stability of the structure, and chemical lifetime which represents the duration of the chemical effects of the material long after the material has ceased to perform its function. It will be important to explicitly specify the mechanical performance lifetime required of the cements by the design, because it may be possible to obtain modern high performance formulations that will perform a mechanical function throughout the retrieval period, and perhaps stretching into some of the period after closure. However, it may not be necessary (or even possible) to engineer (or prove the stability of) a cement with a performance lifetime of thousands of years.

It is highly likely that long after the mechanical "performance lifetime" of the cementitous materials has ended, these materials could perform chemical functions such as sorbing radionuclides, especially if the formulation were to contain zeolites as aggregate or pozzolana. In fact, at the point in the evolution of the repository where sorption is required, an invert a material that is considered to have low very long term mechanical performance properties may be an asset. This is because large surface areas predominantly determine the effectiveness of a sorbant, and thus a cementitious material that becomes greatly fractured or disaggregated increases the effectiveness of the constituent sorbant materials.

6.2.1.3 Metals. Metals that are introduced into a repository environment as a result of construction are used for many different functions (see previous section) and are composed of almost as many different alloys. Thus the concern of the introduced materials studies are far different from those that are intended to select a material for the waste package. Many of the high tech alloys considered for waste packaging materials are not used widely in construction. Conversely, the alloys that are used in construction are the more common and cheaper metals that may not make the best waste package. Fortunately, most of the metals used in construction have been used for many years and provide a foundation of knowledge in this area. For that reason, although a significant construction material metals have not been emphasized in these studies to date.

Metals that may be introduced into the WP environment for construction purposes will be primarily iron and iron alloys, which can degrade through several mechanisms. Oxidation is one common degradation process. Such processes are strongly dependent upon the Eh and pH of the environment within which oxidation occurs. Cast iron, if present in large volumes, has the potential to consume large quantities of oxygen and influence the atmospheric chemistry around waste containers. Experimental studies of copper corrosion in sea water and in the presence of sulfide ions (Mor and Beccaria, 1975) indicate that a variety of copper sulfides can form that are also dependent upon pH. The specific conductivity and resistance to corrosion of the metal are dependent upon the corrosion product, which is pH-dependent. In general, the rate at which metal ions are added to the water is dependent on the corrosion products.

Much of our understanding of the long term chemical processes involving metals that may be used in a radioactive waste repository will be based on a firm understanding of historical analogs. Many of the processes that will affect metal construction materials are identical to those that have affected metal archaeological artifacts. Outside the Yucca Mountain Project, interest in the degradation of metals is found in disparate sources from the U.S. Naval Oceanographic and Atmospheric Research Laboratory to many oil companies. Because of this interest, and also because of the length of time that man has been working with metal materials, much more information is available on the long term degradation of metals than most other manufactured materials. A literature review on the corrosion of metal artifacts has been conducted in support of waste package design.

Studies of metal artifacts from a variety of ages demonstrate that some phases that form cannot be predicted from our present knowledge of material degradation. Some products of these man-made materials rarely occur naturally and are therefore not

necessarily predictable from a geochemical data base. Botallackite, a rare hydroxide of copper chloride, for example, has been observed associated with the corrosion of a copper object exposed to chloride ion (Pollard et al., 1989). Stability fields and reactive sequences of the basic copper (II) chlorides have only recently been proposed (Pollard et al., 1989) on the basis of this and other historical data as a complement to experimental data, where experimental data alone has previously failed. That diffusion-controlled phenomena should be expected over time periods of at least 2,000 years is apparent from investigations of corrosion phenomena in ancient bronzes (Scott, 1985). Development of some phases appears to be mediated by the activity of microorganisms (McNeil et al., 1990).

In addition, information on the long-term corrosion of materials is being assembled from the New Zealand analog site (Bruton et al., 1995). In the respect that this data represents materials that are more similar to present construction materials and methods, some data from the New Zealand (e.g., Foster and Tombs, 1962; Soylemezoglu and Harper, 1982; Braithwaite and Lichti, 1981) and other geothermal fields (e.g., Dodd et al., 1960; Hermannsson, 1970; Hanck, and Nekoksa, 1980; Culivicchi et al., 1985) may be more useful to chemical model assessment than much older archaeological artifacts.

6.2.1.4 Polymers. Assessments of the long term chemical affects of those polymers and their reaction products in the repository are based on current understanding in polymer science which can be translated into models, but given the relatively new nature of these materials, experimental data must be gathered to test these models. Several sources have cautioned that polymer behavior can not be compared with that of simpler but similar molecules. Therefore, no conclusions should be made about polymers based on the behavior of smaller molecules. However, some correlations may be made between synthetic and natural polymers and between modern polymers and their predecessors (assuming one is aware of the cautions mentioned previously). Natural polymers such as keratin, cellulose and starch as a rule degrade much more easily than synthetic polymers. One reason is that they are more hydrophilic and another is that nature is more equipped to get rid of them (i.e., enzymes). Correlations may also be drawn between silicone and silica which have the same ancestry. It must be stressed, though, that only general correlations may be drawn and that the specific polymer must be investigated for specific information.

The primary modes of degradation for synthetic polymers are thermal degradation, oxidation, and photodegradation. Biodegradation will also be discussed in the section below. The degradation of a polymer can not be followed by observing the behavior of a similar but simpler molecule. First, there are many small chemical differences between

polymers and less complex molecules. The differences in termination of polymers are dependent on preparation. Often, side branches are incorporated during saturation. Polymers often undergo changes with the environment which are different from similar simpler molecules. Second, the length of polymers makes many reactions possible which are impossible in smaller molecules and reactions can be rapid in long chain molecules. Polymer degradation occurs by one of two primary structural changes: cross-linking or chain scission. Models have been developed to predict specific degradation processes over times significant to a radioactive waste repository (Burnay, 1990) however most models are for normal life times and under normal service conditions (Kenny, 1993). An activation energy must be reached before degradation begins (Ravanetti and Zini, 1992) which can be derived from thermal analysis. The Arrhenius equation is often used to predict the half lives of materials (Barr-Kumarakulasinghe, 1994). It has been found that thermal degradation rate is increased by higher temperatures, the presence of a radiation flux, oxidative agents, some chemical contaminants and light. In addition, many polymers can exhibit dose rate effects or synergism between radiation and temperature or chemical contamination (Burnay, 1990).

Hydrolysis involves the substitution of an OH for an OR of the polymer. For example, in *polyurethane*, a break would most readily occur at the carbon oxygen single bond and hydrolysis would form toluene diamine and polyether, which are almost identical to the starting material. Another method of polyurethane degradation is glycolysis, which involves the "dissolution of polyurethane (usually foam) in hot glycols, polyethers or polyamines. In this way additional monomer can be added to the solution which can then be used for a new product. However, given the difficulty with which glycolysis and hydrolysis are carried out for the purpose of recycling, the processes may not be relevant.

There are two types of thermal degradation. The first, depolymerization, involves the breaking of the main polymer chain backbone so that at any intermediate stage, the monomer units can be recognized (Grassie, 1985). This is common for polymers which give high values of chain scission at ambient temperature (Garrett et al., 1990). The second, substitution reaction, involves the substituents attached to the backbone of the polymer molecules such that the chemical nature of the repeat unit is changed even though the chain structure may remain intact. In this case, volatile products will be unlike the monomer (Grassie, 1985)."

Leedy and Watters (1994) found that rock bolt *epoxy* degrades at temperatures as low as 50°C and should thus not be used long term mechanical support in areas that

will be exposed to elevated temperature. However a variation in degradation behavior exists, probably dependent on the epoxy. It has been found that at 125°C the primary degradation mechanism for epoxy resins is initiated by oxygen attacks rather than a free radical mechanism. Many epoxy resin systems manifest significant oxidative degradation in air at temperatures as low as 100°C (Burton, 1993). A change in mass begins just below 250°C. To 310°C the degradation reaction is primarily dehydration and is identical in air and an inert atmosphere. Chain scission occurs above 310°C with evolution of SO_2. The rates of weight loss are maximal at 350 and 520°C (Rose et al., 1993). Although Tg varies dependent upon the exact epoxy, epoxies tend to have Tgs from 110°C to 135°C (Kaplan, 1991). Improved crystallinity decreases degradation at high temperatures while aromatic linear groups improve stability. Epoxy resins should not be included in the permanent structure, without detailed long term tests.

Kevlar is extremely heat resistant relative to other polymers with a degradation temperature of 601°C; at this temperature, kevlar will degrade at a rate of about 10 percent per minute (Kutty et al., 1992). However, exposure to thermal environments can alter kevlar's properties and performance. It has been found that "after 250 and 6 h exposure to 250 and 350°C, respectively, the fibers turned brittle and crumbled with handling (Parimala and Vijayan, 1993)." Fibers treated at 150°C remained unaffected over known lifetimes. However, given the relative youth of this material, and thus the lack of historical analogs, it is not possible to predict the response to thousands of years of degradation and an extended (100-200 year) thermal pulse at the 100-200°C range.

Neoprene degrades by a scission reaction accompanied by cross-linking. The metal oxides are consumed during the degradation process of primarily auto-oxidation. Chemical products are dependent on additives and temperature, and should be the subject of analysis should neoprene be considered as part of the permanent repository structure.

Depolymerization and extensive chain fragmentation of *polybutadiene* generally take place at temperatures greater than 300°C, when the activation energy needed for degradation is reached, and becomes appreciable at temperatures greater than 380°C. Below this temperature, some volatile products are released as well as some structural changes such as crosslinking but these are minute. The products of thermal degradation of polybutadiene are primarily larger "fragments" but also include monomer, hydrocarbons and "volatile" products (Brandrup and Immergut, 1975). The degradation process is exothermic up to 380°C and above that, it is endothermic. At about 200°C, polybutadiene becomes insoluble, "presumably in consequence of some degree of crosslinking. From NMR and IR spectroscopy, it has been found that "the polymer first

undergoes a saturation-cyclization process, in which the vinyl groups are the first to disappear. But, at 300°C, it becomes soluble again; in fact, after only half an hour at this temperature, "the product becomes soluble, the content of olefinic hydrogens drops to a mere 2.6%, and aromatic structures begin to appear (Schneider et al., 1993). When studying the thermal degradation of polybutadiene (PB) it must be taken in account that different proportions of the possible structural units (cis-1,4, trans-1,4, and 1,2) can be present, and consequently differences in the overall thermal behavior may be expected (Chiantore, 1989). The composition of the solid and condensed liquid products of thermal degradation of PB depends on temperature and time. By prolonged heating at a lower temperature, products comparable to those obtained at higher temperature cannot be generated (Schneider et al., 1993).

Two main thermal degradation products of *polycarbonate* at temperatures up to 400°C are monomer (and dimer and trimer) and *p*-cresol (Imasaka et al., 1992).

At temperatures above the melting temperature at long time periods, *polyesters* undergo chain scission. With PET, this reaction leads to carboxyl and vinyl ester groups. These react to an acetyl ester intermediate to form carboxylic anhydride linkages and acetaldehyde. Polyester salt complexes have been synthesized for potential battery applications. It was found that the thermal stability of these complexes was significantly less than for polyester (Kay et al., 1993). However, it is unknown whether these complexes would occur outside a laboratory.

The thermal degradation of *polyethylene* is dependent on the degree of side branching; the more linear the polymer, the higher the stability. It is assumed that the molecular weight of polyethylene increases due to long-chain branching which increases the polymer viscosity at about 200°C. However, after one hour of heating at 300°C, the spectrum of branched polyethylene exhibits no chemical or conformational changes (Svoboda et al., 1990).

After heating an isotactic (probably high percent crystallinity) *polypropylene* sample at 300°C, polypropylene does not exhibit chemical change. It is assumed that the molecular weight of polyethylene increases due to long-chain branching which increases the polymer viscosity at about 200°C (Svoboda et al., 1990) while the primary degradation mechanism is chain scission Polypropylene has been converted to gasoline range chemicals in the presence of zeolite-catalysts (Mordi et al., 1992). The process took about 2 hours at 350°C and no solid polymer remained at the end of the process. The addition of carbon black decreases the thermal stability while the addition of red pigment increases the stability (Wallius, 1993).

Poly(styrene) is known to undergo thermal degradation above 250°C to yield mainly monomer (Garrett et al., 1990). Between 200 and 300°C, the molecular weight of PS falls, but volatilization is not significant below 300° C (McNeill et al., 1990). Degradation occurs via scission of the carbon backbone, either randomly or at weak links with a peak in degradation at 392°C. Above 300°C, the polystyrene degrades into monomer, small amounts of toluene and a-methylstyrene, and oligomers (very short chains made up of monomer). Among other products, toluene and ethylbenzene have also been found in the decomposed products of polystyrene (Sato et al., 1990; Imasaka et al., 1992).

When exposed to high temperatures (in excess of 300°C), *Teflon* degrades to pure monomer. At high pressures (1013 mbar or higher) Teflon primarily degrades to three and four carbon fluoro-carbons and a poisonous gas monomer

Polyurethane can be subjected to high temperatures in the absence of oxygen to obtain the original petrochemical reactants; isocyanates and alcohols (Kutty et al., 1992). It is common knowledge that the addition of reinforcing high temperature fibers to a polymer system improves many properties such as thermal resistance. In the case of polyurethane reinforced with kevlar fibers, the degradation begins at 245 to 255°C and reaches peaks at 383°C and 448°C (Kutty et al., 1992). However, the transition temperature of polyurethane alone is significantly lower. Serious decrease of foam thermal stability begins above 160°C. The first evidence of weight loss in un-aged PUR foam is at temperatures between 200-300°C and it is caused by rupture of the primary bonds in the polymer. At temperatures between 240-540°C weight loss involves thermal and oxidative degradation. Aged foams showed similar but more pronounced weight loss. The Tg of polyurethane is 82.5°C, the melting temperature 182.5°C and the decomposition temperature 250°C at which the polyurethane foam degraded to urethane units (Rek et al., 1990).

When *PVC* is exposed to elevated temperatures, even below its melting point, PVC loses chlorine which forms HCl and becomes discolored, leading to deterioration of properties (Okieimen and Ebhoaye, 1992; Bisi et al., 1994). The T_g of PVC is about 81°C (Naqvi, 1991). The steps of PVC degradation (initiation, fast zip-elimination of HCl and simultaneous formation of [polyethylenes], and termination of the zip) are the same irrespective of the type of degradation (thermal, thermo-oxidative, photo or mechanical) (Ivan et al., 1991). Between room temperature and 185°C minimal weight change is observed for untreated PVC. HCl is produced between 185°C and 375°C. Structural reorganization occurs between 375°C and 550°C. Structural degradation in which hydrocarbons are evolved occurs above 550°C (Chatterjee et al., 1994). The Yucca Mountain Project will be primarily concerned with the first two stages. In air, the HCl

generation is doubled (Nass and Heiberger, 1986). Since HCl is corrosive and highly reactive, its presence in a potential repository will be of significance. In addition, the formation of chlorinated toxic compounds and/or other noxious substances depend on the different additives commonly used in commercial grade PVC (heat and light effect stabilizers, lubricants, extenders, pigments, dyes, etc.) (Bisi et al., 1994). PVC is intrinsically thermally unstable. PVC undergoes chain scission in the presence of metal soaps.

The great commercial importance of PVC is due to the development of effective means of stabilization. Thermal degradation is generally considered to be initiated at unstable sites within the polymer structure. Thermal stabilizers are known to function by replacing labile atoms in PVC; they inhibit or suppress the elimination of HCl and interrupt the formation of conjugated polyene sequence in the polymer (Okieimen and Ebhoaye, 1992). It has been shown that soaps from rubber seed oil are effective in preventing dehydrochlorination. Metal sterates ($PbSt_2$, $CdSt_2$, $BaSt_2$, $CaSt_2$, and $ZnSt_2$) have been used as stabilizers, reducing the rates of free HCl evolution destroying peroxides and peroxide radicals (Ivan et al., 1991). The main cause of instability in PVC is abnormal internal structures. The rate of dehydrochlorination may depend on internal double bonds, and allylic chlorines located at chain-end (Xu et al., 1989a). The terminal double bonds of PVC affect the intrinsic thermal stability. Fewer or greater terminal double bonds than the optimum has lower thermal stability (Xu et al., 1989b).

Silicone rubber has a useful life of up to 20 years at 120°C or up to five years at 150°C (Lynch, 1978) which is considered outstanding relative to other polymers.

The presence of oxygen in the environment of a polymer almost always speed up degradation. If the polymer contains hetero-atoms, then polarity governs the rate of oxidation. In addition, it is important to note that stability to thermal degradation is not always the same as stability to oxidative degradation for a given polymer. Oxygen susceptibility is dependent on the state of the polymer. For example, polystyrene oxidizes readily in solution but not in solid form. In addition to chemical structure, physical structure affects the rate of oxidation.

Polyethylene is unstable in the presence of oxygen in air, eventually degrading to carbon dioxide and water. This process takes a about 18,000 hours at 20°C, but is expedited at higher temperatures, 31 hours at 80°C (Barr-Kumarakulasinghe, 1994).

The oxidation of *polypropylene* causes the melting point to decrease (Wallius, 1993).

Plasticization and swelling result when solid polymers are exposed to various solvents (Kaplan, 1991), some of which may be present, or may be produced in a repository setting. In a poor solvent, where the interactions within the polymer chain

are strong and the interactions with the solvent are weak, the polymer molecule will have a tight conformation. A stronger solvent causes the molecule to spread out so that there is more interaction between solvent and polymer. In addition, chemicals can degrade polymers. When placed in a swelling agent such as water, hydrophilic glassy polymer networks swell and form gels (Khare et al., 1992). Environmental factors affect the solvent interaction. Often, an increase in pH will lead to an increase in swelling force. Temperature also has an influence on solvent interaction and appears to be consistent with Arrhenius activation theory. The kinetics of equilibrium concentration can be explained by the first-order kinetic rate equation. In addition, most polymer/solvent systems follow Fickian diffusion (Khinnavar and Aminabhavi, 1992).

Epoxy resins vary in sorption characteristics with different cures and different resins. The huge variety of resins, curing agents, additives exacerbate the difficulties in understanding how solvent damage occurs. In addition swelling and plasticization occur to different extents depending on the solvent. Studies conducted at 22, 40 and 50°C indicate that water produces absorption to about 3 percent (Kaplan, 1991). In contrast, methanol, ethyl acetate, 1,2-dichloroethane and toluene are taken up rapidly by the epoxy from 10 to 20 percent. An increase in temperature increases the sorption of various solvents. This is because as temperature increases, there is more motion in the molecular chains and thus more interaction with solvents (Kaplan, 1991).

Polypropylene interacts with a wide variety of solvents in which it either swells or degrades.

PET, in crystalline form and at room temperature, is resistant to dilute aqueous mineral acids, nonbasic salts and many organic compounds while being vulnerable to oxidizing reagents and aqueous alkalis.

The conversion of *PS* to low molecular weight products is dependent upon both the kind of solvent used and the solvent concentration. The conversion was low in solvents that are hydrogen donors. The decrease in solvent concentration brought a rise in the conversion and the tendency was significant in good hydrogen donor solvents. These results were explained through hydrogen abstraction processes from the solvents by the polymer radicals (Murakata et al., 1993)." Specifically, "the conversion of PS to low molecular weight products [is] dependent on the hydrogen donating ability of the solvents used: Solvents with greater donating ability [result] is less conversion of PS (Sato et al., 1990)."

Polymer deformation often occurs when a polymer comes into contact with heat or a highly reactive solvent. Likewise, *polyurethane* elastomers have been found to react with solvents depending on the solvent and the temperature. In tetrahydrofuran, dioxane,

cyclohexanol, acetophenone and benzyl alcohol, the polymer swells, even at room temperature. In pyridine and aniline, there is a loss of physical integrity which leads to chemical degradation reactions (Aminabhavi and Aithal, 1990). Furthermore, the addition of a basic solution would also break down the polyurethane structure.

Silicones have very good chemical resistance and remain chemically resistant at higher temperatures. In contrast, most other polymers loose their chemical resistance at higher temperatures (Lynch, 1978).

6.2.1.5 Radiation Effects. The effect of radiation on polymeric materials has been studied since the construction of the first nuclear power plants in the 1950s. When exposed to high-energy radiation, polymeric materials undergo chemical changes. The energy from the radiation excites the polymer molecules leading to chemical change. Most energy is deposited in the substrate by Compton scattering, whereby the ejection of a valence electron is accompanied by deflection of the incident photon by the electron cloud around the atom. At lower energies, the incident photon is completely absorbed by the substrate atom to produce ionization. Radiation degradation can be measured from changes in the molecular weight from which, the degree of cross-linking and scission can be determined. After irradiation, polymers continue to undergo changes. For example, irradiation in air leads to the formation of peroxides and these compounds have characteristic rate versus temperature relationships for decomposition, usually with significant rates in the range 50°-150°C (O'Donnell, 1990).

Radiation enhances degradation, especially thermal effects, which often occur in parallel with radiation exposure. As energy is added to a system, the temperature is raised. The reaction rates are often quite different in a glass and rubber of a given polymer and undergo changes at the transition temperatures. The deterioration in the properties of polymers may be markedly increased by relatively small rises in temperature (Garrett et al., 1990). This tends to be the case with most chemical reactions due to the energy provided by an increase in temperature. An increase in temperature when combined with radiation leads to an increase in chain scission. Radical reaction kinetics are dependent upon the polymer morphology, crystallinity, molecular weight distribution and the main chain stability as well as its higher structure (morphology) (Kaplan, 1991). Time-temperature-dose rate models have been developed to predict the long-term aging of polymers exposed to radiation (Gillen and Clough, 1989).

The surface effects of radiation tend to be much greater than the effects to the core of a sample due to greater exposure of the surface. The polymer can be affected directly by the radiation or by the products of radiation from the polymer's environment, specifically the thermal and chemical characteristics of the environment. As a result of

energy transfer, molecular components present in only small amounts may be the main sites of chemical change (O'Donnell, 1990). In addition, hydrogen atoms are often yielded due to radiation which can lead to cross-linking. The penetration of low-molecular-weight liquids into the volume of many polymers leads to a decrease in the radiation yield of cross linking (Smirnov and Dubova, 1992). Because light is a type of radiation, some correlations can be made between degradation caused by light (photo-degradation) and gamma radiation. The energy from light is sufficient to break chemical bonds, especially short ones. In addition, chromophoric groups (double bonds) are necessary to absorb the radiation. Strong absorbers are expected to decompose roughly three orders of magnitude faster than weak absorbers (17). Because absorption of radiation is an essential first step to photo degradation, strongly absorbed radiation will be attenuated as it passes through the polymer and reaction will be concentrated in the surface layers. Thus, photolysis is often identified by the evolution of hydrogen, the *development of insolubility* and discoloration. In addition, UV radiation often initiates oxidation. Photo degradation can not readily be predicted from the chemical structure due to small impurities and abnormalities often present in polymer chains. It must be tested experimentally.

Thermosets have much more stability to irradiation that thermoplastics. Counterintuitively perhaps, thermosets exposed to radiation in air degrade more, the *lower* the dose rate. This is because of the oxygen concentration in the interior of samples. The dissolved oxygen reacts with the radiation induced radicals and builds peroxides. Thus, the thermoset becomes unstable and slowly decays by chain scission. The longer the irradiation time, the more complete is the break down of the peroxides and the damage to the material (Wilski, 1990).

Epoxy resins tend to be quite radiation resistant with fillers providing even more stabilization. Most studies have irradiated the epoxy with high doses at short time intervals. In all cases, epoxy plastics proved to be extraordinarily resistant to radiation (7). Samples exposed to a low dose rate for ten years showed the same effects as the short term, high dose samples. Strength remained the same, however surface-dependent properties were markedly influenced by the does rate (Gilfrich and Wilski, 1992).

Not surprisingly, the irradiation of *nylon (polyamide)* is reflected in the mechanical properties. As radiation dose is increase, the structural integrity is decreased. In one particular study on nylon 6 fibers, it was found that melting temperature decreased, as did degree of crystallinity, with radiation dose (Ellison et al., 1989). The presence of oxygen enhanced the effects of the radiation.

Polybutadiene crosslinks when exposed to radiation. The degree of cross-linking can be established using NMR to determine the amount of carbon-carbon double bonds. Radiation causes free radicals to form which then crosslink. "Upon reaching the glass-transition temperature of the elastomers, more than half of the initial radical concentration had decayed (Dole, 1973)." As energy is increased, temperature increases. Once the Tg has been surpassed, segmental motion begins.

The degradation products of *PET (polyester)* exposed to radiation are carbon dioxide, carbon monoxide, methane and hydrogen gas. The products are affected by the exact structure of the PET, chemical composition and the presence of other reactants such as moisture and oxygen (Dole, 1973).

The degree of degradation due to the irradiation of *polythylene* is a function of its crystallinity; the higher crystallinity samples were found to be mechanically stronger after irradiation (Torikai et al., 1990). In addition, irradiation of low density PE yields a lot of cross-linking while chain scission is primarily achieved in medium and high density PE. It is thought that segmental motion of the polymer chains affects the polymer stability (Torikai et al., 1994). Radiation increases the degradation of *polyethylene*, especially when in contact with a solvent such as toluene, xylene or benzene (Smirnov and Dubova, 1992). The degradation products have little effect on plutonium solubility (Greenfield et al., 1993), however the potential formation of colloids is not known. Radiation causes both cross-linking and oxidative degradation. Irradiation of polyethylene caused both oxidative degradation and crosslinking, and the kinetics of the first process were controlled by diffusion of atmospheric oxygen into the bulk of the material (Spadaro, 1993). In addition, the temperature affects the mobility of free radicals.

In the case of *polypropylene*, the lower the crystallinity, the lower the irradiated degradation. In addition, the narrower the molecular weight distribution, the more stable the polymer is to radiation degradation. Four main radical species formed during the irradiation of polypropylene are alkyls, allyls, polyenyls and peroxys (Williams, 1990). Radiation effects on polypropylene are greatest when oxygen is present due to oxidation which is accelerated by radiation. This leads to discoloration and embrittlement. Oxidation occurs at a greater rate on the surface of samples and the degradation continues after radiation exposure. Published results show that post-irradiation degradation of [polypropylene] occurs by oxidative mechanism due to the free macro-radicals trapped in the crystalline regions (Khoylou and Katbab, 1993). One study followed post-radiation affects for 12 months and found that degradation continued via chain scission mechanism. The recommendation was that semi-crystalline

polypropylene should be stabilized against post-irradiation degradation, if it is going to be irradiated by high energy radiation sources (Khoylou and Katbab, 1993). Quenched polypropylene with a lower crystallinity has a higher radiation durability in than unquenched polypropylene. Also, higher molecular weight polypropylene degrades less than does lower molecular weight polypropylene (Ishigaki and Yoshii, 1992).

Polystyrene is quite radiation resistant and has been used in many early applications (Dole, 1973). However, radiation exposure expedites the degradation process. In the case of polystyrene, IR spectrometry has shown that the aromatic and aliphatic groups are broken down exponentially while carbonyl groups are increased (El-Agramy and Shabaka, 1990). Radiation was found to enhance the rate of thermal degradation, corresponding to an increase in temperature of about 100°C (Garrett, 1990).

Although *Teflon* has superior thermal and chemical stability, its well known sensitivity to radiation limits its use in many cases (Wheeler and Pepper, 1990). Radiation damage is usually concentrated on the surface of the material. X-ray photoelectron spectroscopy (XPS) has been used to model Teflon and it is thought that the surface is made up of a network of branched or cross-linked fluorocarbon chains. With radiation, there is a loss of fluorine and an appearance of unsaturation as saturated fluorocarbon gas is evolved (Svoboda et al., 1990). This continues until a certain level of damage is reached, after which the material degrades into saturated and unsaturated fluorocarbons.

As with other polymers, exposure to radiation accelerates degradation reactions. According to Nass and Heiberger (1986), "If unstabilized *PVC* is exposed to heat (temperatures above 100°C), ultraviolet light, or gamma radiation, then depending on the intensity of the exposure and the type of PVC, a cleavage of HCl accompanied by polyene sequence formation and cross-linking along the chain or intermolecularly can occur," which is intensified by the presence of oxygen. However, PVC has been shown to have little effect on plutonium solubility even after extensive α-irradiation (Imasaka et al., 1992).

When *silicone* is exposed to radiation, it initially forms crosslinks but as the radiation generates more heat in the silicone, it degrades. The crosslinks cause the silicone to become more rigid. Thus, the physical lifetime of silicone exposed to radiation is often dependent on the flexibility needed from the sample (Lynch, 1978).

6.2.1.6 Colloid Sorption and Chelation. Colloids exist naturally as fracture-lining materials, clays, bacteria, algae, and humic acid, but they can also be the product of degradation of man-made materials and debris, such as glass, fuels and greases, metals, biomass evolved on introduced materials and organic waste (see e.g., Meike and

Wittwer, 1994). A number of processes have already been identified as potential originators of radionuclide sorbing colloids in the WP environment (Olofsson et al., 1981, 1982a,b). These are:

1. Leaching of the waste form by groundwater.
2. Corrosion of canister material (iron oxides and hydroxides).
3. Degradation of backfill material (if present).
4. Naturally occurring colloids such as clays, organics, and precipitates.
5. Organic materials that result from man-made modification of the NFE.
7. Extracellular and cellular microbial biomass.

Hydrocarbons that result from the thermal decomposition of greases, paints, and other organic items can form ligands that may enhance radionuclide transport. The little data that exists on this subject suggests that organics more effectively complex radionuclides than inorganic complexes or single ions (Raloff, 1990). The presence of colloidal and organic products may thus produce an environment that greatly enhances radionuclide migration. As a result, the movement of radionuclides may not be predictable through inorganic chemistry alone. The number and significance of other materials to be used in the repository that fall into this same category are still unknown.

Polymers do not readily sorb metals, however, there have been many polymers which have been chelated in order to promote sorption of metals. The stereochemistry and the nature of the complexes are markedly dependent upon the molar ratios of the reactants, the pH of the system and the nature of the anions involved (El-Sonbati et al., 1994). There are also data for metal complexes involving aliphatic alcohol compounds binding through deprotonated hydroxyl groups. The data for these complexes indicated that deprotonated hydroxyl binding is strong compared to carboxylate binding, especially at higher pH values (Greenfield et al., 1993). An extensive project undertaken by Raber and Garrison (1983) to determine which materials would limit the effects of radionuclide sorption. It was found that polypropylene and polyethylene sorbed the least.

There have been many studies of metal chelates of polymers for high performance and filtering applications, especially of epoxy. In one study (Kurnoskin, 1992), it was found that synthesized metalliferous epoxy chelate polymers have high thermal stability and chemical resistance when compared to the polymer alone.

Metal adsorption sites on *polypropylene* are likely to be carboxyl and carbonyl groups formed as the surface degrades under the influence of oxygen, heat or light, other sites are contributed by catalysts, plasticizers and fillers (Kim and Hill, 1993). Polypropylene is known to absorb significant amounts of lead from solutions. A study which

compared the sorption of lead to polypropylene and borosilicate glass found that at pH 7.0, polypropylene "adsorbed significantly more lead than borosilicate glass and that at pH 5.5 polypropylene adsorbed less than the glass," indicating a fundamental change in the nature of the polypropylene surface (Kim and Hill, 1993).

Many chelating resins have been developed with the intent to separate and recover metal ions (i.e., from dilute solutions). It has been found that the hydrophobic character of the *polystyrene* backbone negatively affects the access of metal ions to the chelating groups in the resin. The presence of hydrophilic ligands in the polymer network improves chelation (Chessa et al., 1991). Column experiments have shown that pH is also a factor owing to the different rate of formation of the immobilized chelated species. At pH=6, Pt(IV) flows unaffected from a mixture of Pd(II), Pt(IV) and Au(III), whereas Au(III) and Pd(II) are both retained and successively separated by selective elution. From the same mixture at pH ≤ 0 only Au(III) is sorbed by anionic exchange (Chessa et al., 1991).

Russian studies have suggested that the sorption of various radionuclides from sea water on *Teflon* is time dependent. Others have shown that in the presence of tetraphenylboron, there is selective sorption of trace amounts of cesium from aqueous solution onto the hydrophobic surfaces of polyethylene and Teflon (Raber and Garrison, 1983). This same study found that Teflon was the least sorptive of all the polymers tested.

General Significance to YMP. It has been found that at elevated temperatures, and for many polymers, temperatures within the range of potential repository conditions, polymers are quite susceptible to degradation, so much so that the most of the polymers will degrade within hours rather than the thousands of years which the repository must contain the waste. Given this, it may be possible to plan to observe the impacts of polymer degradation during the retrieval period. However, some care will need to be taken with respect to polymers because the high temperature effects will not be observed. Further studies and modeling should then be conducted with such rates in mind. For example, much of the chemical modeling of long-term chemical effects on the NFE may be conducted with the final products of the polymer degradation as reactants. The final products of most polymers are known, the majority are monomer, hydrocarbons and some volatile products such as toluene, xylene and cresol. Polymer resins should not be used in any structural applications and chemical significance should be assessed for each material. Because of a number of potential thermal degradation effects, epoxy resins should not be included in the permanent structure, without detailed long term tests.

6.2.2 Biotic Chemistry (microbially mediated chemistry)

There is growing awareness that biotic factors could affect the integrity of the repository by a number of processes. These include microbially induced corrosion (MIC) of the waste package and construction materials, alteration of the chemical environment, and contributions to the transport of radionuclides. A variety of different types of bacteria normally inhabit the deep subsurface. In the course of construction both new materials and non-endogenous bacteria will be introduced to the repository environment. Conditions after waste emplacement are expected to alter dramatically. Extremely elevated temperatures with accompanying desiccation, and possible radiation exposure, are among the environmental conditions expected to result from radionuclide decay. Microbes can survive and adapt to extreme environmental conditions, take advantage of microenvironments, and remain active in generated spatial gradients. Microorganisms employ extremely diverse modes of metabolism. For the purpose of repository performance, this translates to mean that microbes can be involved in a wide variety of processes in a geological setting (see Horn and Meike, 1995 for a detailed discussion of the issues). Information on the degradation of various materials of significance to a repository are being gathered from diverse sources (see the section on polymer biodegradation below) of particular use are the data that have been collected with respect to the bioremediation of landfills and other forms of chemical waste.

Microbially mediated chemical processes can significantly alter the geochemical environment and have direct impacts on repository materials. Microbes are capable of utilizing a wide range of organic compounds to serve as sources of carbon. Autotrophic organisms are capable of carbon dioxide fixation to satisfy carbon requirements for synthesis of cellular materials. Energy can be derived from either reduced organic or inorganic compounds. Hydrogen gas, nitrogen, ammonia, nitrite, ferrous iron, and reduced sulfur compounds, for example, can all be used as energy sources by various microbial groups. Similarly, oxygen or a wide array of inorganic compounds may be utilized as a terminal electron sink. Nutrient supply, rate of nutrient transport, and the composition of the repository community will govern the specific types of metabolic activities that occur. Bacteria can also bind metals, secrete metal-complexing compounds, and transform metal ions to altered speciation states. These capabilities may enable the transport of radionuclides from the near-field environment. These considerations demonstrate that microbial biota are integral to environmental mass transfer. Thus, microbial contributions to overall environmental chemistry cannot and should not be ignored if prediction of the long-term integrity of a nuclear repository is

aimed at accurately reflecting environmental processes. In this paper we examine the potential effects of microbial activity on repository performance and present a perspective for future directions to better understand and predict these effects. Specifically, we provide an assessment of standard and non-standard microbiological techniques with respect to their potential for providing information of use to the Yucca Mountain Project.

6.2.2.1 Biodegradation of Polymers. While natural polymers are readily broken down by microbes, synthetic polymers are more resistant. One reason for this is that a main source of energy for micro-organisms is the breaking of the carbon-hydrogen bonds which release energy. Another reason is that the enzymes required to break down these synthetic polymers are not found in nature. The biodegradation of polymers is also dependent upon the intrinsic viscosity and the product structure. For example, a flexible foam will degrade faster than a rigid foam which will degrade faster than a solid product. A last reason is that the most important type of enzymatic polymer cleavage reaction is hydrolysis which occurs exclusively inside microbial cells. Thus high molecular mass polymers would need to enter the cytoplasm before depolymerization (Schink et al., 1992). It would seem that by copolymerizing a synthetic polymer with a natural polymer, degradation could be achieved. This, however, is not the case. Studies in which starch is incorporated into the polymer structure have shown that while the starch components do degrade, the synthetic polymer structure only collapses into smaller pieces which still resist degradation. However, many degradation products of polymers are biodegradable.

Because *polyamides* are hydrophilic it seems that they might be susceptible to microbial attacks. This, however, has been refuted in many tests and "it is well known that these compounds are generally resistant to microbial degradation as their chemical structures are not found in natural polymers (Andreoni et al., 1993). Although, polyamides have been created which can be degraded, this is a far cry from the degradation of a commercial nylon product. Even nylon 6, which tends to have less desirable properties than the widely used nylon 6,6 are not biodegradable when the number average molecular weight is greater than 1000 (Andreoni et al., 1993) (a polymer of this small size would not be useful for any commercial products).

Polyesters used in the manufacture of a polyurethane have been shown to be degraded by fungi. The polyester segment of a the polymer is the main site for attack which could be degraded within two weeks (Kay et al., 1993). However, these experiments were supplemented with yeast and the assumption was made that the polymer was consumed as a result of cometabolism. In another study of bacterial

degradation of polyester polyurethane (Kay et al., 1991), it was found that bacteria could not degrade the polymer within a 12 week test period. Clearly as in most cases of biodegradation the type of microorganism and the environmental conditions are important variables.

There has been some study of the possible degradation of *polyethylene* as it would be something desirable from the standpoint of diminishing the growth of land fill. It has been found that polyethylene does not readily biodegrade. One study tested several types of bacteria on their ability to degrade polyethylene. It was found that only one type could degrade the polyethylene and then only when the sample was put in a medium which was desirable for the bacteria; no degradation of the control samples occurred. The study further hypothesized that polyethylene is degraded into its simple components (Awasthi, 1993). In addition, it was found that degradation increased when oxygen levels were increased. Polyester *polyurethanes* have been found to degrade via microbial attack. Polyether *polyurethanes* have been found to be more resistant polyester polyurethanes (Kay, 1993). Thus, it is assumed that the weak "link" is the polyester rather than the polyurethane. In another study, it was found that polyester polyurethane could not be degraded by bacteria (Kay, 1991).

6.2.2.2 Microbes at Yucca Mountain. Given the wide variety of microbially mediated effects and the complexity of microbial processes, studies to assess potential impacts of microbial activity on the Yucca Mountain repository should include a variety of techniques. These investigations should include laboratory studies of Yucca Mountain-derived microbial isolates (representative of both native and introduced populations) chosen to determine bounding conditions for various microbially-mediated reactions. Carefully chosen analog studies can also supplement characterization of in situ reaction rates to best predict long-term microbial effects. Assessment of microbially-mediated transport of radionuclides can best be examined using perfusion analyses and determination of the binding and transformative capabilities of Yucca Mountain microbial community members. Traditionally, microorganisms are grouped and identified using physiological and metabolic typing criteria. Identification of organisms therefore provides a means of estimating their potential involvement in significant chemical impacts. These studies will generate a roster of the organisms present to the level of genus (and species, where possible and necessary), under selected temperature, humidity, and radiation conditions. The identification of entire microbial communities will allow the establishment of boundary conditions for microbial survival and activity. Traditional culturing techniques that rely on the growth of collected organisms as a means of identification are not entirely

representational. Therefore, these techniques should be supplemented with molecular means of characterizing and quantifying extant Yucca Mountain microorganisms under varying conditions.

The next step is to determine whether these activities are ongoing in both perturbed and unperturbed microbial communities, and assess the magnitude and rates of those reactions that are expected to alter the repository environment. Traditional biochemical assay techniques are available to determine biogenic acid production, hydrogen sulfide generation, metal transformations, and the soluble gas evolution. However, these techniques are not wholly amenable for the determination of in situ reaction rates. Therefore, they too can be supplemented with more advanced molecular techniques to better predict the impact of microbial affects on geochemistry and repository components.

Growth of Whole YM Communities. Samples of Topopah Spring tuff were initially aseptically collected from a mined Fran Ridge outcrop (the Large Block Test Site, LB), and rock excavated during construction of the Exploratory Studies Facility (ESF, Yucca Mountain, NV). The aim was to collect rock samples which had been exposed to construction activities and were representative of the post-construction repository environment. Bacteria which had been introduced by construction machinery, introduced materials, and human intervention could thus be included in subsequent isolations and testing.

Growth rates of YM-derived microbial communities were determined by adding 10 g of crushed rock samples (1.7-2.4 mm grain size) to 50 mL of R2 broth, a low nutrient formulation (Reasoner and Geldreich, 1985). Samples were incubated aerobically by shaking in covered flasks at ambient temperature, 30 °C, and 50 °C. Sterile controls were prepared by repeated cycles of autoclaving (120 °C) and incubation. Growth was monitored by periodic live plating of appropriate dilutions on R2 agar (Difco).

Growth rates of whole communities of YM-derived microorganisms in low nutrient R2 broth varied somewhat, depending on the temperature of incubation. While communities grown at room temperature or 30 °C showed altered doubling times with respect to those grown at 50 °C, all cultures, demonstrated significant increases in cell numbers, ranging to over 20,000 cells/mL of media, at the conclusion of the 30 h growth period (Fig. 6-21). Additionally, it was found that some bacterial isolates, most likely spore-forming species, survived repeated exposure to 120 °C.

These results reveal that even a modest nutrient source supports significant logarithmic growth of native and introduced YM bacteria, and total microbial cell

densities reach similar levels regardless of the temperature of incubation (Fig. 6-21). Probable spore-forming microbial species were able to survive repeated autoclaving (120 °C), demonstrating that even at the highly elevated temperatures expected to occur after waste emplacement in the repository, some of the endogenous microbiota may be able to survive through these extended periods of intense heat.

Isolation of Individual YM Bacterial Strains. Microorganisms were isolated both aerobically and anaerobically from whole and aseptically-crushed (1.7-2.4mm) rock samples at room temperature by plating directly, or washing rock samples with Artificial Pore Water (APW, equivalent in composition to J13 well water in the YM area; Amy et al., 1992), and plating onto low nutrient R2 agar. Organisms that survive in nutrient-depleted environments and at elevated temperature were isolated from crushed samples (1.0 g) after extended growth (aerobic incubation, 72 h.; anaerobic incubation, 17 days) in R2 broth at room temperatures and 50 °C. After extended cultivation, samples were incubated on R2 agar at the temperature of previous growth.

Plating of whole and crushed rock/washes at room temperature on R2 agar showed higher species diversity contained in LB samples than those obtained from ESF samples. Also, crushed rock/washes displayed generally lower species diversity and cell numbers than those arising from whole rock (e.g., Fig. 6-22). Finally, greater diversity and cells numbers were obtained after growth under aerobic conditions than under anaerobic culture conditions.

Extended growth at room temperature and 50 °C showed generally a low diversity of microbial forms (one to three cell types). However, high cell numbers were reached after extended growth under aerobic conditions (2×10^8-10^9 cells/mL), while anaerobic conditions produced low cell densities (e.g., 140 cells/mL), and no growth was evident after extended anaerobic incubation at 50 °C.

Since manipulation of rock samples has been reported to alter the kinds and numbers of organisms recovered (Haldeman et al., 1994), our results regarding the number and types of organisms from whole versus crushed rock are thus consistent with past findings.

YM tuff was collected and crushed exposed to the ambient air, also initial transfers of organisms cultivated on oxygen-depleted agar plates and broth were briefly exposed to air. Therefore, it must be assumed that those organisms cultivated under reduced conditions are either somewhat aero-tolerant (i.e., oxygen is not completely toxic to them, for at least brief periods), or they are capable of both oxic and anoxic growth (so-called "facultative anaerobes"). This became more evident in the results of subsequent experiments (below).

It may also be expected that both higher temperatures and anoxic conditions could result in lower cell numbers and diversity of those microbes obtained under these culture conditions. Topopah Spring tuff and its associated pore water has been characterized as generally containing a significant amount of oxygen (Buscheck and Nitao, 1994), such that strictly anaerobic, or even facultatively anaerobic organisms, might be expected in lower abundance relative to strict aerobes. Since elevated temperatures are not the norm in the subsurface, those organisms adapted to growth at 50 °C may not likewise be immediately expected to be present in high abundance. However again, the demonstration that at least some organisms at the YM site are capable of growth at higher temperatures and under lower oxygen tensions shows that a subset of the extant YM microbial community harbor the potential to grow and survive at elevated temperatures and under reducing conditions.

LB samples, originating from a Fran Ridge outcrop that more closely resembles the geological characteristics of the repository unit, display greater microbial diversity (on R2 agar) than those from the ESF-excavated rock, which had not yet reached the repository horizon. Thus, greater microbial diversity may be extant in the repository horizon than in overlying geological units.

The paucity of microbial forms after extended growth is expected. It is accepted that under stressed conditions, such as those created by the depletion of nutrients, that only a few members of the community are equally well-adapted to exploit the minimal resources available; these will outgrow those species less able to compete.

While any given growth media (e.g., R2) permits only the growth of a small fraction of a microbial community (Atlas, 1982; Roznak and Colwell, 1987), a multiplicity of microbial types were still detected from whole and crushed YM rock on R2 media; henceforth these were treated as a sample of the total microbial community present at this site. A representative group of distinct individual isolates were purified by repeated streaking of single colonies, many of these were identified by fatty acid analysis (Welch, 1991; Analytical Services, Inc., VT), but some remain unidentified. All purified isolates (ca. 60) were preserved for use in further experiments.

Identified and preserved YM bacterial isolates included representatives of the following genera: *Bacillus, Arthrobacter, Cellulomonas, Corynebacterium, Pseudomonas, Staphylococcus, Xanthomonas,* and *Flavobacterium.* These bacterial classes collectively contain members that are capable of forming spores, producing acids, degrading a wide variety of organic compounds, and remaining active under both oxic and anoxic conditions.

Enrichment of Corrosion-Specific Bacteria from YM Tuff. The oxidation of Fe(II) to Fe(III) and the reduction of sulfate to sulfide are elements of different microbial metabolic pathways that have been linked to metal corrosion processes (Lee et al., 1994; Borenstein, 1994). Therefore, efforts were made to culture organisms that carry out these transformations from YM geologic samples.

Iron oxidizers, such as species of bacteria of the genus *Thiobacillus*, utilize Fe(II) as an energy (electron) source with the concomitant production of Fe(III), and they obtain carbon for cellular growth by fixing carbon dioxide from the surrounding atmosphere. The ferric iron produced by these bacteria can react with iron sulfide (pyrite) spontaneously to form more ferrous ions and sulfuric acid. As a result, iron oxidizing bacteria have evolved to function under very acidic conditions.

Iron oxidizing microorganisms were cultured from YM tuff by inoculating 5 g samples of crushed tuff into media previously reported to support the growth of these organisms (i.e., ATCC Media #64, containing Fe(III), no exogenous carbon source, and at pH 2.8; Gherna et al., 1989). As a control for suitable growth conditions, three known and characterized iron-oxidizing microbial strains were grown in parallel with those enriched from YM tuff (*Thiobacillus ferrooxidans* ATCC#21834, #14119, #33020; Gherna et al., 1989).

Sulfate reducing bacteria use sulfate as a terminal electron sink, thereby transforming it to sulfide. These organisms typically are grown with lactate as a carbon and electron source. Thus, to encourage the growth of these organisms from YM geologic media, 5 g samples of aseptically ground tuff were similarly inoculated into two types of media containing sulfate and lactate (Baar's media and sulfate-reducing media; Gherna et al., 1989; Atlas of Microbiological Media-ref). The suitability of growth conditions was judged by the growth of a known sulfate-reducer, *Desulfovibrio vulgaris* ATCC#29579 (Gherna et al., 1989), grown in parallel with test samples.

All cultures were incubated at room temperature and periodically, 5-10% of the culture was transferred to fresh media; a total of four transfers were made over several months of incubation. In this fashion, if iron-oxidizing or sulfate-reducing organisms were extant within the samples, their growth would be encouraged due to hospitable culture conditions, over other members of the microbial community.

All control strains grew well under the conditions provided, showing that the media and conditions used did allow growth of these types of organisms. The iron-oxidizing enrichments from both LB and ESF geologic samples, likewise produced iron-oxidizing cultures (as judged by later plating on solid ISP media; Manning, 1975; e.g., Fig. 6-23). However, sulfate reducing bacteria were not recovered from all ESF geologic samples,

despite repeated attempts using two types of sulfate reducing media and the growth of the control strain under the same conditions. Sulfate reducing bacteria were recovered using the same enrichment techniques from some select sites within the ESF however, demonstrating that the presence of sulfate reducing bacteria, key players in the corrosion process, are not ubiquitous.

Enrichment cultures may or may not be a single bacterial species or strain. Thus, it must be assumed in the absence of further characterization, to be a consortium of bacteria having either predominantly sulfate-reducing or iron-oxidizing metabolic modes. Iron-oxidizing enrichment cultures were frozen for preservation and use in further experiments, as were the sulfate reducers that were obtained outside the immediate YM site.

Iron reducing strains, which use Fe(III) as a terminal electron acceptor producing Fe(II), may effect corrosion directly by anodic depolarization (Westlake et al., 1986), and affect the availability and source of Fe(II) for subsequent microbial iron oxidation. As an initial attempt to enrich these organisms from YM rock, 5 g of crushed ESF and LB material was inoculated into a media formulation that provided lactate as a carbon and energy source and nitrate as an electron acceptor (Meyers and Nealson, 1990). This type of media has been shown to support the growth of iron reducing strains under aerobic growth conditions, however it should be noted that it will also support the growth of other types of organisms as well. A characterized iron reducer, *Shewanella putrifaciens* ATCC#8071 (Gherna et al., 1989), was grown in parallel as a control. Growth was observed of both the control strain and arising from crushed YM rock samples, and periodic transfer of the cultures were carried out (as above). Finally, after four transfers, the enrichment culture was frozen for future analysis.

Calorimetric assays for determining the concentrations of Fe(II) and Fe(III) using ferrozine reagent (Lovley and Phillips, 1987; Greenberg et al., 1985) were tested using water as a solvent. Linear standard curves were obtained [with a dynamic range extending 5-100 ppm Fe(II)] under these conditions. Iron oxidizing and possible iron-reducing consortia will be analyzed to quantify their rates of iron reduction/oxidation using these assay techniques.

Screening for Acid-Producing Bacteria. The production of organic acids as products of microbial central metabolism is well-documented (Horn and Meike, 1995). The generation of acids has been both directly and indirectly linked to metal corrosion. Microbially-generated acids have been shown to directly dissolve the protective calcareous film on stainless steel (Little, 1987). Coupling of protons with electrons results in electron removal from the cathode (Borenstein, 1994), and forms hydrogen

which is a substrate for microbial sulfate reduction (Fig. 6-24; Pope et al., 1994). Therefore, the library of YM isolates that were recovered from LB and ESF geologic samples (above) were screened for those that demonstrated a decrease in pH during active growth.

As an initial screen to identify acid-producing strains among the preserved YM microbial isolates, all isolated strains were grown separately in R2B media (with or without amendment of 0.5% glucose), using the pH indicators bromocresol purple ($pK_{indicator}$=5.3) or methyl red ($pK_{indicator}$=4.1). Under these conditions, a change in the color of the culture indicates the production of acid, thereby providing a rapid means of assessing acid production by the 46 strains tested. Anaerobically-grown strains were incubated under anaerobic conditions, while aerobically-isolated strains were cultivated with aeration, and all strains were incubated at either room temperature or 50 °C, depending on their temperature of isolation. Sterile, uninoculated controls were included in all experiments. The pH endpoint was determined using a standard pH meter for at least one trial.

Results revealed that both growth and acid production were generally more rapid when the media was amended with glucose. This is not surprising given that acid production is largely a result of carbon utilization; addition of glucose provides at once more carbon and energy for growth, together with a greater potential rate of acid generation. When 46 bacterial isolates were tested with glucose amendment, 10 (21.7%) of these displayed a decrease in pH (from about pH 7.0) to pH 5.3 or less after a period of growth lasting from 3 to 16 days. When glucose was not added to the media, only 5 strains tested showed similar extents of acid production. Sterile control cultures maintained the initial pH of the media. While there was some interference of the pH indicator with measurement of the pH endpoint (probably due to titration of protons by the indicator) and even growth in some instances, the lowest pH attained was 4.46 after a 76 hour incubation by a *Pseudomonas stutzeri* LB isolate in media with added glucose and the methyl red indicator.

These results indicated that microbially-induced metal corrosion will be accelerated with inclusion of a readily metabolizable carbon source which promotes both growth and acid production. Thus, materials testing should include added glucose in the media, as glucose will contribute towards accelerated testing conditions. Compilation of the screening results revealed eleven strains that produce acid under the described conditions of growth, which included members of the genera *Cellulomonas, Pseudomonas, Flavobacterium, Bacillus,* and *Arachnia.* (Table 6-12). Five of these strains were further analyzed to determine their rates and extents of acid generation, and to further

determine conditions under which acid is produced; these strains would be considered for specific inclusion in accelerated materials testing (below).

Screening for Sulfide Producing Bacteria. Microbially-produced sulfide may be corrosive to metals, as are the ferrous sulfides that form when produced sulfide reacts with solubilized ferrous ions. Most often these activities are associated with sulfate reducing bacteria, which directly promote corrosion by depolarizing the cathode through consumption of available hydrogen from the metal surface (Borenstein, 1994). Attempts to isolate sulfate reducers from the immediate YM environs demonstrated that these organisms are not uniformly distributed. However, microbes can also produce sulfide by the decomposition of proteins, a process known as "putrefaction" or "desulfurylation," in which the sulfur-containing amino acids methionine and cysteine are broken down, releasing sulfide in the process.

While the evidence that sulfide and ferrous sulfide *directly* contribute to metal corrosion is not entirely conclusive (Licina, 1988), a screening technique was devised to detect desulfurylating microbes among the preserved isolates contained in the YM library. These efforts were aimed at determining whether YM microorganisms harbor desulfurylation capabilities, assessing the potential contribution of desulfurylation to metal corrosion (i.e., the direct effects of sulfide and ferrous sulfide), and to ascertaining those alloys that may be more resistant to these microbial products.

All preserved isolates were screened in test tubes containing R2 agar supplemented with 0.75% proteose peptone #3 (Difco), to provide an excess supply of amino acids for desulfurylation reactions (R2 normally contains only 0.05% of peptone; Reasoner and Geldreich, 1985). Additionally, the media contained 0.05% lead acetate, which precipitates as lead sulfide when sulfide is produced as result of microbially-driven peptone decomposition; the resulting lead sulfide is detected by its blackening of the agar medium.

The library of YM bacteria were each individually inoculated into R2+peptone+lead acetate agar media contained in screw-top test tubes, by streaking on top of the agar surface (exposed to the air in the headspace of the tube) and stabbing into the agar within the tube (under which conditions growth is anoxic or micro-aerobic). Sterile, uninoculated control tubes were monitored in parallel with inoculated ones. All samples were incubated at room temperature or 50 °C, depending on the temperature of strain isolation. Growth and (lead) sulfide generation was monitored over a 34 day period.

Twenty-one of the forty-five aerobic strains tested (46.7%) demonstrated sulfide production in the oxic area of the culture (none of these were strains that were isolated

and incubated at 50 °C), whereas only three of the aerobically-isolated strains (all 50 °C isolates) showed sulfide production in the anoxic area of the culture. Three of the 17 (17.6%) anaerobically-isolated bacteria tested showed sulfide production in the anoxic butt of the tube, one of these had significant sulfide production under aerobic conditions as well. A total of 7 of the 17 (41.2%) anaerobic isolates displayed some detectable sulfide production under aerobic conditions. No sulfide production was detected in any of the sterile controls.

These results demonstrate that a significant proportion of YM bacterial isolates are capable of producing sulfide *via* putrefaction under both oxic and anoxic conditions, at least when provided with excess protein substrate. Isolates of *Pseudomonas, Flavobacterium, Bacillus, Arachnia,* and *Cellulomonas* were all found to produce sulfide; four of these isolates were found to produce both acid and sulfide using these screening techniques. The use of these putrefying bacteria in accelerated corrosion tests should allow a more precise determination of whether hydrogen sulfide and associated metal sulfides are directly capable of causing corrosion to waste package alloys. Since these microbes generate sulfides in the absence of sulfate reduction (and hydrogen utilization), the effects of *only* sulfides on corrosion can be assessed absent cathodic depolarization effects.

All strains were incubated under aerobic conditions, by streaking on top of the agar, as well as under [somewhat] reducing conditions by stabbing into the semi-solid agar surface. Many of the aerobic strains were capable of growth within the agar (all of the 50 °C-incubated cultures grew well under these anoxic conditions), and some of the anaerobes were also capable of growth under aerobic conditions. This may have been expected since the selection and transfer protocols used (above) precluded the isolation of "strict" anaerobes (i.e., those to which oxygen is toxic). Employed methods resulted in isolation of organisms that were at least tolerant to limited exposure to oxygen or so-called "facultative anaerobes," which are capable of both oxic and anoxic metabolism. Likewise, some of the "aerobes" can be facultatively capable of anoxic growth. Several of the identified sulfide producers were further quantitatively analyzed for their rates and extents of sulfide production (below).

Screening for Slime under Varying Culture Conditions. The production and export of polysaccharides (long chain sugar polymers) to the exterior of cells is characteristic of many bacterial species. Exopolysaccharide production results in the build-up of a slime layer which protects, embeds, and allows anchorage of cells to solid surfaces. The microenvironments contained within slime layers (or "biofilms") can be drastically altered from the general conditions in the exterior meileu, and from other

areas within the biofilm. Generally, it can be expected that differential nutrient concentrations, relative humidity, and oxygen tensions exist throughout the film (Costerton and Geesey, 1985). Consortia composed of different microbial species can become embedded by polysaccharide produced by one or more consortial members. These slime capsules provide a three dimensional spatial matrix that permits concentration gradients and facilitates intermicrobial interactions. Slime producing organisms probably indirectly contribute to corrosion by permitting adherence and facilitating interactions among the different types of organisms that cause corrosion. Direct effects of slime on corrosion include the creation of differential aeration cells and localized elevations of ions, which in turn form crevices under which corrosion is accelerated (Borenstein, 1994; Costerton and Boivin, 1991).

Since slime production is an integral element of microbially-induced corrosion, the library of YM bacterial isolates was screened for slime production first on R2 agar and then R2 + 0.5% glucose agar, R2 + 0.75% peptone agar, and R2 + 0.5% glucose + 0.75% peptone agar. All isolates were incubated anaerobically or aerobically at room temperature or 50 °C, depending on their mode of isolation. Slime production was assessed by observation of gross colony morphology: the appearance and quantity of a viscous slime layer was noted and scored (e.g., Fig. 6-25).

Prodigious amounts of polysaccharide were produced by two *Bacillus* isolates and two as yet unidentified isolates with very similar colony morphologies. All of these strains were identified as sulfide producers in former screening analyses, however none of these were identified acid-producers. Moderate quantities of slime were generated by five other YM strains that included representatives of the genera *Arthrobacter* and *Pseudomonas*. Retesting of six of these slime generators on R2 agar supplemented with peptone and glucose revealed that slime production varied with media type. The greatest degree slime production occurred on media containing glucose for two of the strains tested. This observation is in agreement with the fact that the synthesis of polysaccharides requires sugar precursors; amended glucose provides a source of building blocks to support slime synthesis. The other isolates showed little difference in the quantity of polysaccharide produced between media types, and one strain showed no growth at all on R2 + peptone. A single anaerobic isolate demonstrated copious slime generation on R2 agar.

These results demonstrate that YM isolates are capable of slime production under low nutrient conditions, and could therefore play a role in corrosion of waste package materials. Generally it appears that the availability of carbohydrates could increase slime production, and possibly accelerate corrosive microbial activities.

Rates of Acid Production Under Varying Growth Conditions. Five strains identified in preliminary screening for the production of acids (above) were further analyzed for their rates and extents of acid generation in R2 media containing additional peptone and glucose. Each strain was separately inoculated into R2, R2+0.5% glucose, R2+0.75% peptone, and R2+peptone+glucose. Cultures were incubated either anaerobically in serum bottles with pre-reduced media, or aerobically in shake flasks at either 30 °C or 50 °C, depending upon the mode of isolation. The pH was monitored in withdrawn samples periodically over a three to five day period (Fig. 6-26).

The two anaerobic strains (one a possible *Arachnia propionica*, the other unidentified) showed a negligible effect of added glucose and peptone, and the pH did not fall below pH5.2 in either of these cultures. The aerobically-incubated strains, however, showed greater dependence of the composition of the growth media on the production of acids. The *Pseudomonas stutzeri* isolate, LB-71h-RT-13, only generated acid when glucose was added to the R2 media, displaying a decrease to pH4.2. The pH probably did not decrease coordinately after growth of the *P. stutzeri* in R2+glucose+peptone media due to deamination of amino acids contained in the added peptone, which releases alkaline amines, counteracting the effects of acid production. This counter-effect of added peptone was not as evident in the *Flavobacterium esteroaromaticum* isolate, ESF-71h-RT-4, which showed decreases in pH after growth in both R2+glucose and R2+glucose+peptone, as did a 50 °C-isolated strain, LB-71h-50-3 (most probably a *Bacillus*) (Fig. 6-26).

In summary, the effect of available nutrients on the production acids by YM isolates varies by strain. Some isolates are only capable of acid production when supplied with an added carbon source, others are less affected by this requirement and are capable of acid generation even when available carbohydrate concentrations are minimal. Also, the presence of other metabolizable nutrient sources can affect overall pH; if end products include alkaline compounds (such as amines produced by deamination of amino acids), then acid production can be mitigated. The rates of acid production, in view of the long time spans that must be considered to evaluate the integrity of the YM repository, are significant. Rates of acid production over a three to seven day period are measurable and result in orders of magnitude differences in proton concentrations.

Rates of Sulfide Production by YM Isolates. Seven YM isolates identified as sulfide producers (*via* desulfurylation) were analyzed for their rates of sulfide production under aerobic and anaerobic conditions, because it had already been shown that many isolates are capable of growth at high or low oxygen tensions (above). All strains were inoculated into R2 media amended with 0.75% peptone. Both anaerobic (contained in

serum bottles with pre-reduced media, cysteine as a reducing agent and rezasurin as a redox indicator) and aerobic (contained in flasks) were incubated at 30 °C or 50 °C unshaken to minimize air stripping of the produced hydrogen sulfide. Uninoculated media was also incubated to detect spontaneous abiotic sulfide production. Periodically, samples were withdrawn, cells removed by filtration, and the supernatants analyzed using a modification of the methylene blue assay, which relies on the reaction of sulfide, ferric chloride and dimethyl-*p*-phenylenediamine to produce methylene blue (measured spectrophotometrically, 664 nm; Greenberg et al., 1985). Standard curves were prepared using sodium sulfide diluted in the appropriate media, and sample sulfide concentrations were calculated by interpolation of the standard curve.

Preliminary results (depicted in Fig. 6-27) showed that sulfide production *via* desulfurylation increased for all tested strains within a two day incubation period, even in anaerobic cultures which metabolize and grow more slowly than do aerobic cultures. Sulfide concentrations increased to about 500 ppb for all strains grown under anaerobic conditions and to approximately 150 ppb for the same isolates incubated aerobically. Sulfide concentrations continued to increase in aerobically grown cultures, reaching a maximum of approximately 330 ppb over a 7 day period, although extents of maximal sulfide concentrations varied between the strains tested. Thereafter, aerobic sulfide production, in general, decreased until 22 days after initiation of growth, when there was again a trend towards increasing sulfide found in the media.

These aerobic incubation results could be explained by volatilization of hydrogen sulfide from the culture (or precipitation from the soluble phase), combined with an initial growth phase, followed by cell death. In "batch" cultures such as those tested (which are not continually fed), growth of aerated cultures continues for a relatively short time, probably at the most for a week, after which nutrients are exhausted. While efforts were made to minimize the loss of sulfide through volatilization, sulfide losses could have resulted from inadvertent air-stripping or precipitation by media components in the death phase of the cultures where little or no new sulfide production could replace that which had been lost. The final increase at day 22 may be due to the growth of surviving cells on those that had died, with concomitant sulfide production resulting from metabolism of the amino acid content of dead cells.

Anaerobically-grown cultures also displayed a decrease in sulfide concentrations, starting after two days of incubation. In most cases, these decreased to zero over a 17 day period of incubation. These cultures were contained in sealed vials, and maintained under reducing conditions. Thus, loss of hydrogen sulfide from the media through volatilization is unlikely. Rather, since the employed assay only detects the presence of

soluble sulfides, it is likely that sulfide may have precipitated by interacting with other media components.

While these preliminary analyses are not entirely conclusive, it is important to note that microbially induced sulfide production increased significantly above background levels, was detected among a wide variety of YM isolates under both aerobic and anaerobic conditions, at least when strains were provided with an excess amino acid source (in the form of added peptone). These preliminary results additionally aid in determining conditions under which to conduct accelerated testing of alloy candidates, and which strains to include in accelerated corrosion tests.

Significance to YMP. Native microorganisms reside within the potential repository environment. Microbial communities have been characterized from a variety of deep subsurface environments, and ongoing work has already identified some of the native microbiota in the Yucca Mountain region (e.g., Russell et al., 1994).

Microbes vary widely in their types of metabolic activities, and the consequent alterations to the surrounding environment that they can facilitate (Horn and Meike, 1995). Historically, bacteria (and the closely related *Archea*) have been classified according to their individual metabolic types. The potential reactions actually performed by bacteria are dictated by both innate metabolic ability, and the conditions to which they are exposed. The type of metabolic activities that are possible are governed by the availability of substrates. For example, sulfate reduction with the concomitant generation of hydrogen sulfide is only possible if sulfate reducing bacteria are present and sulfate is available to this class of organisms. Presumably, native microbes that are currently present have or have had adequate resources. The establishment of bacteria introduced through drift construction will likewise be dependent on adequate nutrient supplies and their rates of adaptation to the repository environment.

Conditions anticipated upon waste emplacement in the proposed Yucca Mountain repository will include extreme heat, desiccation, and possibly high levels of ionizing radiation. The initial presence of extreme conditions within the repository may not completely preclude microbial activity; even if general conditions extend beyond those able to support microbial activity there may be microenvironments in which environmental extremes are mitigated. In any case, eventual repopulation of the near-field environment through reentry of water carrying both nutrients and microbes, is anticipated as overall repository conditions become less extreme. We may expect that organisms that thrive at high temperatures and those that form spores under adverse conditions will be extant within the native or introduced microbial communities at

Yucca Mountain, and maintain or regain activity as conditions become favorable. Microbial populations may acidify and otherwise alter the pore water chemistry of the near field repository environment, as well as directly affect the corrosion of repository waste packages. The degradation of materials and the consequent alteration of the aqueous chemical environment, with accompanying effects on repository performance, will depend on the presence of adequate nutrients and water to maintain at least a minimum level of activity.

The demands of establishing boundary conditions for microbial activity in the context of a radioactive waste repository extend beyond the information that is presently available in the literature. As a first step organisms collected from the ESF have been cultured and assembled into a YMP library. These microbes were grown in low nutrient media with various amendments and screened for various activities of significance to the long term chemical and hydrological properties of the NFE. Both the production of acid and slime was assessed under these conditions. The generation of both acid and slime for at least some isolates was increased when an easily metabolized carbohydrate (glucose) was incorporated into the media. Other culled YM acid and slime producers did not demonstrate a dependence of corrosion activities on sugar availability. It might be noted however, that the availability of carbohydrates should increase growth rates of those organisms depending on reduced carbon sources for food, such that even if sugars are not required directly for these processes, increased growth rates might be expected to indirectly contribute to increasing acid and slime production rates. These microbes have been used in estimating the required conditions for corrosion-related microbial activities, and to further optimize conditions for accelerated testing of candidate barrier alloys.

The analysis of acid production in different media types revealed that other metabolites (i.e., bacterial products), might ameliorate the results of acid production. If alkaline products are secreted to the media then acid generation is mitigated.

Taken together, while media composition plays a part in the rates and extents of acid and slime production for some isolates, it appears to have little direct effect on other isolated organisms. This demonstrates that even with a minimal supply of nutrients both of these processes are possible. Further analyses should include assessment of these activities under a broader set of conditions, including those which more closely mimic anticipated repository conditions.

Sulfide and metal sulfides have been identified as probable corrosive bacterially-generated products, most often associated with the activity of sulfate reducing microorganisms. The distribution of sulfate reducers at the proposed YM repository site

was not found to be ubiquitous, thus an alternative pathway for microbial sulfide production was explored. Many of the YM microbes contained within the assembled library were found to have the capacity to make sulfides through desulfurization of sulfur-containing amino acids; this process occurred under both anaerobic and aerobic conditions when a supplementary source of amino acids was added to the media. YM microorganisms were not tested for sulfide production in the absence of amended amino acids, however it was found in preliminary experiments that the rates of desulfurylation and concomitant sulfide accumulation increased quickly up to 0.5 ppm. Thereafter, most probably due to the culture conditions employed, sulfide concentrations were found to decrease.

Use of these desulfurylating YM organisms alone in accelerated corrosion tests should indicate the degree to which they can promote corrosion. If the contribution of sulfides and their metal derivatives is significant in increasing corrosion rates, then these processes should be analyzed further to determine their bounding conditions, rates, and contribution to other corrosive processes. The rates of these processes were very rapid when compared to the long term periods that must be considered for repository performance. Given adequate nutrients, slime, acid and sulfide generation rose to their highest levels within a matter of days or weeks. Thus, the period required for these organisms to reach their greatest corrosive potential, given the right conditions, is almost instantaneous in comparison to the functional lifetime of the repository.

6.2.3 Discussion

It is clear that the addition of man-made materials to the near-field environment (NFE) may modify the chemical environment and influence the geochemical reactions that may occur. An example of the interaction between introduced materials, rock and water is as follows. The repository horizon and the adjacent horizons contain zeolites, or they may develop zeolites during interaction of water with rock at elevated temperatures. Zeolites are common molecular sieves and sorbates. Clinoptilolite, for example, is used as a molecular sieve for the ammonium ion (Barrer, 1978b; Breck, 1974), which has the potential to degrade the repository environment. This potential beneficial effect may be counteracted by other man-made materials that could destroy the zeolite structure or provide preferentially adsorbed ions. The balance of these effects at the repository is unknown at present. Application of geochemical models to this area, where the appropriate databases exist will provide guidance and some bounding

constraints for repository design and performance assessment. Modeling and databases are described in the next section.

6.3 Understanding the Processes

6.3.1 Experimental Studies

In order to predict chemical properties over a long period of time we need to know fundamental properties of the appropriate materials. These fundamental properties are often better known for geological materials because the interest in very long term chemical prediction has existed for decades. A similar interest in fabricated materials has appeared only relatively recently, and most commonly in relationship to radioactive waste disposal efforts. Previous efforts in the area of fabricated materials has focused on optimizing fabrication conditions. This is hardly the data that is needed for predicting processes in which the environment w ill not be controlled. It is for this reason that an application driven program finds itself in need of generating fundamental data.

6.3.1.1 Data Availability and Modeling Requirements Regarding Cementitious Materials. Of the major reactant phases of cement powder—alite, belite, possible residual glass, gypsum, and ferrite [$C_2(A,F)$] (See Appendix B for standard cement formula nomenclature)—only the thermochemical data for gypsum are complete. Data are available for the pure calcium end-member equivalents of alite and belite (Haas et al., 1981), but not for their solid solutions. The significance of solid-solution characteristics of alite and belite to performance assessment may be great because not only do alkalis and other minor impurities stabilize phases, but substitution of Al_2O_3 and Fe_2O_3 may affect reaction kinetics. It is suspected that aluminum and iron substitution do not affect early hydration but slow hydration over a period of 24 hr (Ghosh, 1983). The stabilization of phases by alkali substitution has been investigated (Xiuji and Shizong, 1986) but remains poorly understood. Most of the detailed kinetic studies of hydration have employed the pure calcium end-members C_3S and β-C_2S. The thermochemical data for the calcium aluminates have been rigorously evaluated by Ellezer et al. (1981). However, no calorimetric measurements were found for the $C_2(A,F)$ solid solution, which has been characterized structurally by Jeffrey (1964).

Most of the hydrous phases of cement and the anhydrous and hydrous solid solutions lack calorimetric data. The kinetics of transformation of C-S-H into other phases at its upper temperature limit is significant to predictions of cement behavior in the repository, which will stay at 80 to 120°C for an extended time. Of prime importance

for 25°C performance modeling are calorimetric data for ettringite and tobermorite and well characterized solid solutions of these phases. The prediction of chemical reactions at greater temperatures requires more data than is presently available. Geochemical codes are also useful in the absence of these data for conducting a sensitivity analysis to determine the solid solutions or end-member phases that are critical for calorimetry. The original ΔH of formation (20°C) from CaO and silica gel thermodynamic data for all Ca_2SiO_4 phases are evaluated by Haas et al. (1981). Qualitative rate information has been obtained for ettringite components (Majling et al., 1985). Other than an enthalpy of dehydration (Maycock et al., 1974) and C_p data (Ederova and Satava, 1979) obtained over the range of 273 to 333°K, thermochemical data for ettringite are calculated (Sarker et al., 1982; Babushkin et al., 1985). The only experimental data for "monosulfate" (C_4ASH_{12}) located to date is C_p data from 273 to 353°K (Ederova and Satava, 1979). As discussed previously, the kinetics of the relevant reactions are even less well understood.

Comparisons of cement leachates with calculations performed using available data and standard thermochemical tables (Barnes and Roy, 1983) suggest the best agreement with the solutions buffered by tobermorite and possibly gyrolite. Calculated activity products have been compared with (1) experimentally obtained solution compositions (Ca^{++}, Na^+, K^+, pH, and $SO_4^=$, but not Al or $CO_3^=$) from cement hydrated for up to 3 hr (Gartner et al., 1985), and (2) pure C_3S. The comparisons suggest that although no difference in supersaturation was observed with respect to portlandite, gypsum, and syngenite [$CaK_2(SO_4)_2 \cdot H_2O$], thermodynamic equilibrium is not achieved during early hydration (Moragues et al., 1987, 1988), and high ionic concentrations of the solutions cause departure from Debye-Huckel theory. The most successful chemical models to date have been achieved by working with a limited number of equations that include C-S-H solid solutions, monosulfate solid solution, and ferrite solid solution. Glasser et al. (1985) analyze a simplified cement system as the ternary CaO-SiO_2-H_2O. Barret and Bertrandie (1986) make a similar analysis of the system CaO-Al_2O_3-CO_2-H_2O. Incorporation of aggregate into repository concrete will increase the complexity of geochemical modeling. Calculations that include portland cement, special cements, and concretes that incorporate bfs, fly ash, and silica fume (Berner, 1987) have achieved some success for equilibrium-solid-phase and pore-solution-composition data obtained from experiment, but they do not readily take reaction progress into account.

The use of numerical simulations to integrate the effects of the variables described in Sec. 6.2 complements experimental and historical investigations. Eventually, coupled chemical effects that are difficult or inaccessible through experiment can be examined.

However, even the present chemical data base (Sarker et al., 1982; Babushkin et al., 1985), although limited, can be manipulated to obtain insight into some effects that may be expected due to man-made materials. Conversely, the data base will be enhanced over time by incorporation of new thermodynamic data from the experimental and historical investigations.

6.3.1.2 Generation of short term thermodynamic data. The work that has been conducted in the area of generating more thermodynamic data has focused on phases that are expected to be part of the drift scale chemical system at elevated temperatures if OPC cement is a significant element of drift construction. As described by Meike (1995), much of the data required for long term modeling of the same caliber that presently allows us to predict the chemical interactions of the natural system is unavailable. A program was begun to obtain that data. Synthesis of Ca-Si-H_2O phases had been completed and measurement of thermodynamic data had just begun when the program was halted in November 1995. Heat capacity and entropy measurements were obtained for 11Å tobermorite using heat pulse calorimetry, but the data has not yet been analyzed. The work on other phases was halted.

In order to provide a means of verifying experimental data, and ultimately developing a means to calculate necessary thermodynamic parameters and better understand the relationship between relative humidity and the stability of Ca-Si-H_2O phases a program was initiated to conduct electronic structure calculations of Ca-Si-Hydrates (Sterne and Meike, 1995). Given the difficulties inherent in direct measurement of the thermodynamic parameters of these phases we have undertaken a set of first principles electronic structure calculations.

Electronic structure calculations, and the Linear Muffin Tin Orbital (LMTO) theory in particular are standard methods for approaching the physical properties of metals and metal alloys, semi-conductors and simple insulators (see, for example, Anderson, 1975; Skriver, 1984). In the past these methods have been confined to small systems of less than 20 atoms in a unit cell. Thus calculations for wollastonite and xonoitlite, which contain a 30 atom unit cell and 62 atom unit cell respectively would have been out of reach normally. However, recent developments in algorithms and computer power have brought larger systems within the range of these calculational techniques.

The goal of this modeling effort is to determine the energetics of hydration for crystalline Ca-Si-hydrate phases. The work performed to date represents an initial step in this direction. The initial results for the first phases undertaken for phases representing the water poor end members, wollastonite ($CaSiO_3$) and xonotlite

($Ca_6Si_6O_617(OH)_2$). The results, reported in Sterne and Meike (1995), are summarized below.

The calculated ground state properties of wollastonite and xonotlite are in very good agreement with experiment, and provide equilibrium lattice parameters within 1–1.4% of the experimentally reported values. The roles of the different types of oxygen atoms, which are fundamental to understanding the energetics of crystalline Ca-Si-hydrates, examined in terms of their electronic state densities, appear to be in good agreement with experiment for the lattice parameters and internally consistent when comparisons are drawn between the two structures. The exercise, completed with wollastonite and xonotlite, demonstrates the applicability of these electronic structure methods in calculating the fundamental properties of these phases. The electronic structure calculation methods are demonstrated to give reliable results, even for the relatively large wollastonite and xonotlite unit cells. Thus, the application of this new approach to the study of calcium silicate hydrates appears to be fruitful not only in terms of the ability to calculate heats of formation, but also by virtue of the insight that it can provide into the nature of hydration and dehydration.

6.3.1.3 Generation of short term kinetic data. The need for kinetic data is similar to that described above for thermodynamic data, but was also halted in November 1995. However, in the process of conducting the diesel fuel experiments described above, we have obtained some data regarding the degradation of cementitious material, specifically Fibercrete™. In all experiments containing Fibercrete™ (DF3, DF4, and DF6), 11Å-tobermorite formed. Thus, 11Å-tobermorite appears to be a stable, or at least metastable, phase at 200°C. As is observed in experiment DF6, the precipitation of 11Å-tobermorite, calcite and cristobalite may control geochemistry and effect porosity and permeability for waters contacting both cements and Topopah Spring tuff. The importance in the dissolution and precipitation kinetics can be seen in the slow changes in solution pH and dissolved silica concentrations and the small fraction of the initial starting material dissolved to form secondary precipitates at the Fibercrete™ and Topopah Spring tuff surfaces. In the absence of Fibercrete™, cristobalite appears to be the dominant secondary mineral formed in Topopah Spring Tuff experiments, in agreement with previous studies (Knauss et al., 1985; Knauss and Peifer, 1986; Knauss et al., 1987).

Calculations using the current data base appear to be contradictory. Aqueous chemical modeling results suggest that mesolite should precipitate from the solution. They predict that the chemical system is saturated with respect to quartz and calcite after 20 days of reaction and undersaturated with respect to 11Å-tobermorite. Zeolites

were not detected in any of the experiments, suggesting either that the thermodynamic data is not correct, that zeolite nucleation from solution has a very large activation energy, or that zeolite precipitate rates are very slow even in very supersaturated solutions. Given the painful lack of thermodynamic and kinetic data pertinent aqueous degradation of Ca-Si-H_2O phases the first option is very likely. Thermodynamic data for Ca-Si-H_2O phases are sparse and contradictory (Vieillard and Rassineux, 1992; Bruton et al., 1994; Meike et al., 1994). The constant 11Å-tobermorite saturation index after 40 days of reaction and the identification of 11Å-tobermorite in the final solid material indicates that the solubility of 11Å-tobermorite is over estimated in the current data base. Previous experiments which have investigated the stability of various phases are typically only a couple of days (Lea, 1971). Atkins et al. (1991) determined the solubility of cement hydrate phases after four weeks of reaction at 25°C. Clearly longer reaction periods are required for the crystalline phases to reach equilibrium.

From the present work, it is possible to calculate a 11Å-tobermorite solubility constant (K) at 200°C to be $10^{39.7(\pm 0.6)}$, using the experimental ion activity product for the following solubility expression for each aqueous sample after 20 days of reaction:

$$Ca_5(SiO_2)_6(OH)_{10}{\cdot}0.5H_2O + 10H^+ = 5Ca^{2+} + 6SiO_2 + 10.5H_2O \quad (8)$$

$$IAP(200°C) = \frac{[Ca^{2+}]^5[SiO_2]^6}{[H+]^{10}} \quad (9)$$

assuming $aH_2O = 1$ and unit activity of the solid phase. This simplifying assumption is also taken that only crystalline tobermorite of pure composition is involved in the chemical reaction. In the absence of other data, this IAP may prove to be a useful guide. However, the derivation does not allow for the interaction of complexes or other amorphous or crystalline Ca-Si-H_2O phases that are known to precipitate under these conditions. This calculation thus requires verification using independent checks for internal consistency.

6.3.1.4 Material behavior as a function of pH. A major unknown in the prediction of the chemistry of the potential Yucca Mountain repository is pH. A large part of that has to do with cementitious materials, if they are present as invert or stabilizing material. The pH of water in contact with relatively young cement can be relatively high (10-12). However, there are a number of considerations that lend a good deal of uncertainty to a general assumption that the pH of water in contact with cement will be high throughout the lifetime of the repository.

The first consideration is the temperature. The reason that the pH of water in contact with cements equilibrates at such a high value is that the water is in equilibrium with the amorphous Ca-Si-H_2O gel and other metastable phases. These phases will transform into less hydrous and more stable crystalline phases with time and with elevated temperature. It has not been established that the newly formed Ca-Si-H_2O phases also are in equilibrium with water at such elevated pH. In fact, there is evidence to the contrary. Hillebrandite and wollastonite, water poor end-members of the Ca-Si-H_2O system do not produce such elevated pH.

The second consideration is microbial. In general the microbial activity of pumping protons through a chemical system serves to reduce pH. This is beneficial for the microorganism because it tends to solubilize solids and thus provide nutrients.

6.3.1.5 Material behavior as a function of RH. Water adsorption studies of okenite ($Ca_{10}Si_{18}O_{46}\cdot 18H_2O$) conducted at ambient temperature, (Martin et al., 1995) demonstrate the extreme sensitivity of some of the crystalline Ca-Si-H_2O phases to relative humidity.

As part of an experimental and modeling program to characterize the effect that cement will have on the water budget at the potential Yucca Mountain repository, water sorption studies of crystalline calcium silicate hydrate phases are being performed. An adsorption study was conducted on okenite ($Ca_{10}Si_{18}O_{46}\cdot 18H_2O$) at ambient temperature over a range (3.5-97%) of relative humidity (RH) conditions. A sample of okenite from Poona, India, equilibrated at ambient RH, was divided and dried over phosphorus pentoxide (P_2O_5) and placed in chambers containing saturated salt solutions to control the RH. X-ray diffraction analysis (XRD) indicated that interlamellar swelling occurred along the (001) axis. An increase in the d(001) spacing with hydration was on the order of 2.5Å at a RH of 11% and remained unchanged at higher RH. This swelling is consistent with a monomolecular water layer in the interlamellar space. Comparison of the XRD peak positions from the 97% RH sample with an undried, natural sample (33% RH) indicates that the interlamellar water adsorption is reversible. A broadening of the XRD peaks after drying the sample over P_2O_5 was noted and the peaks remained broad with subsequent wetting suggesting that the dehydration process caused some disordering. A comparison of the adsorption isotherm with the XRD data allows us to conclude that water adsorbed at 97% RH (11% by weight) included water located within the crystal structure as well as that externally adsorbed and capillary condensate. Future experiments will be performed at elevated temperatures with a sorption system fitted with an evaporator to control the RH and the results will be compared with those at ambient temperature.

6.3.1.6 Material behavior as a function of growth of microbial biomass. The impacts of the native and introduced bacteria on the performance of geologic nuclear waste disposal facilities were evaluated because these bacteria could promote corrosion of repository components and alteration of chemical and hydrological properties of the surrounding engineered and rock barriers. As a first step towards investigating these potentialities, native and introduced bacteria obtained from post-construction Yucca Mountain (YM) rock were isolated under varying conditions, including elevated temperature, low nutrient availability, and the absence of available oxygen. Individual isolates are being screened for activities associated with microbially induced corrosion of metals (MIC). Preliminary determination of growth rates of whole YM microbial communities under varying conditions was also undertaken. This work is reported in Horn et al. (1996).

Methods. Samples of Topopah Springs tuff collected from a mined Fran Ridge outcrop, and rock excavated during construction of the Exploratory Studies Facility tunnel (Yucca Mountain, NV) were collected aseptically. Microorganisms were isolated both aerobically and anaerobically from whole and aseptically crushed (1.7-2.4 mm) rock samples at room temperature by plating onto low nutrient R2 agar (Difco). Organisms that survive in nutrient-depleted environments and at elevated temperature (50°C) were isolated from crushed samples (1.0 g) using low nutrient R2[1] broth. The resulting whole microbial communities were grown for extended periods (aerobic incubation, 72 h; anaerobic incubation, 17 days) at room temperatures and 50°C. After extended cultivation, samples were incubated on R2 agar at the temperature of previous growth. A representative group of morphologically distinct individual isolates were purified by repeated streaking of single colonies, which were identified primarily using fatty acid analysis. The growth of microbes that possess sulfate-reducing and iron-oxidizing capabilities was encouraged from crushed rock samples using other specialized growth media.

Growth rates were determined by adding 10g of crushed rock samples to 50 mL of R2 broth. Samples were incubated aerobically by shaking in covered flasks at ambient temperature, 30°C, and 50°C. Sterile controls were prepared by repeated cycles of autoclaving (120°C) and incubation. Growth was monitored by periodic live plating of appropriate dilutions on R2 agar.

Crude calorimetric screens were used to identify individual strains that produced the greatest quantity of a range of MIC-related capabilities. Acid producers were identified after growth of individual isolates in R2 broth containing pH indicators, the color change of which gave a qualitative indication of acid production. Production of

hydrogen sulfide by individual isolates was detected by the ability to precipitate ferrous iron after growth in various media. Generation of exopolysaccharide capsular material was assessed after gross examination of colony morphology. Ferrous iron was assayed calorimetrically using ferrozine reagent.[2]

Results. While any given growth media permits only the growth of a small fraction of a microbial community, a multiplicity of microbial types were still detected from whole and crushed YM rock on R2 media; henceforth these were treated as a sample of the total microbial community present at this site. In general, the greatest diversity of those microorganisms culturable on R2 arose from plated rock samples grown under aerobic conditions at room temperature, although 17 anaerobic strains were purified from rock samples incubated at ambient temperature under anoxic conditions. Extended growth at room temperature and 50°C showed a low diversity of microbial forms (one or two cell types). However, high cell numbers were reached after extended growth under aerobic conditions (2×10^8–10^9 cells/mL), while anaerobic conditions produced low cell densities (e.g., 140 cells/mL), and no growth was evident after extended anaerobic incubation at 50°C. In total, a group of over 60 isolates were preserved for further study. After one month, growth of iron oxidizers and sulfate reducers is not evident in specialized media, although efforts continue to isolate these types of organisms.

Growth rates of whole communities of YM-derived microorganisms in low nutrient R2 broth varied depending on the temperature of incubation. While communities grown at room temperature or 30°C showed an average mean doubling time of 1.8 h, those growing at 50°C demonstrated doubling times of 3.2 h over a 9 or 10 hour growth period. All cultures, however, demonstrated significant increases in cell numbers, ranging to over 20,000 cells/mL of media, at the conclusion of the 10 h growth period.

Preliminary screening of over 60 YM-isolates shows that 27% produced enough acid to decrease the pH of the growth media (pH $\leq$ 5.3) under aerobic conditions; 5 of these strains produced acid when incubated at 50°C. 44% of those examined after growth in anoxic conditions generated acid. Several isolates demonstrated marked production of capsular exopolysaccharide material. Studies aimed at screening isolates for sulfide production and iron oxidation are ongoing.

Discussion. We expect that both native microorganisms and those introduced as a result of construction activities are represented in our samples. While identification of *all* microbial community members requires application of alternative techniques (i.e., ribosomal DNA analyses), these studies examined that portion of the YM community capable of growth on R2 media under the conditions specified. These primary findings

demonstrate that microbes present at the YM site are capable of survival and growth under conditions approaching those anticipated after waste deposition. Some examined members of the total microbial community can grow in the absence of oxygen and at temperatures of at least 50°C. Growth rates are measurable at ambient and elevated temperatures, and probable spore-forming organisms are even capable of surviving repeated exposure to 120°C. Further *in vitro* determinations will aid in determining *in situ* rates of growth, which can then be correlated with hydrologic flow rates. Depleted nutrient conditions favor the growth of only a select group of community members, but these are capable of reaching high cell densities under aerobic conditions, even at 50°C. Of those anaerobic isolates capable of growth on R2 media, it appears the combination of elevated temperatures and depleted nutrients are deleterious to growth.

Initial studies of MIC-associated activities demonstrate that YM microbial inhabitants possess the abilities to both produce acidic conditions and biofilm-generating materials. Production of biofilm "slimes" could facilitate the growth of organisms even at a very low relative humidity. Other microbial activities identified with MIC are currently being assessed and crude screening methods are being followed by more refined analysis to better characterize those isolates identified in primary screening protocols. Finally, microbial isolates that demonstrate the highest MIC-associated activity rates will be used to assess the MIC resistance of various alloys intended for use in waste deposition.

Clearly, further correlation of environmental conditions and their effects on relevant microbial activities is required to accurately predict the effects of microorganisms on waste containment. However, these studies provide evidence that microbial impacts are pertinent to risk assessment of nuclear waste storage facilities.

6.3.1.7 Material behavior as a function of gradients of chemical potential, concentration, temperature. As was discussed previously, at the drift scale a radioactive waste repository is extremely heterogeneous. This heterogeneity is the basis for the existence of gradients in chemical composition, temperature, relative humidity and even porosity. These gradients are the basis of thermodynamic driving forces: chemical potential, fugacity, concentration, temperature. As such they can drive reactions and cause substances to dissolve and precipitate in a manner that is not predicted based on average values for those parameters.

6.3.2 Historical Analogs as Long Term Experiments

In order to verify predictive capability we need to compare predictions to test cases where similar processes are occurring. These analogs need not mimic the potential

repository in all aspects, but rather must be able to provide information regarding a significant process in detail.

6.3.2.1 New Zealand. Microbially influenced degradation (MID) of concrete is thought to occur when microorganisms present in the environment produce mineral or organic acids that dissolve or disintegrate the concrete matrix. Three groups of bacteria are known to create conditions which are conducive to destroying concrete integrity. These microorganism are ubiquitous in the environment. They will, therefore, eventually be found in any repository facility, regardless of depth, because of the free movement of environmental contaminates into the confined space. The concrete facility of interest is an operational, passive cooling tower shell located at the Ohaaki Power Station near Wairakei, New Zealand.

Concrete samples from the tower walls were obtained by coring, chiseling, and scraping. Biofilm was retrieved by peeling it from the wall surface. Holes left from the removal of cored samples were used for the emplacement of five concrete specimens (including two proposed for the YMP) made from different cement formulations.

Altogether a total of 29 specimens were recovered. The presence of microbes known to be involved in MID have been verified. Further work in this area was canceled due to lack of funds.

Reference concrete and concrete-waste package composite specimens were emplaced in hydrothermal springs along with the specimens described in the geochemistry section. The samples were retrieved, but have not been analyzed because the program was canceled.

6.3.3 Modeling Activities

The license application (LA) for a potential nuclear waste repository at Yucca Mountain in Nevada must be submitted in the near future. As part of this application process, we must better understand the long-term chemical implications of introducing natural and fabricated materials as well as microbes into a radioactive waste repository. Some of these materials are introduced as a necessity of construction and others are introduced passively and even unintentionally. Of the former explicitly chosen materials, there may be an option to substitute alternates for some materials. Other materials may not be interchangeable.

There are three reasons for using modeling to understand the chemical modifications of the natural environment in a repository setting. The first is that the chemical consequences of some of the materials under consideration are not common to our experience for the long periods of time and/or the conditions of an underground

radioactive waste repository. Computer modeling using fundamental chemical principles allows us to project chemical conditions far into the future and to examine the system from selected points in time. The second reason is that modeling can significantly reduce the number of experimental trials required to demonstrate a similar understanding of chemical processes. Modeling chemical processes is economical and efficient for both simulating long periods of time and for investigating the consequences of multiple combinations of materials. The third reason is to maintain the flexibility required to support repository design and performance assessment efforts at this stage in the design decision process where the advantages and disadvantages of multiple options are being considered.

Modeling is effective, not as an end in itself, or as a tool to be used independently of other efforts, but rather as a facet of a program that is coordinated with experimental and historical analog activities. Such a coordinated program on a small scale is demonstrated in progress report on the long-term chemical impact of diesel exhaust (Meike et al., 1994). The strategy to model drift scale chemistry has been to focus on two areas. First, we are developing materials specific modules that can be either operated independently or can be inter-connected to simulate design and construction options under consideration. Secondly and concurrently to the first, we are developing the capability to simulate and visualize chemical processes in three-dimensions within the geological context of the Yucca Mountain. Conceptually, the modeling program was most advanced in the area of cementitious materials (ordinary Portland cement (OPC) grouts and concretes.

The most important role of the material specific chemical module is to reflect the material's chemical significance in the most streamlined manner possible. Thus, if it can be demonstrated that a material has no effect on the chemical environment, then it can be eliminated from the modeling of that scenario. Similarly, and probably more realistically, if it can be demonstrated that a material is involved to a significant extent only in certain chemical processes, then there is only need for computer simulation of those processes. Of course, the modules are only as robust as their foundations, and thus the chemical role that any materials play must be examined carefully across the range of changing parameters to assure that overly simplistic assumptions have not been made. If done correctly the modular approach can streamline the computer modeling significantly without affecting the capability to comment on questions significant to repository design.

At present our chemical modeling strengths lie in the ability to model the abiotic geological system over long periods and a range of temperature and chemical

conditions using aqueous geochemical modeling packages such as EQ3/6. This code is based on fundamental chemical principles and thus should be adaptable to any materials. However, the adaptation of this code to simulate the long term chemical degradation of non-traditionally geologic materials involves two considerations: first, the adequate representation of significant chemical processes, and second the representation of data for the appropriate phases in materials specific databases that support the modeling packages. The database needs will be described in detail below with respect to cement. In the process, it is hoped that some general considerations involving the databases will become clear. There are two aspects of chemical processes to consider. First are those processes that have not yet been included in the code, abiotic processes such as redox processes that are fundamentally important to modeling the degradation of metals (and this is presently being developed within the Geochemical Modeling Task). Second are those processes which were not intended to be part of the code. These include all biotic processes, specifically the chemical consequences of microbial activity.

With respect to biotic processes, the needs of chemical modeling in the repository diverge significantly from the abilities of the traditional geological models. Abiotic chemistry has seemed to adequately describe the rates and results of chemical processes in systems of traditional geological interest. This may not be the case for a radioactive waste repository. The abiotic chemistry is only one part of the chemical needs because, in a natural system even in the deep subsurface, as is discussed by Horn and Meike (1995) microbes are bound to be present (native and introduced), and many of the materials that may be introduced into a radioactive waste repository may provide nutrient sources to initiate microbial blooms.

At present no work is being conducted in the modeling area.

6.3.3.1 Drift scale thermochemical models. Our intent is to work from drift scale to repository and ultimately mountain scale progressively establishing those spatial and temporal characteristics that need to be transferred to the next larger scale. Thus, we have not chosen a software program that has provided ease in initial rendering of the engineered features. Rather, we have worked closely with a software company (Dynamic Graphics, Inc.) to push the limits of a geological modeling program (EarthVision™) in its ability to render engineering details.

The purpose of this work was to determine whether it would be possible to represent repository design features at an appropriate level of detail within the EarthVision™ software modeling framework. This is not a simple computer generated architectural design (CAD) program. In fact, developing the visual display was much

less straight forward than might be immediately apparent. The various features that are shown in these models were produced by routines that were originally formulated to produce geological features. Therefore, all of the physical features were produced by combinations of faulting, deposition, erosion and drilling "wells".

Certainly the work that went into producing these three-dimensional representations of potential repository designs would not be worthwhile if they were only intended as graphical representations. However, once built, the potential ultimate benefits are great. Our goal is to use these representations for drift, repository and mountain scale hydrological and chemical modeling that include modifications due to construction. The advantage of this software is that physical attributes can be assigned to the various forms and thus they can be used to visualize the evolution of complex chemical, hydrological and coupled chemical-hydrological models. An additional intention is to locate materials, calculate volumes with ease, and locate the interfaces between materials of interest.

EarthVision™ software has a number of significant potential advantages: 1) the ability to use existing Nevada State Survey coordinate data to interface with existing geochemical and hydrogeologic models. 2) the ability to develop an interactive approach between drift, repository and mountain scales to address hydrological and chemical questions. We expect that the first use of this software will be in support of drift scale hydrological and chemical modeling, using the chemical formulations for grout and steel that have been used in the ESF.

This exercise has pushed the limits of the EarthVision™ software in a number of ways. The capabilities of the software are demonstrated in the figures. The representation of a repository layout presently under consideration (Fig. 6-28) is plotted using Nevada State coordinate grid references, so that it can easily be placed into any other EarthVision representation of Yucca Mountain processes. The actual relative sizes of main and emplacement drifts are shown. We have demonstrated a level of detail sufficient to initiate modeling in support of major hydrological and chemical questions concerning repository construction.

Figures 6-29 and 6-30 illustrate various aspects of the emplacement tunnel. The cut-away view of the emplacement tunnel demonstrates the capability of the EarthVision™ software to represent discontinuous shapes (Fig. 6-29). It was found that waste packages were more easily modeled with rounded ends. Although the depiction in this case is for computational simplicity, the shape may have some merits for structural integrity. Figure 6-30 is illustrated to scale: a 25 m section of 4.3 m diam. emplacement tunnel, with concrete invert, gantry tracks and concrete waste package supports.

Various aspects of the service tunnel are depicted in Figs. 6-31 through 6-33. The simplified cross-section rendering of a 20-m section of 7.6 m diam. service tunnel (Fig. 6-31) shows concrete invert, shotcrete layer, and rockbolts for the metal grate platform anchored into the surrounding rock. The metal platform supports are placed at roughly 2 m intervals. A similar length of exposed service tunnel (Fig. 6-32) demonstrates the level of detail that can be obtained for chemical and hydrological modeling at the scale of tens of meters. The cementitious materials, concrete invert and shotcrete are illustrated. The metal materials illustrated are the gantry car rails, platform supports, platform and platform anchor rockbolts. Rock support rockbolts are illustrated in Figs. 6-33 through 6-37. The oblique view of the service tunnel (Fig. 6-33) illustrates rockbolt holes. Given standard spacing (1.5 m) as depicted on engineering drawings, 104 rockbolts would be found in this length of tunnel. A cross-sectional rendering (Fig. 6-34) and cut-away view (Fig. 6-35) of service tunnel showing rockbolt holes. The cross-sectional rendering (Fig. 6-36) and cut-away view (Fig. 6-37) show 36 rockbolts in a 20-m section of emplacement tunnel, given the standard spacing (1.5 m) as depicted on engineering drawings. Using these visual/calculational tools we can examine the chemical and hydrological effects of a plume of fluids equilibrated with cement (e.g. elevated pH) moving into the mountain. It is also clear that the orientation and spacing of rockbolts can heavily influence hydrology. Using EarthVision™ software it will be possible to examine the influence of rockbolts on hydrology on a number of scales from single drifts to the repository and the entire mountain.

Because of its level of detail, EarthVision™ allows the display and manipulation of individual rockbolts with grout (Figures 6-38, 6-39). We have also pushed the ability to model finite objects. Calculation of material volumes is straightforward, as is illustrated in the calculation of the volume of cementitious materials (approximately 54.1 m^3) (Fig. 6-40), and the calculation of volume of metal materials (approximately 14.4 m) (including the waste packages of wall thickness ~0.2 m) in a 20-m section of 4.3 diam. emplacement drift (Fig. 6-41).

6.3.3.2 Abiotic Models. The EQ3NR/EQ6 software package (Wolery, 1992; Wolery and Daveler, 1992) is composed of three executable programs (EQPT, EQ3NR and EQ6) and a number of databases that are used at the modeler's discretion (Fig. 6-42). EQPT simply formats databases to be readable by EQ3NR and EQ6, and is not shown in the figure. The input file for EQ3NR contains the analytical composition of the solution (including total concentrations of dissolved components, pH, Eh and oxygen fugacity). The code calculates the distribution of chemical species, using thermodynamic data located in the selected database. The output consists of an output and a pickup file,

which is used to initialize the EQ6 input file. EQ6 models the reaction of the aqueous solution with a set of minerals and gases, as well as fluid mixing and temperature changes. A set of five data files is now available. Three of these (COM, SUP and NEA) may be used with either the Davies equation, or the B-dot equation to calculate the activity coefficients. Their use is restricted to rather dilute solutions (ionic strength less than the sea water reference value). The two other data files (HMW, PIT) use Pitzer's equations (Pitzer, 1979), and are suitable for the modeling of high concentrations solutions. These databases are outlined below.

1. *SUP database.* Based entirely on the SUPCRT92 program (Johnson et al., 1992), this database has a high level of internal consistency. The database covers a wide range of chemical species. However for the purpose of drift scale chemical modeling it doesn't contain necessary data related to calcium-silicate-hydrate species that might be formed in cements at temperatures between 60 and 300°C.
2. *NEA database.* This database was produced by the Data Bank of the Nuclear Energy Agency of the European Community (Grenthe, 1992), and is specifically tailored to conduct uranium studies.
3. *HMW database.* This dataset is based on Harvie, Moller and Weare (1984). It can be applied to both dilute solutions and concentrated brines, at 25°C. It has also a very high degree of internal consistency but it only treats the components present in the "sea-salt-water" system. Important elements to the modeling of cement in a geologic repository, like Al and Si are not included in this database.
4. *PIT database.* This database is based primarily on data summarized by Pitzer (1979). This data file can also be applied to concentrated brines between 25°C and 100°C. It covers a larger set of species than the HMW database, but it does not address the silica and inorganic carbon species that are necessary to model cement in a geologic repository. In addition, it contains some internal inconsistencies.
5. *COM database.* This dataset represents a melange of data found in the SUP and NEA datasets, as well as data from the HMW dataset. Other data in this database have been obtained by correlation or interpolation. This set therefore offers the least assurance of internal consistency. However, it is the only means available to model problems with a high degree of compositional complexity.

The development of a cement specific database that would allow the modeling of cement-water, and ultimately cement-water-rock interactions has been interrupted.

EXPLORER™ software is most often utilized to visualize complex data sets from existing FORTRAN and C programs, especially those for which properties are linked to

a three dimensional spatial coordinate system. However, because it has the capacity to accept user-built modules it can also be used to encapsulate an existing program (in FORTRAN or in C) into a "module" (Fig. 6-43). Our intention is to utilize the complex chemical modeling capabilities and the modular format to develop materials specific modules and preserve entire complex

It is our intention is to use EXPLORER™ as a tool to encapsulate the EQ3/6 software package into three modules: EQPT, EQ3NR and EQ6. The ability to produce module maps and to imbed whole maps inside modules creates a functional hierarchy of computational maps that facilitates the series of complex and repetitive calculations that must be conducted over a number of levels as the scenarios are developed and compared. Each three module set will be encapsulated into a material specific module using the appropriate default settings, databases and integrating the appropriate biotic modules.

The material specific modules are powerful tools for repository design. They allow the flexibility to deal with variable levels of uncertainty and the ability to model and compare materials specific drift scale implications of repository design.

The material specific modules are the building blocks of design specific drift scale modeling that can be saved as "maps" in Explorer. The maps, which store complex chemical modeling paths at a level above what can be done with current modeling routines, can thus be used to retrace complex calculational steps and minimize operator error. As such it also represents a step forward in the documentation of computer modeling. The maps will interface with the EarthVision model described above to provide access to time stepped three-dimensional understanding of repository chemistry and hydrology.

6.3.3.3 Biotic Models (modeling microbiological activities). Although it is not possible to produce rigorous models of microbially related chemistry at this time, much progress can be made toward determining the relative significance of microbial effects with a simple box model. A box model treats microbial processes as a simplified chemical reactor. We can view microbial reactions as enzymatically-controlled chemical processes which are governed by the size, identity and metabolic state of the microbial community as well as the traditional abiotic chemical parameters such as pH and temperature. Each microbe must have an energy supply, a source of carbon, and a set of nutrients essential for life. The energy supply generally involves an electron acceptor-donor process, the carbon supply is usually some form of organic matter or carbon dioxide, and most microbes need sufficient amounts of nitrogen, phosphorous, and sulfur to live. Other elements are needed in trace amounts but are generally not limiting

in terms of microbial growth, especially in a heterogeneous repository environment. Water is also essential, and temperature is an important limiting factor. For a review of these considerations with regard to a potential repository at Yucca Mountain, see Horn and Meike (1995). Although specific microbes exist over subsets of this range, it is possible to establish, for this first step, a range of temperature over which microbes are active, as opposed to inactive (e.g. spore, dormant or dead state).

The first step in using a box model to understand microbial effects in a repository is to establish limits to the total amount of microbial activity possible in the repository based on the microbial needs listed above (e.g. energy, carbon, nutrients, water, appropriate temperature). This type of approach is described well by McKinley & Hagenlocher (1993) for the Swiss High Level Waste (HLW) and Low/Intermediate Level Waste (ILLW) repositories. They examine the energies available from all redox reactions possible for the materials present in the repository which can be utilized by microbes. This information is combined with an estimate of how much energy is needed to synthesize the compounds which make up biomass (this number is 0.1 mole of ATP to produce one gram of dry cell mass, which is equivalent to 450 kJ/mol if the efficiency of energy utilization is 10%). With this approach, the total biomass that can be sustained can be related to the masses of redox species that are present. Finally, if one can assume an average biomass metabolic rate, then the chemical effects of the biomass in terms of corrosion enhancement, ligand production, gas production or any other rate of chemical change can be estimated and related to overall repository behavior.

A similar simplified approach can be used to determine the maximum possible biomass based on the amounts of essential nutrients (phosphorous, nitrogen, and sulfur) present in the repository. An average biomass is defined in McKinley & Hagenlocher (1993), to have the composition $C_{160}(H_{250}O_{80})N_{30}P_2S$. The total amount of possible biomass is simply the total amount of accessible nutrient divided by its weight fraction in biomass.

This is complicated somewhat by the fact that nutrient availability may be a function of corrosion rates of repository materials, whose rates themselves depend on active biomass. Some nutrients are available only if they are released during corrosion of repository materials. The overall process is therefore coupled and amenable to modeling provided that some quantitative information on the type of coupling is available.

Applying this approach to the Swiss HLW repository, McKinley & Hagenlocher (1993) found that for a bounding calculation not limited by microbe mobility, the overall biomass was limited by energy availability, and not nutrient availability. The amounts

of nitrogen, phosphorous, and sulfur available in the backfill in particular are much higher than the total mass of electron donors needed to fuel microbial growth. The only exception is during the first ten years of repository existence where the availability of oxygen is expected to be high and, as a consequence, energy availability should also be high. The availability of O_2 over time in a potential Yucca Mountain repository drift is still under discussion. This is because the availability of air through the mountain's fracture system, the amount of time that the repository drifts will be ventilated artificially, and the amount of chemically conditioned backfill that may affect the fO_2 have not yet been bounded. The proposed Yucca Mountain repository differs from the Swiss in many ways, for example, the former is an unsaturated environment. However although the Swiss conditions are not necessarily analogous to the Yucca Mountain repository in many important aspects including, for example fO_2, it is illustrative to follow through the calculation as an exercise.

The biomass production rates calculated for the Swiss HLW repository range decrease from an initial rate of about 300 grams dry biomass/year/waste package to long-term rates of about 0.3 g/y/wp. These values can be used to constrain likely production rates of by-products such as organic ligands and gas generation, which in turn affect radionuclide transport rates and repository performance. For this case, even at maximum biological activity, the total production of organic complexing agents is only approximately equal to the estimated release rates of radionuclides. The net effect of microbial activity in terms of solubilization of radionuclides is therefore small for this repository.

Given that the conditions of the Swiss repository (e.g. granitic rock, repository design, saturated rock) are quite different, the findings of McKinley & Hagenlocher (1993) cannot be directly applied to the proposed Yucca Mountain repository. Information gained from this simple box model approach should be used to prioritize and guide more detailed work on microbial effects. More sophisticated models of microbial effects should then be generated using this more detailed information. However, because of the complex nature of microbial processes, and in particular their abilities to evolve with time, express new genes when environmental conditions change, and the diverse nature of microbial communities, it is unlikely that we could produce a reliable mechanistic chemical model for microbial behavior in the short term. Our best approach is to use our information on microbial behavior to define worst-case scenarios, identify parameters that limit microbial productivity, and incorporate these results into our task of designing the engineered barrier system.

Thermal and other perturbations of a microbially mediated chemical system occur as a complex function of microbial identity, microbial activity and colony growth (biomass). In addition, individual species function over a relatively narrow temperature range. Thus, even with respect to the traditional chemical parameters, biological reactions operate according to different laws than the abiotic reactions. However, although not identical to the abiotic case, it should be productive to take an approach similar to existing abiotic chemical modeling to use the chemical laws of microbial chemistry to predict long-term chemistry. This approach is also consistent with the ultimate goal which is to develop models which can be operated in tandem with the abiotic models.

The net chemical effect of a community of microbes can be thought of as a set of mass inputs and outputs. For example, an autotrophic bacteria may take in bicarbonate as a carbon source, and oxidize iron to ferrous iron as an energy source. As by-products, the bacteria may make acetate and as a consequence of oxidizing iron, lower the pH. Based on experimental observations of this type of bacteria in an environment similar to an anticipated repository environment, it should be possible to write a reaction that describes the overall chemical effects of this bacterial population. For each gram of active biomass, there can be related a positive flux of acetate and acid generation, and a negative flux of iron and bicarbonate.

At the most simple level, models of microbial activity can be used as input into EQ3/6 (Wolery, 1992). This approach offers the potential for modeling at a fairly high level of complexity in a short period of time. Although microbial activity is not explicitly provided for, the overall effect of microbial activity on repository corrosion processes can be. Such an approach allows the net effects, in terms of how microbes alter the local chemistry of their environments, to be accounted for. Thus the chemical effects of microbial activity can be rigorously coupled to materials interactions in the repository without specific identification of all microbial species in the repository or explicitly providing for the details of microbial activity.

This type of model obviously lacks feedback from system parameters to the microbial processes. Feedback between environmental conditions and microbial activity is the most difficult part of implementing microbial activity into the simulation. But if empirical relationships between microbial activity and environmental parameters such as temperature and pH are available, they can readily be incorporated into the simulation. For example, microbial productivity is almost certainly pH dependent. Most bacteria live only over a restricted pH range.

The next step in making this type of model more realistic would be to incorporate feedback between environmental parameters and microbial productivity. If the pH changed significantly, it is likely that a new type of microbial population would exist, with a different set of chemical effects. Likewise, if microbial activity were to change the pH, the equilibrium condition between the aqueous fluid and the material with which it is in contact, is changed. EQ3/6 currently has the capability to incorporate these types of complexities into the simulation. Experimental data on the biomass production rates of any variety of microbial populations which are dependent on pH, or on any other parameter related to the chemical response or influence of microbial activity, can be entered as reactants in the simulation. Kinetic control of these rates is also possible if appropriate rate data are known. Given the complexity and interdependency of some of these factors, it may be necessary to enter the numerical relationships as reactants into EQ3/6 and in a step-wise or iterative fashion to take into account the chemical effects of the microbial population.

The presence of other repository materials can also be included in the simulation so that coupling between all chemical processes is properly accounted for. For example, the simulation may include the host rock, a metal canister, and cement. As the reaction proceeds, the effect of acid generation on pH stability, the effect of acetate generation on metal corrosion, the affects of bicarbonate utilization are all accounted for. The system will evolve and have a pH which is controlled by the coupled interactions of all these pH-dependent reactions. Likewise, the complete solution composition can be calculated for any step along this reaction progress. The ability to do this stage of modeling will be enhanced by the use of Explorer™ software.

Our ultimate aim is to find an approach that can be integrated into a sophisticated feedback linkage with the existing EQ3/6 code. We aim to frame descriptions of microbial activity in forms that mimic the abiotic thermodynamic and kinetic descriptions. To do this we must distinguish between the two types of processes: those that can be seen as perturbations from an equilibrium state, or as part of a new, microbially mediated equilibrium state and thus comprise a module that will interact with EQ3, and those considerations that affect rates of change and thus the kinetics and thus comprise a module that will interact with EQ6 (Fig. 6-44). In developing the descriptions we seek to define microbial activities in terms of three types of processes: processes or conditions that can represent standard states, processes that can be described in terms of rates of change, and processes in which transfer of mass, energy or other quantifiable units sum to zero. The advantage of these definitions is that they translate well into the pre-existing abiotic thermodynamic/kinetic framework. We will

define standard states as points of reference that will allow us to quantify deviations from those points. Describing processes in terms of equations that sum to zero has many advantages. For example it ensures internal consistency and provides a foundation for expanding from simple to multi-component systems.

6.4 Summary and Conclusions

Progress has been made in the identification and quantification of materials that may be used as part of the construction of a radioactive waste repository at Yucca Mountain. The major significant processes affecting the chemical impact of those materials on the Near Field Environment and the waste packages have also been identified, as well as the data that is required to be able to predict the outcome of many of these processes over long periods of time. In the past we have emphasized those processes and materials that would take the water chemistry or certain processes outside of the bounds that are assumed based on the natural geochemistry, or the limited knowledge of long term behavior. Our work in the near future is to use this information to provide some bounds for chemical and mechanical modeling, but also to narrow those bounds where they make a significant difference to performance assessment modeling. Many of the fundamental tools are in place to better bound chemistries and behaviors, but others are still missing.

To date the most significant unknowns that have been identified in the area of introduced materials are the effects of microbial activity on water chemistry and degradation rate of important materials (and our ability to model those effects), the effects of cement-water-rock chemistry over time, and the effect of metals corrosion over time.

6.5 Acknowledgments

W. Bourcier, M. Caffee, L. Clodic, S. A. Carrol, A. Miller, M. Sprague, and P. A. Sterne contributed to this chapter.

6.6 References

Aminabhavi, T. M., and U. S. Aithal (1990), *J. Appl. Polym. Sci.* **41**, 2113–2131.

Andersson, K., B. Allard, M. Bengtsson and B. Magnusson (1989) Chemical composition of cement pore solutions. *Cem. Concr. Res.* **19**, 327-332.

Andreoni, V., G. Baggi, C. Guaita, and P. Manfrin (1993). *Int. Biodeterioration Biodegradation* **31**, 41–53.

Atkins, M., F. P. Glasser, A. Kindness, and D. E. Macphee (1991), *Solubility Data for Cement Hydrate Phases (25°C)*, U.S. Department of Energy, Washington, DC, DOE/HMIP/RR/91/032.

Atlas, R. M. (1982), *Enumeration and Estimation of Biomass of Microbial Components in the Biosphere, in Experimental Microbial Ecology*, R. G. Burns and J. H. Slater, Eds., (Blackwell Scientific Publishers, Oxford, England), pp. 84–102.

Awasthi, S. (1993), *Natl. Acad. Sci. Lett.* 16, 143–144.

Babushkin, V. I., G. M. Matveyev and 0. P. Mchedlov-Petrossyan (1985) *Thermodynamics of Silicates*. Springer-Verlag. 459 pp.

Barnes, I., T. S. Presser, M. Saines, P. Dickson, and A. F. K. van Groow (1982), "Geochemistry of Highly Basic Calcium Hydroxide Groundwater" in *Jordan, Chem. Geol.* 35, 147–154.

Barnes, M. W., and D. M. Roy (1983), The Buffering Mechanisms in Leaching of Composites of Cement with Radioactive Waste, Mater. *Res. Soc. Symp. Proc.* 15, 159–166. NNA.19920131.0250

Barns, S. M., R. E. Fundyga, M. W. Jeffries, and N. R. Pace (1994), Remarkable Archael Diversity Detected in a Yellowstone National Park Hot Spring Environment, *Proc. Natl. Acad. Sci USA* 91, 1609–1613.

Barr-Kumarakulasinghe, S. A. (1994), *Polymer* 35, 995–1003.

Barrer, R.M., (1978), *Zeolites and Clay Minerals as Sorbents and Molecular Sieves*, Academic Press, New York, 497 p.

Barret, P. and D. Bertrandie (1986) Fundamental hydration kinetic features of the major cement constituents: Ca_3SiO_5 and b-Ca_2SiO_4. *J. Chemie Phys.* 83, 765-775.

Bell J. L. S., D. A. Palmer, and H. L. Barnes (1992), *Acetate in Hydrothermal Solutions: Decomposition Kinetics and Metal Complexation, in Water-Rock Interaction*, Y. Kharaka and A. Maest, Eds., (Balkema, Rotterdam), pp. 307–310.

Bennett, P. C., M. E. Melcer, D. I. Siegel, and J. P. Hassett (1988), The Dissolution of Quartz in Dilute Aqueous Solution of Organic Acids at 25°C, *Geochim. Cosmochim. Acta* 52, 1521–1530. NNA.19921106.0027

Bensted, J. (1983a) *Hydration of portland cement*. p. 307-347 in Ghosh, 5. N. (ed.) (1983a).

Bensted, J. (1983b) Early hydration of portland cement - effects of water/cement ratio. *Cem. Concr. Res.* 13, 493-498.

Bensted, J. (1989) Oil well cements - a general review. *Chem. Ind.*, 20 Feb. 1989, p. 100-105.

Berner, U. R. (1987). Modelling porewater chemistry in hydrated portland cement. *Mat. Res. Soc. Symp. Proc.* 84, 319-330.

Berry, W. E. (1983), *Durability of Marker Materials for Nuclear Waste Isolation Sites*, Office of Nuclear Waste Isolation, Battelle Memorial Institute. NNA.19920131.0430

Bethke, C. M. *The Geochemist's Workbench™ A Users Guide to RXN, ACT2, TACT, REACT, and GTPLOT*. Urbana, Illinois: C. Bethke, c1992.

Bish, D. L., F. A. Caporuscio, J. F. Copp, B. M. Crowe, J. D. Purson, J. R. Smyth, and R. G. Warren (1981), *Preliminary Stratigraphic and Petrologic Characterization of Core Samples from USW G-1, Yucca Mountain, Nevada*, Los Alamos National Laboratory, Los Alamos, NM, LA-8840-MS. NNA.19870406.0099

Bisi, M., C. Nicolella, E. Palazzi, M. Rovatti, and G. Ferraiolo (1994), *Chem. Eng. Technol.* 17, 67–72.

Borenstein, S.W. (1994). *Microbially Influenced Corrosion Handbook*. New York, NY, Industrial Press Inc.

Braithwaite, W. R., and K. A. Lichti (1981), *Surface Corrosion of Metals in Geothermal Fluids at Broadlands, New Zealand*, American Society for Testing and Materials.

Brandrup, J., and E. H. Immergut, Eds. (1975), *Polymer Handbook* (John Wiley, New York, NY).

Breck, D.W. (1974). *Zeolite Molecular Sieves*, J. Wiley and Sons, New York, 771 p.

Brock, T. D., and M. T. Madigan (1991), *Biology of Microorganisms* (Prentice-Hall, Englewood Cliffs, NJ).

Brown, P. W., E. Franz, G. Frohnsdorff, and H. F. W. Taylor (1984). Analyses of the aqueous phase during early C_3S hydration. *Cem. Concr. Res.* 14, 257-262.

Brown, P. W., J. Pommersheim and G. Frohnsdorff (1985). A kinetic model for the hydration of tricalcium silicate. *Cem. Concr. Res.* 15, 35-41.

Bruton, C. J., B. L. Phillips, A. Meike, S. Martin, and B. E. Viani (1994), Cement Minerals at Elevated Temperature: Thermodynamic and Structural Characteristics, *Mater. Res. Soc. Symp. Proc.* 333, 327–334, UCRL-JC-115796. NNA.19940318.0011

Bruton, C. J., W. E. Glassley, et al. (1995), *Geothermal Areas as Analogues to Chemical Processes in the Near-Field and Altered Zone of the Potential Yucca Mountain, Nevada Repository*, LLNL, Lawrence Livermore National Laboratory, Livermore, CA, UCRL-ID-119842. MOL.19960408.0210

Burnay, S. G., Ed. (1990), *A Practical Model for Prediction of the Lifetime of Elastomeric Seals in Nuclear Environments* (American Chemical Society, Washington, DC), pp. 524–533.

Burnett, N. C., R. D. Hooton, R. B. Heimann and M. Onofrei (1985). The development of durable cementitious materials for use in a nuclear fuel waste disposal facility. *Mat. Res. Soc. Symp. Proc.* 50, 461-468.

Burton, B. L. (1993). *J. Appl. Polym. Sci.* 47, 1821–1837.

Buscheck, T.A. and J.J. Nitao (1994). *The impact of buoyant gas-phase flow and heterogeneity on thermo-hydrological behavior at Yucca Mountain.* Proceedings of the International High Level Radioactive Waste Management Conference, 22-26 May, 1994, Las Vegas, NV and Dept. of Energy, Lawrence Livermore Natl. Laboratory Report #UCRL-JC-115351.

Carlson, V. E.O. Bennett, and J.A. Rowe. (1961). Microbial flora in anumber of oilfield water injection systems. *J. Soc. Pet. Eng.* 1, 72.

Carroll, S. A., M. Alai, and S. A. Copenhaver (in press), *Experimental Investigation of Hydrous Pyrolysis of Diesel Fuel: Potential Impact on the Proposed High-Level Radioactive Waste Repository, Yucca Mountain, Nevada,* Lawrence Livermore National Laboratory, Livermore, CA, UCRL-ID (in press).

Chapman, N. and I. McKinley (1990), Radioactive Waste: Back to the Future? *New Scientist* (May 5, 1990), 36–40.

Chapman, N., P. Cloke, et al. (1995), *Applications of Natural Analogue Studies to Yucca Mountain as a Potential High Level Radioactive Waste Repository,* The Natural Analogue Review Group. MOL.19960508.0064

Chessa, G., G. Marangoni, B. Pitteri, N. Stevanato, and A. Vavasori (1991), *Reactive Polym.* 14, 143–150.

Chiantore, O., M. P. L. d. Cortemigilia, and M. Guaita (1989), *Makromolekulare Chemie* 190, 3143–3152.

Costerton, J.W. and G.G. Geesey. (1985) The microbial ecology of surface colonization and of consequent corrosion. *Proceedings of the International Conference on Biologically Induced Corrosion, June 10-12, 1985,* Gaithersburg, MD.

Costerton, J.W. and J. Boivin. (1991) *The role of biolfilms in microbial corrosion in Microbially Influenced Corrosion and Biodeterioration,* N.J.E. Dowling, M.W. Mittleman, and J.S. Danko, eds. National Association of Corrosion Engineers, Houston, TX.

Coughlin, J. P. and C. J. O'Brien (1957). High temperature heat contents of calcium orthosilicate. *Am. Chem. Soc. J.* 61, 767-769.

Crammond, N. (1996) *The thaumasite form of sulphate attack-Discussion of possible reaction mechanisms* Gordon Research Conference, Plymouth, New Hampshire, July, 1996.

Culivicchi, G., C. G. Palmerini, and V. Scholari (1985). Behaviour of Materials in *Geothermal Environments, Geothermics* 14(1), 73–90.

Dickie, R. A., J. W. Holubka, and J. E. Devries (1990), *J. Adhesion Sci. Technol.* 4, 57–67.

Dodd, F. J., A. E. Johnson, and W. C. Ham (1960), Material and Corrosion *Testing at the Geysers Geothermal Power Plant*, Department of Eng. Research, Pacific Gas and Electric Company.

Dole, M., Ed. (1973), *The Radiation Chemistry of Macromolecules* (Academic Press, New York, NY).

Ederova, J. and V. Satava (1979). Heat capacities of C_3AH_6, C_4ASH_{12} and $C_6AS_3H_{32}$. *Thermochim. Acta* 31, 126-128.

El-Agramy, A. A. Shabaka (1990), *Isotopenpraxis* 26, 229–231.

El-Sonbati, A. Z., A. A. El-Bindary, M. A. Diab, M. A. El-Ela, and S. A. Mazrouh (1994), *Polymer* 35, 647–652.

Ellezer, I., N. Ellezer, R. A. Howald and P. Viswanadham (1981). Thermodynamic properties of calcium aluminates. *J. Phys. Chem.* 85, 2835-2838.

Ellison, M. S., S. H. Zeronian, and Q. Xie (1989), *Textile Res. J.* 59, 657–660.

EPA (Environmental Protection Agency), 1985, *Environmental Standards for the Management and Disposal of Spent Nuclear Fuel, High-Level and Transuranic Wastes: Final Rule*, U.S. Code of Federal Regulations, 40 CFR Part 191, Washington, DC. HQO.19871113.0033

Fein, J. B. (1991), Experimental Study of Aluminum-, Calcium-, and Magnesium-Acetate Complexing at 80°C, *Geochim. Cosmochim. Acta* 55, 955–964.

Fontana, M. G., and N. D. Breen (1978), *Corrosion Engineering* (McGraw-Hill Publishing, New York, NY), pp. 263–265. NNA.19891018.0176

Foster, P. K., and A. Tombs (1962), Corrosion by Hydrothermal Fluids, *New Zealand J. Science* 5 (1), 28–41.

Freemantle, M. (1994), Chemical Techniques Help Conserve Artifacts Raised from Titanic Wreck, *Chem. Eng. News*, 49–52.

Fujii, X. and W. Kondo (1983). Estimation of thermochemical data for calcium silicate hydrate (C-S-H). *Am. Ceram. Soc. J.* 66, C220-C221.

Garrett, R. W., et al. (1990), *Temperature Dependence of the Radiation Chemistry of Polymers* (American Chemical Society, Washington, DC).

Gartner, E. M., F. J. Tang and S. J. Weiss (1985). Saturation factors for calcium hydroxide and calcium sulfates in fresh portland cement pastes. *Am. Ceram. Soc. J.* 68, 667-673.

Gestsdottir, K., and D. A. C. Manning (1992), *An Experimental Study of the Dissolution of Albite in the Presence of Organic Acids, in Water-Rock Interaction*, Y. Kharaka and A. Maest, Eds., (Balkema, Rotterdam), pp. 315–318.

Gettens, R. J. and C. Frondel (1956). *Studies in Conservation*, 2, 64.

Ghema, R., P. Pienta, and R. Cote., eds. (1989). *Catalogue of Bacteria and Bacteriophages*. 17th edition. Rockville, MD, American Type Culture Collection.

Ghosh, S. N. (1983) Portland cement phases: polymorphism, solid solution, defect structure and hydraulicity. in Ghosh (ed) *Advances in Cement Technology*. Pergamon Press. pp. 289-305.

Gilfric, H. P., and H. Wilski (1992), *Int. J. Rad. Applic. Instrumen.* C 39, 401–405.

Gillen, K. T., and R. L. Clough (1989), *Polymer Degradation and Stability* 24, 137–168.

Glasser, F. P., A. A. Rahman, D. Macphee, M. Atkins, N. Beckley and E. E. Lachowski (1986) *Immobilization of radioactive waste in cement-based matrices*. United Kingdom Dept. of the Environment Report DOE RW 86.084. 110 pp.

Glasser, F. P., S. Diamond and D. M. Roy (1987b) Hydration reactions in cement pastes incorporating fly ash and other pozzolanic materials. *Mat. Res. Soc. Proc.* 85, 167-186. [This paper also appears in Mat. Res. Soc. Proc. 86]

Glasser, F. P., M. J. Angus, C. E. McCulloch, D. Macphee and A. A. Rahman (1985) The chemical environment in cements. *Mat. Res. Soc. Proc.* 44, 849-858.

Grassi, N., and G. Scott, Eds. (1985), *Polymer Degradation and Stabilisation* (Cambridge Univerisity Press, Cambridge).

Greenberg, A.E., R.R. Trussell, L.S. Clesceri, and M.A.H. Franson, eds. (1985). *Standard Methods for the Examination of Water and Wastewater*. 16th edition. Washington, D.C., American Public Health Association.

Greenfield, B. F., C. M. Linklater, A. D. Moreton, M. W. Spindler, and S. J. Williams (1993), The Effects of Organic Degradation Products on Actinide Disposal, *AEA Technol.*

Grutzeck, M. W. and A. R. Ramachandran (1987) An integration of tricalcium silicate hydration models in light of recent data. *Cem. Concr. Res.* 17, 164-170.

Haas, J. L. Jr., G. R. Robinson, Jr. and B. 5. Hemingway (1981) Thermodynamic tabulations for selected phases in the system CaO-Al_2O_3-H_2O at 101.325 KPa (1 atm) between 273.15 and 1800 K. *J. Phys. Chem. Ref. Data* 10, 575-669.

Hajash, A., S. P. Franklin and C. L. Reed (1992), Experimental Feldspar Dissolution in Acetic and Oxalic Acids at 100°C, in *Water-Rock Interaction*, Y. Kharaka and A. Maest, Eds., (Balkema, Rotterdam), pp. 325–328.

Haldeman, D. L., and P. S. Amy (1993), Bacterial Heterogeneity in Deep Subsurface Tunnels at Rainier Mesa, Nevada Test Site, *Microb. Ecol.* 25, 183–194.

Haldeman, D. L., P. S. Amy, D. Ringelberg, and D. C. White (1993), Characterization of the Microbiology within a 21-m^3 Section of Rock from the Deep Subsurface, *Microb. Ecol.* 26, 145–159.

Haldeman, D.L., P.S. Amy, D.C. White, and D. Ringelberg. (1994). Changes in bacteria recoverable from subsurface volcanic rock samples during storage at 4°C. *Appl. Environ. Microbiol.* 60, 2697-2703.

Hanck, J. A., and G. Nekoksa (1980), *Corrosion Rate Monitoring at The Geysers Geothermal Power Plant*, Department of Eng. Research, Pacific Gas and Electric Company.

Hedges, R. E. M. (1976), On the Occurrence of Bromine in Corroded Silver, Studies in *Conservatism* 21, 44–46. NNA.19931005.0006

Hedrick, D. B., and D. C. White (1986), Microbial Respiratory Quinones in the Environment. I. A Sensitive Liquid Chromatographic Method, *J. Microbiol. Meth.* 5, 243–254.

Heimann, R. B. (1988a) Interaction of cement and radioactive waste forms in multicomponent systems tests at 200°C. Part 1: Leaching and sorption of cesium, strontium and actinides. *Cem. Concr. Res.* 18, 389-400.

Heimann, R. B. (1988b) Interaction of cement and radioactive waste forms in multicomponent systems tests at 200°C. Part 2: Mineralogical changes of cement. *Cem. Concr. Res.* 18, 554560.

Heimann, R. B. and R. D. Hooton (1986) Mineralogical changes of various cement formulations during reaction with groundwater in the presence of Ca and Na-bentonite at 150°C. *Can. Min.* 24, 289-302. Also issued as AECL-8895.

Hermannsson, S. (1970), Corrosion of Metals and the Forming of a Protective Coating on the Inside of Pipes Carrying Thermal Waters Used by the Reykjavik Municipal District Heating Service, *Geothermics* 2 (Special Issue: U.N. Symposium on the Development and Utilization of Geothermal Resources, Pisa), pp. 1602–1611.

Horn, J. M., and A. Meike (1995), *Microbial Activity at Yucca Mountain*, Lawrence Livermore National Laboratory, Livermore, CA, UCRL-ID-122256.

Horn, J. M., and A. Meike (1996), A Program to Assess Microbial Impacts on Nuclear Waste Containment, in *Proceedings of the 1996 High Level Radioactive Waste Meeting*, Las Vegas Nevada, Lawrence Livermore National Laboratory, Livermore, CA, UCRL-JC-122732. MOL.19960409.0194

Horn, J. M., B. Economides, A. Meike, and R. D. McCright (1996), Initial Studies to Assess Microbial Impacts on Nuclear Waste Disposal, in *Proceedings of the 1996 High*

Level Radioactive Waste Meeting, Las Vegas Nevada, Lawrence Livermore National Laboratory, Livermore, CA, UCRL-JC-122587. MOL.19960409.0710

Imasaka, T., M. Hozumi, and N. Ishibashi (1992) *Anal. Chem.* 64, 2206–2209.

Ishigaki, I., and F. Yoshii (1992), Radiation Physics and Chemistry, *Int. J. Rad. Applic. Instrum. C* 39, 527–533.

Ivan, B., B. Turcsanyi, T. Kelen, and F. Tudos (1991), *Die Angewandte Makromolekulare Chemie* 189, 35–49.

Jackson, K. J., A. K. Burnham, R. L. Braun, and K. G. Knauss (1992), *Measurement of Pressure Effects on N-Hexadecane Cracking Rates*, 37, 1614–1620.

Jackson, K. J., and S. A. Carroll (1994), Experimental Investigation of Hydrous Pyrolysis of Diesel Fuel and the Effect of Pyrolysis Products on Performance of the Candidate Nuclear Waste Repository at Yucca Mountain, *Mater. Res. Soc. Symp. Proc.* 333, 841–847, UCRL-JC-116352. MOL.19950728.0064

Jeffrey, J. W. (1964) The crystal structures of the anhydrous compounds. pp. 131-164 in Taylor, H.F.W. (ed.) *The Chemistry of Cements*. Academic Press.

Johnson, A. B. J., and B. Francis (1980), *Durability of Metals from Archaeological Objects, Metal Meteorites, and Native Metals*, Pacific Northwest Laboratory, U.S. Department of Energy. NNA.19910604.0005

Johnson, J. W., and S. R. Lundeen (in press), *GEMBOCHS Thermodynamic Data Files for Use with the EQ3/6 Software Package*, Lawrence Livermore National Laboratory, Livermore, CA, UCRL-ID.

Jones, P. A. (1992), *Principles and Prevention of Corrosion* (MacMillan Publishing, New York, NY), 392–393.

Kaplan, M. L. (1991), *Polym. Eng. Sci.* 31, 689–698.

Kay, M. J., L. H. G. Morton, and E. L. Prince (1991), *Int. Biodeterioration* 21, 204–222.

Kay, M. J., R. W. McCabe, and L. H. G. Morton (1993). *Int. Biodeterioration Biodegradation* 31, 209–225.

Kenny, J. M., L. Torre, and L. Nicolais (1993), *Thermochim. Acta* 227, 97–106.

Kharaka, Y., P. D. Lundegard, G. Ambats, W. C. Evans, and J. L. Bischoff (1993), Generation of Aliphatic Acid Anions and Carbon Dioxide by Hydrous Pyrolysis of Crude Oils, *Appl. Geochem.* 8, 317–324.

Khare, A. R., N. A. Peppas, G. Massimo, and P. Colombo (1992), *J. Controlled Release* 22, 239–244.

Khinnavar, R. S., and T. M. Aminabhavi (1992), *J. Appl. Polym. Sci.* 46, 909–920.

Khoury, H. N., E. Salameh, and Q. Abdul-Jaber (1985), Characteristics of an Unusual Highly Alkaline Water from the Maqarin Area, Northern Jordan, *J. Hydrol.* 81, 79–91. NNA.19920131.0287

Khoylou, F., and A. A. Katbab (1993), *Radiation Phys. Chem.* 42, 219–222.

Kim, N. D., and S. J. Hill (1993), *Environ. Technol.* 14, 1015–1026.

Knauss, K. G., and W. J. Beiriger (1984), *Report on Static Hydrothermal Alteration Studies of Topopah Spring Tuff Wafers in J-13 Water at 150°C*, Lawrence Livermore National Laboratory, Livermore, CA, UCRL-53576. HQS.19880517.2007

Knauss, K. G., W. J. Beiriger, and D. W. Peifer (1985a), *Hydrothermal Interaction of Solid Wafers of Topopah Spring Tuff and J-13 Water at 90, 150, and 250°C Using Dickson-Type, Gold-Bag Rocking Autoclaves: 1. Short-Term Experiments*, Lawrence Livermore National Laboratory, Livermore, CA, UCRL-53645. NNA.19900207.0282

Knauss, K. G., W. J. Beiriger, and D. W. Peifer (1985b), *Hydrothermal Interaction of Crushed Topopah Spring Tuff and J-13 Water at 90, 150, and 250°C Using Dickson-Type, Gold-Bag Rocking Autoclaves*, Lawrence Livermore National Laboratory, Livermore, CA, UCRL-53630. NNA.19931005.0010

Knauss, K. G. and D. W. Peifer (1986), *Reaction of Vitric Topopah Spring Tuff and J-13 Groundwater under Hydrothermal Conditions Using Dickson-Type, Gold-Bag Rocking Autoclaves*, Lawrence Livermore National Laboratory, Livermore, CA, UCRL-53795. NNA.19891102.0017

Knauss, K. G., W. J. Beiriger, and D. W. Peifer (1987), *Hydrothermal Interaction of Solid Wafers of Topopah Spring Tuff with J-13 Water and Distilled Water at 90 and 150°C Using Dickson-Type, Gold-Bag Rocking Autoclaves: Long-Term Experiments*, Lawrence Livermore National Laboratory, Livermore, CA, UCRL-53722. NNA.19870713.0081

Komarneni, S. and D. M. Roy (1983) Hydrothermal interactions of cement or mortar with zeolites or montmorillonites. *Mat. Res. Soc. Symp. Proc.* 15, 55-62.

Kurnoskin, A. V. (1992), *J. Appl. Polym. Sci.* 46, 1509–1530.

Kutty, S. K. N., T. K. Chaki, and G. B. Nando (1992), *Polym. Degradation Stability* 38, 187–192.

Larrabee, C. P., and W. L. Mathay (1963), in F. L. LaQue and H.R. Copsum, Eds., *Corrosion Resistance of Metals and Alloys* (Reinhold Publishing Co.), 319–323. NNA.19870406.0431

Lea, F. M. (1971), *The Chemistry of Cement and Concrete* (Chemical Publishing Co.), 727 pp. NNA.19890713.0195

Leed, W. T., and R. J. Watters (1994), Assessment of Rock Bolt Systems for *Underground Waste Storage. High Level Radioactive Waste Management, Las Vegas, Nevada,* American Nuclear Society, Inc. American Society of Civil Engineers.

Licina, G.J. (1988). *Sourcebook for Microbiologically Influenced Corrosion in Nuclear Power Plants.* EPRI NP-5580, Electric Power Reasearch Institute, Palo Alto, CA.

Little, B.J., P.A. Wagner, and D. Duquette. (1987) Microbially induced cathodic depolarization. *Corrosion/87,* National Association of Corrosion Engineers, Houston, TX.

Livingston, R. A., P. E. Stutzman, R. Mark and M. Erdik (1992) Preliminary analysis of the masonry of the Hagia Sophia Basilica, Istanbul. *Mat'l.Res. Soc. Symp. Proc.* Vol. 267, 721-735.

LLYMP9603087 (1996), Memo from A. Meike to J. Montgomery of M&O/Morrison-Knudsen Corp. *Subject: Assessment of Dust Suppression Additives.*

Lovley, D.R. and E.J.P. Phillips. (1987). Rapid asay for microbially reducible ferric iron in aquatic sediments. *Appl. Environ. Microbiol.* 53, 1536-1540.

Lucey, V. F. (1972), Developments Leading to the Present Understanding of the Mechanism of Pitting Corrosion of Copper, *Br. Corrosion J.* 7, 36–41.
NNA.19891004.0341

Lundegard, P. D., Y. K. Kharaka, and R. J. Rosenbauer (1992), Petroleum as a Potential Diagenetic Agent: Experimental Evidence, in *Water-Rock Interaction* Y. Kharaka and A. Maest, Eds., (Balkema, Rotterdam), pp. 329-335.

Lynch, W. (1978), *Handbook of Silicone Rubber Fabrication.* (Van Nostrand Reinhold Company, New York, NY).

Macphee, D. E., K. Luke, F. P. Glasser and E. E. Lachowski (1989) Solubility and aging of calcium silicate hydrates in alkaline solutions at 25°C. *Am. Ceram. Soc. J.* 72, 646-654.

Majling, J., V. Tomkova and E. Istenikova (1985) Calorimetric study of reactions in the system C_4A_3S - CH - CS - H. *Thermochim. Acta* 85, 219-222.

Manning, H.L. (1975). New medium for isolating iron-oxidizing and heterotrophic acidophilic bacteria from acid mine drainage. *Appl. Microbiol.* 30, 1010-1016.

Mark, H. S., N. M. Bikales, C. G. Overberge, G. Menge, and J. I. Kroschwitz, Eds. (1985), *Encyclopedia of Polymer Science and Engineering* (John Wiley, New York, NY).

Marshall, E. (1990), Clovis Counterrevolution, 249(August 17, 1990), pp. 738–741.

Martin, S. I, B. Viani, and A. Meike (1995), Synthesis of 1.1 nm Tobermorite: A Cement Phase Expected under Repository Conditions, in *Proceedings of the 1995 High*

Level Radioactive Waste Management Meeting, Las Vegas, Nevada, Lawrence Livermore National Laboratory, Livermore, CA, UCRL-JC-119131, MOL.19950913.0005

Martin, S. I, B. Viani, and A. Meike (1996), *Water Adsorption by Okenite ($Ca_{10}Si_{18}O_{46}{\cdot}18H_2O$) at Ambient Temperature*, Lawrence Livermore National Laboratory, Livermore, CA, UCRL-ID (in preparation).

Maycock, J. N., J. Skalny and R. 5. Kalyoncu (1974) Thermal decomposition of cementitious hydrates. pp. 697-711 in R. 5. Porter and J. F. Johnson, eds. *Analytical Calorimetry*. Plenum.

McNeil, M.B., D.W. Mohr and B.J. Little (1990). *Correlation of laboratory results with observations on long-term corrosion of iron and copper alloys. Proceedings of the Materials Research Society 1990 Spring Meeting, Symposium on Materials Science in Archeology* (in press).

McNeill, I. C., M. Zulfiqar, and T. Kousar (1990), *Polym. Degradation Stability* 28, 131–151.

Meike, A. (1993), *Chemical and Mineralogical Concerns for the Use of Man-Made Materials in the Post-Emplacement Environment*, Lawrence Livermore National Laboratory, Livermore, CA, UCRL-ID-113383. MOL.19930809.0021

Meike, A. (1994), Chemical Implications for the Presence of Introduced Materials in the Post-Emplaceent Environment, *Mater. Res. Soc. Symp. Proc.* 333, 835–840. NNA.19940408.0028

Meike, A., and C. Wittwer (1994), Introduced Materials and Colloid Formation: A Report on the Current State of Knowledge, in *Proceedings of the Materials Research Society* (Fall 1993), pp. 783–789, UCRL-JC-114122. NNA.19940316.0115

Meike, A., M. Onofrei, C. J. Bruton, and B. E. Viani (1994), Progress in Understanding the Structure and Thermodynamics of Calcium Silicate Hydrates, in High Level Radioactive Waste Management, *Proceedings of the Fifth Annual International Conference* (Las Vegas, NV, May 1994), pp. 2590–2596, UCRL-JC-116358. NNA.19940517.0127

Meike, A., W. L. Bourcier, M. Alai, D. L. Haldeman, P. S. Amy, T. Lagadinos, and L. Hersman (1994), *Long-Term Chemical Effects of Diesel Fuel Emissions on a Mining Environment: A Preliminary Assessment Based on Data from a Deep Subsurface Tunnel at Rainier Mesa, Nevada Test Site*, YMP-MOL-73. MOL.19950406.0141

Meike, A., and M. Spragge (1995) *Progress Report #1 on the Materials Identification, Characterization and Evaluation Activity: Acquisition of Materials Data from the Exploratory Studies Facility*, Yucca Mountain Site Characterization Project Milestone Report #MOL132. MOL.19960415.0416

Meike, A., Ed. (1995), *Potential Long-Term Chemical Effects of Diesel Fuel Emissions on a Mining Environment: A Preliminary Assessment Based on Data from a Deep, Subsurface Tunnel at Rainier Mesa, Nevada Test Site*, Lawrence Livermore National Laboratory, Livermore, CA, UCRL-ID-121046. MOL19950406.0141

Meike, A. (1996) Man-Made Materials, *Chapter 6 in Preliminary Near-Field Environment Report Update Volume II: Scientific Overview of Near-Field Environment and Phenomena*, D. G. Wilder, Ed., Lawrence Livermore National Laboratory, Livermore, CA, UCRL-ID (in prepration).

Meike, A., Ed. (in press), *The State of Chemical Modeling Modules for the Degradation of Concrete and Cements*, Lawrence Livermore National Laboratory, Livermore, CA, UCRL-ID 123275.

Milestone, N. B., T. Sugama, L. E. Kukacka and N. Carciello (1987) Carbonation of geothermal grouts - part 3: CO_2 attack on grouts containing bentonite. *Cem. Concr. Res.* 17, 295-306.

Mor, E. D., and A. M. Beccaria (1975), Behaviour of Copper in Artificial Sea Water Containing Sulphides, *Br. Corrosion J.* 10(1), 33–38. NNA.19920506.0040

Moragues, A., A. Macias and C. Andrade (1987) Equilibria of the chemical composition of the concrete pore solution. Part I: Comparative study of synthetic and extracted solutions. *Cem. Concr. Res.* 17, 173-182.

Moragues, A., A. Macias and J. Losada (1988) Equilibria of the chemical composition of the pore concrete solution, part II: Calculation of the equilibria constants of the synthetic solutions. *Cem. Concr. Res.* 18, 342-350.

Mordi, R. C., R. Fields, and J. Dwyer (1992), *J. Chem. Soc. Chem. Commun.* (Febuary 15, 1992), 374–375.

Murakata, T., Y. Saito, T. Yosikawa, T. Suzuki, and S. Sato (1993), *Polymer* 34, 1436–1439.

Naqvi, M. K. (1991), *Polym. Degradation Stability* 33, 367–375.

Nas, L. I., and C. A. Heiberger, Eds. (1986), *Resin Manufacture and Properties* (Marcel Dekker, New York, NY).

Neal, C. and G. Stanger (1984) Calcium and magnesium hydroxide precipitation from alkaline groundwaters in Oman, and their significance to the process of serpentinization. *Min. Mag.* 48, 237-241.

Neal, C., and G. Stanger (1984), Calcium and Magnesium Hydroxide Precipitation from Alkaline Groundwaters in Oman, and Their Significance to the Process of Serpentinization, *Min. Mag.* 48, 237–241. NNA.19920131.0315

NRC (Nuclear Regulatory Commission), 1988, *Disposal of High-Level Radioactive Wastes in Geologic Repositories: Licensing Procedures*, Code of Federal Regulations, Energy, Title 10, Part 60, Washington, DC. NNA.19890715.0655

O'Donnell, J. H., and S. W. Shalabys, Eds. (1990), *Chemistry of Radiation Degradation of Polymers. Radiation Effects on Polymers* (American Chemical Society, Washington DC).

Okieimen, F. E., and J. E. Ebhoaye (1992), *Europ. Polym. J.* 28, 1423–1425.

Olofsson, U., Allard, B., Andersson, K., and B. Torstenfelt (1981), Formation and Properties of Radiocolloids in Aqueous Solution-A Literature Survey. *Programradet for Radioaktivt Abfall*, National Council for Radioactive Waste, Report Proav 4.25.

Olofsson, U., Allard, B., Andersson, K., and B. Torstenfelt (1982a), Formation and Properties of Americium Colloids in Geologic Systems. *Scientific Basis For Nuclear Waste Management*, 4, S. Topp, Ed.

Olofsson, U., Allard, B., Torstenfelt, B. and K. Andersson (1982b), Properties and Mobilities of Actinide Colloids in Geologic Systems. *Scientific Basis For Nuclear Waste Management*, 5, W. Lutze, Ed., 755-764

Onofrei, M. (1987) Leaching studies of concrete materials for nuclear fuel waste immobilization containers. pp. 351-396 in Brookins, D. G. ed. *The Geological Disposal of High Level Radioactive Wastes*. Athens, Greece: Theophrastus Publications.

Pace, N. R., D. A. Stahl, D. J. Lane and G. J. Olsen (1986), The Analysis of Natural Microbial Populations by Ribosomal RNA Sequences, *Adv. Microb. Ecol.* 9, 1–55.

Palmer, D. A., and S. E. Drummond (1986), Thermal Decarboxylation of Acetate. Part I. The Kinetics and Mechanism of Reaction in Aqueous Solution, *Geochim. Cosmochim. Acta* 50, 813–823.

Parimala, H. V., and K. Vijayan (1993), *J. Mater. Sci. Lett.* 12, 99–101.

Pollard, A.M., R.G. Thomas and P.A. Williams (1989), Synthesis and stabilities of the basic copper (II) chlorides atacamite, paratacamite and botallackite, *Mineral. Mag.*, 53, 557-563.

Pope, D. H., S. Lockwood, A. Lee, R. Skultety, and K. Keas. (1994). Mitigation of microbiologically influenced corrosion in natural gas storage facilities. *Corrosion/94* National Association of Corrosion Engineers, Houston, TX.

Raber, E., and J. Garrison (1983), *Radioactive Waste Management and the Nuclear Fuel Cycle* 4, 41–52.

Raloff, J. (1990), The colloid threat, *Science News*, March 17, 1990, p. 169.

Ravanetti, G. P., and M. Zini (1992), *Thermochim. Acta* 207, 53–64.

Reasoner, D. J., and E. E. Geldreich (1985), A New Medium for the Enumeration and Subculture of Bacteria from Potable Water, *Appl. Environ. Microbiol.* 49, 1–7.

Rek, V., D. Hace, M. Bravar, and A. Jagodar (1990), *Die Angewandte Makromolekulare Chemie* 176, 135–146.

Rhoderick, J. E. (1981) *Examination of samples of grout after 63 years exposure underground*. ONWI-248. 6 pp.

Rhoderick, J. E., and A. D. Buck (1981a), *Petrographic Examination of Several Four-Year-Old Laboratory Developed Grout Mixtures*, U.S. Army Engineer Waterways Experiment Station, Structures Laboratory. SRX.19830722.0111

Rhoderick, J. E., G. S. Wong, et al. (1981b), *Examination of Samples of Bell Canyon Test 1-FF Grout*, U.S. Army Engineer Waterways Experiment Station, Structures Laboratory. SRX.19811020.0177

Rhoderick, J. E., and A. D. Buck (1981c), *Examinations of Simulated Borehole Specimens*, U.S. Army Engineer Waterways Experiment Station. SRX.19830107.0010

Rogers, R.D. (1995), *Assessment of the Effects of Microbially Influenced Degradation on a Massive Concrete Structure. Final Report to Introduced Materials Task. July 8, 1995*, Lawrence Livermore National Laboratory, Livermore, CA, UCRL-CR-122068.

Rose, N., M. L. Bras, R. Delobel, B. Costes, and Y. Henry (1993), *Polym. Degradation Stability* 42, 307–316.

Roy, D. M., and C. A. Langton (1983), *Characterization of Cement Based Ancient Building Materials in Support of Repository Seal Materials Study*, BMI/ONWI-523. 139 pp. SRX.19870127.0146

Roy, D. M., and C. A. Langton (1989), *Studies of Ancient Concrete as Analogs of Cementitious Sealing Materials for a Repository in Tuff*, Los Alamos National Laboratory, Los Alamos, NM, LA-11527-MS. 101 pp. HQS.19880517.3281

Roy, D. M. and C. A. Langton (1989) *Studies of ancient concrete as analogs of cementitious sealing materials for a repository in tuff*. LA-11527-MS. 101 pp.

Roznak, D.B. and R.R. Colwell. (1987). Survival strategies of bacteria in the natural environment. *Microbiol. Rev.* 51, 365-379.

Russell, C. E., R. Jacobsen, D. L. Haldeman and P. S. Amy. (1994). Heterogeneity of deep subsurface microorganisms and correlations to hydrogeological and geochemical parameters. *Geomicrobiol. J.* 12, 37-51.

Sarker, A. K., M. W. Barnes and D. M. Roy (1982) *Longevity of borehole and shaft sealing materials: Thermodynamic properties of cements and related phases applied to repository sealing*. ONWI-201. 47 pp.

Sato, S., T. Murakata, S. Baba, Y. Saito, and S. Watanabe (1990), *J. Appl. Polym. Sci.* 40, 2065–2071.

Schneider, B., D. Doskocilova, J. Stokr, and M. Svoboda (1993), *Polymer* 34, 432–436.

Scott, D.A. (1985), Periodic corrosion phenomena in bronze antiquities, *Studies in Conservation*, 30, 49-57.

Seyfried, W. E., D. R. Janecky, and M. E. Berndt (1987), *Rocking Autoclaves for Hydrothermal Experiments. II. The Flexible Reaction-Cell System, in Hydrothermal Experimental Techniques*, G. C. Ulmer and H. L. Barnes, Eds. Wiley and Sons, New York. pp. 216–239.

Shewmon, P. G. (1963), *Diffusion in Solids* (McGraw-Hill, New York, NY).

Shrivastava, 0. P. and F. P. Glasser (1986) Ion-exchange properties of ll-A tobermorite. *React. Solids* 2, 261-268.

Smirnov, V. V., and E. B. Dubova (1992), *High Energy Chem.* 26, 173–177.

Soo, P. and L. W. Milian (1989) *Sulfate-attack resistance and gamma-irradiation resistance of some portland cement based mortars.* NUREG/CR-5279. 35 pp.

Soylemezoglu, S., and R. Harper (1982), Oxygen Ingress into Geothermal Steam and Its Effect on Corrosion of Low Carbon Steel at Broadlands, New Zealand, *Geothermics* 11(1), 31–42.

Spadaro, G. (1993), *Europ. Polym. J.* 29, 851–854.

Sterne, P. A., and A. Meike (1995), Electronic Structure Calculations of Calcium Silicate Hydrates, in *Proceedings of the Materials Research Society* (Boston, MA, December 1995), Lawrence Livermore National Laboratory, Livermore, CA, UCRL-JC-121437.

Suzuki, S., and E. Sinn. (1993), 1.4 nm Tobermorite-Like Calcium Silicate Hydrate Prepared at Room Temperature from $Si(OH)_4$ and $CaCl_2$ Solutions, *J. Mater. Sci. Lett.* 12, 542.

Svoboda, M., J. Stokr, and B. Schneider (1990), *Collection of Czechosovak Chemical Communications* 55, 2233–2243.

Tannenbaum, E., and I. R. Kaplan (1985), Low-M_r Hydrocarbons Generated during Hydrous and Dry Pyrolysis of Kerogen, *Nature* 317, 708–709.

Taylor, H. F. W. (1986) Proposed structure for calcium silicate hydrate gel. *Am. Ceram. Soc. J.* 69, 464-467.

Taylor, H. F. W. (1990), *Cement Chemistry* (Academic Press, London, San Diego), 123 pp.

Taylor, H. F. W. and D. M. Roy (1980) *Structure and composition of hydrates.* 7th Int. Congr. Chem. Cement II-2/1-13.

Taylor, H. F. W. (1987) Bound water in cement pastes and its significance for pore solution compositions. *Mat. Res. Soc. Symp. Proc.* 85, 47-53.

Torikai, A., R. Geetha, and S. Nagaya (1990), *J. Polym. Sci. A, Polym. Chem.* 28, 3639–3646.

Torikai, A. (1994), *Die Angewandte Makromolekulare Chemie* 216, 225–241.

Tylecote, R. F. (1979), *The Effect of Soil Conditions on the Long-Term Corrosion of Buried Tin-Bronzes and Copper*, British Nuclear Fuels Limited.

Van Konynenburg, R.A. (1986), *Radiation Doses in Granite Around Emplacement Holes in the Spent Fuel Test - Climax* (Final Report). UCRL-53580. Lawrence Livermore National Laboratory, Livermore, CA.

Vieillard, P., and F. Rassineux (1992), Thermodynamic and Geochemical Modelling of the Alteration of Two Cement Matrices, *Appl. Geochem. Suppl.* 1, 125–136.

Wallius, S. (1993), *Die Angewandte Makromolekulare Chemie* 212, 103–119.

Ward, D. M., R. Weller, and M. M. Bateson (1990), ^{16}S rRNA Sequences Reveal Numerous Uncultured Microorganisms in a Natural Community, *Nature* 345, 63–65.

Warren, R. S., F. M. Byers, and F. A. Caporuscio (1984), *Petrography and Mineral Chemistry of Units of the Topopah Spring, Calico Hills, and Crater Flat Tuffs, and Older Volcanic Units, with Emphasis on the Samples from Drill Hole USW G-1, Yucca Mountain, Nevada Test Site*, Los Alamos National Laboratory, Los Alamos, NM, LA-10003-MS. HQS.19880517.2569

Welch, D.F. (1991). Applications of cellular fatty acid analysis. *Clin. Microbiol. Rev.* 4, 422–438.

Weres, O., A. S. Newton, and L. Tsao (1988), Hydrous Pyrolysis of Alkanes, Alkenes, Alcohols and Ethers, *Org. Geochem.* 12, 433–444.

West, K. A. (1988), *Nevada Nuclear Waste Storage Investigations Exploratory Shaft Facility Fluids and Materials Evaluation*, Los Alamos National Laboratory, Los Alamos, NM, LA-11398-MS. NNI.19981213.0021

Westlake, D.W.S., K.M. Semple, and C.O. Obuekwe (1985). Corrosion by ferric iron-reducing bacteria isolated from oil production systems. *Proceedings of the International Conference on Biologically Induced Corrosion*, June 10–12, 1985, Gaithersburg, MD.

Wheeler, D. R., and S. V. Pepper (1990), *J. Vac. Sci. Technol.* 8, 4046–4056.

Williams, J. L., Ed. (1990), *Stability of Polypropylene to Gamma Irradiation* (American Chemical Society, Washington, DC), pp. 554–568.

Wilski, H. (1990), *Influence of Ionizing Radiation on Thermoset Plastics* (American Chemical Society, Washington, DC).

Winograd, I. J. (1986), *Archaeology and Public Perception of a Trans-Scientific Problem: Disposal of Toxic Wastes in the Unsaturated Zone*, U.S. Geological Survey. NNA.19910627.0007

Woese, C. R. (1987), Bacterial Evolution, *Microbiol. Rev.* 51, 221–271.

Wolery, T., K. J. Jackson, et al. (1990), *Current Status of the EQ3/6 Software Package for Geochemical Modeling, in Chemical Modeling in Aqueous Systems II*. Lawrence Livermore National Laboratory Report. NNA.19900716.0363

Wu, Z-Q. and J. F. Young (1984) Formation of calcium hydroxide from aqueous suspensions of tricalcium silicate. *Am. Ceram. Soc. J.* 67, 48–51.

Xiuji, F. and L. Shizong (1986) Investigation of the effect of minor ions on the stability of b-C_2S and the mechanism of stabilization, *Cem. Concr. Res.* 16, 587–601.

Xu, P., D. Zhou, and D. Zhao (1989a), *Europ. Polym. J.* 25, 581–583.

Young, J. F., H. S. Tong and R. L. Berger (1977) Compositions of solutions in contact with hydrating tricalcium silicate pastes. *Am. Ceram. Soc. J.* 60, 193–198.

Appendix A: Polymer Chemistry

Polymerization. Polymerization occurs via addition or condensation polymerization. These basic chemical reactions are achieved through one of four primary techniques by which polymers are formed from monomers (bulk, solution, suspension, and emulsion). There are three properties which differentiate addition polymerization from condensation polymerization. First, the repeat unit in the polymer and the monomer have the same composition, although the bonding is different in each for addition polymerization. Second, the mechanism of these reactions places addition polymerization in the kinetic category of chain reactions, with either free radicals or ionic groups responsible for propagating the chain reaction. Lastly, the product molecules usually have a carbon chain backbone, with pendant substituent groups. Chain growth polymers include polyethylene, polystyrene, polyvinylchloride (PVC), polyisobutylene, and Teflon.

Chemical characterization. Chemical characterization of polymers is a complex issue because even within a given polymer class, it is not possible to make correlations between polymers and simpler but chemically similar molecules, because each polymer has its own unique set of properties that depend on chemical structures, chain lengths, conformations, and degrees of branching and crystallinity. This diversity is further complicated by the addition of filler, plasticizers, stabilizers as well as other additives. Two products of the same polymeric substance but with different additives can react differently to the same conditions. Thus, in order to completely understand the affects of a given product, the range of chemical composition must be known. Beginning in the 1920s cellulose nitrate and cellulose acetate became widely used as well as phenol-formaldehyde (Bakelite) which was the first synthetic thermoset (crosslinked) polymer. Given this relatively recent arrival, limited insight can be gained on long-term behavior through historical analogs. Thus, extension back in time will require a sound understanding of fundamental chemical principles, which are outlined below. It must be emphasized that the degradation behavior is based on relatively short term experiments and should only act as a first estimate for the prediction of long-term stability in the context of a radioactive waste repository.

Molecular Weight Distribution. A polymeric material is made up of many polymer molecules which are held together by entanglements and intermolecular forces and crosslinks. It is the exception when polymerization is carried out so that all polymers have the same degree of polymerization. Thus it is difficult to define useful

thermodynamic parameters for these materials. Molecular weight distribution reflects the number of bonds or degree of polymerization and is a fundamental diagnostic polymer property. Properties that are dependent on the number of molecules in a system, called colligative properties, are osmotic pressure, boiling point, and freezing point. Measurement of these properties can thus be used to determine the average molecular weight and the degree of polymerization. Colligative properties have also been used to assess the thermodynamic behavior of polymers in solution. The molecular weight distribution represents the variation from the average of the polymers within the material. A broad distribution in the degree of polymerization of a polymer population is represented as a large "degree of freedom".

Theta Condition. When a polymer is in the theta condition, the tendency to spread out is exactly balanced with the excluded volume effect (real polymer conformations should be more spread out than those predicted because only one polymer segment can take up a certain space at a given time). Solvents which yield this "equilibrium" are referred to as theta solvents and the temperature at which the theta condition is reached for a given polymer/solvent pair is known as the theta temperature.

Many parameters are known for a theta polymer thus, interpretation can be less complex if the polymer is in the theta condition. Given that much information about polymers is in the realm of synthesis, where a theta condition may be sought, it is to be expected that information for conditions outside of the theta condition (which will be the rule rather than the exception under repository conditions) are far less complete.

Thermoplastics vs Thermosets. All solid polymers can be categorized as either thermoplastics and thermosets. The polymer molecules of thermoplastics are held together by intermolecular forces. Thermoplastics soften when heated but do not degrade until a certain temperature. They can be molded and remolded with the use of heat. Examples of thermoplastics are nylon and polystyrene. Thermosets on the other hand contain polymer molecules which are joined by chemical crosslinks. They are achieved by a chemical reaction which creates a crosslinked polymer which can not be remolded once it is set. The crosslinks prevent bond motion (in some cases, the crosslinked polymer can be stretched but the crosslinks prevent the remolding possible with thermoplastics). Examples of thermosets are epoxy and vulcanized rubber. The polymer is still a polymer before crosslinking but it is primarily used in its crosslinked form. Polyester is an example of a polymer that is used as a thermoplastic and which can be crosslinked to become a thermoset.

Polymer Elasticity. Depending on the length of the polymer chains and on the temperature, a particular type of polymer may occur as a viscous liquid, a rubbery

solid, a glass or a partially crystalline solid. The longer the average length of the polymer chains, the less viscous the polymer at a given temperature. The polymer chains are coiled and intertwined with each other. If the polymer is stretched, then the chains slowly untangle and the polymer appears to flow. The relative movement of polymer chains can be decreased by connecting the polymer chains with chemical bonds called crosslinks. When the crosslinked network is stretched, the coils become elongated, but when the stress is released or more energy is put into the system, the polymer network returns to its original coiled state.

Transition Temperature. The physical state of polymers is temperature dependent. Like most materials, polymers have a melting point (T_m). In addition, within the solid state ($T < T_m$), polymers can be in a "glassy" state or in a "rubber" state (different from a crosslinked rubber). The glass transition temperature (T_g) determines the turning point between "glass," where there is not rotation around bonds and "rubber," where segmental bond motion begins. A polymer in the glass state, is stiff and often brittle, but upon passing through its glass transition temperature becomes flexible and malleable. Thus T_g and factors that affect T_g determine the mechanical characteristics of the polymer.

The T_g increases with molecular weight or degree of polymerization, as well ass crystallinity. Side branching usually decreases T_g by leading to a less ordered structure as does heterogeneity of the polymer chain (i.e. copolymers). Chemical composition and configuration (syndiotactic, atactic, isotactic) both affect T_g. In addition, T_g can be lowered by the addition of plasticizers (a plasticizer is defined as any substance which when added to the polymer, lowers its glass transition temperature). For example, water acts as a plasticizer in nylon. Most thermoplastic polymers for consumer applications (e.g. plastic bags, nylon running shorts and 2-L soda bottles) have a glass transition temperature below room temperature for flexibility .

Crystalline and Amorphous States. The orientation of a polymer chain can be ordered by physical force. This is how fibers, as well as most plastic consumer products are formed. A force is applied to the material above the T_g and then the material is cooled. Because it is now a glass, the polymer will not return to its original disordered state. However, as soon as the thermoplastic polymer is heated, it will return to its original form. Crystalline regions are created by the packing of molecular chains together. The crystallinity is dependent on the material itself as well as the production method. For example, an isotactic polymer can be more easily packed than an atactic polymer. Crystals can only be formed above the T_g and below the melting temperature (T_m). Crystallinity can also be achieved by adding particles to the polymer melt which

create an area of reduced energy so that a crystal can propagate(more order means more energy). Crystallinity affects most polymer properties including T_g (increased crystallinity increases T_g), and wettability (crystallinity reduces wettability).

The noncrystalline or amorphous regions are important determinants of polymer properties. Amorphous regions allow for wettability and elasticity in the polymer. Many structures of polymers in terms of crystalline and amorphous regions have been suggested but the exact structure of polymers are not known.

Additives. Additives to polymer resins improve strength, flexibility, flame retardance, or appearance. The term antioxidant is broadly used to refer to inhibitors for autoxidation: heat stabilizers, melt stabilizers, light stabilizers, antifatigue agents and antiozonants. All of these agents interfere with the free radical reactions that lead to the incorporation of oxygen into macromolecules. For example, N-phenyl B-napthylamine and butylated hydroxytoluene respectively are added to elastomers and plastics to reduce deterioration related to autoxidation (Mark et al., 1985). Plasticizers lower the glass transition temperature of a material making processing easier and the polymers more flexible. Phtalic esters are common plasticizers (Mark et al., 1985; Khinnavar and Aminabhavi, 1992).

Appendix B: Curing of Cementitious Material

Cement is predominantly composed of calcium-bearing phases that crystallize when water is added to a mixture of carbonate, silicate, and other phases. Table B-1 briefly describes the nomenclature and standards of cement chemistry. The reactions and structural changes take place over time scales of a few seconds to a year or longer and are sensitive to temperature within the range of interest to the repository. Table B-2 summarizes the chemistry of the major cement hydration reactions. Hydration reactions that predominate below 100°C as well as those that predominate above 100°C are summarized (Bensted, 1989). Table B-3 lists formulas of cement phases.

The most important reaction in curing cement at ambient conditions is probably the hydration of calcium silicates. Alite, C_3S, is known to hydrate considerably faster than belite, an impurity-stabilized form of C_2S at 25°C, and the former is thus the primary contributor to the early strength of concretes. Alite has often been chosen for detailed study because of this kinetic advantage. Other important phases in the hydration and crystallization process include a calcium silicate hydrate gel, C-S-H (no stoichiometry, crystallinity, structure, or degree of polymerization is implied), which is common to most cements. The literature distinguishes at least two forms of this "gel": an early phase that consumes most of the anhydrous starting material within about 28 days (Glasser et al., 1987), and a more polymerized phase that increases in length as the material ages. Although the details are poorly documented, some structural characteristics of the C-S-H phase are well known. The quasi-crystalline C-S-H phases that develop with aging are considerably more crystalline, with either an imperfect tobermorite-like structure or a jennite-like structure. Tobermorite-like phases appear to be favored as aging progresses in cements that contain siliceous blending agents (Shrivastava and Glasser, 1986). The microstructural changes that accompany these solid-state phase transformations may affect virtually all measurable thermal, mechanical, and physical properties. These effects have not been described, and they remain unpredictable. The polymers appear to incorporate a range of ions, and the C:S ratio can also vary. As a consequence, the kinetics and degree of polymerization may differ as a function of the composition of the starting materials.

Kinetic data are limited primarily to the formation of C-S-H from pure beta-C_2S and C_3S. A review of the literature on the kinetics of belite and alite hydration (Barret and Bertrandie, 1986) suggests that the mechanisms may be debated, but that the markedly slower hydration of belite is thought to be similar to alite. In both cases, rapid

dissolution within a few minutes of hydration is followed by a somewhat linear increase to a maximum ion concentration that represents supersaturation with respect to portlandite. Subsequently, the concentration decreases, first rapidly, then slowly and linearly (Wu and Young, 1984; Brown et al., 1984). Competition between chemical reactions that start at different times and differ in progress of reaction will determine the overall rate. Brown et al. (1985) proposed that an initial hydrate forms that eventually nucleates a more stable hydrate. The consequent increase in the rate of Ca^{++} and OH^- liberation eventually supersaturates the solution with respect to $Ca(OH)_2$, which precipitates. The subsequent hydration of C_3S is diffusion-controlled. Grutzeck and Ramachandran (1987) propose that a precipitate of a very-fine-grained C-S-H initially forms on the surface of C_3S as a result of supersaturation and controls subsequent hydration via diffusion. New material forms at the solid/hydrate interface while the fine-grained outer layer dissolves. A sufficiently supersaturated solution at a pH of 11.5 will form relatively-coarse-grained C-S-H(II) at the expense of the fine-grained initial C-S-H. Bensted (1983a) finds that most of the initial ettringite is formed from C_3A at the greatest rate during the first 5 min, followed by a steady increase for up to 2 hr. After 8 to 26 hr, when the gypsum is gone, ettringite reacts with C_4AH_{13} to form monosulfate (Bensted, 1983b). The iron from ferrite is thus freed to participate in hydrous phases. Alkalis, whether present in the original grout or contributed by additives or aggregate, are released in temperature-sensitive reactions from clinker phases to the pore fluids within days (Glasser and Marr, 1984; Glasser et al., 1985), and reach concentrations of 0.05 to 1.0*M*. The presence of alkalis depresses calcium solubility and thus (1) determines the pH of the pore fluid (Macphee et al., 1989), and (2) affects the hydration of alite and belite (Wu and Young, 1984).

Ettringite is the most prevalent sulfate-bearing hydration product below 80°C and is an important trivalent-ion-bearing phase. Within broad limits, ettringite appears to form independently of the degree of hydration (Bensted, 1983a,b), but it is not stable above 75 to 80°C under 100% relative humidity. Prediction of the fate of much of the Al^{+++} and $SO_4^=$ in the hydrated cement, and possibly Fe^{+++}, is dependent on the knowledge of ettringite thermochemistry. Ettringite formed from aluminate and ferrite phases composes a continuous hydrated solid-solution. Analogous solid-solutions of other phases may be formed from ferrite and aluminate. Above about 100°C, iron-rich monosulfate often forms as a consequence of reactions that consume ettringite, which loses much of its structural water on heating to 60°C and transforms to $C_6AS_3H_8$ at 110°C (Taylor, 1987) at pH 11. Ettringite ultimately decomposes to gypsum, aragonite, and $Al(OH)_3$ (Grounds et al., 1985), and to crystalline calcium silicates that include

tobermorite, xonotolite, gyrolite, hydrogarnet, stratlingite, alpha-C_2SH, and $C_6S_2H_3$ (Bensted, 1989). Tobermorite-11Å is a disordered structure (Taylor, 1964) that precipitates in water at temperatures greater than 100°C, but which has been observed from cements leached at 25°C and those cured at 60°C (Barnes and Roy, 1983). "Normal" tobermorite-11Å decreases to 9.3-Å spacing by 300°C. These products are also expected of cement formed at ambient conditions, cured, and subsequently heated to ≥100°C (Scheetz and Roy, 1989a,b), a scenario that is anticipated for the waste repository.

The consequences of incorporating aggregate materials, blending agents, and other additives such as fly ash, blast furnace slag (bfs), silica fume, rice husk ash, and natural pozzolan into cement have been investigated to a limited extent (Glasser et al., 1986; Macphee et al., 1989; Andersson et al., 1989). Glasser et al. (1987) provide a summary of the chemical and mineralogical effects of these cement additives. Pozzolanic aggregate materials react chemically to give the cement advantageous properties. A pertinent example of natural aggregates that behave as pozzolanas are some siliceous welded tuffaceous rocks. Other materials that may be added to cements to influence the rate at which they cure include an anhydrous material, "clinker" which is produced by cement kilns, and gypsum. Gypsum, which is added to prevent flash setting, can lose water during grinding with clinker to form hemihydrate. Rehydration of gypsum when water is added to the cement can compete with cement minerals such as ettringite and influence their aging kinetics. An aggregate of bfs creates a reducing environment and thus may influence the mobility of ions and complexes that are sensitive to oxidation conditions. The bfs additive contains materials foreign to the usual cement chemistry: large amounts of ferrous iron, considerably more Mg^{++} than is present in usual cement formulations, and, possibly, dispersed iron metal and iron sulfide. Mg^{++} is known to react with C-S-H to form $Mg(OH)_2$ and thus destroy the main cohesive phase of concretes. The oxidation of S and Fe could cause significant volumetric changes.

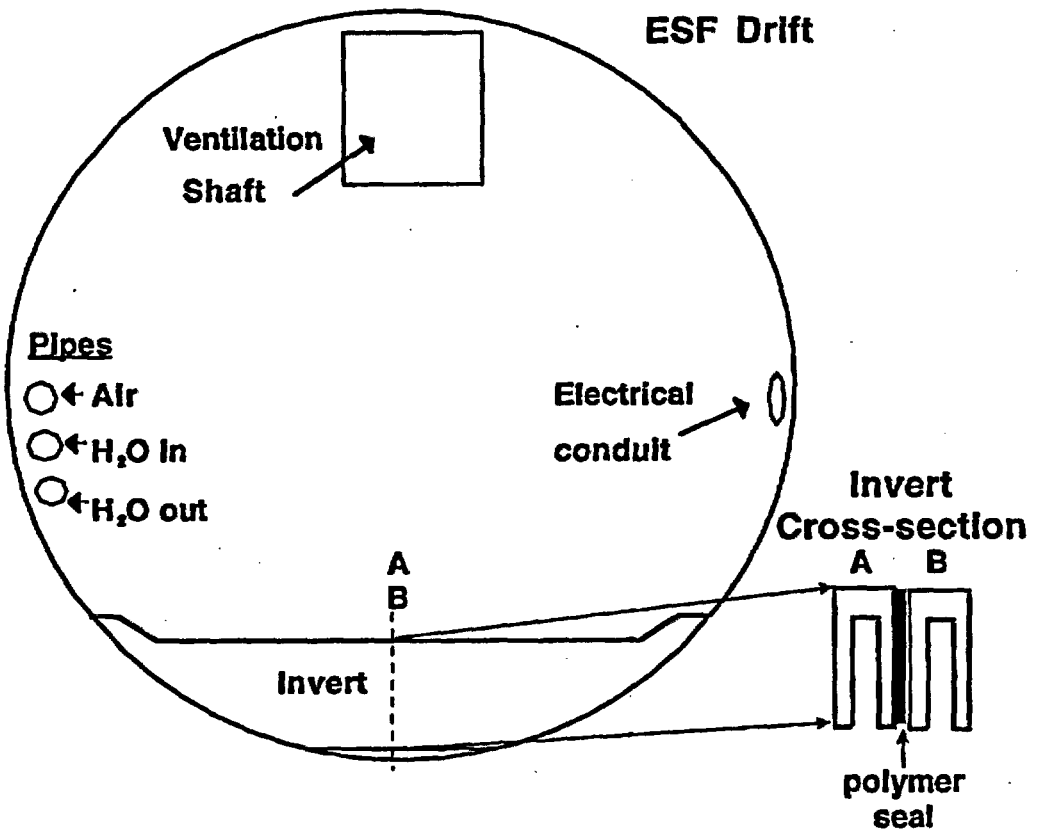

Figure 6-1. Schematic view (not to scale) of ESF drift cross-section illustrates the placement of some materials. The shape of the invert is illustrated in tunnel cross-section, and the invert cross-section parallel to the tunnel axis.

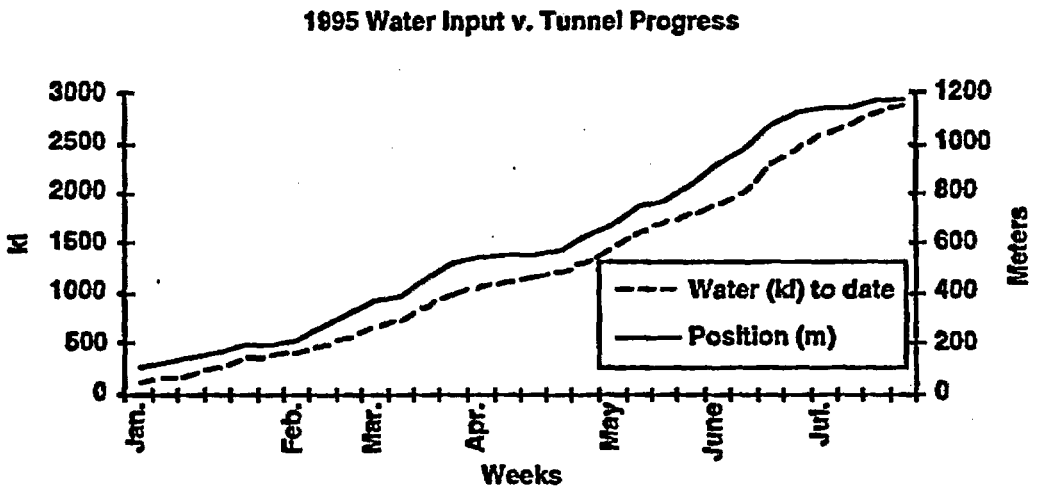

Figure 6-2. Total water usage and total meters excavated are plotted as a function of time. It is clear that the limit specified in the DIE, no more than 7.4 cubic meters of water per linear meter of tunnel excavated, has not been exceeded. Total water usage to date averages roughly 2.47 kL/m.

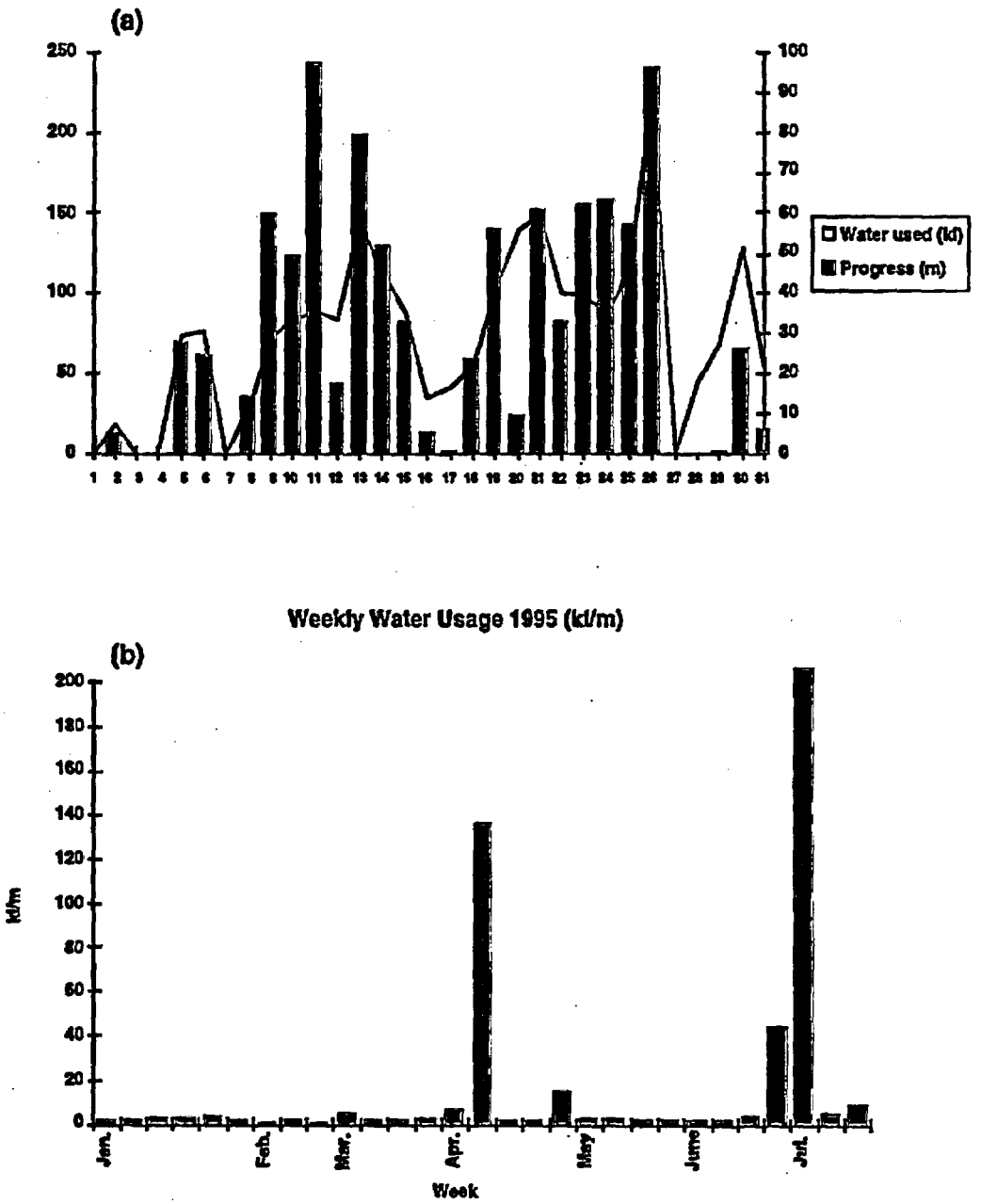

Figure 6-3. (a) A plot of weekly water usage and weekly excavation progress as a function of time suggests a strong correlation between water usage and excavation progress. (b) A plot of water usage as a function of time demonstrates that an average amount of water usage of between 2 and 4 kL/m is punctuated by episodes of large water usage.

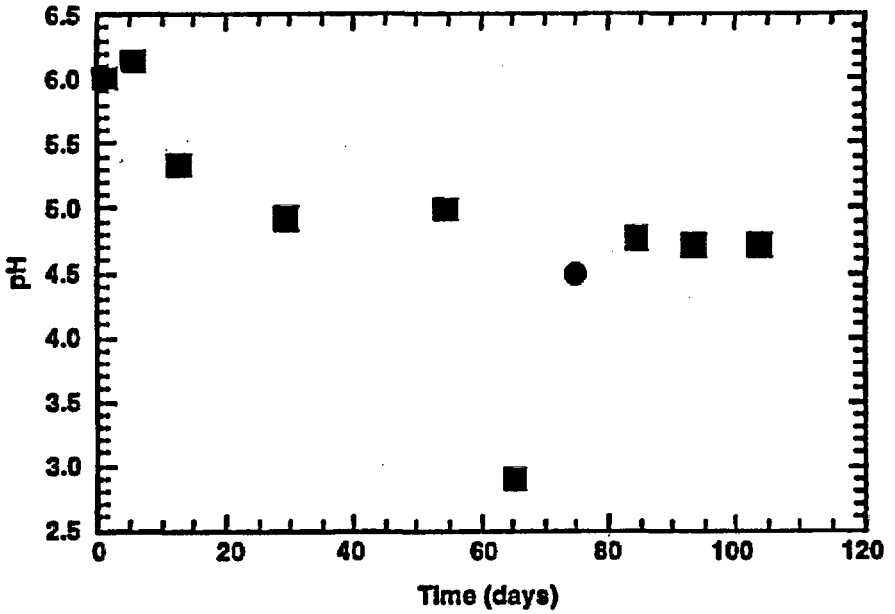

Figure 6-4. Experimental pH (25 °C) as a function of time from diesel fuel hydrous pyrolysis experiments DF1 at 200 °C (circle) and DF2 at 315 °C (squares).

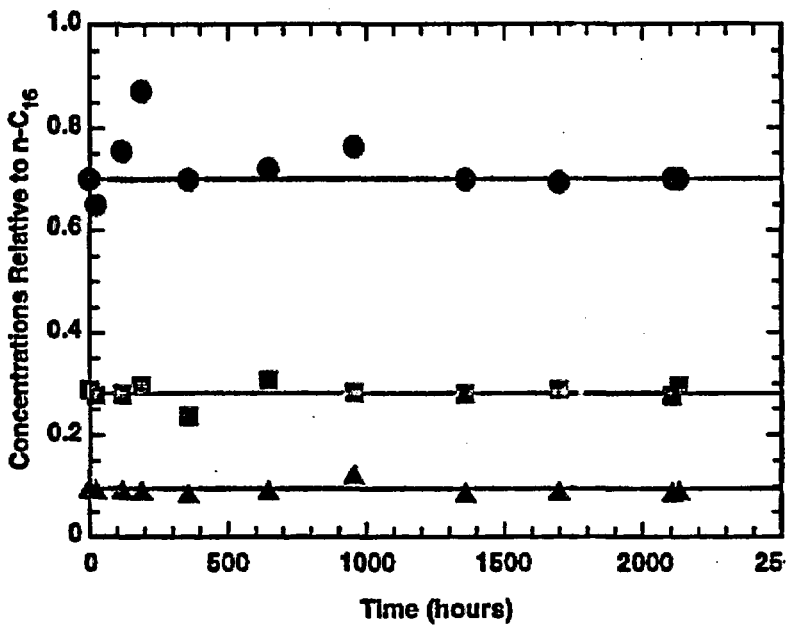

Figure 6-5. Diesel fuel relative concentrations of C_{10-14} normalized with respect to C_{16} as a function of time for experiment DF1. The circles, squares, and triangles are alkanes, C_{14}, C_{12}, and C_{10} respectively.

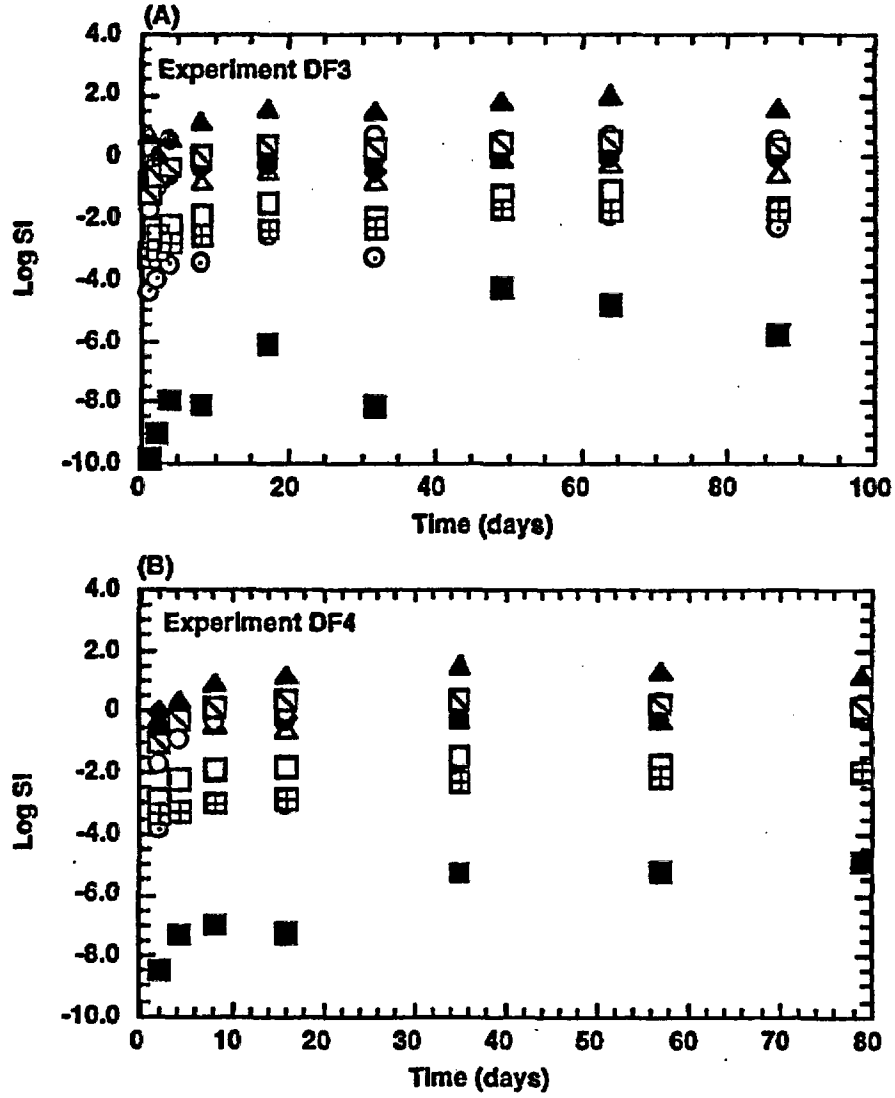

Figure 6-6. Experiment DF3 (A) and DF4 (B) Fibercrete™-water interactions plotted as the log SI with respect to quartz (solid circle), wollastonite (solid diamond), K-feldspar (square with a slash), albite (open circle), anorthite (open square), calcite (open triangle), mesolite (solid triangle), gyrolite (open circle with center dot), 11Å-tobermorite (solid square), and bassanite (open square with cross). The saturation index (SI) is equal to the IAP / K_{eq} for a given mineral. A log SI greater than, equal to, or less than zero, indicates that the solution is supersaturated, saturated, or undersaturated respectively in regard to a given mineral, where IAP is the ion activity product and K_{eq} is the equilibrium constant.

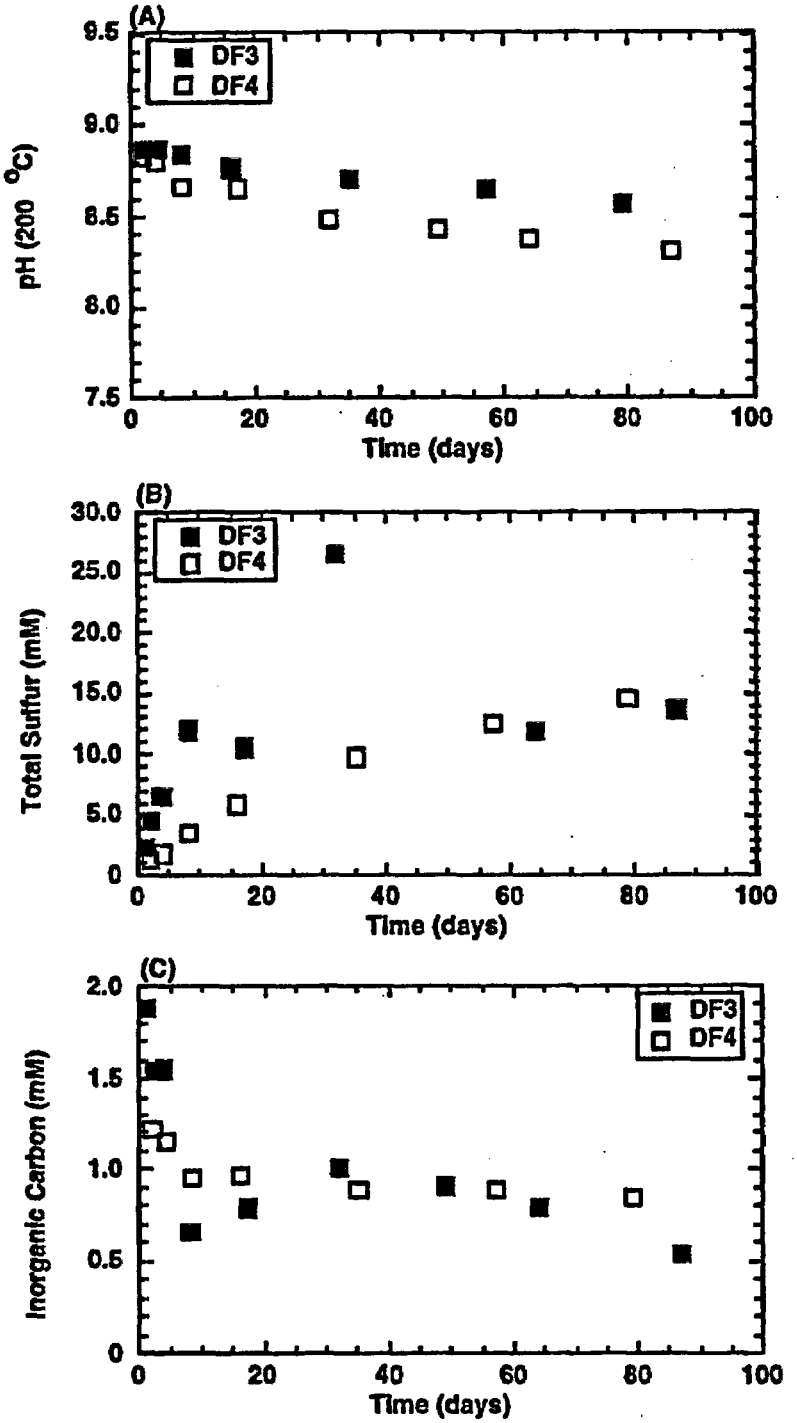

Figure 6-7. Aqueous composition of experiments DF3 and DF4. (A) pH (200 °C), (B) total sulfur, and (C) inorganic carbon are plotted as a function of time.

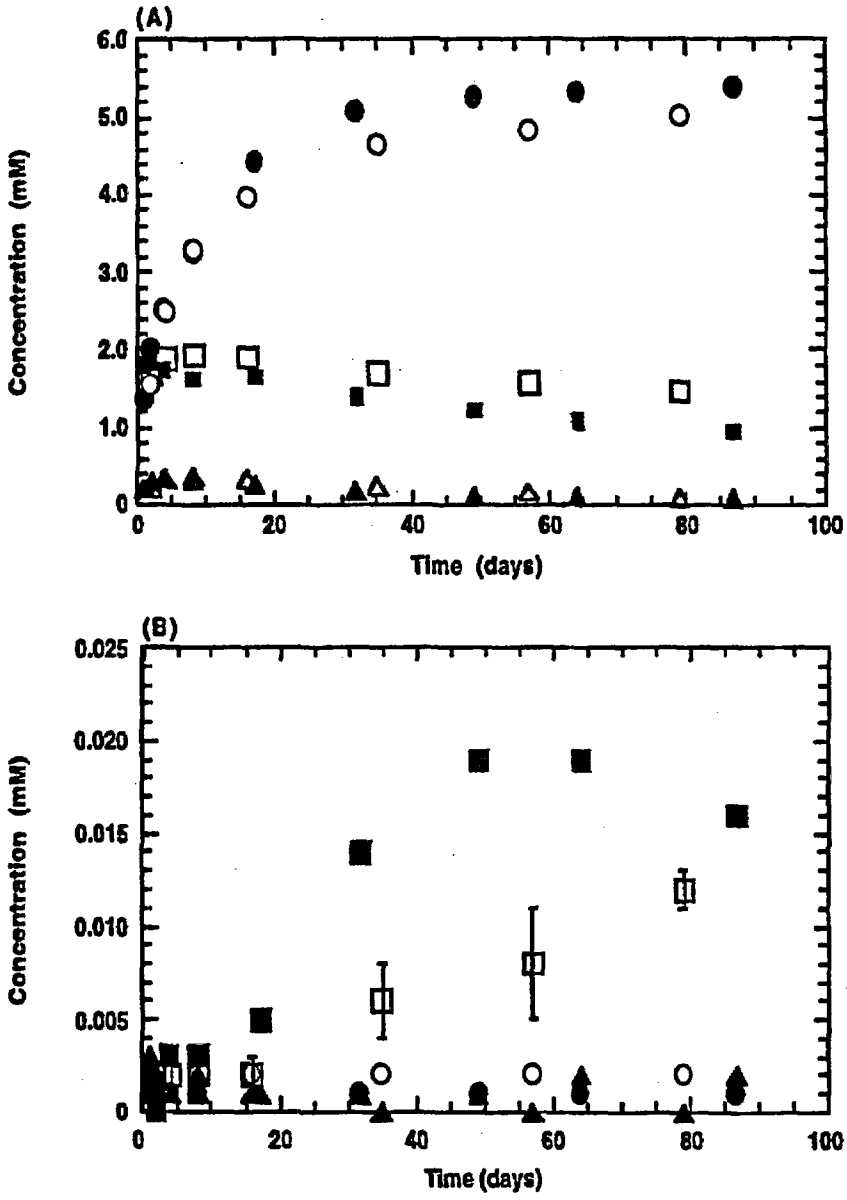

Figure 6-8. Aqueous composition of experiment DF3 (solid symbols) and DF4 (open symbols) plotted as function of time. (A) Si (circles), Al (triangles) and K (squares) and (B) Ca (squares), Mg (circles) and Fe (triangles).

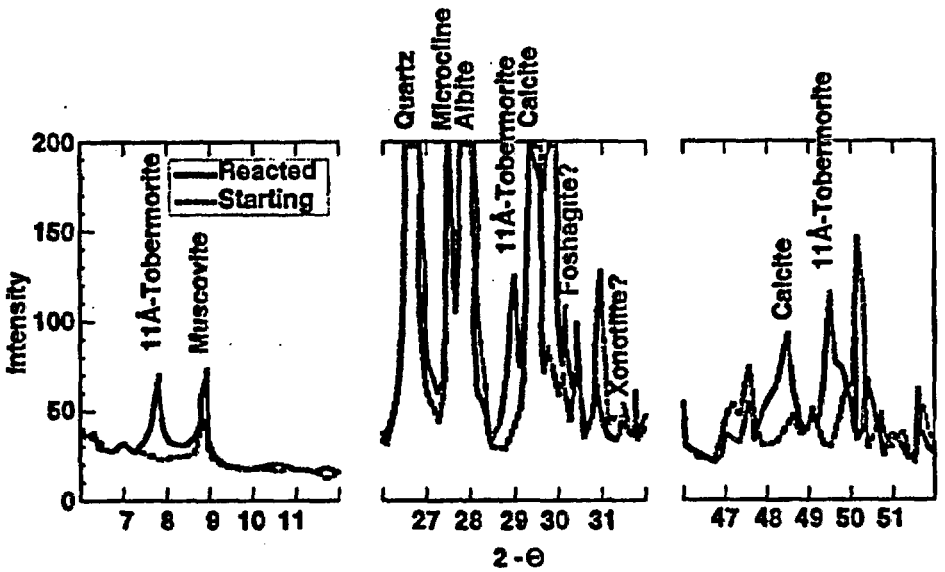

Figure 6-9. XRD pattern showing the three most intense peaks for 11Å-tobermorite in the reacted Fibercrete™.

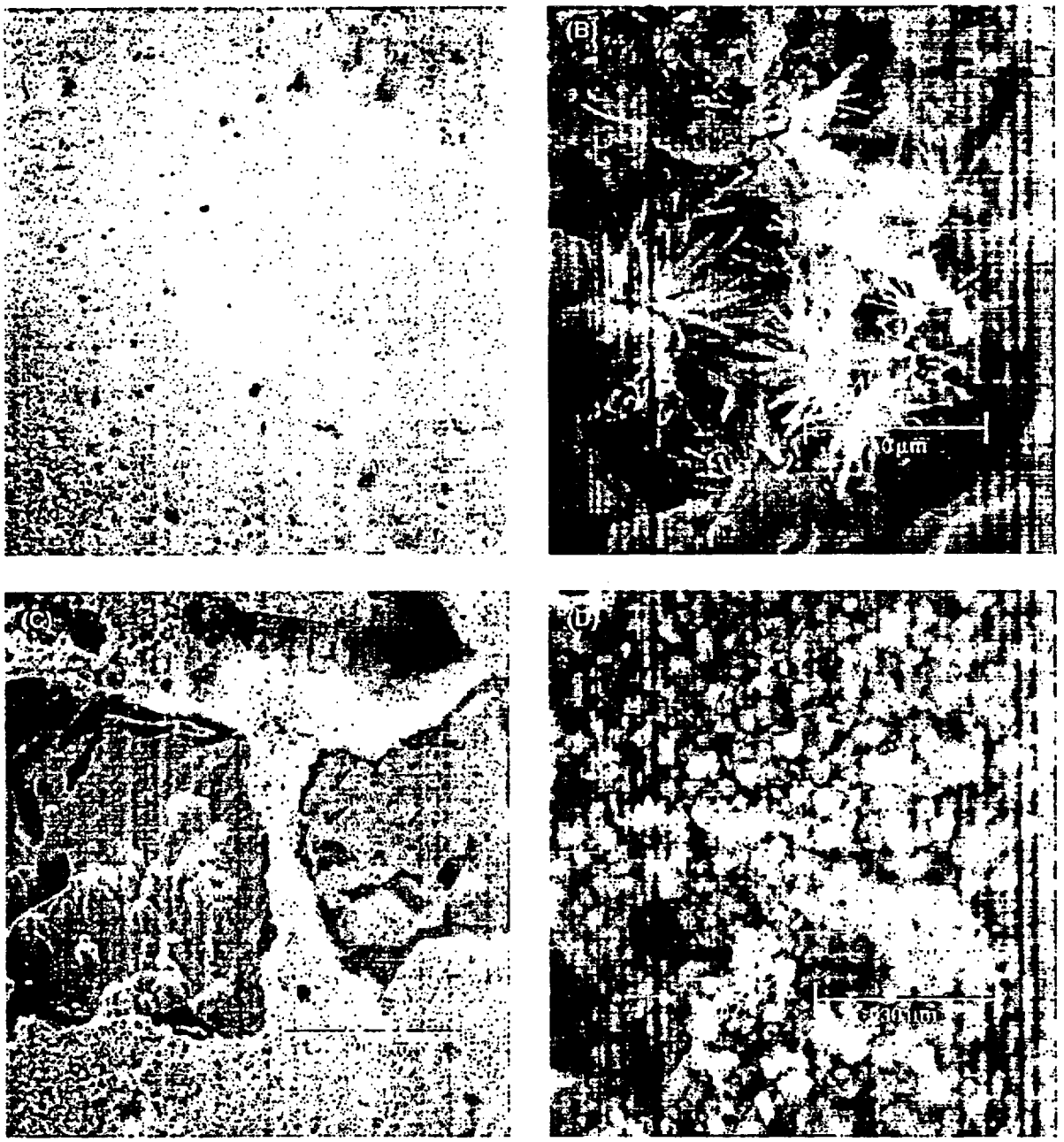

Figure 6-10. SEM photomicrographs of unreacted (A, B) and reacted Fibercrete™ (C, D). (A) Fibercrete™ consists of large quartz and feldspar aggregate minerals and steel fibers (light area near center) in a grout matrix. (B) Magnification of the grout matrix showing crystallites. (C) Reacted Fibercrete™ showing both dissolution precipitation features on the quartz aggregate minerals and the precipitation of Ca-rich phase at the Fibercrete™ surface. (D) Enlargement of the Ca-rich phase showing blocky morphology.

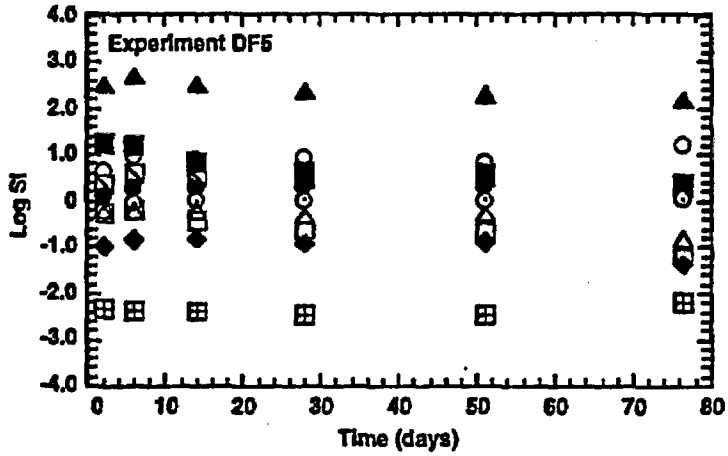

Figure 6-11. Experiment DF5. Topopah Spring tuff - water - diesel fuel interactions plotted as the log SI with respect to quartz (solid circle), cristobalite (open circle with center dot), wollastonite (solid diamond), K-feldspar (square with a slash), albite (open circle), anorthite (open square), muscovite (solid square), calcite (open triangle), mesolite (solid triangle), and bassanite (open square with cross).

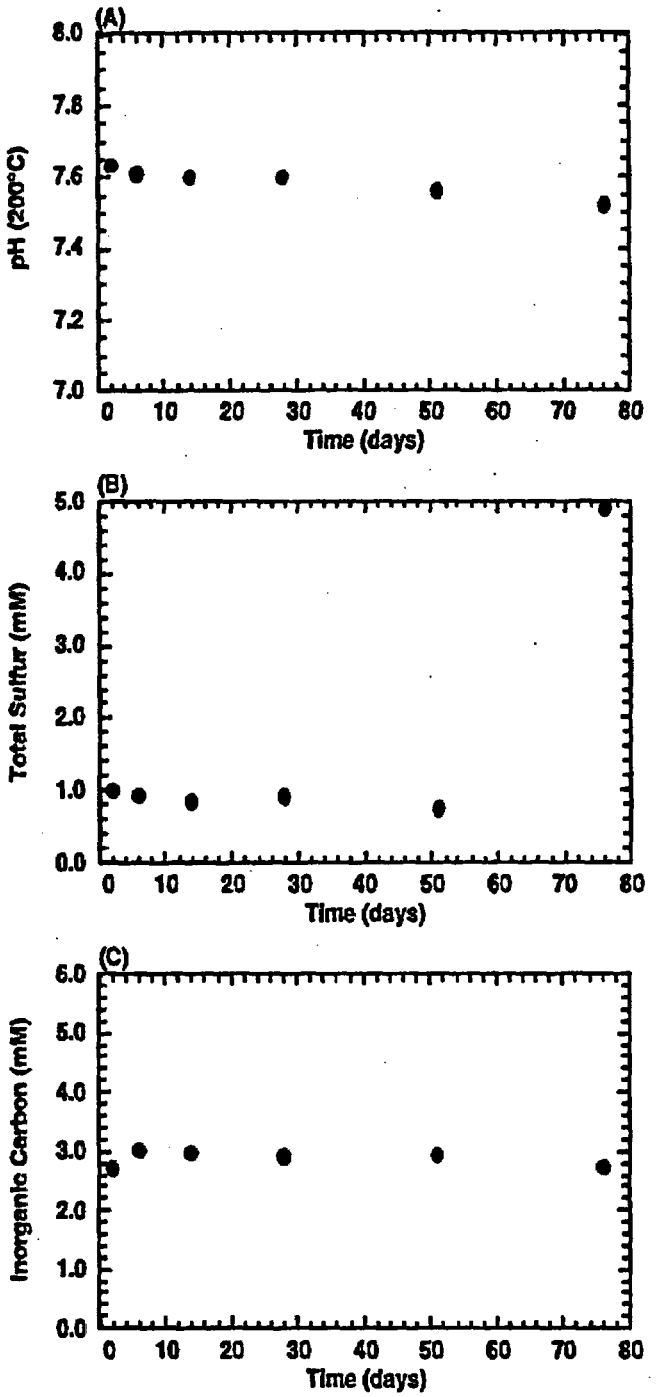

Figure 6-12. Aqueous (A) pH (200 °C), (B) total sulfur, and (C) inorganic carbon of experiment DF5 plotted as a function of time.

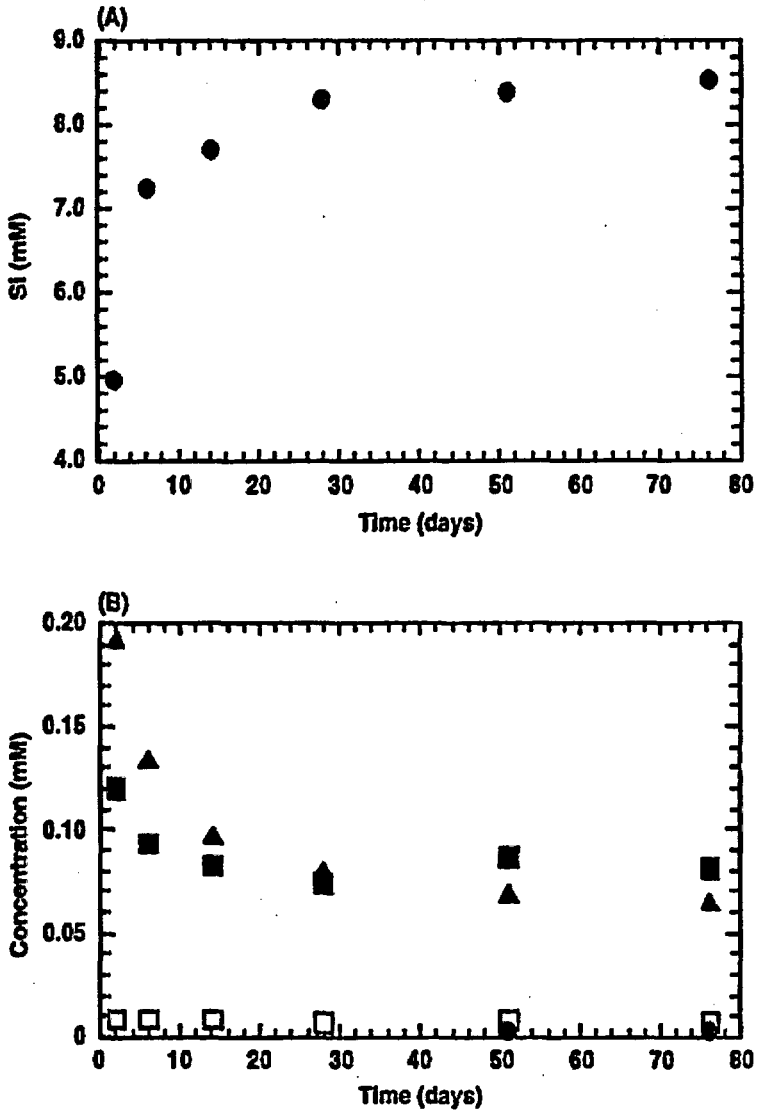

Figure 6-13. Aqueous (A) Si (circles) (B) Al (triangles), K (squares), Ca (open squares), and Mg (circles) of experiment DF5 plotted as function of time.

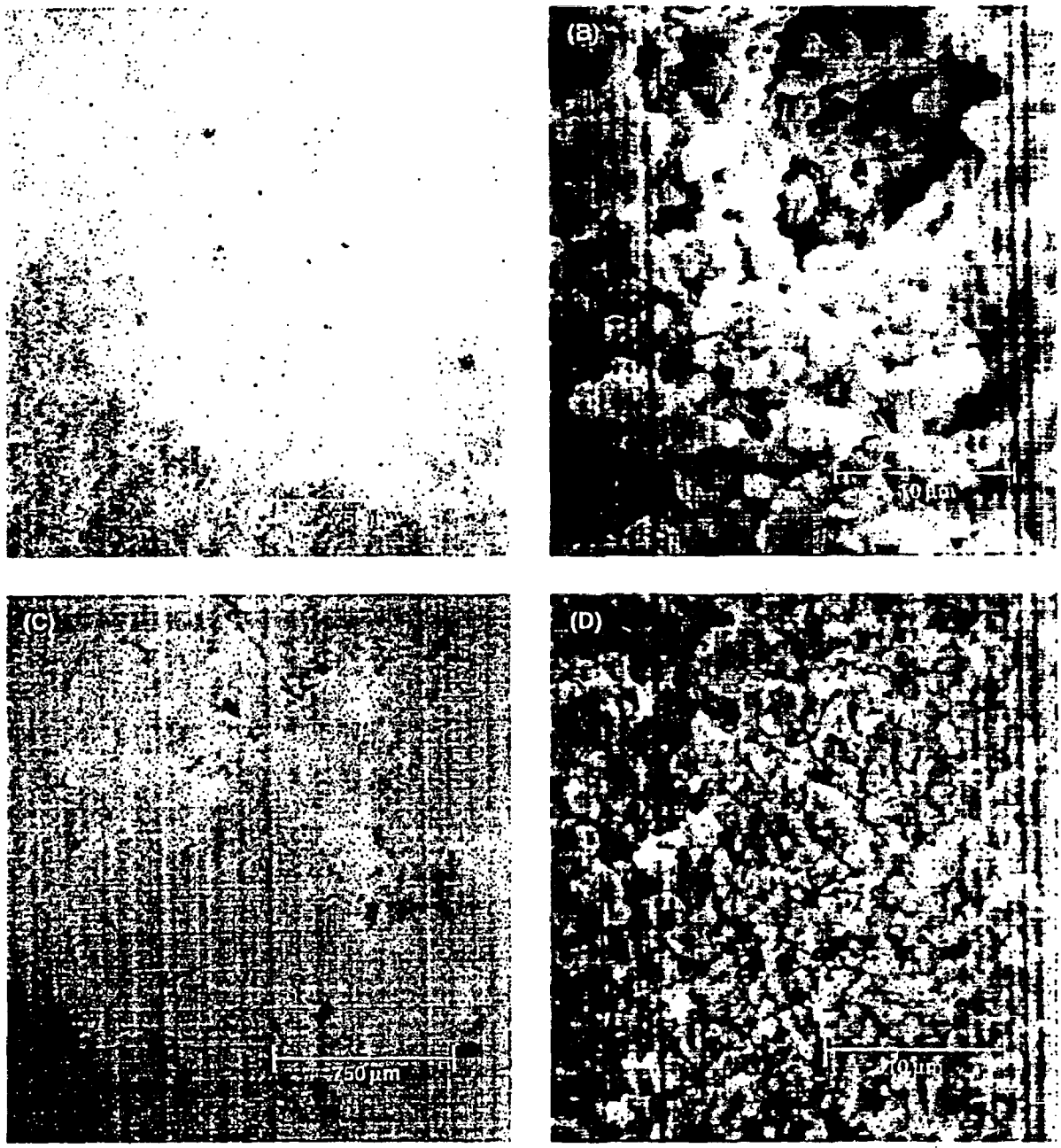

Figure 6-14. SEM photomicrographs of unreacted (A, B) and reacted Topopah Spring tuff (C, D). (B) Magnification of the glassy matrix in the tuff. (C) Reacted Topopah Spring tuff showing a precipitated Si-rich phase (D) Enlargement of the Si-rich precipitate.

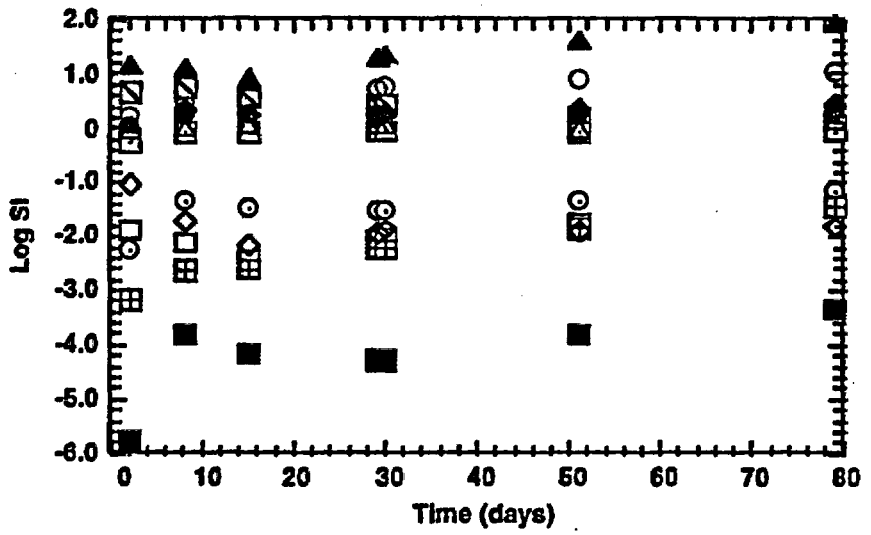

Figure 6-15. Experiment DF6. Topopah Spring tuff - Fibercrete™-water - diesel fuel interactions plotted as the log SI with respect to quartz (solid circle), cristobalite (open square with center dot), wollastonite (solid diamond), K-feldspar (square with a slash), albite (open circle), anorthite (open square), muscovite (open diamond), calcite (open triangle), mesolite (solid triangle), bassanite (open square with cross), gyrolite (open circle with center dot), and 11Å-tobermorite (solid square).

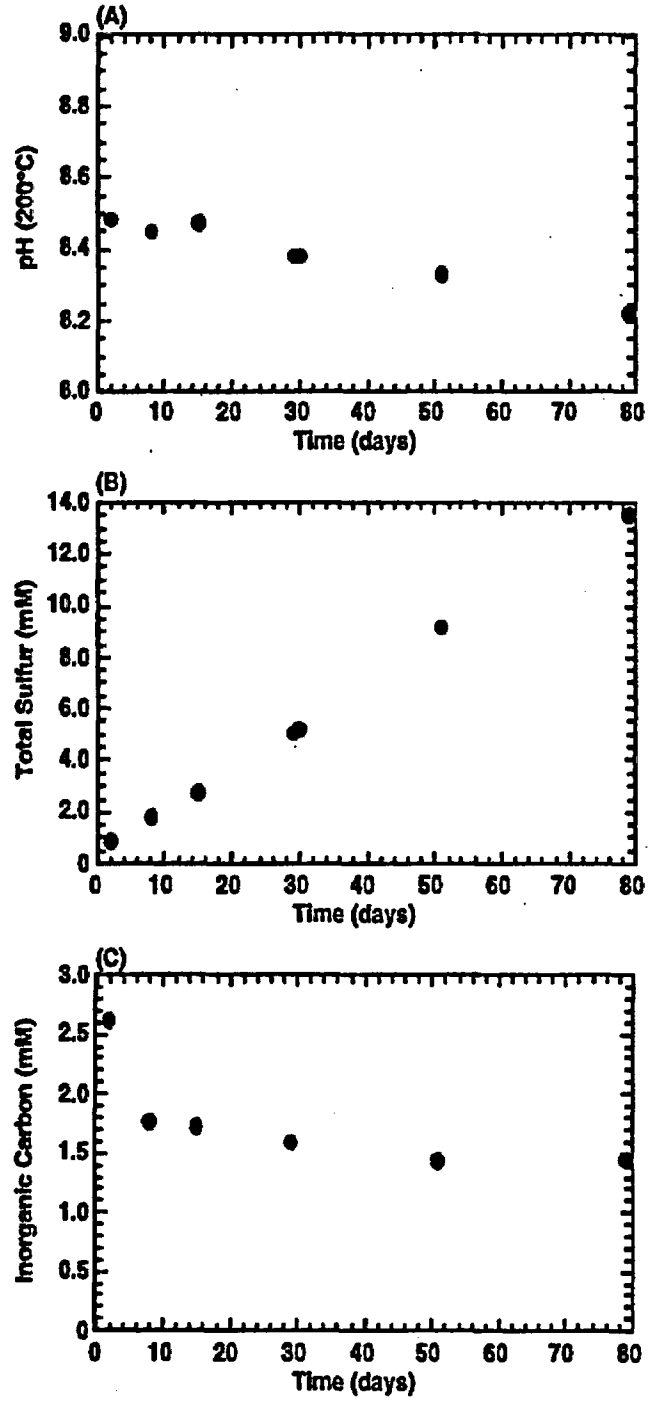

Figure 6-16. Aqueous (A) pH (200 °C), (B) total sulfur, and (C) inorganic carbon of experiment DF6 plotted as a function of time.

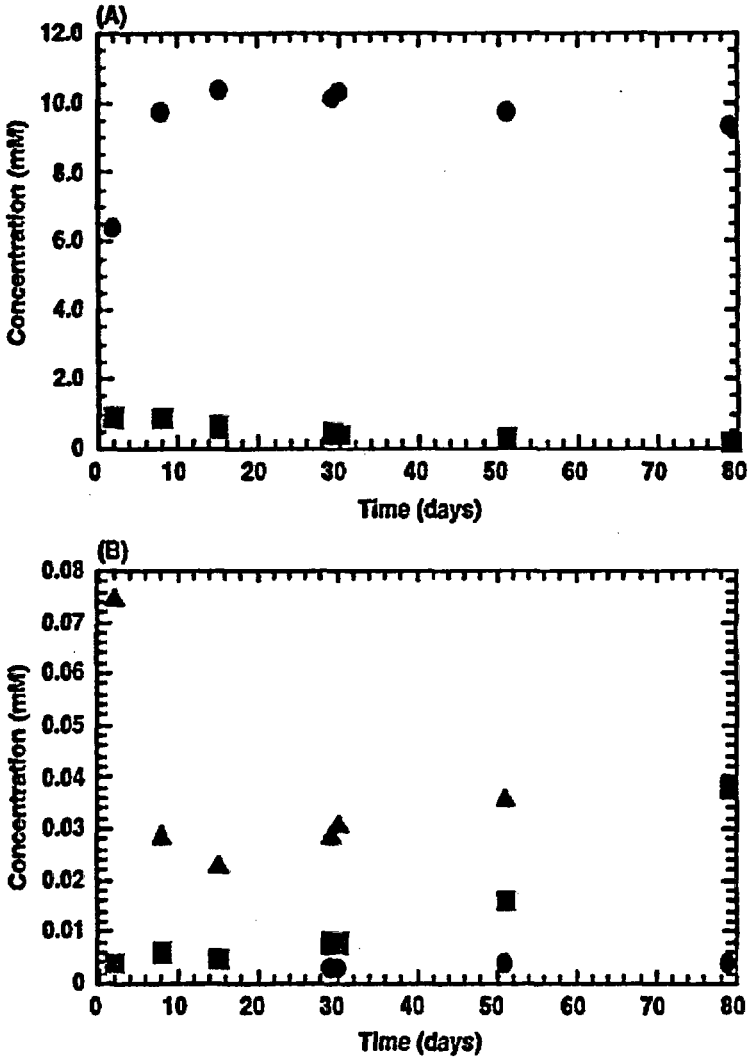

Figure 6-17. Composition of aqueous phase plotted as function of time, experiment DF6. (A) Si (circles) and K (squares) (B) Al (triangles), Ca (squares), and Mg (circles).

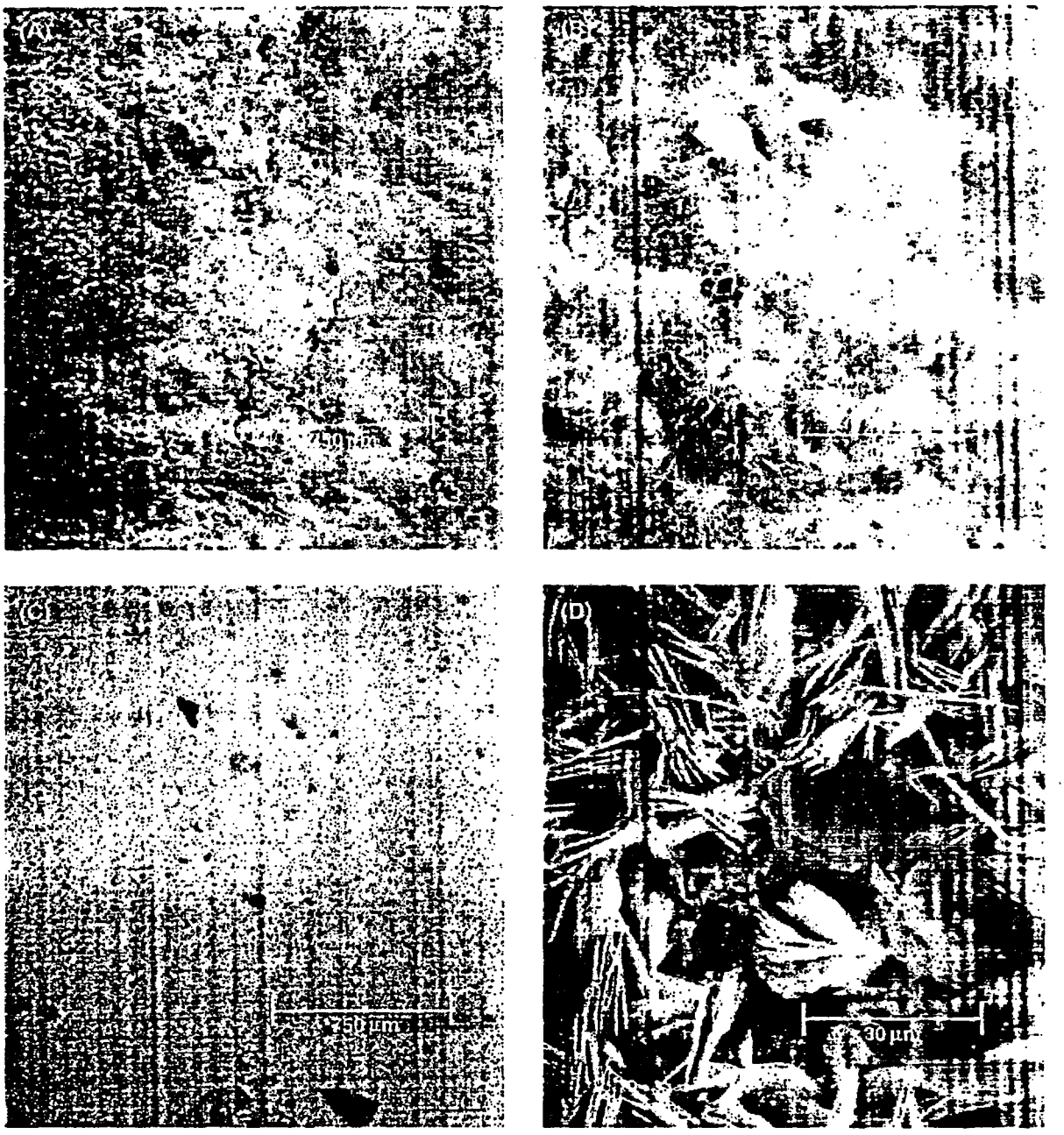

Figure 6-18. SEM photomicrographs from experiment DF6 of reacted Topopah Spring tuff (A, B) and reacted Fibercrete™ (C, D). (B) Enlargement of the precipitates that form on the tuff surface, showing books of layered Ca-silicate, calcite rhombs, and smaller pure silicate precipitate which may be cristobalite. (D) Enlargement of the Ca-silicate phase found on the reacted Fibercrete™ surface.

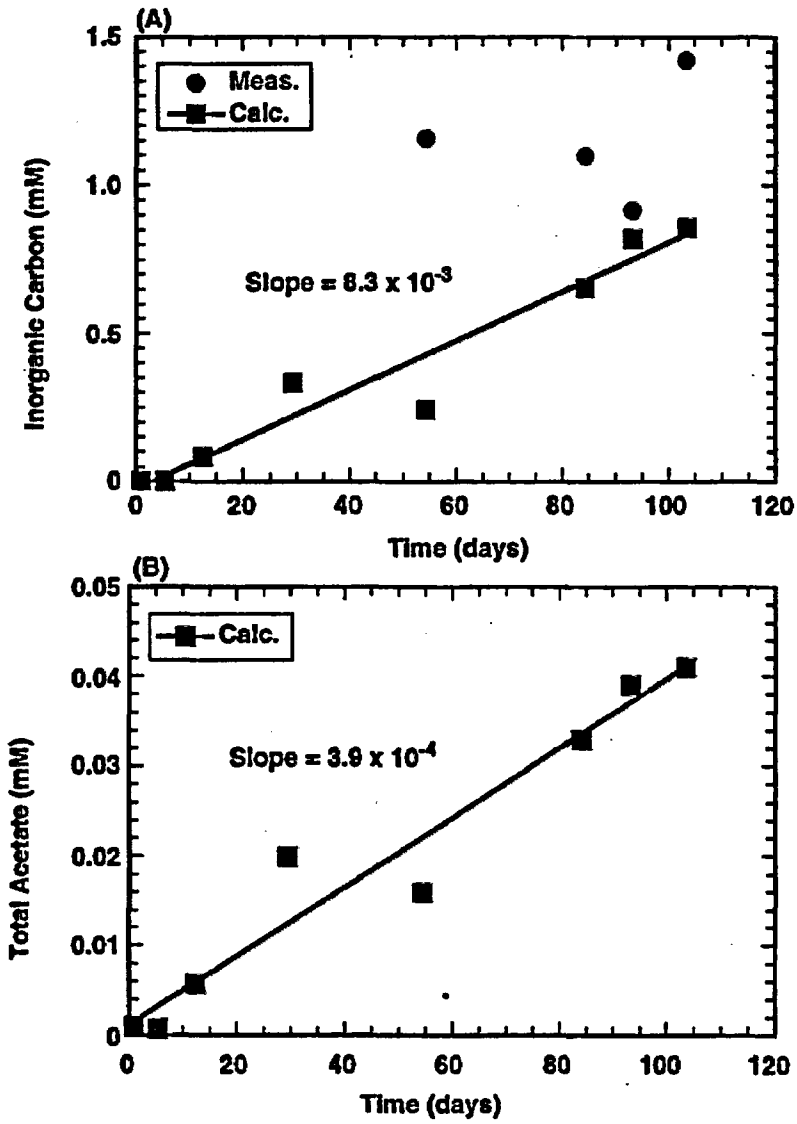

Figure 6-19. The calculated (A) inorganic carbon concentration, and (B) total acetate concentration in a solution of changing pH as a function of time. See text for detailed description of the assumptions and calculations.

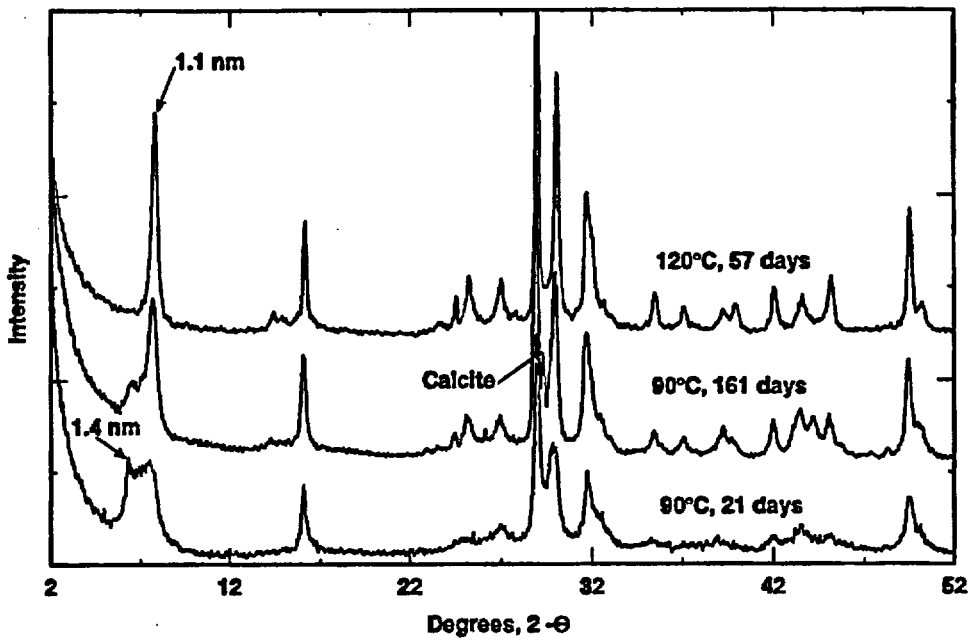

Figure 6-20. XRD patterns of tobermorite run products; the 90 °C XRD patterns show a peak shift from 1.4 to 1.1 nm tobermorite with time; the 120 °C XRD pattern shows only a single phase tobermorite; crystallinity increased with longer run times and higher temperature.

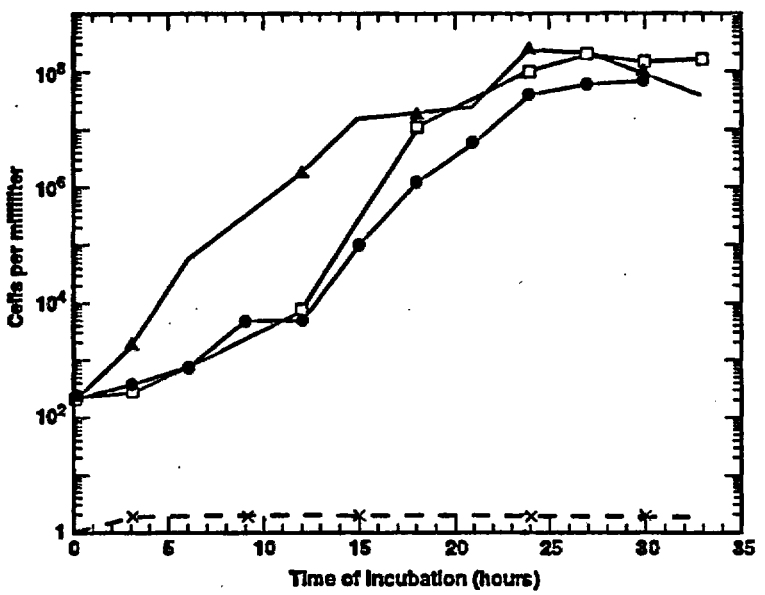

Figure 6-21. Effect of temperature on the growth rates of whole YM microbial communities in R2 media. Rates varied depending on temperature of incubation. Crushed YM tuff was inoculated in media and incubated aerobically at 20°C(●), 30°C (□), or 50°C (▲). Periodically samples were withdrawn and cell count was determined by live planting (×), sterile uninoculated media incubated at 20°C.

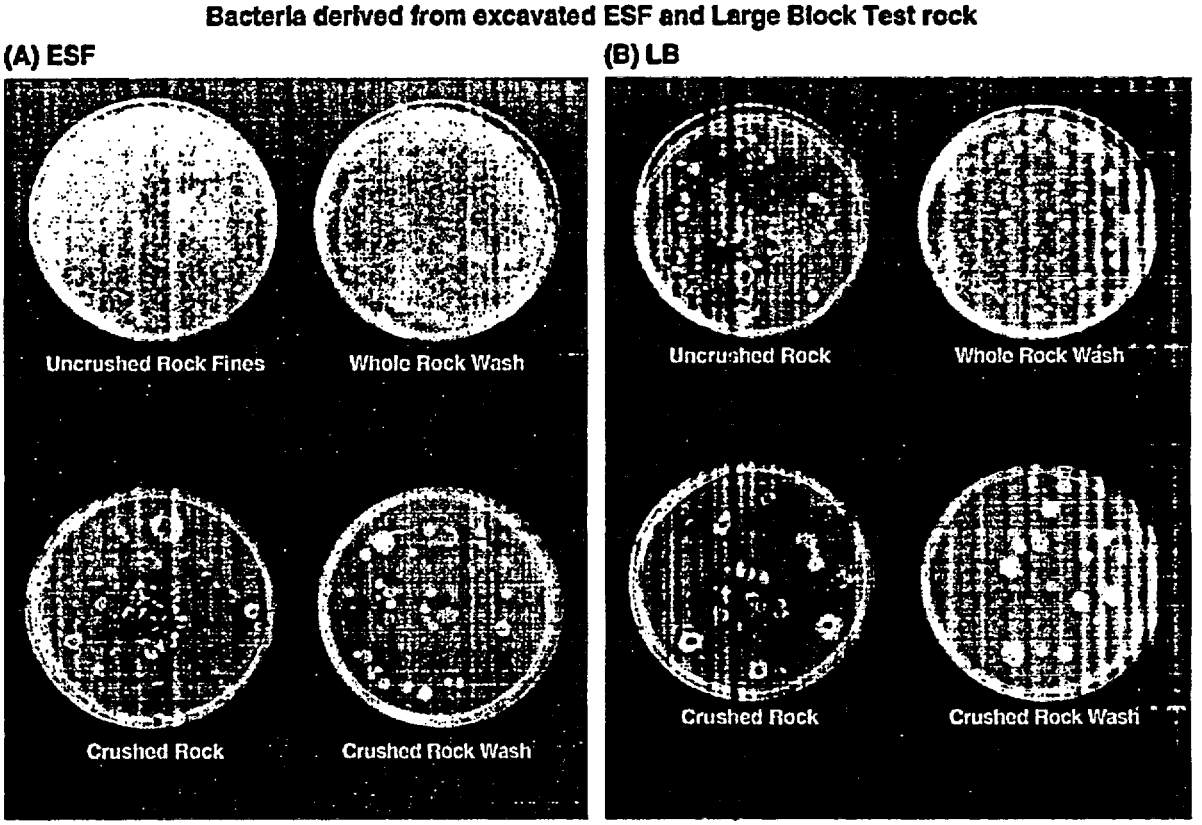

Figure 6-22. Plated samples of whole and crushed rock and rock washes (using sterialized artificial pore water) obtained from (A) the ESF muck pile and (B) the Large Block (LB) Test area suggest that the LB samples show greater culturable species diversity. Future DNA analyses will better indicate total diversity of culturable and unculturable species.

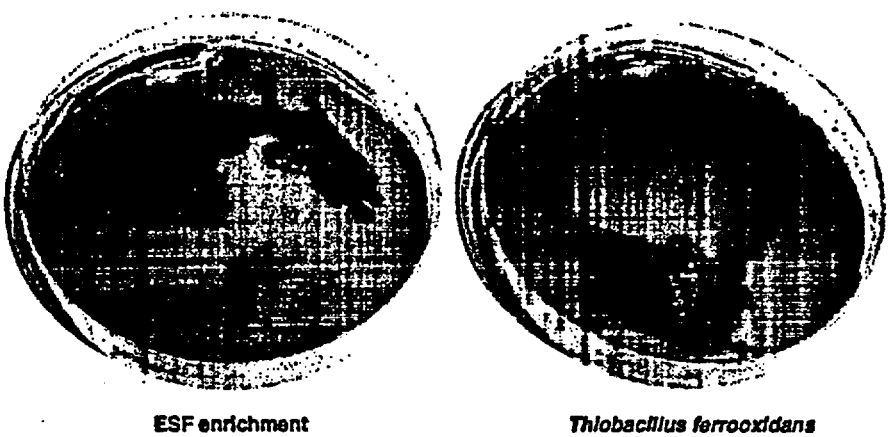

Figure 6-23. Screening tests for iron oxidizers indicate that ESF samples produced iron-oxidizing cultures.

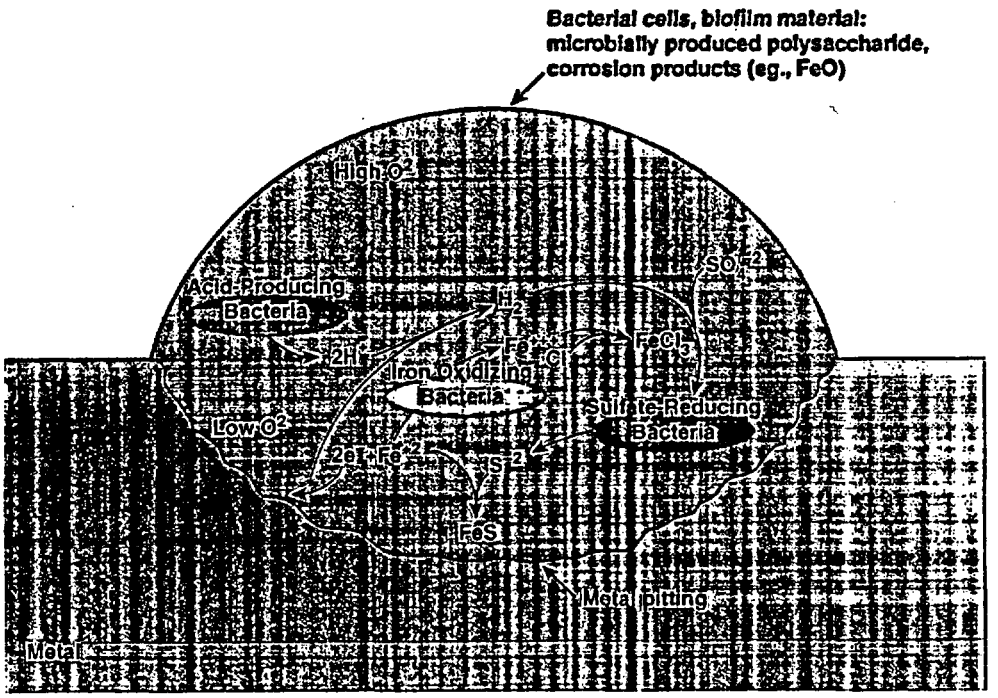

Figure 6-24. Microbially induced corrosion (MIC). Microbially-generated acids directly dissolve the protective calcareous film on stainless steel. Coupling of protons with electrons results in electron removal from the cathode, and forms hydrogen which is a substrate for microbial sulfate reduction.

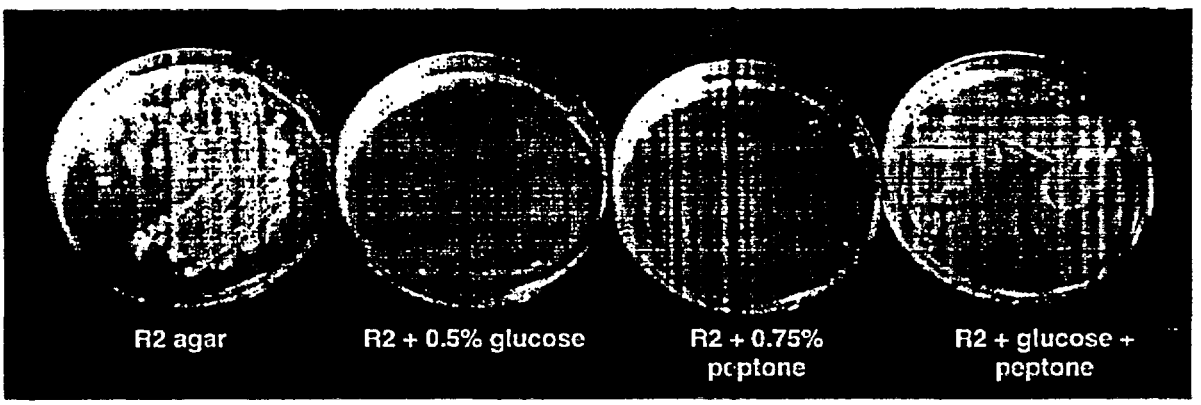

Figure 6-25. Screening tests for slime producers indicate that large quantities of slime can be produced by some bacteria that are extant in the ESF and LB.

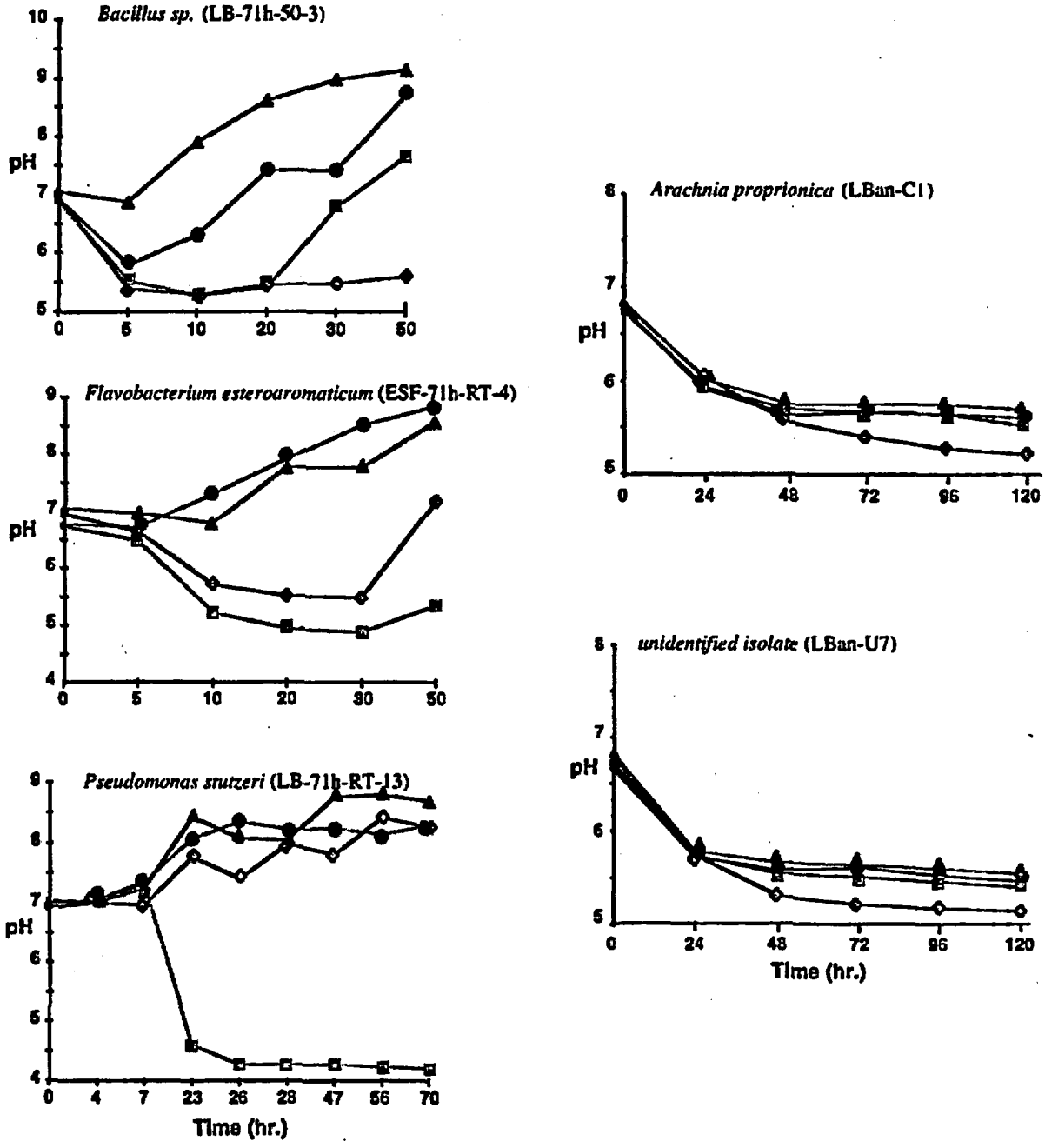

Figure 26. Effect of nutrients and growth on acid production in individual YM isolates. Each indicated isolate was inoculated into R2 media (●), R2 + 0.5% glucose (■), R2 + 0.75% proteose peptone #3 (▲), and R2 + glucose and peptone (◇). Periodically, through subsequent growth the pH of the media was determined.

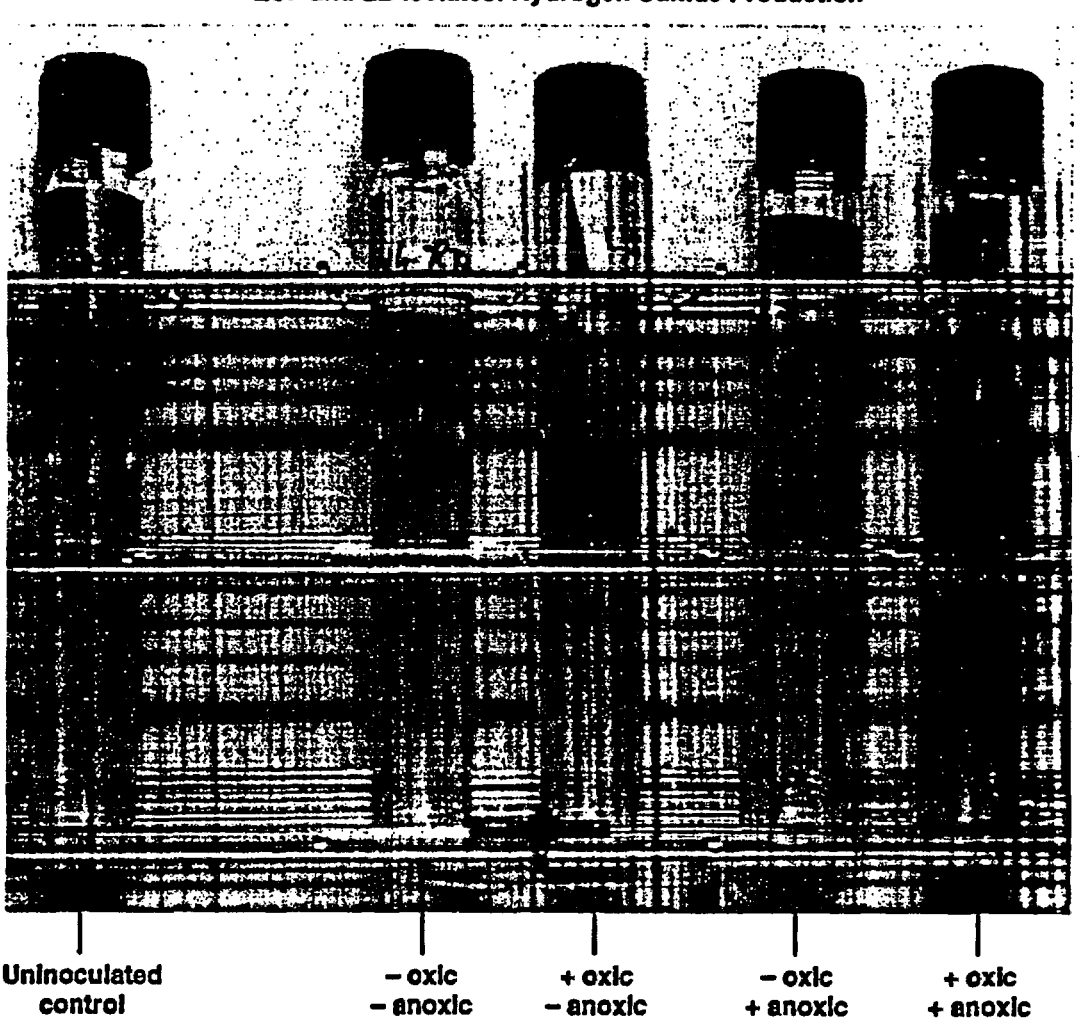

Figure 6-27. Preliminary results showed that sulfide production *via* desulfurylation increased for all tested strains within a two day incubation period, even in anaerobic cultures which metabolize and grow more slowly than do aerobic cultures. R2B media + 0.75% Proteose peptone #3, lead acetate 12 days incubation at room temperature and at 50°C.

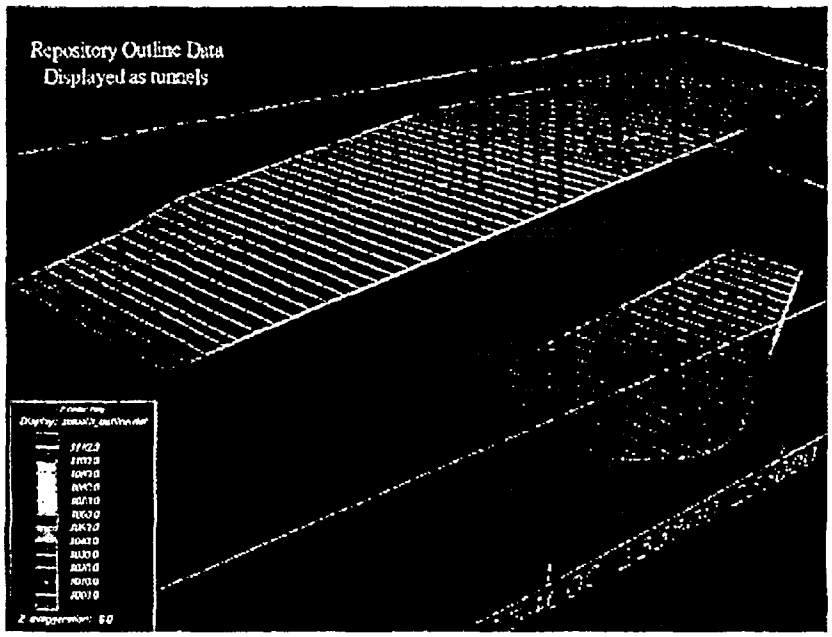

Figure 6-28. Emplacement tunnel footprint is illustrated in the Nevada State coordinate grid, which will allow for easy integration of existing Yucca Mountain geological data. Relative sizes of main and emplacement drifts are shown. Colors indicate elevation (see legend).

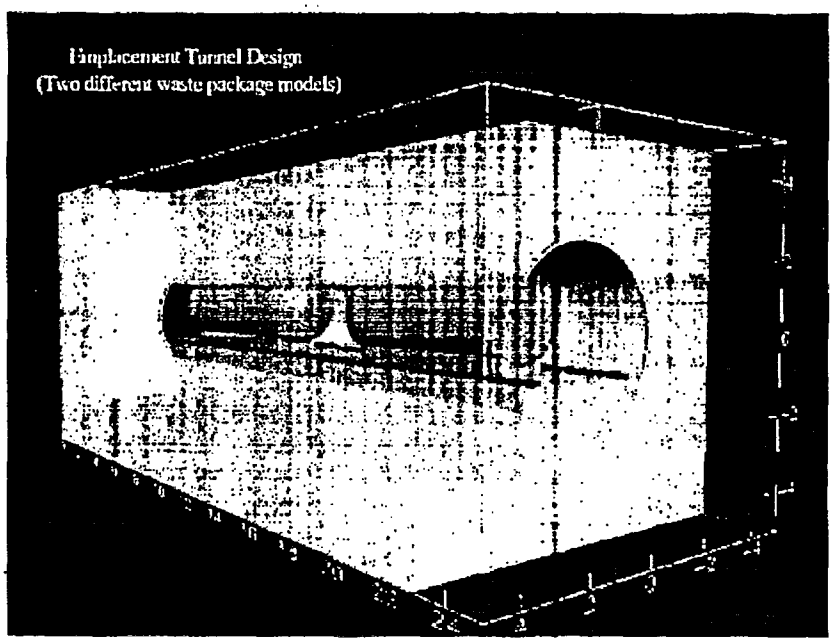

Figure 6-29. Cut away view of the emplacement tunnel demonstrates the capability of the EarthVision™ software to represent discontinuous shapes (scale bar in meters). In this simplified model waste packages (blue; 6 m x 0.2 m diam), cementitious materials (pink and lavender) gantry tracks (red) are installed in the surrounding rock (green).

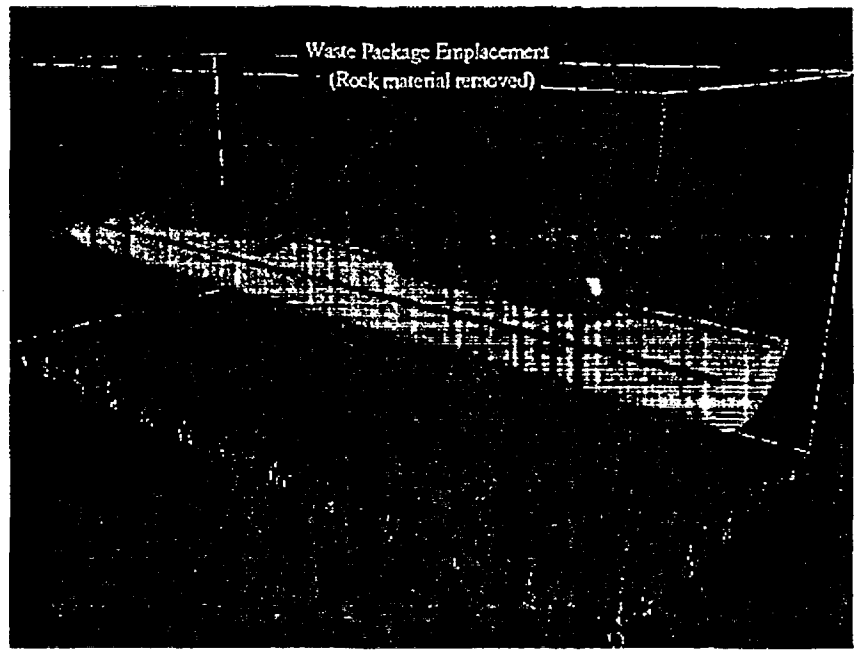

Figure 6-30. Illustration of a 25 m section of 4.3 m diam. emplacement tunnel (scale bar in meters). Waste packages (blue; 6.5 x 1.75 diam.), concrete invert (green; roughly 1.5 m x 4 m), gantry tracks (red; roughly 3.5 m between tracks), and concrete waste package supports (gold; 5.3 m length) are shown to scale.

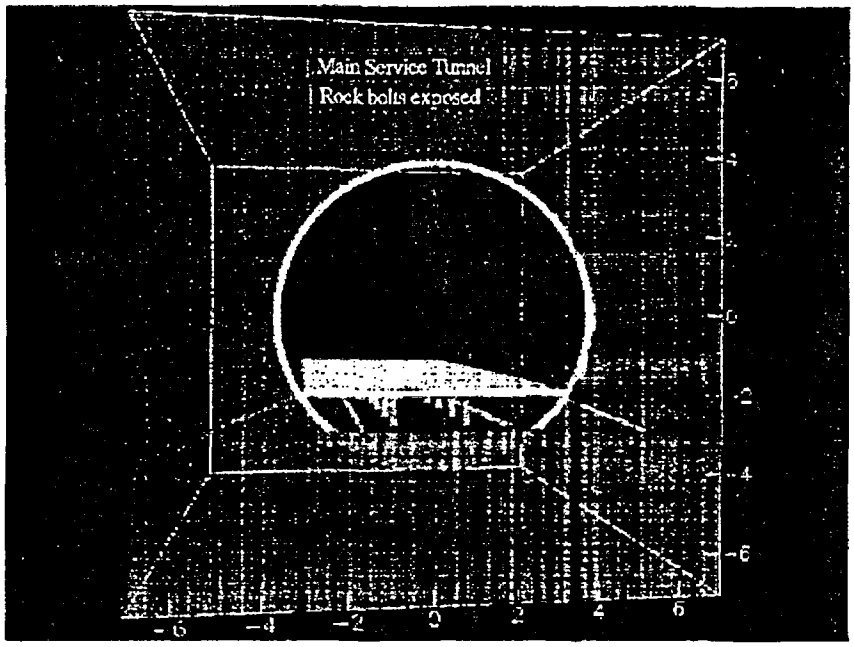

Figure 6-31. Simplified cross-section rendering of a 20-m section of 7.6-m diam. service tunnel (scale bar in meters) shows rockbolts (pink; approximately 3 m long and 0.10 diam.) for the metal grate platform (yellow; approximately 0.2 m thick) anchored into the surrounding rock (brown). The metal platform supports (light blue; approximately 0.2 x 0.3 x 1.0 m) are placed at roughly 2 m intervals. A concrete invert (purple; roughly 1.5 m) and shotcrete layer (gold; 0.2m thick) are shown.

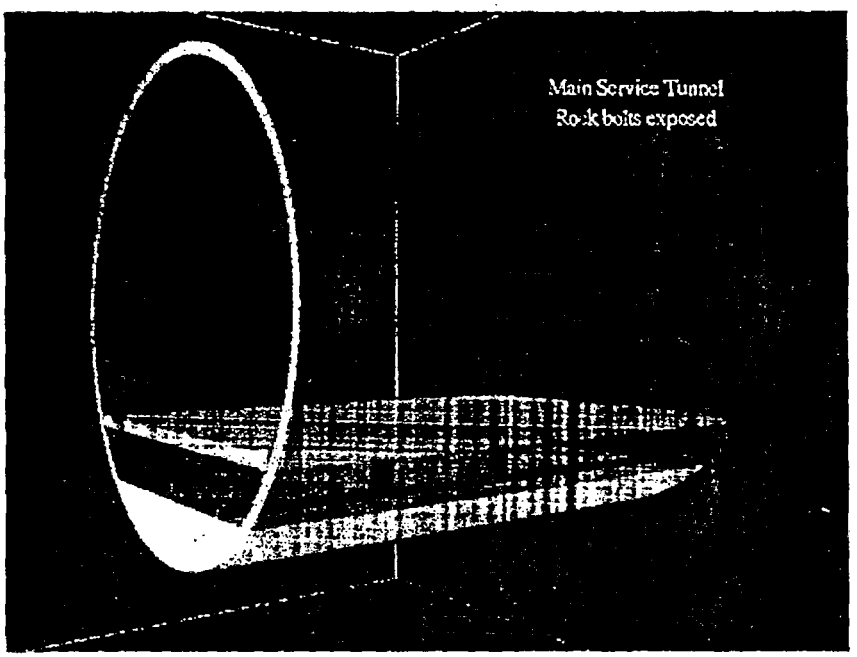

Figure 6-32. Exposed 20-m section of 7.6-m diam. service tunnel (scale bar in meters) demonstrates the level of detail that can be obtained for chemical and hydrological modeling at a scale of meters. Concrete invert (green) and shotcrete (gold) are the cementitious materials that are shown. Metal materials illustrated are the gantry car rails (turquoise) platform supports (blue) platform (yellow) and platform anchor rockbolts.

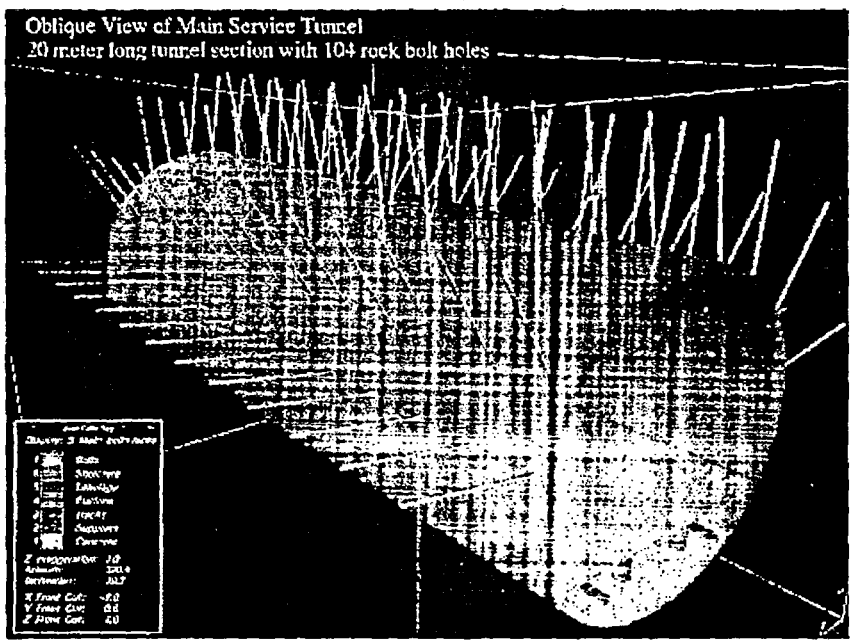

Figure 6-33. Oblique view of 20-m section of 7.6-m diam. service tunnel showing rockbolt holes. Given standard spacing (1.5 m) as depicted on engineering drawings, 104 rockbolts would be found in this length of tunnel.

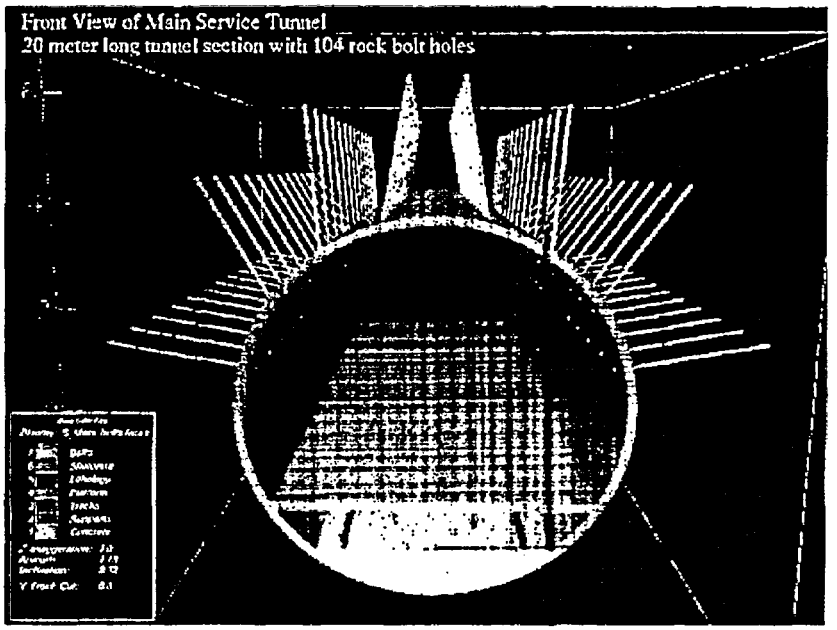

Figure 6-34. Cross-sectional rendering of 20-m section of 7.6-m diam. service tunnel showing rockbolt holes

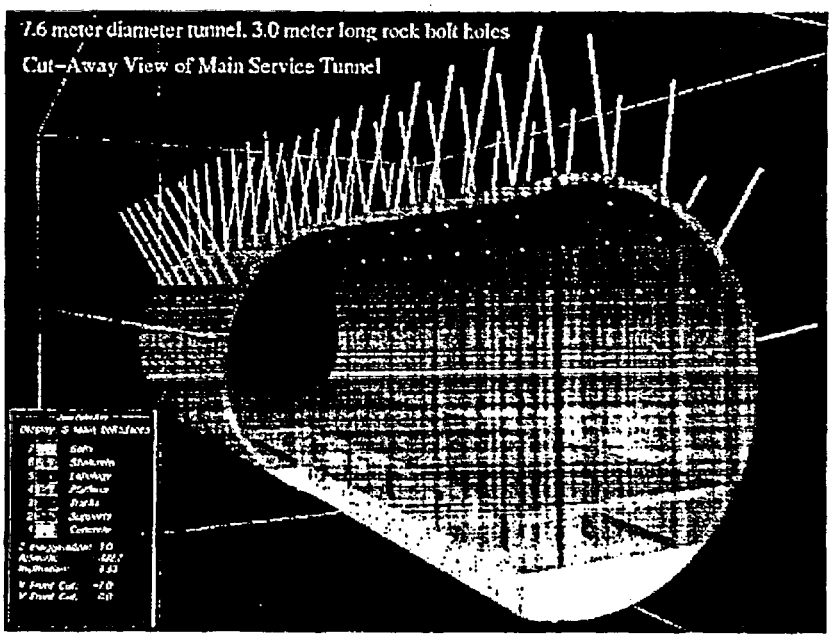

Figure 6-35. Cut-away view of 20-m section of 7.6-m diam. service tunnel showing rockbolt holes.

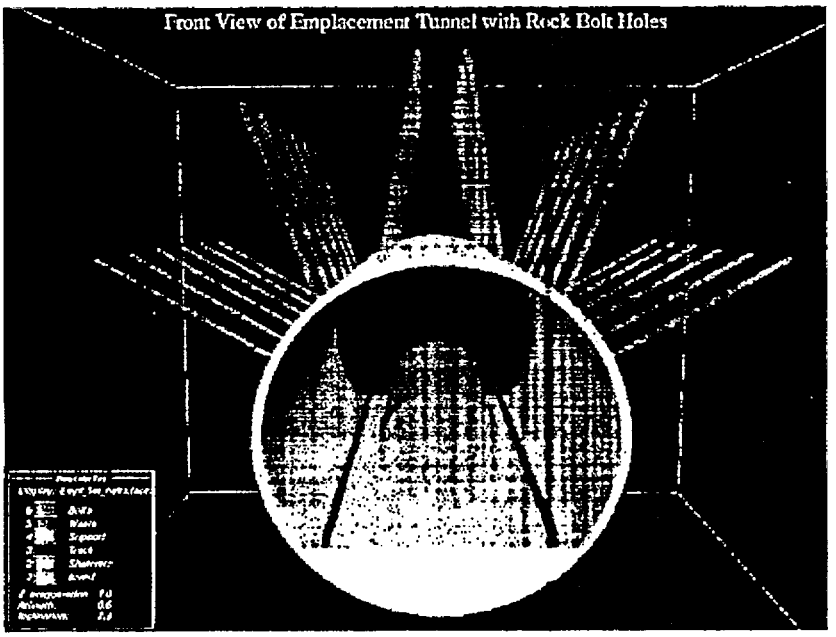

Figure 6-36. Cross-sectional rendering of 20-m section of 5.0-m diam. emplacement tunnel showing rockbolt holes. Given standard spacing (1.5m)as depicted on engineering drawings, 36 rockbolts would be found in this length of tunnel.

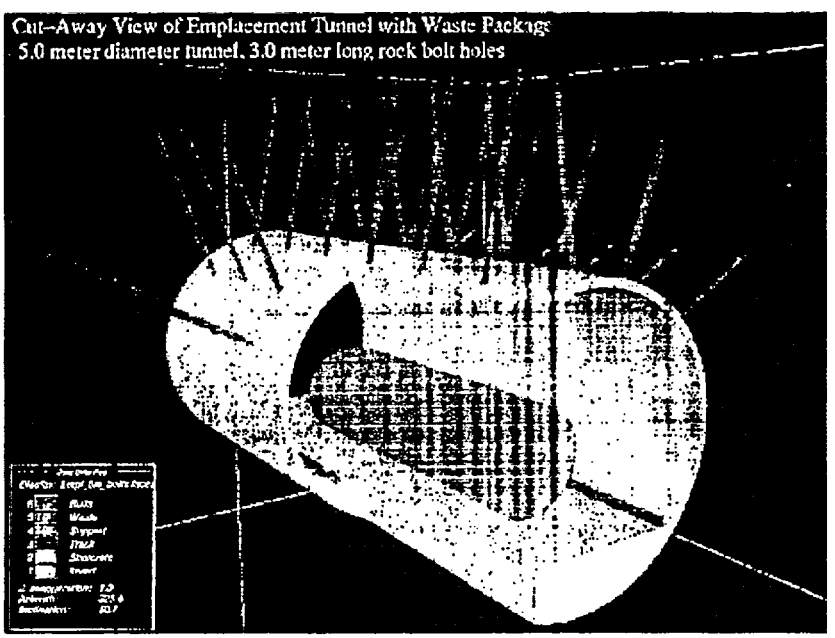

Figure 6-37. Cut-away view of 20-m section of 5.0-m diam. service tunnel showing rockbolt holes.

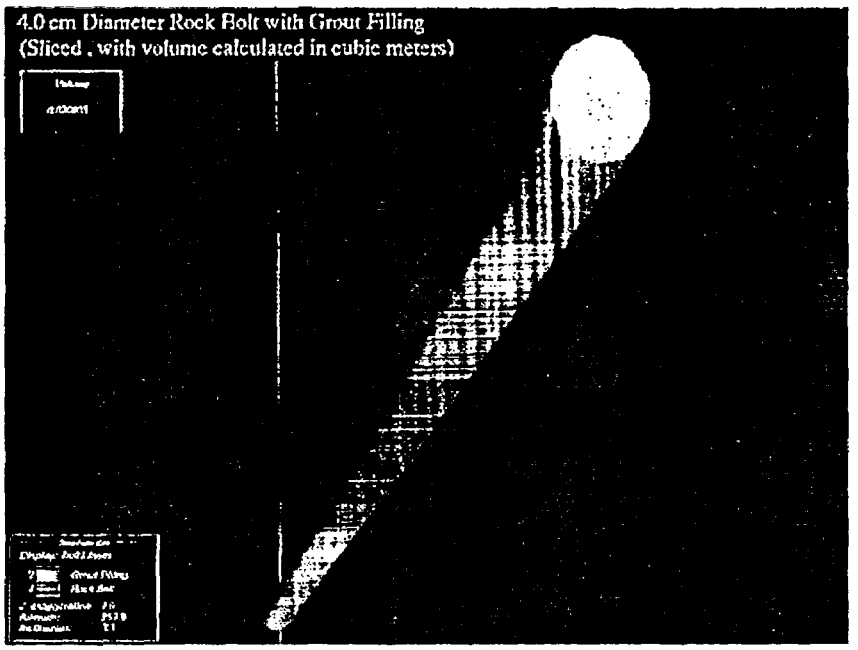

Figure 6-38. Rockbolt detail showing steel rockbolt (gray) and exterior grout filling.

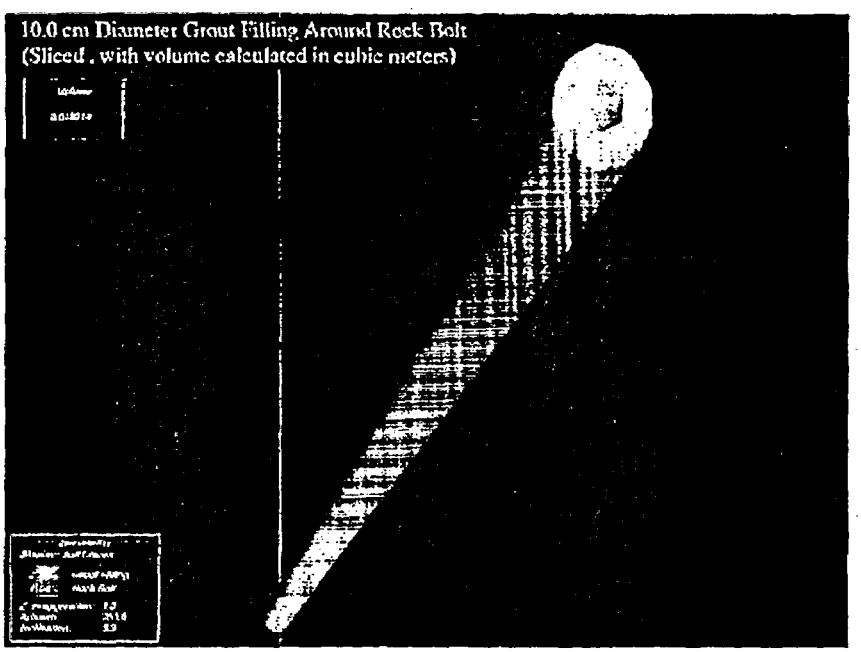

Figure 6-39. Calculational detail of volume of grout (0.018214 m) used for one rockbolt.

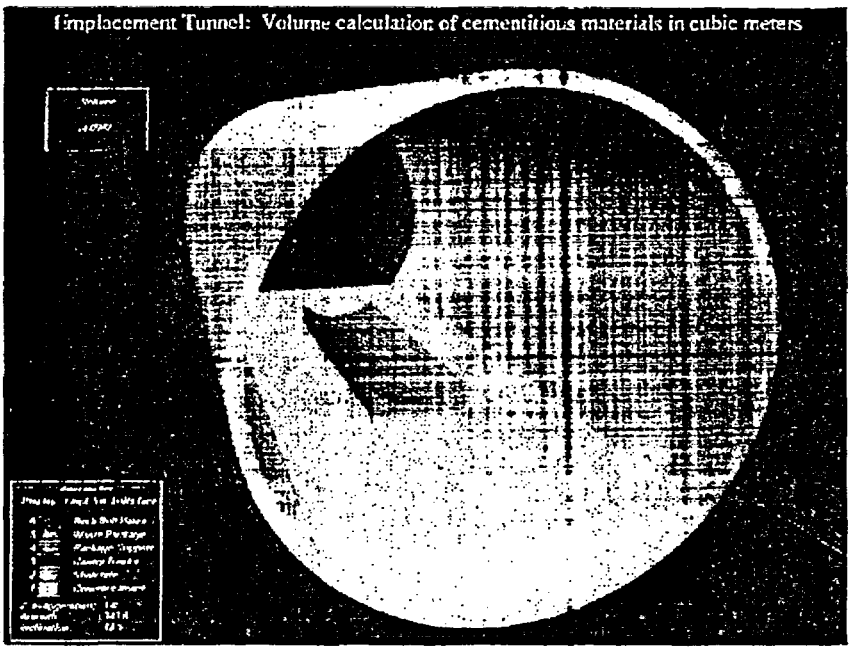

Figure 6-40. Calculation of material volumes is straightforward, as is illustrated in this calculation of the volume of cementitious materials (approximately 54.1 m^3) in a 20-m section of 4.3 diam. emplacement drift.

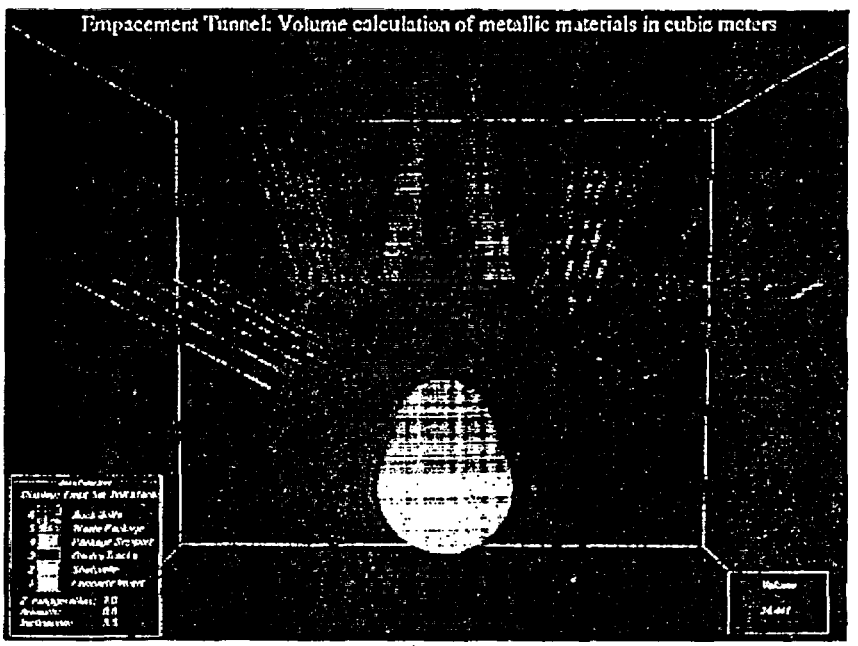

Figure 6-41. Calculation of volume of metal materials (approximately 14.4 m^3) (including the waste packages of wall thickness of roughly 0.2 m) in a 20-m section of 4.3 diam. emplacement drift.

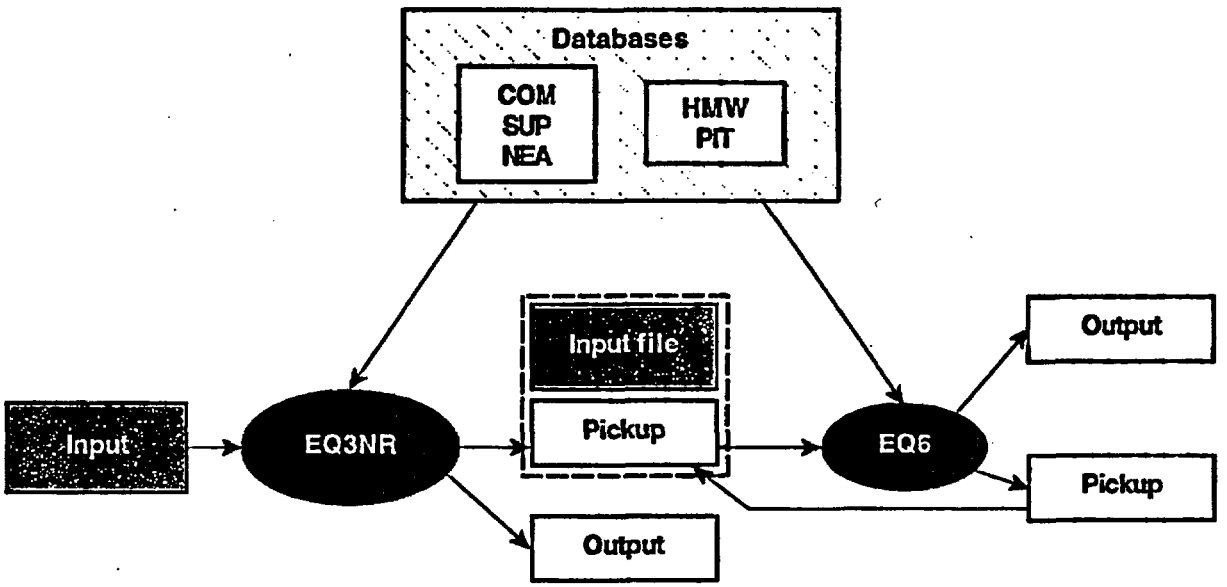

Figure 6-42. Diagram of interaction between various parts of EQ3/6. At present these interactions are conducted manually by the modeler. In order to simulate systems at a higher level of complexity, it will be necessary to automate some of these steps.

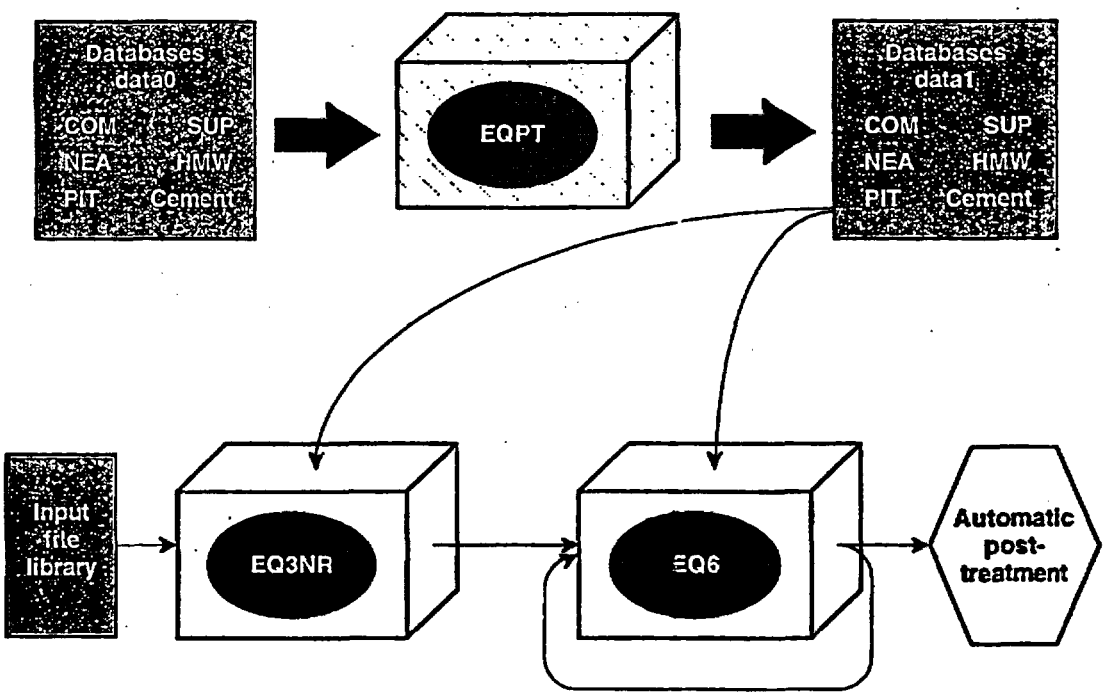

Figure 6-43. Schematic diagram of the flow of information between EQ3NR, EQ6, the databases and the input and output files.

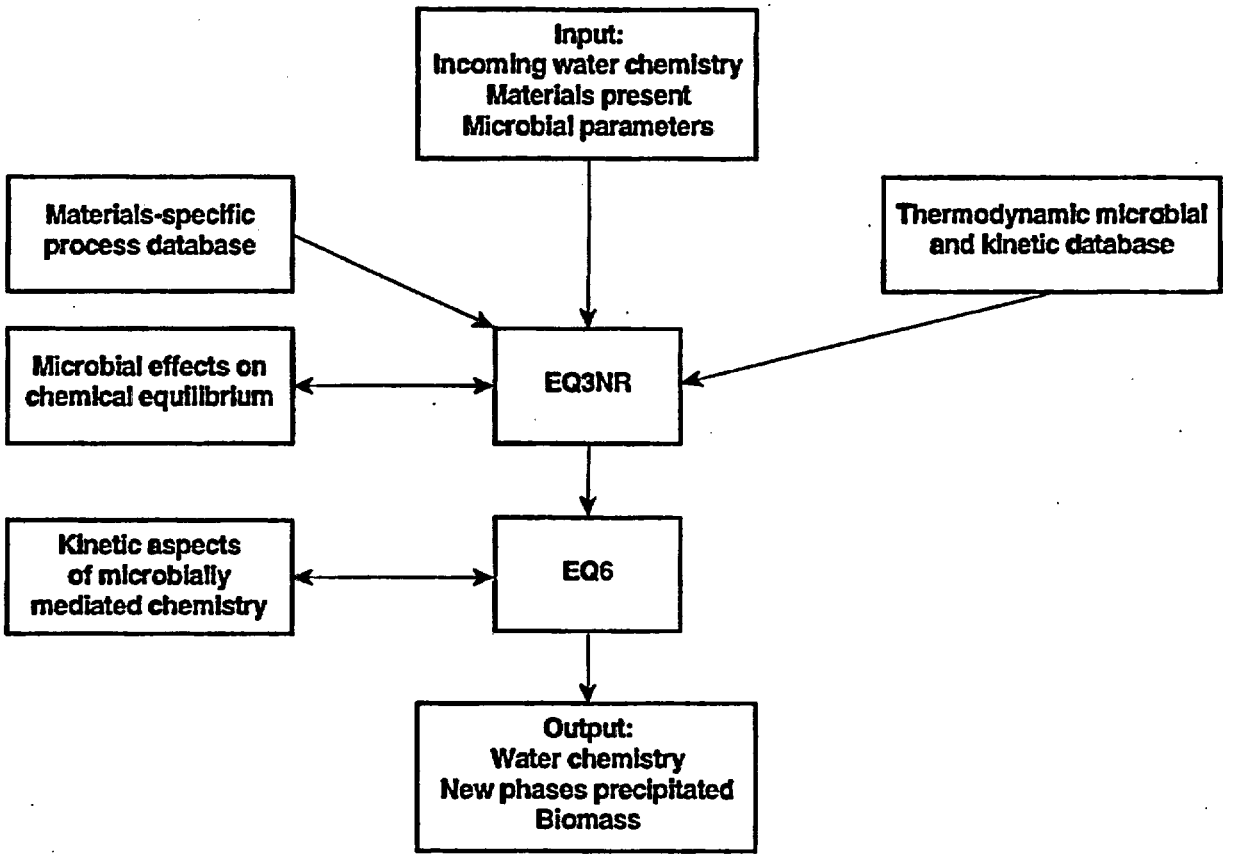

Figure 6-44. Conceptual view of interaction between EQ3/6 modules and modules that simulate biotic effects.

Table 6-1. Steel set materials and ESF locations.

Component *	Quantity between 00 + 58 and 02 + 00 ft	Quantity between 02 + 00 and 04 + 00 ft	Quantity between 04 + 00 and 06 + 00 ft
Item #1	116	83	132
Item #2	232	166	264
Item #3	232	166	264
Item #4	232	166	264
Item #5	468	835	1879
Item #6	3521	3567	6017
Item #7	1276	891	1430

*(1)Top component, MK#1A
(2) Bottom components, MK#1B (2 parts per set)
(3) Side components, MK#1C (2 parts per set)
(4) Steel set, shims and Dutchmen (2 parts per set)
(5) Steel Set Shims (reference drawing BABEAB000-01717-2100411102-03)
(6) Steel Lagging, C8 x 11.5# Channel for Steel Sets ~4 ft in length
(7) Tie rods for steel sets (reference drawing BABEAB000-01717-2100-41102-03)

Table 6-2. Rockbolt types and associated materials

Rockbolt type	Explicitly referred to on engineering diagrams	Associated materials
Super Swellex™1 (long and short)	long only (3000 mm. nom.)	water is applied at a regulated pressure to inflate the bolt
Solid #8 Threaded1 (long and short)	long only (3000 mm. nom.)	grouted into place
Williams™ Hollow Core[1]	(3000 mm. nom.)	grouted
Split Set [2]	no	unknown

[1] BABEABOOO-01717-2100-40157-01.
[2] Personal communication, Eugene Pokorny.

Table 6-3a. Grout mineralogy of Fibercrete™.

Grout mineralogy	Formula	Composition (wt%)
Tricalcium silicate	3(CaO)SiO2	61
Dicalcium silicate	2(CaO)SiO2	15
Tricalcium aluminate	3(CaO)Al2O3	6
Tetracalcium aluminoferrite	4(CaO)Al2O3Fe2O3	9

Table 6-3b. Grout composition of Fibercrete™.

Oxide	Composition (wt%)
SiO_2	21.4
Al_2O_3	4.3
Fe_2O_3	2.9
CaO	64.9
MgO	1.7
SO_3	2.7
Na_2O	0.53
Loss on ignition	0.87
Insoluble residue	0.2

Table 6-3c. Steel fiber composition of Fibercrete™.

Element	Composition (wt%)
Fe	99.8
C	0.018
Mn	0.075
P	0.040
S	0.050

Table 6-4. Details of spills 001 through 010.

Spill No.	Date	Tunnel station	Affected surface	Fluid
SRP-001	12/10/94	0+87	invert	oil
SRP-002	01/07/95	1+09	invert	oil
SRP-003	02/23/95	02+84	TBM	oil
SRP-004	03/03/95	04+05	invert segment	oil
SRP-005	03/21/95	04+60	unknown	oil
SRP-006	03/24/95	05+03	TBM	hydraulic fluid
SRP-006a	03/24/95	05+01	TBM	oil
SRP-007	03/25/95	05+13^{76}	TBM	oil
SRP-008	03/25/95	05+16^{67}	TBM	oil
SRP-009	03/28/95	05+10	TBM	hydraulic fluid
SRP-010	04/14/95	05+45	TBM	hydraulic fluid

Table 6-5. Spills reported through 09-August-95.

Spill No.	Date
SRP-011	05/06/95
SRP-012	05/31/95
SRP-013	06/01/95
SRP-014	06/06/95
SRP-014a	06/21/95
SRP-015	06/24/95
SRP-016	06/20/95
SRP-017	06/30/95
SRP-018	07/05/95
SRP-019	07/22/95
SRP-020	07/24/95
SRP-021	08/03/95
SRP-022	08/09/95

Table 6-6. Dust control agents that have been considered for use in the ESF.

Product name	Constituents	Company
Bio Cat 300-1	unknown	Applied Natural Systems, Inc.
Soil Master	PVAC/acrylic latex/tripolycate	ESSI/ EBCO
Petrotac	asphalt, vacuum gas, oil, metal tallate	SynTech Products Corp.
Coherex	petroleum hydrocarbons	Witco
Lignosite	calcium lignin sulfonate and sugars	Georgia Pacific
R-8376 Surfactant	sodium dodecylbenzene sulfonate	Nevada Dust Control
Agriloc	assumed hydrocarbon based on decomposition products	Swift Adhesives
Chem Loc 411	Vinyl acetate and acetaldehyde	Golden West Industries, Inc.
EMC Squared	assumed hydrocarbon based on physical properties	Soil Stabilization Products
Dustcon	citrus oil	Polo Citrus

Table 6-7. ^{14}C analyses of 50 mL diesel fuel samples collected at the ESF. Five samples were taken from the storage tank and three were collected from the locomotive motor. Prior to measurement using accelerator based mass spectrometry (AMS) an aliquot from each sample was combusted to graphite.

CAMS No.	Sample name	Fraction modern	±	$D^{14}C$	±	^{14}C age
26826	IM-DF-95-1	0.0003	0.0007	-999.7	0.7	>51200
26827	IM-DF-95-2	0.0005	0.0007	-999.5	0.7	>50300
26828	IM-DF-95-3	-0.0007	0.0007	-1000.7	0.7	>52800
26829	IM-DF-95-5	0.0001	0.0008	-999.9	0.8	>52200
26830	IM-DF-95-4	0.0006	0.0009	-999.4	0.9	>49900
26831	IM-DF-95-6	0.0009	0.0008	-999.1	0.8	>48800
26832	IM-DF-95-8	0.0001	0.0007	-999.9	0.7	>52200
26833	IM-DF-95-9	0.0000	0.0009	-1000.0	0.9	>52800
26834	IM-DF-95-7	0.0007	0.0007	-999.3	0.7	>49500

Table 6-8. Experimental matrix. Diesel Fuel Hydrous Pyrolysis.

Exp. No.	Temp. (°C)	Nominal pressure (bars)	Duration (days)	Rocking	Water comp.	Sample composition	Solid analysis	Organic liquid analysis	Aqueous phase analysis	Gas analysis
DF1	200	70	75	not continuous	MilliQ	1 water: 1 diesel fuel	n/a	GC (CS_2 dilution)	HPLC	GMS
DF2	315	150	105	no	MilliQ	10 water: 1 diesel fuel	n/a	n.a.	HPLC GC CO_2 gas anal.	GMS
DF3	200	70	87	continuous after 66 days	3 mM $NaHCO_3$	water + Fibercrete wafer	XRD SEM /EDS	n.a.	ICP-AES IC CO_2 gas anal.	GMS
DF4	200	70	80	yes	3 mM $NaHCO_3$	10 water: 1 diesel fuel + Fibercrete wafer	XRD SEM /EDS	n.a.	HPLC GC CO_2 gas anal. ICP-AES IC	GMS
DF5	200	70	76	yes	3 mM $NaHCO_3$	10 water: 1 diesel fuel + Tpt wafer	XRD SEM /EDS	n.a.	HPLC GC CO_2 gas anal. ICP-AES IC	GMS
DF6	200	70	79	yes	3 mM $NaHCO_3$	10 water: 1 diesel fuel + Tpt and Fibercrete wafers	XRD SEM /EDS	n.a.	HPLC GC CO_2 gas anal. ICP-AES IC	GMS

n/a: not applicable, n.a.: not analyzed

Table 6-9. Starting diesel fuel (LLNL motor pool) compositions measured by GC of CS_2 extractions.

Carbon No.	Average % peak area
C_6-C_9	4.7 ± 0.6
C_{10}-C_{14}	29.5 ± 1.6
C_{15}-C_{19}	52.6 ± 2.6
C_{20}-C_{26}	13.3 ± 1.9
Total	100.1

Table 6-10. Organic compounds identified by GMS analyses of gas extraction from aqueous samples from experiments DF1, DF2, DF4, DF5 and DF6.

Organic compound	Formula	DF1	DF2	DF4	DF5	DF6
methane	CH_4	Y	Y	Y		
ethane	C_2H_6		Y	Y		Y
propylene	C_3H_6	Y	Y			
n-butane	C_4H_{10}	Y	Y	Y		
i-butane	C_4H_{10}	Y	Y	Y		
trans-2-butene	$C4H_8$		Y			
propane	C_3H_8	Y	Y	Y		
i-pentane	C_5H_{12}		Y	Y	Y	
n-pentane	C_5H_{12}	Y	Y			
2-pentene	C_5H_{10}	Y	Y			
2-methylpentane	C_6H_{14}		Y		Y	
2-methyl-1-pentene	C_6H12		Y			
cyclohexene	C_6H_{10}		Y			
2,2-dimethylbutane	C_6H_{14}		Y			
benzene	C_6H_6		Y	Y	Y	
2,hexene (cis,trans)	C_6H_{12}		Y			
n-heptane	C_7H_{16}		Y			
1-heptene	C_7H_{14}		Y			
ethylcyclopentane	C_7H_{14}		Y			
toluene	C_7H_8		Y	Y	Y	Y
1-methylcyclohexene	C_7H_{12}		Y			
1,1-dimethylcyclopentane	C_7H_{14}		Y			
1,2-dimethylcyclopentane	C_7H_{14}		Y			
1-ethylcyclohexene	C_8H_{14}		Y			
xylene	C_8H_{10}		Y	Y	Y	
n-octane	C_8H_{18}		Y			
n-nonane	C_9H_2O		Y			

Table 6-11. Major hydrocarbons and their abundances relative to maximum peak area as determined by GCMS of final aqueous samples from experiments DF4, DF5, and DF6.

Retention time (min)	Compound	Boiling point (°C)	Percent of maximum peak area		
			DF4	DF5	DF6
13.06	benzene	80.1	23.66	18.32	25.87
18.86	toluene	110.6	100	100	100
24.56	ethyl benzene	136.2	31.37	28.21	21.65
25.19	p-xylene & m-xylene	138.3	82.19	80.45	66.77
26.51	o-xylene	144.4	49.38	40.82	35.79
30.22	1-ethyl 3-methyl benzene	161.3	26.90	24.43	17.27
30.56	1, 3, 5- trimethyl benzene	165	16.03	14.53	10.73
30.96	1-ethyl 2-methyl benzene	165.2	16.00	13.97	11.09
31.63	1,2,4-trimethyl benzene	169	52.67	49.77	37.08
32.64	1,2,3-trimethyl benzene)	176	30.60	26.84	21.05
33.03	indane	177.8	14.78	13.39	10.55
36.62	1-methyl-2-(2-propenyl) benzene	198	24.05		
36.91	tetrahydro naphthalene	207.6	20.48	14.74	12.53
37.44	naphthalene	218	39.45	33.9	30.35

Table 6-12. Yucca Mountain bacterial isolates displaying corrosion-related activities.

Strain#[a]	Species Identification[b]	Acid Production[c]	Sulfide Production[d]	Slime Production[e]
ESF-C1	*Cellulomonas flavigena*	X	X (oxic)	
LB-71h-RT-13	*Pseudomonas stutzeri*	X		
ESF-71h-RT-4	*Flavobacterium esteroaromaticum*	X	X (oxic)	
LBan-U7	uncharacterized	X		
LBan-UW2	*Cellulomonas turbata*	X		
LB-71h-50-3	probably *Bacillus sp.*	X		
ESFan-U4	*Bacillus circulans*	X		
LBan-C1	*Arachnia propionica* (poor match)	X	X (oxic/anoxic)	
LBan-UW2	*Cellulomonas turbata*	X		
LBan-U1	*Cellulomonas galida*	X		
LBan-U2	*Bacillus pabuli*	X	X (anoxic)	
LBan-U3	*Bacillus pantothenticus*		X (anoxic)	X
LB-71h-50-2	*Bacillus pumilus* subgroup B		X (anoxic)	
LB-71h-50-4	*Bacillus subtilus*		X (anoxic)	X
LB-71h-50-6	probably *Bacillus sp.*		X (anoxic)	X
ESF-71h-RT-1	*Flavobacterium esteroaromaticum*		X (oxic)	
LB-C1	uncharacterized		X (oxic)	X
LB-C2	uncharacterized		X (oxic)	
LB-C7	*Pseudomonas stutzeri*		X (oxic)	
LB-71h-RT-15	*Pseudomonas pseudoflava*			X
LB-71h-RT-4	*Pseudomonas pseudoflava*			X
LB-CW-6	*Arthrobacter oxydans*			X

[a]ESF=Exploratory Study Facility; LB=Large Block; an=isolated under anaerobic conditions; C=crushed rock isolate; U=uncrushed rock isolate; W=isolated from after washing rock; 71h=isolated after 71 hours of growth; RT=room temperature isolate; 50=50°C. isolate.

[b]Determined by fatty acid analysis using the MIDI/Hewlett Packard microbial identification system (MIS; Analytical Services, Inc., VT); identification of given isolates may be tentative due to a lesser degree of similarity with type organisms contained in the MIS database.

[c]Determined after growth in R2 media (Reasoner and Geldreich, 1985) with or without 0.5% glucose and pH indicators bromocresol purple and methyl red.

[d]Determined after growth in R2 agar media (Difco) containing 0.75% proteose peptone #3 (Difco) and lead acetate.

[e]Determined after growth on R2 agar (Difco).

Table B-1. Cement nomenclature and standards. Designations for cements are standardized by organizations such as the American Society for Testing and Materials (ASTM) and the American Petroleum Institute. Cement chemists have developed a nomenclature for phase composition that is based on ratios of oxides; the notation carries no structural implications. The following shorthand is standard.

Letter designation	Phase composition
C	CaO
S	SiO_2
M	M_gO
H	H_2O
$\bar{C}$	CO_2
$\bar{S}$	SO_3
N	Na_2O
P	P_2O_5
A	Al_2O_3
F	Fe_2O_3
K	K_2O
AFt	Calcium aluminum trisulfate (e.g., ettringite)
AFm	Calcium aluminum monosulfate (e.g., "monosulfate")
OPC	Ordinary portland cement
SRPC	Sulphate-resisting portland cement

Table B-2. Summary of major hydration reactions (Bensted, 1989).

Below 100°C

(1) *Tricalcium silicate (alite):* $2C_3S + 6H \Rightarrow (C_3S_2H_3) + 3CH$ (C-S-H)

(2) *Dicalcium silicate (belite):* $2C_2S + 4H \Rightarrow (C_3S_2H_3) + CH$

(3) *Tricalcium aluminate (aluminate):*

(a) $C_3A + 3C\bar{S}\ H_2 + 26H \Rightarrow C_3A.3C\bar{S}\ .H$ (ettringite)

(b) When the gypsum is used up: $C_3A + CH + 12H \Rightarrow C_4AH_{13}$

(c) This then reacts with the ettringite formed: $C_3A.3C\bar{S}\ .H_{32} + 2C_4AH_{13} \Rightarrow 3(C_3A.C\bar{S}\ .H_{12}) + 2CH + 2OH$ ("monosulphate")

(4) *Calcium aluminoferrite (ferrite):*

(a) $C_2A_{0.5}F_{0.5} + CH + 3CSH_2 + 25H \Rightarrow C_3A_{0.5}F_{0.5}3C\bar{S}\ .H_{32}$ (ettringite)

(b) When the gypsum is used up: $C_2A_{0.5}F_{0.5} + 2CH + 11H \Rightarrow C_4A_{0.5}F_{0.5}H_{13}$

(c) This then reacts with the ettringite formed: $2C_4A_{0.5}F_{0.5}H_{13} + C_3A_{0.5}F_{0.5}3C\bar{S}\ .H_{32} \Rightarrow 3(C_3A_{0.5}F_{0.5}.C\bar{S}\ .H_{12}) + 2CH + 2OH$

Above 100°C

(1) Main product is α-dicalcium silicate hydrate, C_2SH, which has high permeability and low compressive strength; above 200°C it forms tricalcium silicate hydrate, $C_6S_2H_3$.

(2) Additions of ~35 to 40% silica yield tobermorite, $C_5S_6H_5$, which has low permeability and good compressive strength; above 150°C it forms xonotlite, C_6S_6H and gyrolite, $C_2S_2H_2$, which has higher permeability and lower compressive strength.

(3) Hydrogarnet, $Ca_3(Al, Fe)_2[SiO_4/(OH)_4]_3$ and stratlingite $Ca_2(Al,Fe)_2SiO_7{\cdot}8H_2O$ are also formed from the ferrite and aluminate phases.

Table B-3. Names, formulas, and standard terms of cement phases. CA is the chemical abstracts number.

Name	Formula	Cement Std	CA#
Hydrous (Product) Phases			
Calcium hydroxide			
Portlandite	$Ca(OH)_2$	CH	1305-62-0
Calcium silicate hydrates			
Afwillite	$Ca_3Si_2O_6(OH)_2{\cdot}2H_2O$	$C_3S_2H_3$	16291-79-5
	$Ca_3Si_2O_7{\cdot}3H_2O$		24189-31-9
C-S-H gel		$C_1S_1H_1$	14404-64-9
C-S-H(I)		$C_5S_{4-6}H_x$	
C-S-H(II)		$C_9S_{4-6}H_x$	
Foshagite	$Ca_4(SiO_3)_3(OH)_2$	C_4S_3H	12214-32-3
	$4CaO.3SiO_2.H_2O$		
	$Ca_8[Si_6O_{17}](OH)_6$		
Gyrolite	$Ca_{16}Si_{24}O_{60}(OH)_8{\cdot}14H_2O$	$C_2S_3H_2$	66899-82-9
	$Ca_4[Si_6O_{15}](OH)_2{\cdot}4H_2O$		
			16225-87-9
Hillebrandite	$2CaO.SiO_2{\cdot}H_2O$	C_2SH	15669-77-9
	$2CaO.SiO_2{\cdot}xH_2O$		67412-69-5
	anhydrous		13572-91-3
Jennite	$Ca_9(Si_6O_{18}H_2)(OH)_8{\cdot}xH_2O$	$C_9S_6H_{11}$	63701-45-1
Metajennite	$Ca_9(Si_6O_{18}H_2)(OH)_8{\cdot}2H_2O$	$C_9S_6H_7$	12427-05-3
Nekoite	$Ca_3Si_6O_{15}{\cdot}7H_2O$	$C_3S_6H_7$	
	$3CaO.6SiO_2{\cdot}8H_2O$	$C_3S_6H_8$	
	$CaSi_2O_5{\cdot}xH_2O$		32237-29-9
	$CaO.2SiO_2{\cdot}2H_2O$		
Okenite	$Ca_{10}Si_{18}O_{46}{\cdot}18H_2O$	$C_3S_6H_6$	
	$CaSi_2O_4(OH)_2{\cdot}H_2O$	CS_2H_2	14654-13-8
Plombierite	$Ca_{10}[Si_{12}O_{31}](OH)_6{\cdot}18H_2O$	$C_5S_6H_{10.5}$	12420-83-6
Reyerite[1]	$(Na,K)_2Ca_{14}(Si,Al)_{24}O_{58}(OH)_8{\cdot}6H_2O$		12424-04-3
Riversideite-9Å	$Ca_5H_2(SiO_3)_6{\cdot}2H_2O$		14706-42-4
Tobermorite-14Å	$Ca_5Si_6O_{16}(OH)_2{\cdot}8H_2O$	$C_5S_6H_9$	
	$Ca_5Si_6O_{16}(OH)_2{\cdot}5H_2O$		1319-31-9
	$Ca_5Si_6O_{16}(OH)_2{\cdot}xH_2O$		11074-26-3
	$Ca_6Si_5O_{12}(OH)_8{\cdot}2H_2O$		58471-00-0
		$CSH_{1.66}$	68810-15-1
		$C_5S_6H_{1.5}$	67412-68-4
		CSH_x	67070-27-3
		$C_5S_6H_{2.5}$	66732-74-9
		$C_5S_6H_6$	12423-17-5
		$C_3S_2H_3$	12323-54-5
		$C_4S_5H_5$	12141-65-0
Tobermorite-11Å	$5CaO.6SiO_25{\cdot}5H_2O$	$C_5S_6H_5$	
	$Ca_{4.5}(Si_6O_{15}(OH)_3){\cdot}2H_2O$		
	$Ca_4(Si_6O_{14}(OH)_4){\cdot}2H_2O$		
	$Ca_5(Si_6O_{16}(OH)_2){\cdot}2H_2O$		
	$Ca_6(Si_6O_{18}){\cdot}2H_2O$		
Tobermorite-10Å			
Tobermorite-9Å	$5CaO.6SiO_2{\cdot}3H_2O$	C_5S_6H	

Table 6-3. (Continued.)

Name	Formula	Cement Std	CA#
Anhydrous (Reactant) Phases			
Calcium oxide			
Lime	CaO	C	1305-78-8
Calcium silicates			
Belite	beta-Ca_2SiO_4	β-C_2S	14981-10-3 10034-77-2
Alite	Ca_3SiO_5	C_3S	12168-85-3
Calcium aluminates			
	$CaAl_4O_7$	CA_2	
	$CaO.Al_2O_3$	CA	
	$Ca_3Al_2O_6$	C_3A	12042-78-3
Calcium iron aluminates			
"Ferrite"	$Ca_4Fe_4O_{10}$ – $Ca_4FeAl_3O_{10}$ solid solution	$C_2(A,F)$	

[1] Formula for end-member (Ca-Si-H_2O system) is not yet determined.

Contents

Chapter 7.0 Integrated Testing

Brian E. Viani

7.1 Introduction

The role of the Integrated Radionuclide Release: Tests and Model Development activity (Integrated Testing) is to bound the flux of radionuclides that pass the Engineered Barrier System/Near Field Environment (EBS/NFE) (Viani, 1995a). The purpose of this activity is to measure and model the transport of radionuclide elements from the waste form through the introduced materials, their alteration products, and altered host rock that will comprise the post-containment near field environment of the potential repository at Yucca Mountain. Experimental measurements will be combined with conceptual and mechanistic models to bound the concentrations of radionuclide elements that will be released from the EBS/NFE for any given release from the waste form. The estimated releases will be used by the EBS/NFE Subsystem Performance Assessment task (EBS/NFE PA) to calculate the source term to be used in Total System Performance Assessment (TSPA).

7.1.1 Scope of Integrated Testing Activities

Integrated Testing activities are directly concerned with measuring and modeling the effects that hydrothermally altered EBS/NFE materials have on the transport of radionuclides released from the waste form as it interacts with groundwater re-entering the repository after the dry-out period. These interactions, which may include sorption, precipitation, and matrix imbibition, are an important element of the strategy for evaluating the Yucca Mountain site (CRWMS M&O, 1996). The most important materials to be addressed include: waste package corrosion products, backfill/packing, cementitious materials, and altered repository rock (Viani, 1995b).

7.1.2 Relationship of Integrated Testing Activities to Other YMP Activities

To address the issues of radionuclide dispersion, retardation, and depletion in the EBS/NFE, Integrated Testing activities will require material, data, and models from the following activities: ambient and altered zone geochemistry and thermohydrology, waste package materials and waste form testing, and man-made materials (Viani, 1995a).

7.1.2.1 Current Status of Integrated Testing Activities. As a result of the change in reference repository design from a borehole emplaced waste package to a drift emplaced waste package, the scope of Integrated Testing activities has expanded to include the interaction of materials other than the host repository rock adjacent to the waste package. Earlier Integrated Testing activities were focused on the processes expected to play a role in controlling radionuclide transport in the altered host rock. Because of the expanded scope there are many areas that have not been addressed that are important to the overall waste isolation strategy put forward by the project (CRWMS M&O, 1996). To date, the Integrated Testing activity has addressed data and models related to:

1. Diffusion of radionuclides through, and pore-size distribution of, repository rocks.
2. Characterization of colloids in Yucca Mountain groundwaters and in experimental fluids passed through repository rocks.
3. Transport of soluble conservative tracers through fractured repository rock at elevated temperatures.
4. The role of diffusion in controlling sorption by the zeolite clinoptilolite.
5. Testing cation exchange and surface complexation models against field data for a fractured aquifer system.

7.2 Data Inputs Required for Bounding Transport and Source Terms

To assess the role of the EBS/NFE in controlling the flux of radionuclides leaving the repository, the following information is necessary.

Near field environment properties that will be required include:

1. The temperature range over which transport will occur.
2. The flux of radionuclide-bearing groundwater exiting the waste canister.
3. The mode of groundwater flow; i.e., saturated, unsaturated, episodic, etc.
4. The saturation state of the EBS/NFE materials comprising the flow path.
5. The potential of water in the system; i.e., $p/p^{o}_{H_2O}$.

EBS/NFE flow-path-component material properties that will be required include:

1. The composition of the radionuclide-bearing groundwater after it contacts the waste form (pH, soluble species, colloidal species).
2. The elemental, mineralogical, microbial, and physical properties of container corrosion products, hydrothermally altered backfill material, hydrothermally

altered concrete and other introduced materials, and hydrothermally altered repository rock.

7.3 Chemical, Mineralogical, and Physical Characteristics of EBS/NFE Components Expected to Significantly Affect Radionuclide Transport Through the EBS/NFE

Except for episodic fracture flow, the low water flux expected in the post-emplacement and post-containment environment will result in the fluid chemistry being controlled by the flow-path component through which the fluid is passing. The chemical and mineralogical properties of certain of the EBS/NFE materials comprising the effective flow path of radionuclide-bearing groundwaters are expected to play a major role in the transport of radionuclides. The following sections summarize and highlight some of the features that can be important to transport. The reader is to refer to reports and papers regarding the flow-path elements listed below, some of which can be found in the Geochemistry, Man-Made Materials, and Altered Zone sections of this report.

7.3.1 Waste Form

The waste form will control the rate at which radionuclides are released to the contacting groundwaters. An expected scenario for water to contact the waste form would include the following events:

1. During the period of complete containment, container materials are corroded by interaction with liquid and vapor-phase water at elevated temperature.
2. After containers are breached, waste forms interact primarily with vapor phase water during the period of rehydration of the repository, at a temperature above ambient.
3. Liquid water contacts the vapor-altered waste and flows across it and eventually out of the containers into the surrounding altered EBS/NFE materials.
4. Without explicit provision for an oxygen sink, the EBS/NFE environment is assumed to be oxygenated during the time period of radionuclide transport through it.

Because of the unsaturated nature of the repository environment, and the expected low flux of water contacting the waste form following breaching of the waste container, waste forms will have an important effect on the composition of the groundwater leaving the container; i.e., the fluid exiting the waste container will

be strongly conditioned by the waste itself (and by interaction with the ancillary materials in the container; e.g., filler, spacers, etc.).

Groundwater reacting with spent fuel will have reduced levels of Si and other constituents compared with ambient groundwater as a result of formation of uranium silicates and other silicates (Wilson, 1990; Bates et al., 1995a). Layer silicate, uranium-oxide, and uranium-silicate colloids will be released during the interaction of groundwater with spent fuel (Bates et al., 1995a).

Interactions of groundwater with glass waste form may yield a distinctly different chemistry than spent fuel. Laboratory experiments have shown that fluids reacted with glass at high solid to solution ratios (saturated, and under dripping conditions) have relatively high pH, and elevated levels of Si, B, and Li, and distinctly different colloids than spent fuel (Bates et al., 1995b). The actual pH expected in the repository will also depend on the reservoir of CO_2 in gas phase in the system. A large reservoir of CO_2 could buffer the system at a lower pH than is observed in laboratory experiments. Colloids released from glass are predominantly layer silicates with some colloidal phosphates also observed.

We may expect that fluids emanating from the waste package are likely to contain considerable quantities of radionuclide-bearing colloids, be depleted in dissolved oxygen and Si (for spent fuel), and potentially high in pH (for glass). The stability of the colloids that do leave the container is an issue that has not been resolved.

7.3.2 Container Corrosion Products

It would be expected that breaching the waste container would occur as a result of corrosion of the metallic components of the waste package in the humid, elevated temperature regime anticipated during the repository cool-down period. Hence, the first materials likely to be encountered by radionuclide-bearing fluids leaving the container are the corrosion products from the waste container. These corrosion products are likely to be oxides and/or silicates of the metals comprising the container wall and the internal structures of the container.

Mineralogically, these products would be expected to be dominated by oxides and oxy-hydroxides of iron that may be substituted with various other metal elements, and may be intermixed with other oxides formed from other metallic constituents of the waste package. Physically, these materials would be expected to be finely divided porous media that, depending on whether they were contained by

surrounding materials, could be loose (i.e., a pile of sloughed off material) or relatively compact.

Chemical interaction of radionuclide-bearing fluids with canister corrosion products is expected to be dominated by surface chemical effects. Retardation of U, Np, and other metals via surface complexation reactions (Meijer, 1990; Dzombak and Morel, 1990) would be considerably greater than in Yucca Mountain tuffs (Table 7-1). Adsorption of inorganic carbon and dissolved silica may also be significant (Van Geen et al., 1994; Waite et al., 1994; Dzombak and Morel, 1990).

Because the corrosion products are expected to be finely divided, there may be a potential for addition of iron oxide and other metallic oxide colloids to the groundwater. There will also be a potential for filtration of waste-form derived colloids.

7.3.3 Backfill

Although the emplacement of backfill has yet to be finalized, if tuff is used, its chemical effects will be moderate in comparison with its physical effects. Hydrothermal alteration of the tuff is not expected to alter its mineralogical or chemical composition outside the range displayed by the tuffs presently existing at Yucca Mountain (Viani and Bruton, 1992b). However, redistribution of relatively small quantities of silica, coupled with precipitation/dissolution of sorptive minerals could significantly change the behavior of a specific crushed tuff with respect to radionuclide transport. A crushed tuff of coarse sand to gravel would present an effective barrier to transport as long as it remains unsaturated (Conca, 1990). However, episodic flow might short circuit the backfill and potentially entrain significant quantities of colloids. The colloids derived from this material should be similar in composition, but not in quantity, to those found in present day Yucca Mountain groundwaters.

7.3.4 Characterization of Natural Colloids at Yucca Mountain

We have characterized the types of colloids that are found naturally in Nevada Test Site (NTS) and Yucca Mountain groundwaters and in core flow experiments using TSw2 tuff (Buchholtz-ten Brink et al., 1990, 1992; Martin et al., 1991; Viani and Martin, 1994b).

The transport of radionuclides through the EBS/NFE and the far field may be affected by the presence and/or formation of colloids suspended in the fluid phase (Triay et al., 1993a). Suspended colloids may affect the transport of radionuclides by

increasing the partitioning of the radionuclide into the fluid phase, by changing the flow path of the radionuclide, and by reducing the groundwater travel time to the accessible environment. The primary focus of colloid studies carried out in the Integrated Testing activity has been to develop techniques to identify inorganic colloidal particles (<1 μm) that may be present in natural and experimental aqueous fluids. The methods developed were used to characterize colloids in groundwater collected from the NTS, including water from well J13, and in fluid obtained from laboratory core-flow experiments (Viani and Martin, 1994a).

7.3.4.1 Colloids in Yucca Mountain groundwaters. Groundwaters from 10 wells were sampled and the suspended colloids characterized by filtration and gravimetric analysis, x-ray diffraction (XRD), x-ray fluorescence (XRF), light scattering, scanning electron microscopy (SEM), and transmission electron microscopy (TEM) [including energy dispersive x-ray spectroscopy (EDS) and selected area electron diffraction (SAED)] (Viani and Martin, 1994b).

The gravimetrically measured concentration of suspended particles >0.15 μm was on the order of 1 mg/L. In light of previously published colloid concentrations for deep groundwaters (McCarthy and Degueldre, 1993) and for water from Well J13 (Ogard, 1987), it is likely that these measurements overestimate the *in situ* groundwater colloid load. Given the strong relationship between pumping rate and colloid load (Puls et al., 1992), it is probable that colloids may have been stripped from the well-bore area during sampling.

Characterization of the colloids using the instrumental techniques listed showed that with the exception of a few particles that were obvious contaminants (e.g., metal particles), the colloidal particles that were identified were consistent with the lithology of the aquifer from which the groundwater was drawn. Of the particles identified by SAED and EDS, a large fraction are layer silicates. Based on the mineralogy of the groundwater-bearing rocks, it appears that these particles are present in the groundwater at a greater fraction than they are in the rock. This may represent a bias toward fracture-filling minerals, which are often layer silicates, or it could represent a pervasive contaminant. There may also be a bias toward identifying layer silicates because of their stability under the electron beam (contrasted with zeolites) and because they may dominate the larger (>0.5 μm) particles that were suitable for identification by SAED. Colloidal silica polymorphs (quartz, cristobalite, amorphous silica) and iron oxides were also identified in the groundwater samples.

7.3.4.2 Colloids in J13 groundwater. Groundwater from Well J13 was analyzed for colloids on samples collected about 2.5 yr apart. The colloid concentration from the earlier sampling was determined by filtration and gravimetry. For the later sampling[1], colloid concentration was determined by counting particles retained on 0.015-μm polycarbonate filters.

The number of particles ranged between 0.6 and 1.5×10^{10} particles/L. These values are similar to Degueldre's estimate for an earlier sampling of Well J13 groundwater (GIT, 1993). If the number of particles counted in the later sample of J13 (<0.4-μm fraction) is converted to mass according to McCarthy and Degueldre's formula (1993) (assuming a density of 2 g/cm^3), the concentration would range between 0.007–0.016 and 0.05–0.125 mg/L, for 100 and 200 nm spherical particles respectively. These estimates are similar to Ogard's (1987) estimate, but are one to two orders of magnitude smaller than the concentration for J13 measured gravimetrically (1.7 mg/L). It is likely that the latter value overestimates the colloid load because of contamination or too rapid a pumping rate during sampling.

The role that natural colloids may play in transporting radionuclides through the EBS/NFE will depend directly on their affinity for radionuclide species that may sorb to them, the reversibility of sorption, and their concentration. For linear instantaneous sorption of a radionuclide species on suspended colloids, the ratio of the radionuclide carried in the solution in the presence of the colloid to that in the absence of the colloid is approximated by:

$$C_{c+s} / C_s = + m_c K_d ,$$

where, m_c is the concentration of colloid in suspension, and K_d is the equilibrium linear partition coefficient for the radionuclide species on the colloid. This relationship holds for soluble radionuclide species whose concentrations are controlled by either a solubility limit or by partitioning to the host rock. It is apparent that very large K_d's (>10^5 mL/g) and colloid concentrations (>2 mg/L) are required to increase the radionuclide carrying capacity of the solution by a significant amount (Fig. 7-1). Of the colloids identified, only illite and clinoptilolite (for Cs), and the iron oxides (U, Np) have the potential for K_d's above 10^4 mL/g. Waste package corrosion products have the potential to add considerable quantities of colloidal

[1] Water samples were collected under the direction of Ines R. Triay, LANL. Unfiltered, 0.4-μm, and 0.05-μm filtered samples were collected on 11/16/93 and sent to LLNL where they were refrigerated until analyzed.

oxides to the EBS/NFE. Because Np has been identified by total system performance analysis (TSPA) calculations as a major contributor to released dose, the issue of colloidal transport of Np will need to be addressed.

7.3.4.3 Colloids in effluent from flow experiments. Suspended particles in samples of fluids that had passed through a saw-cut fracture (25-μm aperture) in a core of Topopah Spring tuff (Viani and Martin, 1993, 1994a) were analyzed by TEM, EDS, and SAED. These particles consisted of iron oxides (hematite) and layer silicates (mica, illite), and could be reasonably ascribed to the core sample or derived from the tools used to create the fracture.

7.3.5 Cementitious Materials

The most likely flow-path component a radionuclide-bearing fluid will encounter after passing through waste package corrosion products is the hydrothermally altered remains of concrete-bearing invert or other structures. The chemical effect of these materials on radionuclide transport will be most important. The pH of fluids within this flow-path component would be expected to be quite high (>12) when the cement is relatively fresh (young). Calcium aluminosilicate gels present in fresh cement will eventually alter to crystalline phases. Because the thermodynamic data for cement minerals are sparse (Bruton et al., 1993), predicting the mineralogical and chemical composition of the hydrothermally altered cements, and the effect of this alteration on radionuclide transport, is uncertain.

Experiments and modeling have suggested that the pH of fluids passing through concretes at ambient temperatures would be expected to remain very high for tens of thousands to hundreds of thousands of years (Atkinson et al., 1989). However, the pH, sorptive capacity, and ability of the hydrothermally altered material to sequester radionuclides could be significantly different from unaltered concrete.

Radionuclide partition coefficients, K_d's, measured for cements (Table 7-1) appear quite favorable in comparison to K_d's for Yucca Mountain devitrified tuffs, especially for U and Np (the radionuclide with the greatest long-term impact on repository performance). It is possible that the K_d's that are measured for U (potentially Np as well) in cement may reflect the precipitation of a relatively insoluble phase in addition to sorption (Atkins et al., 1988).

At least during the early stages of the repository, the cement components would be expected to release significant quantities of colloids (Ramsay et al., 1988). It is not known whether this release of colloidal material would continue after the cement

has undergone chemical and mineralogical alteration associated with long-term heating.

The physical state of concretes and other cementitious materials may evolve from a consolidated and fractured porous medium to a highly fractured and/or crushed porous medium as a result of chemical and physical alteration.

7.3.6 Altered Host Rock Adjacent to the Engineered Barrier

The host rock immediately adjacent to the EBS that will likely be altered by hydrothermal interaction with groundwater and the potentially reactive fluids leaving the repository is the last flow-path component considered part of the EBS/NFE.

In the absence of influx of alkaline fluids, the alteration products and chemistry of the flow-path component would be expected to be similar to that of a crushed-tuff backfill flow-path component. However, interaction of alkaline fluids derived from cementitious materials with the repository host rock may cause significant alteration of the flow-path, especially the hydrologic connection between fracture and matrix. A potential for dissolution of rock at the contact with cement or concrete by alkaline fluids, and subsequent downstream precipitation of calcite, calcium silicates, and zeolites could potentially reduce the porosity adjacent to the fracture and also the permeability in a direction normal to the fracture wall, thus "armoring" the fracture, and reducing the extent of radionuclide retardation due to matrix imbibition and diffusion (Steefel and Lichtner, 1994). This could also potentially decrease the permeability so that fluid flow rates might be significantly reduced, resulting in longer travel times.

7.4 Transport Studies in Host Rock and Minerals

7.4.1 Characterization of Repository Rock Pore Size Distribution and Diffusion of Actinides

Based on the earlier concept of waste package emplacement in boreholes within the repository rock, Integrated Testing studies focused on diffusive transport of radionuclides in near-field TSw2 rock. Pore size distribution measurements (Buchholtz-ten Brink et al., 1992; Klavetter and Peters, 1986) and direct measurement of elemental tracer concentration profiles in TSw2 samples exposed to actinide-bearing solutions (Phinney et al., 1987, McKeegan et al., 1989) are in agreement. A volumetrically small (< ~2-5%) proportion of the interconnected rock

porosity permits relatively rapid diffusion (on the order of the limit in aqueous solutions; i.e., 1×10^{-5} cm^2/s @ 25°C). A slower diffusive component, having apparent diffusion coefficients on the order of 1×10^{-16} cm^2/s (@ 90°C), is also observed.

7.4.1.1 Pore-size-distribution. Mercury porosimetry measurements (Buchholtz ten Brink et al., 1992; Klavetter and Peters, 1986) have shown that the large majority (>95%) of pores in the matrix of TSw2 are on the order of several hundredths of a micrometer. A small component of porosity is contained in pores on the order of one to several micrometers. This porosity appears to be associated with micro-fractures.

7.4.1.2 Diffusion. Secondary Ion Mass Spectrometry (SIMS) allows the direct measurement of the concentration profile of a diffusing species in a solid. The concentration profile can be used to determine the diffusion coefficient for the element. Analysis of polished wafers of Tsw2 samples that were exposed to radionuclide-bearing solutions shows diffusion to be bimodal. Long-term exposures of the tuff samples to radionuclide-tracer solutions (180 d @ 90°C) yielded concentration profiles that could be modeled assuming a single diffusion coefficient on the order of 1×10^{-16} cm^2/s (Phinney et al., 1987). In short-term exposures (8 h @ 25°C), concentration profiles could not be modeled using a single diffusion coefficient. Elevated levels of tracer (3–40 × background) were observed at depths of ~10–15 μm, indicating that fast paths allow a proportion of the diffusing species to be transported at rates approaching that in solution (McKeegan et al., 1989). These fast paths may not be identifiable visually or by scanning electron microscopy or optical microscopy. The resulting distribution of diffusing species is distinctly non-uniform and reflects the non-uniform distribution of the μm-scaled fast paths. These results suggest both fast and slow diffusional paths will need to be accounted for to realistically predict retardation of radionuclides due to matrix imbibition.

In contrast to these results, Rundberg (1987) inferred from the concentration variation with time for Cs and Sr tracer solutions in contact with Yucca Mountain tuff wafers that diffusion is relatively rapid (1×10^{-6} cm^2/s) but mass transport is limited by slow (1×10^{-14} cm^2/s) intracrystalline diffusion in zeolite and smectite cation exchangers. The diffusion of actinide tracers were not able to be modeled using this approach, presumably because they were excluded from the internal regions of the cation exchangers. Because zeolites and smectite exchangers are not

abundant (< 2%) in TSw2, intracrystalline diffusion cannot explain the concentration profiles determined using SIMS.

7.4.2 Diffusion of Radionuclides in Clinoptilolite

Hydrothermal alteration of TSw2 repository rock and other tuffs in the EBS/NFE (e.g., crushed tuff backfill and/or invert) may create additional masses of sorbing minerals such as clinoptilolite or smectite. Although not abundant in the TSw2, smectite and clinoptilolite are significant phases lining fractures that are expected to be the main hydraulic pathways for radionuclide migration from the waste package (Carlos, 1985). The retardation of radionuclides due to interaction with these minerals via cation exchange will be less than expected if the cation exchange reaction is limited by the rate of intracrystalline diffusion. Secondary ion mass spectrometry (SIMS) was used to obtain information regarding the rate of intracrystalline diffusion of Cs and Sr during cation exchange (Roberts et al., 1995; Viani et al., 1994).

Clinoptilolite crystals oriented to either the (010) or (001) crystallographic face by mounting in epoxy were rendered nominally homoionic with respect to Na, K, and Ca by exchange with NaCl, KCl, or $CaCl_2$ salt solutions as verified by quantitative wavelength dispersive spectroscopy using an electron microprobe (EMP). The homoionic crystals were then exposed to either a Cs/cation or Sr/cation (cation = Na, K, Ca) solution at two different temperatures (30–32°C and 90°C). The mounted crystals were placed in the bottom of a teflon Erlenmeyer flask and 100 mL of the relevant diffuser/cation solution was added to the flask. The sealed flasks were placed in an orbital shaker for the ambient temperature experiment (~30–32°C); and a shaking water bath held at 90°C for the higher temperature experiment.

The geochemical modeling code EQ3/6 (Wolery et al., 1990) was used to select binary solution compositions that would not change significantly (<5%) during the course of the diffusion experiment so as to maintain a constant concentration boundary condition. Solution compositions were selected so that the equilibrium amount of diffusing trace cation in clinoptilolite (Cs or Sr) would be small (~1 mol-% of the exchange cations), and the concentration of the trace cation in solution would be analytically measurable.

Concentration vs. depth profiles were then determined by SIMS. These were obtained for Cs, Sr, Ca, Na, K, Rb, Al, and Si by sputtering through the crystal while rastering the ion beam over a 100 μm square. The conversion of sputtering time to depth was made by measuring the depth of the sputtered raster using a profilometer.

Figure 7-2 shows the SIMS depth profile for the Cs/Ca ambient temperature experiment. The SIMS raw data has been corrected for background, ratioed to the Al signal, and then normalized to a nominal surface concentration value of 0.01 (consistent with EQ3/6 modeling predictions and with the post-diffusion EMP Cs analysis data). An attempt was made to fit this data to a single (constant) diffusion coefficient using the analytical solution to the diffusion equation for a constant concentration boundary condition and an infinite half-plane (Viani et al., 1994). The shape of the experimental data is such that no choice of a constant diffusion coefficient will reasonably match the data.

In contrast, if the binary interdiffusion coefficient D, is compositionally dependent, and is functionally related to composition and trace diffusion coefficients according to (Lanford et al., 1979):

$$D = \frac{D_{in} D_{out}}{X_{in} D_{in} + (1 - X_{in}) D_{out}} ,$$

where X_{in} is the mole or equivalent fraction (relative concentrations) of the inward diffusing component and D_{in} and D_{out} are the trace diffusion coefficients for the inward and outward diffusing components, then it is possible to effectively match the observed data by appropriate choice of D_{in} and D_{out}. The inward and outward tracer diffusion coefficients that result from matching model to data are 2.0×10^{-13} and 1.5×10^{-18} cm^2/s, respectively. Although no direct measurements of diffusion coefficients have been reported for clinoptilolite, these data agree with radiochemical measurements of self diffusion coefficients of Cs and Ca in a similar zeolite, mordenite (Breck, 1984), and with diffusion coefficients inferred from batch adsorption experiments for clinoptilolite-bearing tuffs (Rundberg, 1987). Further analysis of the SIMS data for this experiment, for experiments conducted at other concentrations of Cs and Sr, and at other diffusion times are necessary before this simple two-component model can be verified.

Analysis of Cs diffusion profiles into nominally Ca clinoptilolite for ambient and 90°C, and for Sr diffusion into Ca clinoptilolite at ambient temperature reveal several important points:

1. Using a binary interdiffusion model, the ambient temperature diffusion of Cs can be reasonably modeled.

2. The tracer diffusion coefficients estimated from the Cs and Sr diffusion profiles in the ambient temperature experiments indicate diffusion coefficients on the order of 10^{-13} and 10^{-18} cm^2/s for Cs and Sr, respectively.
3. The diffusion of Cs into the Ca clinoptilolite at 90°C was rapid enough to increase the Cs content several orders of magnitude above background to a depth of at least 35 μm (the maximum depth probed) over a 12-day exposure.
4. It is apparent that small amounts of Na, K, and trace levels of Rb are present in the nominal Ca clinoptilolite crystals and their concentrations are not constant with depth. It is possible that at least some of the observed diffusion of Cs may occur by preferential exchange with the residual monovalent cations in the Ca exchanged crystal.

The experimental data and the parameters derived from them indicate that diffusion of Cs and Sr into clinoptilolite is probably not rapid enough to allow the assumption of local cation-exchange equilibrium for situations in which groundwater flow is relatively rapid and clinoptilolite crystal size is relatively large; e.g., in fractures. Applying equilibrium distribution coefficients obtained from batch adsorption experiments using fine-grained clinoptilolites (1–2 μm) to predict adsorption during flow through fractured media may not be justifiable.

7.4.3 Flow and Transport Through Topopah Spring Tuff

Fracture flow is expected to dominate the flux of H_2O in the altered repository host rock. Matrix flow, if it occurs, will be very slow in comparison. Physical processes related to high suction potential and a potentially discontinuous waste phase will tend to limit flow even beyond the limits imposed by low permeability. Baseline information regarding the potential for retardation and matrix imbibition of soluble radionuclides and/or colloids is necessary to assess flow and transport. In addition, the effects on radionuclide transport of alteration of the host rock by hydrothermal interaction with groundwater, or with reactive fluids derived from EBS/NFE introduced materials, needs to be addressed.

This section summarizes results of flow and tracer tests using core samples of devitrified Topopah Spring tuff containing saw-cut fractures. Experiments were undertaken using ~5.1-cm-diameter by 5.1-cm-long cylindrical cores. A saw-cut parallel to the length of the core was made and two 1/8-inch-wide 1-mil (~25-μm)-thick gold shims inserted to maintain a fixed aperture between the surfaces. The core sample was mounted in an apparatus in which confining pressure, downstream pore pressure, flow rate, and core temperature could be varied

(Fig. 7-3). Initial experiments were performed using a pump without the ability to maintain constant upstream pressure or constant flow. Subsequent experiments were performed using a pump that maintained constant flow. Pressures, temperatures, and cumulative flow (initial device) or flow rate (late experiments) were monitored and periodically logged to a computer. Confining pressures were maintained between 35 and 50 bar; pore pressures varied between 0.1 and ~5 bar. Details of the apparatus and the sample treatment are given in Viani and Martin (1993, 1994a).

7.4.3.1 Bacterial plugging of flow path. To prevent the growth of bacteria during the flow test, a core sample was sterilized by autoclaving in-situ by raising the temperature of the flow test device to 120°C for approximately 12 hours. After cooling to ambient temperature, the temperature was again raised to 120°C for 12 hours. Filtered (0.05 μm), deionized (milli-Q) water was pumped through the core and permeability monitored for two flow tests lasting approximately 6 and 8 weeks.

Despite sterilization of the core, flow rate, differential pressure, and permeability varied, apparently as a result of bacterial fouling of the fracture aperture. In one test, permeability showed a relatively strong correlation with differential pressure (Fig. 7-4). The observed flow behavior suggested that the fracture gradually closed due to material filling the aperture, and that by increasing the differential pressure, this material was forced out. To test this, samples of the effluent fluid were taken at times when the flow rate, differential pressure, and permeability were high (Fig. 7-4) and analyzed using transmission and scanning electron microscopy to see if particles were present that could account for the decrease in permeability.

TEM and SEM analyses identified bacteria and inorganic particles in the effluent samples. The most abundant particles appeared to be rod shaped bacteria (~1–1.5 μm long) and were observed in all three samples. Although no obvious source of carbon was introduced into the system, it is apparent that the growth of this bacterium was sufficient to essentially close the 25-μm-fracture aperture. Differential pressures on the order of 0.5 bar and flow rates on the order of 5 mL/h were necessary to "cleanse" the aperture. However, as shown in Fig. 7-4, even after increasing the flow rate by increasing the differential pressure, closing of the aperture occurred subsequently. In subsequent tests, using a constant flow pump, plugging was not observed, even though the sample was not sterilized. Although plugging is not observed under constant-flow regime, bacterial growth is almost certainly occurring. Apparently, the bacteria are continuously eluted from the fracture without building up enough to close it. Bacterial growth in the subsurface could significantly impact

the path that fluids will take in the fractured flow-path components of the EBS/NFE.

7.4.3.2 Summary of flow test results. To obtain consistent hydraulic data, the constant flow pump was used for subsequent tests. A series of flow tests were performed for a single core sample at three temperatures (23, 59, and 92°C) and two flow rates (0.2 and 2.0 mL/h). Bromide and iodide were used as tracers. The average permeability at 23°C was on the order of 0.06 millidarcy (md) and was independent of the flow rate and average pore pressure (Table 7-2). This value is approximately one third to one fifth that of the lowest permeabilities previously observed for the same core sample (Viani and Martin, 1994a), and for a different sample having the same fracture aperture (Viani and Martin, 1993). This could reflect the growth of a bacterial population in the fracture channel as noted above, or may reflect small differences in effective fracture aperture.

The observed permeability is more than 2 orders of magnitude smaller than would be predicted (de Marsily, 1986) for a 25-μm aperture with smooth walls (33 md). If one assumes all the flow is via the fracture, the effective aperture width is calculated to be 3.1 μm. It is possible that some reduction in the gold shim thickness may have occurred upon loading. Deformation of the core sample itself under confining pressure may also contribute to the low permeabilities observed; however, based on an analysis of the effect of confining pressure on permeability (Fig. 7-5), it appears unlikely that this could explain the observation. At 59°C, the average permeability is slightly larger (~0.1 md) and also appeared to be independent of the flow rate and average pore pressure.

At 92°C, the average permeability varied between 0.08 and 2.34 md and was independent of the flow rate but dependent on average pore pressure. For flow tests in which the average pore pressure was less than 0.1 bar (5 runs) the average permeability was ~0.2 md. For runs in which the average pore pressure was greater than 0.5 bar (7 runs) the average permeability was ~1.9 md (Table 7-2).

It is clear that pore pressure has a significant effect on the permeability at 92°C. This effect is non-linear; i.e., increasing pore-pressure above the ~0.5 bar threshold does not result in a continued increase in permeability. However, the phenomenon does appear to be reasonably reversible, because sequential runs taken at pore pressures below and above 0.5 bar yielded similar results to the previous runs at equivalent pore pressures. If the phenomenon were related to changes in aperture width, a reversible change of ~5 μm would be required. One possibility is that exsolution of dissolved air from the feed solution (between 23 and 92°C, a liter of

H_2O would exsolve about 5 cm^3 of gas at 92°C and 1 bar) may partially block the aperture. This blockage would lessen at higher pore pressures. However, the exsolution would also be expected to have affected the runs at 59°C as well, and this was not observed.

Permeability also varied with confining pressure. The variation in instantaneous permeability with confining pressure can be explained by a change in the fracture aperture that depends on confining pressure. In the example shown (Fig. 7-5), the effective aperture width need only change by ~0.06 μm to cause the change in permeability observed. This response is reversible. Similar observations were made by Roberts and Lin (1995) and Mohanty et al. (1995) for fractured welded tuffs.

7.4.3.3 Tracer experiments. A dilute Na–Cl–HCO_3 solution containing Br^- or I^- tracer was eluted through the core under constant flow conditions. Following a period of flow of the standard feed solution (dilute NaCl, $NaHCO_3$, pH ~7.5), a 560 μL pulse of either NaBr or NaI tracer solution (0.75 mM) was injected upstream from the core. The average recovery of tracer downstream from the core was 95 and 102% for Br^- and I^-, respectively. These recoveries are within experimental error of 100%; under these conditions both Br^- and I^- are considered to be conservative tracers.

Figure 7-6 shows an example of I^- tracer breakthrough curves for replicated run conditions. The generally excellent reproducibility in the tracer breakthrough curves suggest complete flushing of the tracer between runs and no measurable changes to the hydrologic or chemical state of the sample. These results also indicate that pore-pressure, confining pressure, and flow rate effects are essentially reversible.

7.4.3.3.1 Effect of flow rate, pore pressure, and temperature on breakthrough of tracer. Figure 7-7 shows the effect of flow rate on elution of conservative tracer. The tracer elutes slightly sooner (in terms of volume eluted) and exhibits less tailing at a lower flow rate. This effect appears to be independent of pore pressure. Early breakthrough may reflect a relatively greater impact of longitudinal dispersion at the lower flow rate. The reduced tailing region for the breakthrough curve for the lower flow rate suggests that a given volume of post-pulse solution is more effective in "sweeping out" tracer that has diffused into the matrix during passage of the tracer pulse through the fracture. At the slower flow rate, the rate of mass transfer of tracer from matrix to fracture via diffusion relative to advection of tracer through the fracture is greater than at the higher flow rate. For the flow rates and tracer pulse

volumes utilized, it is probable that diffusion into the matrix occurs primarily via the fast paths described in section 7.4.1.

Figure 7-8 shows the effect of pore pressure on the breakthrough of the tracer. This figure shows that the initial breakthrough is retarded, and the tailing region of the pulse is extended relative to the case where pore pressure is low. This suggests that pore pressure controls the fracture/matrix connectivity possibly by controlling the width of micro-fractures that may emanate from the main fracture pathway. At higher pore pressure the number and/or width of micro-fractures intersecting the saw-cut fracture may increase. This would increase the mass transfer of tracer into the matrix during passage of the pulse, and the volume of matrix containing tracer that must be flushed following the pulse.

Figure 7-9 shows the role that temperature plays in controlling the initial breakthrough and the extent of tailing in the tracer pulse. The volumetric elution of the tracer occurs earlier, and the tailing is less pronounced the greater the temperature of the experiment. This may reflect an increase in the diffusion coefficient of the tracer. Physical retardation expected to result from the diffusion of radionuclides into the matrix may be reduced with increasing temperature.

7.4.3.3.2 Composition of effluent. Table 7-3 shows chemical analyses for selected elements in the feed solution and after the breakthrough of the tracer. The major observation is the positive correlation of dissolved Si and negative correlation of Ca and Mg with temperature, and the negative correlation of Si, Ca, and Mg with flow rate at 92°C. The silica concentrations observed in the 0.2 mL/h runs at both 23 and 92°C indicate slight supersaturation with respect to equilibrium with quartz but significant undersaturation with respect to cristobalite. If the length of the core were longer, or the flow rate slower, it would be expected that the concentration of silica in the effluent would approach saturation with cristobalite.

The effects of confining pressure, pore pressure, flow rate, and temperature on permeability and transport of a conservative tracer through a saw-cut sample of Topopah Spring tuff have been measured and are likely to affect the degree of retardation of radionuclides in fractured materials in the near-field environment. Increasing pore pressure tends to increase the retardation due to matrix diffusion; increasing temperature has the opposite effect.

These findings strengthen the argument that transport experiments for fractured samples must be undertaken using flow-test apparatuses that allow the variation of confining and pore pressures, because not only is the permeability of the sample affected, but the so is the nature of the breakthrough curve. Experiments that have

previously been conducted with core samples that were epoxied in place do not provide data to test phenomena which would be expected to play a role in the transport of radionuclides through fractured media at Yucca Mountain. Hence, relationships between physical variables such as pore pressure and confining pressure, and chemical phenomena such as radionuclide transport, will not be adequately accounted for in transport and performance assessment models unless transport experiments are undertaken using the type of apparatus used in this study. The study of biological impact on flow and transport will require experimental apparatuses that will be able to mimic the flow regime expected in the EBS/NFE; otherwise, important phenomena may be missed.

7.5 Field Testing Sorption Models Under Conditions of Fracture Dominated Flow

Modeling the chemical processes likely to impact the transport of radionuclides through the EBS/NFE will require coupled flow and chemical reaction models capable of predicting the effects that dissolution/precipitation, adsorption/desorption, and aqueous speciation have on radionuclide transport. In the EBS/NFE, transport will be strongly influenced by adsorptive retardation in flow-path components (e.g., waste package corrosion products, concrete, altered TSw2). Previous application of surface chemical models to laboratory experiments and field observations (Viani and Bruton, 1992a,b) resulted in model refinement and a better understanding of the limits of model applicability. However, there are limits to the application of laboratory experiments to confidence building and testing modeling approaches. Field testing can play an important role in this confidence building process.

The underground hard rock laboratory in Äspö, Sweden (HRL) afforded a unique opportunity in a well-constrained field test to assess the ability and utility of cation exchange and surface complexation models to explain the evolution of fluid composition over time in a fractured aquifer (Bruton, 1996; Viani and Bruton, 1996a,b). The matrix rock at the HRL is predominantly granite. Although its chemical and hydraulic properties would be expected to differ from the matrix rocks at Yucca Mountain, the processes accounting for mass transfer between fracture and matrix, sorption and diffusion, are identical to those expected to retard radionuclide movement at Yucca Mountain.

Construction of the HRL laboratory initiated relatively rapid downward flow of dilute shallow groundwater through fractures that were intersected by the

underground excavation. The groundwater in one of the intersected fracture zones (Redox Zone) was sampled just prior to the intersection of the underground tunnel with it (@70 m) and regularly thereafter for a period of several years. The shallow groundwater was also sampled before and following the initiation of flow at a depth (<15 m) just below where the fracture zone is expressed at the ground surface. Fractures in the dominantly granitic rocks are lined with a variety of sorbing minerals, including illite/smectite, chlorite, sericite, and iron oxides (Tullborg, 1995b).

The groundwater at tunnel depth is considerably more saline than the shallow groundwater (ionic strength 0.006 vs. 0.18 m). Hence, the induced flow of groundwater into the tunnel is also accompanied by mixing of the two water types. Cation exchange has been hypothesized to play a role in controlling the observed variation in fluid chemistry (Banwart et al., 1994). A comparison of simulated mixing of groundwater using geochemical modeling codes with the observed evolution of groundwater at Äspö suggests that the groundwater mixing is accompanied by mass transfer between fluid and fracture minerals via cation exchange and surface complexation reactions.

7.5.1 Cation Exchange

7.5.1.1 Modeling approach. The geochemical modeling package EQ3/6 (Wolery et al., 1990; version 3245R116), to which a cation-exchange model was added (Viani and Bruton, 1992a,b), was used with an associated thermodynamic data base (version DATA0R19) to simulate the mixing between the shallow (HBH02) and native (tunnel depth; KA0483A) fluids. A cation-exchange model employing the Vanselow convention (Sposito, 1981) was used for the simulations. Details of the implementation of this option in EQ3/6 and examples of its application may be found in Viani and Bruton (1992a,b). Fluid chemistries predicted to result from mixing were compared with those monitored from boreholes intersecting the fracture zone.

The conceptual model of fluid mixing imposed by EQ3/6 is a simplified approximation of the actual process that is occurring at Äspö. Inherent to this simplification is the assumption that the shallow groundwater undergoes no compositional change (i.e., no reaction with its surroundings) prior to mixing with the native groundwater, and that mixing occurs only in the presence of a cation exchanger that is initially in equilibrium with the native groundwater.

not the same as that predicted by the cation exchange model (Fig. 7-10). A number of causes might contribute to this discrepancy:

1. The actual mixing of fluids in the fracture system is not adequately simulated by the simple mixing algorithm embodied in EQ3/6. Because of the potentially large ratio of cations on the exchanger to those in the fluid, differences between the simulated mixing process and the actual mixing process would probably have the greatest effect on the most dilute mixed fluids.
2. More than two "endmember" fluids may be involved in the mixing and cation exchange process (Laaksoharju et al, 1995).
3. The chosen cation-exchange model, exchange energies, or assumption of exchange equilibrium may not be correct. Of these potential shortcomings, only exchange disequilibrium would likely result in significantly different predictions. As observed for exchange equilibrium in clinoptilolite (section 7.4.2), exchange disequilibrium would likely occur only if exchange were limited by inter and intracrystalline diffusion of exchange cations in the fracture-lining exchangers. The diffusion rate in undisturbed fracture fill at the HRL has not been measured.

7.5.1.4 Predicting the level of exchangeable Cs. The ability to model the partitioning of trace elements such as Cs and Sr is a major rationale for using cation-exchange models. Previous work has shown that cation-exchange models can relatively accurately predict the partitioning of Sr and Cs to zeolitized tuff from Yucca Mountain (Viani and Bruton, 1992a, 1992b).

Data available from the HRL allowed a comparison of observed vs. predicted partitioning of Cs in a field situation. Samples of fracture filling minerals collected at the intersection of the HRL tunnel with the fracture zone were analyzed for Cs and other trace elements using sequential extraction techniques to determine the proportion associated with the exchange sites on the minerals (Landström and Tullborg, 1995). The concentration of exchangeable Cs in the fracture fill for Redox Zone fracture was ~0.6 ppm. Assuming that all of the exchangeable Cs is associated with the illite and/or sericite components of the fracture filling, and assuming their abundance to be 5%, the predicted concentration of exchangeable Cs in the fracture fill based on the measured concentration of Cs in the groundwaters collected at those fractures varied between 0.9 and 1.2 ppm (Viani and Bruton, 1996). The predicted values are in reasonable agreement with the measured values which gives further confidence in the model.

Geochemical modeling simulations of the role of cation exchange in fluid mixing and in trace metal partitioning suggest that this phenomenon plays an important role in the short-term chemical dynamics that are occurring in the Redox Zone fracture system. We conclude:

1. Because of the similarity of the exchange properties of smectite and those of the planar site in illite, the major cation occupancies (Na, Ca, and Mg) predicted for the illite exchanger are very similar to those predicted for a smectite exchanger.
2. Cation exchange is a plausible mechanism to explain apparent sources and/or sinks for Ca, Sr, and Na during mixing of dilute shallow groundwater and native groundwater in the Redox Zone.
3. Cation-exchange simulation of the partitioning of Cs and Rb onto illite predicts that almost all of the "mobile" pool of these elements is associated with the exchanger. The predicted level of exchangeable Cs and that measured by sequential extraction of fracture gouge are in reasonable agreement.
4. The quantity of exchanger (~0.1 equiv/L of groundwater) necessary for the simulation to match the observed fluid data is physically reasonable, and is consistent with the observed fracture mineralogy. This estimate agrees with estimates by Banwart et al. (1995b) that are based on modeling and on fracture fill material properties.

7.5.2 Surface Complexation

As shown above, the observed variability of fluid chemistry at the Äspö Hard Rock Laboratory is not fully described by conservative fluid mixing models. Ion exchange may account for some of the observed discrepancies. It is also possible that variably charged solids such as oxyhydroxides of Fe can serve as sources and sinks of anions and cations through surface complexation.

The most successful models describing adsorption onto iron and other oxides are surface complexation models (Dzombak and Morel, 1990). Surface complexation reactions on hydrous ferric oxides involve sorption of both cations and anions. Because U, Np, and other metals are strongly sorbed by iron oxides (Table 7-1), it is important to gain confidence in applying these models to predict the retardation of these radionuclides through the various oxides expected in the EBS/NFE (sec. 7.3.2).

Geochemical modeling of the surface chemistry of hydrous ferric oxides (HFOs) in equilibrium with shallow (HBH02) and native (KA0483A) HRL Redox Zone

waters shows that HFOs can serve as significant, pH-sensitive sources and sinks for cations and anions (Bruton and Viani, 1996).

A variety of cations (e.g. H^+, Ca^{++}, Sr^{++}, Ba^{++}) and anions (HCO_3^-, SO_4^{--}, HPO_4^-) are known to sorb onto hydrous ferric oxides at 25°C (Dzombak and Morel, 1990). Hematite and Fe-oxyhydroxide are commonly found as fracture fillings at Äspö (e.g., Tullborg, 1995b). Banwart et al. (1994) estimated that the abundance of hematite in altered granite is 1–2%, and that the abundance of Fe(III)-oxyhydroxides in the fracture coatings is 4%. Microfractures close to the fracture surface contain what appears to be iron oxyhydroxide.

The approach used to simulate the effect of sorption onto iron oxides via surface complexation is similar to that taken by Viani and Bruton (1994, 1996) to test the hypothesis that ion exchange affects the composition of groundwaters sampled from boreholes in the HRL tunnel. Geochemical modeling computer codes containing surface complexation models capable of simulating sorption onto HFOs were used to:

1. Calculate the potential for HFOs to serve as reservoirs and sinks of ions. The dependencies of ion sorption on pH in shallow and deep waters from the Redox Zone at Äspö were calculated to evaluate the potential for changes in major element chemistry during fluid mixing owing to the sorptive behavior of HFOs.
2. Simulate mixing between the shallow and deep waters that are believed to contribute to the observed changes in fluid chemistry with time in the Large Scale Redox Experiment.

Surface complexation refers to chemical reactions between reactive functional groups exposed on a solid surface and aqueous species in an adjacent fluid. Surface complexation reactions lead to the sorption and desorption of anions and cations. The reactive functional groups at the solid surface (often referred to as "sites") derive from unsatisfied bonds created by the discontinuity of a three-dimensional structure.

The reactive sites on the surfaces of oxide minerals may be negative, neutral or positive depending on the extent of their protonation. Hence, the net charge on the surface may be positive or negative, depending on the pH of the solution. Because the charge of reactive sites in oxides is controlled by pH, surface complexation reactions are much more sensitive to pH than ion exchange; the extent of ion sorption can change drastically within a few pH units.

The surface complexation reactions comprising the sorption model are provided for in the *React* geochemical modeling code. *React* is a part of The Geochemist's Workbench™ (Bethke, 1994) set of software tools for calculating fluid-mineral-gas equilibria. *React* combines the calculational abilities of EQ3 and EQ6. EQ3/6, used by Viani and Bruton (1994, 1996) to describe ion exchange, could not be used as it does not provide for surface complexation reactions.

React can simultaneously provide for aqueous speciation in the fluid phase, mineral dissolution and precipitation, and surface complexation onto a sorbent, such as HFO. However, mineral dissolution and precipitation reactions were not considered in the calculations described here.

React employs the generalized two-layer surface complexation model of Dzombak and Morel (1990). The generalized two-layer model is an extension of the diffuse double layer model, with provision for two types of sorption sites (weak and strong) and surface precipitation (see Dzombak and Morel, 1990 for an extensive discussion of the models).

React contains a data base of surface complexation constants from Dzombak and Morel (1990) assuming a generalized two-layer surface complexation model. Although the most comprehensive compilation of constants to date, Dzombak and Morel's data set lacks complexation constants for carbonate species.

At low pH values, anions such as sulfate and carbonate tend to be sorbed by HFOs. Preliminary calculations with Dzombak and Morel's data set suggested that sulfate surface complexes dominate the total mass of sulfate in the fluid+sorbent system. However, the Dzombak and Morel (1990) data set does not provide for competition between sulfate and carbonate for sorption sites. Therefore, a literature search was made to identify experimental studies yielding carbonate complexation constants that could be added to the Dzombak and Morel (1990) data set.

Waite et al. (1994) determined carbonate complexation constants as part of a larger study to measure U(VI) sorption onto HFOs. They used a two-site diffuse double layer model. Van Geen, Robertson, and Leckie (1994) focused on complexation of carbonate species at the goethite surface and used a single-site diffuse double layer model to extract complexation constants from their sorption experiments.

The complexation constants from both papers were incorporated into two new versions of the *React* complexation constant data base from Dzombak and Morel (1990). Simulations were carried out with each of the three data bases (a) Dzombak and Morel (1990), (b) Dzombak and Morel plus carbonate complexation data from

Waite et al. (1994), and (c) Dzombak and Morel plus carbonate complexation data from Van Geen, Robertson, and Leckie (1994) for comparison.

Scoping calculations using all three data bases suggested that the data of Van Geen, Robertson, and Leckie (1994) predicted significantly greater amounts of carbonate sorption than data from Waite et al. (1994). Because Van Geen, Robertson, and Leckie's (1994) study focused more closely on carbonate sorption than Waite et al. (1994), data bases from (a) Dzombak and Morel (1990) and (b) Dzombak and Morel plus carbonate complexation data from Van Geen, Robertson, and Leckie were used to explore the impact of sorption on fluid chemistry.

For these calculations, goethite was used as a proxy for a variety of iron oxyhydroxides such as ferrihydrite and hematite that can act as sorbents. Goethite was assumed to contain 0.205 moles of sorption sites (0.2 weak, 0.005 strong) per mole of Fe (Dzombak and Morel, 1990). Iron oxyhydroxides can vary significantly in terms of their surface area and corresponding total number of surface sites per mole of Fe. However, by relating our calculations to the number of surface sites available for reaction, we obtain a common frame of reference for all forms of HFOs. The mass of goethite per kilogram of H_2O was varied from 0.1 to 10 g/kg H_2O to illustrate the effects of variations in sorbent:fluid ratio. The relations between mass of goethite, number of surface sites, and fluid mass are discussed below.

The result of surface complexation reactions of goethite in the shallow and native groundwaters are shown in Fig. 7-13 and Fig. 7-14 as a function of pH. One gram of goethite, serving as a proxy for Fe-oxyhydroxides, was assumed to be in equilibrium with 1 kg of H_2O having the composition of the shallow or native groundwater. Sorbed fraction in Fig. 7-13 and Fig. 7-14 refers to the fraction of a given element that resides on HFO surfaces relative to the total amount of that element in the fluid+sorbent system. It is calculated as the sum of the concentrations of sorbed species containing a given element, divided by the sum of the amount of the element in solution and the amount of the element sorbed. For example, a sorbed fraction of 0.5 implies that if there are 100 mg/kg SO_4 in solution, 100 mg/kg SO_4 are bound to the HFO surface as surface complexes.

The sorbed fraction is a useful measure of the effectiveness of a sorbent as a reservoir of ions. When the sorbed fraction exceeds 0.5, the mass of the sorbed element is greater than that in the fluid. A change in solution composition, such as pH, could release those ions and significantly increase the ion concentration in the fluid.

Carbonate surface complexes comprise a significant fraction of total carbonate in the fluid+sorbent system. For example, Table 7-6 shows that over 10 times as much carbonate (1121 mg/kg expressed as bicarbonate) is sorbed onto HFO surfaces as is contained in the fluid (114 mg/kg) given a sorbent:fluid ration of 10 g of goethite per kilogram of H_2O. Thus, the calculations suggest that HFOs at shallow depths may serve as important reservoirs or sources of carbonate if conditions, such as an increase in pH, favor desorption of carbonate.

Competition for surface sites can be appreciated by considering the results of simulations for which carbonate surface complexes are excluded (not shown). Under these conditions, the percent sulfate predicted to be adsorbed is 5 to 50 times greater for the shallow groundwater and 3 to 4 times greater for the native groundwater. It is apparent that carbonate species are sorbed to a much greater extent than sulfate.

To relate the calculations described in this report to attributes of natural systems, we must establish the relevance of the masses of goethite used per kg H_2O. For a given fracture width, we calculated the thickness of a continuous goethite fracture coating yielding 1and 10 grams of goethite per kg H_2O (Fig. 7-15), assuming a fully saturated system. Goethite, hematite, and iron oxide stains are common in the fracture fill at Äspö, with estimated abundances as great as several percent by weight of the fracture fill (Banwart et al., 1994, 1995; Tullborg, 1995a,b). For a fracture fill with a fractional porosity of 0.1, a rock density of 2800 kg/L, and 0.1% by weight of iron oxide, approximately 25 g of iron oxide would be associated with each kg of pore water. Thus, considering the petrographic observations of the abundance and distribution of HFOs observed at Äspö, the quantities of goethite per kg of H_2O used in the calculations are reasonable and conservative. Based on 0.205 mol of sites/mol Fe (Dzombak and Morel, 1990), there are 2.31×10^{-3} moles of surface sites per gram of goethite. Even though goethite does not form continuous surface layers in nature, the calculation nonetheless demonstrates that the masses of goethite considered in this report are conservative, yet can account for a great deal of surface complexation.

The results of geochemical simulations such as those described here are only as reliable as the surface complexation constants and the complexation model upon which the predictions are based. For example, if the carbonate complexation constants from Van Geen, Robertson and Leckie (1994) overestimate the degree of formation of surface carbonate complexes, the degree of SO_4 sorption would increase.

pressure, and confining pressure; hence thermo-mechanical effects of repository construction and waste emplacement may significantly alter the transport properties of the existing fracture network.

In addition to chemical effects of introduced materials, the presence of significant biological activity could significantly affect flow paths by plugging fractures.

Natural groundwater colloids are ubiquitous, but may not be present in large enough quantities to significantly affect radionuclide transport. Introduced materials, such as container corrosion products, backfill, and cements will add to the colloid population that is available for transporting radionuclides.

Surface chemical models that describe sorption via cation exchange and surface complexation approaches have been used to simulate mixing of groundwater mixing in a fractured aquifer and found to be consistent with observation. This enhances our confidence that these models/approaches will have applicability to Yucca Mountain and can be applied once material and design issues are resolved.

7.7 Summary of Gaps in Information Required to Bound Radionuclide Transport in the EBS/NFE

Very little experimental data exists for radionuclide transport through EBS/NFE materials at the temperatures and fluxes expected in the repository. Hence, modeling efforts to derive the flux of radionuclides through the EBS/NFE will not be constrained by data. In addition to basic thermodynamic data regarding solubility and speciation of radionuclides at elevated temperature in the chemical environments expected in the EBS/NFE, bounding the flux of radionuclides through the EBS/NFE will also require:

1. Sorptive/chemical properties of the altered internal components of the waste package.
2. Sorptive properties of waste package corrosion products. Experimental measures of transport of critical soluble and/or colloidal radionuclides through waste package corrosion products at elevated temperatures.
3. Mineralogy and physical status of altered cementitious materials. Characterization of the mode of interaction of actinides with altered cementitious materials. Experimental measures of transport of critical soluble and/or colloidal radionuclides through altered cementitious materials. Characterization of colloids derived from altered cementitious materials.

7.8 References

Albinsson, Y., Andersson, K., Borjesson, S., Allard, B. 1993. *Diffusion of radionuclides in concrete/bentonite systems*. Swedish Nuclear Fuel and Waste Management Co. Technical Report 93-29. Stockholm, Sweden.

Atkins, M., Beckley, A.N., and Glasser, F.P. 1988. Influence of cement on the near field environment and its specific interactions with uranium and iodine. *Radiochimica Acta* 44/45:255–261.

Atkinson, A., Everitt, N.M., and R.M. Guppy. 1989. Time dependence of pH in a cementitious repository. Mat. Res. Soc. Proc. Vol. 127:813-821. Mat. Res. Soc. Proc. Vol. 127:439–446.

Banwart, S., Gustafsson, E., Laaksoharju, M., Nilsson, A-C., Tullborg, E-L. and Wallin, B., 1994. Large-scale intrusion of shallow water into a vertical fracture zone in crystalline bedrock: Initial hydrochemical perturbation during tunnel construction at the Äspö Hard Rock Laboratory, southeastern Sweden. *Water Resources Res.*, v. 30, p. 1747–1763.

Banwart, S., Laaksoharju, M., Pitkänen, P., Snellman, M., and Wallin, B. 1995. Development of a site model for reactive element dynamics. pp. 188–218. *In* Banwart, S. (ed.) *The Redox Experiment in Block Scale: Final Reporting of Results from the Three Year Project*. SKB Äspö Hard Rock Laboratory Progress Report 25-95-06, Stockholm.

Bates, J.K., Brown, N.R., Buck, E.C., Dietz, N.L., DiSanto, T., Ebert, W.L., Ellison, A.J.G., Emery, J.W., Fortner, J.A., Hafenrichter, L.D., Hoh, J.C., Mazer, J.J., Surchik, M.T., Wolf, S.F., and Wronkiewicz, D.J. 1995b. *ANL Technical Support Program for DOE Environmental Restoration and Waste Management*. ANL-95/20. Argonne National Laboratory, Argonne, IL.

Bates, J.K., Fortner, J.A., Finn, P.A., Wronkiewicz, D.J., Hoh, J.C., Emery, J.W., Buck, E.C., and Wolf, S.F. 1995a. *Yucca Mountain Project - Argonne National Laboratory Report, FY 1994*. ANL-94/42. Argonne National Laboratory, Argonne, IL.

Bethke, C.M. 1994. *A Users Guide to Rxn, Act2, Tact, React, and Gtplot*. Copyright Craig M. Bethke, University of Illinois, Champaign, IL.

Breck, DW. 1984. *Zeolite Molecular Sieves*. R.E. Krieger Pub., Malabar, FL, pgs. 559 and 574–575. (NNA.19890522.0211)

Brouwer, E., Baeyens, B., Maes, A., and Cremers, A. 1983. Cesium and rubidium ion equilibria in illite clay. *J. Phys. Chem.* 87: 1213

Bruggenwert, M.G.M., and Kamphorst, A. 1982. Survey of experimental information on cation exchange in soil systems. pp. 141–203. *In* Bolt, G.H. (ed.) *Soil Chemistry B. Physico-Chemical Models*. Elsevier, Amsterdam.

Bruton, C.J., and Viani, B.E. 1996. *Ion Sorption onto Hydrous Ferric Oxides: Effect on Major Element Fluid Chemistry at Aspo, Sweden*. Lawrence Livermore National Laboratory report UCRL-JC-124329. Livermore, CA.

Bruton, C.J., Meike, A., Viani, B.V., Martin, S., and Phillips, B.L. 1993. Thermodynamic and structural characteristics of cement minerals at elevated temperature. *Proc. Topical Meeting on Site Characterization and Model*

Validation, FOCUS '93, Las Vegas, NV, pg. 150–156, American Nuclear Soc., La Grange Park, IL. (MOL. 19940913.0047)

Buchholtz-ten Brink, M., Martin, S.I., Viani, B.E., Gerlach, D.C., and Rego, J.H. 1990. Characterization and transport of colloidal particles in groundwaters from the Nevada Test Site. AGU 1990 Fall Mtng., Abstr., *EOS, Trans.*, Vol. 71, p. 1306.

Buchholtz-ten Brink, M., Martin, S.I., Viani, B.E., Smith, D.K., and Phinney, D. 1992. Heterogeneities in radionuclide transport: Pore-size, particle-size, and sorption. *in* McCarthy, J.F. (ed.), *Concepts in Manipulating Groundwater Colloids for Environmental Restoration*. Lewis publishers, Chelsea, MI. (NNA.19910523.0101)

Carlos, B.A. 1985. *Minerals in Fractures of the Unsaturated Zone from Drill Core USW G-4, Yucca Mountain, Nye County, Nevada*. Los Alamos National Laboratory report LA-10415-MS. (NNA.19920506.0037)

Conca, J.L. 1990. Diffusion barrier transport properties of unsaturated Paintbrush tuff rubble backfill. *Proc. First International Meeting High Level Radioactive Waste Management*, Las Vegas, NV, Vol 1, pg. 394–401, American Nuclear Soc., La Grange Park, IL. (NNA.19900710.0198).

Cornell, R.M. 1993. Adsorption of cesium on minerals: A review. *J. Radioanalytical Nucl. Chem., Articles*. 171:483–500.

CRWMS M&O. 1996. *Strategy for Focused Evaluation of Waste Containment and Isolation at the Yucca Mountain Site*. Civilian Radioactive Waste Management System Management and Operation Contractor, Las Vegas, NV.

De Marsily, G. 1986. *Quantitative Hydrogeology*. p. 55 Academic Press, Inc. New York.

Dzombak, D.A., and Morel, F.M. 1990. *Surface Complexation Modeling: Hydrous Ferric Oxide*. Wiley, New York.

Fletcher, P. and Sposito, G. 1989. The chemical modeling of clay-electrolyte interactions for montmorillonite. *Clay Minerals*, v. 24, p. 375–391.

Gast, R.G. 1972. Alkali metal cation exchange on Chambers montmorillonite. *Soil Sci. Soc. Amer. Proc.* 36:14.

GIT (YMP Geochemistry Integration Team) 1993. Claude Degueldre measured the particulates in a sample of J13 collected by W. Steinkampf (USGS) and found 1.7 × 107 particles/mL. Minutes of the October 18, 1993 Geochemistry Integration Team Teleconference.

Ho, C.H., and Miller, N.H. 1986. Adsorption of uranyl species from bicarbonate solution onto hematite particles. *J. Coll. Inter. Sci.* 110:165–171.

Klavetter, E.A. and Peters, R.R. 1986. *Estimation of Hydrologic Properties of an Unsaturated, Fractured Rock Mass*. Report SAND-84-2642, Sandia National Laboratory, Albuquerque, NM. (NNA.19870317.0738)

Laaksoharju, M., Banwart, S., Skarman, C., Gustafsson, E., Pitkänen, P., and Snellman, M. 1995. Hydrochemistry overview. pp. 17–46. *In* Banwart, S. (ed.) *The Redox Experiment in Block Scale: Final Reporting of Results from the Three Year Project*. SKB Äspö Hard Rock Laboratory Progress Report 25-95-06, Stockholm.

Landström, O., and Tullborg, E-L. 1995. *Interactions of Trace Elements with Fracture Filling Minerals from the Äspö Hard Rock Laboratory*. SKB Technical Report 95-13, Swedish Nuclear Fuel and Waste Management Co., Stockholm, Sweden.

Lanford, W.A., Davis, K., Lamarche, P., Laursen, T., Groleau, R., and Doremus, R.H. 1979. Hydration of soda-lime glass. *J. Non-Crystalline Solids* 33:249–266. (NNA.19900306.0089)

Martin, S.I., Buchholtz-ten Brink, M., and Viani, B.E. 1991. Characterization of colloids in groundwaters using transmission electron microscopy. AGU 1991 Fall Mtng., Abstr., *EOS, Trans.*, Vol. 72, Supplement, p. 154.

McCarthy, J.F., and Degueldre, C. 1993. Sampling and characterization of colloids and particles in ground water for studying their role in contaminant transport. *in* van Leeuwen, H.P. and Buffle, J. (eds.), *Environmental Particles*, IUPAC Environmental Analytical and Physical Chemistry Series, Vol. II, Lewis Publishers, Chelsea, MI. (NNA.19930607.0075)

McKeegan, K.D., Phinney, D., Oversby, V.M., Buchholtz ten Brink, M., and Smith, D.K. 1989. Uranium transport in Topopah Spring tuff: An ion-microscope investigation. Mat. Res. Soc. Proc. Vol. 127:813–821. (NNA.19900620.0330)

Meijer, A. 1990. A strategy for the derivation and use of sorption coefficients in performance assessment calculations for the Yucca Mountain site. Pg 9–40. *Proceeding of the DOE/Yucca Mountain Site Characterization Project Radionuclide Adsorption Workshop at Los Alamos Laboratory*. LA-12325-C. (NNA.19930629.0011)

Mohanty, S., Manteufel, R.D., Chowdhury, A.H., and Philip J. 1995. Fracture permeability under effect of normal and shear stress: A preliminary experimental investigation. *Proc. Sixth International Meeting High Level Radioactive Waste Management*, Las Vegas, NV, pg. 41–43, American Nuclear Soc., La Grange Park, IL.

Ogard, A. 1987. Importance *of radionuclide transport by particulates entrained in flowing groundwaters in Groundwater Chemistry at Yucca Mountain, Nevada, and Vicinity*. Los Alamos National Laboratory Report LA-10929-MS. Los Alamos, NM. (NNA.19870507.0017)

Phinney, D.L., Ryerson, F.J., Oversby, V.M., Lanford, W.A., Aines, R.D., and Bates, J.K. 1987. Integrated testing of the SRL-165 glass waste form. *Mat. Res. Soc. Proc.* Vol. 84:433–446. (NNA.19891120.0003)

Puls, R.W., Clark, D.A., Bledsoe, B., and Powell, R.M. 1992. Metals in ground water - Sampling artifacts and reproducibility. *Hazardous Waste & Hazardous Materials.* 9:149–162.

Ramsay, J.D.F., Avery, R.G., and Russell, P.J. 1988. Physical characteristics and sorption behaviour of colloids generated from cementitious systems. *Radiochimica Acta* 44/45:119–124. (NNA.19931005.0015)

Roberts, J.J., and Lin, W. 1995. Permeability of fractured tuff as functions of temperature and confining pressure. *Proc. Sixth International Meeting High Level Radioactive Waste Management*, Las Vegas, NV, pg. 44–45, American Nuclear Soc., La Grange Park, IL. (MOL19950501.0025)

Roberts, S., Viani, B.E., and Phinney, D. 1995. *Radionuclide Diffusion in Clinoptilolite*. Yucca Mountain Project Milestone M0L133.(M0L.19951213.0093)

Rundberg, R.S. 1987. *Assessment Report on the Kinetics of Radionuclide Adsorption on Yucca Mountain Tuff*. Los Alamos National Laboratory Report LA-11026-MS, Los Alamos, NM (NNA.19930405.0075)

Sposito, G. 1981. Thermodynamics *of Soil Solutions*. Oxford University Press, New York, NY. (NNA.19900416.0124)

Steefel, C.I., and Lichtner, P.C. 1994. Diffusion and reaction in rock matrix bordering a hyperalkaline fluid-filled fracture. *Geochim. Cosmochim. Acta* 58:3595–3612.

Thomas, K.W. 1987. *Summary of Sorption Measurements Performed with Yucca Mountain, Nevada Tuff Samples and Water from Well J-13*. Report LA-10960-MS. Los Alamos National Laboratory, Los Alamos, NM.(NNA.19890602.0026)

Ticknor, K.V. 1994. Uranium sorption on geological materials. *Radiochimica Acta* 64:229–236. (MOL.19950117.0119)

Todorovic, M., Milonjic, S.K., Comor, J.J., and Gal, I.J. 1992. Adsorption of radioactive ions $^{137}Cs^{+}$, $^{85}Sr^{2+}$, and $^{60}Co^{2+}$ on natural magnetite and hematite. *Sep. Sci. Tech.* 27:671–679.

Triay, I., Simmons, A., Levy, S., Nelson, S., Nuttall, H., Robinson, B., Steinkampf, W., and Viani, B. 1993a. *Colloid-facilitated radionuclide transport at Yucca Mountain*. Los Alamos Report LA-12779-MS. Los Alamos, NM. (NNA.19930628.0067)

Triay, I.R., Robinson, B.A., Mitchell, A.J., Overly, C.M., and Lopez, R.M. 1993b. Transport of neptunium through Yucca Mountain tuffs. *Mat. Res. Soc. Symp. Proc.* 294:797–802. (NNA.19930924.0106)

Tullborg, E-L. 1995a. Mineralogical/geochemical investigations in the fracture zone. pp. 81–101. *In* Banwart S. (ed) *The Redox Experiment in Block Scale: Final Reporting of Results from the Three Year Project*. SKB Äspö Hard Rock Laboratory Progress Report 25-95-06, Stockholm.

Tullborg, E-L. 1995b. *Mineralogical and Chemical Data on Rocks and Fracture Minerals from Äspö*. Äspö Hard Rock Laboratory Technical Note 25-95-07g, Stockholm.

Van Geen, A., Robertson, A.P. and Leckie, J.O., 1994. Complexation of carbonate species at the goethite surface: Implications for adsorption of metal ions in natural waters. *Geochim. et Cosmochim. Acta*, v. 58, p. 2073–2086. (NNA.19940210.0041)

Viani, B.E. 1995a. *Scientific Investigation Plan for YMP WBS Element 1.2.3.10.3.1 Integrated Radionuclide Release: Tests and Model Development (Integrated Testing)*. SIP-IT-01. Rev. 0. Lawrence Livermore National Laboratory, Livermore, CA. (M0L.19960329.0044)

Viani, B.E. 1995b. *Strategies for Integrating Materials Properties Activities with Integrated Radionuclide Transport Activities*. YMP Milestone Rept. M0L135. (M0L.19960307.0233)

Viani, B.E., and Bruton, C.J. 1996. *Assessing the Role of Cation Exchange in Controlling Groundwater Chemistry During Fluid Mixing in Fractured Granite at Aspo, Sweden*. Lawrence Livermore National Laboratory report UCRL-JC-121527. Livermore, CA. (M0L.19960419.0049)

Viani, B.E., and Bruton, C.J. 1994. Effect of cation exchange on major cation chemistry in the Large Scale Redox Experiment at Äspö. In Banwart, S., ed., *Proc. Äspö International Geochemistry Workshop*, June 2-3, 1994, Äspö Hard Rock Laboratory, p. B-78-B-96. Also issued as Lawrence Livermore National Laboratory report UCRL-JC-118592. Livermore, CA.

Viani, B.E., and Bruton, C.J. 1992a. Modeling ion exchange in clinoptilolite using the EQ3/6 geochemical modeling code. In Kharaka, Y. and Maest, A.S., eds., *Water-Rock Interaction*, Proceedings of the 7th International Symposium, vol. 1, A.A. Balkema, Brookfield, VT, p. 73-77. (MOL.19960607.0056)

Viani, B.E., and Bruton, C.J. 1992b. *Modeling Fluid-Rock Interaction at Yucca Mountain, Nevada: A Progress Report.* Lawrence Livermore National Laboratory, Livermore, CA, UCRL-ID-109921, 61 p. (NNA.19920805.0002)

Viani B.E., and Martin, S.I. 1994a. *Core Flow Experiment Protocol.* YMP Milestone Report M0L04. (M0L.19950727.0022)

Viani B.E., and Martin, S.I. 1994b. *Groundwater Colloid Characterization.* YMP Milestone Report M0L03. (M0L.19950622.0014)

Viani, B.E., and Martin, S.I. 1993. *Core-Flow Through Apparatus: Letter Report Documenting Testing Phase.* YMP Milestone Report M0L06. (NNA.19940120.0124)

Viani, B.E., Roberts, S., Martin, S.I., and Phinney, D. 1994. YMP Milestone report M0L05: *Progress Report on Diffusion of Radionuclides in Clinoptilolite.* (M0L.19950406.0145)

Waite, T.D., Davis, J.A., Payne, T.E., Waychunas, G.A., and Xu, N., 1994. Uranium(VI) adsorption to ferrihydrite: Application of a surface complexation model, *Geochim. et Cosmochim. Acta*, v. 58, p. 5465–5478.

Wilson, C.N. 1990. *Results from NNWSI Series 3 Spent Fuel Dissolution Tests.* Pacific Northwest Laboratory report PNL-7170. Pacific Northwest Laboratory, Richland, WA. (NNA.19900329.0142)

Wolery, T.J., Jackson, K.J., Bourcier, W.L., Bruton, C.J., Viani, B.E., Knauss, K.G., and Delany, J.M. 1990. Current status of the EQ3/6 software package for geochemical modeling. pp. 104–116. In Melchior, D.C. and Bassett, R.L. (eds.) *Chemical Modeling of Aqueous Systems II.* American Chemical Society, Washington, D.C. (NNA.19900716.0363)

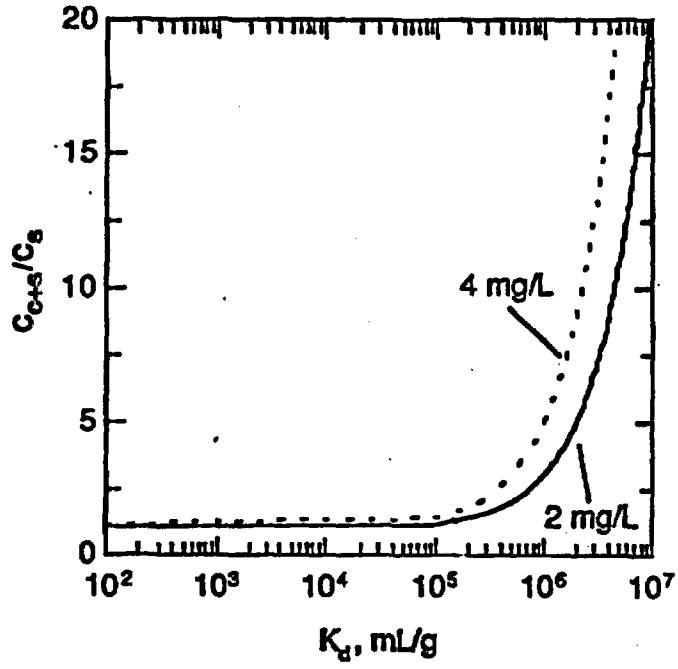

Figure 7-1. Relationship between ratio of concentration of radionuclide carried by solution in presence of colloid to that in absence of colloid, C_{c+s}/C_s, vs. K_d for radionuclide on colloid, at two concentrations of colloid.

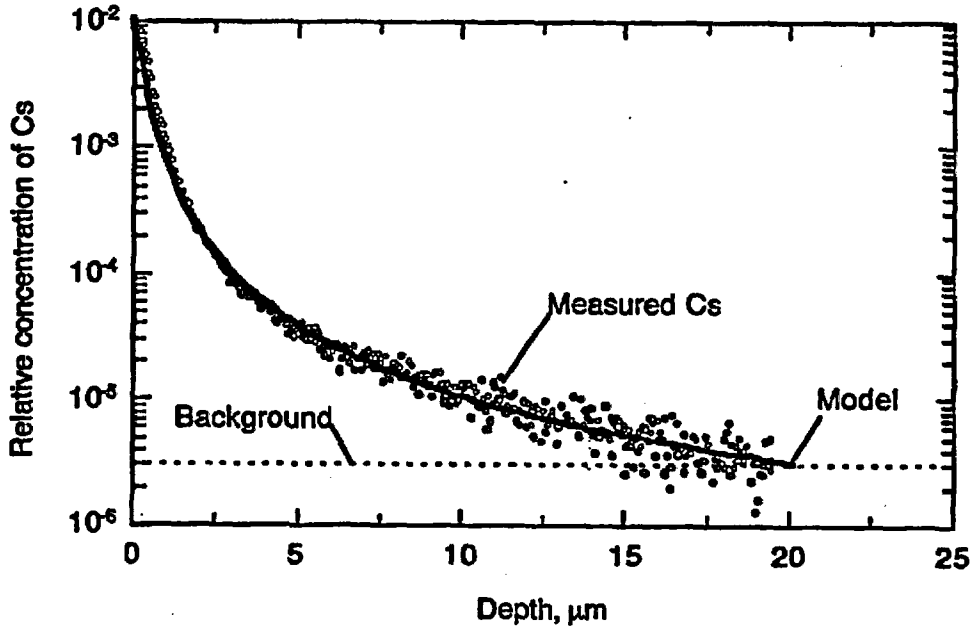

Figure 7-2. Variation of Cs with depth as measured by SIMS for nominally homoionic Ca-clinoptilolite in contact with a Cs/Ca solution at 30 °C for 32 d. Open circles are data points; solid line represents binary interdiffusion model with $D_{in,Cs} = 2.0 \times 10^{-13}$ and $D_{out,Cs} = 1.5 \times 10^{-18}$ cm^2/s; dashed line represents background required to fit the model to the data.

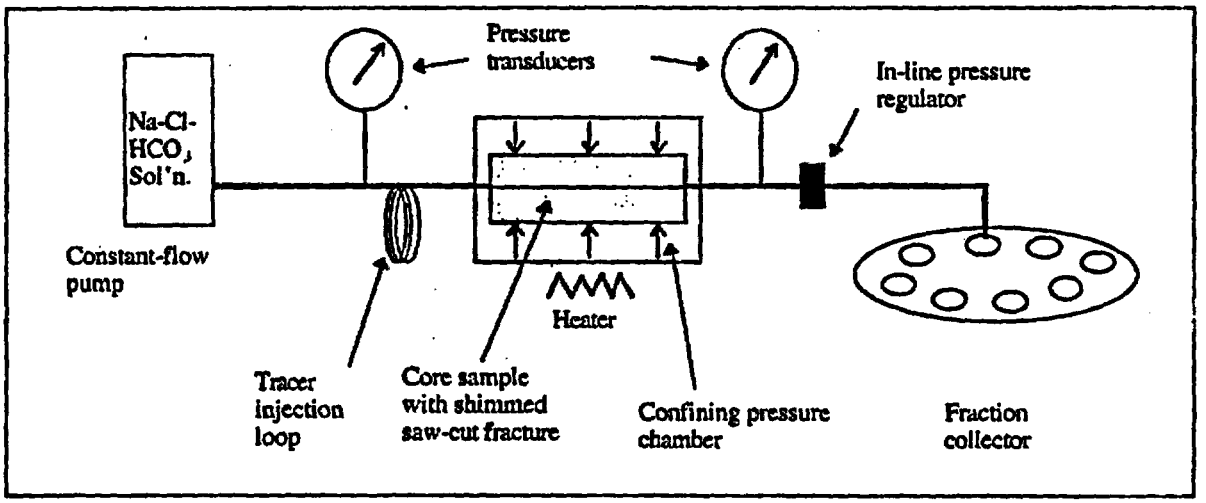

Figure 7-3. Schematic diagram of device used for flow and tracer tests.

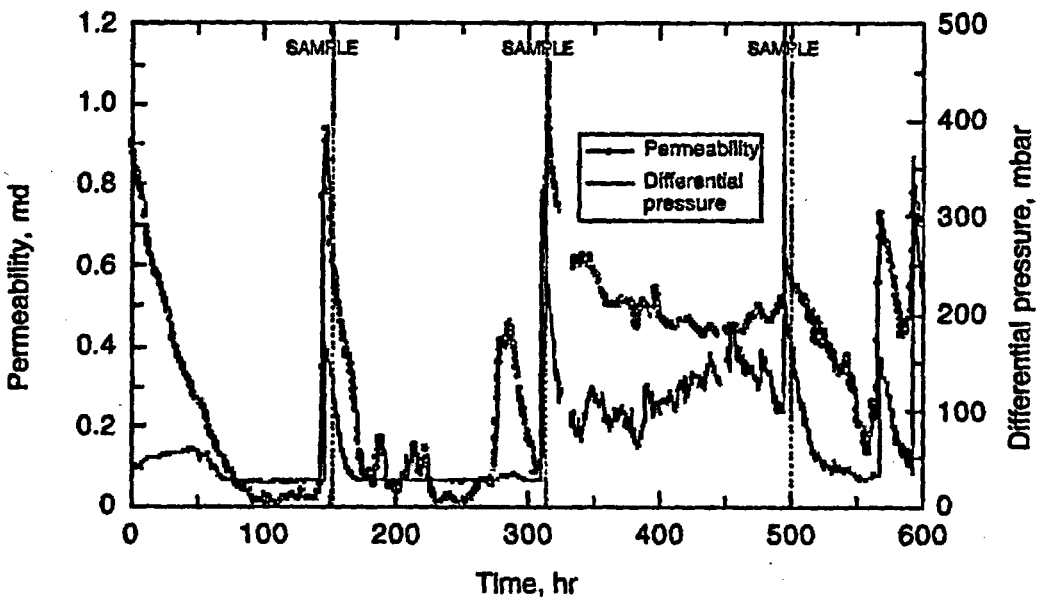

Figure 7-4. Variation of permeability and differential pressure with time for partial segment of flow test (FT040293) at 22 °C, showing repetitive loss of permeability due to bacterial plugging of a saw-cut fracture. Dotted vertical lines indicate points at which samples were taken for microscopic analysis. The apparatus used for this flow-test did not have the ability to maintain a constant flow rate.

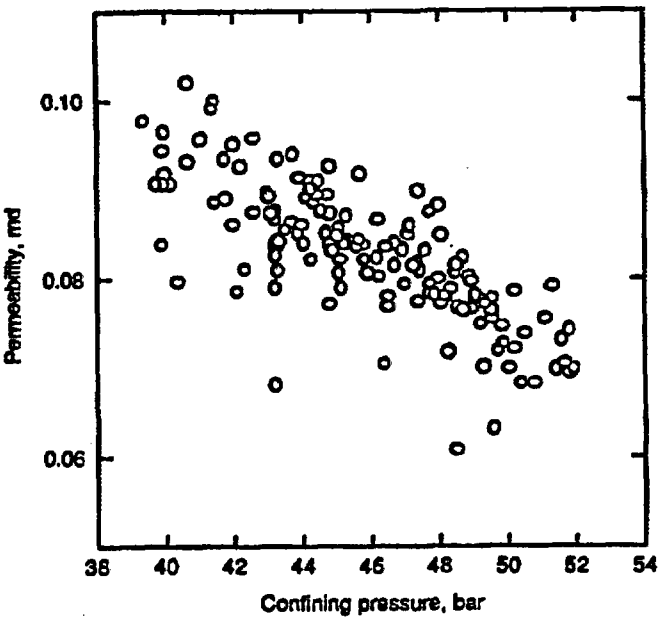

Figure 7-5. Variation in instantaneous permeability due to variation in confining pressure. (T = 59 °C; flow rate = 0.2 mL/h, FT050295).

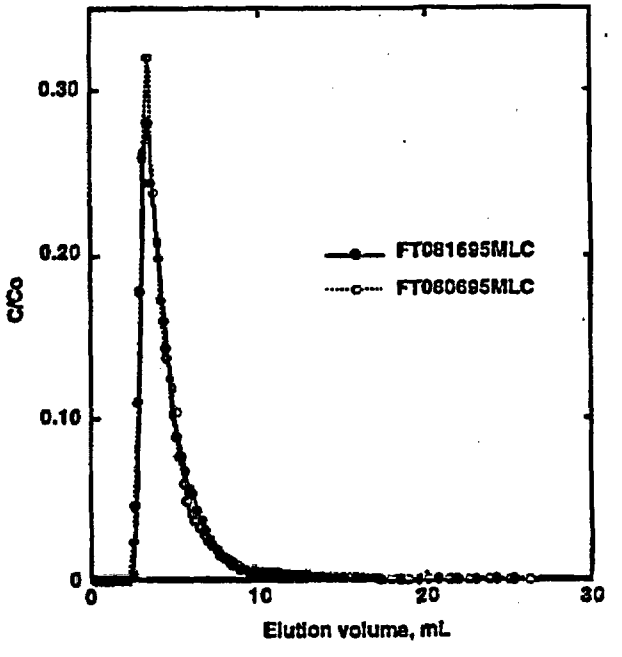

Figure 7-6. Relative concentration (C/C_o) breakthrough of two separate 560-µL pulses of I^- tracer for 0.2 mL/h flow rate, 92 °C, and low pore pressure (collected 10 days apart).

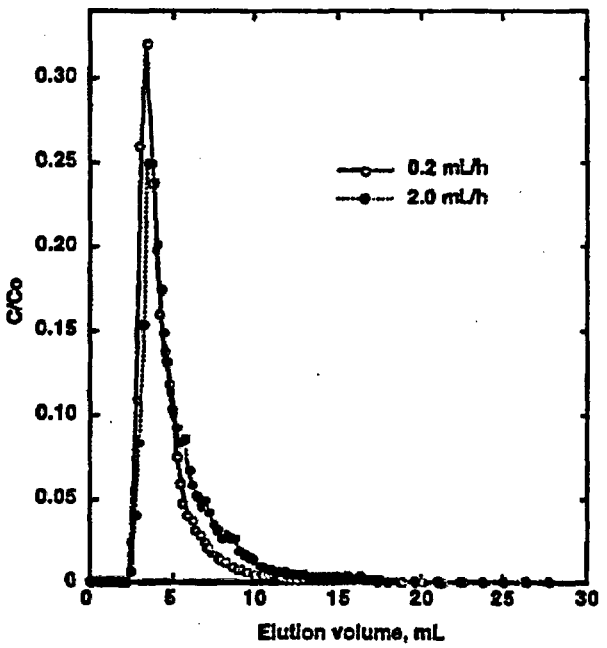

Figure 7-7. Relative concentration (C/C_o) breakthrough of 560-µL pulse of I^- tracer for 0.2 (FT080695MLC) and 2.0 (FT072695MLC) mL/h flow rates at 92 °C and low pore pressure.

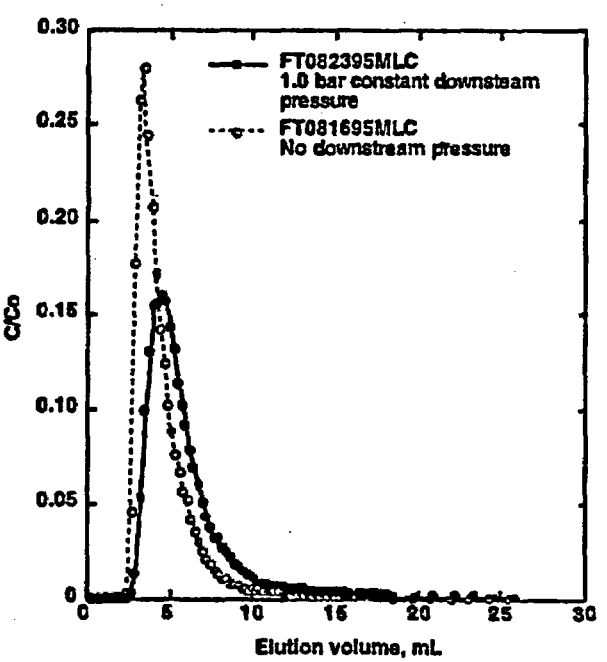

Figure 7-8. Relative concentration (C/C_o) breakthrough of 560 µL pulse of I^- tracer for 0.2 mL/h flow rate at 92 °C and 1 bar (FT082395MLC) and low (FT081695MLC) pore pressure.

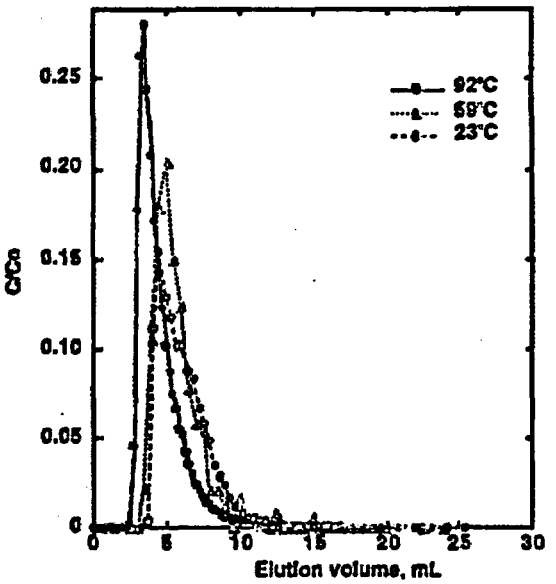

Figure 7-9. Relative concentration (C/C_o) breakthrough of 560 µL pulse of I^- tracer for 0.1 and 0.2 mL/h flow rates at 23 (FT040495MLC), 59 (FT051295MLC) and 92 (FT081695MLC) °C and low pore pressure.

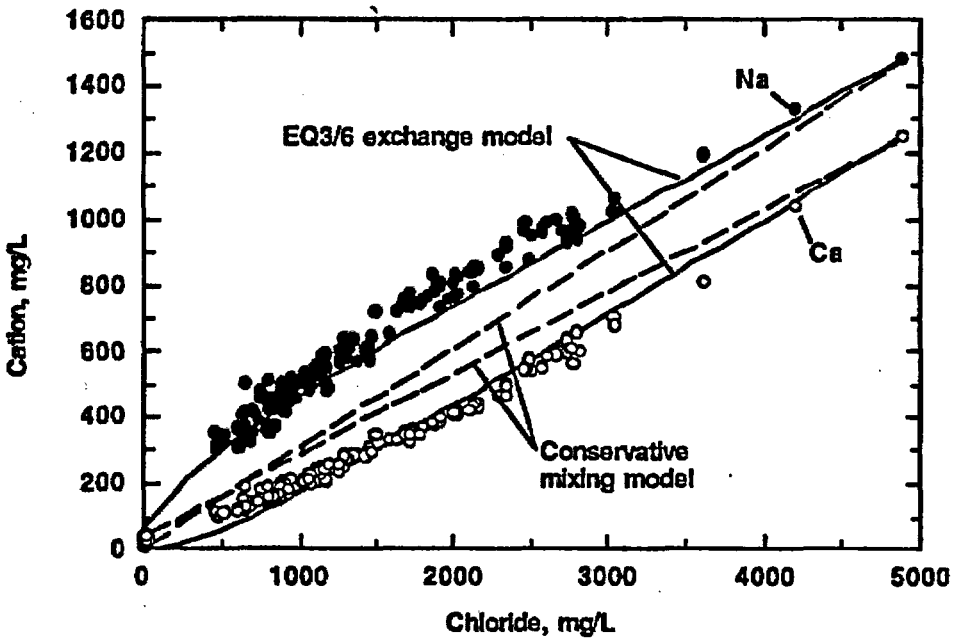

Figure 7-10. Comparison of EQ3/6 simulation of the variation of Na and Ca concentrations vs. Cl expected for mixing shallow (HBH02) and native (KA0483) groundwaters in the presence of 0.1 equiv/kg H_2O illite exchanger (solid lines) with the observed groundwater composition [solid (Na) and open (Ca) circles], and with predictions based on conservative mixing model (dashed lines).

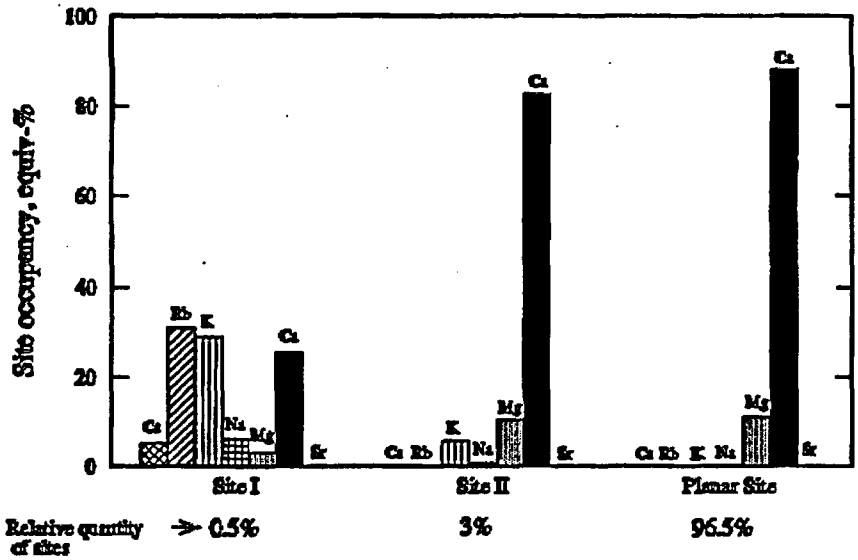

Figure 7-11. Predicted occupancies of exchange sites for illite in equilibrium with shallow (HBH02) groundwater.

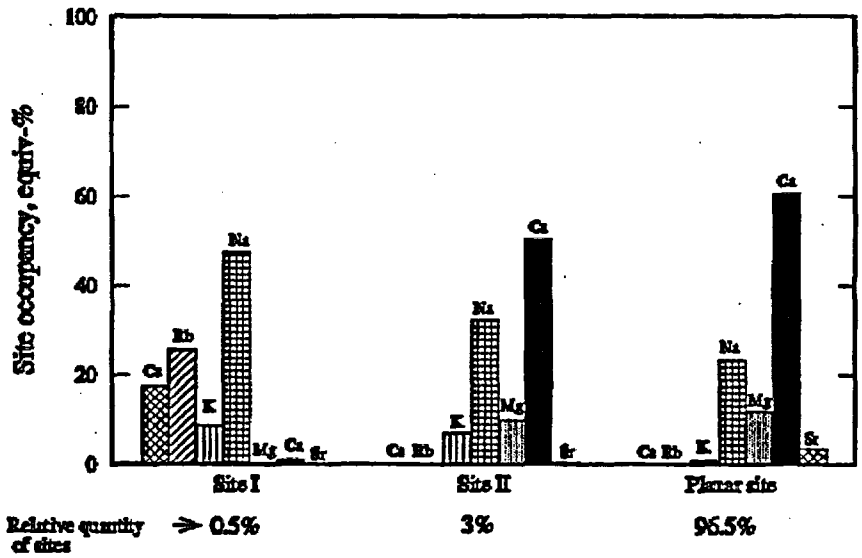

Figure 7-12. Predicted occupancies of exchange sites for illite in equilibrium with native (KA0483) groundwater.

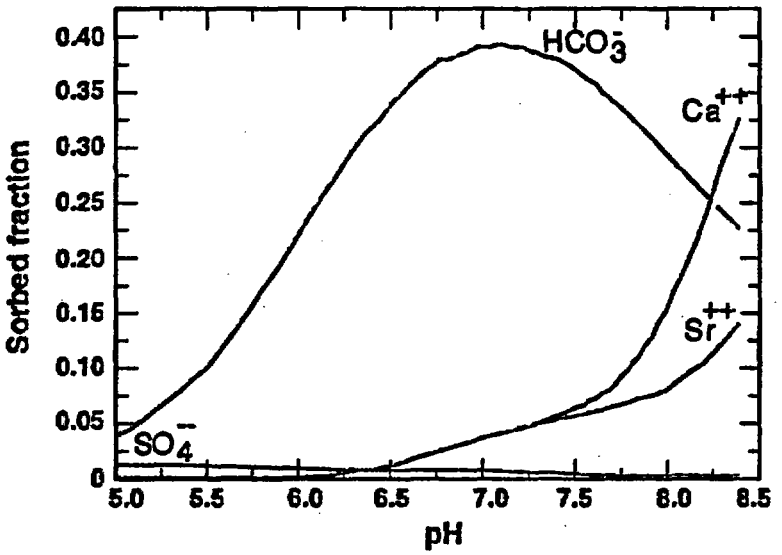

Figure 7-13. Fraction of total quantity of HCO_3, SO_4, Ca, and Sr sorbed onto 1 g goethite/kg H_2O in shallow (HBH02) groundwater at 25 °C using Dzombak and Morel (1990) surface complexation data with carbonate surface species from Van Geen, Robertson, and Leckie (1994). Electrical balancing on HCO_3.

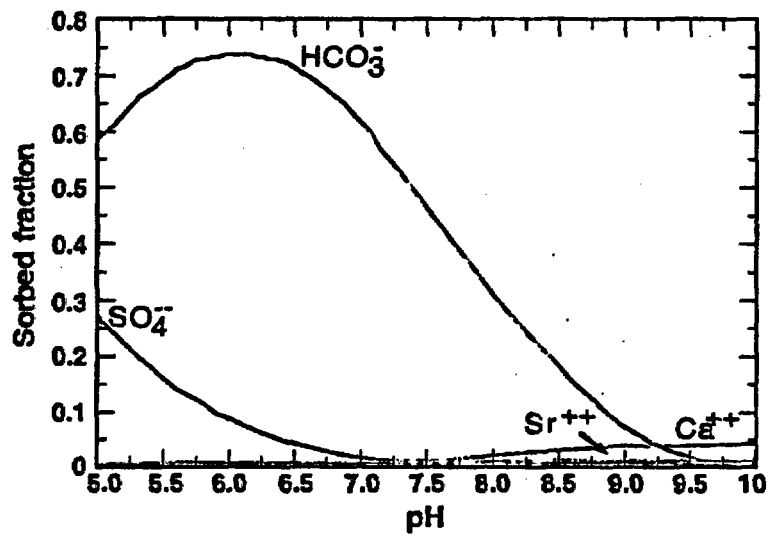

Figure 7-14. Fraction of total quantity of HCO_3, SO_4, Ca, and Sr sorbed onto 1 g goethite/kg H_2O in native (KA0483A) groundwater at 25 °C using Dzombak and Morel (1990) surface complexation data with carbonate surface species from Van Geen, Robertson, and Leckie (1994). Electrical balancing on Cl.

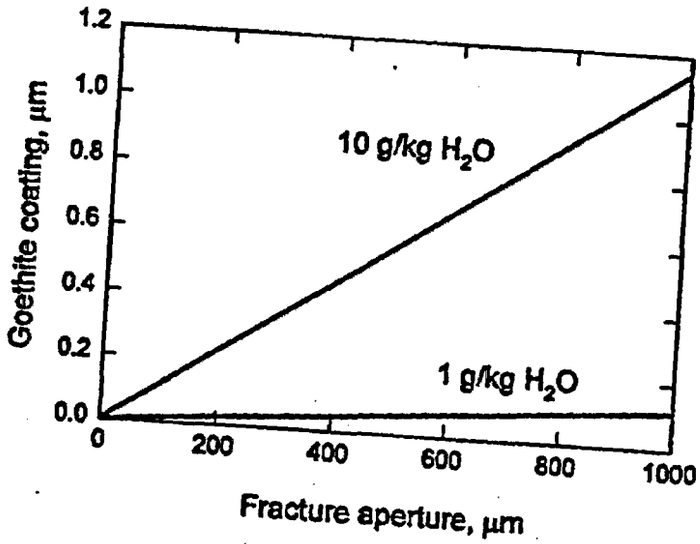

Figure 7-15. Variation in thickness of goethite coating with fracture aperture corresponding to 1 and 10 g of goethite per kg of H^2O contained in fracture.

Table 7-1. Summary of partition coefficient (K_d) ranges for selected elements with selected EBS/NFE flow-path components.[1]

Flow-Path Component	Cs	Np mL/g	U
Iron Oxide	1×10^0 - 1×10^1 [2]	3×10^2 - 9×10^3 [3]	2×10^3 - 2×10^4 [4]
Cement [5]	1×10^0 - 1×10^1	2×10^3 - 3×10^4	1×10^2 - 6×10^3
Devitrified Tuff	1×10^1 - 1×10^3 [6]	0 - 1×10^1 [7]	0 - 1×10^1 [7]

(1) K_d's depend on solution composition, solid/solution ratio, specific surface of adsorbent, and concentration of uranium. The K_d ranges listed for devitrified tuff and iron oxide are for dilute carbonate-bearing solutions with pH's between ~7 to ~8.5; similar to what would be expected at Yucca Mountain. The solution composition for cements is controlled by the interaction with pore water and cement and would be expected to be similar for any dilute groundwater that interacts with it.
(2) Hematite; Cornell, 1993; Todorovic et al., 1992.
(3) Hematite; Triay et al., 1993b.
(4) Hematite; Ticknor, 1994; Ho and Miller, 1986.
(5) Yucca Mountain tuff; Meijer, 1990
(6) Portland cements; Albinsson et al., 1993.
(7) Yucca Mountain tuff; Thomas, 1987.

Table 7-2. Summary of flow tests with saw-cut Topopah Spring core sample.

Temperature °C	Flow Rate mL/h	Pore Pressure [1] bar	Permeability [2] md	Hydraulic Aperture µm
23	0.1, 0.2, 2.0	0.1 - 2.0	0.060±0.005	3.1
59	0.2, 2.0	0.1 - 2.5	0.10±0.035	3.6
92	0.2, 2.0	0.06 - 0.09	0.19±0.14	4.5
92	0.2, 2.0	0.5 - 3.1	1.86±0.47	9.6

(1) Pore pressures are average values computed over the duration of each flow test. The tabulated values show the range in average pore pressures observed for runs at that temperature and the indicated flow rates.
(2) The permeabilities are average values calculated from the average of the instantaneous permeabilities for a given flow test. Instantaneous permeabilities varied with confining pressure, and over time.

Table 7-3. Composition of feed solution and effluent from pooled samples taken after breakthrough of the tracer.

Element	Feed solution	Effluent		
		23 °C 0.2 mL/h	92 °C 0.2 mL/h	92 °C 2.0 mL/h
Ca	0.05	4.54	3.62	2.46
Mg	<0.01	1.08	0.83	0.53
Na	33	37	34	31
K	<0.01	0.4	1.7	1.2
Si	0.08	2.65	22.49	6.91
Sr	<0.02	0.12	0.09	0.06

Table 7-4. Cation-exchange energies for illite and smectite at 25 °C[1].

	Exchange Energy, kcal/equiv			
	Illite			Smectite
Exchange Reaction	Site I	Site II	Planar Site	
Na → 0.5 (Ca, Mg, Sr, Ba)[2]	1.4	0.2	0[3]	-0.12
Na → K	-2.2	-2.3	-1.22	-0.35
Na → Rb	-6.5	-4.2	-1.62	-0.63
Na → Cs	-7.8	-4.2	-2.10	-1.08
Relative fraction of sites	0.005	0.03	0.965	1.00

(1) Data for illite from Brouwer et al. (1983; Tables I and II). Data for smectite from Fletcher and Sposito (1989) except for Na → (Rb, Cs) which are from Gast (1972). Note: these data are strictly accurate at 25 °C only. It was assumed that for the purposes of these simulations, the variation of exchange energy between 25 °C and the groundwater temperature (~10 °C) is a second order effect.

(2) A Na → 0.5 (Ca, Mg, Sr, Ba) signifies the conversion of 1 equivalent of exchanger from the Na form to the Ca, Mg, Sr, or Ba form.

(3) The exchange energy for Na → 0.5 (Ca, Mg, Sr, Ba) deduced from Brouwer et al. (1983) data for the planar site was adjusted to be consistent with their data for Cs → Na, Rb → Na, and Rb →(Ca, Mg, Sr, Ba) exchange.

Table 7-5. Ratio of predicted mass of cation on exchanger[1] to mass of cation in fluid for three groundwaters at Äspö.

Cation	Shallow (HBH02) 15 m	Native (KA0483A) tunnel depth
Na	1.3	0.30
Ca	41.7	1.07
Mg	41.7	1.21

(1) Calculations assume 0.1 equiv/kg of H_2O.

Table 7-6. Predicted sorbed fractions and concentrations of sorbed Ca, Sr, SO_4, and HCO_3, in mg/kg, in shallow (HBH02) groundwater as a function of mass of goethite/kg H_2O.[1]

Mass of goethite g/kg H_2O	Predicted sorbed fraction and concentration (mg/kg, in parentheses) of sorbed species.			
	Ca	Sr	SO_4	HCO_3
0.1	0.0015 (0.06)	0.0016 (0.0003)	0.0022 (0.04)	0.09 (11.21)
1.	0.015 (0.63)	0.016 (0.003)	0.022 (0.43)	0.50 (112.1)
10.	0.13 (6.31)	0.14 (0.03)	0.18 (4.31)	0.91 (1121)
Concentration in coexisting fluid phase, mg/kg	42.8	0.16	19.5	114.

(1) Calculated using Dzombak and Morel (1990) surface complexation data base with carbonate complexation constants from Van Geen, Robertson, and Leckie (1994). The sorbed fractions are calculated assuming the goethite is in equilibrium with an aqueous solution having the composition of the shallow groundwater.